



國立中央大學天文研究所
鹿林天文台年報

2019

No.17

國立中央大學天文研究所 編

目錄

研究論文

Face changing companion of the redback millisecond pulsar PSR J1048+2339, Yap, Y. X.; Li, K. L.; Kong, A. K. H.; Takata, J.; Lee, J.; Hui, C. Y., <i>Astronomy & Astrophysics</i> , Volume 621, id.L9, 6 pp., January 2019.....	1
Diagnosing the Clumpy Protoplanetary Disk of the UXor Type Young Star GM Cephei, P. C. Huang, W. P. Chen, M. Mugrauer, et al., 2019 February, <i>The Astrophysical Journal</i> , 871:183 (12pp).....	8
2012 TC4 - An unusual fast-rotating PHA with C-type taxonomy, Lin, Zhong-Yi; Ip, Wing-Huen; Ngeow, Chow-Choong, February 2019, <i>Planetary and Space Science</i> , Volume 166, p. 54-58.....	20
The fast, luminous ultraviolet transient AT2018cow: extreme supernova, or disruption of a star by an intermediate-mass black hole? Daniel A Perley, Paolo A Mazzali, Lin Yan, et al., <i>Monthly Notices of the Royal Astronomical Society</i> , Volume 484, Issue 1, March 2019, Pages 1031–1049.....	25
Research of activity of Main Belt Comets 176P/LINEAR, 238P/Read and 288P/(300163) 2006 VW139, Shi, Jianchun; Ma, Yuehua; Liang, He; Xu, Ruiqi, <i>Scientific Reports</i> , Volume 9, id. 5492, April 2019.....	44
Lulin Widefield Telescope (LWT): a Robotic Telescope for the Near-Earth Object Follow-up Observation, 黃健峯, 饒兆聰, 2019/06國立中央大學天文所碩士論文, 105229005.....	51
Finding New Cepheids in the Open Clusters with Their Location in the Color-Magnitude Diagram—Tests with Existing Data and Known Cepheids, 駱世昌, 饒兆聰, 2019/06, 國立中央大學天文所碩士論文, 104229008.....	53
The beamed jet and quasar core of the distant blazar 4C 71.07, Raiteri, C M, Villata, M and Carnerero, et al. August 2019, <i>Monthly Notices of the Royal Astronomical Society</i> , Volume 489, Issue 200.....	56
Triple Range Imager and POLarimeter (TRIPOL)—a compact and economical optical imaging polarimeter for small telescopes, Sato, Shuji; Chieh Huang, Po; Chen, Wen Ping; Zenno, Takahiro; Eswaraiah, Chakali; Su, Bo He; Abe, Shinsuke; Kinoshita, Daisuke; Wang, Jia Wei, September 2019, <i>Research in Astronomy and Astrophysics</i> , Volume 19, Issue 9, article id. 136.....	69
Investigating the multiwavelength behaviour of the flat spectrum radio quasar CTA 102 during 2013–2017, D’Ammando, F, Raiteri, C M, Villata, M, et al., October 2019, <i>Monthly Notices of the Royal Astronomical Society</i> , Volume 489, Issue 2.....	79

GROWTH on S190425z: Searching Thousands of Square Degrees to Identify an Optical or Infrared Counterpart to a Binary Neutron Star Merger with the Zwicky Transient Facility and Palomar Gattini-IR, Michael W. Coughlin ¹ , Tomás Ahumada ² , Shreya Anand, et al., 2019 November, The Astrophysical Journal Letters, 885:L19 (13pp).....	96
Evidence for Late-stage Eruptive Mass Loss in the Progenitor to SN2018gcp, a Broad-lined Ic Supernova: Pre-explosion Emission and a Rapidly Rising Luminous Transient, Anna Y. Q. Ho, Daniel A. Goldstein, Steve Schulze et al., 2019 December, The Astrophysical Journal, 887:169 (24pp).....	109

工作報告

鹿林天文台觀測時數統計(2003-2019).....	134
鹿林天文台LOT 觀測研究計畫統計 (2019).....	137
鹿林天文台工作報告2019.....	141
鹿林天文台團體參觀及觀測教學2019.....	147
鹿林天文台三色偏振相機 (TRIPOL) 介紹.....	150
Follow-Up Observations of Gravitational Wave Events from Lulin Observatory.....	155
利用鹿林廣視場望遠鏡對近地天體做自動化的追蹤觀測.....	157
Lulin Widefield Telescope (LWT): a Robotic Telescope for the Near-Earth Object Follow-up observation.....	158

新聞報導

新聞報導.....	160
-----------	-----

研究論文

LETTER TO THE EDITOR

Face changing companion of the redback millisecond pulsar PSR J1048+2339

Y. X. Yap¹, K. L. Li², A. K. H. Kong¹, J. Takata³, J. Lee⁴, and C. Y. Hui⁵

¹ Institute of Astronomy, National Tsing Hua University, Hsinchu 30013, Taiwan

e-mail: yapyeexuan@gapp.nthu.edu.tw

² Department of Physics, UNIST, Ulsan 44919, Korea

³ School of Physics, Huazhong University of Science and Technology, Wuhan 430074, PR China

⁴ Department of Space Science and Geology, Chungnam National University, Daejeon, Republic of Korea

⁵ Department of Astronomy and Space Science, Chungnam National University, Daejeon, Republic of Korea

Received 31 October 2018 / Accepted 20 December 2018

ABSTRACT

We present optical observations of the redback millisecond pulsar PSR J1048+2339, which is a 4.66 ms radio pulsar in a compact binary with an orbital period of six hours. We obtained high-quality light curves of PSR J1048+2339 with the Lulin 1 m Telescope. The system shows two distinct six-hour orbital modulations, in which an ellipsoidal modulation changes into a sinusoidal-like profile in less than 14 days. In addition to the change, the brightness of the companion increased by one magnitude, suggesting that the latter type of modulation is caused by the pulsar wind heating of the companion and that the heating became dominant in the system. While the changes are not unexpected, such a timescale is the shortest among similar systems. We performed modeling analysis to extract the properties of the system. We obtained a derived pulsar mass of $2.1 M_{\odot}$ and a companion star mass of $0.4 M_{\odot}$ for the system. The irradiation power increased by a factor of 6 during which the pulsar wind heating dominates. We also report on the two archival *Chandra* X-ray observations and discuss several possibilities that might cause the varying heating on the companion.

Key words. pulsars: individual: PSR J1048+2339 – X-rays: binaries

1. Introduction

PSR J1048+2339 (hereafter J1048+2339) is a 4.66 ms millisecond pulsar that was discovered by Cromartie et al. (2016) using Arecibo Observatory. It was later confirmed as a redback system by Deneva et al. (2016) with multiwavelength observations. The system has an orbital period of six hours and spin-down power $\dot{E} = 1.2 \times 10^{34}$ erg s⁻¹. This object is more than just a radio pulsar; it has a gamma-ray counterpart, which is 3FGL J1048.6+2338 in the *Fermi* Large Area Telescope (LAT) four-year point source catalog (3FGL; Acero et al. 2015). J1048.6+2338 was originally associated with a BL Lac active galactic nuclei (AGN; NVSS J104900+233821) in 3FGL, however the improved localization in the recent preliminary LAT eight-year source list (FL8Y)¹ ruled out the possibility that it is an AGN. In a previous optical study with the Catalina Real-Time Transient Survey (CRTS), Palomar Transient Factory (PTF), Sloan Digital Sky Survey (SDSS), and Pan-STARRS survey data, the light curves indicated intrinsic variability in the system. While there are no significant X-ray (the *Neil Gehrels Swift*-XRT) and gamma-ray (*Fermi*-LAT) pulsations detected, Deneva et al. (2016) proposed that J1048+2339 has a minimum mass of $0.3 M_{\odot}$ and effective temperature T_{eff} of 3350 K, with assumptions of a $1.4 M_{\odot}$ mass neutron star and an inclination of 90°. In this Letter, we present the optical observations of J1048+2339 taken in 2018 March and April, in which the orbital

modulation changes from ellipsoidal to pulsar wind heating in less than 14 days. We also include light curve modeling to constrain the geometry of the binary and an independent X-ray analysis based on the two archival *Chandra* observations.

2. Observations and data analysis

2.1. Optical observations

We observed J1048+2339 with the Lulin 1 m telescope (LOT) on six separate nights from 2018 March 11 to April 23. Each image is exposed for 300 s and alternated between SDSS r' and g' filters. These raw images are then processed with IRAF V2.15 with standard calibration procedures, including bias and flat-field corrections. In addition, we have data from the 2 m Liverpool Telescope (LT; Steele et al. 2004) taken in late March, which were flat- and bias-corrected. The r' and g' filters are alternated with 180 s exposure time, except for the g' band data taken on 2018 March 25 and 26, which were exposed for 300 s per image. In total, there are 189 images (15.23 h total integration time) with the r' filter, and 147 images (12.07 h total integration time) with g' filter. A summary of all observations is recorded in Table 1. We obtained the magnitude information by performing differential photometry to the reduced images with the IRAF package *phot*. We used ten isolated and nonsaturated stars to compute the relative magnitudes for J1048+2339. The relative magnitudes were then converted to apparent magnitudes using a nearby star SDSS J104840.81+234018.0 of which the magnitudes in

¹ See <https://fermi.gsfc.nasa.gov/ssc/data/access/lat/fl8y/>

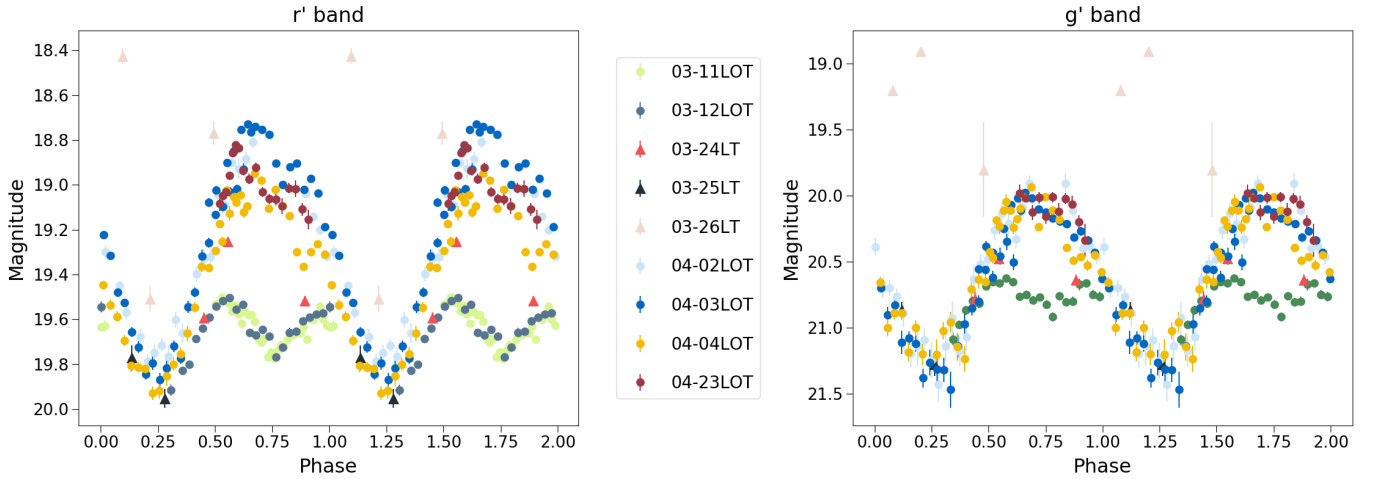


Fig. 1. Light curves of PSR J1048+2339 companion star with the SDSS r' and g' band filter between 2018 March 11 and April 23, folded with an orbital period of 6 h and $T_0 = \text{MJD } 56637.598177$. While the pulsar wind heating and ellipsoidal variation are clearly seen in both bands, the magnitude in the g' band has larger variation compared to that of the r' band. An orbital phase of 0.25 corresponds to the inferior conjunction of the companion star.

Table 1. Summary of observations.

Date	Telescope	Filter (SDSS)	Phase range	Number of images	Exposure (s)	Apparent magnitudes
11.3.2018	LOT	r'	0.50–0.01	36	300	19.50–19.77
12.3.2018	LOT	r'	0.31–0.00	24	300	19.50–19.92
12.3.2018	LOT	g'	0.34–0.99	23	300	20.62–21.09
24.3.2018	LT	r'	0.45–0.89	3	180	19.25–19.59
24.3.2018	LT	g'	0.44–0.88	3	180	20.48–20.78
(25–26).3.2018	LT	r'	0.09–0.49	5	180	18.43–19.95
(25–26).3.2018	LT	g'	0.08–0.48	5	300	18.91–21.28
(2–4).4.2018	LOT	r'	0.01–0.99	100	300	18.83–19.93
(2–4).4.2018	LOT	g'	0.00–0.99	104	300	19.91–21.80
23.4.2018	LOT	r'	0.52–0.91	18	300	18.82–19.16
23.4.2018	LOT	g'	0.64–0.92	11	300	19.98–20.34

the r' band and g' band are 16.53 and 17.90, respectively. We folded the light curves using the orbital period of 0.250519045 d and ascending node $T_0 = \text{MJD } 56637.598177$ from the radio ephemeris (Deneva et al. 2016). The folded light curves are presented in Fig. 1. The quantity $\phi = 0$ corresponds to the ascending node of pulsar.

2.2. Face changing companion

We observed a pronounced six-hour modulation in the first two nights of observation (2018 March 11 and 12). We detected two minima at $\phi = 0.25$ and $\phi = 0.75$, and two maxima at $\phi = 0.55$ and $\phi = 0$, which resemble an ellipsoidal modulation of the companion star. Ellipsoidal modulation is a consequence of the orbital motion for a tidally distorted star, which is commonly seen among redback systems (e.g., PSR J2129–0429; Hui et al. 2015; Bellm et al. 2016). In Fig. 1, we see that the minima at $\phi = 0.25$ is deeper than $\phi = 0.75$ by ~ 0.1 mag.

Subsequent observing runs with LT were carried out from 2018 March 24–26. On March 24, we observed an increase of 0.3 mag (compared to the previous data taken at the same phase) at $\phi = 0.55$ in r' band. Similar changes are also observed in the g' band. On March 25, data points were taken close to the

companion inferior conjunction ($\phi = 0.25$), and they agree well with the minimum seen in other observations. On March 26, the r' magnitude at $\phi = 0.09$ increased by 1 mag (compared to the previous data taken at the same phase) and then decreased quickly by 1.1 mag at $\phi = 0.21$, whereas the corresponding g' magnitude, which was taken slightly earlier, increased instead. To make sure there was no random error involved, we plot J1048+2339 against one of the comparison stars to compare their light curves (cf. Fig. 2). The light curve of the comparison star is relatively stable, indicating the observed variation in the companion is likely genuine. This might be because of a spontaneous flaring event of some kind of transition that arose in late March.

J1048+2339 was observed again in early April with LOT. As shown in Fig. 1, the folded light curves have a minimum at $\phi = 0.25$ and a maximum at $\phi = 0.65$, which are very different compared to the March light curves. The April light curves resemble pulsar wind heating. As discussed in Romani & Sanchez (2016), a direct pulsar irradiation toward the companion star would be expected to give a peak at $\phi = 0.75$, but intrabinary shock can accounted for the peak observed slightly before 0.75. Heating from the intrabinary shock was also discussed in Takata et al. (2014) and Li et al. (2014). From our observations, the pulsar

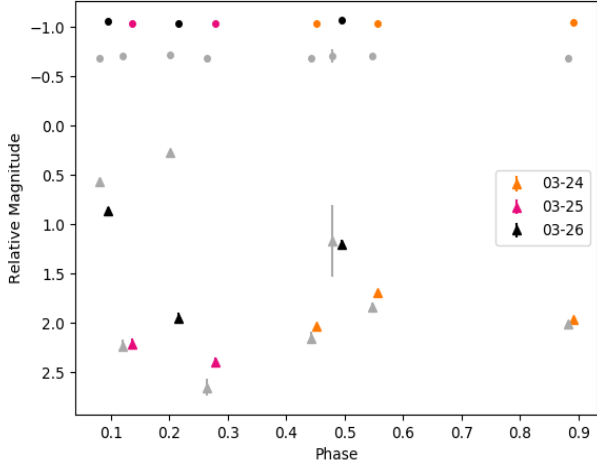


Fig. 2. Close examination of PSR J1048+2339 companion in late March 2018. The light curve of the companion star (triangle) and a nearby comparison star (circle) are plotted to confirm the magnitude decrease/increase at $\phi = 0.21$ observed in the g' (gray) and r' (colored) band. The comparison star is relatively stable, indicating the observed variation at $\phi = 0.21$ in J1048+2339 companion is likely genuine.

heating effect at $\phi = 0.75$ was affected by the minimum in the ellipsoidal modulation. The trace of ellipsoidal modulation can still be seen even when pulsar heating becomes dominant. That implies that the flux produced from the irradiated companion takes on a considerable proportion of the total flux detected. In addition, the g' band light curve has larger variation than that of the r' band light curve, indicating a larger temperature variation. The distinct changes from March to April light curves suggest that a face changing mechanism took place in less than two weeks. The heating effect in J1048+2339 was evident up until our observation in late April.

2.3. Chandra observation

We also explored the X-ray properties of J1048+2339 with two archival *Chandra* data, which were taken on 2017-03-08 (obsID 19039; 22.6 ks) and 2017-07-04 (obsID 19038; 24.7 ks). In both observation, J1048+2339 was imaged with the back-illuminated CCD ACIS-S3. The data were reprocessed using standard *Chandra* Interactive Analysis of Observations (CIAO) software and updated *Chandra* Calibration Database (CALDB). All the subsequent analysis are restricted in 0.3–8 keV energy range.

An X-ray point source is clearly detected at the pulsar position with no hint of any extended X-ray emission. The phase-averaged spectrum were extracted from a 3 arcsec source region. The background spectra were sampled from a nearby source-free region in each observation. After background subtraction, we obtained 91 and 122 net counts for the respective observations. For each spectrum, we binned the data to have at least 10 counts per spectral bin. This led to an approximately Gaussian distribution of the binned data so that we can adopt chi-square as the fit statistic. We then performed spectral analysis using the absorbed power-law model. We found that the best-fit spectral parameters and fluxes deduced from both observations are consistent within the tolerance of the statistical uncertainties. Therefore, we fitted both spectra simultaneously in order to maximize the photon statistics and obtain tighter constraints for the spectral parameters.

As the column absorption N_{H} cannot be constrained properly, we fixed it at the total Galactic HI column density,

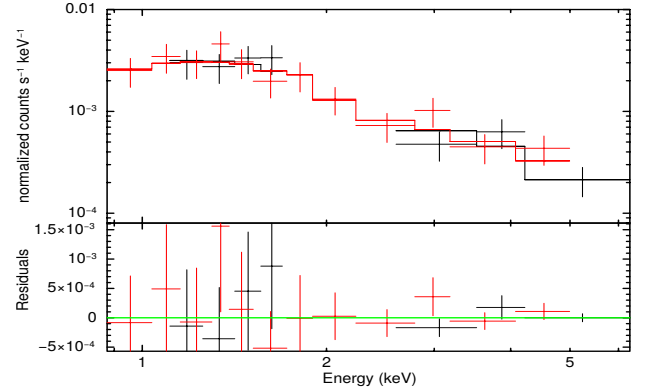


Fig. 3. X-ray spectra of PSR J1048+2339 obtained from both *Chandra* observations (ObsIDs: 19038 and 19039) with the best-fit absorbed power-law model (*top panel*) and the fitting residuals (*bottom panel*).

$N_{\text{H}} = 2.3 \times 10^{20} \text{ cm}^{-2}$, in the direction of J1048+2339 (Kalberla et al. 2005). The best-fit with a power-law yield a photon index of $\Gamma = 1.64 \pm 0.15$ (c.f. Fig. 3) and a goodness-of-fit of $\chi^2 = 7.64$ for 17 d.o.f. The photon index is similar to the typical value of redbacks (Lee et al. 2018). The unabsorbed X-ray flux in 0.3–8 keV is $f_X = 7.25^{+0.54}_{-0.51} \times 10^{-14} \text{ erg s}^{-1} \text{ cm}^{-2}$. At a distance of 852 pc as estimated by *Gaia* (Bailer-Jones et al. 2018), the 0.3–8 keV X-ray luminosity is $L_X = 6.29^{+0.47}_{-0.45} \times 10^{30} \text{ erg s}^{-1}$. We also considered a pure thermal scenario by fitting the spectra with an absorbed blackbody model. However, the goodness-of-fit is found to be undesirable ($\chi^2 = 28.7$ for 17 d.o.f.).

After barycentering the arrival times in both observations, we folded the data from each observation at the same orbital period and T_0 defined previously for the optical light curves. We did not identify any significant differences between the two observations. In the top panel of Fig. 4, we show the orbital modulation of J1048+2339 in 0.3–8 keV by combining the data from these two observations. The X-ray emission is found to attain the peak just before the companion enters the superior conjunction ($\phi = 0.75$). We also examined if there is any differences in the modulation in the soft band (0.3–2 keV) and hard band (2–8 keV) (cf. middle panel of Fig. 4). However, there is no significant variation of X-ray hardness can be found (cf. bottom panel of Fig. 4).

3. Optical light curve modeling

We use the eclipsing light curve code (ELC) by Orosz & Hauschildt (2000) to generate light curve models for two groups of data according to their modulation. We combined 2018 March 11 and 12 light curves (ellipsoidal modulation) into one group (group 1) and 2018 April 2 and 3 light curves (pulsar heating modulation) into another (group 2). We save computing time by doing so and most importantly, this grouping is adequate for exploring the heating effect seen from the two distinct groups that are three weeks apart. In the modeling analysis, we assumed the following: convective envelopes for both stars, a nonspherical shape of the companion, absence of an accretion disk, and point source X-ray heating. Owing to the difficulty in measuring the spot locations, no spots are added to the models, although it can be accounted for the different maximum observed at the ascending and descending node of the ellipsoidal-modulated light curve. We also supply a SDSS atmosphere model to the ELC. We use the optimisers provided in the ELC to fit the folded g' and r' band light curves

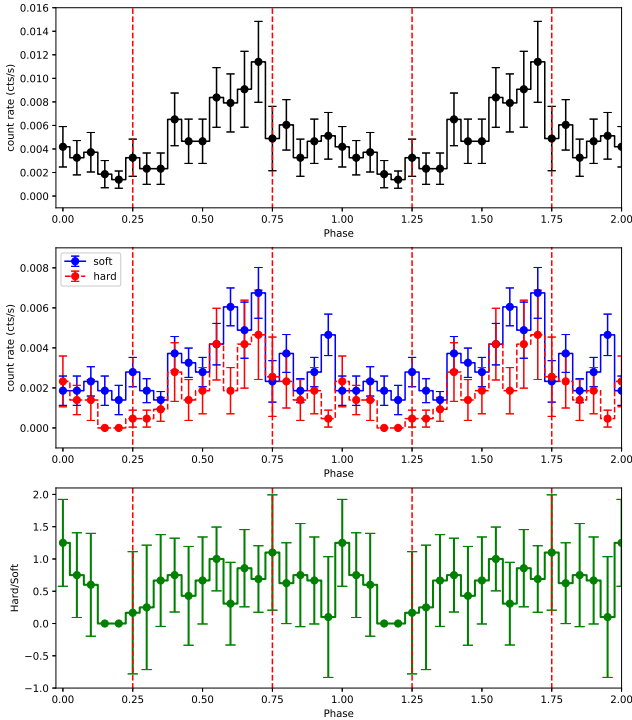


Fig. 4. *Top panel:* X-ray orbital modulation of PSR J1048+2339 in 0.3–8 keV with both *Chandra* observation combined. The phase zero is at same epoch as that in Fig. 1. The time bin size is about 2000 s. The red vertical lines illustrate the locations of inferior conjunction ($\phi = 0.25$) and superior conjunction ($\phi = 0.75$) of the companion. *Middle panel:* blue solid and red dashed lines illustrate the orbital modulation in soft band (0.3–2 keV) and hard band (2–8 keV), respectively. *Bottom panel:* variation of X-ray hardness across the orbit.

simultaneously; the parameters are listed in Table 2. We first use GridELC to search around the initial guess, by performing a “grid search” with the assigned grid size, until a minimum χ^2 is obtained. We then use differential evolution Monte Carlo Markov chain (demcmcELC) to explore the probability of these fitted parameters. Each fit evolved over 2000 generations with 50 members in the population.

Initial fitting results inferred that the companion fully filled its Roche lobe ($f_1 = 0.99$), but other parameters were not well constrained. We tried fixing $f_1 = 1$ and the results are shown in Fig. A.1 (top panels). For instance, the pulsar irradiation in Group 2 increased by a factor of 19, compared to that of Group 1. The fitted inclinations are 40° – 60° while the effective temperatures (corresponding to the night side temperature of the star) are around 4000 K. The mass ratio in both groups are unconstrained but both have a median around 4.4–5.5. We attribute this scenario to the lack of radial velocity measurements. At the fitted inclinations, the mass ratios imply a pulsar mass of around $3 M_\odot$, which is too massive for a neutron star. For a typical pulsar, the above mass ratios inferred a higher inclination. Furthermore, the difference in the pulsar irradiation is too large to be justified. In the subsequent analysis, we fixed the inclination to a theoretical upper limit of 76° for which an X-ray eclipse was not observed, using the derived pulsar mass of $2.1 M_\odot$ and a companion star mass of $0.4 M_\odot$, obtained from the light curve fitting. The results are shown in Fig. A.1 (bottom panels), in addition to Table 2. We obtained a factor of ~ 6 increment in the Group 2 pulsar irradiation, in comparison to the irradiation in Group 1. The filling factors and effective temperatures are ~ 0.8 and ~ 4200 K in both groups.

Table 2. ELC modeling results.

Parameter	Group 1 ^a	Group 2 ^b
Pulsar irradiation (erg s^{-1})	$10^{33.14^{+0.19}_{-0.20}}$	$10^{33.88^{+0.12}_{-0.10}}$
Roche-lobe filling factor	$0.83^{+0.03}_{-0.03}$	$0.86^{+0.02}_{-0.02}$
Mass ratio ($M_{\text{pulsar}}/M_{\text{companion}}$)	$4.92^{+1.02}_{-0.92}$	$5.60^{+0.40}_{-0.70}$
Effective temperature (K)	4253^{+247}_{-288}	4123^{+81}_{-80}
Inclination ($^\circ$)	fixed at 76°	fixed at 76°
Derived pulsar mass	$2.06 M_\odot$	$2.14 M_\odot$
Derived companion mass	$0.40 M_\odot$	$0.41 M_\odot$

Notes. ^(a)2018 March 11 & 12. ^(b)2018 April 2 & 4.

4. Discussion

We observed a face changing companion of the redback system J1048+2339, in which the modulation changes evidently from ellipsoidal to pulsar heating. The changing timescale took no more than 14 days. It is not clear if the timescale of ≤ 14 days is only exclusive to J1048+2339. Based on our LT data, the unusual brightening at $\phi = 0.21$ might be a precursor of a huge flaring taking place in the system. More recently, Cho et al. (2018) reported an optical brightening and an X-ray flaring event of the system. The optical emission at orbital phase $\phi = 0.75$ increased by 0.5 mag on 2018 April 18 (compared to their previous detection) and went back to quiescence ($R \gtrsim 20.5$ mag) in the 2018 May 20 observation. An X-ray flare was detected by *Chandra* on 2018 July 8 at $\phi = 0.9$. By comparing with our observations, it follows that the pulsar wind heating timescale is at most ~ 2 months.

The observed brightening of the companion star and the X-ray modulation provide us the information of the heating source for the companion star. From the observed and estimated properties of the system, the separation of the two stars, a , and the Roche-lobe radius, R_{rb} , of the companion star are estimated as $a = 1.5 \times 10^{11}$ cm and $R_{\text{rb}}/a = 0.25$. With the ELC model, we find the required irradiation luminosity of $L_{\text{irr}} \sim 10^{33-34}$ erg s^{-1} (cf. Table 2), if we assume the heating source is located at the position of the pulsar. In this case, a fraction of the luminosity absorbed by the companion star would be estimated by $\delta \sim (R_{\text{rb}}^2/4a^2) \sim 0.016$. Hence, we may estimate the rate of the energy absorbed by the companion star as $L_{\text{ab}} \sim \delta L_{\text{irr}} \sim 5 \times 10^{31}$ erg $\text{s}^{-1} (\delta/0.016) (L_{\text{irr}}/10^{33.5}$ erg $\text{s}^{-1})$.

There are several possibilities for the sources of the heating: the pulsar wind (Harding & Gaisser 1990), gamma-ray radiation from the pulsar (Takata et al. 2012), and the intrabinary shock emission (Sanchez & Romani 2017). For J1048+2339, the gamma-rays from the magnetosphere, for which the luminosity is usually 10% of the spin-down power, are not the main heating source, since the magnetospheric emission are steady and cannot explain the observed brightening (~ 1 mag) of the companion star. The change of the gamma-ray emission from the pulsar magnetosphere has been observed for young pulsar PSR J2021+4026 (Zhao et al. 2017). However, such a flux change is accompanied by a large glitch of the neutron star. For millisecond pulsars, such a large glitch has not been observed yet.

The observed X-ray luminosity from the intrabinary shock of this system is on the order of $L_X \sim 10^{31}$ erg s^{-1} , which is comparable to the required energy of the absorption L_{ab} . Hence if the shock emission is the main heating source, the intrabinary shock should be located near/on the companion star source. In such a case, a natural explanation of the observed X-ray modulation

with the flux peak around the superior conjunction is a consequence of the obstruction of the X-ray emitting region by the companion star. As demonstrated in [Bogdanov et al. \(2011\)](#), however, the modulation expected by this scenario has a sinusoidal shape and the expected width of the peak (≥ 0.5 orbital phase) is wider than the observed one peak (say, ~ 0.3). This scenario would also be difficult to explain the observed large amplitude (factor of 10, cf. Fig. 4), unless our view is almost edge-on. In fact, our results imply a high inclination of the system, consistent with the recent work by [Strader et al. \(2018\)](#) in which a near to edge-on orbit for J1048+2339 is suggested using radial velocity measurements.

Alternatively, the X-ray peak can be interpreted as the Doppler boosting effect of the pulsar wind flow (see [Huang et al. 2012](#)). In this scenario, the pressure of the stellar wind is stronger than the pulsar wind pressure and the shock cone wraps the pulsar. The Doppler boosting effect enhances (or weakens) the observed X-ray flux when the pulsar wind moves toward (or away from) the Earth. PSR J2129-0429, for example, shows a double peak structure at a small dip at the superior conjunction ([Kong et al. 2018](#)). It has been suggested that since the spin of the companion is synchronized with the orbital period, the stellar magnetic field of the companion star is enhanced to several kilogauss (kG) by the stellar dynamo process ([Sanchez & Romani 2017](#)). The X-ray peak (cf. Fig. 4) is not symmetric. Depending on the inclination angle of the binary, a double peak can be produced if the viewing angle is within the shock cone, while single peak is expected if the viewing angle is outside the shock cone.

If the intrabinary shock is located far from the companion star surface and wraps the pulsar, the observed X-ray luminosity, $L_X \sim 10^{31} \text{ erg s}^{-1}$, is insufficient to explain the heating of the companion star. To overcome this difficulty, [Sanchez & Romani \(2017\)](#) proposed that a portion of pulsar wind particles duct along the magnetic field of the companion star to the companion star surface, although it is uncertain how a fraction of the pulsar wind particles can cross the contact discontinuity of the MHD shock ([Wadiasingh et al. 2017](#)). If we assume that the pulsar wind particles carry an energy of $L_{\text{PW}} \sim L_{\text{sd}} = 1.2 \times 10^{34} \text{ erg s}^{-1}$ and assume that several percent of the wind energy, which is required to explain the observed X-ray luminosity for J1048+2339, is stopped by the intrabinary shock, a several percent of the shocked pulsar wind particles will reach the companion star surface. The pairs trapped by the magnetic field of the companion star will increase their pitch angle and lose their energy via synchrotron radiation as they move toward the stellar surface. This radiation could be one of the sources of the heating. Since the pairs with a large pitch angle cannot reach the star surface owing to the magnetic mirror, only pairs with small pitch angle can deposit on and directly heat up the companion surface.

Light curve modeling shows that the heating energy increased by a factor of 6 in less than three weeks. We speculate that this is related to the activity of the companion star, and the magnetic field of the companion star could play an important role by connecting to the shock region and guides the pair plasmas to the companion star surface. For instance, after 2018 March 12, more pair plasmas are guided to the companion star. In the event that the magnetic field of the companion star is suddenly weakened, the location of the intrabinary shock moves toward the companion star surface, and increases the heating energy in late March. Interestingly, there is a spontaneous flaring

event on 2018 March 26 before the launch of the pulsar heating modulation and the color variation suggests that the flare emission is hot. It is likely due to some heating effect related to magnetic activity on the tidally locked companion instead of reprocessing. Future multicolor monitoring will allow us to investigate the face changing mechanism of this intriguing redback system.

Another speculative scenario is that the outflow from an unaccreting dead disk stops the pulsar wind located close to the pulsar ([D'Angelo & Spruit 2010](#); [Takata et al. 2012](#)). In this scenario, the irradiated gamma rays on the disk are absorbed by the disk, if the column density is greater than a critical value of $\sigma \sim 60 h/l \text{ g cm}^{-2}$, where h and l is the thickness of the disk and propagating length of the gamma rays in the disk. The absorbed energy will be converted into the outflow from the disk, which could block the pulsar wind near the pulsar. After 2018 March 12, the disk column density could be lower than the critical value, and no formation of the outflow from the disk, therefore allowing the intrabinary shock to move toward the companion star and thus increase the heating.

Acknowledgements. We thank K. S. Cheng for helpful discussions. This work has made use of data collected at Lulin Observatory, partly supported by the Ministry of Science and Technology of the Republic of China (Taiwan) through grant 105-2112-M-008-024-MY3. The scientific results reported in this article are based on data obtained from the Chandra Data Archive. The Liverpool Telescope is operated on the island of La Palma by Liverpool John Moores University in the Spanish Observatorio del Roque de los Muchachos of the Instituto de Astrofísica de Canarias with financial support from the UK Science and Technology Facilities Council. Y.X.Y and A.K.H.K. are supported by the Ministry of Science and Technology of the Republic of China (Taiwan) through grants 105-2119-M-007-028-MY3 and 106-2628-M-007-005. J.T. is supported by NSFC grants of Chinese Government under 11573010, 1166116 1010, U1631103, and U1838102. J.L. is supported by BK21 plus Chungnam National University and the National Research Foundation of Korea grant 2016R1A5A1013277. C.Y.H. and K.L.L. are supported by the National Research Foundation of Korea grant 2016R1A5A1013277.

References

- Acerro, F., Ackermann, M., Ajello, M., et al. 2015, *ApJS*, **218**, 23
 Bailer-Jones, C. A. L., Rybizki, J., Fouesneau, M., Mantelet, G., & Andrae, R. 2018, *AJ*, **156**, 58
 Bellm, E. C., Kaplan, D. L., Breton, R. P., et al. 2016, *ApJ*, **816**, 74
 Bogdanov, S., Archibald, A. M., Hessels, J. W. T., et al. 2011, *ApJ*, **742**, 97
 Cho, P. B., Halpern, J. P., & Bogdanov, S. 2018, *ApJ*, **866**, 71
 Cromartie, H. T., Camilo, F., Kerr, M., et al. 2016, *ApJ*, **819**, 34
 D'Angelo, C. R., & Spruit, H. C. 2010, *MNRAS*, **406**, 1208
 Deneva, J. S., Ray, P. S., Camilo, F., et al. 2016, *ApJ*, **823**, 105
 Harding, A. K., & Gaisser, T. K. 1990, *ApJ*, **358**, 561
 Huang, R. H. H., Kong, A. K. H., Takata, J., et al. 2012, *ApJ*, **760**, 92
 Hui, C. Y., Hu, C. P., Park, S. M., et al. 2015, *ApJ*, **801**, L27
 Kalberla, P. M. W., Burton, W. B., Hartmann, D., et al. 2005, *A&A*, **440**, 775
 Kong, A. K. H., Takata, J., Hui, C. Y., et al. 2018, *MNRAS*, **478**, 3987
 Lee, J., Hui, C. Y., Takata, J., et al. 2018, *ApJ*, **864**, 23
 Li, K. L., Kong, A. K. H., Takata, J., et al. 2014, *ApJ*, **797**, 111
 Orosz, J. A., & Hauschildt, P. H. 2000, *A&A*, **364**, 265
 Romani, R. W., & Sanchez, N. 2016, *ApJ*, **828**, 7
 Sanchez, N., & Romani, R. W. 2017, *ApJ*, **845**, 42
 Steele, I. A., Smith, R. J., Rees, P. C., et al. 2004, in *Ground-based Telescopes*, ed. J. M. Oschmann, Jr., *Proc. SPIE*, **5489**, 679
 Strader, J., Swihart, S. J., Chomiuk, L., et al. 2018, *ApJ*, submitted [arXiv:1812.04626]
 Takata, J., Cheng, K. S., & Taam, R. E. 2012, *ApJ*, **745**, 100
 Takata, J., Li, K. L., Leung, G. C. K., et al. 2014, *ApJ*, **785**, 131
 Wadiasingh, Z., Harding, A. K., Venter, C., Böttcher, M., & Baring, M. G. 2017, *ApJ*, **839**, 80
 Zhao, J., Ng, C. W., Lin, L. C. C., et al. 2017, *ApJ*, **842**, 53

Appendix A: Additional figure

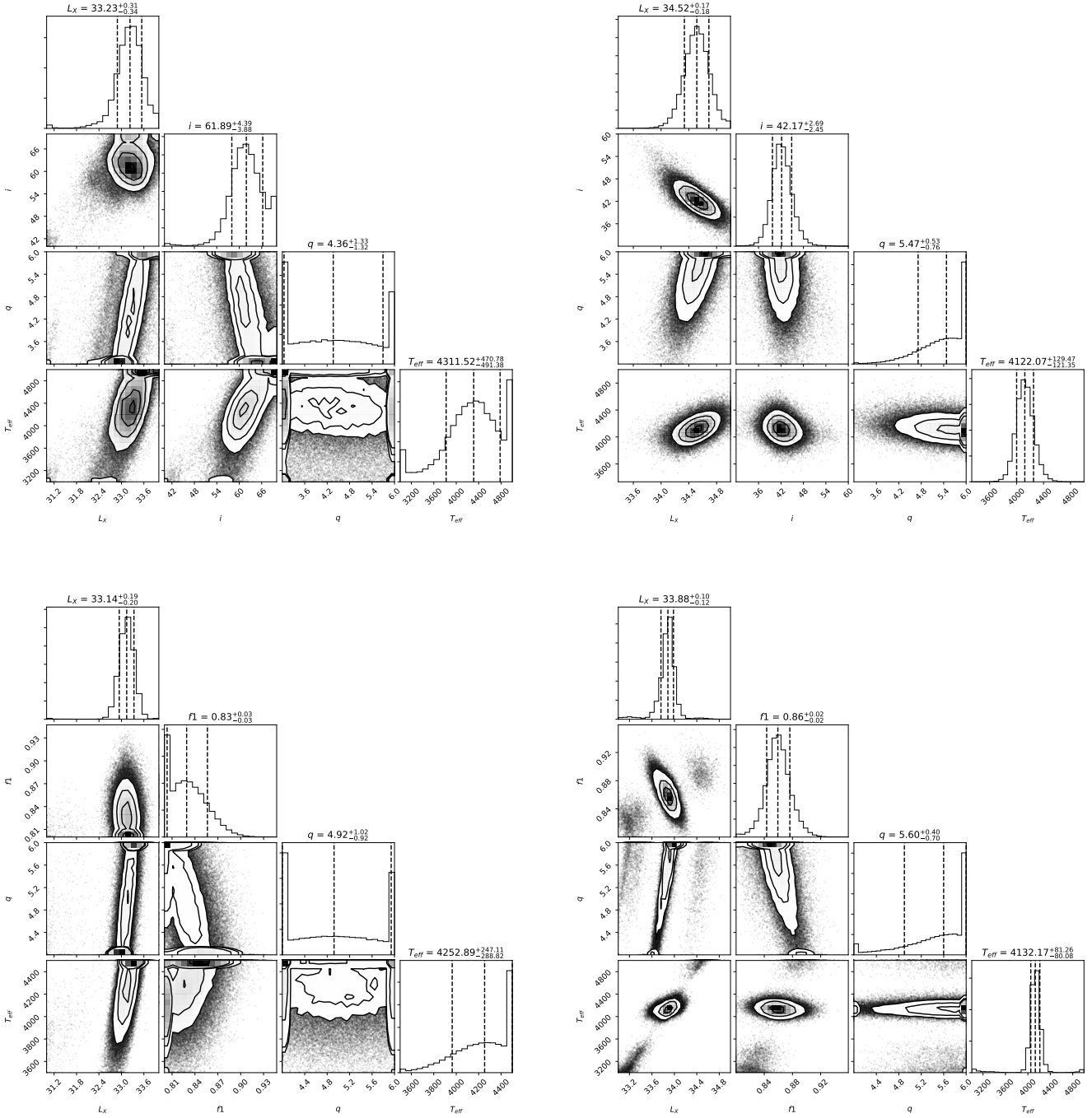


Fig. A.1. Corner plot of the fitted parameters: luminosity L_x , filling factor f_1 , mass ratio q , and effective temperature T_{eff} . *Top left:* Roche-lobe filling factor of 1 is assumed in Group 1 (ellipsoidal modulation) fitting. *Top right:* Roche-lobe filling factor of 1 is assumed in Group 2 (pulsar heating modulation) fitting. *Bottom left:* inclination angle of 76° is assumed in Group 1 (ellipsoidal modulation) fitting. *Bottom right:* inclination angle of 76° is assumed in Group 2 (pulsar heating modulation) fitting. The best-fit parameter is displayed with 1σ confidence interval for a 2D histogram.



Diagnosing the Clumpy Protoplanetary Disk of the UXor Type Young Star GM Cephei

P. C. Huang¹, W. P. Chen^{1,2} , M. Mugrauer³, R. Bischoff³, J. Budaj⁴, O. Burkhonov⁵, S. Ehgamberdiev⁵, R. Errmann^{6,7}, Z. Garai⁴, H. Y. Hsiao¹, C. L. Hu⁸, R. Janulis⁹, E. L. N. Jensen¹⁰ , S. Kiyota¹¹, K. Kuramoto¹², C. S. Lin¹, H. C. Lin¹, J. Z. Liu¹³, O. Lux³, H. Naito¹⁴, R. Neuhauser³, J. Ohlert^{15,16}, E. Pakštienė¹⁷, T. Pribulla⁴, J. K. T. Qvam¹⁸, St. Raetz^{19,20}, S. Sato²¹, M. Schwartz²², E. Semkov²³ , S. Takagi¹², D. Wagner³, M. Watanabe²⁴ , and Yu Zhang¹³ 

¹ Graduate Institute of Astronomy, National Central University, 300 Zhongda Road, Zhongli, Taoyuan 32001, Taiwan; pochiehuang1@gmail.com

² Department of Physics, National Central University, 300 Zhongda Road, Zhongli, Taoyuan 32001, Taiwan

³ Astrophysikalisches Institut und Universitäts-Sternwarte, FSU Jena, Schillergäßchen 2-3, D-07745 Jena, Germany

⁴ Astronomical Institute, Slovak Academy of Sciences, 059 60 Tatranská Lomnica, Slovak Republic

⁵ Ulugh Beg Astronomical Institute of the Uzbek Academy of Sciences, 33 Astronomicheskaya str., Tashkent 100052, Uzbekistan

⁶ Centre for Astrophysics Research (CAR), University of Hertfordshire, Hatfield Hertfordshire, AL10 9AB, UK

⁷ Abbe Center of Photonics, Friedrich-Schiller-Universität Jena, Max-Wien-Platz 1, D-07743 Jena, Germany

⁸ Taipei Astronomical Museum, 363 Jihe Road, Shilin, Taipei 11160, Taiwan

⁹ Institute of Theoretical Physics and Astronomy, Vilnius University, Saulėtekio av. 3, 10257 Vilnius, Lithuania

¹⁰ Department of Physics and Astronomy, Swarthmore College, 500 College Avenue, Swarthmore, PA 19081, USA

¹¹ Variable Stars Observers League in Japan (VSOLJ), 7-1 Kitahatsutomi, Kamagaya, Chiba 273-0126, Japan

¹² Department of Cosmosciences, Hokkaido University, Kita 10, Nishi 8, Kita-ku, Sapporo, Hokkaido 060-0810, Japan

¹³ National Astronomical Observatories, Xinjiang Observatory, Chinese Academy of Sciences, 150, Science 1-Street, Urumqi, Xinjiang 830011, People's Republic of China

¹⁴ Nayoro Observatory, 157-1 Nisshin, Nayoro, Hokkaido 096-0066, Japan

¹⁵ University of Applied Sciences, Wilhelm-Leuschner-Strasse 13, D-61169 Friedberg, Germany

¹⁶ Michael Adrian Observatory, Astronomie Stiftung Trebur, Fichtenstrasse 7, D-65468 Trebur, Germany

¹⁷ Institute of Theoretical Physics and Astronomy, Vilnius University, Saulėtekio av. 3, 10257 Vilnius, Lithuania

¹⁸ Department of Physics, University of Oslo, P.O. Box 1048 Blindern, NO-0316 Oslo, Norway

¹⁹ Freiburg Institute of Advanced Studies (FRIAS), University of Freiburg, Albertstraße 19, D-79104 Freiburg, Germany

²⁰ Institute for Astronomy and Astrophysics Tübingen (IAAT), University of Tübingen, Sand 1, D-72076 Tübingen, Germany

²¹ Astrophysics Department, Nagoya University, Nagoya, 464-8602, Japan

²² Tenagra Observatory, 221 Calle Coco, Rio Rico, AZ 85648, USA

²³ Institute of Astronomy and National Astronomical Observatory, Bulgarian Academy of Sciences, 72 Tsarigradsko Shosse Blvd., 1784 Sofia, Bulgaria

²⁴ Department of Applied Physics, Okayama University of Science 1-1 Ridai-cho, Kita-ku, Okayama, Okayama 700-0005, Japan

Received 2018 September 16; revised 2018 December 2; accepted 2018 December 9; published 2019 January 30

Abstract

UX Orionis stars (UXors) are Herbig Ae/Be or T Tauri stars exhibiting sporadic occultation of stellar light by circumstellar dust. GM Cephei is such a UXor in the young (~ 4 Myr) open cluster Trumpler 37, showing prominent infrared excess, emission-line spectra, and flare activity. Our photometric monitoring (2008–2018) detects (1) an ~ 3.43 day period, likely arising from rotational modulation by surface starspots, (2) sporadic brightening on timescales of days due to accretion, (3) irregular minor flux drops due to circumstellar dust extinction, and (4) major flux drops, each lasting for a couple of months with a recurrence time, though not exactly periodic, of about two years. The star experiences normal reddening by large grains, i.e., redder when dimmer, but exhibits an unusual “blueing” phenomenon in that the star turns blue near brightness minima. The maximum extinction during relatively short (lasting ≤ 50 days) events, is proportional to the duration, a consequence of varying clump sizes. For longer events, the extinction is independent of duration, suggestive of a transverse string distribution of clumps. Polarization monitoring indicates an optical polarization varying $\sim 3\%$ – 8% , with the level anticorrelated with the slow brightness change. Temporal variation of the unpolarized and polarized light sets constraints on the size and orbital distance of the circumstellar clumps in the interplay with the young star and scattering envelope. These transiting clumps are edge-on manifestations of the ring- or spiral-like structures found recently in young stars with imaging in infrared of scattered light, or in submillimeter of thermalized dust emission.

Key words: circumstellar matter – occultations – protoplanetary disks – stars: individual (GM Cephei) – stars: pre-main sequence – stars: variables: T Tauri, Herbig Ae/Be

1. Introduction

Circumstellar environments are constantly changing. A young stellar object (YSO), with prominent chromospheric and coronal activities, interacts intensely with the surrounding accretion disk by stellar/disk winds and outflows. The first few million years of the pre-main-sequence (PMS) evolution coincide with the epoch of possible planet formation, during which grain growth, already taking place in prestellar molecular cores up to micron sizes, continues on to centimeter sizes, and then to planetesimals (Natta et al. 2007). The detailed

mechanism to accumulate planetesimals and eventual planets is still uncertain. Competing theories include planetesimal accretion (Weidenschilling 2000) versus gravitational instability (Safronov 1972; Goldreich & Ward 1973; Johansen et al. 2007). Given the ubiquity of exoplanets, planet formation must be efficient to complete the dissipation of PMS optically thick disks in less than 10 Myr (Mamajek et al. 2004; Briceño et al. 2007; Hillenbrand 2008).

YSOs are known to vary in brightness. Outbursts arising from intermittent mass accretion events are categorized into two major classes: (1) FU Ori-type stars (or FUors) showing

erupt brightening up to 6 mag from quiescent to the high state in weeks to months, followed by a slow decline in decades (Hartmann & Kenyon 1985), and (2) EX Lup-type stars showing brightening up to 5 mag, sometimes recurrent, with roughly the same timescale of months in both rising and fading (Herbig 1989). Sunlike PMS objects, i.e., T Tauri stars, may also display moderate variations in brightness and colors (Herbst et al. 1994) due to rotational modulation by magnetic/chromospheric cool spots or accretion/shocking hot spots on the surface. There is an additional class, owing its variability to extrinsic origin, of UX Ori type stars (UXors; Herbst et al. 1994), that displays irregular dimming caused by circumstellar dust extinction. In addition to the prototype UX Ori itself, examples of UXors include CO Ori, RR Tau, and VV Ser.

The YSO dimming events can be further categorized according to the levels of extinction and the timescales. The “dippers” (Cody & Hillenbrand 2010), with AA Tau being the prototype (Bouvier et al. 1999, 2003), have short (1–5 days) and quasi-periodic events thought to originate from occultation by warps (Terquem & Papaloizou 2000; Cody et al. 2014) or by funnel flows (Blinova et al. 2016) near the disk truncation radius and induced by the interaction between the stellar magnetosphere and the inner disk (Romanova et al. 2013). The “faders,” with KH 15D being the prototype (Kearns & Herbst 1998; Hamilton et al. 2001), show prolonged fading events, each lasting for months to years with typically large extinction up to several magnitudes, thought to be caused by occultation by the outer part of the disk (Bouvier et al. 2013; Rodriguez et al. 2015, 2016). The target of this work, GM Cephei (hereafter GM Cep), a UXor star known to have a clumpy dusty disk (Chen et al. 2012), displays both dipper and fader events.

As a member of Trumpler (Tr) 37, a young (1–4 Myr, Marschall et al. 1990; Patel et al. 1995; Sicilia-Aguilar et al. 2005; Errmann et al. 2013) star cluster as a part of the Cepheus OB2 association, GM Cep (R.A. = $21^{\text{h}}38^{\text{m}}17^{\text{s}}.32$, decl. = $+57^{\circ}31'22''$, J2000) possesses observational properties typical of a T Tauri star, such as emission spectra, infrared excess, and X-ray emission (Sicilia-Aguilar et al. 2008; Mercer et al. 2009). *Gaia*/DR2 (Gaia Collaboration et al. 2018) measured a parallax of $\varpi = 1.21 \pm 0.02$ mas ($d = 826_{-13}^{+14}$ pc), consistent with being a member of Tr 37 at ~ 870 pc (Contreras et al. 2002).

The spectral type of GM Cep reported in the literature ranges from a late F (Huang et al. 2013) to a late G or early K (Sicilia-Aguilar et al. 2008). The star has been measured to have a disk accretion rate up to $10^{-6} M_{\odot} \text{ yr}^{-1}$, which is thought to be 2–3 orders higher than the median value of the YSOs in Tr 37 and is 1–2 orders higher than those of typical T Tauri stars (Gullbring et al. 1998; Sicilia-Aguilar et al. 2008). The broad spectral lines suggest a rotation $v \sin i \sim 43.2 \text{ km s}^{-1}$ much faster than the average $v \sin i \sim 10.2 \text{ km s}^{-1}$ of the members of Tr 37 (Sicilia-Aguilar et al. 2008).

Sicilia-Aguilar et al. (2008) presented a comprehensive collection of data on GM Cep, including optical/infrared photometry and spectroscopy, plus millimeter line and continuum observations, along with the young stellar population in the cluster Tr 37 and the Cep OB2 association (See also Sicilia-Aguilar et al. 2004, 2005, 2006a, 2006b). Limited by the time span of their light curve, Sicilia-Aguilar et al. (2008) made the incorrect conclusion that the star belonged to the EXor type. Later, with a century-long light curve derived from archival photographic plates, covering 1895 to 1993,

Xiao et al. (2010) classified the star as a UXor, which was confirmed by subsequent intense photometric monitoring (Chen et al. 2012; Semkov & Peneva 2012; Semkov et al. 2015; Huang et al. 2018). Chen et al. (2012) speculated on a possible recurrent time of ~ 1 yr based on a few major brightness dimming events, but this was not substantiated by Semkov et al. (2015).

GM Cep has been studied as part of the Young Exoplanet Transit Initiative (YETI) project (Neuhäuser et al. 2011), which combines a network of small telescopes in distributed time zones to monitor young star clusters, with the goal to find possible transiting exoplanets (Neuhäuser et al. 2011). Any exoplanets thus identified would have been newly formed or in the earliest evolution, providing a comparative sample with the currently known exoplanets that are almost exclusively found in the general Galactic fields, so are generally older). While so far YETI has detected only exoplanet candidates (Garai et al. 2016; Raetz et al. 2016), the data set serves as a valuable inventory for studies such as stellar variability (Errmann et al. 2013; Fritzewski et al. 2016).

The work reported here includes light curves in *BVR* bands on the basis of the photometry collected from 2008 to 2018. Moreover, polarization measurements in *g'*-, *r'*-, and *i'*-bands have been taken at different brightness phases, enabling simultaneous photometric and polarimetric diagnosis of the properties of the circumstellar dust clumps that cause the UXor variability. Section 2 summarizes the data used in this study, including those collected in the literature, and our own photometric and polarimetric observations. Section 3 presents the results of photometric, color, and polarimetric variations. On the temporal behavior of these measurements, we then discuss in Section 4 the implications on the properties of the dust clumps around GM Cep. We summarize our findings in Section 5.

2. Data Sources and Observations

Optical data of GM Cep consist mostly of our own imaging photometry since mid-2008, and polarimetry since mid-2014, up to mid-2018. These are supplemented by data adopted from the American Association of Variable Star Observers (AAVSO) database, covering timescales from days/weeks to years. Sicilia-Aguilar et al. (2008) summarized the photometry from the literature, e.g., those of Morgenroth (1939), Suyarkova (1975), and Kun (1986), and from databases such as VizieR, SIMBAD, and SuperCOSMOS (Monet et al. 2003), along with the infrared data from *IRAS* and *MSX6C*. Xiao et al. (2010) expanded the light-curve baseline and presented a-century-long photometric measurements, with a photometric uncertainty of ~ 0.15 mag, derived from the photographic plates collected at the Harvard College Observatory and from Sonneberg Observatory. Previous optical monitoring data include those reported by Chen et al. (2012, in *BVR* covering end of 2009–2011), by Semkov & Peneva (2012), and by Semkov et al. (2015, in *UBVRI* to end of 2014). The AAVSO data were adopted only from the observer “MJB” after checking photometric consistency with our results.

2.1. Optical Photometry

The imaging photometry covering 10 years has been acquired by 16 telescopes, including seven of the YETI telescopes (Neuhäuser et al. 2011). The Tenagra Observatory in Arizona

Table 1
Parameters of Telescopes

Observatory/Telescope	CCD Type	Size (pixels)	Pixel Size (μm)	FOV (arcmin^2)	RON (e^-)	# Nights
YETI Telescopes						
0.4 m SLT (Lulin)	E2V 42-40	2048 \times 2048	13.5	30.0 \times 30.0	7	541
0.81 m TenagraII (Tenagra)	SITe SI-03xA	1024 \times 1024	24	14.8 \times 14.8	29	463
0.25 m CTK-II (Jena) ^a	E2V PI47-10	1056 \times 1027	13	21.0 \times 20.4	7	104
0.6 m STK (Jena) ^b	E2V 42-10	2048 \times 2048	13.5	52.8 \times 52.8	8	79
1.0 m LOT (Lulin)	Apogee U42	2048 \times 2048	13.5	11.0 \times 11.0	12	48
0.61 m RC (Van de camp)	Apogee U16M	4096 \times 4096	9	26.0 \times 26.0	7	13
0.6 m Zeiss 600/7500 (Stara Lesna)	FLI ML 3041	2048 \times 2048	15	14.0 \times 14.0	5	11
Other Telescopes						
1.6 m Pirka (Nayoro) ^c	EMCCD C9100-13	512 \times 512	16	3.3 \times 3.3	13	133
1.5 m AZT-22 (Maidanak)	SI 600 Series	4096 \times 4096	15	16.0 \times 16.0	5	120
1.0 m NOWT (XinJiang)	E2V 203-82	4096 \times 4096	12	78.0 \times 78.0	5	108
1.2 m TIT (Michael Adrian)	SBIG STL-6303	3072 \times 2048	9	10.0 \times 6.7	15	12
0.51 m CDK (Mayhill)	FLI ProLine PL11002M	4008 \times 2072	9	36.2 \times 54.3	9	12
1.0 m ESA's OGS (Teide) ^d	Roper Spec Camera	2048 \times 2048	13.5	13.76 \times 13.76	8	10
1.5 m P60 (Palomar)	AR-Coated Tektronix	2048 \times 2048	24	11.0 \times 11.0	9	7
0.35 m ACT-452 (MAO)	QSI 516	1552 \times 1032	9	37.6 \times 25.0	15	2

Notes.^a Mugrauer (2016).^b Mugrauer & Berthold (2010).^c Nayoro observatory equips EMCCD camera with their Multi-Spectral Imager (MSI) instrument (Watanabe et al. 2012).^d Schulz et al. (2014).**Table 2**
Photometric Reference Stars Adopted from Xiao et al. (2010)

Ref. Star	R.A. (J2000) (deg)	Decl. (J2000) (deg)	<i>B</i> (mag)	<i>V</i> (mag)	<i>R</i> (mag)
Star B	324.529226	57.508117	16.015	14.961	14.364
Star C	324.563184	57.492816	15.445	14.837	14.455
Star D	324.543391	57.505287	15.333	14.357	13.770
Star F	324.586443	57.487231	14.389	13.358	12.770
Star G	324.600939	57.556202	13.374	12.829	12.513

and Lulin Observatory in Taiwan contributed about four-year baseline coverage each from mid-2010 to mid-2018, respectively. The Tenagra II telescope, a 0.81 m, Ritchey–Chrétien type telescope, carried out the *BVR* monitoring from 2010 October to 2014 June. No observations were taken in July/August because of the monsoon season, or during February/March because of the invisibility of the target. The SLT 0.4 m telescope, located at Lulin Observatory, acquired a few data points in *BVR* bands every night from 2014 September to date, weather permitting. Technical parameters of additional telescopes contributing to the data are listed in Table 1.

For each observing session, darks and bias frames were obtained every night when science frames were taken, except for the STK and CTK-II, for which darks already include biases. The sky flats were obtained when possible. For those nights without sky flats, we used the flats from the nearest previous night. The standard reduction with dark, bias, and flat field correction was performed with IRAF. For the Maidanak Observatory, Nayoro Observatory, and the ESA's OGS, the images were only corrected with bias and flat because of the low temperatures of the CCD detectors used.

The brightness of GM Cep and photometric reference stars was each measured with the aperture photometry procedure

“aper.pro” of IDL, which is similar to the “IRAF/Daophot” task, with an aperture radius of $8''.5$ for the target, and an annulus of the inner radius of $9''.5$ and outer radius of $13''$ for the sky. The seven reference stars from Xiao et al. (2010, their Table 2) were originally used by Chen et al. (2012), but later we found that Star A varied at ~ 0.1 mag level, and Star E was likely a member of the young cluster, so would be likely also variable. Excluding these two stars, the remaining five, listed in Table 2, were used as reference stars in the differential photometry of GM Cep reported here.

Photometric measurements at multiple bands were taken at different epochs in a night, and sometimes with different telescopes. In order to facilitate a quantitative comparison, e.g., between the *B*- and *V*-band light curves, and hence the *B* – *V* color curve, the epoch of each observation was rounded to the nearest integer Modified Julian Date (MJD), and the average in each band was taken within the same MJD. For periodicity analysis, the actual timing was used, so there would be no round-off error.

2.2. Optical Polarimetry

The optical polarization of GM Cep was measured by TRIPOL2, the second unit of the Triple-Range Imaging POLarimeter (TRIPOL; W. P. Chen et al. 2019, in preparation) attached to the LOT. This imaging polarimeter measures polarization in the Sloan *g'*-, *r'*-, and *i'*-bands simultaneously by rotating a half-wave plate to four angles, 0° , 45° , 22.5° , and 67.5° . To reduce the influence by sky conditions, every polarization measurement reported in this work was the mean value of at least five sets of images having nearly the same counts in each angle. This compromises the possibility to detect polarization variations on timescales of less than about an hour, but ensures the reliability of nightly measurements.

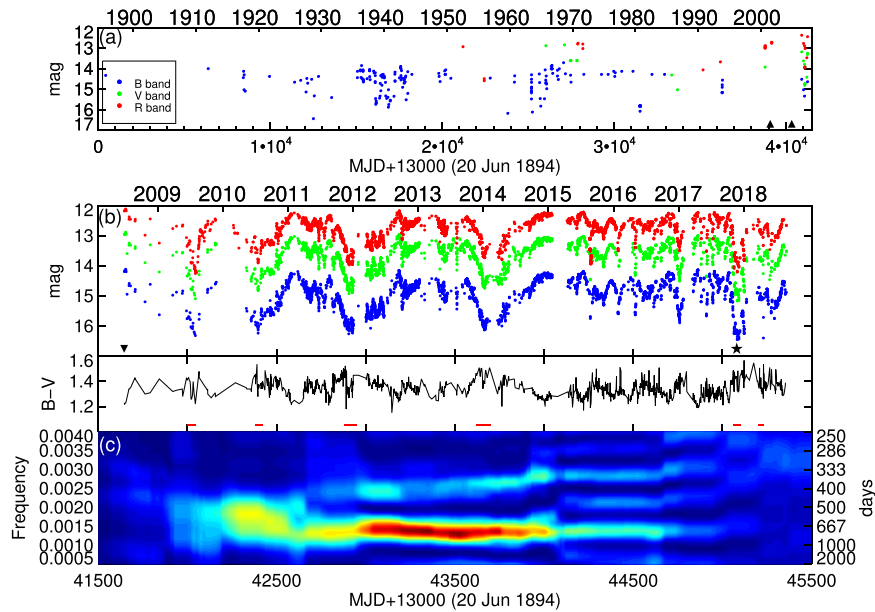


Figure 1. The light curve of GM Cep from 1894 to 2018. (a) The century-long data reported by Sicilia-Aguilar et al. (2008) and Xiao et al. (2010). (b) The light curves and $(B - V)$ color curve from 2008 to 2018 reported in this work. Epochs at which spectral measurements were reported in the literature are marked, with a triangle symbol for Sicilia-Aguilar et al. (2008), an upside down triangle for Semkov et al. (2015) and an asterisk for Giannini et al. (2018). (c) Dynamical period analysis of the input light curve of (b), with a window size of 2000 days and a step of 1 day. The color represents the power of the periodogram, from high in red to blue. The vertical axis represents either the frequency (on the left) or the corresponding period (right).

For TRIPOL2, we acquired the sky flats if weather allowed, or else we used the sky flats from the nearest adjacent night. Several unpolarized and polarized standard stars (Schmidt et al. 1992) were observed to calibrate the instrumental polarization and angle offset (W. P. Chen et al. 2019, in preparation). The correction for the dark and flat field was performed for all the images following the standard reduction procedure. The fluxes at four angles were measured with aperture photometry, and the Stokes parameters (I , Q , and U) were then calculated, from which the polarization percentage ($P = \sqrt{Q^2 + U^2}/I$) and position angle ($\theta = 0.5 \arctan(U/Q)^{-1}$) were derived. A typical accuracy $\Delta P \lesssim 0.3\%$ in polarization could be achieved in a photometric night (W. P. Chen et al. 2019, in preparation).

3. Results and Discussions

3.1. Photometric Variations

Figure 1 exhibits the light curves of GM Cep, including data taken from the literature covering more than a century since 1895 (Figure 1(a)), and our intense multiband observations starting in 2008 (Figure 1(b)). Since last reported (Chen et al. 2012; Semkov & Peneva 2012; Semkov et al. 2015), the star continued to show abrupt brightness changes. There are three main kinds of variations. Most noticeable are the major flux drops, ~ 1 – 2.5 mag at all B -, V -, and R -bands, with prominent ones, each lasting for months, occurring in mid-2009, mid-2010, 2011/2012, beginning of 2014, end of 2016, and end of 2017 (Munari et al. 2017). The list is not complete, limited by the time coverage of our observations. In addition, there are minor flux drops (~ 0.2 – 1 mag), each with the duration of days to weeks. The third kind, with a typical depth of 0.05 mag and occurring in a few days, is not discernible on the display scale of Figure 1, and will be discussed later.

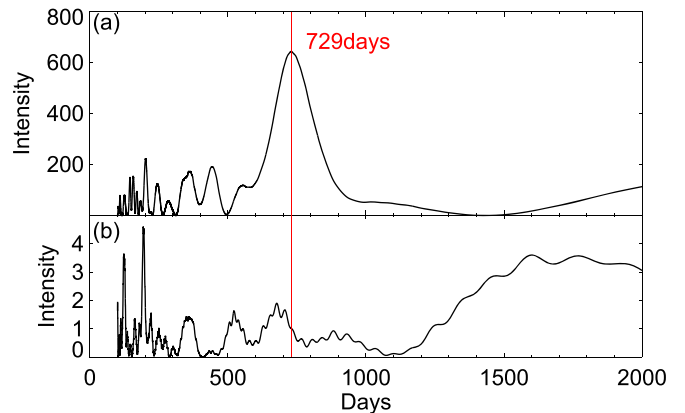


Figure 2. (a) The periodogram of the V -band light curve, where the red line marks the peak of the power spectrum. (b) The periodogram of the sampling function.

3.1.1. Periodicity Analysis

Deep Flux Drops: The UXors are thought to have irregular extinction events, despite the attempts to search for cyclic variability (Grinin et al. 1998; Rostopchina et al. 1999). For GM Cep, period analysis by the Lomb–Scargle algorithm (Lomb 1976; Scargle 1982) was performed, and the result is shown in Figure 2. A significant power is seen at ~ 730 days, which does not show up in the power spectrum of the sampling function (i.e., a constant magnitude at each sampling point). The secondary peak around 350 days, also visible in the sampling function, is the consequence of annual observing gaps. A dynamical period analysis was performed by repetitive Lomb–Scargle computation within a running window of 2,000 days with a moving step of one day. For example, the power spectrum at date 42500 (plus MJD+13000) was calculated by the data within the window ranging from 41500 to 43500.

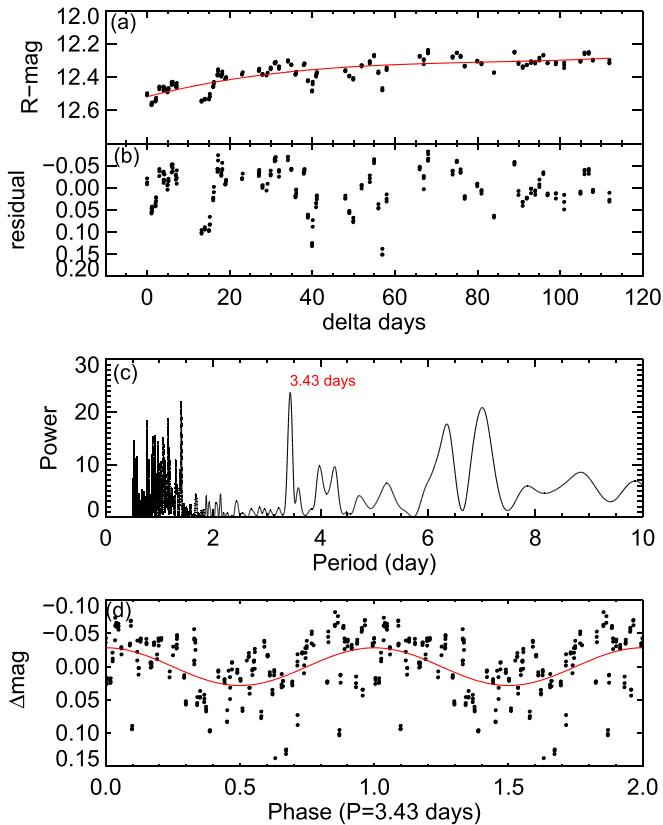


Figure 3. (a) The bright state in mid-2014 of the R -band light curve. (b) The scaled light curve after removal of the slow-varying trend. (c) The power spectrum of (b), from which a period of 3.43 days is detected. (d) The folded light curve with $P = 3.43$ days found in (c). The solid curve shows the best-fit sinusoidal function.

Enough padding was applied to the edges of the light curve. A peak around ~ 700 days persists, evidenced in Figure 1(c).

An independent investigation of the periodicity was performed by computing the autocorrelation function. The light curve was resampled to be equally spaced with a step of one day, and for each day, the average of data within 300 days from date 41500 to date 45500, or within 100 days from date 42300 to date 45500, centered on the day was adopted. A time lag of ~ 700 – 800 days is reaffirmed. This is the timescale between the few prominent minima (i.e., near 42900 and 43700).

Rotational Modulation: To investigate possible variability on much shorter timescales, we extracted the segment of the light curve from mid-2014 to the end of 2014, when the star was in the bright state so that there should be little influence by major flux drops. The light curve was fitted with, and then subtracted by, a third-order polynomial function to remove the slow-varying trend. The Lomb–Scargle analysis led to an identification of a period of ~ 3.43 days in the detrended light curve, and Figure 3 exhibits the original and the detrended light curves, together with the power spectrum and the folded light curve. This variation is caused by modulation of stellar brightness by dark spots on the surface with the rotational period of the star (Strassmeier 2009). Note that this period coincides roughly with the expected rotational period of a few days for the star, given its measured rotation $v \sin i \sim 43 \text{ km s}^{-1}$, and a radius of a few solar radii, estimated from the PMS evolutionary tracks (Sicilia-Aguilar et al. 2008).

Guided by the periodicity derived from the short segment of the light curve, we then processed the entire light curve using a more aggressive detrend technique than a polynomial fit to deal with the large fluctuations. The original light curve was smoothed by a running average, with an eight-day window. This effectively removes low-frequency signals slower than about 10 days. To investigate possible period changes, we divided the light curve into three segments, with the MJD ranges (plus MJD+13000) (1) 41500 to 43000, (2) 43000 to 44250, and (3) 44250 to 45500, respectively, based on a judicious choice to have sufficiently long trains of under-sampled data to recover periods on timescales of days. Figure 4 presents the power spectrum and the phased light curve for each segment, and in each case a significant period stands out, with the period and amplitude, $P_1 = 3.421$ days, $A_1 = 0.039$ mag, $P_2 = 3.428$ days, $A_2 = 0.036$ mag, and $P_3 = 3.564$ days, $A_3 = 0.020$ mag. The seemingly large scattering in each folded light curve is not the noise in the data, but the intrinsic variation in the star’s brightness, e.g., by differing total starspot areas. Because such a variation is not Gaussian, a least-squares analysis may not be appropriate to render a reliable estimate of the amplitude. Still, the sinusoidal behavior seems assured.

Therefore, a rotation period of roughly 3.43 days is found to persist throughout the entire time of our observations. Moreover there is marginal evidence of a lengthening period with a reduction in amplitude. This can be understood as latitudinal dependence of the occurrence of starspots due to surface differential rotation, in analog to the solar magnetic Schwabe cycle, in which sunspots first appear in heliographic mid-latitudes, and progressively more new sunspots turn up (hence covering a larger total surface) toward the equator (hence with shortening rotational periods). GM Cep therefore has an opposite temporal behavior, suggestive of an alternative dynamo mechanism at work (e.g., Küker et al. 2011). Further observations with a shorter cadence should be able to confirm this period shift and to provide a more quantitative diagnostic.

The detrended light curve shows mostly dimming events with occasional brightening episodes. The dimming must be the consequence of rotational modulation by surface starspots, whereas the brightening arises from sporadic accretion. The amplitude $\lesssim 0.2$ mag is consistent with the 0.01–0.5 mag variation range typically observed in T Tauri stars caused by cool or hot starspots (Herbst et al. 1994). Also, the amplitude of variation is marginally larger at shorter wavelengths, namely in V and B , lending evidence of accretion.

The excessive accretion rate of GM Cep reported by Sicilia-Aguilar et al. (2008), 10^{-7} to $5 \times 10^{-6} M_{\odot} \text{ yr}^{-1}$, was estimated by the U -band luminosity (Gullbring et al. 1998). Using the H_{α} velocity as an alternative diagnostic tool (Natta et al. 2004), the accretion rate would be 5×10^{-8} to $3 \times 10^{-7} M_{\odot} \text{ yr}^{-1}$ (Sicilia-Aguilar et al. 2008). Similarly, measuring also the H_{α} velocity, Semkov et al. (2015) derived $1.8 \times 10^{-7} M_{\odot} \text{ yr}^{-1}$. Giannini et al. (2018) presented spectra of GM Cep at different brightness phases and, on the basis of the dereddened H_{α} luminosity and its relation to the accretion luminosity (Alcalá et al. 2017), and then to the accretion rate (Gullbring et al. 1998), derived an average accretion rate of $3.5 \times 10^{-8} M_{\odot} \text{ yr}^{-1}$ with no significant temporal variations. Each of these methods has its limitation. The U -band flux may be contributed by thermal emission from the hot boundary layer (the accretion funnel) between the star and the disk. The H_{α} emission, on the other hand, may be contaminated by absorption

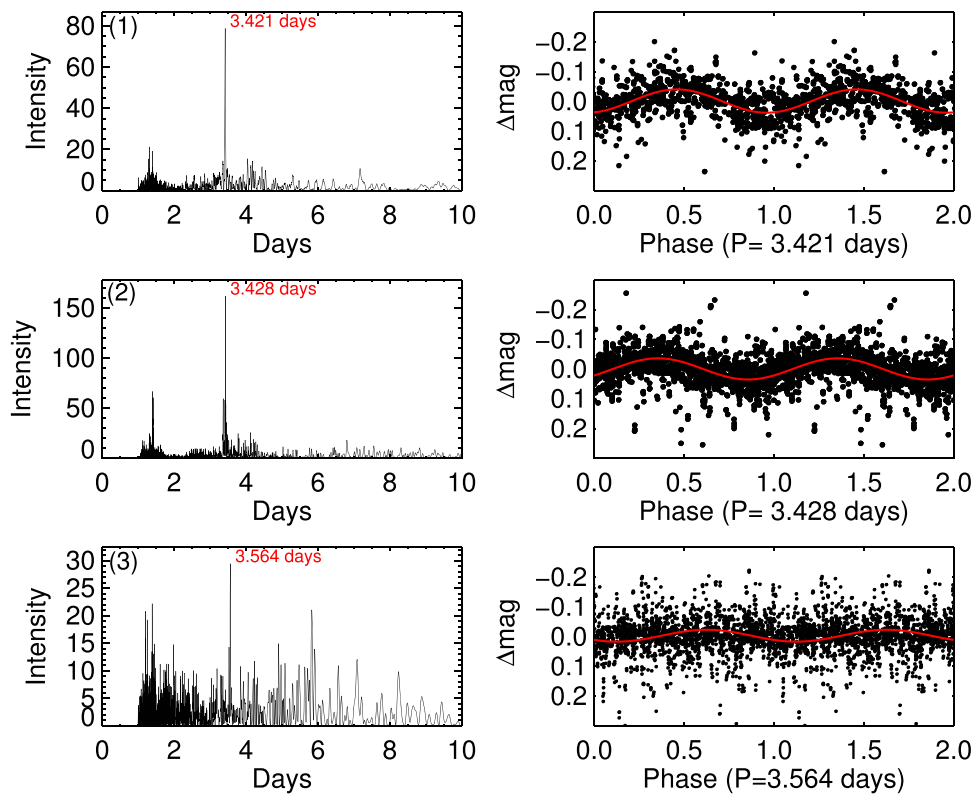


Figure 4. Power spectrum and phased light curve for (plus MJD+13000) (a) 41500–43000, (b) 43000–44250, and (3) 44250–45500. In each case the solid curve is the best-fit sinusoidal function, from which the amplitude is derived.

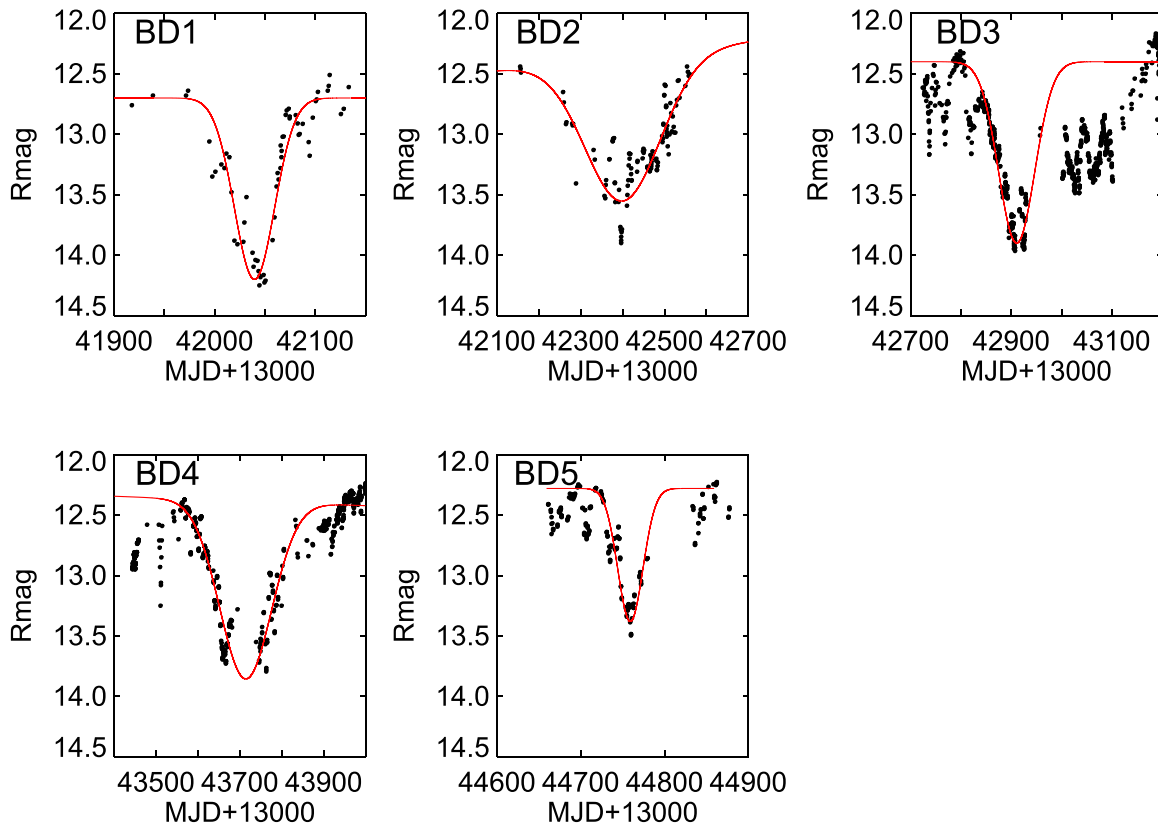


Figure 5. Gaussian fitting to each of the major flux drop events.

Table 3
Flux Drop Events

ID	MJD	Duration (days)	ΔB (mag)	ΔV (mag)	ΔR (mag)	(Remarks)
Major Events						
BD01	55039	100	1.45	1.50	1.50	
BD02	55401	450	1.45	1.40	1.20	
BD03	55910	180	1.70	1.60	1.50	
BD04	56713	310	1.75	1.64	1.47	
BD05	57759	75	1.45	1.30	1.10	
Minor Events						
SD01	55736	10	0.79	0.75	0.67	
SD02	55767	30	0.82	0.75	0.63	
SD03	55818	35	0.80	0.70	0.65	
SD04	56205	25	1.05	0.85	0.78	
SD05	56415	13	0.87	0.80	0.72	
SD06	56429	10	0.52	0.44	0.40	
SD07	56510	11	0.65	1.05	0.70	<i>V</i> includes AAVSO data
SD08	56553	15	0.37	0.32	0.30	
SD09	56763	13	0.35	0.55	0.68	
SD10	56784	13	0.55	0.48	0.48	
SD11	56865	13	...	0.40	...	
SD12	56944	13	0.33	0.18	0.20	
SD13	56972	3	0.22	0.17	0.15	
SD14	56989	3	0.22	0.20	0.18	
SD15	57184	8	0.49	0.40	0.36	
SD16	57263	25	1.10	1.10	1.40	incomplete sampling in <i>B</i> and <i>V</i>
SD17	57291	10	0.40	0.35	0.30	
SD18	57333	10	0.30	0.35	0.35	
SD19	57415	28	0.95	...	0.87	
SD20	57511	20	1.10	1.00	0.92	
SD21	57591	15	0.45	0.35	0.30	
SD22	57656	10	0.61	0.54	0.48	
SD23	57946	15	1.05	0.85	0.80	

in the H_{α} profile, or by chromospheric contribution not related to accretion. In any case, GM Cep does not seem to be unusually active in accretion activity compared to typical T Tauri stars or Herbig Ae/Be stars. The prominent flux variations are the consequences of dust extinction, not the FUor kind of flares. In Figures 1(a) and (b), the epoches at which literature spectroscopic measurements are available are marked, at date 39091 (Sicilia-Aguilar et al. 2008) and at date 41645 (Semkov et al. 2015), both when the star was in a bright state, and at date ~ 45080 (Giannini et al. 2018) when the star was in a faint state. Among the three data sets, the accretion rate does not seem to correlate with the apparent brightness.

3.1.2. Event Duration and Extinction

We parameterize a flux drop event by its duration and the maximum depth, with a least-squares fit by a Gaussian function. Only events sampled at more than half of the duration, e.g., an event lasting for roughly 10 days must have been observed for more than 5 nights, are considered to have sufficient temporal coverage to be included in the analysis. Figure 5 illustrates how the duration, taken as five times the standard deviation, or about 5% below the continuum, and the depth, as the minimum of the

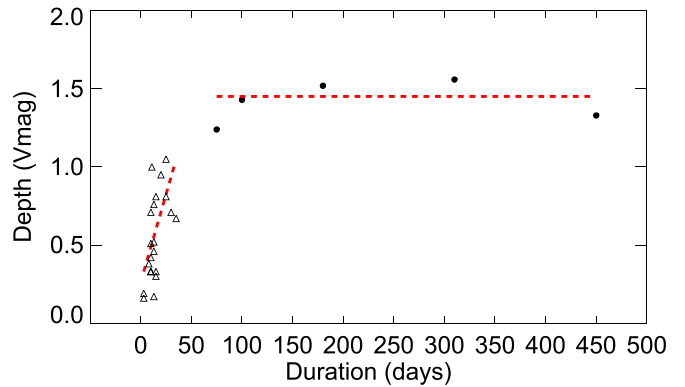


Figure 6. Depth vs. duration of occultation events. Each event is parameterized by a Gaussian fit to the light curve as illustrated in Figure 5. There is a linear trend for short events (triangles), whereas for long events (circles) the extinction depth levels off.

Gaussian function, are derived for each major event. The parameters are summarized in Table 3, in which the columns list for each event the identification, the MJD, duration, depths in B -, V -, and R -bands, and the comments.

Figure 6 exhibits the duration versus depth of the flux drop events. Two distinct classes of events emerge. For the short events the duration in general lengthens with the depth, roughly amounting to $A_V \sim 1$ mag per 30 days. This is understood as the various sizes of occulting clumps, so a larger clump leads to a longer event along with a deeper minimum. The extinction depth levels off for longer ($\gtrsim 100$ days) events to $A_V \sim 1.5$ mag, suggesting that these events are not caused by ever larger clumps. We propose that each long event consists of a series of events, or a continuous event, by clumps distributed along a string or a spiral arm. In this case, the duration gets longer, but the depth is not deeper.

The depth-duration relation of T Tauri stars has been discussed by Findeisen et al. (2013) with 3 yr monitoring of Palomar Transient Factory for the North America Nebula complex. In their sample of 29 stars, there are fading events with a variety of depth (up to ~ 2 mag) and duration (1–100 days). Stauffer et al. (2015), with a high-cadence light curve from the *CoRoT* campaign for NGC 2264, identified YSO fading events up to 1 mag. Guo et al. (2018) summarized event parameters for different stars, including those in Stauffer et al. (2015), and found those with durations less than 10 days varied typically with a depth of ≤ 1 mag, whereas those lasting more than ~ 20 days have a roughly constant amplitude ~ 2 –3 mag. All these studies made use of samples of different stars with diverse star/disk masses, ages, inclination angles, etc., and no clear correlation was evidenced between depth and duration. In comparison, our investigation is for a single target with distinct correlations for the short and for the long events.

3.2. Color Variations

Along with the light curves, Figure 1 also presents the $B - V$ color curve, i.e., the temporal variation. Figure 7(a) illustrates how the B magnitude of GM Cep varies with its $B - V$ color. In this color-magnitude diagram (CMD), GM Cep in general becomes redder when fainter, suggesting normal interstellar extinction/reddening. The slope of the reddening vector, marked by an arrow, is consistent with a total-to-selective extinction law of $R_V = 5$ (Mathis 1990), rather than with the

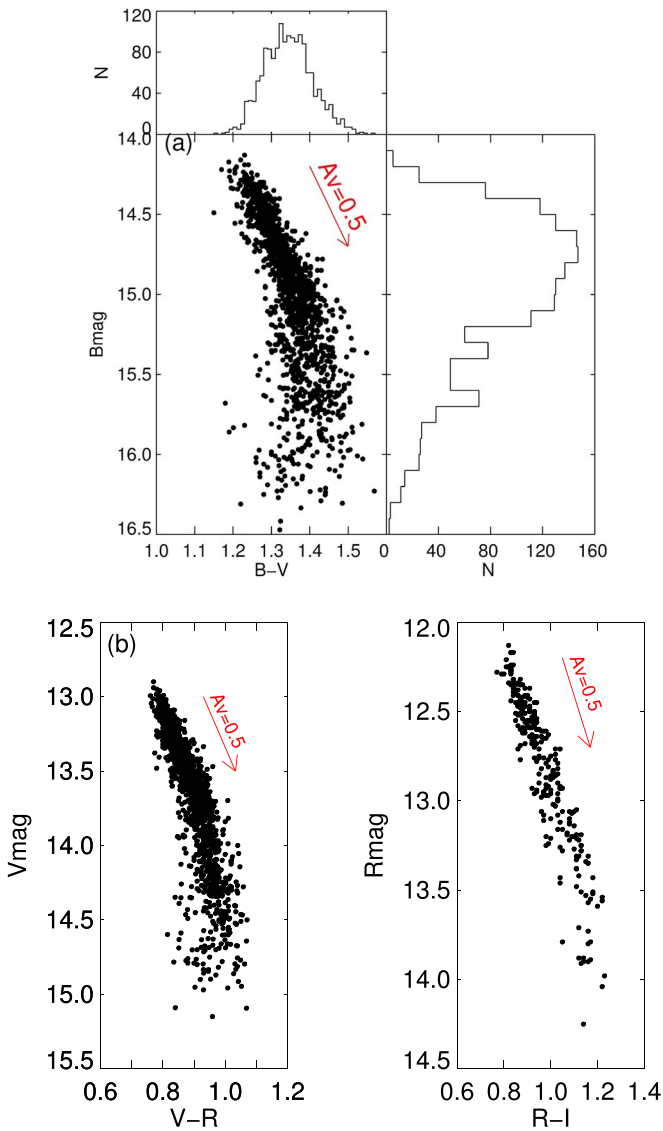


Figure 7. (a) The B magnitude vs. $B - V$ color for GM Cep, using data in Figure 1. The panel on the right plots the histogram of the brightness in B , whereas the panel on the top plots the histogram of the $B - V$ color. The arrow marks the reddening vector for $A_V = 0.5$ mag assuming a total-to-selective extinction of $R_V = 5.0$. (b) The same as in (a) but for V vs. $V - R$ and R vs. $R - I$.

nominal $R_V = 3$, implying larger dust grains than in the diffuse interstellar clouds. Between $B \sim 15.2$ mag and $B \sim 15.7$ mag, the extinction appears independent of the $(B - V)$ color, indicative of gray extinction by even larger grains ($>10 \mu\text{m}$, (Eiroa et al. 2002). The trend is yet different toward the faint state; namely the color turns bluer when fainter. This color reversal, or the “bluing effect,” has been known (Bibo & The 1990; Grinin et al. 1994; Grady et al. 1995; Herbst & Shevchenko 1999; Semkov et al. 2015), with the widely accepted explanation being that during the flux minimum, when direct starlight is heavily obscured by circumstellar dust, the emerging light is dominated by forward scattered radiation into the field of view.

The bluing phenomenon is also illustrated in Figure 1, where a few deep minima are marked, each by a thick red line, during which the corresponding color turns blue near the flux minimum. Additional CMDs in V versus $V - R$, and R versus $R - I$, where the data in I are adopted from those reported by

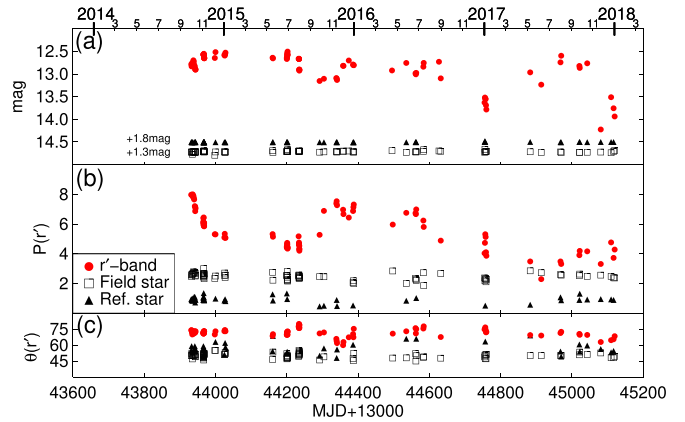


Figure 8. (a) The r' -band light curve (in black) for GM Cep, together with one of the photometric reference stars (filled triangles) and one field star (squares), in the same field of images. (b) The changing polarization level of GM Cep, in comparison to the two comparison stars. (c) The polarization angle for GM Cep remaining steady (72°) during three years of monitoring.

Semkov et al. (2015), indicate also normal reddening in the bright state, whereas the bluing tends to subside toward longer wavelengths, in support of the scattering origin, as shown in Figure 7(b).

3.3. Polarization

Figure 8 presents the linear polarization in r' -band of GM Cep, and of two comparison stars including one of the photometric reference stars and a field star. GM Cep displays a varying polarization with $P = 3\% - 8\%$ but with an almost constant position angle of $\sim 72^\circ$. The two comparison stars remain steadily polarized, each of $P \lesssim 2\%$ with a variation $\lesssim 1\%$.

Adding up the TRIPOL measurements at four polarizer angles gives the total flux. As seen in Figure 8, the TRIPOL r' light curve, albeit with lower cadence, allows for diagnosis of simultaneous photometric and polarimetric behavior. The broadband light curves in turn serve to indicate the overall brightness states at which the polarization data are taken.

Figure 9(a) plots the polarization in each band, $P_{g'}$, $P_{r'}$, and P_V . The polarization exhibits a slowly varying pattern, declining from 6% to 9% in the fall of 2014 to 3%–5% in 2015 July/August, and reclining to 5%–7% near the end of 2015. A similar pattern seems to exist also in 2017 but with a variation of 2%–5%. At the same time, the slow brightness change in each case, notwithstanding abrupt flux drops, seems to have a reverse trend. In particular, the smooth brightening in late 2014, where polarization data are densely sampled, is clearly associated with a monotonic decrease in polarization. A similar brightness-polarization pattern is seen from early 2017 to early 2018, for which the brightening and fading in the light curve is associated with a decreasing-turn-increasing trend in polarization.

Note that in general the polarization is higher at shorter wavelengths, but at certain epochs, particularly at flux minima, e.g., at the end of 2015 and the beginning of 2017, an “anomalous” wavelength dependence seems to emerge, so that the g' band becomes the least polarized.

4. The Clumpy Disk Structure in GM Cep

The photopolarimetric measurements enable inference on the occultation configuration in a qualitative way. For example, a sequential blockage of the circumstellar environs and the star

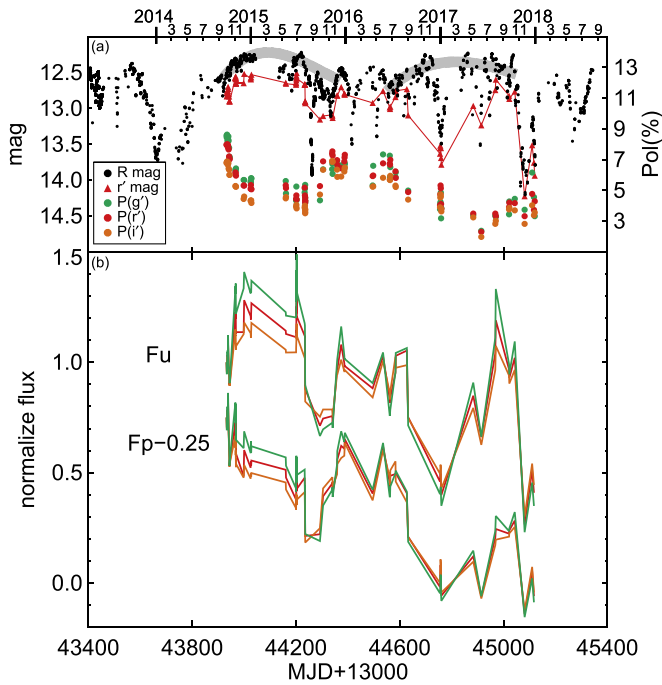


Figure 9. (a) The photopolarimetric r' -band light curve (in red) vs. the R -band light curve (in black), and shown below the polarization levels in g' (in green), r' (in red), and i' (in brown). The gray shades represent the slow brightness changes and simultaneous behavior of the polarization. (b) The light curves for unpolarized flux (F^u) and polarized flux (F^p), with the same color symbols as in (a).

will result in a certain photometric and polarimetric behavior. The high-cadence light curves, furthermore, allow quantitative derivation of the depth, duration, etc., of the occulting body. We present the analysis and interpretation of both kinds in this section.

4.1. Occultation Geometry Inferred By the Polarization Data

The level of polarization at wavelength λ is defined as

$$P_\lambda(\%) = \frac{F_\lambda^p}{F_\lambda^t} = \frac{F_\lambda^p}{F_\lambda^p + F_\lambda^u} = \frac{1}{1 + F_\lambda^u/F_\lambda^p},$$

where F^t is the total flux, which is decomposed into polarized flux (F^p) and unpolarized flux (F^u), with $F^t = F^p + F^u$. At each observing epoch, P_λ and F^t are measured, therefore F^p and F^u can be derived. In general the starlight is not polarized, but the scattered light from the inner gaseous envelope/disk is, which is fainter and bluer in color than the direct starlight.

The temporal variations of F_λ^p , F_λ^u , and F_λ^t , plus the wavelength dependence of these variations, provide clues on the geometry of a clump, or a string of clumps, relative to the stellar system (star plus disk). The last part of the equation suggests that (1) if F_λ^u remains the same, P_λ changes with F_λ^p in the sense that as F_λ^p decreases, so does P_λ . The dust reddening by occultation makes this dependence stronger at shorter wavelengths. But (2) if F_λ^u changes, because it dominates the brightness over F_λ^p , so, for example, as F_λ^u decreases, P_λ increases.

Figure 9(b) exhibits how the decomposed polarized (F^p) and unpolarized (F^u) components vary, respectively, at different wavelengths. To facilitate the comparison, each curve is scaled to its first data point to demonstrate the relative level of flux changes. The decomposition makes it clear that the decreasing

polarization near the end of 2014, with $P_{g'} > P_{r'} > P_{i'}$ (see Figure 9(a)), corresponding to the brightening of the star system, is the result of a fading F_λ^p alongside with a brightening F_λ^u , as evidenced in Figure 9(b), both leading to a decreasing P_λ in every wavelength. In the occultation scenario, the star system would be just coming out of a major event, and during such an egress, the clump was unveiling the star and blocking a progressively larger part of the envelope. Incidentally the deep flux drop event at the beginning of 2017 has polarization measured. At the brightness minimum, the level of polarization changes little, but with the anomaly $P_{r'} > P_{i'} > P_{g'}$. Inspection of the decomposition result reveals that both F_λ^u and F_λ^p decline to almost an all-time low, particularly at shorter wavelengths. This is the configuration when the star and the envelope are both heavily obscured.

On YSO photometric and polarimetric variability, Wood et al. (1996) and Stassun & Wood (1999) modeled the rotationally modulated multiwavelength photopolarization due to scattering of light by stellar hot spots, under different simulation parameters, such as the size and latitude of the hot spot, inclination, truncation radius, and geometry (e.g., flat or flared) of the disk. In general, the simulations suggested an amplitude of polarization variability due to a warped disk is similarly low, as demonstrated in the case of AA Tau, a prototype of dippers, with a variation of $\sim 0.5\%$ in the V -band during the occultation (O'Sullivan et al. 2005).

Recent modeling by Kesseli et al. (2016) of the photopolarimetric variability of YSOs plus accretion disks considered the spot temperature, radius of inner disk, structure, and inclination of the warp disk. Only star and dust emission was included, with no gas emission, but still, the typical polarization is expected to vary by less than $\sim 1\%$. It is interesting that the polarization level of I -band normally is always higher than that of the V -band, consistent with the wavelength dependence of our observations, albeit with limited time coverage, near flux minima. Hot starspots or a warped inner disk alone apparently cannot account for the large polarization variability seen in GM Cep. An additional gaseous envelope likely plays an important role.

4.2. Clump Parameters by the Light-curve Analysis

The long-term light curves render conclusive evidence that the major flux drops detected in GM Cep are caused by occultation of the young star and the envelope by circumstellar dust clumps. These dust grains are large in size, inferred by the reddening law (see Section 3.2), and distributed in a highly nonuniform manner. This density inhomogeneity could signify the protoplanetary disk evolution in transition from grain growth (of μm size) to planetesimal formation (of kilometer size; Chen et al. 2012).

Accretion plus viscous dissipation heats up a young stellar disk early on. As the accretion subsides and grains get clumpy, the disk becomes passive, in the sense that the dust absorbs starlight, warms up, and reradiates in infrared (Chiang & Goldreich 1997). The frequent occultation events imply a geometry that would have led to a significant stellar extinction and a flat spectral energy distribution (SED). Instead, however, because of the grain coagulation, GM Cep (1) has a moderate $A_V = 2-3$ mag, partly of interstellar origin, despite the copious dust content evidenced by the elevated fluxes in far-infrared and submillimeter wavelengths (Sicilia-Aguilar et al. 2008), and also (2) has an SED characteristic of a T Tauri star (Sicilia-Aguilar et al. 2008) with a noticeable infrared excess. In a

passive disk, hydrostatic equilibrium results in a structure to flare outward (Kenyon & Hartmann 1987; Chiang & Goldreich 1997), so the dust intercepts more starlight than a geometrically thin disk.

Ring- or spiral-like structure in YSO disks seems ubiquitous, as evidenced by, e.g., recent ALMA imaging in molecular lines or in continuum of the Herbig Ae/Be star AB Aur (Tang et al. 2012, 2017), the class II object Elias 2–27 (Pérez et al. 2016), or by HiCIAO/Subaru polarimetric imaging of FUors (Liu et al. 2016). Such a structure may be induced by a planet companion (Zhu et al. 2015) or by gravitational instability (Kratte & Lodato 2016). All these rings or spirals have some tens to hundreds of astronomical units in extents.

The most enlightening finding relevant to our work is the detection in the T Tauri star HL Tau at 7 mm of a distribution of clumps along the main ring of thermalized dust found earlier by at shorter wavelengths, where large grains reside (Carrasco-González et al. 2016, see their Figure 2). The most prominent one, at ~ 0.1 from the star, or ~ 14 au at a distance of 140 pc, with an estimated mass of 3–8 M_{\oplus} , is considered by these authors as a possible planetary embryo.

We have no knowledge of the location of the (strings of) clumps in the GM Cep disk, or of their geometric shape. But we present the following exercise, using theoretical disk models, to shed light on the possible constraints on clump parameters. The largest clumps in GM Cep, as seen in Figure 6, cause a maximal extinction of $A_V^c = 1.5$ mag with a timescale of ~ 50 days. Note that here A_V^c refers to the extinction caused by the occultation of the clump, to be distinguished from the interstellar plus circumstellar extinction of the star. The maximal extinction provides information on the column density of dust, and the duration time on the scale of the clump. The fiducial disk by Chiang & Goldreich (1997) adopts a stellar temperature $T_* = 4000$ K, mass $M_* = 0.5 M_{\odot}$, and radius $R_* = 2.5 R_{\odot}$. With veiling and line blending due to fast rotation, the spectral type of GM Cep is uncertain, ranging from an F9 (Huang et al. 2013) to G5/K3 (Sicilia-Aguilar et al. 2008). In any case the star is hotter (with higher pressure) but more massive (with stronger gravitational pull), and the hydrostatic conditions in the disk turn out to be similar. This means the disk height (H) is scaled with the radius (r) $H/r \approx 0.17(r/\text{au})^{2/7}$ (Chiang & Goldreich 1997). A clump at $r = 14$ au thus would subtend an opening angle (viewing the rim from the star) of $\sim 20^\circ$; at $r = 1$ au, the angle would become $\sim 10^\circ$, for which the disk has to be close to edge-on for occultation to take place. Assuming $2 M_{\odot}$ for GM Cep, a clump at 4–14 au has a projected Keplerian speed up to 11 km s^{-1} . So for a clump to traverse the GM Cep system, the linear size would be 0.3 au for $r = 14$ au. In the case $r = 1$ au, the orbital speed is faster, so the linear scale would be 1.2 au.

Alternatively, the clumps may be located closer in to the central star. The disk may not be monotonically flared, as the innermost disk is irradiated by starlight, and dust evaporation at temperature $T_{\text{evap}} \sim 1500$ K results in an inner hole, hence an inner rim or “wall” in the flaring disk, which accounts for the bump near 2–3 μm observed in the SEDs of some YSOs (Dullemond et al. 2001; Eisner et al. 2004). This temperature corresponds to a distance from the central star, $r_{\text{rim}} = (L_*/4\pi T_{\text{rim}}^4 \sigma)^{1/2} (1 + (H_{\text{rim}}/r_{\text{rim}}))^{1/2}$, where L_* is the luminosity of the star, $T_{\text{rim}} = T_{\text{evap}}$ is the temperature at the rim, H_{rim} is the vertical height of the inner rim, and σ is the Stefan–Boltzmann constant (Dullemond et al. 2001). Given

$L_* = 26 L_{\odot}$ for GM Cep (Sicilia-Aguilar et al. 2008), adopting $H_{\text{rim}}/r_{\text{rim}} = 0.2$ (Dullemond et al. 2001), the estimated inner rim radius is roughly $r_{\text{rim}} \sim 0.4$ au, corresponding to an opening angle $\arctan(H_{\text{rim}}/r_{\text{rim}}) \sim 11^\circ$. Even though the chance of occultation is higher with a clump closer to the star, a faster Keplerian speed would lead to a linear size of 1.7 au. We conclude that the “clump,” or the region of density enhancement in the disk has a length scale up to roughly 0.1–1 au across the line of sight.

The depth, or the length scale along the line of sight, is related to the maximum $A_V^c = 1.5$ mag, or the column density of dust. Integration requires detailed disk structure, such as the vertical and radial density profiles, grain size distribution, midplane settling, etc. Such a complexity is beyond the scope of this paper and in fact not justified by our data. Here we again attempt to gain some physical insights on the clump properties.

For a uniform disk, the volume mass density of dust $m_d = (N_d/\ell) M_{\text{grain}}$, where N_d is the column density of dust, ℓ is the length of the sightline through the dusty medium, and M_{grain} is the mass of each grain. Each term is evaluated as follows.

The column density N_d is related to the extinction: $A_V^c = 1.086\tau_V = N_d \sigma_d Q_{\text{ext}}$, where τ_V is the optical depth at V-band, $\sigma_d = \pi a^2$ is the geometric cross section of each (assuming spherical) grain of radius a , and Q_{ext} is the optical extinction coefficient, which, for grains large in size compared to the wavelength ($2\pi a \gg \lambda$), $Q_{\text{ext}} \approx 2$ (Spitzer 1978; van de Hulst 1957). Therefore, $N_d = 1.6 \times 10^5 A_V^c [10 \mu\text{m}/a]^2 \text{ cm}^{-2}$, and for each dust grain, assuming a material bulk density of 2 g cm^{-3} , the mass is $M_{\text{grain}} = 8.4 \times 10^{-9} [a/10 \mu\text{m}]^3 \text{ g}$. Given a gas density n_g , and a nominal gas-to-dust mass ratio of 100, $m_d = n_g m_H / 100$, and so

$$\ell = \frac{5.4 \times 10^9}{n_g} A_V^c \left(\frac{a}{10 \mu\text{m}} \right) [\text{au}].$$

For GM Cep, $A_V^c = 1.5$ mag, and adopting a gas density $n_g = 10^{10}$ (Barrière-Fouchet et al. 2005), $\ell \sim 0.8$ au for $a = 10 \mu\text{m}$ grains. For truly large grains, such as $a = 1$ mm, the extinction efficiency becomes much smaller, thus ℓ 100 times longer, to $\ell \sim 80$ au.

Admittedly, none of the simple assumptions we have made in the estimation is likely valid. Still, it is assuring that both the crossing time and the flux drop of occultation by a dust clump could end up with reasonable solutions, namely a region tens of astronomical units across in the young stellar disk, perhaps in a ring or a spiral configuration located tens of astronomical units from the star, consisting of primarily $10 \mu\text{m}$ grains or larger. Given the overall low extinction of the star, small grains likely exist but not in quantity, as they had been agglomerated into large bodies.

5. Conclusion

Optical photometric and polarimetric monitoring of the UX Ori star GM Cep for nearly a decade reveals variations in brightness and in polarization of different amplitude and timescales. The essential results of our study are:

1. GM Cep exhibits (1) brightness fluctuations $\lesssim 0.05$ mag on timescales of days, due partly to rotational modulation by surface starspots with a period of 3.43 days, and partly to accretion activity; (2) minor flux drops of amplitude

- 0.2–1.0 mag with duration of days to weeks; and (3) major flux drops up to 2.5 mag, each lasting for months, with a recurrent time, but not exactly periodic, of about 2 years.
- The flux drops arise from occultation of the star and gaseous envelope by orbiting dust clumps of various sizes.
 - The star experiences normal dust reddening by large grains, i.e., the star becomes redder when fainter, except at the brightness minimum during which the star turns bluer when fainter.
 - The maximum depth of an occultation event is proportional to the duration, about 1 mag per 30 days, for the events lasting less than ~ 50 days, a result of occultation by clumps of varying sizes. For the events longer than about 100 days, the maximum depth is independent of the duration and remains $A_V \sim 1.5$ mag, a consequence of transiting strings or layers of clumps.
 - The $g'r'i'$ polarization levels change between 3% and 8%, and vary inversely with the slow brightness change, while the polarization angle remains constant. The polarization is generally higher at shorter wavelengths, but at flux minima, there is a reversal of wavelength dependence, e.g., the g' -band becomes the least polarized. Temporal variations of polarization versus brightness, once the total light is decomposed into polarized and unpolarized components, allow diagnosis of the occultation circumstances of the dust clumps relative to the star and envelope.
 - Our data do not provide direct information on the size or location of the clumps, but the duration of an occultation sets constraints on the transverse size scale of the clump, while the maximum extinction depth is a measure of the column density of dust, hence a dependence of the line-of-sight length through the dusty medium. It is possible that GM Cep is an edge-on manifestation of the ring- or spiral-like structures found recently in young stars with imaging in infrared of scattered light, or in submillimeter of dust emission.

The NCU group acknowledges the financial support of the grants MOST 106-2112-M-008-005-MY3 and MOST 105-2119-M-008-028-MY3. We greatly thank the Jena group H. Gilbert, T. Zehe, T. Heyne, A. Pannicke, and C. Marka for kindly providing us with their efforts on acquiring data from Jena Observatory, which is operated by the Astrophysical Institute of the Friedrich-Schiller-University. Furthermore, we would like to thank the Thuringian State (Thüringer Ministerium für Bildung, Wissenschaft und Kultur) in project number B 515-07010 for financial support. The work by the Xinjiang Observatory group was in part supported by the program of the Light in China's Western Region (LCWR, grant No.2015-XBQN-A-02) and National Natural Science Foundation of China (grant No.11661161016). J. Budaj, Z. Garai, and T. Pribulla acknowledge VEGA 2/0031/18 and APVV 15-0458 grants as well as V. Kollar, J. Lopatovsky, N. Shagatova, S. Shugarov, and R. Komzik for their help with some observations. This research has made use of the International Variable Star Index (VSX) database, operated at AAVSO, Cambridge, Massachusetts, USA. We thank the referee for constructive comments that greatly improve the quality of the paper.

ORCID iDs

W. P. Chen  <https://orcid.org/0000-0003-0262-272X>
 E. L. N. Jensen  <https://orcid.org/0000-0002-4625-7333>
 E. Semkov  <https://orcid.org/0000-0002-1839-3936>
 M. Watanabe  <https://orcid.org/0000-0002-3656-4081>
 Yu Zhang  <https://orcid.org/0000-0001-7134-2874>

References

- Alcalá, J. M., Manara, C. F., Natta, A., et al. 2017, *A&A*, **600**, A20
 Barrière-Fouchet, L., Gonzalez, J.-F., Murray, J. R., Humble, R. J., & Maddison, S. T. 2005, *A&A*, **443**, 185
 Bibo, E. A., & The, P. S. 1990, *A&A*, **236**, 155
 Blinova, A. A., Romanova, M. M., & Lovelace, R. V. E. 2016, *MNRAS*, **459**, 2354
 Bouvier, J., Chelli, A., Allain, S., et al. 1999, *A&A*, **349**, 619
 Bouvier, J., Grankin, K., Ellerbroek, L. E., Bouy, H., & Barrado, D. 2013, *A&A*, **557**, A77
 Bouvier, J., Grankin, K. N., Alencar, S. H. P., et al. 2003, *A&A*, **409**, 169
 Briceño, C., Hartmann, L., Hernández, J., et al. 2007, *ApJ*, **661**, 1119
 Carrasco-González, C., Henning, T., Chandler, C. J., et al. 2016, *ApJL*, **821**, L16
 Chen, W. P., Hu, S. C.-L., Errmann, R., et al. 2012, *ApJ*, **751**, 118
 Chiang, E. I., & Goldreich, P. 1997, *ApJ*, **490**, 368
 Cody, A. M., & Hillenbrand, L. A. 2010, *ApJS*, **191**, 389
 Cody, A. M., Stauffer, J., Baglin, A., et al. 2014, *AJ*, **147**, 82
 Contreras, M. E., Sicilia-Aguilar, A., Muzerolle, J., et al. 2002, *AJ*, **124**, 1585
 Dullemond, C. P., Dominik, C., & Natta, A. 2001, *ApJ*, **560**, 957
 Eisner, C., Oudmaijer, R. D., Davies, J. K., et al. 2002, *A&A*, **384**, 1038
 Eisner, J. A., Lane, B. F., Hillenbrand, L. A., Akeson, R. L., & Sargent, A. I. 2004, *ApJ*, **613**, 1049
 Errmann, R., Neuhäuser, R., Marschall, L., et al. 2013, *AN*, **334**, 673
 Findeisen, K., Hillenbrand, L., Ofek, E., et al. 2013, *ApJ*, **768**, 93
 Fritzewski, D. J., Kitz, M., Mugrauer, M., et al. 2016, *MNRAS*, **462**, 2396
 Gaia Collaboration, Brown, A. G. A., Vallenari, A., et al. 2018, *A&A*, **616**, A1
 Garai, Z., Pribulla, T., Hambálek, L., et al. 2016, *AN*, **337**, 261
 Giannini, T., Munari, U., Lorenzetti, D., et al. 2018, *RNAAS*, **2**, 124
 Goldreich, P., & Ward, W. R. 1973, *ApJ*, **183**, 1051
 Grady, C. A., Perez, M. R., The, P. S., et al. 1995, *A&A*, **302**, 472
 Grinin, V. P., Rostopchina, A. N., & Shakhovskoi, D. N. 1998, *AstL*, **24**, 802
 Grinin, V. P., The, P. S., de Winter, D., et al. 1994, *A&A*, **292**, 165
 Gullbring, E., Hartmann, L., Briceño, C., & Calvet, N. 1998, *ApJ*, **492**, 323
 Guo, Z., Herczeg, G. J., Jose, J., et al. 2018, *ApJ*, **852**, 56
 Hamilton, C. M., Herbst, W., Shih, C., & Ferro, A. J. 2001, *ApJL*, **554**, L201
 Hartmann, L., & Kenyon, S. J. 1985, *ApJ*, **299**, 462
 Herbig, G. H. 1989, in *ESO Workshop on Low Mass Star Formation and Pre-main Sequence Objects*, ed. B. Reipurth (Garching: ESO), 233
 Herbst, W., Herbst, D. K., Grossman, E. J., & Weinstein, D. 1994, *AJ*, **108**, 1906
 Herbst, W., & Shevchenko, V. S. 1999, *AJ*, **118**, 1043
 Hillenbrand, L. A. 2008, *PhST*, **130**, 014024
 Huang, P.-C., Chen, W.-P., Hu, C.-L., et al. 2018, *BSRSL*, **87**, 145
 Huang, Y. F., Li, J. Z., Rector, T. A., & Mallamaci, C. C. 2013, *AJ*, **145**, 126
 Johansen, A., Oishi, J. S., Mac Low, M.-M., et al. 2007, *Natur*, **448**, 1022
 Kearns, K. E., & Herbst, W. 1998, *AJ*, **116**, 261
 Kenyon, S. J., & Hartmann, L. 1987, *ApJ*, **323**, 714
 Kesseli, A. Y., Petkova, M. A., Wood, K., et al. 2016, *ApJ*, **828**, 42
 Kratter, K., & Lodato, G. 2016, *ARA&A*, **54**, 271
 Küker, M., Rüdiger, G., & Kitchatinov, L. L. 2011, *A&A*, **530**, A48
 Kun, M. 1986, *IBVS*, **2961**, 1
 Liu, H. B., Takami, M., Kudo, T., et al. 2016, *SciA*, **2**, e1500875
 Lomb, N. R. 1976, *Ap&SS*, **39**, 447
 Mamajek, E. E., Meyer, M. R., Hinz, P. M., et al. 2004, *ApJ*, **612**, 496
 Marschall, L. A., Karshner, G. B., & Comins, N. F. 1990, *AJ*, **99**, 1536
 Mathis, J. S. 1990, *ARA&A*, **28**, 37
 Mercer, E. P., Miller, J. M., Calvet, N., et al. 2009, *AJ*, **138**, 7
 Monet, D. G., Levine, S. E., Canzian, B., et al. 2003, *AJ*, **125**, 984
 Morgenroth, O. 1939, *AN*, **268**, 273
 Mugrauer, M. 2016, *AN*, **337**, 226
 Mugrauer, M., & Berthold, T. 2010, *AN*, **331**, 449
 Munari, U., Castellani, F., Giannini, T., et al. 2017, *ATel*, **11004**
 Natta, A., Testi, L., Calvet, N., et al. 2007, in *Protostars and Planets V*, ed. B. Reipurth, D. Jewitt, & K. Keil (Tucson, AZ: Univ. Arizona Press), 767
 Natta, A., Testi, L., Muzerolle, J., et al. 2004, *A&A*, **424**, 603
 Neuhäuser, R., Errmann, R., Berndt, A., et al. 2011, *AN*, **332**, 547

- O'Sullivan, M., Truss, M., Walker, C., et al. 2005, *MNRAS*, **358**, 632
- Patel, N. A., Goldsmith, P. F., Snell, R. L., Hezel, T., & Xie, T. 1995, *ApJ*, **447**, 721
- Pérez, L. M., Carpenter, J. M., Andrews, S. M., et al. 2016, *Sci*, **353**, 1519
- Raetz, S., Schmidt, T. O. B., Czesla, S., et al. 2016, *MNRAS*, **460**, 2834
- Rodríguez, J. E., Pepper, J., Stassun, K. G., et al. 2015, *AJ*, **150**, 32
- Rodríguez, J. E., Reed, P. A., Siverd, R. J., et al. 2016, *AJ*, **151**, 29
- Romanova, M. M., Ustyugova, G. V., Koldoba, A. V., & Lovelace, R. V. E. 2013, *MNRAS*, **430**, 699
- Rostopchina, A. N., Grinin, V. P., & Shakhovskoi, D. N. 1999, *AstL*, **25**, 243
- Safronov, V. S. (ed.) 1972, *Evolution of the Protoplanetary Cloud and formation of the Earth and Planets* (Jerusalem: Keter Publishing House), 212
- Scargle, J. D. 1982, *ApJ*, **263**, 835
- Schmidt, G. D., Elston, R., & Lupie, O. L. 1992, *AJ*, **104**, 1563
- Schulz, R., Erd, C., Guilbert-Lepoutre, A., et al. 2014, *AAS/DPS Meeting Abstracts*, **46**, 214.05
- Semkov, E. H., Ibryamov, S. I., Peneva, S. P., et al. 2015, *PASA*, **32**, e011
- Semkov, E. H., & Peneva, S. P. 2012, *Ap&SS*, **338**, 95
- Sicilia-Aguilar, A., Hartmann, L. W., Briceño, C., Muzerolle, J., & Calvet, N. 2004, *AJ*, **128**, 805
- Sicilia-Aguilar, A., Hartmann, L. W., Calvet, N., et al. 2006a, *ApJ*, **638**, 897
- Sicilia-Aguilar, A., Hartmann, L. W., Fürész, G., et al. 2006b, *AJ*, **132**, 2135
- Sicilia-Aguilar, A., Hartmann, L. W., Hernández, J., Briceño, C., & Calvet, N. 2005, *AJ*, **130**, 188
- Sicilia-Aguilar, A., Merín, B., Hormuth, F., et al. 2008, *ApJ*, **673**, 382
- Spitzer, L. 1978, *Physical Processes in the Interstellar Medium* (New York: Wiley)
- Stassun, K., & Wood, K. 1999, *ApJ*, **510**, 892
- Stauffer, J., Cody, A. M., McGinnis, P., et al. 2015, *AJ*, **149**, 130
- Strassmeier, K. G. 2009, *A&ARv*, **17**, 251
- Suyarkova, O. G. 1975, *PZ*, **20**, 167
- Tang, Y.-W., Guilloteau, S., Dutrey, A., et al. 2017, *ApJ*, **840**, 32
- Tang, Y.-W., Guilloteau, S., Piétu, V., et al. 2012, *A&A*, **547**, A84
- Terquem, C., & Papaloizou, J. C. B. 2000, *A&A*, **360**, 1031
- van de Hulst, H. C. 1957, *Light Scattering by Small Particles* (New York: Dover)
- Watanabe, M., Takahashi, Y., Sato, M., et al. 2012, *Proc. SPIE*, **8446**, 84462O
- Weidenschilling, S. J. 2000, *SSRv*, **92**, 295
- Wood, K., Kenyon, S. J., Whitney, B. A., & Bjorkman, J. E. 1996, *ApJL*, **458**, L79
- Xiao, L., Kroll, P., & Henden, A. A. 2010, *AJ*, **139**, 1527
- Zhu, Z., Dong, R., Stone, J. M., & Rafikov, R. R. 2015, *ApJ*, **813**, 88



2012 TC4 - An unusual fast-rotating PHA with C-type taxonomy

Zhong-Yi Lin^{*}, Wing-Huen Ip, Chow-Choong Ngeow

No. 300, Zhongda Rd., Zhongli Dist, Taoyuan City, 32001, Taiwan



ARTICLE INFO

Keywords:

Near earth asteroids
2012 TC4

ABSTRACT

The potentially hazardous asteroid 2012 TC4 made an Earth close approach at a distance of 0.11 lunar distance on 12 October 2017. Photometric observations were carried out between October 11 and October 12 at the Lulin Observatory at short cadence. Data analysis of the light curves shows that this PHA has a fast rotation period of 12.25 min, a light curve variation amplitude of 1.2 ± 0.1 mag corresponding to an axial ratio of about 3.0. Our BVRI photometry also indicates that 2012 TC4 is a C-type asteroid. With the C-type albedo of 0.065 and an absolute magnitude of $H = 26.613 \pm 0.350$, its effective diameter can be derived to be $24.8_{-8.0}^{+19.1}$ m.

1. Introduction

Potentially Hazardous Asteroids (PHAs) are defined as near-Earth asteroids (NEAs) with close approaches to the Earth within a distance of 0.05 AU and the absolute magnitudes less than 22.0. As of January 2018, a total of 1885 PHAs have been found with a size range from a few meters to several kilometers (C. NASA/JPL, 2018a), (C. NASA/JPL, 2018b), (M. P. Center, 2018). The largest known PHA is (53319) 1999 JM8 with an effective diameter of about 3.5 km (Benner et al., 2002) (Benner et al., 2002), but it will not pass the Earth within the PHA limit of 0.05 AU in this century. The small PHA, 2012 TC4, was discovered on October 4, 2012, by the Pan-STARRS telescope in Hawaii during its close approach to the Earth at a distance of 0.247 Lunar distances (LD) or 94800 km. The size of the object was estimated to be 7–34 m (Polishook, 2013) (Polishook, 2013). From the light curve data with a variation amplitude of 0.9 ± 0.1 , 2012 TC4 was found to be rapidly rotating with a spin period of 12.24 ± 0.06 min (Polishook, 2013; Odden et al., 2013; Warner, 2013; Carbognani, 2014); this indicates that it is a monolith instead of a rubble pile (Polishook, 2013) (Polishook, 2013). The Earth pass on October 12, 2017, with a closest approach distance of 0.11 LD (43500 km) provided an excellent opportunity for ground-based observations of this interesting object to obtain more precise information on its mineralogical composition and size. In this paper, our results from measurements at the Lulin Observatory will be summarized.

2. Observations

The photometric observations of 2012 TC4 were made using the Lulin

one-meter telescope (LOT) at the Lulin Observatory, Taiwan. The LOT with a field of view of 11 arcmin was installed in 2002 by the Institute of Astronomy, National Central University. The $2K \times 2K$ CCD camera, U42, manufactured by Apogee Instruments has a pixel scale of 0.52 arcsec per pixel. Image acquisition is done by using the software Maxim DL provided by the Diffraction Limited, Inc., running on Windows operating system. More information can be found in the following website <http://www.cyanogen.com/index.php>. Asteroid 2012 TC4 was observed for two nights from October 10 to 11, 2017 with B, V, R, and I Johnson filters, centered at 0.45, 0.55, 0.67 and $0.81 \mu\text{m}$, respectively. The observational details of the color photometric measurements and light curve photometry are shown in Table 1 and Table 2, respectively. The asteroid phase angle ($\alpha = 33.5^\circ$), geocentric ($\Delta = 0.0068$ AU) and heliocentric ($r = 1.004$ AU) distances, as well as its apparent visual magnitude ($m_V = 17.2$) did not change significantly during color observations. Table 2 shows the time intervals in which light curve photometric measurements were obtained, using R filter. Due to weather condition, the data obtained on October 11, 2017, were only used for rotation period determination. The data reduction followed standard procedures, including bias and dark-frame subtraction and flat-field correction. The dark frames and the flat frames were taken at the beginning and the end of each observation night. To calibrate the resulting magnitudes and colors, a number of photometric standard fields (MarkA, PG2213, and SA113) selected from the list of (Landolt, 1992) were also observed from the 10:46 to 10:56 UT on Oct. 10 2017.

Time-series photometry was obtained from images acquired with the R-filter. The exposure times varied from 5 s to 20 s depending on how fast 2012 TC4 moved. Differential photometry using at least four or more

^{*} Corresponding author.

E-mail address: zylin@astro.ncu.edu.tw (Z.-Y. Lin).

<https://doi.org/10.1016/j.pss.2018.07.012>

Received 9 February 2018; Received in revised form 18 July 2018; Accepted 29 July 2018

Available online 6 August 2018

0032-0633/© 2018 Elsevier Ltd. All rights reserved.

Table 1

Observational details of the color photometric measurements. Information includes UT time slot for color sequence, filters, exposure time (seconds), geocentric (Δ) and heliocentric (r_h) distances, phase angle (α), airmass, and V magnitude.

Time	Filter	Δ	r_h	α	Airmass	V_{obs}
Oct. 10 (UT)	(exp. time (s))	(AU)	(AU)	(degree)		
11:29~11:46	B (120), V (60), R (60), I (60)	0.0068	1.004	33.5	1.70~1.86	17.23±0.03 17.19±0.04

Table 2

Observational details of light curve photometry. Information includes UT time slot for each series of observations, geocentric (Δ) and heliocentric (r_h) distances, phase angle (α), airmass and exposure time for the individual acquisitions.

Time (UT)	Δ	r_h	α	Airmass	Exp. time
Oct. 10	(AU)	(AU)	(degree)		(s)
12:12~12:31	0.0067~0.0066	1.004	33.6~33.7	1.20~1.17	20s
16:38~17:30	0.0059~0.0058	1.003	34.6~34.7	1.67~2.32	20s
Oct. 11					
13:49~15:01	0.0026~0.0024	1.000	39.8~40.7	1.18~1.33	5s

reference stars on all images was carried out by means of IDL routines based on DAOPHOT. Note that different sets of reference stars were used from night to night because the track of 2012 TC4 crossed different star fields. For aperture photometry of both 2012 TC4 and the reference stars, the mean value of the full width half-maximum (FWHM) of the PSFs of reference stars in each image was used. In other words, the flux of the asteroid and those of the reference stars were computed through the same aperture(s). Because the Earth-asteroid and Sun-asteroid distance of 2012 TC4 changed continuously, the estimated magnitudes have to be calibrated from time to time. This leads to the concept of "reduced magnitude" to account for the changing distances, which is defined by

$$V_R = V_{obs} - 5 \log(RD). \tag{1}$$

Where V_{obs} = V magnitude at observation

- R = distance Sun to Asteroid (in AU)
- D = distance Earth to Asteroid (in AU).

It is important to note that the differential magnitude of 2012 TC4 was estimated by subtracting the average magnitudes of the reference

stars with variabilities removed. In lieu of absolute photometry, the photometric data were normalized by using the average magnitude obtained for each light curve when we combined the data from October 10 and 11, 2017. The normalized light curve for both nights is shown in Fig. 1.

3. Results

3.1. Rotation period

We used the Lomb-Scargle method (Lomb, 1976) (Lomb, 1976) to estimate the rotation period of 2012 TC4. Several peaks appeared in the

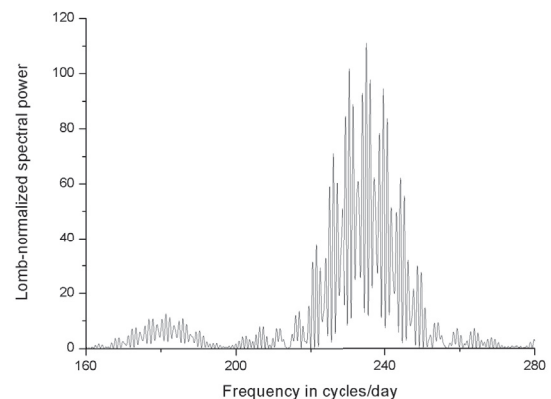


Fig. 2. Power spectrum of asteroid 2012 TC4 from the Lomb periodogram analysis. The peak at 235.10 cycles per day corresponds to a rotation period of 12. 25 min.

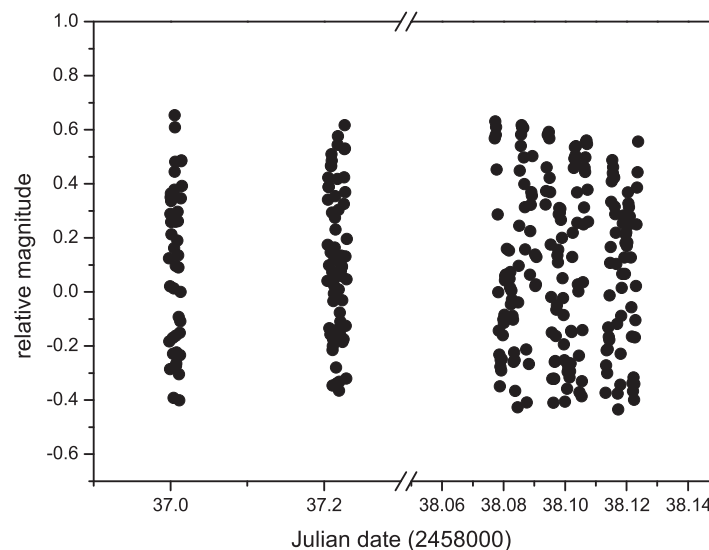


Fig. 1. Fig. 1. Relative magnitudes of the asteroid 2012 TC4 obtained by observations at Lulin between Oct. 10 and Oct. 11, 2017. An estimation of error in magnitude about 0.003 ~ 0.008 is not represented in the figures.

Lomb periodogram (Fig. 2). The peak with the highest spectral power is at 0.102 h, which corresponds to a rotation period of 12.25 min because the folded light curve should have double peaks with two maxima and two minima in one rotation. The derived value is in agreement with the reported values of Polishook (2013) (Polishook, 2013) and Odden et al. (2013) (Odden et al., 2013). But, if we look at every data set individually (Fig. 3), we found that the shape of the lightcurve is complex. This usually indicates that this NEA might be in a tumbling state of rotation. A tumbling state in 2012 TC4 have been reported by Warner et al. (2018) (Warner, 2012), also detected in the light curve analysis presented by Ryan and Ryan (2017) (Ryan and Ryan, 2017), and Sonka et al. (2017) (Sonka et al., 2017). However, our computed periods for each sequence are not shown a second period of 0.1418 h reported by Warner et al. (2018) (Warner, 2012) and Ryan and Ryan (2017) (Ryan and Ryan, 2017). Instead, the values (0.22843, 0.20458, and 0.20460 from top to bottom) were only slightly different and consist with the result by Sonka et al. (2017) (Sonka et al., 2017). The rotational phase curve combining two days of data is shown in Fig. 4. In addition to the spin rate estimation, we can further place a lower limit of 1.2 magnitude on the peak-to-peak light curve variation. If the light curve variability is due to the asteroidal shape approximated by an ellipsoid, 2012 TC4 would have an axial ratio of about 3 which is unusually elongated among small asteroids (Binzel et al., 2004) (Binzel et al., 2004).

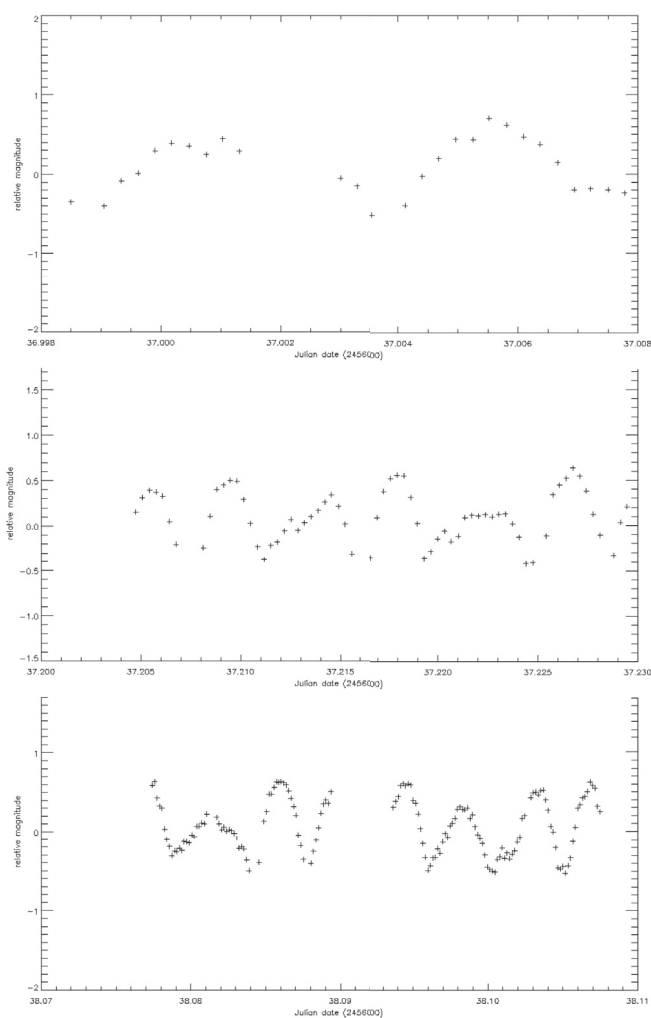


Fig. 3. Three individual lightcurves obtained during the night of 10 and 11 October 2017. Each figure shows the relative magnitude variation versus JD. An estimation of error in magnitude about 0.003 ~ 0.008 is not represented in the figures.

3.2. Taxonomic classification

The measurements of 2012 TC4 at Lulin were carried out in B, V, R and I filters with the aim of deriving its taxonomic type according to its surface colors. The observing sequence (i.e. R-B-R-V-R-I-R ...) was acquired to remove the effect of the magnitude variation due to the asteroid's rotation. But the effect of phase angle was not corrected because the change of phase angle is small (~ 0.1) within the duration of 20 min observation. And the correction of phase reddening is not done here. By subtracting the standard solar colors (B-V = 0.665, V-R = 0.367, and V-I = 0.705, Howell et al., 1995) (Howell, 1995)), we obtained the relative reflectance of 2012 TC4 in Fig. 5. The relative reflectance is normalized to one at 0.55 μm . Through comparing the known relative reflectance (i.e. Bus-DeMeo system), we classified the 2012 TC4 into C-type asteroid. Notes that the computed relative reflectances from the Bus-DeMeo system in Fig. 5 is as follows: we used the template average spectra defined for each taxonomic class from the Bus-DeMeo taxonomic system, and integrated the spectra through the transmissions curves of the Johnson's filters. After convolution, we transform the derived flux to magnitudes and then compute the colors. Because of the similar spectra slopes, we combined the R-type into the V-type and the O-type and the Q-type merged into the Q-complex. More detail color indices for different taxonomic groups (A, C, D, Q, S, V, and X) can be found in Table 2 of Lin et al., 2018) (Lin et al., 2018).

In order to obtain more precise taxonomic classification as spectroscopic observations, the principal component index (PCI) method was adopted (Lin et al., 2018) (Lin et al., 2018)). We obtained equation (2) to derive a principal component index.

$$PCI = (B - V)\cos\theta + (V - R)\sin\theta \quad (2)$$

The angle (θ) of $37.5_{-2.937}^{+2.714}$ is estimating from the known color indices (i.e. B-V and V-R color-color diagram) of hundreds NEAs by a linear fitting. The taxonomic domains according to the Bus-DeMeo system for seven different spectral complexes are shown in Fig. 6. The boundaries of different complexes are resulting from the color indices estimated by convoluting the average spectra of the Bus-DeMeo system. It can be seen that asteroid TC4 should be classified as a C-type while using PCI and the R-I index. This result is further confirmed by the relative reflectances-fitting between 2012 TC4 and a template relative reflectances of the C-type object in Fig. 5.

3.3. Size

The phase angle (α) of an object is the Sun-asteroid-Earth angle. Measuring the relationship between the brightness of an asteroid and phase angle at observation allows an estimate of the absolute magnitude (H), or the brightness of the asteroid at zero phase angle (Bowell et al., 1989) (Bowell et al., 1989). The observed V magnitude first came from the color sequences (Table 1) using photometric standard stars for the photometric calibration. The other V magnitudes were derived and converted from the all the R-band magnitudes of lightcurve data using the result of color sequence (the mean V-R color is 0.351 ± 0.085). Instead of using the standard star catalog of (Landolt, 1992), we used the Pan-STARRS-1 DR1 catalog ((Tonry et al., 2012)) to calibrate R-band magnitude. By assigning a G slope of 0.15 which is the average value of C-type asteroids (Bowell et al., 1989) (Bowell et al., 1989), the absolute magnitude can be determined to be $H_v = 26.613 \pm 0.364$ according to the standard phase curve model described in Bowell et al. (1989) (Bowell et al., 1989). The effective diameter D_{eff} of an asteroid can be estimated by using the formula

$$D_{\text{eff}}(km) = \frac{1329}{\sqrt{p_v}} 10^{-0.2H_v}. \quad (3)$$

where p_v is the geometric visible albedo. From a mean albedo $p_v = 0.065 \pm 0.036$ for the Bus C-type asteroid derived from the space

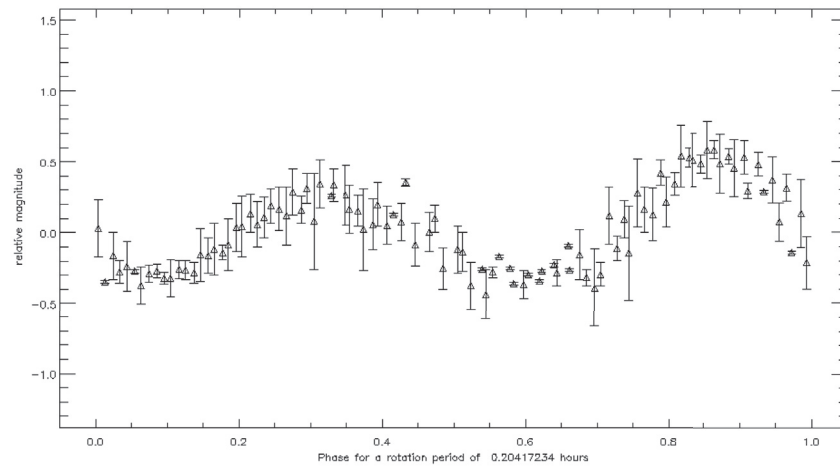


Fig. 4. The light curve of 2012 TC4 folded into rotation phase with a rotation period of 12.25 min.

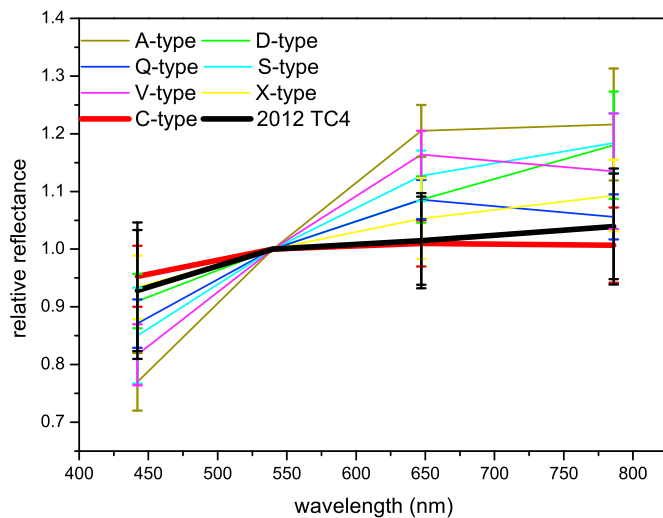


Fig. 5. A comparison of the relative reflectance of 2012 TC4 with the template relative reflectances of different type of asteroids. The C-type relative reflectance was the best fit.

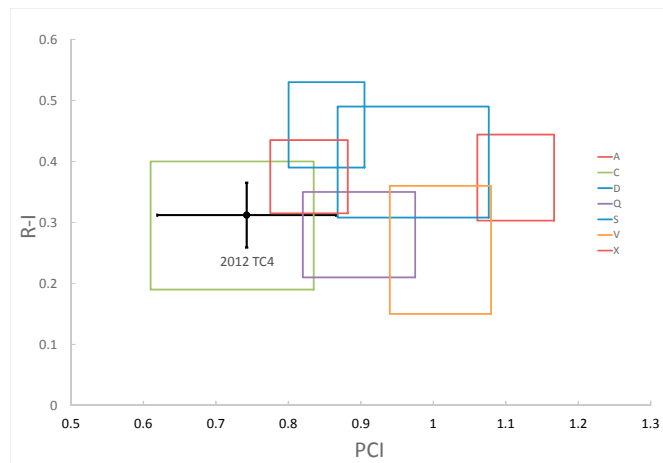


Fig. 6. Boundaries made by Bus-DeMeo's divergence can be used to classify observing data into different taxonomic classes.

telescopes (0.072 ± 0.043 in AKARI, Usui et al., 2013 (Usui et al., 2013)) and 0.058 ± 0.028 in NEOWISE, Mainzer et al., 2011 (Mainzer et al., 2011)), the effective diameter of 2012 TC4 can be computed to be $D^{eff} = D^{eff} 24.8^{+19.1}_{-8.0}$ m.

3.4. Distribution of rotation rates of near-Earth asteroids

Fig. 7 shows the distribution of the near earth asteroids' spin rates and sizes that can provide important information on theories of asteroids' structure and physical processes. The data points were gathered from the NEA database of the European Asteroid Research Node (E.A.R.N., Binzel et al. 2002), the earlier Lulin NEAs survey data (Lin et al., 2018) (Lin et al., 2018) and the Asteroid Lightcurve Database (LCDB, Warner et al., 2009 (Warner et al., 2009)). Note that the CDB data includes a flag to describe data quality ("U"), ranging from 0 (incorrect) to 3 (well-defined). We have only included data with $U = 2$ in Fig. 7. The region defined by rotational periods smaller than the spin barrier (2.2 h) and diameters smaller than 100 m is designated as VSA (Very Small Asteroids) and is mainly populated by S-type asteroids (Fig. 7). The few other spectral types for the four remaining asteroids are the C-group with type C (2012 TC4, and 2012 KP24) and type B (2012 KT42), the X-type (1998 KY26). This means that 2012 TC4 is most likely to be solid, monolithic body and not rubble pile weakly held together by its self-gravity.

4. Discussion

The very fast rotation of 2012 TC4 with a spin period of 12.25 min indicates that this small NEA is most likely to be of monolithic structure. Although our visible colors indicates 2012 TC4 is a C-type asteroid, the associated centrifugal force with such a short rotation period would have destroyed 2012 TC4 if it was composed of an assemble of small fragments in the rubble-pile model with ordinary bulk density. Hatch et al. (2015) (Hatch and Wiegert, 2015) investigated the physical properties of the small near-Earth asteroids ($D \leq 60$ m) and concluded that a large portion of his data set (92 asteroids rapidly rotating) are monolithic. His result is consistent with the suggestion given by Harris (1996) (Harris, 1996) that the rubble pile asteroids cannot spin faster than the spin-cutoff at 2.2 h. Otherwise, they will break apart. Furthermore, C-type asteroid 2012 TC4 is given a high value in a/b ratio referred to a highly-elongated asteroid and might fly apart if it is not made up of a monolithic body. Unfortunately, we only have one sample in this region, the highly-elongated and spin fast asteroids. This could be an observational bias due to their lower albedo or the result of the differences in the physical properties (i.e., material strength and cohesion). In future, to improve the discovery of C-type near-Earth fast asteroids is important because of their more

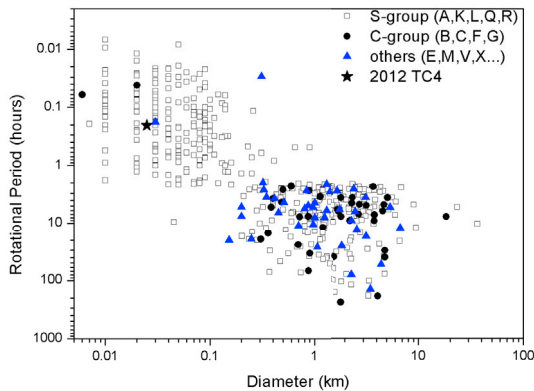


Fig. 7. The diameter-rotational period diagram of asteroids marked with 2012 TC4 (star). The errors for this asteroid is smaller than the symbol. The background population of near-Earth asteroids is divided into three groups, S-group (black squares), C-group (black dots), and others (E, M, V, X, blue triangles). The data for the background population was taken from the Light Curve Data Base, the NEA database of E.A.R.N., and the earlier Lulin NEAs survey data (Lin et al. (2018) (Lin et al., 2018)). (For interpretation of the references to color in this figure legend, the reader is referred to the Web version of this article.)

diverse compositions, which include water, carbon compounds, rock and metal.

5. Summary

Small NEA 2012 TC4 was observed at Lulin Observatory for the nights of October 10 and 11, 2017. Our light curve measurements and multi-filter photometric observations yielded the following results.

- 1 The Lomb periodogram analysis showed a rotation period of 12.25 min and an amplitude of 1.2 magnitudes of the light curve variation. This implies an axial ratio of about 3, assuming a triaxial ellipsoid, and indicates a highly elongated object. These results are in good agreement with the CCD photometric measurements of Polishook (2013), Odden et al. (2013), Warner (2013), and Carbognani (2014) (Polishook, 2013; Odden et al., 2013; Warner, 2013; Carbognani, 2014).
- 2 The multi-color photometry between 400 nm and 800 nm indicates that 2012 TC4 is a C-type asteroid according to the Bus taxonomy.
- 3 Phase function measurements made at phase angles of 33.6–40.6° were used to obtain an absolute magnitude of $H = 26.613 \pm 0.350$ with a G-value of 0.15. The derived effective diameter of $24.8^{+19.1}_{-8.0}$ m based on mean albedo $p_v = 0.065 \pm 0.036$ for the Bus C-type asteroid is consistent with the previous estimate of 10–40 m (Polishook, 2013) (Polishook, 2013).

Acknowledgements

We specially acknowledge that the Lulin staff, Chi-Sheng Lin and Hsiang-Yao Hsiao, Hung-Chin Lin, and Dr. Cheng Yu-Chi have provided assistance in observations. This publication has made use of data collected at Lulin Observatory, partly supported by MOST grant 105-

2112-M-008-024-MY3. This work was also supported by MOST 105-2112-M-008-002-MY3 and MOST 104-2112-M-259-006 from the Ministry of Science and Technology of Taiwan.

References

- Benner, L.A.M., Ostro, S.J., Nolan, M.C., Margot, J.-L., Giorgini, J.D., Hudson, R.S., Jurgens, R.F., Slade, M.A., Howell, E.S., Campbell, D.B., Yeomans, D.K., 2002. Radar observations of asteroid 1999 JM8. *Meteoritics Planet Sci.* 37, 779–792. <https://doi.org/10.1111/j.1945-5100.2002.tb00855.x>.
- Binzel, R.P., Lupishko, D., di Martino, M., Whiteley, R.J., Hahn, G.J., 2002. *Physical Properties of Near-earth Objects*, pp. 255–271.
- Binzel, R.P., Rivkin, A.S., Stuart, J.S., Harris, A.W., Bus, S.J., Burbine, T.H., 2004. Observed spectral properties of near-Earth objects: results for population distribution, source regions, and space weathering processes. *Icarus* 170, 259–294. <https://doi.org/10.1016/j.icarus.2004.04.004>.
- Bowell, E., Hapke, B., Domingue, D., Lumme, K., Peltoniemi, J., Harris, A.W., 1989. Application of photometric models to asteroids. In: Binzel, R.P., Gehrels, T., Matthews, M.S. (Eds.), *Asteroids II*, pp. 524–556.
- C. NASA/JPL, 2018. Neo basics -potentially hazardous asteroids (phas). Retrieved 22 January 2018: https://cneos.jpl.nasa.gov/about/neo_groups.html.
- C. NASA/JPL, 2018. Discovery statistics - cumulative totals. Retrieved 25 April 2018. <https://cneos.jpl.nasa.gov/stats/totals.html>.
- Carbognani, A., 2014. Asteroids lightcurves at oavda: 2012 june - 2013 march. *Minor Planet Bulletin* 41, 4–8.
- Harris, A.W., 1996. The rotation rates of very small asteroids: evidence for 'rubble pile' structure. In: *Lunar and Planetary Science Conference, Vol. 27 of Lunar and Planetary Science Conference*, pp. 473–494.
- Hatch, P., Wiegert, P.A., 2015. On the rotation rates and axis ratios of the smallest known near-Earth asteroids-The archetypes of the Asteroid Redirect Mission targets. *planets* 111, 100–104. <https://doi.org/10.1016/j.pss.2015.03.019> arXiv:1503.07454.
- Howell, E.S., Jan. 1995. Probing Asteroid Composition Using Visible and Near-infrared Spectroscopy. Ph.D. thesis. THE UNIVERSITY OF ARIZONA.
- Landolt, A.U., 1992. UBVR photometric Standard Stars in the Magnitude Range 11.5–16.0 Around the Celestial Equator, *Aj*, vol 104, pp. 340–371. <https://doi.org/10.1086/116242>.
- Lin, C.-H., Ip, W.-H., Lin, Z.-Y., Cheng, Y.-C., Lin, H.-W., Chang, C.-K., 2018. Photometric survey and taxonomic identifications of 92 near-Earth asteroids. *Plan* 152, 116–135. <https://doi.org/10.1016/j.pss.2017.12.019>.
- Lomb, N.R., 1976. Least-squares frequency analysis of unequally spaced data. *apss* 39, 447–462. <https://doi.org/10.1007/BF00648343>.
- M. P. Center, 2018. Unusual minor planets - overview. Retrieved 16 January 2018. <https://www.minorplanetcenter.org/jau/lists/Unusual.html>.
- Mainzer, A., Grav, T., Masiero, J., Hand, E., Bauer, J., Tholen, D., McMillan, R.S., Spahr, T., Cutri, R.M., Wright, E., Watkins, J., Mo, W., Maleszewski, C., 2011. NEOWISE Studies of Spectrophotometrically Classified Asteroids: Preliminary Results, *Apj*, vol 741, p. 90. <https://doi.org/10.1088/0004-637X/741/2/90> arXiv: 1109.6407.
- Odden, C.E., Verhaegh, J.C., McCullough, D.G., Briggs, J.W., 2013. Lightcurve analysis for near-earth asteroid 2012 TC4. *Minor Planet Bulletin* 40, 176–177.
- Polishook, D., 2013. Fast rotation of the NEA 2012 TC4 indicates a monolithic structure. *Minor Planet Bulletin* 40, 42–43.
- Ryan, W., Ryan, E.V., 2017. Spin state of returning fly-by near earth asteroid 2012 TC4. In: *AAS/Division for Planetary Sciences Meeting Abstracts #49, Vol. 49 of AAS/Division for Planetary Sciences Meeting Abstracts*, 204.06.
- Sonka, A.B., Gornea, A.L., Anghel, S., Birlan, M., 2017. Photometric observations of near earth asteroid 2012 TC4. *Rom. Astron. J.* 27, 223–231.
- Tonry, J.L., Stubbs, C.W., Lykke, K.R., Doherty, P., Shivvers, I.S., Burgett, W.S., Chambers, K.C., Hodapp, K.W., Kaiser, N., Kudritzki, R.-P., Magnier, E.A., Morgan, J.S., Price, P.A., Wainscoat, R.J., 2012. The Pan-STARRS1 photometric system. *APJ (Acta Pathol. Jpn.)* 750, 99. <https://doi.org/10.1088/0004-637X/750/2/99> arXiv:1203.0297.
- Usui, F., Kasuga, T., Hasegawa, S., Ishiguro, M., Kuroda, D., Müller, T.G., Ootsubo, T., Matsuhara, H., 2013. arXiv:1211.2889. Albedo Properties of Main Belt Asteroids Based on the All-sky Survey of the Infrared Astronomical Satellite AKARI, *Apj*, vol 762, p. 56. <https://doi.org/10.1088/0004-637X/762/1/56>.
- Warner, E., Nea 2012 tc4 - physical properties (2018). http://2012tc4.astro.umd.edu/2012TC4_properties.shtml.
- Warner, B.D., 2013. Asteroid lightcurve analysis at the palmer divide observatory: 2012 september - 2013 january. *Minor Planet Bulletin* 40, 71–80.
- Warner, B.D., Harris, A.W., Pravec, P., 2009. The asteroid lightcurve database. *Icarus* 202, 134–146. <https://doi.org/10.1016/j.icarus.2009.02.003>.

The fast, luminous ultraviolet transient AT2018cow: extreme supernova, or disruption of a star by an intermediate-mass black hole?

Daniel A. Perley¹  ¹★ Paolo A. Mazzali,^{1,2} Lin Yan,³ S. Bradley Cenko,^{4,5} Suvi Gezari,⁵ Kirsty Taggart,¹ Nadia Blagorodnova,³ Christoffer Fremling,³ Brenna Mockler,^{6,7} Avinash Singh^{8,9} , Nozomu Tominaga,^{10,11} Masaomi Tanaka,¹² Alan M. Watson,¹³ Tomás Ahumada,⁵ G. C. Anupama,⁸ Chris Ashall,¹⁴ Rosa L. Becerra,¹³ David Bersier,¹ Varun Bhalerao,¹⁵ Joshua S. Bloom,¹⁶ Nathaniel R. Butler,¹⁷ Chris Copperwheat,¹ Michael W. Coughlin³ , Kishalay De,³ Andrew J. Drake,³ Dmitry A. Duvvuri,³ Sara Frederick,⁵ J. Jesús González,¹³ Ariel Goobar¹⁹ , Marianne Heida³ , Anna Y. Q. Ho,³ John Horst,²⁰ Tiara Hung,⁵ Ryosuke Itoh,²¹ Jacob E. Jencson,³ Mansi M. Kasliwal³ , Nobuyuki Kawai,²¹ Tanazza Khanam,¹⁵ Shrinivas R. Kulkarni,^{3,18} Brajesh Kumar⁸ , Harsh Kumar,¹⁵ Alexander S. Kuttyrev,^{4,5} William H. Lee,¹³ Keiichi Maeda,²² Ashish Mahabal,^{3,23} Katsuhiko L. Murata,²¹ James D. Neill,³ Chow-Choong Ngeow,²⁴ Bryan Penprase,²⁵ Elena Pian,²⁶ Robert Quimby,^{10,20} Enrico Ramirez-Ruiz,^{6,27} Michael G. Richer,¹³ Carlos G. Román-Zúñiga²⁸ , D. K. Sahu,⁸ Shubham Srivastava,¹⁵ Quentin Socia,²⁰ Jesper Sollerman,²⁹ Yutaro Tachibana²¹ , Francesco Taddia,²⁹ Samaporn Tinyanont,³ Eleonora Troja,^{4,5} Charlotte Ward,⁵ Jerrick Wee³⁰ and Po-Chieh Yu²⁴

Affiliations are listed at the end of the paper

Accepted 2018 December 10. Received 2018 December 10; in original form 2018 August 3

ABSTRACT

Wide-field optical surveys have begun to uncover large samples of fast ($t_{\text{rise}} \lesssim 5$ d), luminous ($M_{\text{peak}} < -18$), blue transients. While commonly attributed to the breakout of a supernova shock into a dense wind, the great distances to the transients of this class found so far have hampered detailed investigation of their properties. We present photometry and spectroscopy from a comprehensive worldwide campaign to observe AT 2018cow (ATLAS 18qqn), the first fast-luminous optical transient to be found in real time at low redshift. Our first spectra (<2 days after discovery) are entirely featureless. A very broad absorption feature suggestive of near-relativistic velocities develops between 3 and 8 days, then disappears. Broad emission features of H and He develop after >10 days. The spectrum remains extremely hot throughout its evolution, and the photospheric radius contracts with time (receding below $R < 10^{14}$ cm after 1 month). This behaviour does not match that of any known supernova, although a relativistic jet within a fallback supernova could explain some of the observed features. Alternatively, the transient could originate from the disruption of a star by an intermediate-mass black hole, although this would require long-lasting emission of highly super-Eddington thermal radiation. In either case, AT 2018cow suggests that the population of fast luminous transients represents a new class of astrophysical event. Intensive follow-up of this event in its late phases, and

* E-mail: d.a.perley@ljmu.ac.uk

of any future events found at comparable distance, will be essential to better constrain their origins.

Key words: Black hole – stars – supernovae: general – supernova: individual: AT2018cow.

1 INTRODUCTION

The development of sensitive, wide-area digital optical sky surveys has led to the discovery of populations of rare, luminous extragalactic transients that evolve on time-scales of just a few days — much faster than typical supernovae, whose light curves are governed by the decay of ^{56}Ni within a massive envelope and typically take weeks to months to fade. Many of these have been reasonably well-explained by known phenomena: shock-breakout flashes from supernovae (e.g. Ofek et al. 2010; Shivvers et al. 2016; Arcavi et al. 2017), early emission from relativistic supernovae (Whitesides et al. 2017), or the shockwave afterglows from gamma-ray bursts (Cenko et al. 2013, 2015; Bhallerao et al. 2017; Stalder et al. 2017).

Other objects are more mysterious, however, and still lack a convincing explanation or firm spectroscopic identification. In particular, populations of optical transients with luminosities comparable to or exceeding those of the most luminous core-collapse supernovae, but rise times of only a few days, have been reported by a variety of different surveys (Drout et al. 2014; Arcavi et al. 2016; Tanaka et al. 2016; Pursiainen et al. 2018; Rest et al. 2018). Nearly all of these events (dubbed fast-evolving luminous transients by Rest et al. 2018) were found at great distances ($z > 0.1$) where they are difficult to study. Furthermore, most were not recognized as unusual events in real time, preventing the acquisition of essential follow-up observations. The few spectra that are available tend to show only featureless blue continua. Because of their origins in star-forming galaxies, these transients are widely interpreted as supernovae, but strong constraints are lacking.

Fortunately, our ability to find and identify fast transients continues to improve, and several surveys are now monitoring almost the entire sky at cadences of a few days or less. The Asteroid Terrestrial-impact Last Alert System (ATLAS; Tonry et al. 2018) observes most of the visible Northern sky down to 19 mag every ~ 2 nights. The Zwicky Transient Facility (ZTF; Kulkarni 2018) observes a similar area to 20.5 mag every three nights, and a significant fraction of it at much higher cadence. ASAS-SN (Shappee et al. 2014) monitors both hemispheres nightly to ~ 17 mag. With these capabilities, it is now possible to find and identify transients in (almost) real time over most of the night sky.

In this paper, we present a detailed observational study of the first fast high-luminosity transient to be identified in the nearby Universe in real time: AT2018cow, discovered by the ATLAS survey and independently detected by ZTF and ASAS-SN. We present our extensive, worldwide observational campaign in Section 2, focusing on observations at ultraviolet, optical, and near-infrared wavelengths (the multiwavelength view of this transient is presented by Ho et al. 2018). We summarize the key properties of this event in Section 3, and illustrate the ways in which AT2018cow is distinct from any well-established class of transient in Section 4. In Section 5, we consider two possible explanations for its origin: a jet-driven supernova erupting into a dense envelope of circumstellar matter, or, alternatively, the tidal disruption of a star around an intermediate-mass black hole located in a small galaxy’s spiral arm. Both models have significant difficulties explaining the full suite of observations, and our observations suggest that the origins of fast luminous transients may be significantly more exotic and complex than previously assumed. We summarize our

results and examine future directions in fast-transient research in Section 6.

2 OBSERVATIONS

2.1 Discovery and pre-imaging constraints

AT2018cow¹ was discovered and promptly announced via the Astronomers Telegram (Smartt et al. 2018) by ATLAS; the discovery and early data are described in detail by Prentice et al. 2018. The first detection of the transient was an image taken at 2018-06-16 10:35:02 UT (MJD 58285.441), appearing as a strikingly bright (14.7 ± 0.1 mag in the ATLAS *o*-band) optical source coincident with the galaxy CGCG 137-068 ($z = 0.0141$, $d = 60$ Mpc; Abolfathi et al. 2018)². The preceding ATLAS observation of the field, four days earlier (MJD 58281.48), registered no detection of any transient object at the same location to a magnitude limit of $o > 20.2$ mag, implying brightening by almost 5 mag within this period. Independent imaging by the Palomar 48-inch telescope (P48) as part of the ZTF public Northern Sky Survey later moved the time of last non-detection one day closer, to only three days before the first ATLAS detection ($i > 19.5$ at MJD 58282.172; Fremling 2018). The ASAS-SN non-detection reported by Prentice et al. 2018 ($g > 18.9$ at MJD 58284.13) provides an even tighter constraint: a rise of > 4.2 magnitudes over < 1.3 days.

A fast rise to a very high optical luminosity ($M < -19$ mag) is unusual for supernovae but similar to cosmological fast-transients of the types discussed in the introductory paragraph. Motivated by these unusual characteristics, we initiated a campaign of observations via the GROWTH (Global Relay of Observatories Watching Transients Happen) network, a world-wide collaboration of predominantly small telescopes co-operating in the study of energetic time-domain phenomena. We also observed it under other telescopic programs. Our observing campaign is described in detail below.

2.2 Ground-based imaging observations

Nightly imaging observations were acquired with the Infrared-Optical imager on the robotic Liverpool Telescope (LT; Steele et al. 2004) in both optical (IO:O) and near-infrared (IO:I) bands. We typically observed with the full suite of available filters (*uBgVrizH*) although on some nights a more limited set was obtained. We also obtained frequent imaging from a variety of other facilities. These include the CCD imager on the Mount Laguna Observatory (MLO; Smith & Nelson 1969) 1 m telescope, the EMCCD demonstrator camera on the Kitt Peak 84-inch telescope (KP84), ANDICAM on the 1.5 m telescope at the Cerro Tololo Interamerican Observatory, the Himalayan Faint Object Spectrograph Camera (HFOSC) on

¹The name of this transient was assigned automatically by the Transient Name Server (<https://wis-tns.weizmann.ac.il/>). It was later redesignated SN2018cow following the emergence of broad features in the spectrum, although we argue here that a SN association is not definite and retain the AT designation. The transient is also known as ATLAS18qqn and as ZTF18abcfcoo.

²We assume $h = 0.7$, $\Omega_M = 0.3$, $\Omega_\Lambda = 0.7$.

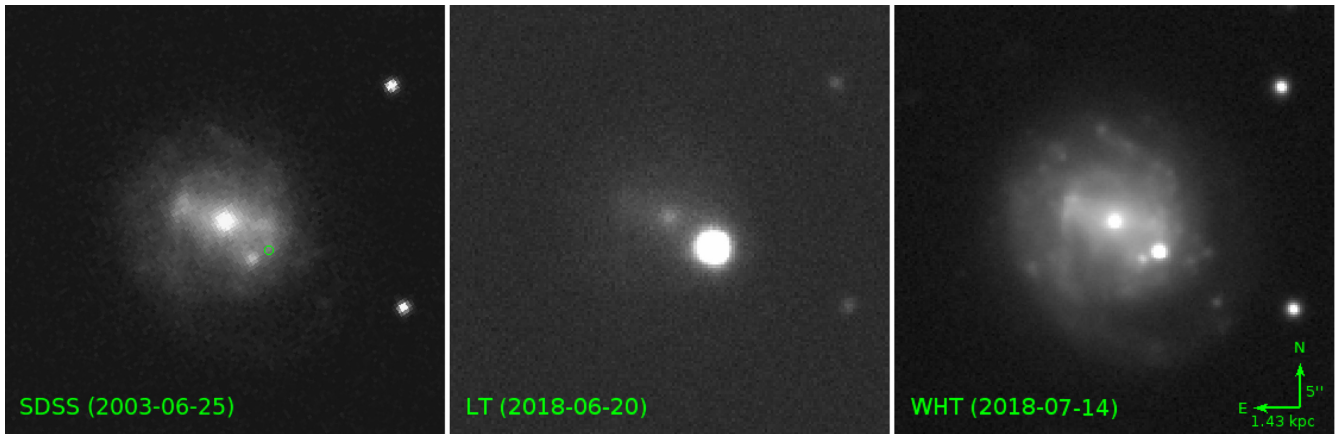


Figure 1. Pre-explosion imaging of AT2018cow from the Sloan Digital Sky Survey compared to imaging with the Liverpool Telescope taken shortly after peak and deep later-time imaging from the William Herschel Telescope. The transient is significantly brighter than its host galaxy at peak. The galaxy itself shows a barred morphology and weak spiral features, one of which underlies the transient. A point-source located at the galaxy nucleus is likely to be a weak AGN, while a fainter compact source slightly southeast of the transient is likely an H II region. No point source lies under the transient itself (position designated by a green circle in left-hand panel), and there are no obvious merger indicators.

the 2 m Himalayan Chandra Telescope (HCT), the COATLI 50 cm Telescope (Watson et al. 2016) at the Observatorio Astronómico Nacional in Sierra San Pedro Mártir, and the Reionization and Transients Infrared instrument (RATIR; Butler et al. 2012; Watson et al. 2012) on the 1.5 m Harold L. Johnson telescope (also at San Pedro Mártir). Observations were taken less regularly with the 0.4 m (SLT) and 1.0 m (LOT) telescopes at Lulin Observatory in Taiwan, the MITSuME 50 cm telescope of Akeno Observatory in Japan, and with the Wide-Field Infrared Camera (WIRC) at the Palomar 200 inch Hale Telescope. Finally, a single epoch of deep r -band imaging was acquired using the Auxiliary Port Camera (ACAM) on the William Herschel Telescope.

Images were reduced using standard methods. A dithered sequence of NIR frames was not available for the ANDICAM NIR images and simple pair subtraction was used to remove the sky.

Host galaxy contribution to the transient flux is not insignificant (especially at late times; Fig. 1). We used a custom image-subtraction tool written in IDL to remove the host galaxy flux from all ground-based optical images consistently by convolving both the transient image and a template image to a common PSF, then subtracting. Imaging from the Sloan Digital Sky Survey (SDSS; Abolfathi et al. 2018) was used to subtract the $ugriz$ measurements. For non-SDSS optical filters ($UBVRI$), we averaged two adjacent filters: e.g. to simulate a B -band image we took a weighted average of the aligned u and g images. The relative weights for each synthetic filter were estimated based on the relative magnitude weights from the Lupton transformation equations.³

Host subtraction for the NIR images is more challenging; the only available pre-explosion reference is the Two Micron All Sky Survey (2MASS), which is shallow and has a very broad PSF. We instead used an SDSS z -band image, but adjusted the flux scale visually to ensure that the extended features of the host galaxy are removed. Photometry was performed uniformly on the subtracted images using a custom IDL-based aperture photometry tool. Calibration of the field was established by comparison of stars in unsubtracted images to SDSS (or, for NIR images, to 2MASS). SDSS $ugriz$

magnitudes of calibration stars are transformed via the Lupton equations to $BVRI$.

The transient is very blue compared to any other object in the field: for example, the transient $u - g$ colour is typically ~ -0.4 for most of its evolution, compared to a range between $+1.48$ and $+3.04$ for bright stars within $5'$. This greatly magnifies the impact of small differences between filter transmission curves for different telescopes (and other wavelength-dependent transmission differences), leading to offsets between different instruments.

Colour terms for the LT optical filters have been determined by Smith & Steele (2017). We colour-corrected SDSS reference stars in the field to the LT system, setting the zeropoint of the transformation as appropriate for an AB colour of 0.0 in all filters. We then recalculated the magnitudes of a series of SDSS bright reference star magnitudes using a set of LT exposures taken under the best weather conditions, and used these as secondary standards for the photometry of all LT images (we employ aperture photometry via a custom routine and seeing-matched apertures.) An additional minor adjustment was made to the B filter (-0.05 mag) to match our spectrophotometry (Section 2.6). For all other telescopes, we calibrated directly to the SDSS magnitudes, but applied an additional, filter-specific constant adjustment to align each filter to the interpolated LT curve in the same filter and remove any systematic offset.

A subset of our photometry is presented in Table 1, and the light curves are plotted in Fig. 2.

2.3 Swift observations

Observations of AT2018cow using the Neil Gehrels Swift Observatory (*Swift*; Gehrels et al. 2004) began at MJD 58288.442. Data were collected with both the Ultraviolet-Optical Telescope (UVOT; Roming et al. 2005) and the X-ray Telescope (XRT; Burrows et al. 2005). The transient was well-detected in both instruments (e.g. Rivera Sandoval & Maccarone 2018) and remained so for the entire monitoring period discussed in this paper.

Raw UVOT images were processed by the pipeline provided by the *Swift* Data Center at the Goddard Space Flight Center (GSFC). The reduced level 2 sky images were downloaded for photometry. We used the software package `uvotsource` and

³<http://www.sdss3.org/dr8/algorithms/sdssUBVRITransform.php>

Table 1. Early photometric observations of AT2018cow from our campaign. No correction for Galactic extinction has been applied. A machine-readable table of all 949 photometric data points will be made available online.

MJD	Instrument	Filter	AB magnitude
58287.2674	P60/SEDM	r	13.93 ± 0.03
58288.3405	P60/SEDM	r	14.18 ± 0.03
58288.4416	Swift/UVOT	w1	13.34 ± 0.05
58288.4421	Swift/UVOT	u	13.57 ± 0.05
58288.4426	Swift/UVOT	b	13.85 ± 0.04
58288.4442	Swift/UVOT	w2	13.29 ± 0.06
58288.4448	Swift/UVOT	v	14.06 ± 0.05
58288.4464	Swift/UVOT	m2	13.40 ± 0.05
58289.0227	LT/IO:O	u	13.97 ± 0.03
58289.0234	LT/IO:O	g	14.10 ± 0.03
58289.0241	LT/IO:O	r	14.35 ± 0.03
58289.0248	LT/IO:O	i	14.78 ± 0.03
58289.0255	LT/IO:O	z	15.01 ± 0.03
58289.1889	KP84/KPED	g	14.18 ± 0.03
58289.1901	KP84/KPED	r	14.43 ± 0.04
58289.1904	P60/SEDM	r	14.38 ± 0.03
58289.1963	KP84/KPED	U	14.03 ± 0.10
58289.2108	P60/SEDM	r	14.39 ± 0.03
58289.2229	Swift/UVOT	w1	13.55 ± 0.03
58289.2246	Swift/UVOT	u	13.92 ± 0.05
58289.2263	Swift/UVOT	b	14.14 ± 0.04
58289.2281	Swift/UVOT	w2	13.58 ± 0.03
58289.2298	Swift/UVOT	v	14.23 ± 0.04
58289.2331	Swift/UVOT	m2	13.63 ± 0.05
58289.3493	P60/SEDM	r	14.34 ± 0.03
58289.6299	HCT/HFOSC	R	14.67 ± 0.03
58289.6336	HCT/HFOSC	I	15.00 ± 0.03
58289.6365	HCT/HFOSC	V	14.37 ± 0.03
58289.6397	HCT/HFOSC	B	14.39 ± 0.03
58289.6434	HCT/HFOSC	U	14.24 ± 0.03
58289.9081	LT/IO:I	H	15.66 ± 0.03
58289.9131	LT/IO:O	z	15.15 ± 0.03
58289.9136	LT/IO:O	i	14.99 ± 0.03
58289.9142	LT/IO:O	r	14.62 ± 0.03
58289.9147	LT/IO:O	g	14.48 ± 0.03
58289.9154	LT/IO:O	u	14.31 ± 0.03

an aperture radius of 3", chosen to minimize the contamination from the extended host galaxy. The final photometry output from `uvotsource` was corrected for aperture loss using the curve-of-growth method.

The background was computed from an off-target sky region without any other sources using an aperture radius of 10". The image frames were visually inspected and frames with large pointing smearing were thrown away. For a small number of frames with slight PSF smearing, we used an aperture radius of 5". For frames with astrometric errors, we manually provide the correct centroids as the input to `uvotsource`.

As the UVOT PSF is stable, we subtracted off the estimated host galaxy contribution to the UVOT PSF in flux space rather than via image subtraction. Photometry from a final epoch (acquired 120.45 days after the reference epoch) was used to estimate the magnitudes within our aperture. In principle, this final epoch could have contained a small amount of transient flux, although the fact that the optical bands are fading steeply between 50 and 80 days while negligible fading is seen in the UVOT between 60 and 120 days suggest that this contribution is very small.)

The XRT data were analysed using an automated reduction routine following the techniques of Butler & Kocevski (2007) and binned to increase the *S/N*. We assume negligible host contamination (although we note that the galaxy likely hosts a weak AGN; Section 3.1).

2.4 Astrosat observations

AT2018cow was observed by the UltraViolet Imaging Telescope (UVIT; Kumar et al. 2012) on-board AstroSat on 2018-07-03 from 13:45:58 UT to 19:54:12 UT (ToO). These observations were performed in the FUV F172M filter with a total exposure time of 5667 s. Images were pre-processed with UVIT L2 pipeline. Aperture photometry was performed using IRAF using an 18-pixel (7.5") aperture, and calibrated following the calibration procedure mentioned in Tandon et al. (2017).

2.5 Other photometry

In addition to our own photometry, we also acquire data from public sources and the literature. In particular, we use the first two epochs of GROND observations from Prentice et al. (2018) to extend our multicolour optical-NIR coverage to earlier times: we caution that these observations are not host-subtracted or colour-corrected and the aperture size is unknown, although the transient was extremely bright at this time (~14 mag) and the host contribution should be negligible. We also use the first epoch of ATLAS photometry from Prentice et al. (2018), *r*-band data from the Palomar 48-inch telescope taken as part of the public ZTF Northern Sky Survey, the ZTF *i*-band point reported by Fremling (2018), and the ASAS-SN limit from Prentice et al. (2018). As these come from imaging-differenced surveys, no host correction is necessary.

2.6 Optical and near-IR spectroscopy

We conducted an extensive campaign to spectroscopically monitor the evolution of the transient at high cadence. Spectroscopic observations began at MJD 58287.268 (1.82 days after the first ATLAS detection, making this the earliest spectrum obtained of the transient that has been reported so far), and continued at least nightly and usually two to three times nightly during the first 12 days after peak. Sub-night cadence during this period was enabled by observations using spectrographs in California, the Canary Islands, and India: specifically, the SED Machine (SEDM) on the Palomar 60-inch Telescope (Blagorodnova et al. 2018), the Spectrograph for the Rapid Acquisition of Transients (SPRAT; Piascik et al. 2014) on the Liverpool Telescope, and the Himalayan Faint Object Spectrograph Camera (HFOSC) on the the Himalayan Chandra Telescope.

Additional spectra were obtained less regularly and at later phases using larger telescopes: the DeVeny spectrograph at the Discovery Channel Telescope (DCT), the Andalucia Faint Object Spectrograph and Camera (ALFOSC) on the Nordic Optical Telescope (NOT), the Double-Beam Spectrograph (DBSP; Oke & Gunn 1982) and the TripleSpec near-infrared spectrograph on the 200-inch Hale Telescope, the Gemini Multi-Object Spectrograph (GMOS) on Gemini-North, and the Low-Resolution Imaging Spectrograph (LRIS; Oke et al. 1995) at Keck Observatory. A log of all spectroscopic observations can be found in Table 2, and all spectra are plotted in Fig. 3.

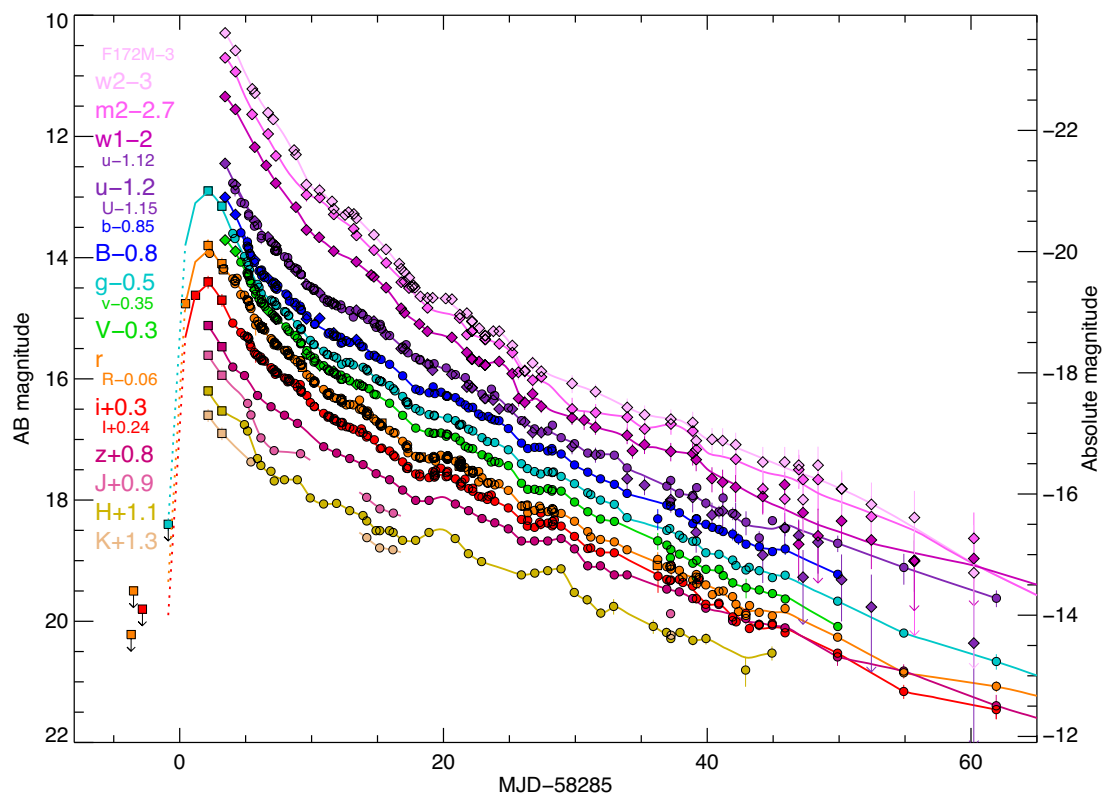


Figure 2. Multiband light curves of the ultraviolet, optical, and near-infrared transient AT2018cow. Small offsets have been applied to the filters for clarity (shown at left). The offsets for the R , I , and U bands, and of the Swift optical filters, have been chosen to align them with the closest optical bands. Only the earliest ZTF and ATLAS observations show a rise: from the first epoch of follow-up the transient fades monotonically with time and experiences no subsequent rise in any band, except for short-lived 1–2 day flares in the near-IR. The coloured curves show a non-parametric interpolation of the observed points in each filter. The line segments on the rise show a simple linear interpolation or the early transient based on available ATLAS, ZTF, and ASAS-SN data assuming no colour evolution. Circles show our ground-based data, diamonds show space-based data, and squares indicate photometric measurements from the literature. Arrows on error bars indicate marginal ($<2\sigma$) UVOT detections.

LT/SPRAT and P60/SEDM data were processed by automated reduction pipelines designed for each facility.⁴ The LPipe reduction pipeline⁵ (Perley et al. in prep) was used to process the LRIS data. Reductions for the remaining spectrographs were performed manually using standard IRAF tools.

After initial reduction and flux calibration, all spectra were absolutely calibrated by comparing synthetic photometry of the spectrum to photometry from our imaging data. The absolute flux scale is established by comparing synthetic r -band photometry calculated from each spectrum to our (true) r -band photometry, interpolated to the appropriate epoch. To correct for imperfections in the calibration related to atmospheric attenuation or wavelength-dependent slit losses, we next colour-correct the spectrum by comparing a synthetic $g - r$ colour to the true photometric $g - r$ colour, and warping the spectra by a power-law correction factor.⁶ Since the spectra unavoidably include some host-galaxy light, we

re-add an estimate of the host-galaxy flux within the slit to the photometry (estimated given the size of the slit and using our host-galaxy model; Section 3.5) prior to the photometric correction, and subtract the host-galaxy model after correction.

3 OBSERVATIONAL PROPERTIES

3.1 Environment and pre-explosion constraints

The transient lies on the sky coincident with the catalogued galaxy CGCG 137-068, an unremarkable dwarf spiral galaxy showing a faint bar and spiral arms (Fig. 1). Two sources are present within the SDSS and PS1 pre-imaging of the galaxy: a reddish point source at the galaxy nucleus (likely a weak AGN) and a compact, but not truly point-like, source approximately $1.9''$ east-southeast of the transient (probably an HII region). AT 2018cow is located far from the centre of the galaxy ($5.9''$ or 1.7 kpc from the nucleus), and no point or pointlike source is visible at the location of the transient itself. Forced photometry on a median-filtered PS1 image limits any contribution from an unresolved source to $g > 22.2$, $r > 22.3$, $i > 21.9$: more than eight magnitudes below the transient at peak.

Additionally, we checked for evidence of pre-explosion variability in both the Catalina Real-Time Survey and iPTF archives. We

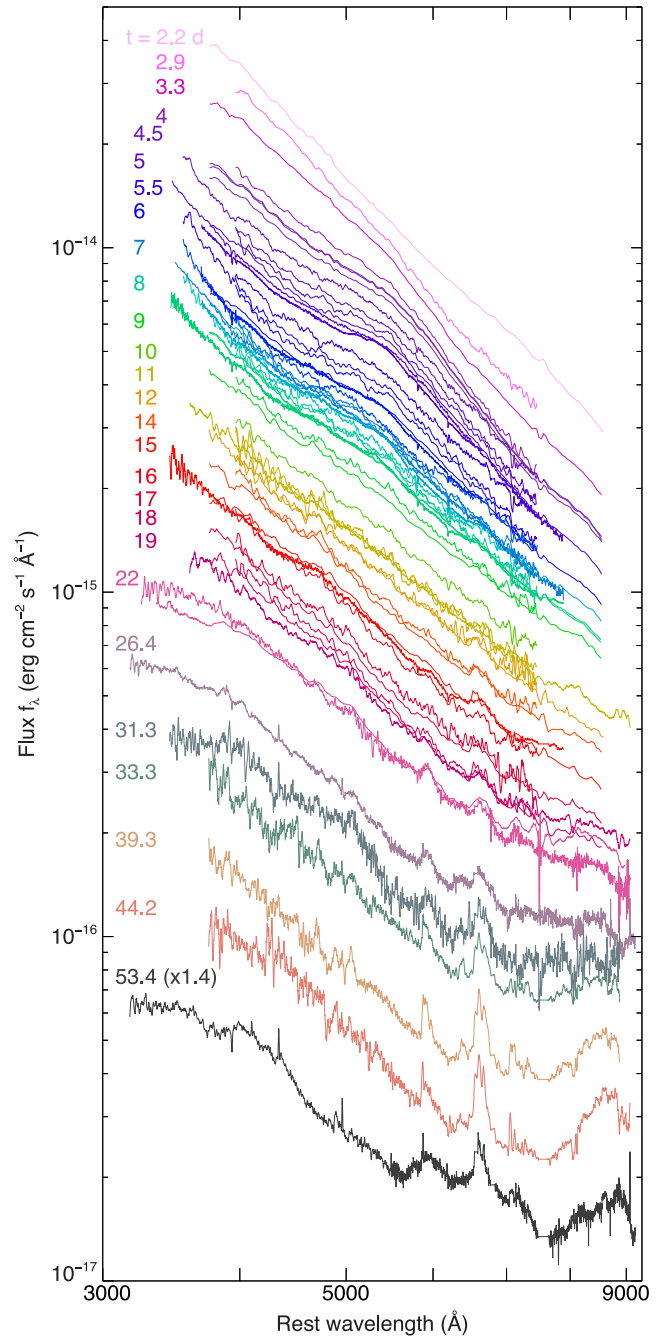
⁴The SEDM pipeline is described at <http://www.astro.caltech.edu/sedm/Pipeline.html>; the SPRAT pipeline is a modification of the pipeline for FrodoSpec (Barnsley, Smith & Steele 2012)

⁵<http://www.astro.caltech.edu/dperley/programs/lpipe.html>

⁶The colour correction was typically quite small: <0.1 mag in nearly all cases.

Table 2. Log of spectroscopic observations of AT2018cow. Times are relative to the reference epoch of MJD 58285.

MJD	t (d)	Exp. (s)	Telescope	Instrument
58287.268	2.268	1600	P60	SEDM
58287.949	2.949	300	LT	SPRAT
58288.341	3.341	1600	P60	SEDM
58289.000	4.000	180	LT	SPRAT
58289.191	4.191	1600	P60	SEDM
58289.211	4.211	1600	P60	SEDM
58289.350	4.350	1600	P60	SEDM
58289.651	4.651	900	HCT	HFOSC
58289.946	4.946	180	LT	SPRAT
58290.097	5.097	450	LT	SPRAT
58290.196	5.196	2500	P60	SEDM
58290.261	5.261	250	DCT	DeVeny
58290.353	5.353	300	P200	DBSP
58290.327	5.327	1800	Gemini-N	GMOS
58290.618	5.618	1200	HCT	HFOSC
58291.020	6.020	450	LT	SPRAT
58291.224	6.224	2500	P60	SEDM
58291.276	6.276	4800	P200	TripleSpec
58291.337	6.337	1800	Gemini-N	GMOS
58291.636	6.636	1000	HCT	HFOSC
58291.939	6.939	240	LT	SPRAT
58292.027	7.027	450	LT	SPRAT
58292.145	7.145	180	DCT	DeVeny
58292.181	7.181	2500	P60	SEDM
58292.374	7.374	1800	Gemini-N	GMOS
58292.648	7.648	1200	HCT	HFOSC
58292.955	7.955	300	LT	SPRAT
58293.018	8.018	450	LT	SPRAT
58293.182	8.182	2500	P60	SEDM
58293.212	8.212	2500	P60	SEDM
58293.288	8.288	1800	Gemini-N	GMOS
58293.821	8.821	1200	HCT	HFOSC
58293.892	8.892	300	LT	SPRAT
58294.182	9.182	2500	P60	SEDM
58294.656	9.656	1200	HCT	HFOSC
58294.989	9.989	300	LT	SPRAT
58295.894	10.894	240	LT	SPRAT
58296.017	11.017	600	NOT	ALFOSC
58296.103	11.103	450	LT	SPRAT
58296.913	11.913	240	LT	SPRAT
58297.245	12.245	2500	P60	SEDM
58297.349	12.349	1800	P200	TripleSpec
58298.916	13.916	240	LT	SPRAT
58299.212	14.212	2500	P60	SEDM
58299.766	14.767	2400	HCT	HFOSC
58300.180	15.180	2500	P60	SEDM
58300.389	15.389	900	Gemini-N	GMOS
58300.622	15.622	2400	HCT	HFOSC
58300.896	15.896	240	LT	SPRAT
58301.990	16.990	600	LT	SPRAT
58302.275	17.275	2500	P60	SEDM
58302.908	17.908	360	LT	SPRAT
58303.180	18.180	2500	P60	SEDM
58304.000	19.028	900	NOT	ALFOSC
58307.034	22.034	900	NOT	ALFOSC
58307.301	22.301	1200	P200	DBSP
58311.397	26.397	1800	Keck I	LRIS
58316.345	31.345	600	P200	DBSP
58318.295	33.295	1200	Gemini-N	GMOS
58324.300	39.300	1800	Gemini-N	GMOS
58329.254	44.254	1800	Gemini-N	GMOS
58338.359	53.359	3180	Keck I	LRIS

**Figure 3.** Our full sequence of spectroscopic observations of AT2018cow. Numbers indicate the time in days since MJD 58285; between days 4 and 22, they indicate approximate times. No scaling has been applied: the relative offsets are due to the intrinsic, steady fading of the source. (The $t = 31.3$ d and $t = 53.4$ d spectra have been slightly scaled for clarity.) We interpolate over host narrow features and (when not corrected) over the telluric A + B bands. Obvious spectral features develop only at late times, although a very broad, blue dip is visible in all spectra between 4 and 8 days post-explosion.

found no evidence for any previous outbursts from the location of the transient.

3.2 A fast, consistently blue transient

Light curves of the transient, assembled by our worldwide telescope network, are shown in Fig. 2. The photometric properties alone

Table 3. Key properties of AT 2018cow.

z	0.0140	Redshift (from host emission)
t_{rise}	~ 2.5 d	Rise time to peak (g)
$t_{\text{rise}, 1/2}$	~ 1.5 d	Time to rise from half-max (r)
$t_{\text{decline}, 1/2}$	~ 3 d	Time to decay to half-max (r)
$M_{g, \text{peak}}$	-20.4	Peak g absolute magnitude
$M_{r, \text{peak}}$	-19.9	Peak r absolute magnitude
$L_{\text{bol}, \text{peak}}$	4×10^{44} erg s $^{-1}$	UVOIR luminosity at optical peak
T_{char}	17000 K	Characteristic temperature
E_{rad}	5×10^{49} erg	Total UVOIR radiative output
v_{spec}	6000 km s $^{-1}$	Velocity width of late emission lines
$M_{*, \text{host}}$	$1.4 \times 10^9 M_{\odot}$	Host stellar mass
SFR_{host}	$0.22 M_{\odot} \text{yr}^{-1}$	Host star-formation rate

exhibit several remarkable features unprecedented for any other extragalactic transient observed at this level of detail.

As we have already noted, the rise time is very fast. Comparing the ATLAS o discovery magnitude (which is dominated by r flux for this blue transient) to the GROND r magnitude indicates a rise from half-max of only 1–2 d. The ASAS-SN g –band limit suggests an explosion time of no more than 1 d prior to the discovery observation, giving a total time from explosion to peak of between 2 and 3 days.

The transient is extremely luminous at peak ($M_r \sim -19.9$ or $M_g \sim -20.4$). This is more luminous than any core-collapse supernova with the exception of a small fraction of Type II n and superluminous supernovae, both of which exhibit very long rise and decay times.

The fading, like the rise, is quite rapid. The time to decline to half of its peak flux is only about 4 days, and there is no subsequent rise to a second, radioactively powered peak: the light curve fades monotonically (except in the NIR, which exhibits minor but significant fluctuations on time-scales of 2–3 d). By around 25 d post-discovery, the transient has a luminosity ($M_r \sim -16$) well below that of a typical core-collapse supernova at the same phase.

Finally, the colour is extremely and persistently blue. In early observations, the colours are close to the Rayleigh–Jeans power-law limit, indicating a thermal origin with a spectral peak far into the UV (Section 3.4). Hot, blue early phases of supernovae are common (shortly after shock breakout and before adiabatic losses have cooled the ejecta), but AT 2018cow retains a high temperature for a remarkably long period: after a month, the optical colours are bluer than most SNe are even in their earliest phases and it remains well-detected in all UV filters.

These properties are summarized in Table 3. Prentice et al. (2018) also independently report the exceptionally fast evolution and blue colour of this transient, as does the recent analysis by Margutti et al. (2018).

3.3 Spectral evolution

The behaviour seen in the spectra is also unprecedented. The earliest spectra in our sequence (Fig. 4), sampling close to the peak time of the transient, show only a hot and smooth continuum: they are particularly lacking in emission or absorption features, except for weak emission from host galaxy H α (not shown in our figures since we interpolate over the host narrow lines). There is no sign of any flash-ionized emission features (e.g. Gal-Yam et al. 2014; Khazov et al. 2016; Yaron et al. 2017).

Beginning around MJD 58299 (day 4 on our plots), a single, extremely broad feature begins to emerge in all of our spectra

and in our photometry. If interpreted as an absorption trough, its centre is at approximately 4600 Å with a full-width of 1500 Å. It is vaguely reminiscent of the Fe II feature seen in broad-lined Ic supernovae around peak light (e.g. Galama et al. 1998), a resemblance that led to early suggestions of a Ic-BL classification (Xu et al. 2018; Izzo et al. 2018). Simultaneously with the emergence of this feature, a very bright radio/submillimeter afterglow was detected (Bright et al. 2018; Dobie et al. 2018; de Ugarte Postigo et al. 2018) which — at the time — seemed to seal the Ic-BL association and led to anticipation that these features would strengthen and a supernova peak would emerge shortly in the light curve.

This is not what happened: while the feature strengthens slightly between days 4 and 5, from then on it begins to dissipate and by day 8 it vanishes entirely, returning to a largely featureless blue continuum (Perley et al. 2018).

Very different evolution sets in after this time. First, a weak and moderately-broad (full-width ~ 200 Å; $v \sim 10\,000$ km s $^{-1}$) emission feature centred at ≈ 4850 Å begins to emerge: it is difficult to recognize because spectra during this period are of low quality owing to the presence of the nearly-full moon, but is seen consistently in both the LT and the SEDM spectra on days 9, 11, 12, and 14 (Fig. 5); it was also independently seen in NOT spectra reported by (Benetti et al. 2018). Its most likely interpretation is He II $\lambda 4686$. The line fades thereafter, but a variety of other lines of similar velocity width and offset begin to appear between 20 and 30 days. Emission features of He I $\lambda 5876$ and He I $\lambda 5015$ are clearly visible starting at ~ 15 days, along with emission from H α (in a blend with He I $\lambda 6678$), H β , H γ , H δ , and a blend of several higher Balmer lines. All of these lines are significantly and consistently offset to the red by about +3000 km s $^{-1}$ at the time of first detection. However, over the subsequent 10–20 d, the profiles evolve blueward, developing a ‘wedge’ shape: the peak (which often contains a weak narrow component) is very close to the rest-frame wavelength, with a steep fall towards the blue and a very gradual one towards the red (Fig. 6). Additional lines, including He I $\lambda 7065$, weak Ca II] $\lambda \lambda 7291, 7324$, and (possibly) O I $\lambda \lambda 6300, 6363$ also begin to emerge at later times (> 30 d). A very strong, broad upturn between 8000 and 9000 (also easily visible in the photometry as a z -band excess) emerges around this time as well, although its origin is unclear: its wavelength is close to that of the Ca II IR triplet but it is much broader than would be expected from this feature alone if it has a similar profile as the H and He lines, especially on the blue wing.

3.4 Physical properties

To characterize the early SED, we first construct coeval sets of photometry by performing a nonparametric interpolation of the light curve for each filter (the same procedure was used in the g and r bands to colour-correct the spectroscopy; Section 2.6). Galactic extinction is corrected using the Fitzpatrick (1999) attenuation curve and $E_{B-V} = 0.07$ (Schlafly & Finkbeiner 2011). We assume no extinction in the host galaxy.

The early SEDs are unambiguously thermal. The UVOIR slope ($F_{\nu} \propto \nu^{\alpha}$) during the first epoch is $\alpha = 1.2 \pm 0.1$ as measured between the u and the z bands: close to the Rayleigh–Jeans $\alpha = 2$ and inconsistent (in particular) with synchrotron emission, which exhibits $\alpha = 0.33$ below the peak frequency and -0.5 to -1.25 above it (e.g. Sari, Piran & Narayan 1998). The colour of the transient becomes gradually less blue as time passes, but it remains effectively thermal throughout, with the peak (in νF_{ν}) remaining in the UV at all times.

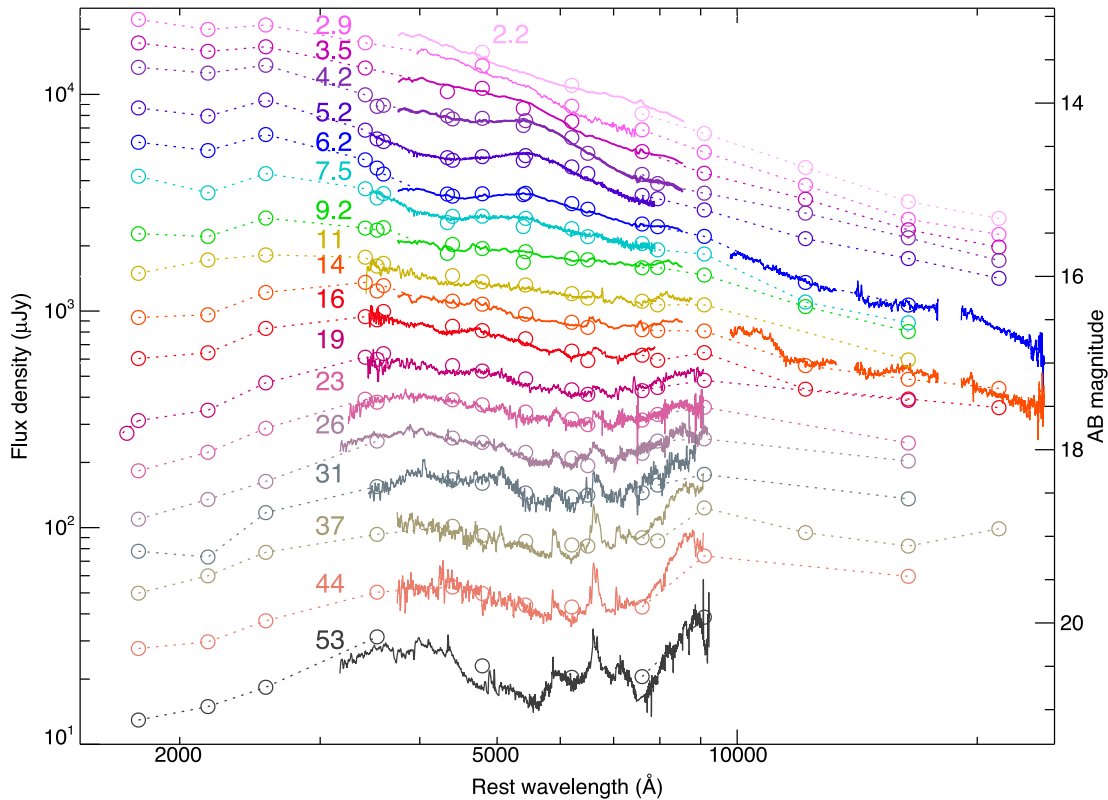


Figure 4. Spectral energy distribution (in f_{ν}) sequence of AT2018cow from the UV to the NIR, with selected spectra overplotted. (The closest high-quality spectrum to each photometric reference epoch is shown, rescaled by a constant factor to match the absolute flux level). The spectrum is initially (days 2–3) hot and featureless. A broad absorption feature develops in the UV/blue region of the spectrum starting around day 4, but disappears again by day 9. Narrower features begin to emerge after >10 days, and the NIR bands become dominated by a red SED component that peaks around 10 000 Å. Our photometry and spectroscopy show good consistency (except in z -band at late times). In particular, both show the early, broad spectral feature between 3500 and 5500 Å.

To characterize the evolution of the photosphere, we fit a Planck function to the UV-optical data at the time of each UVOT epoch. A single Planck function fits the UV and most optical filters well at essentially every epoch, but underpredicts the NIR fluxes after a few days; it also cannot explain the persistent “dip” seen in the uBg filters in several early optical observations (Fig. 7). We thus exclude the uBg filters from the fits, and add an additional red component to the model. The form of this red component is not well-constrained by our data (our light curve coverage in the NIR is very incomplete outside the H -band). We tried both a second blackbody and a power law; we obtain acceptable fits to most bands for a blackbody with a constant, low (~ 3000 K) temperature and a power law with spectral index ($F_{\nu} \propto \nu^{\alpha}$) of $\alpha \sim -0.75$. We prefer the power-law model: a warm blackbody is not well-justified theoretically (the observed temperature is too hot to be easily explained as dust, although similar red components have been seen in some SNe; e.g. Kangas et al. 2016), whereas a synchrotron power law of $\alpha \sim 0.5 - 1.0$ is expected given the bright radio afterglow (and an extrapolation of the flux to the millimeter band provides reasonable consistency with reported millimeter fluxes). The z -band at late times shows strong excess relative to either model and is excluded from our final fits. We fix the spectral index at $\alpha = -0.75$ for all epochs.

At very late times (>45 d), our ground-based coverage becomes sparse, due to both the fading of the transient and the shortening window of observations each night. At these times, we fix our epochs to the ground-based (LT) epochs, interpolating the low- S/N (but numerous) UVOT fluxes via local regression. We caution that

derived parameters in this regime are particularly uncertain due to the absence of NIR coverage, presence of emission features, and systematics associated with the host subtraction. For the last epoch (65 d), the power-law component could not be constrained and is fixed by extrapolation of the preceding epochs.

Results are plotted in Fig. 8 and listed in Table 4. At peak, the object is very hot (30 000 K) and already quite large in size, with an inferred radius of almost 10^{15} cm. This implies fast ejecta: given the ASAS-SN pre-explosion limit, the time of the first SED was only ~ 4 d after the initial explosion time and thus the expansion speed must exceed $>0.1 c$. Alternatively, the rapid expansion of the photosphere could imply a high-velocity shock traversing pre-existing, optically thick material. However, the broad absorption feature independently implies that this material must also be traveling at a velocity of $>0.1 c$ at this time, so if the transient is due to an explosion (cf. Section 5.2) it must represent part of the ejecta.

Surprisingly, after this initial rise, no further expansion is inferred: the photospheric radius *declines* continuously throughout our observations. This is extremely unusual for a supernova: normally, the photosphere expands with the expanding material in the early, optically-thick phases.

The temperature initially declines with time, as expected for most explosive transients. However, this parameter, too, begins to exhibit unusual evolution at later epochs: after 20 days, the temperature curve levels off and in subsequent epochs it actually *increases*, levelling off at about 17 000 K before possibly falling again in the

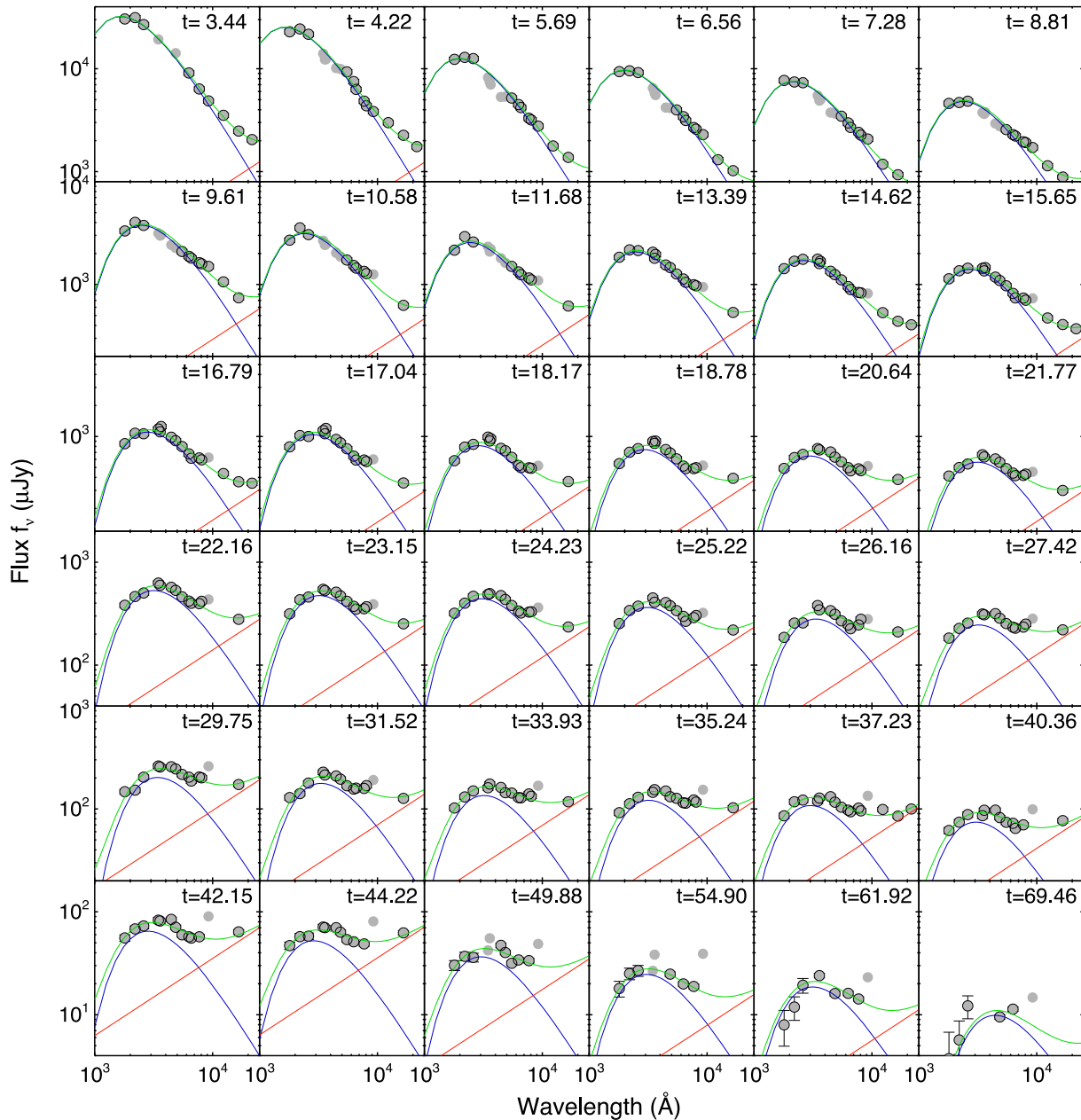


Figure 7. Fits to the multi-epoch photometry using a combined blackbody (blue curve) and power-law (red curve) model. The green curve shows the sum of these models. Data points that are not enclosed in circles are excluded from the fits, usually due to contamination by strong emission or absorption features.

well within the distribution. While clearly star-forming, the galaxy is not particularly young nor is it undergoing a notable burst of star-formation.

4 COMPARISONS TO PREVIOUS EVENTS

4.1 A fast extreme-luminosity transient seen up-close

The fast rise, early peak, and subsequent rapid decay do not resemble any common class of extragalactic transient. While supernovae can show early, luminous peaks associated with shock heating, these are inevitably followed by either a long plateau (as in SNe IIP or IIc) or by a second, radioactively powered peak (in SNe IIB, SNe Ib/c, and GRB-SNe). A few classical examples of this are

shown in the top row of Fig. 10: SN 1993J (Richmond et al. 1996; Barbon et al. 1995) and SN 2006aj (Campana et al. 2006; Ferrero et al. 2006), as well as the double-peaked superluminous supernova SN 2006oz (Leloudas et al. 2012). In all cases the late-time flux of these reference objects exceeds that of AT 2018cow by several magnitudes.

The rest of Fig. 10 shows comparisons between the light curve of AT 2018cow and a variety of luminous, fast-rising transients from different surveys. These transients are diverse, exhibiting differences in both temporal and colour evolution. Several retain a high luminosity for a long period and fail to replicate the fast fading of AT 2018cow. These include iPTF16asu (Whitesides et al. 2017), an initially featureless transient that later developed into a SN Ic-BL; all members of the Arcavi et al. (2016) sample (SNLS04D4ec,

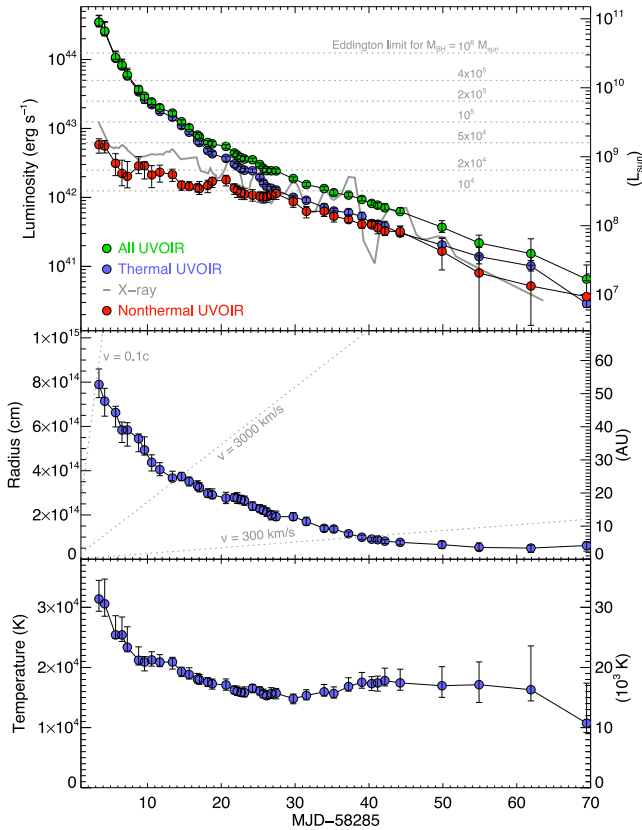


Figure 8. Physical properties based on the blackbody fits shown in Fig. 7. In the top panel, the green data points show the luminosity inferred by summing the total Stefan–Boltzmann luminosity of the thermal component and an integral of the power-law component for $\lambda > 1000 \text{ \AA}$. (Each component is also shown separately as blue and red points, respectively.) The X-ray light curve is also shown in grey.

the fastest of these, is shown); and the unknown transient “Dougje” (Vinkó et al. 2015).

The most convincing matches by far are the luminous members of the PS1 sample from Drout et al. (2014): PS1-11qr and PS1-12bv, shown at bottom right. While not quite as luminous or as fast-evolving as AT 2018cow, these events manage to replicate the fast rise, fast decay, and consistent blue colours around the peak time. (The less luminous objects in that sample are more questionable: in addition to being less luminous by a factor of ~ 10 they fade more slowly and clearly become redder at late times.)⁷

Additionally, both PTF 09uj (Ofek et al. 2010) and KSN-2015K (Rest et al. 2018) also represent good light-curve matches to AT 2018cow. Neither has multi-epoch colour information and they are 1–2 mag fainter at peak, although the pre-peak UV-optical colour of PTF 09uj and the single-epoch colours of KSN-2015K suggest that these transients were indeed similarly blue.

⁷The DES fast transients of Pursiainen et al. (2018) do not yet have publicly available light curves and are not shown in Fig. 10. Like the PS1 transients, they exhibit a variety of luminosities but all are fast-evolving and most are blue at peak. Some also show evidence of sustained high temperatures and contracting photospheres, similar to what observed in AT 2018cow. The HSC transients of Tanaka et al. (2016) were observed only in g and r and generally only during the rising phase, so post-peak constraints are not available.

Table 4. Photospheric parameters derived from a combined synchrotron + blackbody fit to the UV-optical-NIR data. Uncertainty estimates are statistical errors only.

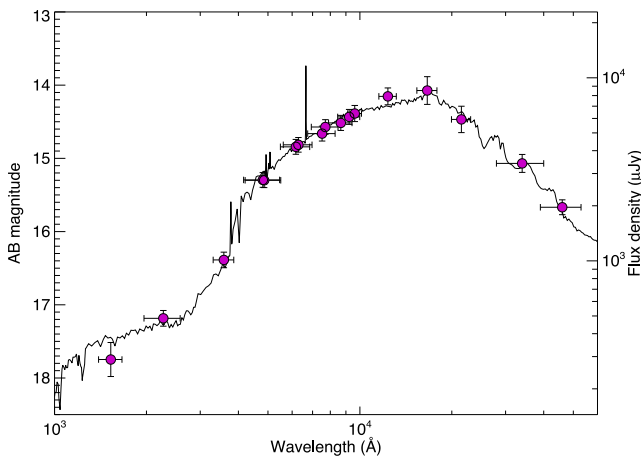
MJD	$L (L_{\odot})$	R (AU)	T (kK)
58288.44	$8.96e+10^{+2.32e+10}_{-1.19e+10}$	$52.77^{+4.70}_{-3.98}$	$31.39^{+3.10}_{-2.04}$
58289.22	$6.64e+10^{+2.46e+10}_{-8.66e+09}$	$47.72^{+3.89}_{-4.51}$	$30.58^{+4.12}_{-2.06}$
58290.69	$2.75e+10^{+6.67e+09}_{-1.70e+09}$	$44.20^{+1.89}_{-4.35}$	$25.42^{+3.19}_{-0.60}$
58291.56	$2.13e+10^{+4.81e+09}_{-2.04e+09}$	$38.99^{+2.44}_{-3.74}$	$25.42^{+2.98}_{-1.08}$
58292.28	$1.53e+10^{+3.91e+09}_{-1.06e+09}$	$39.04^{+2.18}_{-4.88}$	$23.37^{+3.40}_{-0.77}$
58293.81	$9.47e+09^{+1.17e+09}_{-8.92e+08}$	$36.39^{+1.45}_{-3.94}$	$21.20^{+2.22}_{-0.80}$
58294.61	$7.53e+09^{+5.24e+08}_{-1.02e+09}$	$32.99^{+3.97}_{-1.54}$	$20.91^{+0.90}_{-1.49}$
58295.58	$6.23e+09^{+6.60e+08}_{-5.08e+08}$	$29.24^{+2.29}_{-2.59}$	$21.25^{+1.37}_{-1.02}$
58296.68	$5.15e+09^{+5.53e+08}_{-3.42e+08}$	$27.07^{+2.10}_{-1.84}$	$20.90^{+1.24}_{-0.76}$
58298.39	$4.29e+09^{+3.19e+08}_{-4.10e+08}$	$24.51^{+2.08}_{-0.78}$	$20.91^{+0.78}_{-1.17}$
58299.62	$3.22e+09^{+2.12e+08}_{-2.46e+08}$	$24.96^{+1.28}_{-1.25}$	$19.32^{+0.73}_{-0.83}$
58300.65	$2.64e+09^{+2.74e+08}_{-1.64e+08}$	$23.50^{+1.31}_{-1.37}$	$18.84^{+1.11}_{-0.76}$
58301.79	$2.06e+09^{+2.02e+08}_{-9.79e+07}$	$22.19^{+1.52}_{-1.40}$	$18.04^{+0.97}_{-0.64}$
58302.04	$1.95e+09^{+1.64e+08}_{-1.24e+08}$	$21.69^{+1.43}_{-1.35}$	$18.00^{+0.85}_{-0.80}$
58303.17	$1.61e+09^{+1.05e+08}_{-9.91e+07}$	$19.86^{+1.42}_{-1.23}$	$17.57^{+0.75}_{-0.74}$
58303.78	$1.54e+09^{+1.12e+08}_{-1.16e+08}$	$19.47^{+1.79}_{-1.20}$	$17.28^{+0.81}_{-0.89}$
58305.64	$1.41e+09^{+8.66e+07}_{-1.06e+08}$	$18.46^{+1.76}_{-1.66}$	$17.09^{+1.00}_{-0.87}$
58306.77	$1.13e+09^{+7.78e+07}_{-6.57e+07}$	$18.62^{+1.13}_{-1.05}$	$16.23^{+0.70}_{-0.62}$
58307.16	$1.06e+09^{+7.34e+07}_{-7.25e+07}$	$18.46^{+1.66}_{-1.64}$	$16.01^{+0.87}_{-0.68}$
58307.70	$9.69e+08^{+8.19e+07}_{-5.53e+07}$	$18.07^{+1.22}_{-1.34}$	$15.84^{+0.75}_{-0.66}$
58308.15	$9.27e+08^{+8.19e+07}_{-5.71e+07}$	$17.70^{+1.39}_{-1.42}$	$15.81^{+0.96}_{-0.71}$
58309.23	$9.04e+08^{+5.32e+07}_{-5.56e+07}$	$16.00^{+1.34}_{-1.22}$	$16.55^{+0.62}_{-0.76}$
58310.22	$7.73e+08^{+4.16e+07}_{-5.47e+07}$	$15.19^{+1.31}_{-0.78}$	$16.10^{+0.68}_{-0.69}$
58310.70	$6.79e+08^{+5.02e+07}_{-4.02e+07}$	$14.78^{+1.37}_{-1.18}$	$15.55^{+0.84}_{-0.60}$
58311.16	$6.29e+08^{+5.06e+07}_{-3.89e+07}$	$14.30^{+1.18}_{-1.39}$	$15.30^{+0.83}_{-0.55}$
58311.76	$6.26e+08^{+4.82e+07}_{-3.94e+07}$	$13.33^{+1.28}_{-1.45}$	$15.67^{+0.98}_{-0.84}$
58312.42	$6.23e+08^{+4.23e+07}_{-5.01e+07}$	$12.88^{+1.67}_{-1.21}$	$15.71^{+0.81}_{-0.93}$
58314.75	$4.82e+08^{+2.74e+07}_{-3.48e+07}$	$12.82^{+1.25}_{-1.10}$	$14.82^{+0.76}_{-0.86}$
58316.52	$3.96e+08^{+2.91e+07}_{-2.75e+07}$	$11.38^{+1.32}_{-1.11}$	$15.34^{+0.95}_{-0.73}$
58318.93	$3.46e+08^{+2.72e+07}_{-2.22e+07}$	$9.34^{+0.84}_{-1.00}$	$15.94^{+1.22}_{-0.70}$
58320.24	$3.00e+08^{+2.92e+07}_{-2.24e+07}$	$9.13^{+0.85}_{-0.96}$	$15.66^{+1.12}_{-0.74}$
58322.23	$2.78e+08^{+2.42e+07}_{-1.63e+07}$	$7.70^{+0.57}_{-0.80}$	$16.83^{+1.46}_{-0.76}$
58324.03	$2.41e+08^{+2.54e+07}_{-1.14e+07}$	$6.64^{+0.65}_{-0.79}$	$17.53^{+1.64}_{-0.98}$
58325.36	$2.10e+08^{+1.94e+07}_{-1.20e+07}$	$6.06^{+0.60}_{-0.64}$	$17.31^{+1.16}_{-1.15}$
58326.17	$1.99e+08^{+1.70e+07}_{-1.87e+07}$	$5.91^{+0.88}_{-0.69}$	$17.43^{+1.13}_{-1.37}$
58327.15	$1.81e+08^{+2.66e+07}_{-1.22e+07}$	$5.46^{+0.45}_{-0.72}$	$17.81^{+2.07}_{-0.88}$
58329.22	$1.60e+08^{+2.16e+07}_{-8.68e+06}$	$5.09^{+0.64}_{-0.75}$	$17.43^{+2.27}_{-1.21}$
58334.88	$9.52e+07^{+2.32e+07}_{-1.52e+07}$	$4.41^{+1.01}_{-1.16}$	$16.96^{+3.17}_{-1.93}$
58339.90	$5.63e+07^{+1.67e+07}_{-1.90e+07}$	$3.56^{+1.38}_{-0.86}$	$17.14^{+3.79}_{-2.95}$
58346.92	$3.94e+07^{+2.52e+07}_{-8.20e+06}$	$3.37^{+0.90}_{-1.33}$	$16.30^{+7.28}_{-1.86}$
58354.46	$1.68e+07^{+1.02e+07}_{-9.16e+05}$	$4.14^{+1.09}_{-1.70}$	$10.74^{+6.65}_{-1.54}$

None of these transients have been characterized in detail, although the few spectra that exist are generally featureless (PTF 09uj exhibited weak, narrow emission lines of hydrogen.) All were found in star-forming galaxies offset from their host nuclei.

The rate of fast, blue transients was estimated from the Pan-STARRS sample (Drout et al. 2014): they measured a value of 4–7 per cent of the core-collapse supernova rate, equivalent to 1 per year within a radius of 40 Mpc. Given this rate, it seems credible

Table 5. Host–galaxy photometry from pre-imaging observations.

Filter	AB mag	Uncertainty	Survey
FUV	18.376	0.210	GALEX
NUV	17.880	0.038	GALEX
u	16.763	0.036	SDSS
g	15.578	0.003	SDSS
g	15.573	0.010	Pan-STARRS
r	15.021	0.002	SDSS
r	15.048	0.017	Pan-STARRS
i	14.725	0.009	SDSS
i	14.814	0.018	Pan-STARRS
z	14.544	0.020	SDSS
z	14.626	0.024	Pan-STARRS
Y	14.481	0.046	Pan-STARRS
J	14.153	0.054	2MASS
H	14.073	0.081	2MASS
Ks	14.320	0.106	2MASS
W1	15.370	0.007	WISE
W2	16.007	0.017	WISE
W3	14.989	0.032	WISE
W4	14.673	0.242	WISE

**Figure 9.** Spectral energy distribution for the host–galaxy of AT2018cow. Multiband photometry from GALEX, SDSS, 2MASS, and WISE is shown in purple and the best-fit SED model (with $M_* = 1.42^{+0.17}_{-0.29} \times 10^9 M_\odot$, $\text{SFR} = 0.22^{+0.03}_{-0.04} M_\odot \text{ yr}^{-1}$) is shown as a curve.

that one might be detected at 60 Mpc in the first few years of high-cadence all-sky observations by ATLAS or ZTF. (Conversely, given the detection of an event this close within ATLAS/ZTF, it would be surprising if similar events were *not* present in PS1 and other surveys.)

For these reasons, we argue that AT 2018cow is very likely related to the population of fast, blue, luminous transients seen by PS1 (and also by HSC and DES; Tanaka et al. 2016; Pursiainen et al. 2018). Earlier studies almost universally attributed these transients to supernovae undergoing shock breakout into, or interaction with, a dense wind or shell close to the progenitor (Ofek et al. 2010). The extensive additional observations available for AT 2018cow allow us to examine this connection in much more detail.

4.2 A spectroscopically unique transient

AT 2018cow shows at least two distinct spectral phases. Prior to 10 d, it is effectively featureless, save for the short-lived, broad blue

absorption feature. After 12 d, it remains hot and blue but exhibits weak features of (redshifted) H, He, and other light elements in emission.

The early, broad feature⁸ has no obvious analogue in any previous event. It bears some loose resemblance to the Fe II P-Cygni absorption trough seen in SNe Ic-BL, but overlying a much hotter continuum. We attempted to subtract the hot continuum to test this connection more rigorously, but the match is poor, being both too blue and too broad (Fig. 11) compared to even the earliest spectra of SN1998bw or SN2002ap (Patat et al. 2001; Kinugasa et al. 2002), or of the spectrum of SN2008D (Modjaz et al. 2009) during its shock-cooling phase.⁹ As of yet we have no convincing explanation for the origin of this feature, other than that it implies very fast (nearly relativistic) ejecta.

The identities of the features seen in later spectra (H and He in broad emission) are secure. In spite of this, these later spectra bear no obvious resemblance to any class of known supernova. The strongest similarities are to Type II_n supernovae (which can also remain hot for several weeks after explosion, and are emission-dominated by definition): in the bottom panel of Fig. 11, we plot AT 2018cow versus an early spectrum of SN 1998S from Fassia et al. (2001), which shows a similar blue continuum and most of the same H and He transitions. However, the lines in AT 2018cow are not narrow for most of their evolution ($v \sim 6000 \text{ km s}^{-1}$, versus a few hundred km s^{-1} for SN 1998S). Thomson scattering within ionized matter could broaden a line enough to wash out the narrow component, but this would not produce the net redshift in the emission component that we observe. The H and He thus must be in the ejecta itself (and seemingly preferentially in receding ejecta given the net redshift).

In fact, the best spectroscopic analogues to AT 2018cow are not supernovae at all. Our spectra bear a striking resemblance to tidal disruption events: the high temperatures, presence of helium and hydrogen features in emission, and moderate velocities all match what is observed for TDEs. The spectral features in AT 2018cow are substantially weaker than in the examples of TDEs that we are aware of (bottom panel of Fig. 11; comparison spectra are from Holoien et al. 2014, 2016), but the resemblance to a TDE is much stronger than to any supernova.

We summarize the key observational features of AT 2018cow in Table 3.

5 INTERPRETATION

5.1 Supernova models: A jet from a failed supernova?

The location of AT2018cow, and its apparent connection to other cosmological events that have also been found outside the nuclei of their host galaxies, give ample justification to consider a supernova as the most natural interpretation of this event. However, the observational aspects of this event impose severe constraints on any type of stellar explosion.

⁸We emphasize that the existence of this feature is secure: it is seen with a consistent shape and consistent temporal evolution in at least three different independently-reduced spectrographs (SEDM, SPRAT, HFOSC) and is also evident in our photometry via the evolution of the $B - V$ and $g - r$ colours.

⁹This cannot be because the SN features are washed out by a bright afterglow, as was the case for early spectra of SN 2003dh / GRB 030329 (e.g. Hjorth et al. 2003; Deng et al. 2005): the continuum is far too blue to be predominantly synchrotron in origin (Section 3.4).

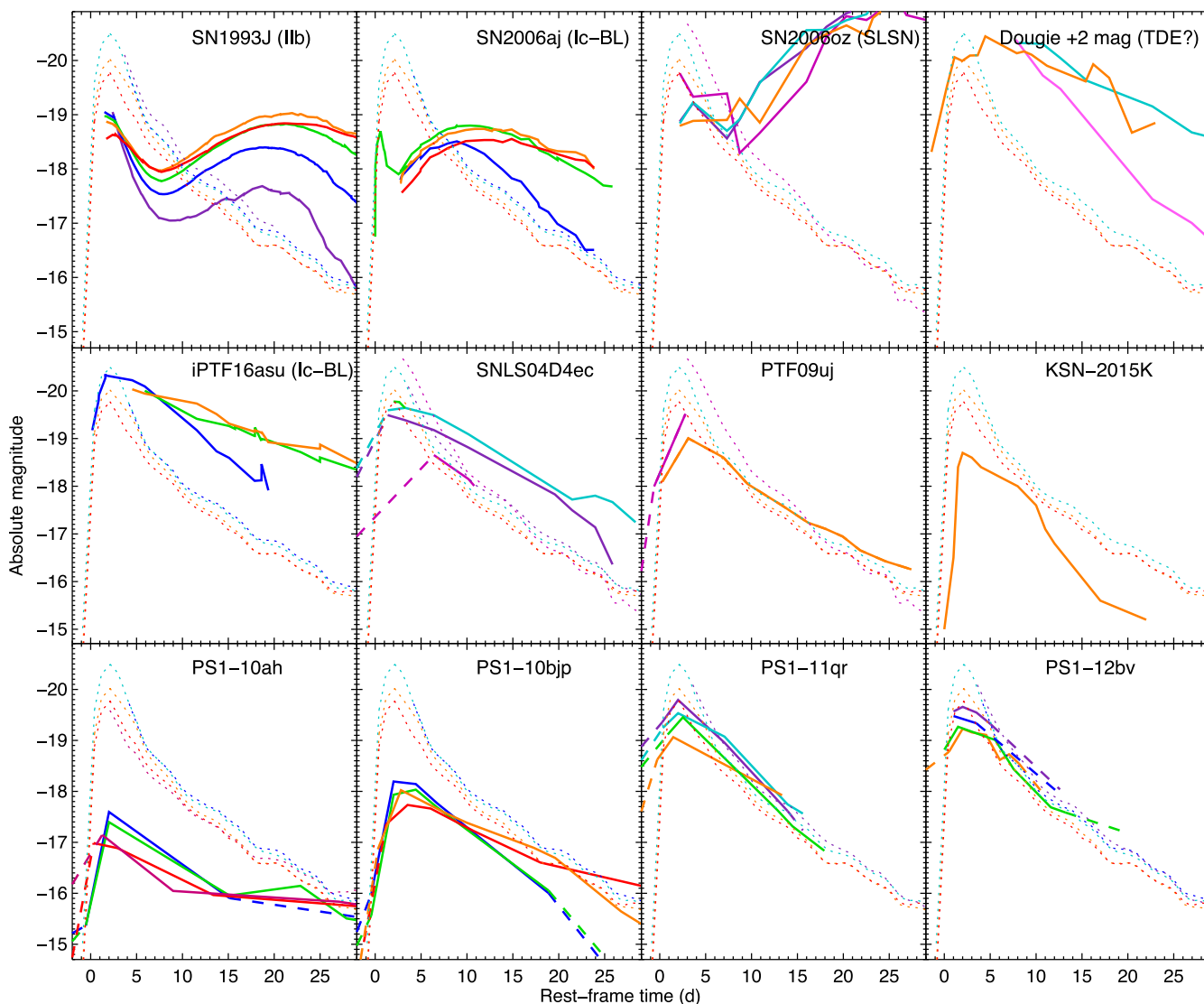


Figure 10. Comparison of the light curve of AT2018cow to other classes of fast-rising or luminous events. The dotted lines show AT2018cow; solid lines indicate comparison objects with dashed lines connecting upper limits to detections. Filter colour codes are the same as in Fig. 2 and are matched to rest-frame wavelengths. AT2018cow is insufficiently luminous at late times compared to GRB-SNe and also far too blue. It is much faster than any known TDE and the thermal SED is entirely unlike the optically thin spectra of GRB afterglows. However, it matches well with the cosmological fast transients found in PS1 and Kepler (and to a lesser extent SNLS) in colour, luminosity, and time-scale.

The first problem for any supernova model is the need to explain the fast rise. Heating from radioactive ^{56}Ni certainly cannot produce it: at least $5 M_{\odot}$ of Nickel would be needed to power the luminosity of AT2018cow at peak, which is orders of magnitude greater than the total ejecta mass that would be inferred from the fast rise given standard assumptions about diffusion ($M_{\text{ej}} \sim (\frac{\text{rise}}{20\text{d}})^2 M_{\odot}$ or approximately $0.01 M_{\odot}$; Arnett 1982; Rest et al. 2018).

A natural alternative is shock heating. Most core-collapse SNe are believed to exhibit an early shock-breakout and shock-cooling phase in which the stellar photosphere is nearly-instantaneously heated to X-ray temperatures by the emergence of the SN shock, producing a rapid rise in the light curve (Waxman & Katz 2017). However, for standard types of stellar progenitor, the shock-cooling rise time is far *too* fast to explain AT2018cow’s 2–3 day rise. A multiday rise could be achieved only if the progenitor was quite extended ($R \sim 10^{14}$ cm, or about 10 AU).

This radius is similar to that of the largest red supergiants. However, a massive stellar envelope of this nature would greatly slow down the later evolution of the SN, producing a “plateau” phase rather than sudden fading. The photosphere at the time of shock breakout thus would have to be unbound, with the shock breaking out into a dense wind or ejected shell associated with recent, intense mass loss.

Evidence has been accumulating in recent years that extreme mass loss shortly before explosion is common (Gal-Yam et al. 2014; Ofek et al. 2014; Yaron et al. 2017), so this may not be surprising. However, other observations place further strong constraints on the nature of this recent mass loss: the lack of any flash-ionization features, the lack of shocked hydrogen or helium, and the lack of further rebrightenings in the light curve all require that the CSM shell be quite localized in extent. This may also be possible, if the previous mass-loss episode is both singular and explosive.

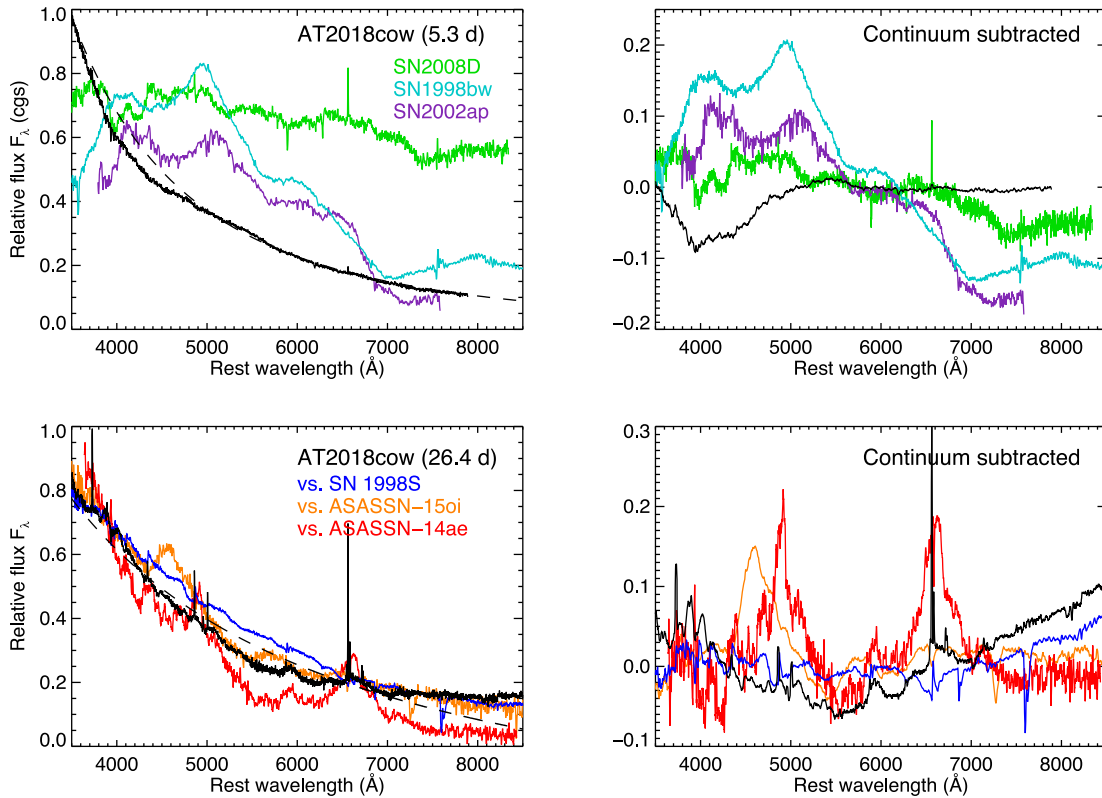


Figure 11. Comparison of an early spectrum of AT2018cow to the early spectrum of SN2008D (Ib) and two SNe Ic-BL (top row), and of a later-time spectrum to SN1998S (IIn) and two tidal disruption events (bottom row). The extremely blue, smooth continuum bears little resemblance to SN Ib/c, even after attempting to subtract the blue continuum. (A power-law plus a constant have been subtracted from AT2018cow; the reference SN spectra have been subtracted by a constant only. The strength of the features in the SNe after subtraction has been suppressed by a factor of 2.) The later-time spectra are dominated by weak emission features of hydrogen and helium; these features are also present in IIn SNe but are much narrower compared to what is seen in AT2018cow. These features are seen in known TDEs with similarly broad widths, although typically much greater strengths.

Further constraints on the explosion can be imposed based on the lack of a second, radioactively powered peak in the light curve. Using the bolometric luminosity at 20 days and scaling relative to SN2002ap (Mazzali et al. 2002; Foley et al. 2003), we estimate $M_{\text{Ni}} < 0.05 M_{\odot}$. While this is in the range of masses inferred for “normal” core-collapse supernovae (Rubin et al. 2016; Müller et al. 2017), a modest ^{56}Ni mass seems hard to reconcile with the energetic shockwave necessary to produce the extraordinary shock-breakout flash and accelerate substantial ejecta to $>0.1c$, as inferred from the broad absorption seen in the spectra at ~ 1 week¹⁰ and by the luminous radio counterpart. (Velocities this high have been previously seen observationally only in GRB-SNe, which have universally high ejecta and nickel masses: Mazzali et al. 2014, although cf. Fynbo et al. 2006).

Perhaps the shock in this SN was driven not by the classical neutrino mechanism (or other forms of energy input from a proto-NS), but solely by an energetic jet driven by a black hole following direct collapse of a massive star to a black hole (analogous to

the original “failed supernova” model of Woosley 1993). No high-energy prompt emission was observed from AT2018cow, but the jet could have been off-axis or (more likely) choked by the stellar envelope. We may then just have seen a short-lived high-velocity pseudo-photosphere in the early spectra, which may be supported by a small amount of material surrounding the jet, either dragged by the jet itself or ejected in a disc wind. This material would contain only a small amount of ^{56}Ni , explaining the lack of a radioactive second peak.

This model (which is similar to that of Quataert & Kasen 2012, but with the addition of circumstellar interaction: see also Kashiyama & Quataert 2015) has some appeal, especially given the observation of bright, self-absorbed radio emission which independently implies substantial interaction (Ho et al. 2018). Even so, it faces formidable challenges. The high-velocity absorption implied by our early spectra suggests material that is expanding outward rapidly ($>0.1c$), but the spectral features seen only two weeks later are quite narrow ($\sim 0.02c$). This could be achieved if the high-velocity ejecta collided with a *second* dense shell of comparable mass — eliminating the broad lines and largely halting the expansion of the photosphere that would normally be expected in a young supernova. But the resulting shock-wave should then have excited narrow-line emission of H and perhaps He which we do not see. (The H and He lines that eventually emerge originate too late and have velocities too broad to be attributed to shock interaction).

Alternative stellar progenitor scenarios beyond core-collapse do not provide any appreciable resolution to these contradictions. Large

¹⁰It could be contested whether the broad feature truly represents Doppler-broadened absorption, given the lack of a clear identification of the line(s) responsible. However, as the SEDs in Fig. 4 make clear, this feature shows up clearly as missing flux from what is otherwise an excellent fit to a single thermal SED; multiple emission components or non-thermal features cannot reproduce this profile. Alternative, non-velocity-broadened sources of absorption (e.g. transient dust extinction with an unknown broad feature) are unlikely.

energies and small ^{56}Ni masses are expected for neutron star merger models, but such events should not possess significant hydrogen or helium. Furthermore, AT2018cow empirically bears no relation to the (much dimmer, fast-cooling, fast-expanding) optical counterpart of GW 170817 (McCully et al. 2017; Kasliwal et al. 2017; Evans et al. 2017; Villar et al. 2017; Pian et al. 2017). White-dwarf explosions (variants on Ia or accretion-induced collapse models; e.g. Brooks et al. 2017; Poznanski et al. 2010) are also likely to be poor in H and He, and heavily suppress the UV via iron line blanketing in the ejecta.

Perhaps, the biggest challenge for any supernova model is the lack of expansion of the photosphere. Pursiainen et al. (2018) noted that a hot, receding photosphere is expected in the wind shock-breakout model due to the rapid expansion of the unbound shock-heated material, but this will only be true during the early phases: the photosphere should eventually reach the dense stellar envelope, after which its evolution should follow that of typical supernovae. Regardless of the progenitor structure, it is difficult to understand how freely-expanding ejecta would maintain a photosphere on a scale of only 10^{14} cm 40 days after the explosion: the material at the photosphere could be expanding no faster than 300 km s^{-1} (much slower than the width inferred by the observed lines at late times.)

5.2 Tidal disruption models: Disruption of a star by an IMBH?

In spite of the circumstantial evidence for a SN origin (the event occurred in a spiral arm) there are many reasons to look more broadly at progenitor models, and in particular to consider a tidal disruption event as an alternative (e.g., Kuin et al. 2019).

Many of the properties of the transient that cause the most difficulty for the SN interpretation are natural components of TDE models. The bolometric light curve declines as a power-law, as expected under simple TDE models (although the decay is steeper than the canonical $t^{-5/3}$). The lack of an early free-expansion phase and the maintenance of a high temperature are also similar to expectations for TDEs, which provide continued energy input via BH accretion and whose potential well hampers free expansion of the ejecta. And a TDE origin would also explain the H and He-rich late-time spectra (which empirically resemble known TDEs more closely than any SN).

Aside from its peculiar location, the primary feature that distinguishes AT2018cow from known TDEs is its time-scale: typical TDEs have rise times of weeks to months and decay times even longer. Faster TDEs have been found more recently (Blagorodnova et al. 2017), but even these have characteristic time-scales an order of magnitude longer than AT2018cow.

A possible resolution is a smaller black hole mass: known TDEs appear to show an empirical time-scale–mass correlation (e.g. Blagorodnova et al. 2017), and there are also reasons to expect one theoretically (Guillochon & Ramirez-Ruiz 2013). To better constrain the black hole mass under a TDE model, we fit the UV/optical data using two different methods: using simple scaling relations, and using a full MCMC fit to the light curve.

We first fit the bolometric (UVOIR) light curve to a power-law decay of the form $L(t) = L_0 \left(\frac{t-t_0}{t-t_D} \right)^{-n}$. We obtain an excellent fit with a power-law index of $n = 3.0 \pm 0.1$ and a time of disruption (t_D) of -1.5 ± 0.3 (relative to MJD 58285). Under this scenario the implied rise-time-to-peak of $t_{\text{peak}} = t_0 - t_D = 5.0\text{d}$, according to the simulations of Guillochon & Ramirez-Ruiz (2013) for a solar-type star, would correspond to a black hole of $1.5 \times 10^4 M_\odot$.

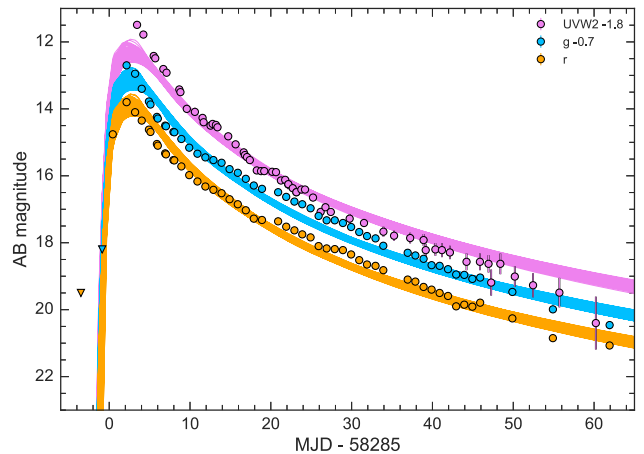


Figure 12. Results from an MCMC fit to the data using the TDE implementation of MOSFiT (Guillochon et al. 2018; Mockler et al. 2018). The rising and falling time-scales of this transient, along with the slow temperature evolution, are well-reproduced by a model involving the disruption of a Solar-type star around an intermediate-mass black hole ($\sim 2 \times 10^4 M_\odot$).

Additionally, we fit the light curve in the g , r , and UVOT $w2$ bands with the MOSFiT TDE model (Guillochon et al. 2018; Mockler, Guillochon & Ramirez-Ruiz 2018). The MOSFiT TDE model uses hydrodynamic simulations of tidal disruption events from (Guillochon & Ramirez-Ruiz 2013) to calculate the fallback rate of stellar debris to the black hole. MOSFiT then converts these fallback rates into bolometric luminosities and passes them through viscosity and reprocessing transformation functions to create optical and UV light curves. Two adjustments to the model were required to obtain a good fit: the peak luminosity was allowed to exceed the Eddington limit, and the maximum photosphere radius was allowed to reach beyond the apocentres of the Keplerian orbits of the stellar debris. Under these circumstances, our fit prefers a black hole with a mass of $M_h = 1.9^{+1.2}_{-0.8} \times 10^4 M_\odot$ and a star with mass $M_* = 0.6^{+2.0}_{-0.5} M_\odot$. This is fully consistent with the scaling-relation solution. Fitted light curves are presented in Fig. 12.

These parameters correspond to the disruption of a main-sequence star around an intermediate-mass black hole (IMBH). This would be a significant discovery: IMBH disruptions were recently theoretically predicted (Fragione & Leigh 2018; Chen & Shen 2018) and if confirmed, would represent evidence for the existence of IMBHs in the low-redshift universe, a topic that remains broadly controversial. A black hole in this mass range would also not conflict with the off-nuclear location: it could originate from a globular cluster or from a massive young star cluster.

However, as the above discussion suggests, the peak luminosity of the transient ($\sim 3 \times 10^{44}$ erg) is much greater than the Eddington luminosity for a black hole of the mass needed to explain its short time-scale ($\sim 10^{42}$ erg for $M_{\text{BH}} = 10^4 M_\odot$). While TDEs are expected to have super-Eddington mass fallback rates (e.g. Strubbe & Quataert 2009), the radiated luminosity is generally expected to be capped at close to the Eddington luminosity (Chen & Shen 2018), since higher luminosities would disrupt the accretion and drive the luminosity back down. Super-Eddington luminosities could be achieved in two ways: by an anisotropic radiation process, or by a heating source not directly associated with accretion.

There is evidence that some TDEs can indeed produce highly anisotropic, relativistic jets (Bloom et al. 2011; Burrows et al. 2011; Levan et al. 2011; Cenko et al. 2012). The bright (and variable)

X-ray and radio emission from AT2018cow (see also Ho et al. 2018; Margutti et al. 2018) suggest a similar phenomenon could be present here as well. However, the optical radiation which gives rise to our luminosity estimates is unambiguously thermal and not easily beamed, so anisotropy is unlikely to resolve the conflict.

Alternatively, it is possible that the early UV/optical emission is related to the circularization process (Piran et al. 2015; Dai et al. 2018), rather than accretion. The similarity of the peak luminosity of AT2018cow to other UV/optical TDEs (Hung et al. 2017) and the expected energy dissipation rate from the circularization process of $10^{44} (M_{\text{BH}}/10^6 M_{\odot})^{-1/6} \text{ erg s}^{-1}$ (Piran et al. 2015) support this interpretation. The self-intersection radius for debris streams around a $\sim 10^4 M_{\odot}$ black hole is $\sim 5 \times 10^{13} \text{ cm}$ (Wevers et al. 2017), which is a factor of 10 smaller than the observed photosphere radius for AT2018cow. If the luminosity is powered by stream–stream intersections, then the photosphere would engulf both the intersection point and the black hole. This optically thick reprocessing layer would need to be in place by the time of our first observations to explain the colour and luminosity of AT2018cow. This could be associated with matter blown to larger radii during an early wind phase (Jiang, Guillochon & Loeb 2016; Metzger & Stone 2016).

Further modelling will be needed to examine the behaviour of tidal disruptions around IMBHs during the super-Eddington phase. If even some of the PS1 and DES events belong to the same class as AT2018cow, there is reason to believe that these events are reasonably common and the current generation of fast-cadence optical surveys may find future examples at similar rates as ordinary, SMBH TDEs.¹¹

6 CONCLUSIONS

Prior to AT2018cow, fast high-luminosity transients were widely attributed to an extreme variant of the shock-breakout scenario that has already been widely appealed to in order to explain a variety of nearby supernovae. To our surprise, the first real-time detection of a nearby event belonging to this empirical class has only deepened the mystery surrounding these events. While the off-nuclear location within a star-forming region seems to imply the explosion of a star as a supernova, the actual observational properties — including high-velocity absorption in early spectra, a long-lived hot photosphere, a complete lack of narrow lines during the first week, and luminous X-ray through radio emission — are all difficult to explain under any existing supernova model. If nothing else, any stellar explosion must involve a radically different progenitor structure and/or explosion mechanism compared to known SNe.

In contrast, disruption by an intermediate-mass black hole provides an excellent description of the qualitative behaviour of the transient and its later-time spectra. However, the highly super-Eddington luminosity of the transient is a formidable challenge for IMBH TDE models, and it remains to be seen whether alternative explanations for the early heating (e.g. circularization of infalling material) provide an adequate interpretation.

Studies of fast optical transients are still in their infancy, and there is much more to learn both observationally and theoretically. While an event as close as AT2018cow may not be a regular occurrence,

its sheer brightness suggests that others of a similar nature are likely to be observed in the near future at somewhat greater distances. Samples of the spatially-resolved galaxy environments, total energetics, and spectroscopic properties of such events are likely to shed light on their nature.

ACKNOWLEDGEMENTS

DAP acknowledges useful discussions with Matt Darnley and Helen Jermak. We thank the referee for helpful comments which improved the quality of this paper.

This work was supported by the GROWTH project funded by the National Science Foundation under Grant No 1545949. GROWTH is a collaborative project between California Institute of Technology, Pomona College, San Diego State University, Los Alamos National Laboratory, University of Maryland College Park, University of Wisconsin Milwaukee (USA), Tokyo Institute of Technology (Japan), National Central University (Taiwan), Indian Institute of Astrophysics (India), Weizmann Institute of Science (Israel), The Oskar Klein Centre at Stockholm University (Sweden), Humboldt University (Germany), and Liverpool John Moores University (UK). This paper used the GROWTH marshal to filter alerts and co-ordinate follow-up.

FT and JS gratefully acknowledge support from the Knut and Alice Wallenberg Foundation. JS acknowledges the support of Vetenskapsrådet through VR grants 2012-2265 and 2017-03699.

AYQH was supported by a National Science Foundation Graduate Research Fellowship under Grant No. DGE-1144469. MC was supported by the David and Ellen Lee Postdoctoral Fellowship at the California Institute of Technology. JSB was supported by a Data-Driven Discovery grant from the Moore Foundation.

C-C Ngeow and P-C Yu thank the Ministry of Science and Technology (MoST, Taiwan) for funding under grant 104-2923-M-008-004-MY5 and 106-2112-M-008-007. This publication has made use of data collected at Lulin Observatory, partly supported by MoST grant 105-2112-M-008-024-MY3.

RI is supported by JSPS and NSF under the JSPS-NSF Partnerships for International Research and Education (PIRE), YT and NK supported by JSPS KAKENHI Grant Numbers JP16J05742 and JP17H06362. YT is also financially supported by Academy for Global Leadership (AGL) of Tokyo Institute of Technology. MITSuME Akeno 50cm telescope is also supported by the joint research program of the Institute for Cosmic Ray Research (ICRR), the University of Tokyo, and Optical and Near-Infrared Astronomy Inter-University Cooperation Program in Japan (KLM).

GCA and VB acknowledge the support of the Science and Engineering Research Board, Department of Science and Technology, India and the Indo-US Science and Technology Forum for the GROWTH-India project. BK acknowledges the Science and Engineering Research Board under the Department of Science & Technology, Govt. of India, for financial assistance in the form of National Post-Doctoral Fellowship (PDF/2016/001563) and BRICS grant DST/IMRCD/BRICS/PilotCall1/MuMeSTU/2017(G).

The Liverpool Telescope is operated on the island of La Palma by Liverpool John Moores University in the Spanish Observatorio del Roque de los Muchachos of the Instituto de Astrofísica de Canarias with financial support from the UK Science and Technology Facilities Council. We acknowledge helpful support from the entire LT staff, including Robert Smith, Jon Marchant, and Iain Steele, and to the LT review panel for approving our requests for Reactive time (JQ18A01).

¹¹ Super-Eddington-luminosity disruptions by more massive black holes are also of interest: the transient ‘Dougie’ was slower than AT2018cow (Fig. 10) but was vastly more luminous, and the preferred TDE model fit by Vinkó et al. (2015) also indicated a highly super-Eddington luminosity, in this case from a somewhat more massive black hole ($M_{\text{h}} = 2.0_{-1.3}^{+13.9} \times 10^5 M_{\odot}$).

We acknowledge the use of public data from the Swift data archive, and thank the Swift team for executing such a thorough observing campaign of this transient.

This work is partly based on observations made with the Nordic Optical Telescope, operated by the Nordic Optical Telescope Scientific Association at the Observatorio del Roque de los Muchachos, La Palma, Spain, of the Instituto de Astrofísica de Canarias. The data presented here were obtained in part with ALFOSC, which is provided by the Instituto de Astrofísica de Andalucía (IAA) under a joint agreement with the University of Copenhagen and NOTSA. The William Herschel Telescope is operated on the island of La Palma by the Isaac Newton Group of Telescopes in the Spanish Observatorio del Roque de los Muchachos of the Instituto de Astrofísica de Canarias.

These results made use of the Discovery Channel Telescope at Lowell Observatory. Lowell is a private, non-profit institution dedicated to astrophysical research and public appreciation of astronomy and operates the DCT in partnership with Boston University, the University of Maryland, the University of Toledo, Northern Arizona University and Yale University. The upgrade of the DeVeny optical spectrograph has been funded by a generous grant from John and Ginger Giovale. We thank Debra Fischer for graciously assisting with our Target of Opportunity request at the DCT.

This work is partly based on observations made with the Kitt Peak EMCCD Demonstrator (KPED) camera on the Kitt Peak 84 inch telescope. The KPED team thanks the National Science Foundation, discretionary funds of SRK, and donors to SRK for support in the building and operation of KPED. In addition, they thank the Chimera project for use of the EMCCD.

Some of the data used in this paper were acquired with the COATLI telescope and interim instrument, and with the RATIR instrument on the 1.5-meter Harold L. Johnson telescope; both at the Observatorio Astronómico Nacional on the Sierra de San Pedro Mártir, Baja California, México. COATLI is funded by CONACyT (LN 232649, 260369, and 271117) and the Universidad Nacional Autónoma de México (CIC and DGAPA/PAPIIT IT102715, IG100414, and IN109408). RATIR is funded by the University of California and NASA Goddard Space Flight Center. COATLI and the Johnson 1.5-m telescope are operated and maintained by the Observatorio Astronómico Nacional and the Instituto de Astronomía of the Universidad Nacional Autónoma de México. We acknowledge the contribution of Leonid Georgiev and Neil Gehrels to the development of RATIR.

Based partially on data from the Gemini Observatory, which is operated by the Association of Universities for Research in Astronomy, Inc., under a cooperative agreement with the NSF on behalf of the Gemini partnership: the National Science Foundation (United States), the National Research Council (Canada), CONICYT (Chile), Ministerio de Ciencia, Tecnología e Innovación Productiva (Argentina), and Ministério da Ciência, Tecnologia e Inovação (Brazil). Data were taken under program GN-2018A-Q-902 and acquired through the Gemini Observatory Archive.

Some data presented herein were obtained at the W. M. Keck Observatory, which is operated as a scientific partnership among the California Institute of Technology, the University of California and the National Aeronautics and Space Administration. The Observatory was made possible by the generous financial support of the W. M. Keck Foundation. The authors wish to recognize and acknowledge the very significant cultural role and reverence that the summit of Maunakea has always had within the indigenous Hawaiian community. We are most fortunate to have the opportunity to conduct observations from this mountain.

The 2m Himalayan Chandra Telescope at the Indian Astronomical Observatory is operated by the Indian Institute of Astrophysics. Support from IAO staff and HCT observation assistants is acknowledged. We also thank all HCT observers who provided part of their time for the observations. The HCT data of 22, 23, 25 and 29 June were obtained under the ToO proposals of both D. K. Sahu (PI) and F. Sutarra (PI).

AstroSat is a dedicated multi-wavelength space observatory funded and facilitated by the Indian Space Research Organisation (ISRO). We thank the AstroSat ToO Time Allocation Committee for granting ToO time, and the operations team for carrying out these observations.

Funding for the SDSS and SDSS-II has been provided by the Alfred P. Sloan Foundation, the Participating Institutions, the National Science Foundation, the U.S. Department of Energy, the National Aeronautics and Space Administration, the Japanese Monbukagakusho, the Max Planck Society, and the Higher Education Funding Council for England. The SDSS Web Site is <http://www.sdss.org/>. The SDSS is managed by the Astrophysical Research Consortium for the Participating Institutions.

The Pan-STARRS1 Surveys (PS1) and the PS1 public science archive have been made possible through contributions by the Institute for Astronomy, the University of Hawaii, the Pan-STARRS Project Office, the Max-Planck Society and its participating institutes, the Max Planck Institute for Astronomy, Heidelberg and the Max Planck Institute for Extraterrestrial Physics, Garching, The Johns Hopkins University, Durham University, the University of Edinburgh, the Queen's University Belfast, the Harvard-Smithsonian Center for Astrophysics, the Las Cumbres Observatory Global Telescope Network Incorporated, the National Central University of Taiwan, the Space Telescope Science Institute, the National Aeronautics and Space Administration under Grant No. NNX08AR22G issued through the Planetary Science Division of the NASA Science Mission Directorate, the National Science Foundation Grant No. AST-1238877, the University of Maryland, Eotvos Lorand University (ELTE), the Los Alamos National Laboratory, and the Gordon and Betty Moore Foundation.

Finally, we thank the developers and maintainers of the Open Supernova Catalog and the Weizmann Spectral Repository, whose databases greatly facilitated the comparisons of this event to other transients.

REFERENCES

- Abolfathi B. et al., 2018, *ApJS*, 235, 42
 Arcavi I. et al., 2016, *ApJ*, 819, 35
 Arcavi I. et al., 2017, *ApJ*, 837, L2
 Arnett W. D., 1982, *ApJ*, 253, 785
 Barbon R., Benetti S., Cappellaro E., Patat F., Turatto M., Iijima T., 1995, *A&AS*, 110, 513
 Barnsley R. M., Smith R. J., Steele I. A., 2012, *Astron. Nach.*, 333, 101
 Benetti S., Pastorello A., Cappellaro E., Turatto M., Tomasella L., Fiore A., Reguitti A., Gromadzki M., 2018, *The Astronomer's Telegram*, 11836
 Bhalerao V. et al., 2017, *ApJ*, 845, 152
 Blagorodnova N. et al., 2017, *ApJ*, 844, 46
 Blagorodnova N. et al., 2018, *PASP*, 130, 035003
 Blanton M. R., Kazin E., Muna D., Weaver B. A., Price-Whelan A., 2011, *AJ*, 142, 31
 Bloom J. S. et al., 2011, *Science*, 333, 203
 Bright J., Horesh A., Fender R., Motta S., Sfaradi I., Titterton D., Perrott Y., Ho A., 2018, *The Astronomer's Telegram*, 11774
 Brooks J., Schwab J., Bildsten L., Quataert E., Paxton B., Blinnikov S., Sorokina E., 2017, *ApJ*, 850, 127

- Burrows D. N. et al., 2005, *Space Sci. Rev.*, 120, 165
- Burrows D. N. et al., 2011, *Nature*, 476, 421
- Butler N. et al., 2012, in *Ground-based and Airborne Instrumentation for Astronomy IV*, SPIE, p. 844610
- Butler N. R., Kocevski D., 2007, *ApJ*, 663, 407
- Calzetti D., Armus L., Bohlin R. C., Kinney A. L., Koornneef J., Storchi-Bergmann T., 2000, *ApJ*, 533, 682
- Campana S. et al., 2006, *Nature*, 442, 1008
- Cenko S. B. et al., 2012, *ApJ*, 753, 77
- Cenko S. B. et al., 2013, *ApJ*, 769, 130
- Cenko S. B. et al., 2015, *ApJ*, 803, L24
- Chabrier G., 2003, *ApJ*, 586, L133
- Chen J.-H., Shen R.-F., 2018, *ApJ*, 867, 20
- Dai L., McKinney J. C., Roth N., Ramirez-Ruiz E., Miller M. C., 2018, *ApJ*, 859, L20
- Deng J., Tominaga N., Mazzali P. A., Maeda K., Nomoto K., 2005, *ApJ*, 624, 898
- de Ugarte Postigo A. et al., 2018, *The Astronomer's Telegram*, 11749
- Dobie D., Ravi V., Ho A., Kasliwal M., Murphy T., 2018, *The Astronomer's Telegram*, 11795
- Drout M. R. et al., 2014, *ApJ*, 794, 23
- Evans P. A. et al., 2017, *Science*, 358, 1565
- Fassia A. et al., 2001, *MNRAS*, 325, 907
- Ferrero P. et al., 2006, *A&A*, 457, 857
- Fitzpatrick E. L., 1999, *PASP*, 111, 63
- Foley R. J. et al., 2003, *PASP*, 115, 1220
- Fragione G., Leigh N., 2018, *MNRAS*
- Fremling C., 2018, *The Astronomer's Telegram*, 11738
- Fynbo J. P. U. et al., 2006, *Nature*, 444, 1047
- Gal-Yam A. et al., 2014, *Nature*, 509, 471
- Galama T. J. et al., 1998, *Nature*, 395, 670
- Gehrels N. et al., 2004, *ApJ*, 611, 1005
- Guillochon J., Nicholl M., Villar V. A., Mockler B., Narayan G., Mandel K. S., Berger E., Williams P. K. G., 2018, *ApJS*, 236, 6
- Guillochon J., Ramirez-Ruiz E., 2013, *ApJ*, 767, 25
- Hjorth J. et al., 2003, *Nature*, 423, 847
- Ho A. Y. Q. et al., 2018, preprint ([arXiv:1810.10880](https://arxiv.org/abs/1810.10880))
- Holoien T. W.-S. et al., 2014, *MNRAS*, 445, 3263
- Holoien T. W.-S. et al., 2016, *MNRAS*, 463, 3813
- Huchra J. P. et al., 2012, *ApJ*, 199, 26
- Hung T. et al., 2017, *ApJ*, 842, 29
- Ilbert O. et al., 2006, *A&A*, 457, 841
- Izzo L. et al., 2018, *The Astronomer's Telegram*, 11753
- Jiang Y.-F., Guillochon J., Loeb A., 2016, *ApJ*, 830, 125
- Kaiser N. et al., 2010, in *Ground-based and Airborne Telescopes III*. p. 77330E
- Kangas T. et al., 2016, *MNRAS*, 456, 323
- Kashiyama K., Quataert E., 2015, *MNRAS*, 451, 2656
- Kasliwal M. M. et al., 2017, *Science*, 358, 1559
- Khazov D. et al., 2016, *ApJ*, 818, 3
- Kinugasa K. et al., 2002, *ApJ*, 577, L97
- Kuin N. P. M. et al., 2019, *MNRAS* accepted ([arXiv:1808.08492](https://arxiv.org/abs/1808.08492))
- Kulkarni S. R., 2018, *The Astronomer's Telegram*, 11266
- Kumar A. et al., 2012, in *Space Telescopes and Instrumentation 2012: Ultraviolet to Gamma Ray*. p. 84431N
- Leloudas G. et al., 2012, *A&A*, 541, A129
- Levan A. J. et al., 2011, *Science*, 333, 199
- Margutti R. et al., 2018, preprint ([arXiv:1810.10720](https://arxiv.org/abs/1810.10720))
- Martin D. C. et al., 2005, *ApJ*, 619, L1
- Mazzali P. A., McFadyen A. I., Woosley S. E., Pian E., Tanaka M., 2014, *MNRAS*, 443, 67
- Mazzali P. A. et al., 2002, *ApJ*, 572, L61
- McCully C. et al., 2017, *ApJ*, 848, L32
- Metzger B. D., Stone N. C., 2016, *MNRAS*, 461, 948
- Mockler B., Guillochon J., Ramirez-Ruiz E., 2018, preprint ([arXiv:1801.08221](https://arxiv.org/abs/1801.08221))
- Modjaz M. et al., 2009, *ApJ*, 702, 226
- Müller T., Prieto J. L., Pejcha O., Clocchiatti A., 2017, *ApJ*, 841, 127
- Ofek E. O. et al., 2010, *ApJ*, 724, 1396
- Ofek E. O. et al., 2014, *ApJ*, 789, 104
- Oke J. B., Gunn J. E., 1982, *PASP*, 94, 586
- Oke J. B. et al., 1995, *PASP*, 107, 375
- Patat F. et al., 2001, *ApJ*, 555, 900
- Perley D. A., Blagorodnova N., Neill J. D., Walters R., 2018, *The Astronomer's Telegram*, 11776
- Pian E. et al., 2017, *Nature*, 551, 67
- Piascik A. S., Steele I. A., Bates S. D., Mottram C. J., Smith R. J., Barnsley R. M., Bolton B., 2014, in *Ground-based and Airborne Instrumentation for Astronomy V*, p. 91478H
- Piran T., Svirski G., Krolik J., Cheng R. M., Shiokawa H., 2015, *ApJ*, 806, 164
- Poznanski D. et al., 2010, *Science*, 327, 58
- Prentice S. J. et al., 2018, *ApJ*, 865, 3
- Pursiainen M. et al., 2018, *MNRAS*, 481, 894
- Quataert E., Kasen D., 2012, *MNRAS*, 419, L1
- Rest A. et al., 2018, *Nature Astron.*, 2, 307
- Richmond M. W., Treffers R. R., Filippenko A. V., Paik Y., 1996, *AJ*, 112, 732
- Rivera Sandoval L. E., Maccarone T., 2018, *The Astronomer's Telegram*, 11737
- Rivera Sandoval L. E., Maccarone T. J., Corsi A., Brown P. J., Pooley D., Wheeler J. C., 2018, *MNRAS*, 480, 146
- Roming P. W. A. et al., 2005, *Space Sci. Rev.*, 120, 95
- Rubin A. et al., 2016, *ApJ*, 820, 33
- Sari R., Piran T., Narayan R., 1998, *ApJ*, 497, L17
- Schlafly E. F., Finkbeiner D. P., 2011, *ApJ*, 737, 103
- Shappee B. J. et al., 2014, *ApJ*, 788, 48
- Shivvers I. et al., 2016, *MNRAS*, 461, 3057
- Smartt S. J. et al., 2018, *The Astronomer's Telegram*, 11727
- Smith C. E., Nelson B., 1969, *PASP*, 81, 74
- Smith R. J., Steele I. A., 2017, *Liverpool Telescope Technical Note 1: Telescope and IO:O Throughput*
- Stalder B. et al., 2017, *ApJ*, 850, 149
- Steele I. A. et al., 2004, in *Oschmann J. M., Jr, ed., Proc. SPIE Vol. 5489, Ground-based Telescopes*. p. 679
- Strubbe L. E., Quataert E., 2009, *MNRAS*, 400, 2070
- Tanaka M. et al., 2016, *ApJ*, 819, 5
- Tandon S. N. et al., 2017, *AJ*, 154, 128
- Tonry J. L. et al., 2018, *PASP*, 130, 064505
- Villar V. A. et al., 2017, *ApJ*, 851, L21
- Vinkó J. et al., 2015, *ApJ*, 798, 12
- Watson A. M. et al., 2012, in *Ground-based and Airborne Telescopes IV*, SPIE 9908, 5, p. 84445L
- Watson A. M. et al., 2016, in *Ground-based and Airborne Instrumentation for Astronomy VI*, SPIE 8444, p. 99085O
- Waxman E., Katz B., 2017, *Handbook of Supernovae*. Springer International Publishing AG, p. 967
- Wevers T., van Velzen S., Jonker P. G., Stone N. C., Hung T., Onori F., Gezari S., Blagorodnova N., 2017, *MNRAS*, 471, 1694
- Whitesides L. et al., 2017, *ApJ*, 851, 107
- Woosley S. E., 1993, *ApJ*, 405, 273
- Wright E. L. et al., 2010, *AJ*, 140, 1868
- Xu D. et al., 2018, *The Astronomer's Telegram*, 11740
- Yaron O. et al., 2017, *Nature Phys.*, 13, 510
- York D. G. et al., 2000, *AJ*, 120, 1579

SUPPORTING INFORMATION

Supplementary data are available at [MNRAS](https://academic.oup.com/mnras) online.

Table 1. Early photometric observations of AT 2018cow from our campaign.

Please note: Oxford University Press is not responsible for the content or functionality of any supporting materials supplied by the authors. Any queries (other than missing mate-

rial) should be directed to the corresponding author for the article.

¹*Astrophysics Research Institute, Liverpool John Moores University, 146 Brownlow Hill, Liverpool L3 5RF, UK*

²*Max-Planck Institut für Astrophysik, Karl-Schwarzschild-Str 1, D-84741 Garching, Germany*

³*Division of Physics, Math, and Astronomy, California Institute of Technology, Pasadena, CA 91125, USA*

⁴*Astrophysics Science Division, NASA Goddard Space Flight Center, 8800 Greenbelt Road, Greenbelt, MD 20771, USA*

⁵*Department of Astronomy and Astrophysics, University of California, Santa Cruz, CA 95064, USA*

⁶*Dark Cosmology Centre, Niels Bohr Institute, University of Copenhagen, Blegdamsvej 17, DK-2100 Copenhagen, Denmark*

⁷*Department of Astronomy, University of Maryland, College Park, MD 20742, USA*

⁸*Indian Institute of Astrophysics, II Block Koramangala, Bengaluru 560034, India*

⁹*Joint Astronomy Programme, Department of Physics, Indian Institute of Science, Bengaluru 560012, India*

¹⁰*Kavli IPMU (WPI), The University of Tokyo Institutes for Advanced Study, The University of Tokyo, Kashiwa, Chiba 277-8583, Japan*

¹¹*Department of Physics, Faculty of Science and Engineering, Konan University, 8-9-1 Okamoto, Kobe, Hyogo 658-8501, Japan*

¹²*Astronomical Institute, Tohoku University, Aoba, Sendai 980-8578, Japan*

¹³*Instituto de Astronomía, Universidad Nacional Autónoma de México, Apartado Postal 70-264, 04510 México, CDMX, México*

¹⁴*Department of Physics, Florida State University, Tallahassee, FL 32306, USA*

¹⁵*Physics Department, Indian Institute of Technology Bombay, Powai, Mumbai 400076, India*

¹⁶*Department of Astronomy, University of California, Berkeley, CA 94720, USA*

¹⁷*School of Earth and Space Exploration, Arizona State University, Tempe, AZ 85287, USA*

¹⁸*Caltech Optical Observatories, California Institute of Technology, Pasadena, CA 91125, USA*

¹⁹*The Oskar Klein Centre, Department of Physics, AlbaNova, Stockholm University, SE-106 91 Stockholm, Sweden*

²⁰*Department of Astronomy/Mount Laguna Observatory, San Diego State University, 5500 Campanile Drive, San Diego, CA 92182-1221, USA*

²¹*Department of Physics, School of Science, Tokyo Institute of Technology, 2-12-1 Ohokayama, Meguro, Tokyo 152-8551, Japan*

²²*Department of Astronomy, Kyoto University, Kitashirakawa-Oiwake-cho, Sakyo-ku, Kyoto 606-8502, Japan*

²³*Center for Data Driven Discovery, California Institute of Technology, Pasadena, CA 91125, USA*

²⁴*Graduate Institute of Astronomy, National Central University, 32001 Taipei, Taiwan*

²⁵*Soka University of America, 1 University Drive, Aliso Viejo, CA 92656, USA*

²⁶*INAF OAS, Via Piero Gobetti, 101, I-40129 Bologna, Italy*

²⁷*Niels Bohr Institute, University of Copenhagen, Blegdamsvej 17, DK-2100 Copenhagen, Denmark*

²⁸*Instituto de Astronomía UNAM, Unidad Académica en Ensenada, 22860 Ensenada BC, México*

²⁹*The Oskar Klein Centre, Department of Astronomy, AlbaNova, Stockholm University, SE-106 91 Stockholm, Sweden*

³⁰*Yale-NUS College, 16 College Avenue West, Singapore 138527, Singapore*

This paper has been typeset from a $\text{\TeX}/\text{\LaTeX}$ file prepared by the author.

SCIENTIFIC REPORTS



OPEN

Research of activity of Main Belt Comets 176P/LINEAR, 238P/Read and 288P/(300163) 2006 VW₁₃₉

Jianchun Shi^{1,2,3}, Yuehua Ma^{1,2}, He Liang^{1,4} & Ruiqi Xu^{1,4}

As a new class of comet, main belt comets (MBCs) have attracted more and more attention in recent years. To study activity and physical properties of three MBCs 176P/LINEAR, 238P/Read and 288P/(300163) 2006 VW₁₃₉, we carried out broadband CCD photometry of three MBCs on UT 2016 November 18–19 with the 1-m optical telescope at Lulin Observatory in Taiwan. By comparing cometary surface brightness profiles to stellar surface brightness profiles, and by comparing cometary absolute magnitude to the expected magnitude of inactive nucleus, we found that 176P/LINEAR was inactive, while 238P/Read and 288P/(300163) 2006 VW₁₃₉ were active. By photometric studies, we obtained the $Af\rho$ values and the dust production rates. Finally, the activity of three MBCs were discussed. Our photometric results show that the total dust mass of 238P/Read and 288P/(300163) 2006 VW₁₃₉ obtained in this work are of the same magnitude as the majority of known MBCs.

Comets are small bodies in solar system, they are distinguished from asteroids by the presence of coma or tail. The activity of comets are driven by water ice or sublimation of volatile admixtures. Before 2006, comets are believed to have formed in the outer solar system, beyond the orbit of Neptune, and to reside in two cold reservoirs: the Oort cloud and the Kuiper belt. Hsieh & Jewitt¹ identified a third reservoir which is located at the main asteroid belt. Some asteroids show evidence for mass loss, these are called active asteroids. Active asteroids include main-belt comets (MBCs) and disrupted asteroids². MBCs exhibit comet-like activity driven by the sublimation of volatile ice, while disrupted asteroids exhibit activity likely due to impacts^{3–5}, rotational disruption^{6–10}, thermal disintegration or electrostatics¹¹.

MBCs have attracted most attention in recent years due to the implication from their activity that the existence of present-day ice in the asteroid belt. This offers opportunities to better understand the thermal and compositional history of our solar system, and place constraints on protosolar disk models. Research of MBCs may also be useful for investigating hypotheses that objects from the main asteroid belt may have played a significant role in the primordial delivery of water to the terrestrial planets^{12–15}. Previous cometary measurements the deuterium-to-hydrogen (D/H) ratios in Jupiter family comets show that most of them are higher than the oceanic D/H ratio and preclude the idea that the water on Earth is delivered from Jupiter family¹⁶. Thus the possibility of the water on Earth is delivered from the main asteroid belt has been enhanced.

There are 8 known unambiguous MBCs, which activity is driven by sublimation of volatiles and the triggering mechanism of activity of these objects are collision with a small impactor. (133P/Elst-Pizarro, 176P/LINEAR, 238P/Read, 259P/Garradd, 324P/2010 R2 (La Sagra), 288P/(300163) 2006 VW₁₃₉, P/2012 T1, 313P/Gibbs¹⁷. But not all of MBCs can reappear activity during the next perihelion passage, this may cast doubt on its sublimation-driven nature of the activity. To further determine whether main-belt objects are true MBCs, we need more observation data of perihelion passage. The objects of our observation are three MBCs 176P/LINEAR (118401), 238P/Read and 288P/(300163) 2006 VW₁₃₉.

176P/LINEAR (hereafter 176P), also known as asteroid 118401, was discovered on September 7, 1999 by LINEAR telescope in Socorro, New Mexico. It is the third discovered member of the MBCs. It was discovered to exhibit cometary nature on 2005 November 26 by the Gemini North telescope on Mauna Kea in Hawaii¹⁸, but it was not exhibit activity during its 2011 perihelion passage, this casts doubt on the sublimation-driven nature of

¹Purple Mountain Observatory, Chinese Academy of Sciences, Nanjing, 210034, China. ²CAS Key Laboratory of Planetary Sciences, Chinese Academy of Sciences, Nanjing, 210034, China. ³CAS Center for Excellence in Comparative Planetology, Hefei, China. ⁴School of Astronomy and Space Science, University of Science and Technology of China, Hefei, 230026, China. Correspondence and requests for materials should be addressed to J.S. (email: jcshi@pmo.ac.cn) or Y.M. (email: yhma@pmo.ac.cn)

Comet	UT date	R_h (au) ^a	Δ (au) ^b	α (°) ^c	ν (°) ^d	$N_{exp} \times \text{filter}^e$	t_{exp} (s) ^f
176P/LINEAR	2016/11/19	2.633 ^I	2.388	22.0	331.0	$5 \times R$	150
238P/Read	2016/11/18	2.371 ^O	1.615	18.7	3.1	$5 \times R$	300
288P/(300163) 2006 VW ₁₃₉	2016/11/19	2.437 ^O	1.954	22.7	8.0	$5 \times R$	225

Table 1. Log of all observations on UT 2016 November 18–19. *Note.* ^aThe heliocentric distance in au, superscripts ^I refers to the comet is inbound (pre-perihelion), ^O refers to the comet is outbound (post-perihelion); ^bThe geocentric distance in au; ^cThe phase angle(Sun-comet-Earth) in degrees; ^dThe true anomaly in degrees; ^eNumber of exposures in the R filter; ^fThe total exposure time in second.

the activity observed in 2005¹⁹. The last perihelion passage of 176P was on 2017 March 12. Hsieh *et al.*²⁰ examined the pole orientation and active region of 176P and suggested that the comet was active due to a seasonal variation of the solar flux at the active area.

238P/Read (formerly P/2005 U1, hereafter 238P) was discovered by M. T. Read using the Spacewatch 36 inch telescope on Kitt Peak on 2005 October 24. It was the second MBC to be discovered. When it was discovered, it showed cometary activity. 238P repeated activity during its 2011 and 2016 perihelion passage^{21–23}. The last perihelion passage of 238P was on 2016 October 22.

288P/(300163) 2006 VW₁₃₉ (also known as asteroid 300163, formerly 2006 VW₁₃₉, hereafter 288P) was discovered in 2006 and first observed to be active on UT 2011 August 30²⁴. 288P was reported the reactivation during its 2016 perihelion passage^{23,25}. The last perihelion passage of 288P was on 2016 November 08. Agarwal *et al.*²⁶ found that 288P is a binary main belt comet which ejected dust grains via ice sublimation and they suggested sublimation torques may play an important part in binary orbit evolution.

In this paper, we present optical observations and the surface brightness profile (SBP) of the above three MBCs observed on November 18–19, 2016. We also obtained the $Af\rho$ values and the dust mass production rates. The activity of three MBCs was discussed. Hsieh *et al.*²³ published a paper about the 2016 reactivations of 238P and 288P recently, they reported observations of 238P and 288P from 2016 July to 2017 January in this paper. Our observation dates are in this time frame, but are not included in their observation Logs. Thus, the photometric results of our observations can be used to help fill in gaps of their observations.

Methods

The three comets were observed by using the 1-m optical telescope at Lulin Observatory in Taiwan on 2016 November 18–19. This telescope has been equipped with an Alta U42 2 k × 2 k CCD camera. The pixel scale of camera is 0.348 arcsec, the field of view (FOV) is 11.9×11.9 arcmin². The average seeing is 1.2 arcsec during the observations.

The three comets were observed through Asahi broad-band R filters. The effective wavelength of the R filter is $\lambda_e = 6578$ Å, the full width at halfmaximum (FWHM) is $\Delta\lambda = 1215$ Å. The observation mode of telescope was set to track the sidereal motion, the exposure times of comets were chosen to make the apparent motion of the comet within the seeing disc. The details of observations are provided in Table 1.

All images were reduced and calibrated in similar procedures (bias subtraction, flat-field correction and cosmic ray cleaning) used in our previous work²⁷. The bias value used in the calibration was an average of several zero-exposure images. The final flat-fields were obtained from several images of the twilight sky. The night sky level used for photometry in the IRAF task PHOT was obtained from the region far from the nucleus. The NOMAD1 catalog was used to perform the magnitude calibration of the images. To minimize the effect of color terms, we selected Standard stars that optical colors were similar to the Sun.

Results

Cometary activity and surface brightness profile. All three MBCs looked like a stellar appearance in each single exposure frame. To increase the signal-to-noise ratios of both our target comets and field stars, we created two composite images per object, one combining all R -band images of each object aligned on the comet, and another combining all images of each object aligned on field stars. The combined frames still appear stellar (Fig. 1). To search possible the extent of coma, we extracted surface brightness profiles (SBPs) of comets and stars from the combined image using the method described in Shi & Ma²⁸. By comparing with the stellar SBP, we find that 176P's SBP is consistent with stellar SBP, 238P and 288P's SBPs show a flux excess in outer region. This means that 176P was inactive or unresolved activity on November 19, 2016, while 238P and 288P were active on November 18, 2016 and November 19, 2016, respectively.

The cometary dust production and dust mass production rate. The cometary dust production is usually made by means of the parameter $Af\rho$ value (cm)²⁹. It is the product of the average grain albedo, the filling factor f (the ratio of the cross section of the dust grains to the field of view of aperture) and the projected radius of the photometric aperture ρ . $Af\rho$ can be given by the formalism

$$Af\rho = \frac{4R_h^2 \Delta^2 10^{0.4(m_\odot - m_{comet})}}{\rho}, \quad (1)$$

where R_h is in AU, Δ and ρ are in cm, m_{comet} is the comet integrated magnitude. For a steady state coma, $Af\rho$ should be an aperture-independent parameter, this parameter can be used to compare measurements concerning the dust continuum produced under different observing conditions, times and instruments.

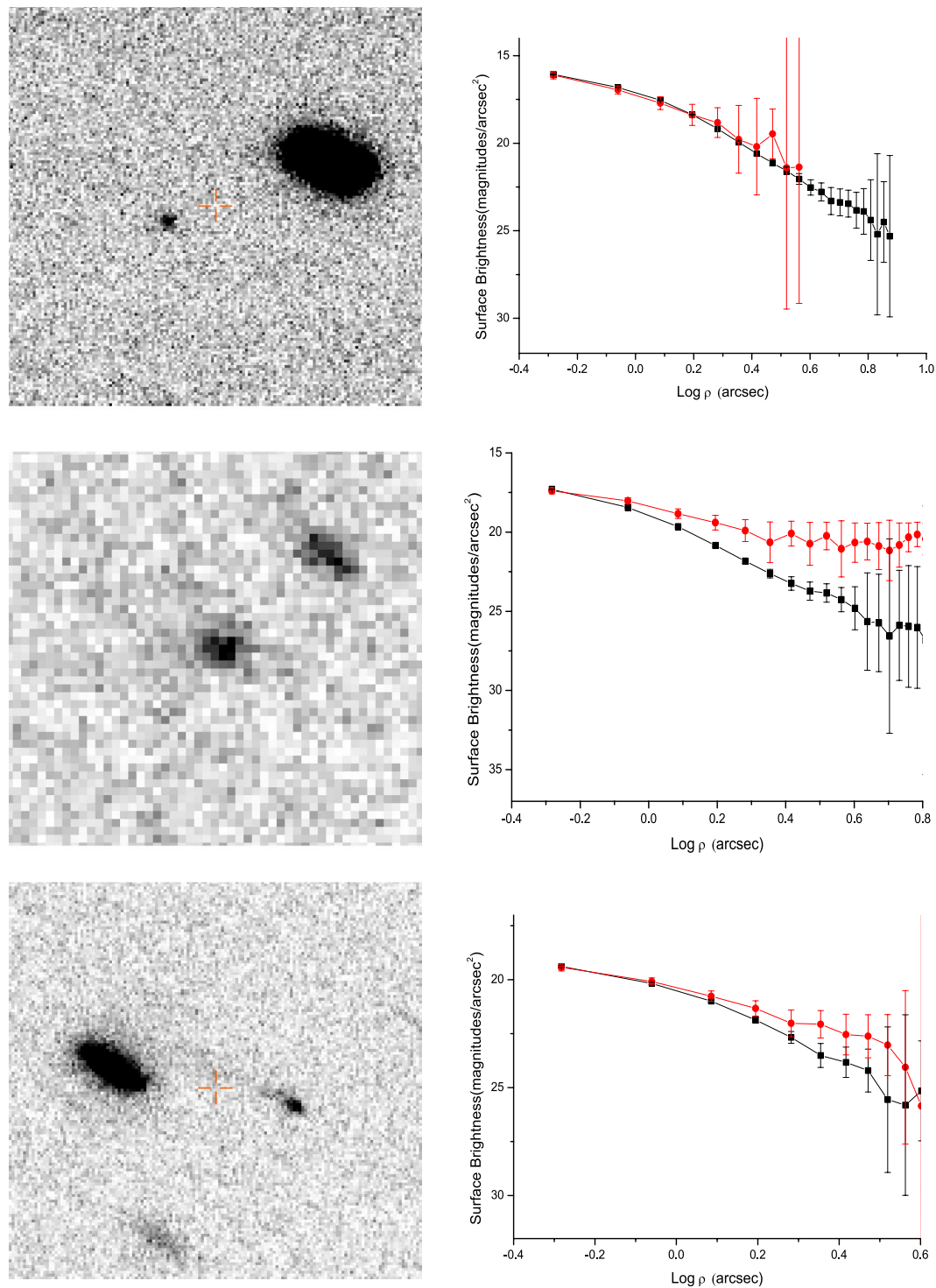


Figure 1. Co-added images (left-hand panels) and SBPs (right-hand panels) of 176P (top panels), 238P (middle panels) and 288P (bottom panels) in the *R* filter on November 19, 2016, November 18, 2016 and November 19, 2016, respectively. All images are oriented north-up (N), east-left (E). The field of view (FOV) of the top panel and bottom panel are 52.2×52.2 arcsec², The field of view (FOV) of the middle panel is 17.4×17.4 arcsec². The square dot line in SBPs represents the stellar SBP within the image, the circle dot line in SBPs represents the cometary SBP within the image.

Theoretically, $Af\rho$ should be calculated using the magnitude of the coma. As the $Af\rho$ values obtained by other works were calculated by using the total magnitude, we used total magnitude m_{TOT} to calculate the $Af\rho$ values to facilitate comparison with other works. For 238P, $Af\rho$ value in the reference aperture of 1.8 arcsec is 5.08 ± 0.59 cm; for 288P, $Af\rho$ value in the reference aperture of 1.8 arcsec is 12.04 ± 1.11 cm (Table 2). The photometry apertures were computed by using the star's FWHM in these coadded images that aligns the field stars.

Comet	m_{TOT} (1.8 arcsec) ^a	m_{TOT} (4.0 arcsec) ^b	$Af\rho$ (cm) ^c	Q_{dust} (kg s ⁻¹) ^d	M_{dust} (10 ⁷ kg) ^e
176P/LINEAR	20.01 ± 0.06	—	—	—	—
238P/Read	20.62 ± 0.05	20.06 ± 0.07	5.08 ± 0.59	1.9	2.8 ± 0.3
288P/(300163) 2006 VW ₁₃₉	19.95 ± 0.04	19.50 ± 0.06	12.04 ± 1.11	4.2	6.9 ± 1.5

Table 2. Magnitude, $Af\rho$, dust mass production rate and total dust mass measured in R -band of comets 176P/LINEAR, 238P/Read and 288P/(300163) 2006 VW₁₃₉. *Note.* ^aThe total magnitude in the reference aperture of 1.8 arcsec; ^bThe total magnitude in the reference aperture of 4.0 arcsec; ^c $Af\rho$ value in the reference aperture of 1.8 arcsec; ^dThe dust mass production rate in the reference aperture of 1.8 arcsec; ^eThe total dust mass in the reference aperture of 4.0 arcsec.

The dust mass loss rate can be calculated by dividing the total dust mass by the time of residence of the dust grains as they travel across the projected photometry annulus³⁰. The coma magnitude between ϕ_1 and ϕ_2 is given by

$$m_d = -2.5 \log_{10}(10^{-0.4m_2} - 10^{-0.4m_1}), \quad (2)$$

where m_1 and m_2 are the magnitudes in apertures of ϕ_1 and ϕ_2 . To minimize the effects of nucleus contribution and sky background, we choose $\phi_1 = 2.4$ arcsec and $\phi_2 = 3.0$ arcsec. The dust mass is given by Jewitt³⁰ as $M_d = \frac{4}{3}\sigma a_{dust} C_d$, where σ is bulk density, a_{dust} is average grain radii, C_d is the total cross-section of the coma dust particles and can be computed from Equation (1). The time of residence of the dust grains in the annulus between ϕ_1 and ϕ_2 is $\tau(R_h) = 1.5 \times 10^{11} \Delta (\phi_2 - \phi_1) / v_{ej}$ ³⁰, where $\tau(R_h)$ is in s, Δ is in AU, ϕ_1 and ϕ_2 are expressed in radians, v_{ej} is the radial outflow speed of the dust grains from the nucleus in m s⁻¹. For comet Hale-Bopp, expansion measurements showed that the radial outflow speed of gas from the nucleus was $v_{R_h} = v_0(r_0/R_h)^{1/4}$ ³¹, where $v_0 = 550$ ms⁻¹ and $r_0 = 5$ au. For spherical grains emitted from a homogeneous nucleus, a dust velocity is about 10 per cent of the gas velocity^{32,33}. So the dust grain ejection velocity is $v_{ej} = v(R_h)/10$. We adopted the dust grain radius value of $a_{dust} = 10 \mu\text{m}$, this value consistent with dust modeling results for 133P³⁴. The grain density was adopted the canonical asteroid density $\sigma = 2000$ kg m⁻³³⁵. For 238P, $m_1 = 20.47 \pm 0.06$, $m_2 = 20.29 \pm 0.06$, the calculated dust production rate is 1.9 kg s⁻¹. For 288P, $m_1 = 19.75 \pm 0.05$, $m_2 = 19.61 \pm 0.05$, the calculated dust production rate is 4.2 kg s⁻¹ (Table 2).

Discussion

For 176P, Hsieh *et al.*²⁰ derived best-fit IAU phase function parameters of $H = 15.10 \pm 0.05$ and $G = 0.15 \pm 0.10$. Using these phase function parameters, Hsieh *et al.*¹⁹ summarized apparent R -band magnitude and absolute R -band magnitude of 176P observed before 2014. To compare previous observation to ours, we computed absolute magnitudes based on the total magnitude using the HG approximation with scattering parameter $G = 0.15 \pm 0.1$ and obtained $m_R(1, 1, 0) = 14.96 \pm 0.22$. Considering rotational variations of 176P is about 0.7 mag (a peak-to-trough photometric range)²⁰. The absolute magnitude obtained in this work is still in the range of rotational variations, this also suggest that it was inactive on November 19, 2016.

Table 3 summarized available R -band photometry results of comet 238P. The inactive photometric behavior of 238P has been previously established by Hsieh, Meech & Pittichová²¹ who derived best-fit IAU phase function parameters of $H = 19.05 \pm 0.05$ mag and $G = -0.03 \pm 0.05$. Using $G = -0.03 \pm 0.05$, we can then compute the equivalent absolute magnitudes (at heliocentric and geocentric distances of $R_h = \Delta = 1$ au and a solar phase angle of $\alpha = 0^\circ$) for all observations of 238P (Table 3). Comparing absolute magnitude and $Af\rho$ values obtained in this work to previous observation, we can find that there is an obvious about 2 mag photometric enhancement in this work than data obtained in 2010 July and August when 238P was observed to be largely inactive, this also suggest that it was active on November 18, 2016. Table 4 summarized available R -band photometry results of comet 288P. Absolute R -band magnitudes (at $R_h = \Delta = 1$ au and $\alpha = 0^\circ$), were computed by using $G = 0.15 \pm 0.1$ ²⁰ (Table 4).

As the determination of the dust production rate of a comet is highly model-dependent and parameter-dependent, we can't compare the dust production rates obtained in this work to other works directly. To compare activity of 238P and 288P in this work to Hsieh *et al.*'s²³ work and other MBCs. We computed the total mass M_{dust} of visible ejected dust by using of equation²³

$$M_{dust} = \frac{4}{3} \pi a_N^2 a_{dust} \rho_d \frac{1 - 10^{0.4(m(1,1,0) - H)}}{10^{0.4(m(1,1,0) - H)}}, \quad (3)$$

where a_N is the nucleus's radius in m. For consistency, we choose dust grain densities of $\rho_d = 2500$ kg s⁻¹, mean effective grain radii of $a_{dust} = 1$ mm and the photometry aperture radius is 4 arcsec, these values are same with Hsieh *et al.*'s work²³. For 238P, the total apparent R -band magnitude measured in aperture radius 4 arcsec is $m_{TOT} = 20.06 \pm 0.07$, the total absolute R -band magnitude computed by using $H = 19.05 \pm 0.05$ mag and $G = -0.03 \pm 0.05$ ²¹ is $m(1, 1, 0) = 15.94 \pm 0.13$, $a_N \approx 0.4$ km²¹, the corresponding total dust mass is $M_{dust} = (2.8 \pm 0.3) \times 10^7$ when 238P was at true anomaly $\nu = 3^\circ.1$ on 2016 November 18. For 288P, the total apparent R -band magnitude measured in aperture radius 4 arcsec is $m_{TOT} = 19.50 \pm 0.06$, the total absolute R -band magnitude computed by using $H = 16.80 \pm 0.12$ and $G = 0.18 \pm 0.11$ ²³ is $m(1, 1, 0) = 15.07 \pm 0.23$, $a_N \approx 1.3$ km³⁶, the corresponding total dust mass is $M_{dust} = (6.9 \pm 1.5) \times 10^7$, when 288P was at true anomaly $\nu = 8^\circ.0$ on 2016 November 19. Hsieh *et al.*²³ reported 238P's total dust mass of $M_{dust} = (2.3 \pm 0.3) \times 10^7$ on 2016 November 5 (when 238P was at $\nu = 4^\circ.2$ and 288P's total dust mass of $M_{dust} = (6.8 \pm 1.4) \times 10^7$ on 2016 November

Active? ^a	UTdate	R_h (au) ^b	Δ (au) ^c	α (°) ^d	ν (°) ^e	m_{TOT} ^f	$m(1, 1, 0)$ ^g	Afp (cm) ^h	References
Perihelion	2005-07-28	2.365	2.276	25.2	0.0	—	—	—	—
yes	2005-11-10	2.436	1.446	0.6	31.4	19.28 ± 0.05	16.41 ± 0.17	7.47 ± 0.86	³⁹
yes	2005-11-19	2.448	1.468	3.8	33.9	19.34 ± 0.05	16.13 ± 0.16	7.23 ± 0.83	³⁹
yes	2005-11-20	2.450	1.471	4.3	34.2	19.46 ± 0.05	16.20 ± 0.15	6.47 ± 0.74	³⁹
yes	2005-11-21	2.451	1.475	4.8	34.5	19.37 ± 0.05	16.07 ± 0.15	7.08 ± 0.82	³⁹
yes	2005-11-22	2.453	1.480	5.3	34.8	19.28 ± 0.05	15.94 ± 0.15	7.69 ± 0.89	³⁹
yes	2005-11-26	2.459	1.499	7.1	35.9	19.72 ± 0.10	16.24 ± 0.17	5.24 ± 1.21	³⁹
yes	2005-12-24	2.504	1.739	17.1	43.6	20.12 ± 0.03	15.79 ± 0.12	4.34 ± 0.30	³⁹
yes	2005-12-25	2.505	1.751	17.4	43.9	20.16 ± 0.03	15.80 ± 0.12	4.24 ± 0.29	³⁹
no	2007-01-27	3.433	2.488	5.2	123.0	24.90 ± 0.40	19.71 ± 0.42	0.14 ± 0.13	³⁹
Aphelion	2008-05-19	3.963	3.276	11.8	180.0	—	—	—	—
no	2010-07-07	2.704	1.821	13.0	−68.2	23.61 ± 0.10	19.19 ± 0.16	0.21 ± 0.05	²¹
no	2010-07-20	2.674	1.709	8.5	−65.2	22.85 ± 0.06	18.82 ± 0.15	0.39 ± 0.05	²¹
no	2010-08-15	2.616	1.608	2.6	−58.9	22.34 ± 0.05	18.88 ± 0.16	0.57 ± 0.07	²¹
no	2010-09-03	2.576	1.643	10.7	−54.1	21.97 ± 0.04	17.99 ± 0.13	0.79 ± 0.07	²¹
yes	2010-09-04	2.574	1.647	11.0	−53.9	22.01 ± 0.05	18.02 ± 0.14	0.76 ± 0.09	²¹
yes	2010-09-05	2.572	1.651	11.4	−53.6	22.02 ± 0.05	18.00 ± 0.14	0.76 ± 0.09	²¹
yes	2010-10-05	2.514	1.869	20.3	−45.7	22.25 ± 0.05	17.62 ± 0.12	0.66 ± 0.08	²¹
yes	2010-11-25	2.433	2.414	23.5	−31.5	21.75 ± 0.05	16.51 ± 0.11	1.27 ± 0.15	²¹
yes	2010-12-09	2.416	2.566	22.5	−27.5	21.86 ± 0.07	16.54 ± 0.12	1.20 ± 0.19	²¹
Perihelion	2011-03-10	2.361	3.277	7.9	0.0	—	—	—	—
Perihelion	2016-10-22	2.366	1.410	8.7	0.0	—	—	—	—
yes	2016-11-18	2.371	1.615	18.7	3.1	20.62 ± 0.05	16.50 ± 0.12	5.08 ± 0.59	This work

Table 3. Summary of available R -band photometry results of comet 238P/Read. *Note.* ^aIs visible activity detected?; ^bThe heliocentric distance in au; ^cThe geocentric distance in au; ^dThe phase angle (Sun-comet-Earth) in degrees; ^eThe true anomaly in degrees; ^fThe total magnitude; ^gAbsolute R -band magnitude; ^h Afp values in R -band.

Active? ^a	UTdate	R_h (au) ^b	Δ (au) ^c	α (°) ^d	ν (°) ^e	m_{TOT} ^f	$m(1, 1, 0)$ ^g	References
Perihelion	2011-07-18	2.438	2.293	24.6	0.0	—	—	—
yes	2011-11-14	2.506	1.561	8.4	33.2	18.62 ± 0.05	15.08 ± 0.27	²⁴
yes	2011-11-14	2.506	1.561	8.4	33.2	18.64 ± 0.05	15.10 ± 0.27	²⁴
yes	2011-11-18	2.510	1.586	10.0	34.3	18.60 ± 0.10	14.95 ± 0.28	²⁴
yes	2011-11-19	2.512	1.596	10.6	34.6	18.64 ± 0.10	14.95 ± 0.27	²⁴
yes	2011-11-30	2.525	1.685	14.4	37.4	19.04 ± 0.05	15.08 ± 0.24	²⁴
yes	2011-12-04	2.530	1.724	15.6	38.5	19.12 ± 0.03	15.07 ± 0.23	²⁴
yes	2011-12-19	2.549	1.895	19.2	42.4	19.68 ± 0.03	15.29 ± 0.22	²⁴
yes	2012-01-07	2.577	2.152	21.7	47.4	20.43 ± 0.10	15.66 ± 0.23	²⁴
yes	2012-10-14	3.111	3.273	17.7	107.1	22.45 ± 0.03	16.49 ± 0.23	³⁶
Aphelion	2014-03-13	3.660	2.697	4.5	180.0	—	—	—
Perihelion	2016-11-08	2.436	1.823	21.3	0.0	—	—	—
yes	2016-11-19	2.437	1.954	22.7	8.0	19.95 ± 0.04	15.48 ± 0.21	This work

Table 4. Summary of available R -band photometry results of comet 288P/300163. *Note.* ^aIs visible activity detected?; ^bThe heliocentric distance in au; ^cThe geocentric distance in au; ^dThe phase angle(Sun-comet-Earth) in degrees; ^eThe true anomaly in degrees; ^fThe total magnitude; ^gAbsolute R -band magnitude.

28 (when 288P was at $\nu = 5^\circ.6$ Examining previously reported photometry of active dust emission, Hsieh *et al.*²³ found that activity of 238P in 2016 were lower than the activity in 2010 and the activity of 288P in 2016 were larger than the activity in 2000. Comparing the total dust mass of 238P and 288P obtained in this work to Hsieh *et al.*'s²³ work, we find that our results are consistent with Hsieh *et al.*'s²³ conclusions. Comparing the total dust mass of 238P and 288P obtained in this work to other MBCs^{37,38}, we find that the total dust mass of 238P and 288P obtained in this work are of the same magnitude as the majority of known MBCs'. This is consistent with the fact that almost all of the MBCs appear to eject nearly identical quantities of dust³⁷.

Data Availability

Observations were carried out with the 1-m optical telescope at Lulin Observatory in Taiwan. The observation data can be obtained from Lulin Observatory.

References

- Hsieh, H. H. & Jewitt, D. A population of comets in the main asteroid belt. *Sci.* **312**, 561–563 (2006).
- Hsieh, H., Yang, B. & Haghighipour, N. Optical and dynamical characterization of comet-like main-belt asteroid (596) scheila. *Astrophys. J.* **744**, 9 (2012).
- Jewitt, D., Weaver, H., Mutchler, M., Larson, S. & Agarwal, J. Hubble space telescope observations of main-belt comet (596) scheila. *Astrophys. J. Lett.* **733**, L4 (2011).
- Bodewits, D. *et al.* Collisional excavation of asteroid (596) scheila. *Astrophys. J. Lett.* **733**, L3 (2011).
- Ishiguro, M. *et al.* Interpretation of (596) scheila's triple dust tails. *Astrophys. J. Lett.* **741**, L24 (2011).
- Jewitt, D., Agarwal, J., Weaver, H., Mutchler, M. & Larson, S. The extraordinary multi-tailed main-belt comet p/2013 p5. *Astrophys. J. Lett.* **778**, L21 (2013).
- Jewitt, D. *et al.* Disintegrating asteroid p/2013 r3. *Astrophys. J. Lett.* **784**, L8 (2014).
- Agarwal, J., Jewitt, D. & Weaver, H. Dynamics of large fragments in the tail of active asteroid p/2010 a2. *Astrophys. J.* **769**, 46 (2013).
- Drahus, M. *et al.* Fast rotation and trailing fragments of the active asteroid p/2012 f5 (gibbs). *Astrophys. J. Lett.* **802**, L8 (2015).
- Sheppard, S. & Trujillo, C. Dynamics of large fragments in the tail of active asteroid p/2010 a2. *Astrophys. J.* **149**, 44 (2015).
- Jewitt, D., Hsieh, H. & Agarwal, J. In *Asteroids IV* (eds Michel, P. *et al.*), 221–241 (Univ. Arizona Press, 2015).
- Morbidelli, A. *et al.* Source regions and time scales for the delivery of water to earth. *Meteorit. Planet. Sci.* **35**, 1309–1320 (2000).
- Morbidelli, A., Lunine, J. I., O'Brien, D. P., Raymond, S. N. & Walsh, K. J. Building terrestrial planets. *Ann. Rev. Earth Planet. Sci.* **40**, 251–275 (2012).
- Mottl, M., Glazer, B., Kaiser, R. & Meech, K. Water and astrobiology. *Chemie der Erde - Geochem.* **67**, 253–282 (2007).
- Owen, T. The contributions of comets to planets, atmospheres, and life: Insights from cassini-huygens, galileo, giotto, and inner planet missions. *Space Sci. Rev.* **138**, 301–316 (2008).
- Altwegg, K. *et al.* 67p/churyumov-gerasimenko, a jupiter family comet with a high d/h ratio. *Sci.* **347**, 1261952 (2015).
- Haghighipour, N., Maindl, T. I., Schäfer, C., Speith, R. & Dvorak, R. Triggering sublimation-driven activity of main belt comets. *Astrophys. J.* **830**, 22 (2016).
- Hsieh, H. H., Jewitt, D. & Pittichova, J. Comet p/1999 re70 = (118401). *IAU Circ.* **8704**, 3 (2006).
- Hsieh, H. H. *et al.* Search for the return of activity in active asteroid 176p/linear. *Astrophys. J.* **147**, 89 (2014).
- Hsieh, H. H., Ishiguro, M., Lacerda, P. & Jewitt, D. Physical properties of main-belt comet 176p/linear. *AJ.* **142**, 29 (2011).
- Hsieh, H. H., Meech, K. J. & Pittichová, J. Main-belt comet 238p/read revisited. *Astrophys. J. Lett.* **736**, L18 (2011).
- Hsieh, H. H., Forshay, P. & Schwamb, M. Comet 238p/read. *CBET.* 4307 (2016).
- Hsieh, H. H. *et al.* The 2016 reactivations of the main-belt comets 238p/read and 288p/(300163) 2006 VW₁₃₉. *AJ.* **156**, 223 (2018).
- Hsieh, H. H. *et al.* Discovery of main-belt comet p/2006 VW₁₃₉ by pan-starrs1. *Astrophys. J. Lett.* **748**, L15 (2012).
- Agarwal, J., Jewitt, D., Weaver, H., Mutchler, M. & Larson, S. Comet 288p/2006 VW₁₃₉. *CBET.* 4306 (2016).
- Agarwal, J., Jewitt, D., Mutchler, M., Weaver, H. & Larson, S. A binary main-belt comet. *Nat.* **549**, 357–359 (2017).
- Shi, J. C., Ma, Y. H. & Zheng, J. Q. Ccd photometry of distant active comets 228p/linear, c/2006 s3 (loneos) and 29p/schwassmann-wachmann 1. *Mon. Not. Roy. Astron. Soc.* **441**, 739–744 (2014).
- Shi, J. C. & Ma, Y. H. Ccd photometry of active centaur 166p/2001 t4 (neat). *Mon. Not. Roy. Astron. Soc.* **454**, 3635–3640 (2015).
- A'Hearn, M. F., Schleicher, D. G., Feldman, P. D., Millis, R. L. & Thompson, D. T. Comet bowell 1980b. *AJ.* **89**, 579–591 (1984).
- Jewitt, D. The active centaurs. *AJ.* **137**, 4296–4312 (2009).
- Biver, N. *et al.* The 1995 2002 long-term monitoring of comet c/1995 o1 (hale bopp) at radio wavelength. *Earth Moon Planet.* **90**, 5–14 (2002).
- Probstein, R. F. In *Probl. Hydrodyn. Continuum Mech. Soc. Indust. Appl. Math.* (eds Bisshopp, F. *et al.*), 568 (Philadelphia, PA, 1969).
- Fulle, M., Cremonese, G. & Böhm, C. The preperihelion dust environment of c/1995 o1 hale-bopp from 13 to 4 au. *AJ.* **116**, 1470–1477 (1998).
- Hsieh, H. H., Jewitt, D. C. & Fernández, Y. R. The strange case of 133p/elst-pizarro: A comet among the asteroids. *AJ.* **127**, 2997–3017 (2004).
- Jewitt, D. The active asteroids. *AJ.* **143**, 66 (2012).
- Agarwal, J., Jewitt, D., Weaver, H., Mutchler, M. & Larson, S. Hubble and keck telescope observations of active asteroid 288p/300163 (2006 VW₁₃₉). *AJ.* **151**, 12 (2016).
- Hsieh, H. H. The nucleus of main-belt comet p/2010 r2 (la sagra). *Icarus.* **243**, 16–26 (2014).
- Jewitt, D., Agarwal, J., Peixinho, N. & Weaver, H. New active asteroid 313p/gibbs. *AJ.* **149**, 81 (2015).
- Hsieh, H. H., Jewitt, D. & Ishiguro, M. Physical properties of main-belt comet p/2005 u1 (read). *AJ.* **137**, 157–168 (2009).

Acknowledgements

This work was based on observations made with the Lulin Observatory whose staff and assistants kindly helped us to finish these observations. We thank Haibin Zhao and Bin Li for discussions about the manuscript. We acknowledge the support of the National Natural Science Foundation of China (Grant Nos U1631128, 11573075, 11633009 and 11761131008); Minor Planet Foundation of Purple Mountain Observatory; “Technology of Space Telescope Detecting Exoplanet and Life” supported by National Defense Science and Engineering Bureau civil spaceflight advanced research project (D030201); the Strategic Priority Research Program on Space Science, the Chinese Academy of Sciences (Grant No. XDA15020302) and the exchange program between Finnish Academy (FA) and NSFC.

Author Contributions

J.C. Shi and Y.H. Ma contributed equally to conceive the research, data analysis and writing of the paper. J.C. Shi prepared all figures and tables. H. Liang and R.Q. Xu participated in the discussions. All authors contributed to the manuscript.

Additional Information

Competing Interests: The authors declare no competing interests.

Publisher's note: Springer Nature remains neutral with regard to jurisdictional claims in published maps and institutional affiliations.



Open Access This article is licensed under a Creative Commons Attribution 4.0 International License, which permits use, sharing, adaptation, distribution and reproduction in any medium or format, as long as you give appropriate credit to the original author(s) and the source, provide a link to the Creative Commons license, and indicate if changes were made. The images or other third party material in this article are included in the article's Creative Commons license, unless indicated otherwise in a credit line to the material. If material is not included in the article's Creative Commons license and your intended use is not permitted by statutory regulation or exceeds the permitted use, you will need to obtain permission directly from the copyright holder. To view a copy of this license, visit <http://creativecommons.org/licenses/by/4.0/>.

© The Author(s) 2019

國立中央大學

天文研究所
碩士論文

Lulin Widefield Telescope (LWT): a Robotic Telescope
for the Near-Earth Object Follow-up Observation

研究生：黃健峯

指導教授：饒兆聰 博士

中華民國 一百零八年 五月

ABSTRACT

Thanks to human beings' endless curiosity about the universe and advances in technology, ground-based telescopes around the world are constructed larger and larger. As a result of the imaging system has been significantly improved, we nowadays are able to observe much fainter celestial objects, i.e. the objects can be discovered at much longer distance from Earth. In order to avoid the demise of human civilization owing to devastating asteroids, we need to keep monitoring the potentially hazardous object (PHO) that may threaten Earth. However, the prerequisite is to confirm and predict their orbits so as for sufficient time to prepare for the incoming risks.

The goal of this paper is to make a telescope automatically follow up the unconfirmed Near-Earth Objects (NEOs) in the Near-Earth Object Confirmation Page (NEOCP) [1] [2] of the Minor Planet Center (MPC) which belongs to the International Astronomical Union (IAU) and participate in the global asteroid warning network on behalf of Taiwan.

We introduced the Lulin Widefield Telescope (LWT), a 0.40 m Officina Stellare 400 Ri-Fast Astrograph [3] installed at the Lulin Observatory, Taiwan, in October 2017, to focus on the follow-up observation of the NEOs. The telescope is equipped with a FLI ProLine [4] PL16803 Monochrome CCD camera, which offers a field of view of about 2 degree squared ($1.4^\circ \times 1.4^\circ$) especially for tracking the NEOs with uncertain orbits.

We describe in detail about the system of the LWT including hardwares and softwares, the characteristics of the camera such as gain, readout noise, dark current and linearity, the quality of site including sky background brightness and limiting magnitudes for *B* and *V* bands, the design of automatic operation ranging from observation to analysis, sending the astrometric observation report of the recovered NEOs to the MPC, and the future plan for upgrading the system or expanding research interests to other areas of time-domain astronomy.

Keywords: Lulin Observatory, Lulin Widefield Telescope (LWT), Near-Earth Objects (NEOs), system testing, robotic telescope

國立中央大學

天文研究所

碩士論文

利用星團中已知造父變星在顏色-星等圖上的位置
尋找新的造父變星

Finding New Cepheids in the Open Clusters with Their
Location in the Color-Magnitude Diagram – Tests with
Existing Data and Known Cepheids

研究生：駱世昌

指導教授：饒兆聰 博士

中華民國一百零八年六月

Finding New Cepheids in the Open Clusters with Their Location in the Color-Magnitude Diagram – Tests with Existing Data and Known Cepheids

Abstract

Cepheids in open clusters can use its period-luminosity relation to determine distance of the open clusters. According to an initial mass function, we expect member stars in open clusters include both low and high mass stars. Based on stellar evolution, 4~20 solar mass stars will eventually enter the instability strip in their lifetime and become Cepheids. However, only 24 Cepheids were found in open clusters. In comparison there are more than 3000 open clusters in our Galaxy, it is not more than 1%.

In this thesis, receiving the Cepheids of open clusters' data from WEBDA and 2MASS database to make the locus of the instability strip in the Color-Magnitude Diagram. We use the instability strip, spatial membership probability, proper motion membership probability, photometric membership probability and age to look for the open clusters that have candidate Cepheids in 2MASS database. Then observed 6 open clusters that have 12 candidate Cepheids in B, V, R, I bands by SLT in Lulin Observatory in 6~7 months. Final, we analyzed these candidate Cepheids by Differential Photometry, LS Periodogram and Mean Magnitude-Standard Deviation of Magnitude Diagram, and we determined that 12 candidate

Cepheids are not Cepheids.

We used 2 new Cepheids of open clusters to examine the filter condition. It showed the instability strip, spatial membership probability, proper motion membership probability and age that can used, but photometric membership probability is not.

Keywords: Cepheid, Open Cluster, Color-Magnitude Diagram

The beamed jet and quasar core of the distant blazar 4C 71.07

C. M. Raiteri ^{1b}, ^{1★} M. Villata,¹ M. I. Carnerero,¹ J. A. Acosta-Pulido,^{2,3}
 D. O. Mirzaqulov,⁴ V. M. Larionov,^{5,6} P. Romano ^{7b}, S. Vercellone ^{7b}, I. Agudo,⁸
 A. A. Arkharov,⁶ U. Bach ^{9b}, R. Bachev,¹⁰ S. Baitieri,¹¹ G. A. Borman,¹²
 W. Boschin,^{2,3,13} V. Bozhilov,¹⁴ M. S. Butuzova ^{12b}, P. Calcidese,¹⁵ D. Carosati,^{13,16}
 C. Casadio,⁹ W.-P. Chen,¹⁷ G. Damljanovic,¹⁸ A. Di Paola,¹⁹ V. T. Doroshenko,^{20†}
 N. V. Efimova,⁶ Sh. A. Ehgamberdiev,⁴ M. Giroletti ^{21b}, J. L. Gómez,⁸ T. S. Grishina,⁵
 S. Ibryamov,²² H. Jermak,²³ S. G. Jorstad,^{5,24} G. N. Kimeridze,²⁵ S. A. Klimanov,⁶
 E. N. Kopatskaya,⁵ O. M. Kurtanidze,^{25,26} S. O. Kurtanidze,²⁵ A. Lähteenmäki,^{27,28}
 E. G. Larionova,⁵ A. P. Marscher,²⁴ B. Mihov,¹⁰ M. Minev,¹⁴ S. N. Molina,⁸
 J. W. Moody,²⁹ D. A. Morozova,⁵ S. V. Nazarov,¹² A. A. Nikiforova,⁵
 M. G. Nikolashvili,²⁵ E. Ovcharov,¹⁴ S. Peneva,¹⁰ S. Righini,²¹ N. Rizzi,³⁰
 A. C. Sadun,³¹ M. R. Samal ^{17b}, S. S. Savchenko,⁵ E. Semkov,¹⁰ L. A. Sigua,²⁵
 L. Slavcheva-Mihova,¹⁰ I. A. Steele,²³ A. Strigachev,¹⁰ M. Tornikoski,²⁷
 Yu. V. Troitskaya,⁵ I. S. Troitsky⁵ and O. Vince¹⁸

Affiliations are listed at the end of the paper

Accepted 2019 August 12. Received 2019 August 5; in original form 2019 June 14

ABSTRACT

The object 4C 71.07 is a high-redshift blazar whose spectral energy distribution shows a prominent big blue bump and a strong Compton dominance. We present the results of a 2-yr multiwavelength campaign led by the Whole Earth Blazar Telescope (WEBT) to study both the quasar core and the beamed jet of this source. The WEBT data are complemented by ultraviolet and X-ray data from *Swift*, and by γ -ray data by *Fermi*. The big blue bump is modelled by using optical and near-infrared mean spectra obtained during the campaign, together with optical and ultraviolet quasar templates. We give prescriptions to correct the source photometry in the various bands for the thermal contribution, in order to derive the non-thermal jet flux. The role of the intergalactic medium absorption is analysed in both the ultraviolet and X-ray bands. We provide opacity values to deabsorb ultraviolet data, and derive a best-guess value for the hydrogen column density of $N_{\text{H}}^{\text{best}} = 6.3 \times 10^{20} \text{ cm}^{-2}$ through the analysis of X-ray spectra. We estimate the disc and jet bolometric luminosities, accretion rate, and black hole mass. Light curves do not show persistent correlations among flux changes at different frequencies. We study the polarimetric behaviour and find no correlation between polarization degree and flux, even when correcting for the dilution effect of the big blue bump. Similarly, wide rotations of the electric vector polarization angle do not seem to be connected with the source activity.

Key words: galaxies: active – galaxies: jets – quasars: individual: 4C 71.07.

1 INTRODUCTION

Blazars are radio-loud active galactic nuclei (AGNs) with the peculiarity that one of the relativistic plasma jets points towards

* E-mail: claudia.raiteri@inaf.it

† Passed away.

us. The jet emission undergoes Doppler beaming, with consequent flux enhancement, contraction of the variability time-scales and blueshift of the radiation. The blazar spectral energy distribution (SED), in the usual $\log(\nu F_\nu)$ versus $\log \nu$ plot, presents two bumps. The low-energy bump is produced by synchrotron radiation, while the origin of the high-energy bump is debated. According to leptonic models, high-energy photons are obtained through inverse-Compton scattering of soft photons on relativistic electrons, while in the hadronic scenario they are produced by acceleration of protons and/or particle cascades.

The blazar class includes BL Lac objects (BL Lacs) and flat-spectrum radio quasars (FSRQs), which were originally distinguished according to the equivalent width of their emission lines (Stickel et al. 1991). Following the unified scheme of AGN, the parent population of blazars are radio galaxies, with FRI and FRII grossly representing the unbeamed counterpart of BL Lacs and FSRQs, respectively (Urry & Padovani 1995). Understanding the affinity between blazars and other AGN classes can benefit from the study of the properties of the unbeamed blazar emission coming from the accretion disc and broad-line region (BLR). This is an extremely difficult task for BL Lacs, which usually have featureless spectra and no signature of disc radiation. In contrast, the spectra of FSRQs generally show broad emission lines. Moreover, their SED displays a big blue bump, and sometimes also a little blue bump, which are interpreted as contributions from the accretion disc and BLR and can reveal important information on the AGN nuclear zone, i.e. their quasar core.

One of the most promising candidates to study the unbeamed properties of blazars is the FSRQ 0836+710 (4C 71.07), whose SED shows a particularly luminous disc (Raiteri et al. 2014). Its redshift was estimated to be $z = 2.172$ by Stickel & Kuehr (1993) from the broad emission lines C IV $\lambda 1549$ and C III] $\lambda 1909$, and $z = 2.18032$ by Lawrence et al. (1996), while McIntosh et al. (1999) derived a systemic redshift of $z = 2.218$ from the [O III] $\lambda 5007$ narrow line in *H*-band spectra. A detailed investigation of the spectroscopic properties of 4C 71.07 is presented in Raiteri et al. (in preparation). They estimated a systemic redshift of $z = 2.213$ from the Balmer H α and H β broad emission lines. In the following, we will adopt this redshift value.

Asada et al. (2010) inferred a Faraday rotation measure gradient from multifrequency VLBI polarimetry, suggesting a helical magnetic field for the jet of 4C 71.07. Evidences in favour of a helical jet structure were presented also by Perucho et al. (2012b) based on very long baseline interferometry data. From the absence of a hotspot in the arcsec jet radio structure, Perucho et al. (2012a) concluded that the jet likely loses collimation and gets disrupted by the growth of helical instabilities.

Akyuz et al. (2013) analysed the multifrequency behaviour of the source during both a quiescent state in 2008–2011 and an active state in 2011. They found that the γ -ray emission correlates with the optical, but not with the radio emission and that the γ -ray spectrum becomes curved in active states.

From the theoretical side, in their analysis of high-redshift blazars, Ghisellini et al. (2010) applied a simple leptonic one-zone synchrotron and inverse-Compton model to the sources SED to derive information on the nuclear and jet physical parameters. For 4C 71.07, they estimated a black hole mass of $3 \times 10^9 M_\odot$, a size of the BLR of 1.5×10^{18} cm, an accretion disc luminosity of 2.25×10^{47} erg s $^{-1}$, a bulk Lorentz factor of 14 at the jet dissipation radius of 5.40×10^{17} cm for a jet viewing angle of 3°.

With the aim of disentangling the beamed from the unbeamed properties of this distant FSRQ to study both the jet and nuclear emission, we organized an intense multiwavelength monitoring effort in the period going from 2014 September to 2016 October. Optical (photometric and polarimetric), near-infrared, and radio monitoring was obtained by the GLAST-Agile Support Program (GASP) of the Whole Earth Blazar Telescope Collaboration¹ (e.g. Villata et al. 2008; Raiteri et al. 2017b, and references therein). These observations were complemented by pointings of the *Swift* satellite approximately once a month, by optical spectroscopic monitoring at the 4.2-m William Herschel Telescope (WHT) and 2.5-m Nordic Optical Telescope (NOT), and by near-infrared spectroscopic observations at the 3.58-m Telescopio Nazionale Galileo (TNG), all in the Canary Islands, Spain. The continuous survey of the sky at γ -rays by the *Fermi* satellite completed the observing coverage at high energies. The γ -ray flaring activity in 2015 October–November detected by the *Astrorivelatore Gamma ad Immagini LEggero* (AGILE) and by *Fermi* has been analysed in Vercellone et al. (2019). A detailed investigation of the broad emission-line properties is presented by Raiteri et al. (in preparation). In this paper, we analyse the photometric and polarimetric data acquired during the WEBT campaign together with the UV and X-ray data from *Swift* and γ -ray data from *Fermi*.

The paper is organized as follows: we first present and analyse in detail the radio-to-ultraviolet data acquired from both ground-based and space observations (Sections from 2 to 5). These data are used in Section 6 to reconstruct the low-energy bump of the source SED, to disentangle the synchrotron from the nuclear thermal emission, and to build an empirical model for the latter. We subsequently analyse the high-energy X-ray (Section 7) and γ -ray (Section 8) data and discuss the broad-band multiwavelength behaviour (Section 9). We finally present optical polarimetric observations (Section 10) and draw conclusions in Section 11.

2 GROUND-BASED OPTICAL, NEAR-INFRARED, AND RADIO DATA

Optical observations for the WEBT campaign were performed at the following observatories: Abastumani (Georgia), Belogradchik (Bulgaria), Calar Alto² (Spain), Crimean (Russia), Lowell (USA; Perkins telescope), Lulin (Taiwan), McDonald³ (USA), Mt. Maidanak (Uzbekistan), Pulkovo (Russia), Roque de los Muchachos (Spain; Liverpool, NOT, TNG, and WHT telescopes), ROVOR (USA), Rozhen (Bulgaria), SAI Crimean (Russia), Sirio (Italy), Skinakas (Greece), St Petersburg (Russia), Teide (Spain; IAC80 and STELLA-I telescopes), Tjarafe (Spain), Valle d'Aosta (Italy), Vidojevica Astronomical Station (Serbia; 60 and 140 cm telescopes).

All data sets were processed with standard procedures. The source magnitude was obtained by differential aperture photometry, using reference stars in the same field of the source (Villata et al. 1997; Doroshenko et al. 2014; Larionov private communication). Further optical photometry was obtained as calibration information in support of the spectroscopic monitoring at the NOT and WHT telescopes (see Raiteri et al., in preparation).

¹<http://www.oato.inaf.it/blazars/webt>

²Calar Alto data were acquired as part of the MAPCAT project: <http://www.iaa.es/~iagudo/research/MAPCAT>.

³In the framework of the telescope network of the Las Cumbres Observatory.

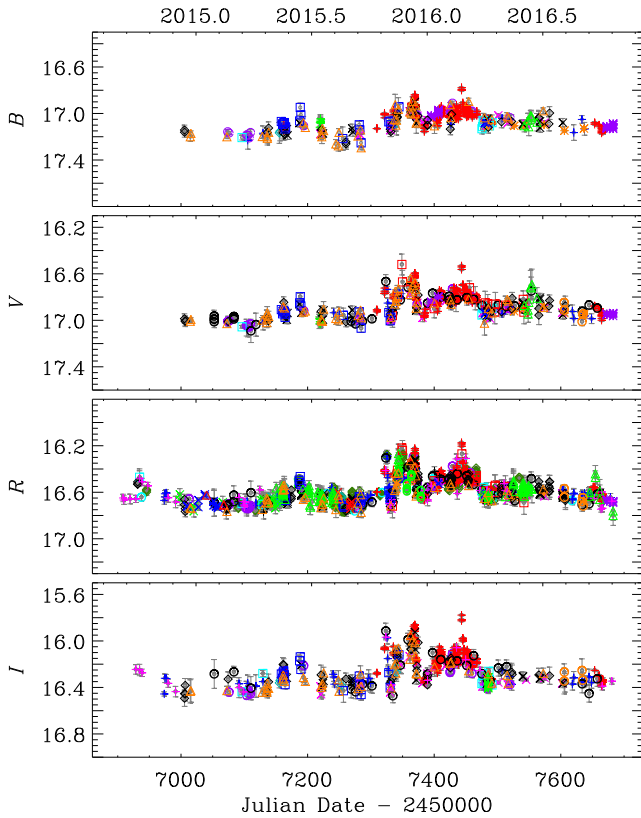


Figure 1. Optical light curves of 4C 71.07 from WEBT observations: observed magnitudes versus Julian Date (-2450000). Different data sets are marked with different colours and symbols.

Overposition of data from different telescopes sometimes revealed offsets that were corrected for by shifting the most deviating data sets. Strong outliers showing up in only one band were removed. In some cases, data scatter was reduced through binning.

Near-infrared data in J , H , and K bands were acquired at the Campo Imperatore Observatory (Italy). Additional data were obtained as calibration photometry for the near-infrared TNG spectra (see Raiteri et al., in preparation).

The final, cleaned, optical, and near-infrared light curves are shown in Figs 1 and 2, respectively. Notwithstanding the large sampling difference, especially between optical and near-infrared data, and different precision, the general increase of the variability amplitude from blue to red is evident and reveals the imprint of the emission contribution from the big blue bump, which is stronger in the blue (see Section 6). Table 1 reports, for each band, the number of data in the final light curves, the variability amplitude $\Delta\text{mag} = \text{mag}_{\text{max}} - \text{mag}_{\text{min}}$ and the mean fractional variation (Peterson 2001)

$$f_{\text{var}} = \frac{\sqrt{\sigma^2 - \delta^2}}{\langle F \rangle},$$

where σ^2 is the data set variance, δ^2 the mean square uncertainty of the fluxes (see Section 5 for the transformation from magnitudes to fluxes), and $\langle F \rangle$ is the mean flux of the data set. The advantage of f_{var} is that it takes into account the data errors. A few flares are visible in the optical light curves in the period from $\text{JD} = 2457320$ to $\text{JD} = 2457370$ and then at $\text{JD} = 2457443$. The optical maxima

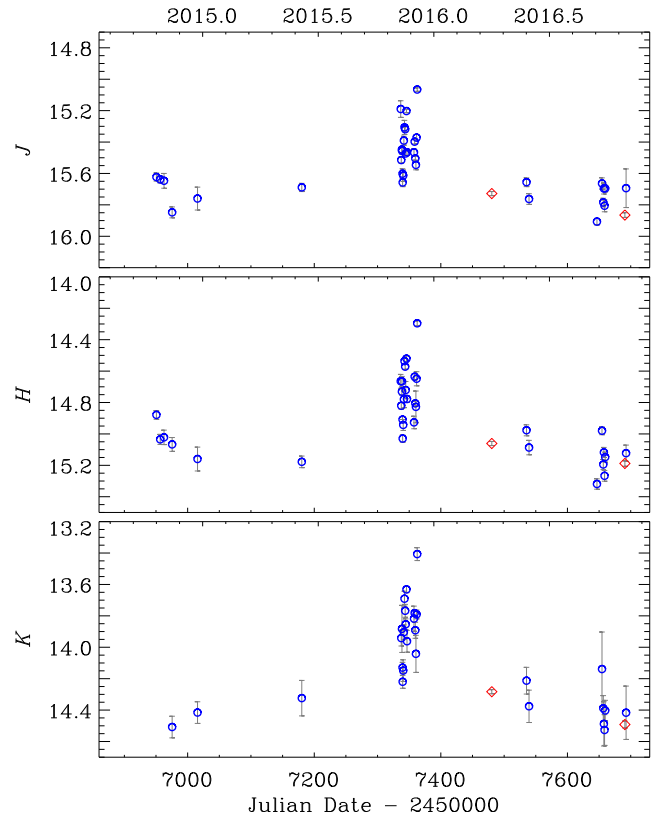


Figure 2. Near-infrared light curves of 4C 71.07 from WEBT observations: observed magnitudes versus Julian Date (-2450000). Blue circles represent data from Campo Imperatore, red diamonds observations taken with the TNG at the Roque de los Muchachos Observatory.

Table 1. Source properties in the various photometric bands: number of data, variability amplitude, mean fractional variation, big blue bump contribution to the flux densities corrected for the Galactic extinction.

Band	N_{data}	Δmag	f_{var}	F_{BBB} (mJy)	$\log(\nu F_{\nu})_{\text{BBB}}$
WEBT					
B	470	0.617	0.07	0.527	-11.443
V	531	0.561	0.09	0.520	-11.543
R	1521	0.717	0.10	0.532	-11.604
I	507	0.715	0.13	0.506	-11.721
J	36	0.841	0.19	0.470	-11.943
H	36	1.023	0.23	0.418	-12.123
K	30	1.120	0.28	0.606	-11.075
UVOT					
$w2$	43	0.47	0.10	0.045	-12.200
$m2$	42	0.48	0.08	0.059	-12.108
$w1$	43	0.48	0.10	0.137	-11.815
u	43	0.38	0.07	0.421	-11.442
b	43	0.35	0.07	0.533	-11.438
v	42	0.55	0.06	0.513	-11.548

were missed by the near-infrared observations, so we can expect that the near-infrared variability amplitude were actually higher than reported in Table 1.

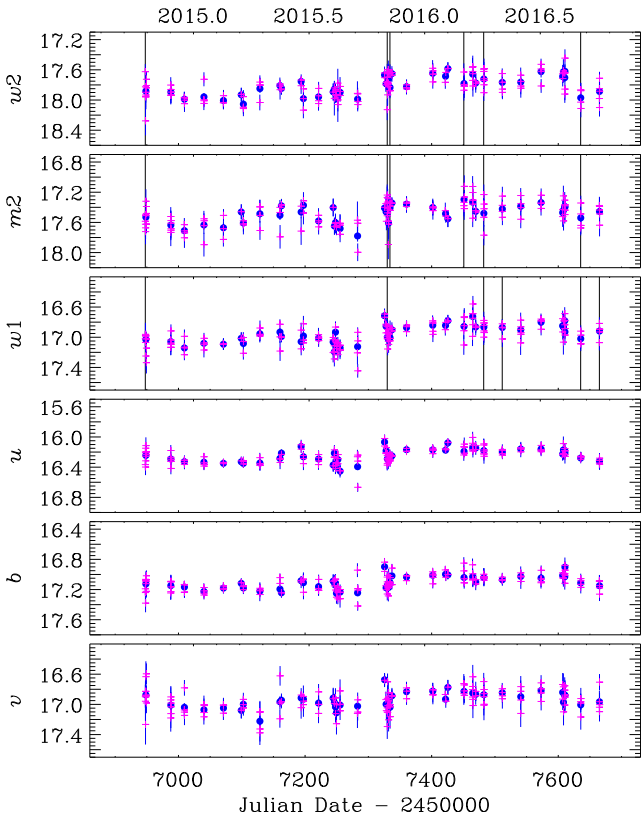


Figure 3. Ultraviolet and optical light curves built with data from the UVOT instrument on board *Swift*. Magenta plus signs represent photometry derived from the single exposures; blue dots that obtained by summing the frames in the same filter at the same epoch. Vertical lines mark the epochs affected by small-scale sensitivity problems.

In the radio band, observations were performed at the Pico Veleta⁴ (Spain; 228 and 86 GHz), Metsähovi (Finland; 37 GHz), and Medicina (Italy; 24, 8, and 5 GHz) observatories. Data reduction and analysis procedures are described in Agudo et al. (2010), Teraesranta et al. (1998), and D’Ammando et al. (2012). Radio light curves have been shown in Fig. 11. The 37 GHz data show some scatter, so we plotted a cubic spline interpolation through the 30-binned data to better distinguish the trend.

3 ULTRAVIOLET AND OPTICAL OBSERVATIONS BY *SWIFT*-UVOT

In the period of the WEBT campaign, *Swift* pointed at the source during 43 epochs. We processed the data with HEASOFT version 6.22. The source counts were extracted from a circular region with 5 arcsec radius centred on the source; the background counts were derived from an annular region centred on the source with inner and outer radius of 10 and 20 arcsec, respectively.

We processed both the single exposures and the images obtained by summing the exposures with the same filter in the same epoch. The results are shown in Fig. 3.

⁴These data were acquired with the IRAM 30 m telescope as part of the POLAMI (Polarimetric AGN Monitoring with the IRAM-30 m-Telescope) and MAPI (Monitoring AGN with Polarimetry at the IRAM 30 m Telescope) programmes.

Observations were checked for small-scale sensitivity (sss) problems, which occur when the source falls on small detector regions where the sensitivity is lower. The problem is more important for the ultraviolet filters. We found 35 snapshots in 8 epochs, where sss effects are recognized by the check procedure,⁵ all in the ultraviolet filters. These epochs are shown in Fig. 3. The data dispersion there is not larger than what happens in other epochs, so there is no need to exclude some of these frames from the analysis. Indeed, the most questionable points, lying out of the general trend common to all filters (e.g. the *v*-band point at JD = 2457128), are not due to sss problems.

As shown by Fig. 3 and Table 1, the source variability is smaller in the UVOT optical bands than in the ultraviolet, and this is a consequence of the fact that, due to the high redshift of the source, the big blue bump peaks in the *u*-*b* bands (see Section 6).

The comparison with the ground-based data shown in Fig. 1 reveals that only the optical flaring period around JD = 2457330 is well covered by UVOT observations, which were triggered by the detection of a high γ -ray flux (Vercellone et al. 2019), while the other optical peaks were missed. As a consequence, the variation amplitude and mean fractional variability reported in Table 1 for the UVOT filters underestimate the actual variability of the source in the considered period.

4 COLOUR BEHAVIOUR

To investigate the source spectral behaviour, we first built ground-based *B* – *V* colour indices by associating the most precise *B* and *V* data (error less than 0.03 mag) acquired within 15 min by the same telescope. We obtained 347 values, with an average index of 0.19 and standard deviation of 0.03.

Fig. 4 shows that the colour indices sample the whole brightness range of the source and clearly indicate a redder-when-brighter behaviour. Linear regression results in a slope of -0.23 . This trend is expected if the source brightening is due to the increasing contribution of a ‘red’ variable synchrotron component to the (quasi) stationary emission of the big blue bump (e.g. Gu et al. 2006; Villata et al. 2006).

In the same figure, we show the *b* – *v* colour indices obtained from UVOT data. We had to relax the constraints on the errors to get a reasonable number of colours. Using data with uncertainties less than 0.06 mag, we obtained 12 indices. They cover only the faintest states and indicate a mean value of 0.18, with standard deviation of 0.04, in agreement with the ground-based data.

5 FROM MAGNITUDES OR COUNT RATES TO FLUXES

Optical and near-IR magnitudes were transformed into flux densities by correcting for Galactic reddening according to the NASA/IPAC Extragalactic Database⁶ (NED) and using the absolute fluxes by Bessell, Castelli & Plez (1998).

By assuming a power-law shape of the optical spectrum $F_\nu \propto \nu^{-\alpha}$, we can derive the optical spectral index from the colours (see Fig. 4). The mean value obtained from the ground-based *B* – *V* indices is $\alpha = 0.18$ with a standard deviation of 0.14.

As seen in the previous section, the average *B* – *V* or *b* – *v* colour is ~ 0.2 mag, which is outside the range of validity of the

⁵http://swift.gsfc.nasa.gov/analysis/uvot_digest/sss_check.html

⁶<http://ned.ipac.caltech.edu>

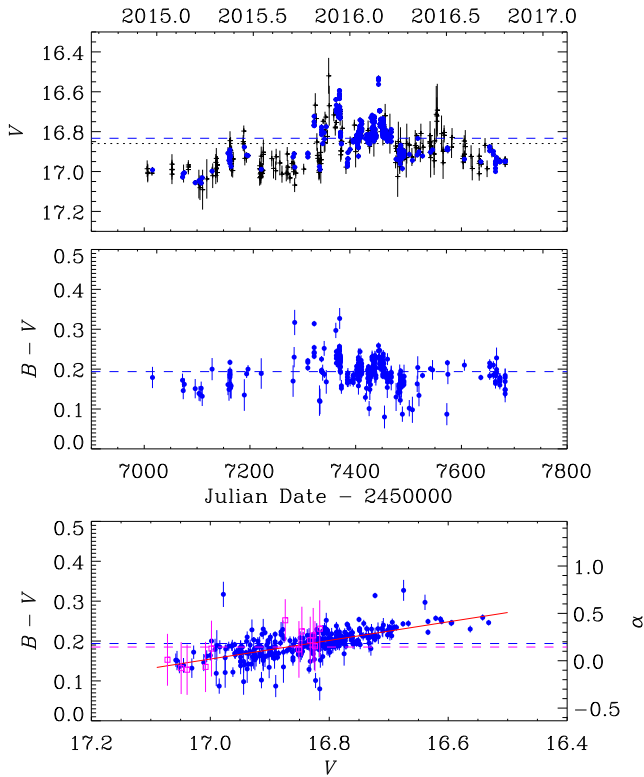


Figure 4. $B - V$ colour indices as a function of time (middle panel) and brightness (bottom panel); the dashed blue line indicates the average value. The light curve in V band is shown in the top panel for comparison. Black plus signs and dotted line refer to the whole data set; blue dots and dashed line to the subset used to get colour indices. The small difference in $\langle V \rangle$ between the whole data set and the subset means that colour indices sample fairly well the range of brightness covered by the source. In the bottom panel, the linear regression line is plotted in red. The spectral index α of the $F_\nu \propto \nu^{-\alpha}$ law is shown on the right. Magenta squares and lines refer to UVOT data.

Breeveld et al. (2011) count rate to flux conversion factors for the UVOT ultraviolet bands. This means that the standard UVOT calibrations in the ultraviolet are not applicable to spectral types like that of our source. Therefore, to convert UVOT magnitudes into fluxes, we followed the recalibration procedure described in Raiteri et al. (2010) and applied to a number of cases thereafter (e.g. D’Ammando et al. 2012; Larionov et al. 2016). We convolve an average source spectrum with the UVOT filter effective areas to derive the effective wavelengths λ_{eff} and count-to-flux conversion factors CF , and further with the mean extinction laws by Cardelli, Clayton & Mathis (1989) to obtain the extinction values A_λ . The procedure is then iterated to check stability of the results. Those reported in Table 2 were obtained with a log-linear fit to the source spectrum.

With respect to the Breeveld et al. (2011) calibrations, the most noticeable differences are a shift of about 100 \AA in the effective wavelengths of the $w1$ and $w2$ bands and a ~ 5 per cent increase of the count-to-flux conversion factor in the $w1$ band.

Starting from the source count rates, we applied the count-to-flux conversion factors of Table 2 and then corrected for the Galactic extinction according to the values in the same table to get deabsorbed flux densities. However, because of the high redshift of the source, the spectral region bluewards of the $\text{Ly}\alpha$ emission line is strongly eroded by a wealth of intervening absorbers

Table 2. Results of the UVOT recalibration procedure and prescriptions to correct for both Galactic and IGM absorption.

	λ_{eff} (\AA)	CF ($\text{erg cm}^{-2} \text{ s}^{-1} \text{ \AA}^{-1}$)	A_λ (mag)	τ_{eff}^a	τ_{eff}^b
$w2$	2148	$6.009 \cdot 10^{-16}$	0.220	1.140	1.481
$m2$	2272	$8.358 \cdot 10^{-16}$	0.231	0.923	1.330
$w1$	2688	$4.405 \cdot 10^{-16}$	0.183	0.529	0.820
u	3491	$1.647 \cdot 10^{-16}$	0.133	0.147	0.205
b	4377	$1.467 \cdot 10^{-16}$	0.111	0.	0.
v	5439	$2.602 \cdot 10^{-16}$	0.084	0.	0.

Notes. ^aDerived following Ghisellini et al. (2010).

^bDerived following Lusso et al. (2015).

(Scott, Bechtold & Dobrzycki 2000; Raiteri et al., in preparation). Therefore, to reconstruct the flux observed in the ultraviolet as it was emitted from the source, we must further correct for this effect. This issue will be addressed in the next section.

6 AN EMPIRICAL MODEL FOR THE QUASAR CORE

Based on infrared data from the *Wide-field Infrared Survey Explorer* (WISE) satellite, the Two Micron All-Sky Survey (2MASS), and the Campo Imperatore and Teide observatories, Raiteri et al. (2014) modelled the SED of 4C 71.07 from the infrared to the ultraviolet with the superposition of a log-parabolic jet component and a nuclear thermal component representing the emission contribution of the accretion disc and broad-line region. Because of the prominence of the big blue bump in this source, the nuclear thermal model was obtained by strengthening the type-1 QSO template by Polletta et al. (2007) with a blackbody. Thanks to the wealth of photometric and spectroscopic data we obtained in the WEBT 2-yr campaign, we can now refine the model for the source quasar core and estimate the thermal contribution of the nuclear emission to the source photometry in the various bands.

Fig. 5 shows the near-infrared to ultraviolet SED of 4C 71.07. All photometric and spectroscopic data have been corrected for the Galactic absorption. To build the core template, we started by considering the range of brightness spanned by the near-infrared, optical, and ultraviolet photometric data in the period considered in this paper. As mentioned before, the variability amplitude increases towards the red, and this is due to the increasing contribution of the very variable synchrotron emission with respect to the less variable thermal emission, which is assumed to be steady in the relatively short period of time we are dealing with.

In Raiteri et al. (in preparation), we present and discuss in detail the results of the spectroscopic monitoring of 4C 71.07 during the WEBT campaign. We obtained 24 optical spectra (12 with the WHT and 12 with the NOT) and 2 near-infrared spectra with the TNG. All of them were carefully calibrated in flux also using photometric supporting data. The average optical and near-infrared spectra are shown in Fig. 5. They have not been corrected for atmospheric absorption and include both a non-thermal emission contribution from the jet and a thermal contribution from the quasar core. To obtain a template for the big blue bump, we must first clean the spectra from the jet component, which we model as a power law. We use the relative difference in flux variability in the various bands to determine the slope of the power law and set the brightness level to have a very strong thermal contribution to the B - and V -band fluxes, as suggested by their observed smaller variability (see Figs 1–3 and Table 1). Although the model normalization is somewhat arbitrary,

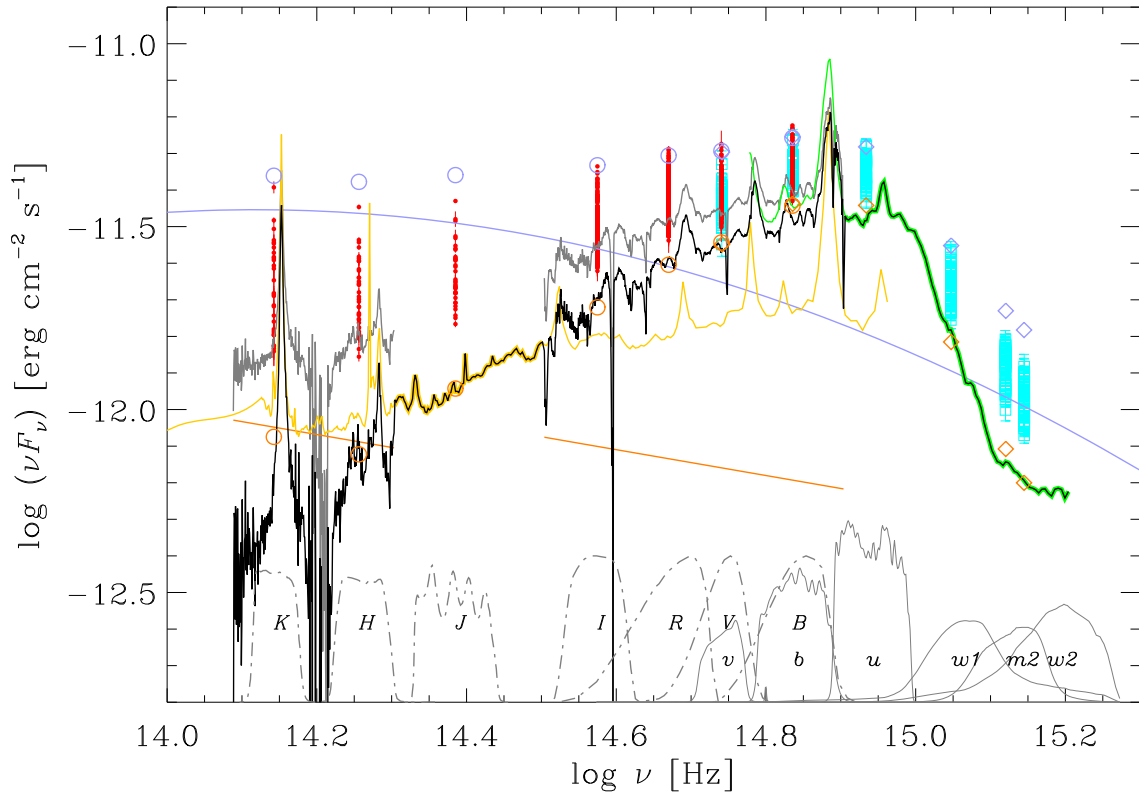


Figure 5. SED of 4C 71.07 from the near-infrared to the ultraviolet. Red dots and cyan squares represent the photometric data acquired by the WEBT and by *Swift*-UVOT, respectively. The average near-infrared and optical spectra by Raiteri et al. (in preparation) are shown in grey; the power laws used to correct them for the synchrotron jet emission contribution are plotted as orange lines. The quasar templates by Polletta et al. (2007) and Lusso et al. (2015) are shown in light orange and green, respectively. The final empirical model for the 4C 71.07 quasar core is plotted as a black line. Its contributions in the various photometric bands (whose transmission curves are shown in the figure bottom) are marked with orange circles (diamonds for the UVOT bands). The violet log-parabola represents a flaring state jet emission. The addition of this contribution to the nuclear thermal emission produces the photometric values shown as violet circles (diamonds for the UVOT filters).

the log-parabolic shape of the thermal-subtracted SED that we will discuss in Section 9 suggests that we are not far from the real, elusive solution. By comparing the spectroscopic with the photometric information, we note that the source brightness level corresponding to the near-infrared spectrum is lower than that corresponding to the optical spectrum, therefore we use a power law with a lower normalization to describe the jet contribution to the near-infrared spectrum. By subtracting the jet flux from the spectral fluxes, we obtain the predicted nuclear component.

We lack source spectra in between the near-infrared and the optical spectrum as well as in the ultraviolet. Therefore, we complete the nuclear thermal model using available quasar templates. We adopted the TQSO1 template by Polletta et al. (2007), shifted to the systemic redshift of $z = 2.213$ (Raiteri et al., in preparation) and properly rescaled to smoothly join our optical and near-infrared spectra, to cover the wavelength range from 14900 to 9400 Å. The comparison between the prolongation of the TQSO1 template and the optical spectrum of 4C 71.07 corrected for the jet emission (see Fig. 5) reveals that the rising part of the big blue bump of this source is much harder than the average quasar spectrum, as found by Raiteri et al. (2014). This may be due to the fact that in other AGN the low-frequency part of the disc SED is usually contaminated by additional softer emission contributions, as suggested by Calderone et al. (2013).

For wavelengths shorter than 3740 Å, we use the ultraviolet quasar-stacked spectrum by Lusso et al. (2015). This was obtained

by combining spectra of 53 quasars with redshift $z \sim 2.4$ acquired with the WFC3 instrument of the *Hubble Space Telescope* (*HST*). The authors present both the observed spectrum and that obtained by correcting for the absorption by the intergalactic medium (IGM). We use the former (Lusso private communication), properly scaled, to complete our ‘observed’ big blue bump template, while the IGM-corrected spectrum will be used to estimate effective opacity values in the photometric bands bluewards of the Ly α .

The final empirical model for the quasar core emission of 4C 71.07 is shown in Fig. 5. By convolving this template with the transmission curve of the Bessels and UVOT filters, we then calculate the photometric contributions of the big blue bump in the various bands.⁷ These are reported in Table 1 and can be used to subtract the thermal contributions to the source photometric observations when the purely non-thermal, jet emission is desired.

To further check the consistency of our procedure, we simulated a high brightness state. The broad-band jet emission is now modelled with a log-parabola, which is often used to describe the synchrotron contribution (e.g. Massaro et al. 2004; Raiteri et al. 2017b), as the power-law approximation would be too rough over such a

⁷We had to apply a correction to the $w2$ values to take into account that the template does not cover the whole range of frequencies spanned by the $w2$ filter. The correction was done by shifting the $w2$ thermal contribution to match the template.

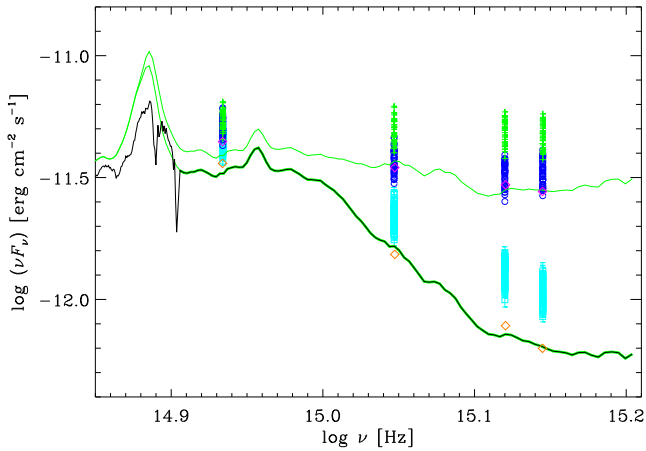


Figure 6. Zoom into the SED of 4C 71.07 in the blue–ultraviolet. The black line represents the quasar core template, which corresponds to the stacked quasar spectrum of Lusso et al. (2015) (lower green line) at wavelengths shorter than 3740 Å. The upper green line shows the IGM-corrected spectrum by the same authors. Orange diamonds mark the big blue bump contributions in the photometric UVOT bands derived from the absorbed template. The magenta diamonds show the big blue bump contributions after correction for the IGM absorption using the IGM-corrected template. Cyan squares represent the UVOT data, while blue circles and green plus signs the same data corrected for IGM absorption with the Ghisellini et al. (2010) and Lusso et al. (2015) prescriptions, respectively.

large frequency range. By summing the log-parabola and nuclear thermal template fluxes, we obtain what we should observe in flaring states. These predictions can then be compared to the highest observed flux levels. In Fig. 5, we see that the optical maxima are satisfactorily reproduced, while the near-infrared maxima are somewhat overproduced. This can be at least partly justified by the fact that we lack near-infrared data at the epochs of the optical flux peaks (see Section 2). In the ultraviolet, the range of the observed data is satisfactorily reproduced too. These are encouraging results, especially when considering that the ultraviolet template we used (Lusso et al. 2015) is an average quasar spectrum and that the jet emission spectrum can likely only approximately be described with a log-parabolic model.

A further step is now necessary to correct for the IGM absorption. Effective opacity values due to such absorption were estimated by Ghisellini et al. (2010) by averaging over all possible lines of sight. We rescaled those values (Ghisellini private communication) to take into account the difference between the old standard effective wavelengths by Poole et al. (2008) and ours. These new effective opacity values τ_{eff} are listed in Table 2. With respect to the estimates of Ghisellini et al. (2010), there is a 6 per cent decrease in the $w2$ band and a 2 per cent decrease in the $m2$ and $w1$ bands. The IGM-corrected flux densities are obtained as $F_{\tau} = F \times \exp(\tau_{\text{eff}})$ and are shown in Fig. 6.

Another way of estimating the correction is to use the IGM-corrected quasar spectrum of Lusso et al. (2015). By convolving this spectrum with the UVOT filters effective areas, we obtain the photometric contributions of the deabsorbed quasar core of 4C 71.07 (see Fig. 6). The differences between deabsorbed and absorbed SED values⁸ allow us to estimate the average effective opacities and to correct the UVOT data for IGM absorption. The opacity values are

⁸The ratio $T_{\lambda} = F_{\lambda,\text{obs}}/F_{\lambda,\text{corr}}$ corresponds to the mean IGM transmission function of Lusso et al. (2015).

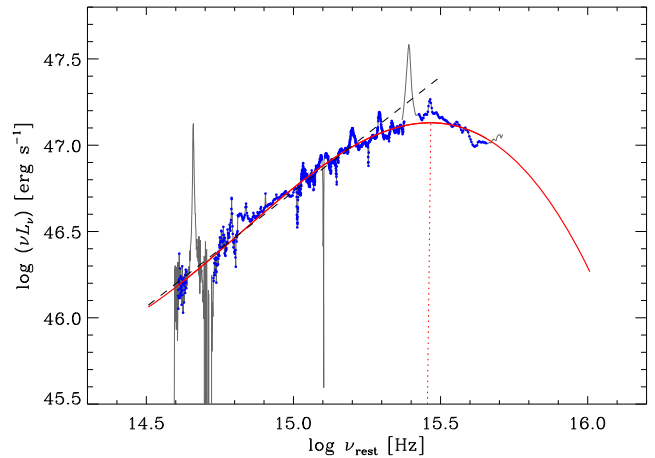


Figure 7. The empirical template for the 4C 71.07 big blue bump corrected for IGM absorption (grey). Blue dots mark the points that were used to obtain a third-order polynomial fit to the thermal continuum (red thick line). The dotted vertical line highlights the peak. The black dashed line represents the $F_{\nu} \propto \nu^{1/3}$ slope of a Shakura & Sunyaev disc spectrum.

reported in Table 2, while corrected data are shown in Fig. 6. As can be seen, following Lusso et al. (2015) leads to a higher correction than estimated by Ghisellini et al. (2010).

A final comment is due to remind that the disc emission of quasars is variable and also in the case of 4C 71.07 a remarkable change (a flux variation of a factor ~ 2.5) has been noted by Raiteri et al. (in preparation). However, this occurred on a time span of more than 30 yr and indeed quasar flux changes are usually of the order of a few tenths of mag on time-scales of several months/years (e.g. Kaspi et al. 2000). This is much less than the variability characterizing the non-thermal radiation from the jet.

7 DISC LUMINOSITY, ACCRETION RATE, AND BLACK HOLE MASS

The empirical model built in the previous section allows us to estimate the disc bolometric luminosity by integrating the thermal continuum. This is obtained by fitting the big blue bump template with a cubic polynomial (see Fig. 7) and leads to the extremely high value $L_{\text{disc}} = 2.45 \times 10^{47} \text{ erg s}^{-1}$, assuming a luminosity distance of 17 585 Mpc. The main uncertainty comes from the high-energy part of the spectrum, which is poorly constrained. However, our estimate is in good agreement with the value $2.25 \times 10^{47} \text{ erg s}^{-1}$ calculated by Ghisellini et al. (2010) with a completely different procedure.

The peak of the thermal continuum is found at $\log \nu_{\text{rest}} \simeq 15.46$ and implies a peak luminosity of $(\nu L_{\nu})_{\text{peak}} = 1.35 \times 10^{47} \text{ erg s}^{-1}$, so that $L_{\text{disc}}/(\nu L_{\nu})_{\text{peak}} = 1.8$, close to the factor of 2 usually assumed (e.g. Calderone et al. 2013; Ghisellini & Tavecchio 2015). Moreover, the peak frequency is in agreement with that predicted by accretion disc models for the same luminosity (e.g. Hubeny et al. 2000).

We note that the rising part of our disc template fairly matches the $F_{\nu} \propto \nu^{1/3}$ spectral distribution of a Shakura & Sunyaev disc (Shakura & Sunyaev 1973) up to $\log \nu_{\text{rest}} \sim 15.25$.

From the equation $L_{\text{disc}} = \eta \dot{M} c^2$ (Shakura & Sunyaev 1973), we can derive the accretion rate \dot{M} once the efficiency of gravitational energy release η is fixed. This can be as small as 0.06 for a Schwarzschild’s black hole and up to 0.32 for a rotating Kerr’s

black hole (Calderone et al. 2013). The disc bolometric luminosity we estimated above then leads to accretion rates of 17 and 3.3 $M_{\odot} \text{ yr}^{-1}$, respectively.

Calderone et al. (2013) proposed a method to estimate the black hole mass and accretion rate from the disc luminosity based on a Shakura & Sunyaev disc. By applying their equations (8) and considering that the isotropic disc luminosity is about one half the bolometric luminosity, we obtain $M_{\text{BH}} = (1.61\text{--}1.62) \times 10^9 M_{\odot}$ and $\dot{M} = (18.0\text{--}18.3) M_{\odot} \text{ yr}^{-1}$ for viewing angles in the range $0^{\circ}\text{--}10^{\circ}$, as expected for a blazar. The Eddington luminosity is then $L_E = 1.6 \times 10^{47} \text{ erg s}^{-1}$ and the Eddington ratio is 0.66, a remarkably high value (e.g. Ghisellini & Tavecchio 2015). The black hole mass is somewhat smaller than that derived by Ghisellini et al. (2010), who found $3 \times 10^9 M_{\odot}$, but the difference is less than a factor of 2, which is the expected uncertainty on the results.

A comparison of the nuclear properties estimated above with those inferred from the analysis of the broad emission lines is deferred to Raiteri et al. (in preparation).

8 SWIFT-XRT

XRT data were processed with version 6.24 of the HEASOFT⁹ package and calibration files dated 20180710. We ran the `xrt-pipeline` on all observations in pointing mode in the period of interest and ended up with 21 observations in WT mode and 43 observations in PC mode. Because all WT observations have less than 1 min exposure, in the following we concentrate on the observations in PC mode. Many of them are piled-up, and the analysis of the source point spread function with the `ximage` tool indicates that the problem affects the inner 3 pixel radius core (1 pixel = 2.36 arcsec). To correct for pile-up, it is necessary to puncture the centre of the region from which the source counts are extracted and to reconstruct the PSF central maximum from the wings. To this aim, we first run the `xrtcentroid` tool to accurately identify the source coordinates on each image. Then, we extracted the source counts from an annulus with 3 and 30 pixel radii and the background counts in an annulus with 40 and 60 pixel radii centred on the source.

The source spectra, grouped in at least 20 counts per energy bin, were analysed in the 0.3–10 keV energy range with the Xspec package. We adopted the Wilms, Allen & McCray (2000) elemental abundances and a value for the Galactic absorption of $N_{\text{H}} = 2.76 \times 10^{20} \text{ cm}^{-2}$ (Kalberla et al. 2005).

The XRT data examined by Ghisellini et al. (2010) were modelled with a power law with Galactic absorption and the fit was very good from a statistical point of view ($\chi^2/\nu = 0.99$). Similarly, an analysis of the X-ray data acquired by *XMM-Newton* in 2001 by Vercellone et al. (2019) found only marginal evidence for absorption larger than the Galactic value; when left free, the hydrogen column density resulted in $N_{\text{H}} = (3.3 \pm 0.2) \times 10^{20} \text{ cm}^{-2}$. They fit the XRT data taken in 2015 with an absorbed power law with N_{H} both free and fixed to the Galactic value. In the former case, values between 3.1 and $7.4 \times 10^{20} \text{ cm}^{-2}$ were obtained as well as higher spectral indices, i.e. softer spectra. Arcodia et al. (2018) studied the IGM absorption towards high-redshift blazars. They applied different models to the X-ray spectra of several sources, and concluded that the best results are obtained when assuming that the intrinsic spectrum is curved (e.g. a log-parabola) and there is some extra-

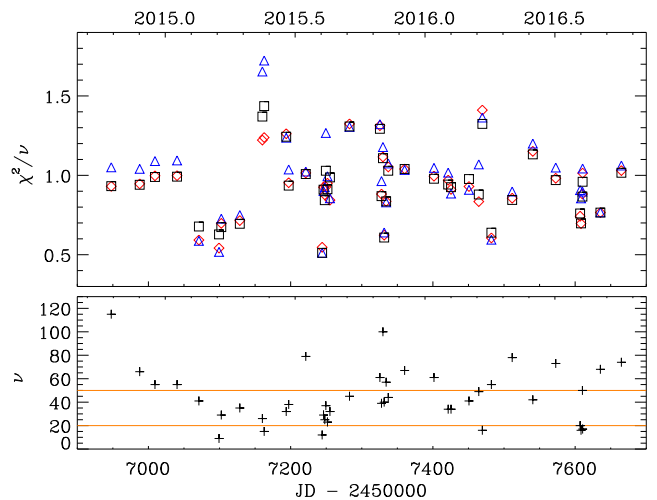


Figure 8. Top: Reduced chi-squared values obtained by fitting the XRT spectra with: a power law with Galactic absorption (blue triangles), a power law with free absorption (red diamonds), and a power law with absorption fixed to our best-guess value $N_{\text{H}}^{\text{best}} = 6.3 \times 10^{20} \text{ cm}^{-2}$ (black squares). Bottom: number of degrees of freedom in the fixed absorption cases.

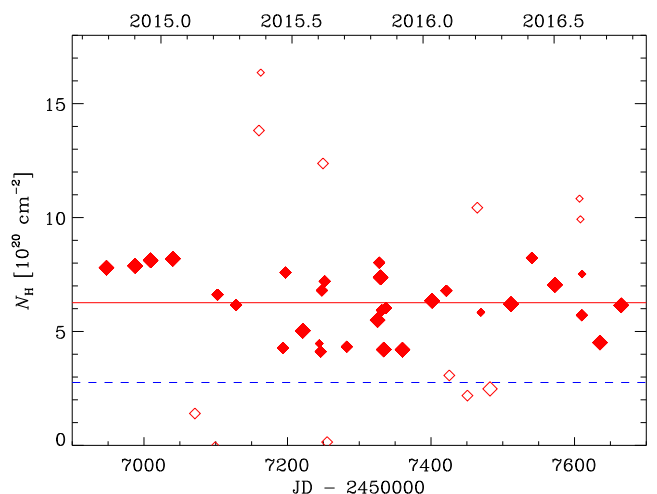


Figure 9. Values of the hydrogen column density obtained by fitting the XRT spectra with a power law with free N_{H} . The red horizontal line indicates the best-guess value $N_{\text{H}}^{\text{best}} = 6.3 \times 10^{20} \text{ cm}^{-2}$, while the blue dashed line marks the Galactic value. Symbols are shown with increasing size for increasing degrees of freedom within the ranges indicated by the orange horizontal lines in Fig. 8. Filled symbols highlight those values that are 1 standard deviation within the mean and that have been considered to estimate the best-guess N_{H} .

absorption. They also noted that 4C 71.07 is an outlier in the $N_{\text{H}}(z)$ versus z relation, showing smaller excess absorption than expected.

In the previous section, we saw that the UV emission of 4C 71.07 is likely to be strongly absorbed by the IGM. Therefore, we need to carefully investigate the role of absorption also at X-ray energies. We first compared the results obtained by fitting the XRT spectra with a power law with Galactic absorption to those obtained when N_{H} is left free to vary. Fig. 8 shows that the improvement of the goodness of fit in the latter case is substantial, especially for some of the spectral fits. The best-fitting N_{H} values are plotted in Fig. 9. They show a large range of values, with a mean $N_{\text{H}} = 6.4 \times 10^{20} \text{ cm}^{-2}$ and a standard deviation of $\sigma = 3.3 \times 10^{20} \text{ cm}^{-2}$. If we discard

⁹<https://heasarc.nasa.gov/lheasoft/>

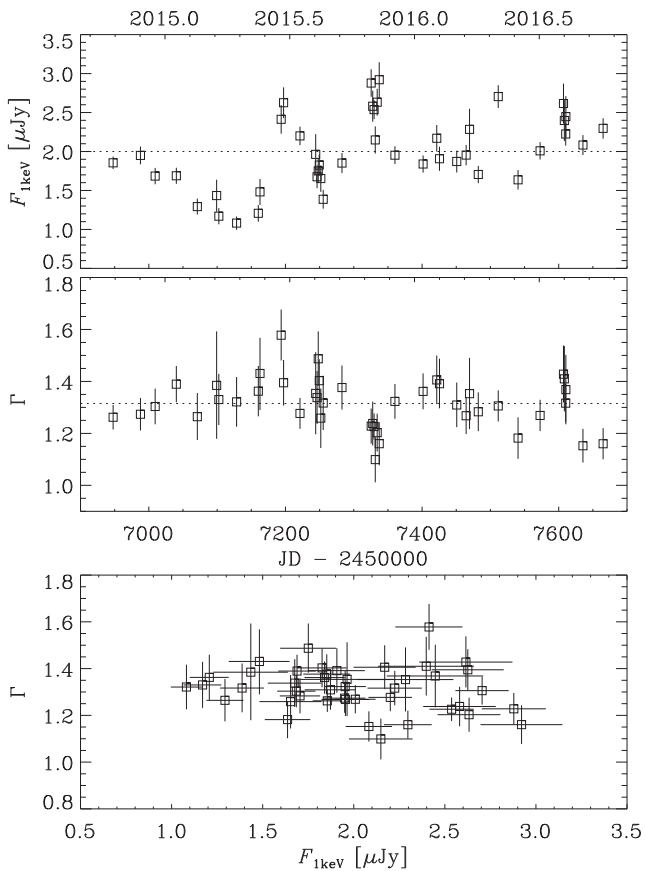


Figure 10. Results of the *Swift*-XRT data analysis when adopting a power-law model with absorption fixed to $N_{\text{H}}^{\text{best}} = 6.3 \times 10^{20} \text{ cm}^{-2}$. Top: X-ray flux density at 1 keV versus time. Middle: Photon index Γ versus time. Bottom: Photon index versus flux density.

the cases that are 1σ out from the mean, we obtain $N_{\text{H}}^{\text{best}} = 6.3 \times 10^{20} \text{ cm}^{-2}$. We consider this value as the best guess we can make for the total absorption affecting the X-ray spectra of 4C 71.07.

We then performed a third fitting run, where the spectra are modelled with a power law with N_{H} fixed to the best-guess value. The corresponding χ^2/ν are shown in Fig. 8. In general, they are very close to the values obtained in the power law with N_{H} free case. The 1 keV flux densities and photon indices Γ are shown in Fig. 10. The 1 keV flux ranges from 1.08 to 2.92 μJy , with a mean value of 2.00 μJy and standard deviation of 0.47 μJy , while Γ goes from 1.10 to 1.58, with a mean value of 1.32 and standard deviation of 0.09. This case implies slightly softer spectra than in the case where N_{H} is fixed to the Galactic value, which yields a mean photon index of 1.23. We note that there is no correlation between the flux and the photon index.

We finally tested the effects of a spectral curvature by fitting a log-parabola model with absorption fixed to $N_{\text{H}}^{\text{best}}$. The curvature parameter showed a very large spread with large uncertainties, so we believe that this case cannot add meaningful information.

9 OBSERVATIONS BY FERMI

We processed the Pass 8 data (Atwood et al. 2013) from the Large Area Telescope (LAT; Atwood et al. 2009) on board the *Fermi* satellite using the SCIENCETOOLS software package version v10r0p5 and following standard procedures (see e.g. Carnerero et al. 2015).

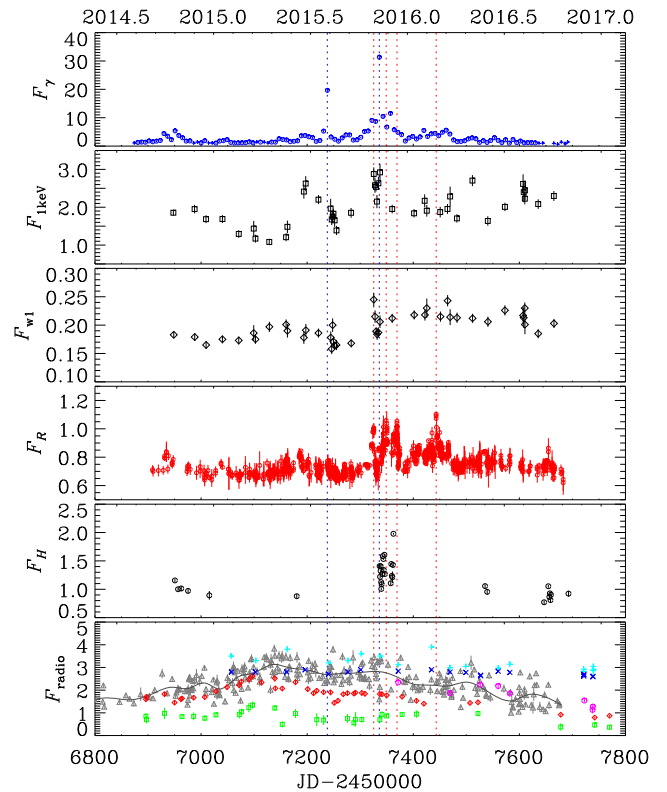


Figure 11. Multiwavelength light curves of 4C 71.07. From top to bottom: (i) 0.1–300 GeV fluxes (circles, $10^{-7} \text{ ph cm}^{-2} \text{ s}^{-1}$) and upper limits (plus signs) from *Fermi*-LAT; (ii) 1 keV flux densities (μJy) from *Swift*-XRT; (iii) *Swift*-UVOT flux densities (mJy) in *w1* band corrected for the Galactic, but not for IGM absorption; (iv) flux densities (mJy) in *R* band corrected for the Galactic extinction; (v) flux densities (mJy) in *H* band corrected for the Galactic extinction; (vi) radio flux densities (Jy) at 5 GHz (cyan plus signs), 8 GHz (blue crosses), 24 GHz (magenta circles), 37 GHz (grey triangles), 86 GHz (red diamonds), 228 GHz (green squares). The solid line represents a cubic spline interpolation on the 30-d binned data. The blue and red vertical lines guide the eye through the γ -ray and optical peaks, respectively.

We considered both a power-law and a log-parabola model for the source spectrum and a week time bin for the light curve. In Fig. 11, we show the γ -ray light curve in the 0.1–300 GeV energy range resulting from the power-law fit.

10 BROAD-BAND MULTIWAVELENGTH BEHAVIOUR

Fig. 11 compares the behaviour of 4C 71.07 at different wavelengths, from the γ -rays to the radio band. The γ -ray light curve shows two prominent maxima at $\text{JD} = 2457238$ and $\text{JD} = 2457336$. We lack *Swift* observations at the time of the first maximum, but the X-ray flux was in a high state shortly before. The X-ray data exhibit a peak simultaneous to the second γ -ray maximum. Interestingly, another X-ray peak at $\text{JD} = 2457325$ corresponds to the maximum of the ultraviolet light curve, which in turn correlates with a major optical flare. The following three optical maxima are not covered by *Swift* observations. Their simultaneous γ -ray data show moderately high states. Other remarkable X-ray levels are reached at $\text{JD} = 2457197$, 2457511 , and 2457607 . The first event was preceded by a minor optical flare and a mild flux increase is also visible in the γ -rays. The second event has a possible, weak

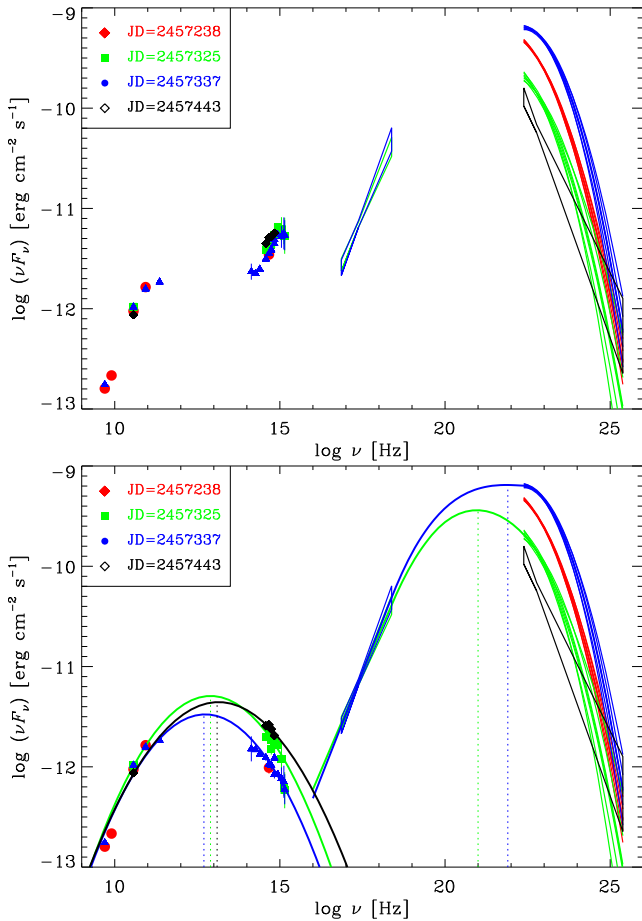


Figure 12. Broad-band SEDs of 4C 71.07 at four epochs, indicated in the upper left inset. Near-infrared and optical data have been corrected for the Galactic extinction. In the top panel, data in the u and ultraviolet bands have also been corrected for the IGM absorption, so that these SEDs represent the total deabsorbed source emission. In the bottom panel, the big blue bump contributions estimated from the template shown in Fig. 5 have been subtracted from the near-infrared, optical and ultraviolet flux densities, so that these SEDs represent the synchrotron jet emission. The X-ray spectra have been obtained with a power-law model with absorption fixed to our best-guess value $N_{\text{H}}^{\text{best}} = 6.3 \times 10^{20} \text{ cm}^{-2}$. γ -ray spectra have been modelled with a log-parabola except for the faintest state, where a power law was preferred. In the bottom panel, the solid lines are log-parabolic fits and cubic spline interpolations to the synchrotron and inverse-Compton components, respectively, to highlight the possible shift of the bump peaks towards higher energies with increasing flux.

γ -ray, but no optical, counterpart, and the third event does not seem to have any counterpart at all.

The near-infrared light curves are undersampled, so we can just notice higher fluxes in the period of increased optical activity. As for the radio bands, the 5 GHz data seem rather scattered, those at 8 GHz show little variability, while at 37, 86, and 228 GHz the flux maximum is reached before the optical, X-ray and γ -ray activity and then the radio flux declines.

Fig. 12 shows broad-band SEDs built with data simultaneous at all frequencies but in the radio band, where a few days distance was accepted because of the smoother flux variations at those wavelengths. We chose four epochs, corresponding to different γ -ray and optical brightness states. Two SEDs correspond to the two peaks in the γ -ray light curve, while the other two SEDs refer to

the first and the fourth optical maxima. *Swift* data are available for only two SEDs. The plotted XRT spectra are obtained with a power-law model with absorption fixed to our best-guess value $N_{\text{H}}^{\text{best}} = 6.3 \times 10^{20} \text{ cm}^{-2}$. *Fermi*-LAT spectra are fitted with log-parabolic models but in the faintest state, where we show the results of a power-law fit, as the curvature parameter of the log-parabolic model was very small.

In the upper panel, the data in the u and ultraviolet bands have been corrected for IGM absorption. Therefore, these SEDs represent the total deabsorbed emission of the source, including the quasar core and beamed jet contributions.

In the bottom panel, we subtracted the big blue bump contributions from the near-infrared, optical and ultraviolet fluxes according to the prescriptions given in Section 6. These SEDs thus represent the pure jet emission. In this representation, it is easier to see that increasing brightness states in the near-infrared to ultraviolet bands correspond to decreasing brightness states in γ -rays.

Log-parabolic fits to the data from the radio to the ultraviolet band highlight that the frequency of the synchrotron peak shifts towards higher values as the near-infrared-to-ultraviolet spectrum rises. A simple interpolation through the X-ray and γ -ray data allows us to verify that the same shift also applies to the inverse-Compton peak. Moreover, we can give a rough estimate of the Compton dominance, i.e. the ratio between νF_{ν} of the two peaks, in the two epochs where *Fermi* data are available. This ratio is about 70 at JD = 2457325 and about 200 at JD = 2457337.

The jet emission SEDs allow us to estimate the jet bolometric luminosity by integrating the synchrotron and inverse-Compton bumps. The result for the JD = 2457325 epoch, which represents a somewhat mean state, is $L_{\text{jet}} = 9.42 \times 10^{49} \text{ erg s}^{-1}$, 98.5 per cent of which is due to the high-energy bump. This extremely high luminosity is linked to the jet power spent in radiation by the relation (Ghisellini et al. 2014): $P_{\text{rad}} \simeq 2 L_{\text{jet}} / \Gamma^2$, where Γ is the bulk Lorentz factor. By considering a range of possible Γ values, from $\Gamma = 14$ (Ghisellini et al. 2010) to $\Gamma = 28$ (Savolainen et al. 2010), we find $P_{\text{rad}} = (2.40\text{--}9.61) \times 10^{47} \text{ erg s}^{-1} \simeq (1\text{--}4) L_{\text{disc}}$. This puts 4C 71.07 close (within $1\text{--}2\sigma$) to the best-fitting linear correlation between radiative jet power and disc luminosity derived by Ghisellini et al. (2014) and confirms the validity of this relation at the highest blazar energies.

11 POLARIMETRIC OBSERVATIONS

Synchrotron emission is polarized and in blazars the degree of polarization (P) and electric vector polarization angle (EVPA) can be extremely variable (e.g. Smith 1996). The polarization properties are expected to mirror the properties of the magnetic field in the emission region(s) and hence they can potentially shed light on the jet physics and structure. Actually, it is not clear yet to what extent stochastic processes due to turbulence act in determining the polarization behaviour in blazars (e.g. Marscher 2014; Kiehlmann et al. 2017; Raiteri et al. 2017a). Large EVPA rotations have been observed that are sometimes correlated with flares detected at γ -rays (e.g. Blinov et al. 2018). The picture appears quite complex, as changes in the jet viewing angle can mimic a stochastic process even when the variations in flux and P , and EVPA rotations, are produced by a deterministic process (Lyutikov & Kravchenko 2017).

Polarization data for this work were acquired at the Calar Alto, Crimean, Lowell, and St. Petersburg observatories. The P and EVPA behaviour in time is plotted in Fig. 13 and compared with the γ and optical light curves. The optical light curve shows the contribution of the jet to the R -band flux densities, $F_{\text{jet}} = F_{\text{tot}} - F_{\text{BBB}}$, where

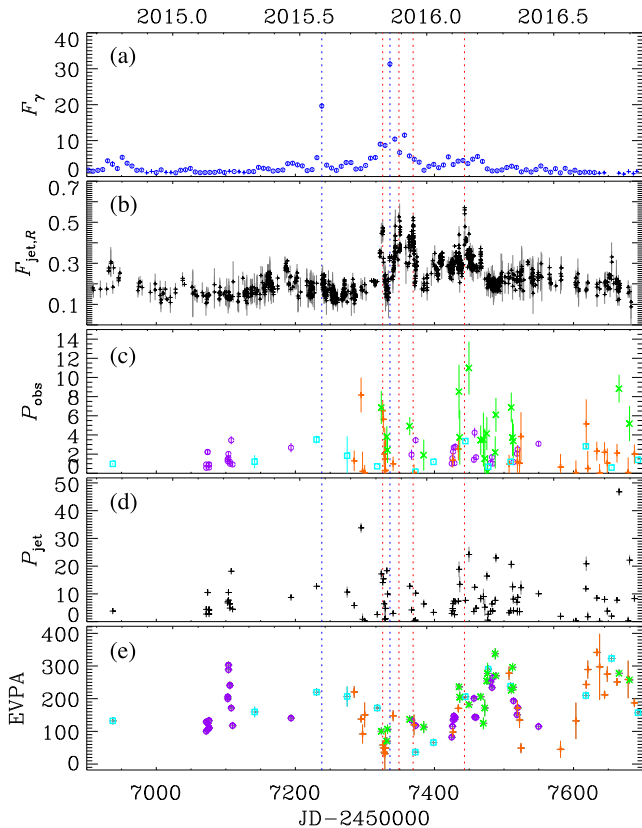


Figure 13. From top to bottom: (a) 0.1–300 GeV γ -ray flux (10^{-7} ph cm $^{-2}$ s $^{-1}$) from *Fermi*-LAT; (b) R -band deabsorbed jet (black plus signs) flux densities (mJy); (c) observed degree of polarization (percent); data are from Calar Alto (cyan squares), Crimean (orange plus signs), Lowell (violet circles), and St. Petersburg (green crosses) observatories; (d) degree of polarization (percent) of the jet contribution (black squares), after correcting the observed values for the dilution effect due to the big blue bump; (e) EVPA (degree; symbols and colours as in panel c) adjusted for the $\pm n \times \pi$ ambiguity. Blue and red vertical dotted lines are drawn to guide the eye through the γ -ray and optical major peaks, respectively.

$F_{\text{BBB}} = 0.532$ mJy is the big blue bump contribution, as obtained in Section 6 and listed in Table 1.

The observed degree of polarization varies very fast, ranging from about zero (0.03 percent) to 11 percent. We have no data simultaneous with the γ -ray and optical peaks, except for the first major optical peak at JD = 2457325.5, where $P_{\text{obs}} = 6.5$ percent. The somewhat sparse sampling and large errors affecting many polarization data points prevent us to draw firm conclusions, but there seems to be a lack of correlation between P and the flux (see also Fig. 14) that remains true even when we correct P_{obs} for the dilution effect of the big blue bump to derive the degree of polarization of the jet: $P_{\text{jet}} = (F_{\text{tot}} \times P_{\text{obs}})/F_{\text{jet}}$. The minimum and maximum values of P_{jet} are 0.11 percent and 47 percent, respectively. The maximum is more than four times higher than the observed maximum value. We recall that the degree of polarization expected for synchrotron radiation from a power-law distribution of particles is $P_{\text{syn}} = (p + 1)/(p + 7/3) = 0.69 - 0.75$ for typical power-law indices $p = 2 - 3$ (Rybicki & Lightman 1979). A value for F_{BBB} higher than what we have assumed would further increase P_{jet} , pushing its maximum towards the above theoretical value. Therefore, polarization can potentially be used to constrain the emission contribution from the big blue bump in FSRQs.

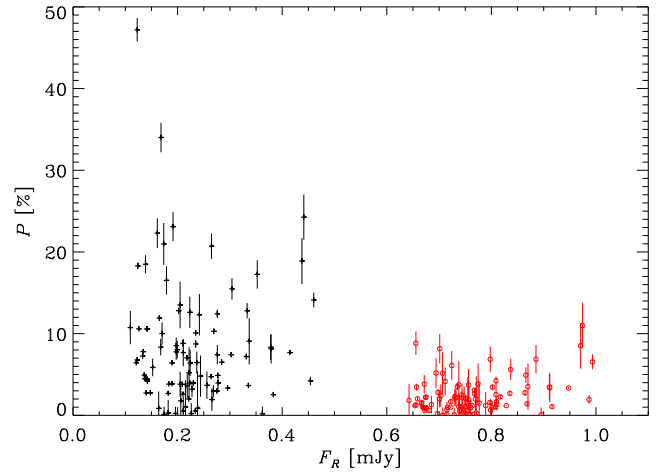


Figure 14. Degree of polarization versus deabsorbed flux density. Black plus signs refer to the jet component, while red circles to observed P and total flux density.

The EVPA presents a $\pm n \times \pi$ ambiguity that can be treated giving a reasonable prescription. The values shown in Fig. 13 have been obtained by simply minimizing the difference between subsequent angles. EVPA rotations both clockwise and counterclockwise are recognizable, a behaviour that has often been ascribed to a stochastic process due to turbulence (Marscher 2014; Raiteri et al. 2017a).

A fast and large clockwise rotation of about 180° occurs around JD \sim 2457104–10, during a period of low γ and optical activity. A counterclockwise rotation of $\sim 140^\circ$ in 12 d precedes the optical ‘sterile’ flare (i.e. without γ -ray counterpart) at JD = 2457443. Other remarkable rotations are seen starting at JD = 2457470 (166° in a week, counterclockwise) and at JD = 2457507 (143° in 15 d and possibly 230° in 17 d, clockwise), in periods when no significant optical or γ -ray flux variations are observed.

12 CONCLUSIONS

Because of the beamed nature of the source, the blazar emission that we observe is usually dominated by the non-thermal radiation from the jet. However, FSRQs often receive considerable thermal emission contributions from their quasar cores, which peak at wavelengths increasing with redshift. But as the redshift becomes higher, the more is the IGM that the blazar radiation must cross and hence the stronger the absorption. The problem of disentangling the jet and big blue bump contributions to the observed emission and that of correcting the observed fluxes for the IGM absorption are key issues when investigating the properties of high-redshift FSRQs.

In this paper, we have analysed the flux and polarimetric behaviour of the high-redshift FSRQ-type blazar 4C 71.07. Optical, near-infrared, and radio light curves have been built with data taken by the WEBT during an intensive campaign in 2014–2016. These have been complemented by ultraviolet and X-ray data from *Swift* and by γ -ray data by *Fermi*.

During the campaign, we also obtained optical spectroscopic data that have been analysed in detail by Raiteri et al. (in preparation). We use here the average optical and near-infrared spectra to construct a model for the source quasar core. We filled the gaps between the near-infrared and the optical frequency range and in the ultraviolet

by making use of the quasar templates by Polletta et al. (2007) and Lusso et al. (2015), respectively. From the model we derived the flux contributions of the big blue bump to the source photometry in the various near-infrared, optical, and ultraviolet bands. These can be subtracted from the observed fluxes to obtain the synchrotron jet fluxes. Following Ghisellini et al. (2010) and Lusso et al. (2015), we also estimate the opacity values that can be applied to the UVOT data to correct for the IGM absorption.

We analysed the XRT data with different models and estimated a best-guess value for the total absorption due to both the Galaxy and IGM of $N_{\text{H}}^{\text{best}} = 6.3 \times 10^{20} \text{ cm}^{-2}$, which is more than twice the Galactic value. The modest number of counts of the XRT spectra does not allow us to distinguish whether some intrinsic spectral curvature is present.

Light curves at different frequencies do not show persistent correlation, in particular among γ -rays, X-rays, and optical fluxes.

Broad-band SEDs present, beside a prominent big blue bump, a very strong Compton dominance. The correction for the IGM absorption makes the ultraviolet spectrum harder and the X-ray spectrum softer, and this implies a smoother connection between them.

We verified that 4C 71.07 is characterized by extreme nuclear and jet properties. Integration of the thermal continuum traced by our big blue bump template allowed us to estimate the disc bolometric luminosity, $L_{\text{disc}} = 2.45 \times 10^{47} \text{ erg s}^{-1}$, and to derive the mass accretion rate, $\dot{M} \simeq 18 M_{\odot} \text{ yr}^{-1}$, and black hole mass, $M_{\text{BH}} \simeq 1.6 \times 10^9 M_{\odot}$, from it in the case of a Shakura & Sunyaev disc. As a consequence, the Eddington ratio is as high as 0.66. On the other hand, we could estimate the jet bolometric luminosity integrating the nuclear-subtracted SED, obtaining $L_{\text{jet}} = 9.42 \times 10^{49} \text{ erg s}^{-1}$. From this, we calculated the jet radiation power, $P_{\text{rad}} = (2.40\text{--}9.61) \times 10^{47} \text{ erg s}^{-1} \simeq (1\text{--}4) L_{\text{disc}}$. The disc and jet luminosities of 4C 71.07 are thus found to fit fairly well into the jet–disc relation for blazars (Ghisellini et al. 2014), confirming it at the highest energy values.

The polarization data acquired during the WEBT campaign display strong variability in both the polarization degree and polarization angle. This variability seems not to be correlated with the flux behaviour. Correction of P for the dilution effect of the thermal radiation from the quasar core brings the maximum from ~ 11 per cent to ~ 47 per cent, but does not lead to a correlation with the flux. Noticeable EVPA rotations are observed, both clockwise and counterclockwise. They mostly occur during periods where the flux does not show significant changes and may be caused by turbulence.

In the light of our results, we conclude by stressing the importance of taking in due consideration the contribution of the quasar core when analysing the emission from FSRQs and the role of IGM absorption when dealing with high-redshift objects.

ACKNOWLEDGEMENTS

We thank an anonymous referee for stimulating comments and Elisabeta Lusso and Gabriele Ghisellini for sharing results of previous publications. The data collected by the WEBT collaboration are stored in the WEBT archive at the Osservatorio Astrofisico di Torino – INAF (<http://www.oato.inaf.it/blazars/webt/>); for questions regarding their availability, please contact the WEBT President Massimo Villata (massimo.villata@inaf.it). This publication uses data obtained at Metsähovi Radio Observatory, operated by Aalto University in Finland. We acknowledge finan-

cial contribution from the agreement ASI-INAF n.2017-14-H.0 and from the contract PRIN-SKA-CTA-INAF 2016. PR and SV acknowledge contract ASI-INAF I/004/11/0. We acknowledge support by Bulgarian National Science Programme ‘Young Scientists and Postdoctoral Students 2019’, Bulgarian National Science Fund under grant DN18-10/2017 and National RI Roadmap Projects DO1-157/28.08.2018 and DO1-153/28.08.2018 of the Ministry of Education and Science of the Republic of Bulgaria. GD and OV gratefully acknowledge the observing grant support from the Institute of Astronomy and Rozhen National Astronomical Observatory, Bulgarian Academy of Sciences via bilateral joint research project ‘Study of ICRF radio-sources and fast variable astronomical objects’ (head – G.Damljanovic). This work is a part of the Projects No. 176011 (‘Dynamics and Kinematics of Celestial Bodies and Systems’), No. 176004 (‘Stellar Physics’), and No. 176021 (‘Visible and Invisible Matter in Nearby Galaxies: Theory and Observations’) supported by the Ministry of Education, Science and Technological Development of the Republic of Serbia. This research was partially supported by the Bulgarian National Science Fund of the Ministry of Education and Science under grants DN 08-1/2016, DN 18-13/2017, and KP-06-H28/3 (2018). The Skinakas Observatory is a collaborative project of the University of Crete, the Foundation for Research and Technology – Hellas, and the Max-Planck-Institut für Extraterrestrische Physik. The St Petersburg University team acknowledges support from Russian Science Foundation grant no. 17-12-01029. The Abastumani team acknowledges financial support by the Shota Rustaveli National Science Foundation under contract FR/217950/16. This work was partly supported by the National Science Fund of the Ministry of Education and Science of Bulgaria under grant DN 08-20/2016, and by funds of the project RD-08-37/2019 of the University of Shumen. The Astronomical Observatory of the Autonomous Region of the Aosta Valley (OAVdA) is managed by the Fondazione Clément Fillietroz-ONLUS, which is supported by the Regional Government of the Aosta Valley, the Town Municipality of Nus and the ‘Unité des Communes valdôtaines Mont-Émilius’. The research at the OAVdA was partially funded by two ‘Research and Education’ grants from Fondazione CRT. This research has made use of the NASA/IPAC Extragalactic Database (NED), which is operated by the Jet Propulsion Laboratory, California Institute of Technology, under contract with the National Aeronautics and Space Administration.

REFERENCES

- Agudo I., Thum C., Wiesemeyer H., Krichbaum T. P., 2010, *ApJS*, 189, 1
 Akyuz A. et al., 2013, *A&A*, 556, A71
 Arcodia R., Campana S., Salvaterra R., Ghisellini G., 2018, *A&A*, 616, A170
 Asada K., Nakamura M., Inoue M., Kamenoi S., Nagai H., 2010, *ApJ*, 720, 41
 Atwood W. B. et al., 2009, *ApJ*, 697, 1071
 Atwood W. B. et al., 2013, *ApJ*, 774, 76
 Bessell M. S., Castelli F., Plez B., 1998, *A&A*, 333, 231
 Blinov D. et al., 2018, *MNRAS*, 474, 1296
 Breeveld A. A., Landsman W., Holland S. T., Roming P., Kuin N. P. M., Page M. J., 2011, in McEnery J. E., Racusin J. L., Gehrels N., eds, *AIP Conf. Proc. Vol. 1358, Gamma Ray Bursts 2010*. Am. Inst. Phys., New York, p. 373
 Calderone G., Ghisellini G., Colpi M., Dotti M., 2013, *MNRAS*, 431, 210
 Cardelli J. A., Clayton G. C., Mathis J. S., 1989, *ApJ*, 345, 245
 Carnerero M. I. et al., 2015, *MNRAS*, 450, 2677
 D’Ammando F. et al., 2012, *MNRAS*, 426, 317

- Doroshenko V. T., Efimov Y. S., Borman G. A., Pulatova N. G., 2014, *Astrophysics*, 57, 176
- Ghisellini G., Tavecchio F., 2015, *MNRAS*, 448, 1060
- Ghisellini G. et al., 2010, *MNRAS*, 405, 387
- Ghisellini G., Tavecchio F., Maraschi L., Celotti A., Sbarro T., 2014, *Nature*, 515, 376
- Gu M. F., Lee C.-U., Pak S., Yim H. S., Fletcher A. B., 2006, *A&A*, 450, 39
- Hubeny I., Agol E., Blaes O., Krolik J. H., 2000, *ApJ*, 533, 710
- Kalberla P. M. W., Burton W. B., Hartmann D., Arnal E. M., Bajaja E., Morras R., Pöppel W. G. L., 2005, *A&A*, 440, 775
- Kaspi S., Smith P. S., Netzer H., Maoz D., Jannuzi B. T., Giveon U., 2000, *ApJ*, 533, 631
- Kiehlmann S., Blinov D., Pearson T. J., Lioudakis I., 2017, *MNRAS*, 472, 3589
- Larionov V. M. et al., 2016, *MNRAS*, 461, 3047
- Lawrence C. R., Zucker J. R., Readhead A. C. S., Unwin S. C., Pearson T. J., Xu W., 1996, *ApJS*, 107, 541
- Lusso E., Worseck G., Hennawi J. F., Prochaska J. X., Vignali C., Stern J., O'Meara J. M., 2015, *MNRAS*, 449, 4204
- Lyutikov M., Kravchenko E. V., 2017, *MNRAS*, 467, 3876
- Marscher A. P., 2014, *ApJ*, 780, 87
- Massaro E., Perri M., Giommi P., Nesci R., 2004, *A&A*, 413, 489
- McIntosh D. H., Rieke M. J., Rix H.-W., Foltz C. B., Weymann R. J., 1999, *ApJ*, 514, 40
- Perucho M., Martí-Vidal I., Lobanov A. P., Hardee P. E., 2012a, *A&A*, 545, A65
- Perucho M., Kovalev Y. Y., Lobanov A. P., Hardee P. E., Agudo I., 2012b, *ApJ*, 749, 55
- Peterson B. M., 2001, in Aretxaga I., Kunth D., Mújica R., eds, *Advanced Lectures on the Starburst-AGN Connection*. World Scientific, Singapore, p. 3
- Polletta M. et al., 2007, *ApJ*, 663, 81
- Poole T. S. et al., 2008, *MNRAS*, 383, 627
- Raiteri C. M. et al., 2010, *A&A*, 524, A43
- Raiteri C. M. et al., 2014, *MNRAS*, 442, 629
- Raiteri C. M. et al., 2017a, *MNRAS*, 466, 3762
- Raiteri C. M. et al., 2017b, *Nature*, 552, 374
- Rybicki G. B., Lightman A. P., 1979, *Radiative Processes in Astrophysics*. Wiley-Interscience, New York
- Savolainen T., Homan D. C., Hovatta T., Kadler M., Kovalev Y. Y., Lister M. L., Ros E., Zensus J. A., 2010, *A&A*, 512, A24
- Scott J., Bechtold J., Dobrzycki A., 2000, *ApJS*, 130, 37
- Shakura N. I., Sunyaev R. A., 1973, *A&A*, 24, 337
- Smith P. S., 1996, in Miller H. R., Webb J. R., Noble J. C., eds, *ASP Conf. Ser. Vol. 110, Blazar Continuum Variability*. Astron. Soc. Pac., San Francisco, p. 135
- Stickel M., Kuehr H., 1993, *A&AS*, 100, 395
- Stickel M., Padovani P., Urry C. M., Fried J. W., Kuehr H., 1991, *ApJ*, 374, 431
- Teraesranta H. et al., 1998, *A&AS*, 132, 305
- Urry C. M., Padovani P., 1995, *PASP*, 107, 803
- Vercellone S. et al., 2019, *A&A*, 621, A82
- Villata M. et al., 1997, *A&AS*, 121, 119
- Villata M. et al., 2006, *A&A*, 453, 817
- Villata M. et al., 2008, *A&A*, 481, L79
- Wilms J., Allen A., McCray R., 2000, *ApJ*, 542, 914
- ¹INAF, Osservatorio Astrofisico di Torino, via Osservatorio 20, I-10025 Pino Torinese, Italy
- ²Instituto de Astrofísica de Canarias (IAC), La Laguna, E-38200 Tenerife, Spain
- ³Departamento de Astrofísica, Universidad de La Laguna, La Laguna, E-38205 Tenerife, Spain
- ⁴Ulugh Beg Astronomical Institute, Maidanak Observatory, Tashkent 100052, Uzbekistan
- ⁵Astronomical Institute, St Petersburg State University, 198504 St Petersburg, Russia
- ⁶Pulkovo Observatory, 196140 St Petersburg, Russia
- ⁷INAF, Osservatorio Astronomico di Brera, Via Emilio Bianchi 46, I-23807 Merate, LC, Italy
- ⁸Instituto de Astrofísica de Andalucía (CSIC), E-18080 Granada, Spain
- ⁹Max-Planck-Institut für Radioastronomie, Auf dem Hügel 69, D-53121 Bonn, Germany
- ¹⁰Institute of Astronomy and NAO, Bulgarian Academy of Sciences, BG-1784 Sofia, Bulgaria
- ¹¹Dipartimento di Fisica G. Occhialini, Università degli Studi di Milano Bicocca, I-20126 Milano, Italy
- ¹²Crimean Astrophysical Observatory RAS, P/O Nauchny, 298409, Russia
- ¹³INAF, TNG Fundación Galileo Galilei, E-38712 La Palma, Spain
- ¹⁴Department of Astronomy, Faculty of Physics, University of Sofia, BG-1164 Sofia, Bulgaria
- ¹⁵Osservatorio Astronomico della Regione Autonoma Valle d'Aosta, I-11020 Nus, Italy
- ¹⁶EPT Observatories, Tijarafe, E-38780 La Palma, Spain
- ¹⁷Graduate Institute of Astronomy, National Central University, Zhongli City, Taoyuan County 32001, Taiwan
- ¹⁸Astronomical Observatory, 11060 Belgrade, Serbia
- ¹⁹INAF, Osservatorio Astronomico di Roma, I-00040 Monte Porzio Catone, Italy
- ²⁰Sternberg Astronomical Institute, M.V. Lomonosov Moscow State University, Moscow 119991, Russia
- ²¹INAF, Istituto di Radioastronomia, Via Piero Gobetti 93/2, I-40129 Bologna, Italy
- ²²Department of Physics and Astronomy, Faculty of Natural Sciences, University of Shumen, BG-9700 Shumen, Bulgaria
- ²³Astrophysics Research Institute, Liverpool John Moores University, Liverpool L3 5RF, UK
- ²⁴Institute for Astrophysical Research, Boston University, Boston, MA 02215, USA
- ²⁵Abastumani Observatory, Mt. Kanobili, 0301 Abastumani, Georgia
- ²⁶Engelhardt Astronomical Observatory, Kazan Federal University, Tatarstan, Russia
- ²⁷Aalto University Metsähovi Radio Observatory, FI-02540 Kylmälä, Finland
- ²⁸Department of Electronics and Nanoengineering, Aalto University, FI-00076 Aalto, Finland
- ²⁹Department of Physics and Astronomy, Brigham Young University, Provo, UT 84602, USA
- ³⁰Osservatorio Astronomico Sirio, I-70013 Castellana Grotte, Italy
- ³¹Department of Physics, University of Colorado Denver, CO 80217, USA

This paper has been typeset from a $\text{\TeX}/\text{\LaTeX}$ file prepared by the author.

Triple Range Imager and POLarimeter (TRIPOL) — a compact and economical optical imaging polarimeter for small telescopes

Shuji Sato¹, Po Chieh Huang², Wen Ping Chen², Takahiro Zenno¹, Chakali Eswaraiah^{2*}, Bo He Su², Shinsuke Abe^{2**}, Daisuke Kinoshita² and Jia Wei Wang³

¹ Astrophysics Department, Nagoya University, Nagoya, 464-8602, Japan

² Graduate Institute of Astronomy, National Central University, Taoyuan 32001; wchen@astro.ncu.edu.tw

³ National Tsing Hua University, Hsin Chu, 30013

Received 2019 March 13; accepted 2019 April 23

Abstract We report the design concept and performance of a compact, lightweight and economical imaging polarimeter, the Triple Range Imager and POLarimeter (TRIPOL), capable of simultaneous optical imagery and polarimetry. TRIPOL splits the beam in wavelengths from 400 to 830 nm into g' -, r' - and i' -bands with two dichroic mirrors, and measures polarization with an achromatic half-waveplate and a wire grid polarizer. The simultaneity makes TRIPOL a useful tool for small telescopes for the photometry and polarimetry of time variable and wavelength dependent phenomena. TRIPOL is designed for a Cassegrain telescope with an aperture of ~ 1 m. This paper presents the engineering considerations of TRIPOL and compares the expected with observed performance. Using the Lulin 1-m telescope and 100 seconds of integration, the limiting magnitudes are $g' \sim 19.0$ mag, $r' \sim 18.5$ mag and $i' \sim 18.0$ mag with a signal-to-noise ratio of 10, in agreement with design expectation. The instrumental polarization is measured to be $\sim 0.3\%$ in the three bands. Two applications, one to the star-forming cloud IC 5146 and the other to the young variable GM Cep, are presented as demonstrations.

Key words: instrumentation: photometers — instrumentation: polarimeters — techniques: photometric — techniques: polarimetric — methods: observational — ISM: magnetic fields

1 INTRODUCTION

Polarization provides information about a celestial object in addition to that acquired by photometry and spectroscopy (Tinbergen 1996; Clarke 2010). Yet a polarimeter is considered to be a specialized instrument when fitted to an optical telescope with a small size aperture. Nowadays, with commercial CCD cameras and other optical and electronic components readily available with good performance, it has become feasible to design and fabricate a compact and economical polarimetric imager to be used for scientific programs with small telescopes. We report on an imaging system, Triple Range Imaging POLarimeter (TRIPOL), capable of simultaneous imaging photometry

and polarimetry in three optical bands (g' , r' , i'). TRIPOL was designed for a telescope with a primary mirror of around one meter in diameter and located at a moderate observing site, with typical seeing of 1 to 2 arcsec. The telescope is assumed to have a Cassegrain f-ratio from F/6 to F/15, and the CCD pixel scale is from 10 to 20 μm to properly sample the point spread function. The optics uses no lenses to magnify or reduce the image, and the elements, such as dichroic mirrors, spectral filters, half-waveplate (HWP) and wire grid polarizer (WGP), are all flat and thin for easy optical alignment. TRIPOL is compact, measuring $300 \times 350 \times 250$ mm in width, length and height respectively, weighs only 15 kg including the data acquisition system, and is easy to operate. It was designed to an accuracy of $\sim 3''$ for alignment, and ~ 0.05 mm for machining and positioning. This paper describes the performance of the first (TRIPOL1) and second (TRIPOL2) units of

* Now at National Astronomical Observatories, Chinese Academy of Sciences, Beijing, China

** Now at Department of Aerospace Engineering, Nihon University, Japan

TRIPOL adapted for use on the Lulin One-meter Telescope (LOT) in Taiwan. In the F/8 beam of the LOT, and hence a $\sim 3^\circ$ cone-angle, effects such as spherical aberration, chromatic aberration, and astigmatism are small compared to the $20\ \mu\text{m}$ pixel size. We compare the design parameters with observational results on the polarization measurements of polarization standard stars, and demonstrate the use of TRIPOL when targeting the star-forming cloud IC 5146 and the young star GM Cep.

2 DESIGN OF TRIPOL

TRIPOL is composed of three parts, the polarization unit, the color-decomposition unit and the data-acquisition unit, plus three CCD cameras and a desktop computer. The overview and layout of the optical components are depicted in Figure 1. Light from the telescope passes through an HWP and a WGP, and is then decomposed by two dichroic mirrors (DM1 and DM2) and band-pass filters (BPFs) into three channels (g' , r' , i'). The incident photons are detected and converted to electrons in the CCD camera with built-in readout electronics.

The polarization unit, consisting of a rotatable HWP and a fixed WGP, working as a phase retarder and polarization analyzer, respectively, is located in front of the color-decomposition unit. The HWP, with size of $33\ \text{mm} \times 33\ \text{mm}$ and thickness of 3 mm, made of SiO_2MgF_2 , was procured from the optical shop Kogaku Giken Co. We employ a commercial (from Edmund Optics Co.) WGP plate composed of an Al wire grid, with size of $50\ \text{mm} \times 50\ \text{mm}$ and thickness of 1.5 mm, sandwiched by thin glass plates, affording a field-of-view as wide as the detector size. While using birefringent materials, such as a Wollaston prism, would allow for, alternatively, a dual beam design, thus minimizing instrumental and sky effects on polarization measurements, our design is much more compact and economical. The WGP is slightly tilted to avoid ghost images due to reflected glare.

For the color-decomposition unit, the central wavelengths (λ_0) and bandwidths ($\Delta\lambda$) are defined by multiplying the transmission or reflection curves of the DMs and BPFs for each of the g' -, r' - and i' -bands. The spectral response functions of the DMs and BPFs are shown in Figure 2.

Even though the TRIPOL optics makes no use of mirrors or lenses with power, astigmatism from tilted DMs and spherical aberration from flat-parallel BPFs may still exist. The g' -band optical train contains the BPF- g' and a CCD camera, the r' -band optical train holds DM1 tilted at an

angle of 30° , and the r' - i' optical train houses DM1 and DM2 at angles of $\pm 30^\circ$.

Ray-tracing was executed using the software ZEMAX for classical Cassegrain-type telescopes with apertures $D=0.7, 1.0$ and $1.5\ \text{m}$, and f -ratios F/6, F/8, F/10, F/12.5 and F/15. We evaluated the tolerance of aberrations by comparing the root mean square (RMS) radius in the spot diagram with the detector pixel size and seeing size. It was confirmed that the RMS radius of the spot, due mostly to astigmatism, was smaller than $50\ \mu\text{m}$, or ~ 2.5 times the pixel size, even near the corners of the detector, and much smaller than the seeing size, $1.5''$. With various parameters for apertures and focal ratios, the optics is found tolerable for an F/7 or slower beam. Astigmatism can be remedied by wedging DM1 and DM2 by 0.18° and 0.24° , respectively, even for a system as fast as F/7.

TRIPOL was designed to use commercially available CCD cameras, with the specific model in accordance with scientific and budgetary requirements. TRIPOL1 and TRIPOL2 employed SBIG ST-9 XEi cameras using KAF-0261E plus TC-237, having 512×512 pixels, each with $20\ \mu\text{m}$ on a side. The detector response shows linearity up to $\sim 50\,000$ counts, or about 1/3 of the full well. The dark current is $10\ [\text{e/s}]$ at temperature $\sim 0^\circ\text{C}$ and the readout noise is $15\ [\text{e}]$ per sampling.

The CCD cameras are located on the bottom plate so as to align each of the array centers to the focal point of the telescope within an accuracy of less than $0.1\ \text{mm}$ (~ 5 pixels) relative to each other. The SBIG ST-9 camera model satisfied our initial need for point-source targets, but that model is no longer available. Subsequent TRIPOL units were upgraded to the camera model STT-8300. A computer (Intel DN2800MT) controls simultaneous readout of the three CCD cameras and the polarization units according to the position angles of the HWP via three USB 2.0 cables. The overall cost of TRIPOL, excluding the cameras and the computer, was about US\$17 000 in 2010.

3 EVALUATION OF PERFORMANCE

In this section, we evaluate the performance of TRIPOL in photometric and polarimetric measurements. In each case, the engineering design parameters are compared with those measured in actual observations.

3.1 Limiting Magnitudes for Photometry

The limiting magnitudes of TRIPOL2 were measured in December 2012 using the LOT, for which each SBIG ST9-

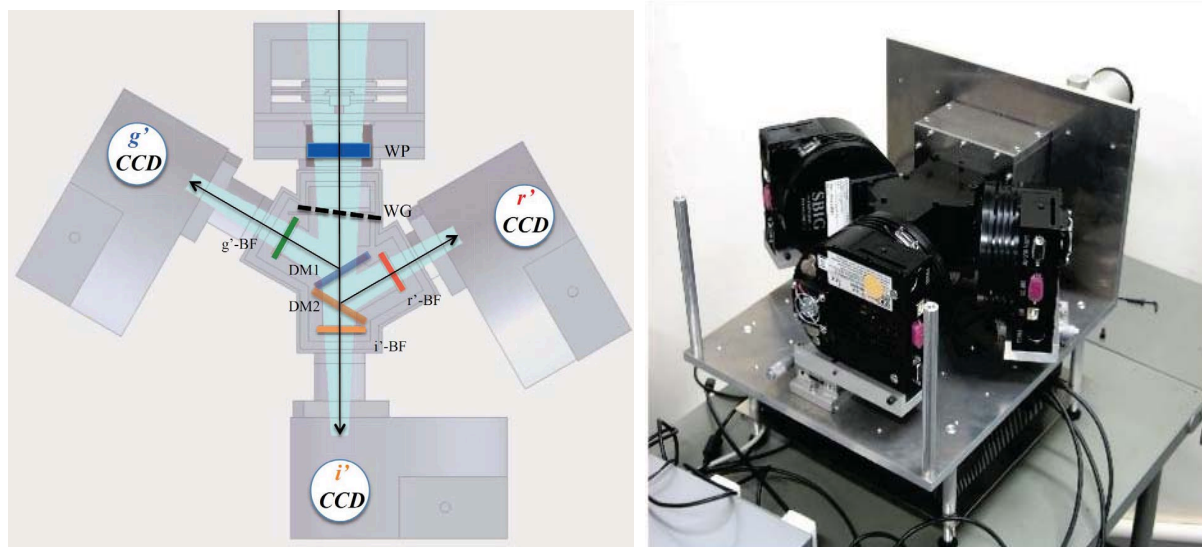


Fig. 1 (Left) Layout of the optical components and CCDs of TRIPOL2. Arrows illustrate the light paths. See the text for abbreviations. (Right) Overview of the components with the control computer utilized for data acquisition beneath the bottom plate.

XEi 20 μm pixel corresponds to $0.5''$, giving a field of view about $4.7' \times 4.7'$.

We observed the Landolt Field 101–404 (Landolt 1992) for 100 s, and analyzed the images of the 12 stars with a photometric aperture of $4.0''$, or 8 pixels in diameter, and derived the limiting magnitudes of 19, 18.5 and 18, for signal to noise ratio (S/N) ~ 10 , respectively, in the g' -, r' - and i' -bands. In every band, the measured and expected values are in agreement with each other within uncertainties of ~ 0.5 mag. For a photometry-only observing run, the WGP could be removed to gain an increase of about 60% in incident flux.

3.2 Efficiency and Reliability of Polarization Measurements

The combination of a rotatable HWP and a fixed WGP, as described in Section 2, follows the same design as the near-infrared (J , H , K_s) polarimeter, SIRPOL, on the InfraRed Survey Facility (Kandori et al. 2006, IRSF). Below, we describe the performance parameters measured in the laboratory, in comparison with observations of standard stars.

3.2.1 Efficiency of the polarization devices

The phase retarder of the HWP was designed and measured by Kogaku Giken Co. to be $180^\circ \pm 2^\circ$ over the wavelength range 400 to 950 nm (see Fig. 3(a)). The transmittance of the WGP was measured in this wavelength range in steps of $\Delta\lambda = 50$ nm. Two identical WGPs were arranged such that one was fixed while the other was rotat-

able. When rotating relative to each other, a silicone photodiode was illuminated with a white light through the intermediate BPFs of $\Delta\lambda = 50$ nm. A single rotation gives a double sinusoidal curve. Fitting with a sinusoidal curve, we obtain $I(\theta) = A \sin 2(\theta - \phi) + B$, where A is the amplitude, B the residual and ϕ the phase-difference. For this we parameterized the transmittances, T_{\max} and T_{\min} , parallel and perpendicular to each other, as plotted in Figure 3(b) and Figure 3(c) respectively. The contrast parameter, defined as the extinction ratio, T_{\max}/T_{\min} , should be as high as possible (infinite for a perfect polarizer), but in practice is considered satisfactory with a value above ~ 100 to substantially suppress the perpendicular component of polarization, i.e., the crosstalk. The contrast parameter measured for TRIPOL, presented as Figure 3(d), increases toward long wavelengths and remains sufficiently high above 500 nm.

3.2.2 Observations of polarization standard stars

The TRIPOL images were reduced by standard procedures for bias and dark subtraction, and corrected with flat-fielding. For each polarization measurement, target frames acquired with each filter at four HWP positions were aligned using DAOPHOT (find, daomaster and daogrow) and IRAF (geomap and geotran) packages. Then multiple frames for each HWP were average-combined using IRAF/imcombine. These four images, taken at each of the four HWP positions, became the science images used for photometry and polarimetry.

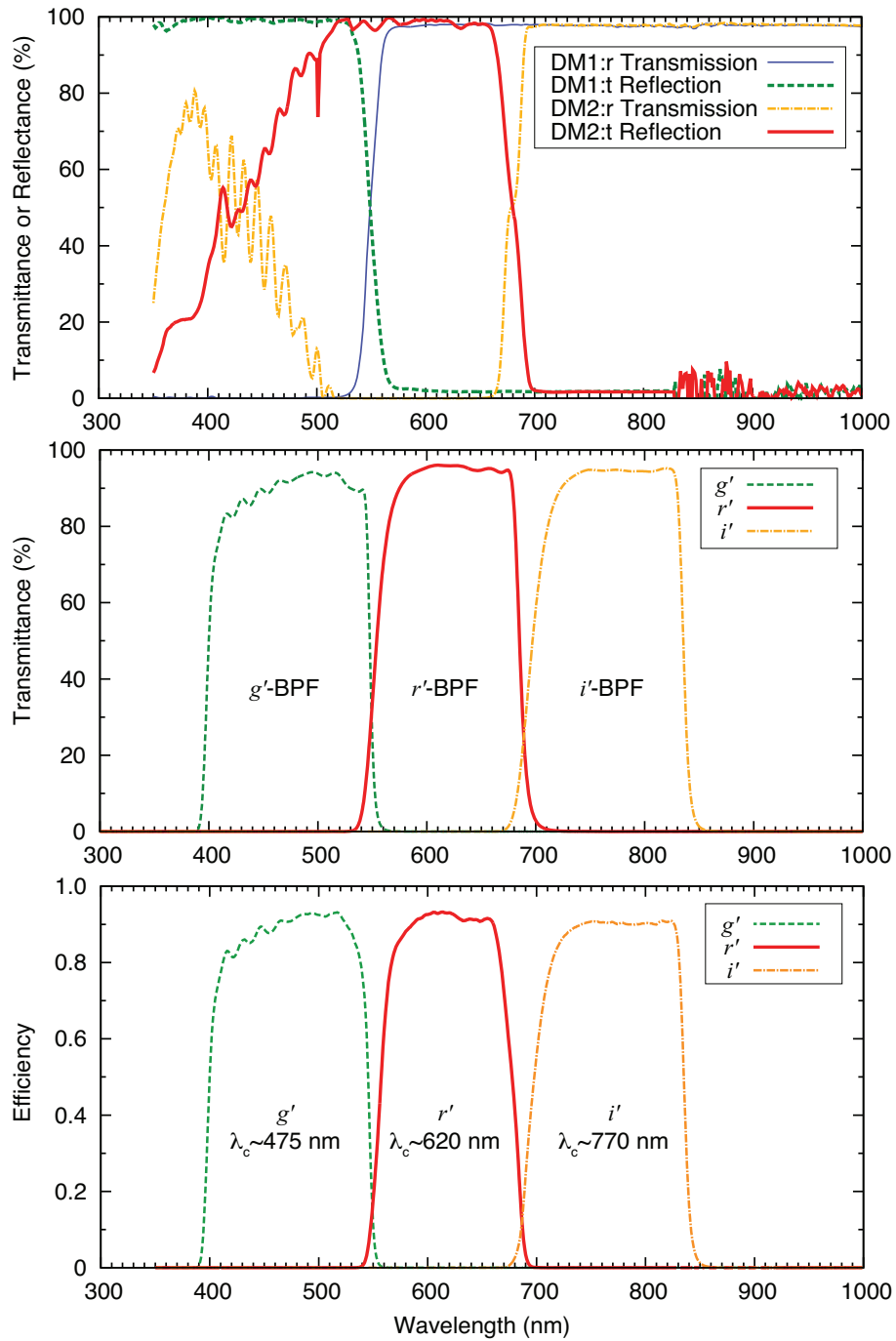


Fig. 2 Transmittance of optical components for the three passbands: (*top panel*) transmission/reflectance of the dichroic mirrors, (*middle panel*) transmission of the BPFs and (*bottom panel*) throughput.

Aperture photometry was performed using DAOFIND (for source detection with a threshold of 5σ for the sky variation) and PHOT (for aperture photometry) tasks of DAOPHOT for point sources. Typical image full widths at half maximum (FWHMs) for these runs varied between 2 and 4 pixels ($1'' - 2''$). The flux of a star at each position of the HWP was estimated using IRAF/DAOPHOT with an aperture size of 2.5 times the FWHM. The inner and outer

sky annuli were chosen to be 5 and 10 pixels more than the star aperture. Fluxes at four angles are used to compute the Stokes parameters as follows:

$$I = 1/2(I_0 + I_{22.5} + I_{45} + I_{67.5}),$$

$$Q = I_0 - I_{45},$$

$$U = I_{22.5} - I_{67.5},$$

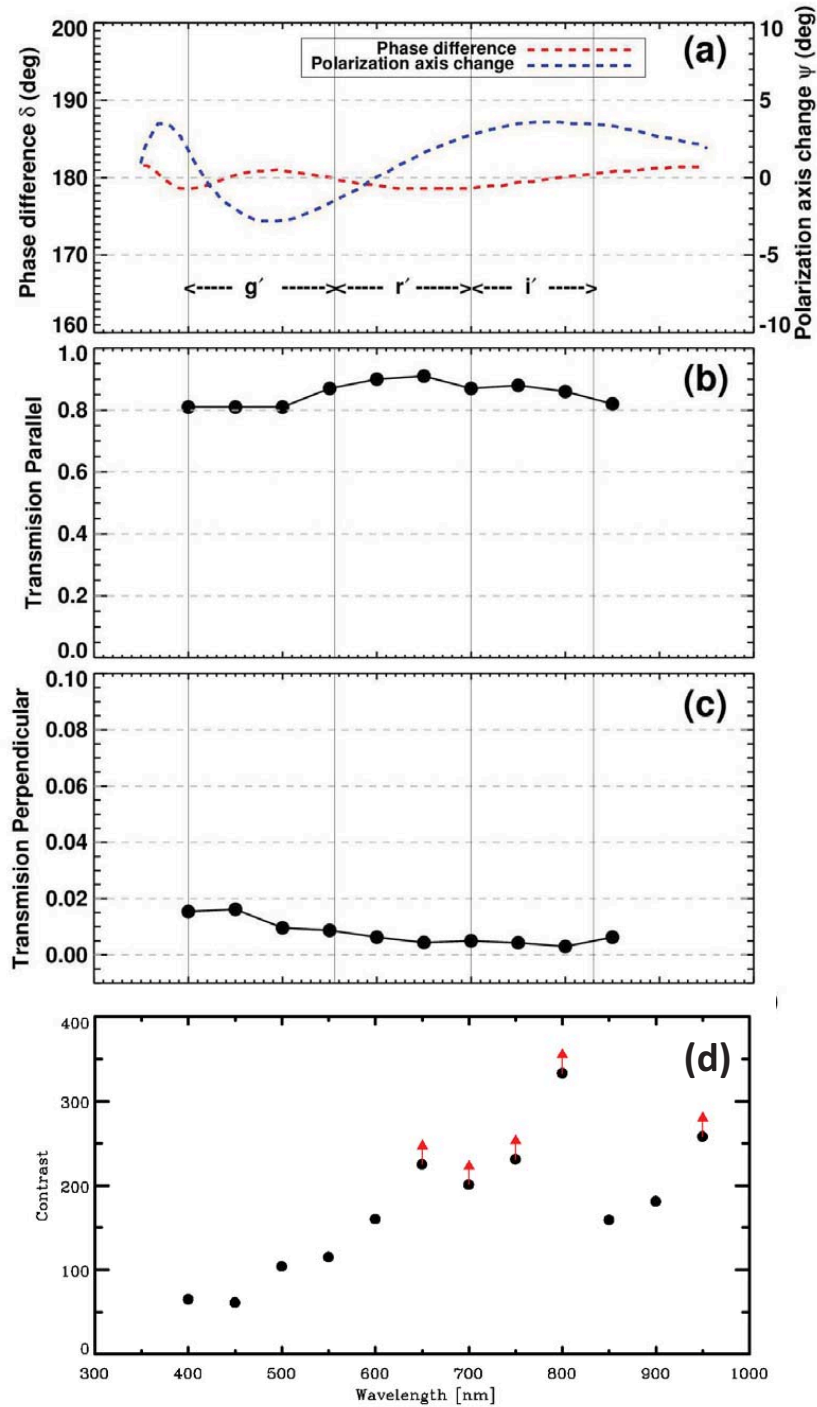


Fig. 3 Performance of the TRIPOL WGP: (a) the phase retardant (in units of deg); (b) transmittance with two polarizers in a parallel configuration; (c) transmittance with two polarizers in a perpendicular configuration; (d) contrast parameter (T_{\max}/T_{\min}). Those with a value greater than 200, each marked with an *upward arrow*, are uncertain because of a small number in the denominator.

where I_0 , $I_{22.5}$, I_{45} and $I_{67.5}$ are the intensities at the four HWP angles in deg respectively, with the corresponding error being the square-root of the sum of the square of each intensity error, i.e., $\delta I = \sqrt{(\delta I_0)^2 + (\delta I_{22.5})^2 + (\delta I_{45})^2 + (\delta I_{67.5})^2}$. The errors δQ and δU are computed similarly.

The level of polarization P (in percentage) and the polarization position angle θ (in deg) are then derived accordingly,

$$P = \sqrt{Q^2 + U^2}/I,$$

$$\theta = 0.5 \arctan(U/Q),$$

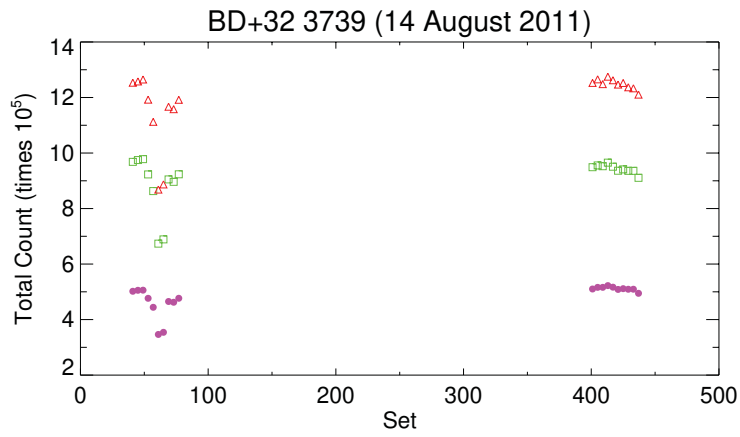


Fig. 4 The total counts of BD+32° 3739 showed inferior sky conditions in all g' - (in green), r' - (in red) and i' -bands for the first half of the night, whereas the sky was relatively stable in the second half.

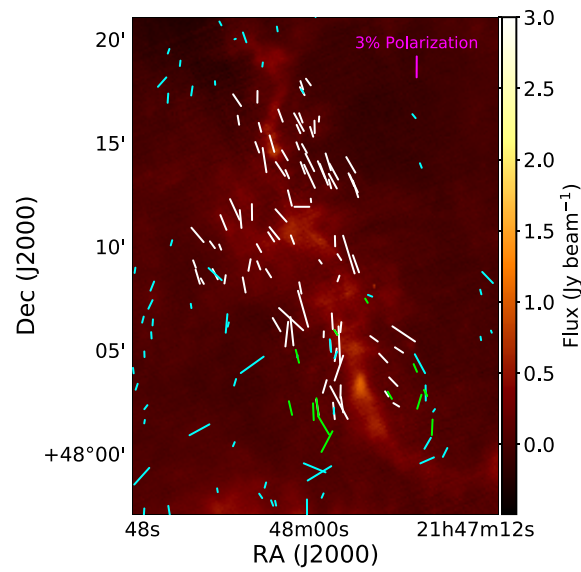


Fig. 5 TRIPOL i' -band polarization vector map (in red) of IC 5146 (Wang et al. 2017). The background image is the *Herschel* 250 μm data (Arzoumanian et al. 2011). Also shown are the polarization vectors measured by AIMPOL at R band (in green) and Mimir at near-infrared H band (in blue).

for which δP and $\delta\theta$ are estimated from the respective δQ and δU .

Because P is positively defined, the derived polarization is overestimated, especially for low S/N sources. To correct for this bias, the debiased value $P_{\text{db}} = \sqrt{P^2 - (\delta P)^2}$ (Wardle & Kronberg 1974) is computed.

A polarization measurement relies on photometry at different polarization angles, and therefore all conditions pertaining to reliable photometric measurements apply. Even under a perfect photometric sky, though, our observations, via a fixed sequence of images taken at 0-45-22.5-67.5 deg, are subject to a small but noticeable flux drift due to airmass changes, leading to spurious polarization signals. Figure 4 depicts the results observed by

LOT/TRIPOL on 2011 August 14 for BD+32° 3739, a standard star known to have null polarization (Schmidt et al. 1992). The total g' count, that is, the sum of $g'_0 + g'_{22.5} + g'_{45} + g'_{67.5}$, indicates varying sky conditions during the first session (a total of 10 sets of data, with each set consisting of images at four polarization angles per filter), starting at UT 12:53 (local time 20:53), but relatively stable skies during the second session (also with 10 sets), starting at local time 02:12. The ratio of the standard deviation of the total counts to the average counts, used as a measure of the sky stability, changed from about 13% in each of the g' -, r' - and i' -bands in the first session, to about 1% in the second session. The data taken in the first session hence should be discarded.

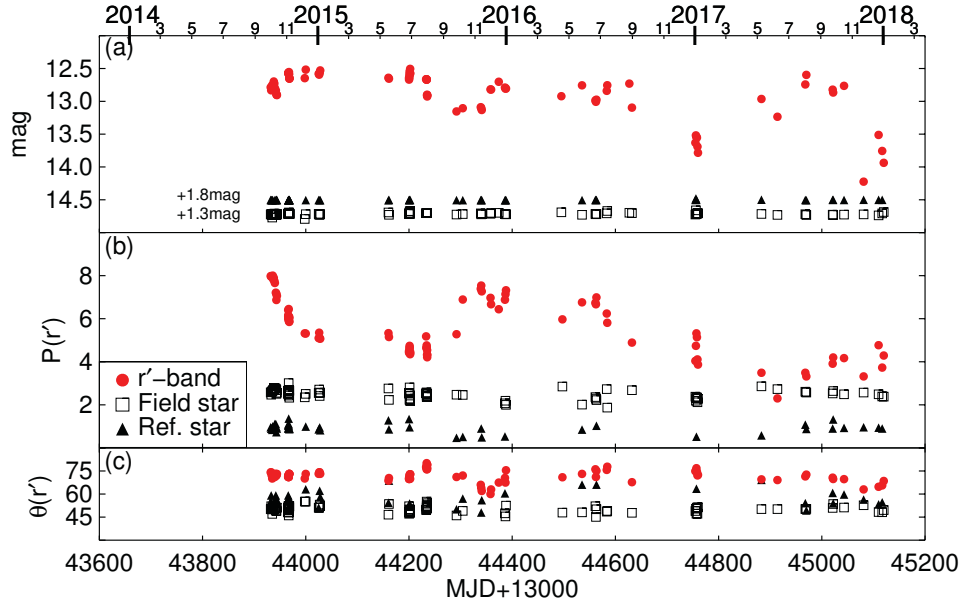


Fig. 6 The r' -band (a) light curve, (b) polarization and (c) polarization angle of the UX Ori-type young star GM Cep measured by TRIPOL from late 2014 to late 2017 (Huang et al. 2019). GM Cep shows a significant temporal change of polarization in comparison with two nearby stars.

Table 1 TRIPOL Measurements of Unpolarized Standard Stars

Star, mag/ P_λ (Schmidt et al. 1992)	Date	$P_{g'}$ (%)	$P_{r'}$ (%)	$P_{i'}$ (%)	
BD+32° 3739, $V = 9.31$	2011 Aug 14	0.12 ± 0.11	0.12 ± 0.10	0.17 ± 0.15	
	$P_B = 0.039 \pm 0.021$	2011 Aug 15	0.14 ± 0.16	0.32 ± 0.14	0.19 ± 0.23
	$P_V = 0.025 \pm 0.017$	2018 Oct 25	0.27 ± 0.27	0.26 ± 0.19	0.32 ± 0.18
	2018 Oct 28	0.20 ± 0.20	0.16 ± 0.16	0.17 ± 0.12	
BD+28° 4211, $V = 10.53$	2011 Aug 15	0.20 ± 0.19	0.34 ± 0.21	0.25 ± 0.10	
	$P_B = 0.063 \pm 0.023$	2011 Aug 17	0.08 ± 0.13	0.29 ± 0.14	0.32 ± 0.28
	$P_V = 0.054 \pm 0.027$	2018 Oct 26	0.25 ± 0.12	0.20 ± 0.20	0.20 ± 0.20
	$P_V = 0.054 \pm 0.027$	2018 Oct 27	0.28 ± 0.13	0.17 ± 0.17	0.21 ± 0.19
HD 212311, $V = 8.10$	2018 Oct 23	0.15 ± 0.05	0.15 ± 0.06	0.20 ± 0.05	
	$P_B = 0.028 \pm 0.025$	2018 Oct 24	0.20 ± 0.09	0.24 ± 0.06	0.13 ± 0.07
	$P_V = 0.034 \pm 0.021$	2018 Oct 25	0.26 ± 0.12	0.23 ± 0.12	0.28 ± 0.14
	2018 Oct 26	0.11 ± 0.11	0.10 ± 0.15	0.32 ± 0.21	
	2018 Oct 27	0.12 ± 0.12	0.23 ± 0.15	0.16 ± 0.16	
	2018 Oct 28	0.07 ± 0.11	0.21 ± 0.10	0.12 ± 0.12	

A further correction is the polarization introduced by the instrument, which is estimated by observing unpolarized standard stars. The mean and standard deviation of the measured polarization of unpolarized standards were found to be $P_{g'} = 0.27 \pm 0.12\%$, $P_{r'} = 0.32 \pm 0.23\%$ and $P_{i'} = 0.25 \pm 0.13\%$. These values, summarized in Table 1, are considered as the instrumental polarization. For the unpolarized standard stars, with brightness up to $V \sim 12$ mag, the overall accuracy of polarization mea-

surements with TRIPOL is estimated to be $\sim 0.3\%$ with an uncertainty of 3° for the polarization angle.

In every TRIPOL run, polarized standard stars should be observed to calibrate the measured polarization angle to the equatorial coordinate system. The TRIPOL measurements of a selected set of unpolarized standard stars and polarized stars are listed in Table 1 and Table 2 respectively, demonstrating general agreement with the published values, given that the observing wavelengths are slightly different. An observing run was carried out exclusively for

Table 2 TRIPOL Measurements of Polarized Standard Stars

Star/mag/ $P_\lambda, \theta_\lambda$ (Schmidt et al. 1992)	Date	$P_{g'}(\%), \theta_{g'}(\text{deg})$	$P_{r'}(\%), \theta_{r'}(\text{deg})$	$P_{i'}(\%), \theta_{i'}(\text{deg})$
HD 154445, $V = 5.61$	2015 Feb 17	$3.8 \pm 0.1, 87 \pm 3$	$3.4 \pm 0.2, 82 \pm 2$	$3.7 \pm 0.1, 67 \pm 3$
$P_V = 3.780 \pm 0.062, \theta_V = 88.79 \pm 0.47$	2015 Feb 26	$3.8 \pm 0.1, 92 \pm 3$	$3.7 \pm 0.2, 90 \pm 2$	$3.7 \pm 0.1, 92 \pm 3$
$P_{Rc} = 3.683 \pm 0.072, \theta_R = 88.91 \pm 0.56$	2015 Feb 27	$3.8 \pm 0.1, 88 \pm 3$	$4.0 \pm 0.2, 86 \pm 2$	$3.5 \pm 0.1, 87 \pm 3$
$P_{Ic} = 3.246 \pm 0.078, \theta_I = 89.91 \pm 0.69$				
HD 161056, $V = 6.32$	2015 Feb 27	$3.9 \pm 0.1, 67 \pm 3$	$4.1 \pm 0.2, 66 \pm 2$	$3.7 \pm 0.1, 67 \pm 3$
$P_V = 4.030 \pm 0.025, \theta_V = 66.93 \pm 0.18$				
$P_{Rc} = 4.012 \pm 0.032, \theta_R = 67.33 \pm 0.23$				
$P_{Ic} = 3.575 \pm 0.030, \theta_I = 67.78 \pm 0.24$				
HD 204827, $V = 7.93$	2011 Aug 11	$5.5 \pm 0.2, 60 \pm 1$	$5.3 \pm 0.2, 61 \pm 1$	$4.7 \pm 0.2, 63 \pm 2$
$P_V = 5.322 \pm 0.014, \theta_V = 58.73 \pm 0.08$	2018 Oct 23	$5.5 \pm 0.3, 59 \pm 3$	$5.0 \pm 0.2, 58 \pm 2$	$4.5 \pm 0.3, 58 \pm 2$
$P_{Rc} = 4.893 \pm 0.029, \theta_R = 59.10 \pm 0.17$	2018 Oct 24	$5.8 \pm 0.2, 61 \pm 1$	$5.3 \pm 0.2, 60 \pm 1$	$4.5 \pm 0.2, 62 \pm 1$
$P_{Ic} = 4.189 \pm 0.030, \theta_I = 59.94 \pm 0.20$	2018 Oct 25	$5.9 \pm 0.1, 59 \pm 1$	$5.3 \pm 0.1, 60 \pm 1$	$4.5 \pm 0.1, 60 \pm 1$
	2018 Oct 26	$5.9 \pm 0.1, 57 \pm 1$	$5.2 \pm 0.0, 59 \pm 1$	$4.2 \pm 0.1, 60 \pm 1$
	2018 Oct 27	$5.6 \pm 0.2, 57 \pm 1$	$5.3 \pm 0.2, 58 \pm 1$	$4.4 \pm 0.2, 58 \pm 1$
	2018 Oct 28	$5.6 \pm 0.1, 59 \pm 1$	$5.1 \pm 0.1, 59 \pm 1$	$4.3 \pm 0.1, 60 \pm 1$
HD 19820, $V = 7.11$	2018 Oct 23	$4.5 \pm 0.1, 115 \pm 1$	$4.4 \pm 0.1, 115 \pm 1$	$4.2 \pm 0.1, 114 \pm 1$
$P_V = 5.322 \pm 0.014, \theta_V = 114.93 \pm 0.08$	2018 Oct 24	$4.6 \pm 0.2, 114 \pm 2$	$4.7 \pm 0.1, 111 \pm 1$	$4.0 \pm 0.1, 115 \pm 2$
$P_{Rc} = 4.893 \pm 0.029, \theta_R = 114.46 \pm 0.17$	2018 Oct 25	$4.9 \pm 0.2, 110 \pm 2$	$4.0 \pm 0.2, 115 \pm 2$	$4.5 \pm 0.1, 117 \pm 2$
$P_{Ic} = 4.189 \pm 0.030, \theta_I = 114.48 \pm 0.20$	2018 Oct 26	$4.2 \pm 0.1, 111 \pm 2$	$3.8 \pm 0.1, 113 \pm 1$	$3.5 \pm 0.1, 115 \pm 2$
(Variable, this work)	2018 Oct 27	$4.4 \pm 0.1, 111 \pm 1$	$4.3 \pm 0.1, 113 \pm 1$	$3.6 \pm 0.1, 115 \pm 1$
	2018 Oct 28	$4.6 \pm 0.2, 114 \pm 1$	$4.6 \pm 0.2, 113 \pm 1$	$4.0 \pm 0.1, 113 \pm 1$

standard star calibration in October 2018 to assess the intranight and internight consistency of the TRIPOL measurements. For unpolarized standard stars, accuracy is kept to two decimal digits, and no polarization angle is listed. For polarized standard stars, the fractional polarization is kept to one decimal digit, with the polarization angle in integers reflecting the uncertainties. In the October 2018 run, each target was measured a few times, and the entries in Table 1 and Table 2 for each date are the average values of individual measurements and the associated errors. Because we relied on the standard stars to correct for the polarization angles (one offset per night for each angle at each band), the values of angles scatter around the offset. From the observations of polarization standards, we conclude that the WGP has a high efficiency for measuring polarized light, and there is no need to correct for instrumental polarization, except for an angular offset.

Note that only standard stars from Schmidt et al. (1992) known not to vary were selected. In the process of our experiment, we found that one target, HD 19820, however, exhibited noticeable variability in the polarization level, but with a relatively steady polarization angle in our measurements. The mechanism of variability is unclear, but this O-type star is reported to be a binary system with a period of 3.366324d (Hilditch & Hill 1975; Hill et al. 1994). Its polarization variability requires further study but, in any case, using it as a standard is not advisable.

4 SCIENTIFIC DEMONSTRATION

Data acquired by TRIPOL provide simultaneous information such as flux, linear polarization and the source coordinates in three bands, enabling study of the spectral energy distribution (SED), color-magnitude and color-color diagrams, and polarization. The combination of wavelength-dependence on polarization with the SED could distinguish various emission and propagation processes, such as synchrotron emission, scattering or extinction.

For imaging photometry, the time resolution of TRIPOL is as fast as about 1 s, whereas for polarimetry it is ~ 15 s. As a single-beam instrument, TRIPOL is susceptible to polarization caused by the instrument itself, and to sky variations. The effects of internal polarization are assessed by observing standard stars. To mitigate the sky effects, multiple sets of observations are taken, and those with comparable total counts in four polarization angles are used in polarization analysis. This compromises the time resolution to a few minutes, but because of the simultaneity in three bands, TRIPOL still proves efficient. TRIPOL should be especially useful for investigating variable phenomena on timescales from a few seconds to years or longer. These include, but are not limited to, gravitational wave counterparts (Morokuma et al. 2016), gamma-ray bursts, cataclysmic variables, eclipsing binaries, Cepheids, novae, supernovae, blazars, Miras and T Tauri stars (Chen et al. 2015; Huang et al. 2019).

We are pursuing several programs for polarimetric monitoring of Galactic star-forming regions. An organized polarization pattern of background stars, as a result of dichroic extinction by magnetically aligned dust grains, provides the magnetic field structure in a dark cloud (Davis & Greenstein 1951), whereas scattered light reveals the radiation fields and spatial distribution of circumstellar matter of young stellar objects. Polarimetric observations with TRIPOL2 on the LOT were carried out for IC 5146 on 2012 July 27 and 28. Seven fields were observed toward the northwest part of this filamentary cloud, with a total exposure time of 1.5 h (22.5 min for each HWP angle). Polarization measurements simultaneously acquired in g' -, r' - and i' -bands were corrected for both instrumental polarization as well as offset polarization angles by observing polarized and unpolarized standard stars. Figure 5 displays the i' -band polarization of the northwest part of IC 5146 (Wang et al. 2017).

Also plotted in Figure 5 are the ARIES Imaging Polarimeter (AIMPOL) R -band and Mimir H -band polarization data. AIMPOL (Reutela et al. 2004), an optical polarimeter installed on the 1.04 m Sampurnanand Telescope of ARIES in Nainital, India, has been calibrated well over the years by observing unpolarized and polarized standard stars (Medhi et al. 2007; Eswaraiah et al. 2013). Mimir is a near infrared imager for polarization measurements (Clemens et al. 2007) mounted on the 1.8 m Perkins Telescope in Arizona, operated by Lowell Observatory.

While TRIPOL2 and Mimir observations each covered a larger part of the filament than AIMPOL data did, the polarization results measured by the three instruments, two working in optical and one in near infrared, are consistent with each other, suggesting a global magnetic field roughly parallel to the long axis of the filament. On average, TRIPOL2 detected more prominent polarization than Mimir, a manifestation of higher fractional polarization in visible wavelengths because the extinction difference is amplified. Infrared polarimetry, on the other hand, probes denser parts of a molecular cloud. A combination of optical and infrared polarimetry, together with millimeter and submillimeter interferometric observations of polarization, hence offers an opportunity to scrutinize the magnetic field structure at scales from a cloud core to the central protostar. Detailed results on IC 5146 can be found in Wang et al. (2017).

Another application of TRIPOL is targeting the point source GM Cep, a 4-Myr T Tauri star undergoing abrupt photometric variations caused by obscuration of protoplan-

etary dust clumps (Chen et al. 2012; Chen & Hu 2014; Huang et al. 2019). The long-term photometric and polarimetric monitoring data, plotted in Figure 6, display a noticeable polarization up to 8% with temporal variability on a timescale of years, while the comparison star exhibits a steady level of polarization, with a standard deviation of less than 1%. Such polarization observations provide valuable information on the distribution and properties of the circumstellar dust clumps, from grain growth from micron-size dust in transition to km-size planetesimals (Huang et al. 2019).

5 SUMMARY

The simultaneous three-color (g' , r' , i') polarimeter, TRIPOL, is simple, compact and economical, suitable for a small telescope at a moderate astronomical site. This paper presents the design concept and compares the performance to data taken on the LOT located in Taiwan. The limiting magnitudes for photometry are found to be $g' \sim 19$ mag, $r' \sim 18.5$ mag and $i' \sim 18$ mag, with an S/N of 10 and an integration time of 100 s. The internal instrumental polarization is at the level of 0.3% for a 100-s integration at all three bands. The simultaneous photometric and polarimetric capability should open up new research opportunities for time-domain astronomy on small or amateur telescopes.

Acknowledgements We are grateful to N. Takeuchi and A. Yamanaka for their laboratory experiments, and to Drs. M. Kino, M. Kurita, T. Nagayama, K. Kawabata, M. Ishiguro and H. Takami for valuable comments throughout the development of this project. We appreciate Dr. Y. Nakajima for his kind assistance with the data reduction and Drs. M. Ishiguro and K. Murata for preparation of the figures. This work is supported by Grant-in-Aid for Science Research from the Ministry of Education, Culture, Sports and Technology of Japan. SS owes his scientific activity to Dr. H. Fujiwara for his generous support of astronomy.

References

- Arzoumanian, D., André, P., Didelon, P., et al. 2011, *A&A*, 529, L6
- Chen, W. P., Hu, S. C.-L., Errmann, R., et al. 2012, *ApJ*, 751, 118
- Chen, W. P., & Hu, S. C.-L. 2014, in *IAU Symposium*, 293, Formation, Detection, and Characterization of Extrasolar Habitable Planets, ed. N. Haghighipour, 74
- Chen, W. P., Su, B. H., Eswaraiah, C., et al. 2015, *Highlights of Astronomy*, 16, 390

- Clarke, D. 2010, *Stellar Polarimetry* (Wiley)
- Clemens, D. P., Sarcia, D., Grabau, A., et al. 2007, *PASP*, 119, 1385
- Davis, Jr., L., & Greenstein, J. L. 1951, *ApJ*, 114, 206
- Hilditch, R. W., & Hill, G. 1975, *MmRAS*, 79, 101
- Hill, G., Hilditch, R. W., Aikman, G. C. L., & Khalessch, B. 1994, *A&A*, 282, 455
- Huang, P. C., Chen, W. P., Mugrauer, M., et al. 2019, *ApJ*, 871, 183
- Kandori, R., Kusakabe, N., Tamura, M., et al. 2006, in *Proc. SPIE*, 6269, 626951
- Landolt, A. U. 1992, *AJ*, 104, 340
- Morokuma, T., Tanaka, M., Asakura, Y., et al. 2016, *PASJ*, 68, L9
- Rautela, B. S., Joshi, G. C., & Pandey, J. C. 2004, *BASI*, 32, 159
- Schmidt, G. D., Elston, R., & Lupie, O. L. 1992, *AJ*, 104, 1563
- Tinbergen, J. 1996, *Astronomical Polarimetry* (Cambridge, UK: Cambridge Univ. Press), 174
- Wang, J.-W., Lai, S.-P., Eswaraiah, C., et al. 2017, *ApJ*, 849, 157
- Wardle, J. F. C., & Kronberg, P. P. 1974, *ApJ*, 194, 249

Investigating the multiwavelength behaviour of the flat spectrum radio quasar CTA 102 during 2013–2017

F. D’Ammando^{1,★}, C. M. Raiteri², M. Villata², J. A. Acosta-Pulido^{3,4}, I. Agudo⁵, A. A. Arkharov⁶, R. Bachev⁷, G. V. Baida⁸, E. Benítez⁹, G. A. Borman⁸, W. Boschin^{3,4,10}, V. Bozhilov¹¹, M. S. Butuzova⁸, P. Calciolone¹², M. I. Carnerero², D. Carosati^{10,13}, C. Casadio^{5,14}, N. Castro-Segura^{4,15}, W.-P. Chen¹⁶, G. Damjanovic¹⁷, A. Di Paola¹⁸, J. Echevarría⁹, N. V. Efimova⁶, Sh. A. Ehgamberdiev¹⁹, C. Espinosa⁹, A. Fuentes⁵, A. Giunta¹⁸, J. L. Gómez⁵, T. S. Grishina²⁰, M. A. Gurwell²¹, D. Hiriart⁹, H. Jermak²², B. Jordan²³, S. G. Jorstad^{20,24}, M. Joshi²⁴, G. N. Kimeridze²⁵, E. N. Kopatskaya²⁰, K. Kuratov^{26,27}, O. M. Kurtanidze^{25,28,29,30}, S. O. Kurtanidze²⁵, A. Lähteenmäki^{31,32}, V. M. Larionov^{6,20}, E. G. Larionova²⁰, L. V. Larionova²⁰, C. Lázaro^{3,4}, C. S. Lin¹⁶, M. P. Malmrose²⁴, A. P. Marscher²⁴, K. Matsumoto³³, B. McBreen³⁴, R. Michel⁹, B. Mihov⁷, M. Mineev¹¹, D. O. Mirzaqulov¹⁹, S. N. Molina⁵, J. W. Moody³⁵, D. A. Morozova²⁰, S. V. Nazarov⁸, A. A. Nikiforova^{6,20}, M. G. Nikolashvili²⁵, J. M. Ohlert^{36,37}, N. Okhmat⁸, E. Ovcharov⁹, F. Pinna^{3,4}, T. A. Polakis³⁸, C. Protasio^{3,4}, T. Pursimo³⁹, F. J. Redondo-Lorenzo^{3,4}, N. Rizzi⁴⁰, G. Rodriguez-Coira⁴¹, K. Sadakane³³, A. C. Sadun⁴², M. R. Samal¹⁶, S. S. Savchenko²⁰, E. Semkov⁷, L. Sigua²⁵, B. A. Skiff⁴³, L. Slavcheva-Mihova⁷, P. S. Smith⁴⁴, I. A. Steele²², A. Strigachev⁷, J. Tammi³¹, C. Thum⁴⁵, M. Tornikoski³¹, Yu. V. Troitskaya²⁰, I. S. Troitsky²⁰, A. A. Vasilyev²⁰, O. Vince¹⁷, (the WEBT Collaboration), T. Hovatta^{46,47}, S. Kiehlmann⁴⁸, W. Max-Moerbeck⁴⁹, A. C. S. Readhead⁴⁸, R. Reeves⁵⁰, T. J. Pearson⁴⁸, (the OVRO Team), T. Mufakharov^{51,52}, Yu. V. Sotnikova⁵³ and M. G. Mingaliev^{52,53}

Affiliations are listed at the end of the paper

Accepted 2019 October 1. Received 2019 October 1; in original form 2019 March 11

ABSTRACT

We present a multiwavelength study of the flat-spectrum radio quasar CTA 102 during 2013–2017. We use radio-to-optical data obtained by the Whole Earth Blazar Telescope, 15 GHz data from the Owens Valley Radio Observatory, 91 and 103 GHz data from the Atacama Large Millimeter Array, near-infrared data from the Rapid Eye Monitor telescope, as well as data from the *Swift* (optical-UV and X-rays) and *Fermi* (γ -rays) satellites to study flux and spectral variability and the correlation between flux changes at different wavelengths. Unprecedented γ -ray flaring activity was observed during 2016 November–2017 February, with four major outbursts. A peak flux of $(2158 \pm 63) \times 10^{-8}$ ph cm⁻² s⁻¹, corresponding to a luminosity of $(2.2 \pm 0.1) \times 10^{50}$ erg s⁻¹, was reached on 2016 December 28. These four γ -ray outbursts have corresponding events in the near-infrared, optical, and UV bands, with the peaks observed at the same time. A general agreement between X-ray and γ -ray activity is found. The γ -ray flux

* E-mail: dammando@ira.inaf.it

variations show a general, strong correlation with the optical ones with no time lag between the two bands and a comparable variability amplitude. This γ -ray/optical relationship is in agreement with the geometrical model that has successfully explained the low-energy flux and spectral behaviour, suggesting that the long-term flux variations are mainly due to changes in the Doppler factor produced by variations of the viewing angle of the emitting regions. The difference in behaviour between radio and higher energy emission would be ascribed to different viewing angles of the jet regions producing their emission.

Key words: radiation mechanisms: non-thermal – galaxies: individual: CTA 102 – galaxies: jets – galaxies: nuclei – gamma-rays: general.

1 INTRODUCTION

Blazars are an extreme class of active galactic nuclei (AGNs) whose bright and violently variable non-thermal radiation across the entire electromagnetic spectrum is ascribed to the presence of a collimated relativistic jet closely aligned to our line of sight (e.g. Blandford & Rees 1978). This peculiar setting implies a strong amplification of the rest-frame radiation because of Doppler boosting, together with a contraction of the variability time-scales, and a blueshift of the frequencies.

The relativistic jets of blazars are able to transport a huge amount of power away from the central engine in the form of radiation, kinetic energy, and magnetic fields. When this power is dissipated, the particles emit the observed radiation, showing the typical double-hump spectral energy distribution (SED) of blazars. The first peak of the SED, usually observed between radio and X-rays, is due to the synchrotron radiation from relativistic electrons, while the second peak, usually observed from X-ray up to TeV energies, is commonly interpreted as inverse Compton (IC) scattering of seed photons, either internal or external to the jet, by highly relativistic electrons. However, the nature of this second hump is a controversial issue and other models involving hadronic and lepto-hadronic processes have been proposed (e.g. Böttcher et al. 2013).

Blazars are traditionally divided into flat-spectrum radio quasars (FSRQs) and BL Lac objects (BL Lacs) based on the presence or not, respectively, of broad emission lines (i.e. equivalent width $> 5 \text{ \AA}$) in their optical and UV spectrum (e.g. Stickel et al. 1991). Recently, a new classification was proposed based on the luminosity of the broad-line region (BLR) in Eddington luminosity (Ghisellini et al. 2011): sources with $L_{\text{BLR}}/L_{\text{Edd}}$ higher or lower than 5×10^{-4} being classified as FSRQ or BL Lacs, respectively, in agreement with a transition of the accretion regime from efficient to inefficient between the two classes.

Blazar emission shows strong and unpredictable variability over all the electromagnetic spectrum, from the radio band to γ -rays, with time-scales ranging from minutes to years. Long-term observations of blazars during different activity states provide an ideal laboratory for investigating the emission mechanisms at work in this class of sources. In this paper we present multifrequency observations of the blazar CTA 102 during 2013–2017. CTA 102 (also known as 4C +11.69) is an FSRQ at redshift $z = 1.037$ (Schmidt 1965). Flaring activity in the optical band has been observed from this source in 1978 (Pica et al. 1988), 1996 (Katajainen et al. 2000), and 2004 (Osterman Meyer 2009). However, simultaneous γ -ray observations were not available for those events. The source was detected for the first time in γ -rays by the *Compton Gamma Ray Observatory* in 1992 with both the EGRET (Hartman et al. 1999) and COMPTEL (Blom et al. 1995) instruments. Unfortunately, no optical observations were available during the γ -ray detec-

tion (Villata et al. 1997). On the other hand, during the *Fermi* era a remarkable outburst was simultaneously observed in 2012 September–October in near-infrared (near-IR) and optical bands by the Whole Earth Blazar Telescope¹ (WEBT) and γ -rays by the Large Area Telescope (LAT) on board *Fermi Gamma-ray Space Telescope*. Correlated variability in the two energy bands suggested a co-spatial origin of the optical and γ -ray-emitting regions during the flaring activity (Larionov et al. 2016).

In 2016 November, CTA 102 entered a new very-high-activity state in γ -rays, as observed by *Fermi*-LAT, reaching a daily flux higher than $1 \times 10^{-5} \text{ ph cm}^{-2} \text{ s}^{-1}$ on 2016 December 16 (Ciprini et al. 2016). This flaring activity continued for a few weeks in γ -rays (e.g. Bulgarelli et al. 2016; Xu et al. 2016). A significant increase of activity was observed over the entire electromagnetic spectrum (e.g. Calciolone et al. 2016; Ojha, Carpenter & D’Ammando 2016; Righini et al. 2016). In particular, an extreme optical and near-IR outburst occurred in 2016 December, with a brightness increase up to six magnitudes with respect to the faint state of the source (Raiteri et al. 2017). In Raiteri et al. (2017) we explained the flux and spectral variations in optical, near-IR, and radio bands by means of an inhomogeneous curved jet with different jet regions changing their orientation, and hence their Doppler factors, in time. Alternative theoretical scenarios have been proposed to explain the 2016–2017 flaring behaviour of CTA 102. According to Casadio et al. (2019) the outburst was produced by a superluminal component crossing a recollimation shock, while for Zacharias et al. (2017, 2019) it was due to ablation of a gas cloud penetrating the relativistic jet in a leptonic or hadronic scenario.

The radio-to-optical and γ -ray emission are produced by two different mechanisms (i.e. synchrotron and IC emission in leptonic models), although related to the same relativistic electron population. Therefore, the γ -ray variability can be used as a further test to verify the geometrical model that we proposed to explain the low-energy flux variability in CTA 102 during 2013–2017. In the geometrical scenario, the γ -ray and optical radiation are produced in the same jet region, therefore the γ -ray and optical fluxes undergo the same Doppler beaming and should be linearly correlated.

In this paper we present a multiwavelength analysis of the CTA 102 emission from radio to γ -rays between 2013 January 1 and 2017 February 9, in particular during the bright flaring activity occurred during 2016 November–2017 February. The radio-to-optical observations performed in the framework of a campaign led by the WEBT, already presented in Raiteri et al. (2017), are complemented by the Atacama Large millimeter/Submillimeter Array (ALMA) at 91 and 103 GHz, the Owens Valley Radio Observatory (OVRO) data at 15 GHz, the Rapid Eye Mount (REM) near-IR data, and a detailed analysis of data collected by the *Neil*

¹<http://www.oato.inaf.it/blazars/webt>

Gehrels Swift Observatory (optical–UV and X rays) and *Fermi* (γ -rays) satellites. The data set used in this paper is the richest in terms of number of data points and broad-band coverage presented in literature for the period considered here.

Sun constraints prevented us to have observations from optical and near-infrared WEBT observatories and *Swift* satellite after 2017 February 9, not allowing us to investigate the connection between the γ -ray flaring activity observed in 2017 March–April (see e.g. Shukla et al. 2018) and the emission from near-IR to X-rays. After that period the infrared-to-X-ray coverage is insufficient to adequately test the geometrical model and to investigate the connection between low-energy and γ -ray emission.

The paper is organized as follows. In Sections 2 and 3 we present *Fermi*-LAT and *Swift* data analysis and results, respectively, whereas in Section 4 we report on the radio-to-optical observations. Multi-frequency flux and spectral variability are discussed in Sections 5 and 6, respectively. The application of the geometrical model by Raïteri et al. (2017) to the γ -ray, optical, and radio variability is discussed in Section 7. We discuss the previous results and draw our conclusions in Section 8. Throughout this paper, we assume the following cosmology: $H_0 = 71 \text{ km s}^{-1} \text{ Mpc}^{-1}$, $\Omega_M = 0.27$, and $\Omega_\Lambda = 0.73$ in a flat Universe (Ade et al. 2016).

2 FERMI-LAT DATA: ANALYSIS AND RESULTS

The *Fermi*-LAT is a pair-conversion telescope operating from 20 MeV to > 300 GeV. Further details about the *Fermi*-LAT are given in Atwood et al. (2009).

The LAT data used in this paper were collected from 2013 January 1 (MJD 56293) to 2017 February 9 (MJD 57793). During this time, the LAT instrument operated almost entirely in survey mode. The Pass 8 data (Atwood et al. 2013), based on a complete and improved revision of the entire LAT event-level analysis, were used. The analysis was performed with the SCIENTOOLS software package version v11r5p3. Only events belonging to the ‘Source’ class (`evclass = 128, evtype = 3`) were used. We selected only events within a maximum zenith angle of 90 deg to reduce contamination from the Earth limb γ -rays, which are produced by cosmic rays interacting with the upper atmosphere. The spectral analysis was performed with the instrument response functions `P8R2.SOURCE.V6` using a binned maximum-likelihood method implemented in the Science tool `gtlike`. Isotropic (‘iso_source_v06.txt’) and Galactic diffuse emission (‘gll_iem_v06.fit’) components were used to model the background (Acero et al. 2016).² The normalization of both components was allowed to vary freely during the spectral fitting.

We analysed a region of interest of 20° radius centred at the location of CTA 102. We evaluated the significance of the γ -ray signal from the source by means of a maximum-likelihood test statistic (TS) defined as $\text{TS} = 2 \times (\log L_1 - \log L_0)$, where L is the likelihood of the data given the model with (L_1) or without (L_0) a point source at the position of CTA 102 (e.g. Mattox et al. 1996). The source model used in `gtlike` includes all the point sources from the 3FGL catalogue that fall within 30° of CTA 102. We also included new candidates within 10° of CTA 102 from a preliminary eight-year point source list (FL8Y³). The spectra of these sources were parametrized by a power law (PL), a log-parabola (LP), or a super exponential cut-off, as in the catalogues.

²<http://fermi.gsfc.nasa.gov/ssc/data/access/lat/BackgroundModels.html>

³<https://fermi.gsfc.nasa.gov/ssc/data/access/lat/fl8y/>

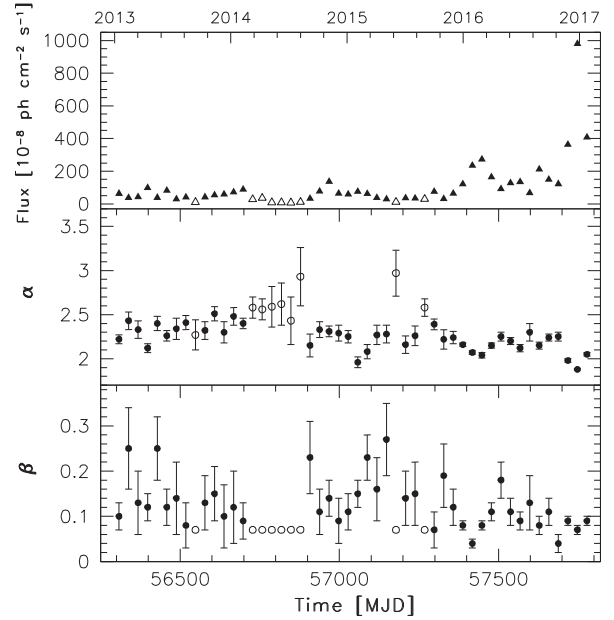


Figure 1. Integrated flux light curve of CTA 102 (upper panel), spectral slope (middle panel), curvature parameter (bottom panel) obtained in the 0.1–300 GeV energy range during 2013 January 1–2017 February 9 (MJD 56293–57793) with 30-d time bins. The open symbols refer to results obtained with β fixed to 0.07 (see the text for details).

A first maximum-likelihood analysis was performed over the whole period to remove from the model the sources having $\text{TS} < 25$. A second maximum-likelihood analysis was performed on the updated source model. In the fitting procedure, the normalization factors and the spectral parameters of the sources lying within 10° of CTA 102 were left as free parameters. For the sources located between 10° and 30° from our target, we kept the normalization and the spectral shape parameters fixed to the values from the 3FGL catalogue.

Integrating over 2013 January 1–2017 February 9 the fit with an LP model, $dN/dE \propto E/E_0^{-\alpha-\beta \log(E/E_0)}$, as in the 3FGL and FL8Y catalogues, results in $\text{TS} = 125\,005$ in the 0.1–300 GeV energy range, with an integrated average flux of $(93.8 \pm 0.6) \times 10^{-8} \text{ ph cm}^{-2} \text{ s}^{-1}$, a spectral slope $\alpha = 2.16 \pm 0.01$ at the reference energy $E_0 = 308$ MeV, and a curvature parameter around the peak $\beta = 0.07 \pm 0.01$. The corresponding apparent isotropic γ -ray luminosity is $(5.1 \pm 0.1) \times 10^{48} \text{ erg s}^{-1}$. As a comparison in the 3FGL catalogue, covering the period 2008 August 4–2012 July 31, the integrated average flux is $(16.1 \pm 0.5) \times 10^{-8} \text{ ph cm}^{-2} \text{ s}^{-1}$, and the spectrum is described by an LP with a spectral slope $\alpha = 2.34 \pm 0.03$ at the reference energy $E_0 = 308$ MeV, and a curvature parameter around the peak $\beta = 0.13 \pm 0.02$. This indicates a moderate change of the average γ -ray spectrum during the period studied here, in which the flux is a factor of approximately six higher than the first four years of LAT operation.

Fig. 1 shows the γ -ray flux (top panel) and spectral parameters (middle panel: spectral slope; bottom panel: curvature parameter) evolution of CTA 102 for the period 2013 January 1–2017 February 9 using an LP model and 30-d time bins. For each time bin, the spectral parameters of both CTA 102 and all sources within 10° from it were left free to vary. For the time bins in which the fit results in a $\text{TS} < 300$ for CTA 102, the statistics is not enough for obtaining a detailed characterization of the spectrum with complex spectral models, therefore we run again the likelihood analysis using

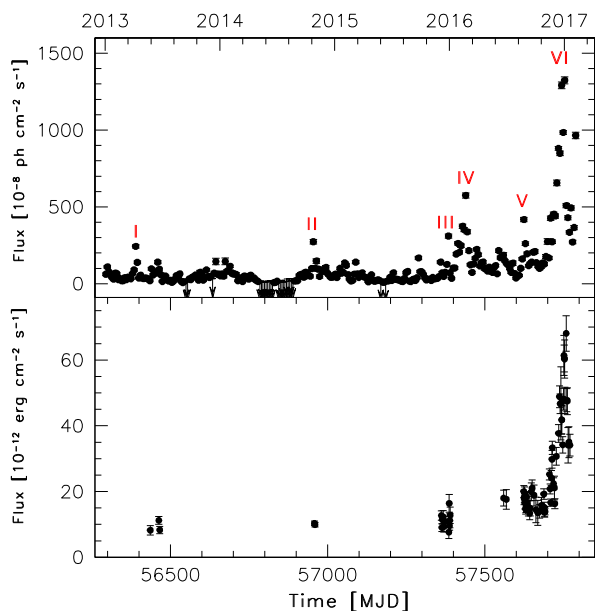


Figure 2. Upper panel: Integrated flux light curve of CTA 102 obtained in the 0.1–300 GeV energy range during 2013 January 1–2017 February 9 with five-day time bins. The arrow refers to 2σ upper limit on the source flux. Upper limits are computed when $TS < 10$. Different outbursts are labelled with an identification number in the plot. Bottom panel: X-ray light curve in the 0.3–10 keV energy range obtained by *Swift*-XRT (see Section 3 for details).

an LP model with the curvature parameter fixed to the value obtained integrating over the entire period (i.e. $\beta = 0.07$). The γ -ray spectrum of CTA 102 shows a remarkable variability on monthly time-scale, with a spectral slope between 1.88 and 2.97 (the average spectral slope is $\langle\alpha\rangle = 2.30 \pm 0.09$), and a curvature parameter between 0.04 and 0.26 (the average curvature parameter is $\langle\beta\rangle = 0.13 \pm 0.04$), although for the latter the uncertainties are relatively large.

For investigating the γ -ray variability on different time-scales, we have produced a γ -ray light curve for the entire period with five-day time bins (Fig. 2). For each time bin, the spectral parameters of CTA 102 and all sources within 10° of it were frozen to the values resulting from the likelihood analysis over the respective monthly time bin. When $TS < 10$, 2σ upper limits were calculated. Six peaks corresponding to periods with fluxes higher than 2×10^{-6} ph cm 2 s $^{-1}$ were observed in 2013 April 4–8 (MJD 56386–56390; I), 2014 October 21–25 (MJD 56951–56955; II), 2015 December 26–30 (MJD 57382–57386; III), 2016 February 19–23 (MJD 57437–57441; IV), 2016 August 22–26 (MJD 57622–57626; V), and 2016 December 30–2017 January 3 (MJD 57752–57756; VI), with an increase of the flux of a factor between 2.5 and 14 with respect to the average flux estimated during 2013–2017.

Finally, we have produced a γ -ray light curve with one-day and 12-h time bins for the period of high activity, i.e. 2016 November 11–2017 February 9 (MJD 57703–57793), as shown in Fig. 3. In the analysis of the sub-daily light curves, we fixed the flux of the diffuse emission components at the value obtained by fitting the data over the entire period analysed in this paper. For each time bin, the spectral parameters of both CTA 102 and all sources within 10° of it were frozen to the values resulting from the likelihood analysis in the monthly time bins. The peak flux of the daily light curve dates 2016 December 28 (MJD 57750), with a flux of $(2158 \pm 63) \times 10^{-8}$ ph cm $^{-2}$ s $^{-1}$, corresponding to a γ -ray

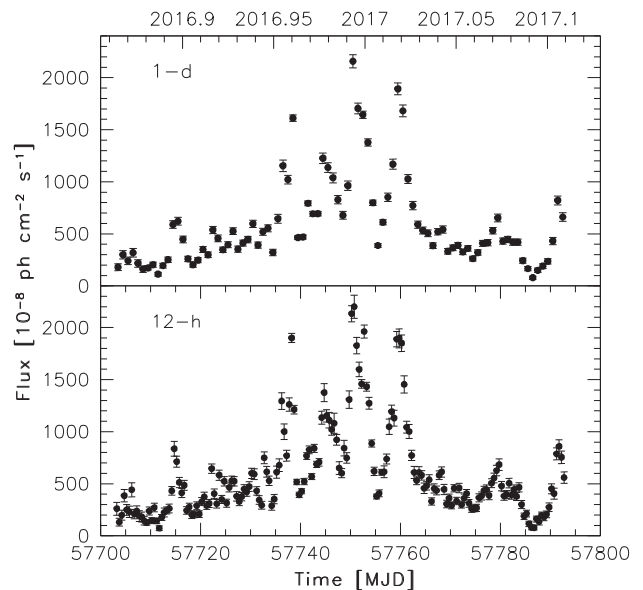


Figure 3. Integrated flux light curve of CTA 102 obtained by *Fermi*-LAT in the 0.1–300 GeV energy range during 2016 November 11–2017 February 9, with one-day time bins (top panel), and 12-h time bins (bottom panel).

luminosity $(2.2 \pm 0.1) \times 10^{50}$ erg s $^{-1}$. A similar peak flux was observed on 12-h time-scales, $(2200 \pm 111) \times 10^{-8}$ ph cm $^{-2}$ s $^{-1}$ in the second bin of 2016 December 28, corresponding to a γ -ray luminosity $(2.2 \pm 0.1) \times 10^{50}$ erg s $^{-1}$. These values are among the highest γ -ray luminosities ever measured for blazars, comparable to what was observed for 3C 454.3 (Abdo et al. 2011) and S5 0836+710 (Oriente et al. 2019). As a comparison, in 2012 the γ -ray flux of CTA 102 reached a peak flux of $\sim 9 \times 10^{-6}$ ph cm $^{-2}$ s $^{-1}$ (Larionov et al. 2016).

The search for variability on very short time-scale in γ -rays is beyond the scope of this paper. Rapid variability on time-scale of minutes was observed in 2016 December, with a peak flux of $\sim 3.5 \times 10^{-5}$ ph cm $^{-2}$ s $^{-1}$ (Gasparyan et al. 2018; Shukla et al. 2018; Meyer, Scargle & Blandford 2019).

3 NEIL GEHRELS SWIFT OBSERVATORY DATA: ANALYSIS AND RESULTS

The *Neil Gehrels Swift Observatory* satellite (Gehrels et al. 2004) carried out 73 observations of CTA 102 between 2013 March 24 (MJD 56436) and 2017 January 18 (MJD 57771). The observations were performed with all three instruments on board: the X-ray Telescope (XRT; Burrows et al. 2005, 0.2–10.0 keV), the Ultraviolet/Optical Telescope (UVOT; Roming et al. 2005, 170–600 nm), and the Burst Alert Telescope (BAT; Barthelmy et al. 2005, 15–150 keV).

The hard X-ray flux of this source turned out to be below the sensitivity of the BAT instrument for such short exposures and therefore the data from this instrument will not be used. Moreover, the source is not present in the *Swift* BAT 105-month hard X-ray catalogue (Oh et al. 2018).

The XRT data were processed with standard procedures (`xrt-pipeline v0.13.3`), filtering, and screening criteria by using the `HEASOFT` package (v6.22). The data were collected in photon counting mode in all the observations. The source position in detector coordinates was optimized for each observation by means of `XIMAGE`. The source extraction region is centred on these

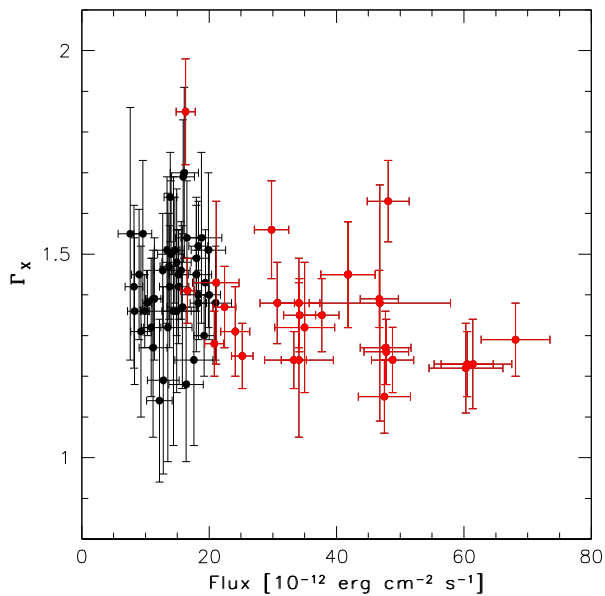


Figure 4. *Swift*-XRT photon index as a function of the 0.3–10 keV unabsorbed flux. The red points highlight the high-activity period.

coordinates. The source count rate in some observations is higher than $0.5 \text{ counts s}^{-1}$: these observations were checked for pile-up and a correction was applied following standard procedures (e.g. Moretti et al. 2005). To correct for pile-up we excluded from the source extraction region the inner circle of three-pixel radius by considering an annular region with outer radius of 30 pixel (1 pixel ~ 2.36 arcsec). For the other observations source events were extracted from a circular region with a radius of 20 pixels. Background events were extracted from a circular region with radius of 50 pixels far away from bright sources. Ancillary response files were generated with `xrtmkarf`, and account for different extraction regions, vignetting and point spread function corrections. We used the spectral redistribution matrices `v014` in the calibration data base maintained by HEASARC.⁴ We fitted the spectrum with an absorbed PL using the photoelectric absorption model `tbabs` (Wilms, Allen & McCray 2000), with a neutral hydrogen column density fixed to its Galactic value in the source direction ($N_{\text{H}} = 2.83 \times 10^{20} \text{ cm}^{-2}$; Kalberla et al. 2005). The results of the fit are reported in Table A1 and the 0.3–10 keV fluxes are shown in Fig. 2 in comparison to the γ -ray light curve obtained by *Fermi*-LAT.

The X-ray flux (0.3–10 keV) varied between 7.6×10^{-13} and $68.1 \times 10^{-13} \text{ erg cm}^{-2} \text{ s}^{-1}$ and the photon index between 1.14 and 1.85, with an average value of $\langle \Gamma_{\text{X}} \rangle = 1.40 \pm 0.15$. In Fig. 4 we plotted the XRT photon index as a function of flux in the 0.3–10 keV energy range. A harder-when-brighter spectral trend has been observed in X-rays in several blazars (e.g. Krawczynski et al. 2004; D’Ammando et al. 2011; Raiteri et al. 2012; Aleksic et al. 2015; Hayashida et al. 2015), although not always present also in the same source (e.g. Hayashida et al. 2012; Aleksic et al. 2017; Carnerero et al. 2017). This behaviour is usually related to the competition between acceleration and cooling processes acting on relativistic electrons. No spectral hardening with increasing flux is observed either in the entire period or in the high-activity period alone for CTA 102. This suggests that a change in the electron energy distribution is not the main driver of the long-term variability in this

energy band. However, at the peak of the X-ray activity the photon index is harder than the average value observed over 2013–2017.

During the *Swift* pointings, the UVOT instrument observed CTA 102 in all its optical (*v*, *b*, and *u*) and UV (*w1*, *m2*, and *w2*) photometric bands (Poole et al. 2008; Breeveld et al. 2010). We analysed the data using the `uvotsource` task included in the HEASOFT package (v6.22). Source counts were extracted from a circular region of five-arcsec radius centred on the source, while background counts were derived from a circular region of 20 arcsec radius in a nearby source-free region. Observed magnitudes are reported in Table B1. An increase of 4.5–5.5 mag with respect to the faint state of the source was observed in the UVOT bands, with a range of values: *v* = 11.44–16.86, *b* = 12.56–17.24, *u* = 11.78–16.27, *w1* = 11.33–16.18, *m2* = 11.36–16.17, *w2* = 11.52–16.46.

Following Raiteri et al. (2010, 2011) to obtain de-absorbed flux densities we used the count rate to flux density conversion factors CF and amount of Galactic extinction A_{Λ} for each UVOT band that have been obtained by folding the quantities of interest with the source spectrum and effective areas of UVOT filters and are reported in Larionov et al. (2016).

Besides correcting flux densities for Galactic extinction, we also subtracted the thermal emission contribution due to the accretion disc and BLR according to the model by Raiteri et al. (2014).

4 OPTICAL-TO-RADIO OBSERVATIONS

CTA 102 has been monitored by the GLAST-AGILE Support Program (GASP) of the WEBT in the optical, near-infrared, and radio bands since 2008. Optical-to-radio GASP-WEBT data collected in 2013–2017 have been presented in Raiteri et al. (2017). That data set is here complemented with data at 15 GHz by the OVRO telescope, at 91 and 103 GHz by ALMA, in the near-IR by the REM telescope, in the optical by the *Swift* satellite. The optical photometric observations used in this paper were acquired at the following observatories: Abastumani (Georgia), AstroCamp (Spain), Belogradchik (Bulgaria), Calar Alto (Spain), Campo Imperatore (Italy), Crimean (Russia), Kitt Peak (USA), Lowell (USA; 70 cm, DCT and Perkins telescopes), Lulin (Taiwan), Michael Adrian (Germany), Mt. Maidanak (Uzbekistan), New Mexico Skies (USA), Osaka Kyoiku (Japan), Polakis (USA), Roque de los Muchachos (Spain; Liverpool, NOT and TNG telescopes), ROVOR (USA), Rozhen (Bulgaria; 200 and 50/70 cm telescopes), San Pedro Martir (Mexico), Sirio (Italy), Skinakas (Greece), Steward (USA; Kuiper, Bok, and Super-LOTIS), St. Petersburg (Russia), Teide (Spain), Tien Shan (Kazakhstan), Tjarafe (Spain), Tucson (USA), Valle d’Aosta (Italy), and Vidojevica (Serbia).

Near-IR data were collected within the WEBT project in the *J*, *H*, and *K* bands at the Campo Imperatore, Lowell (Perkins) and Teide observatories. These data are here complemented with observations performed by REM (Zerbi et al. 2001; Covino et al. 2004), a robotic telescope located at the ESO Cerro La Silla observatory (Chile), in the period 2016 November 15–2016 December 11. All raw near-IR frames obtained with the REM telescope were reduced following standard procedures. Instrumental magnitudes were obtained via aperture photometry and absolute calibration has been performed by means of secondary standard stars in the field reported by 2MASS.⁵ The data presented here were obtained as Target of Opportunity observations triggered by the γ -ray flaring activity of the source (PI: F. D’Ammando). Observed magnitudes are reported in Table C1.

⁴<https://heasarc.gsfc.nasa.gov/docs/heasarc/caldb/>

⁵<http://www.ipac.caltech.edu/2mass/>

Table 1. Variability amplitude estimated over the period 2013 January 1–2017 February 9 in the different energy bands. Values are corrected for Galactic extinction and the thermal emission contribution. For the minimum and maximum flux density the MJD at which the value is collected is reported in parenthesis.

Band	Minimum flux density ($\text{erg cm}^{-2} \text{s}^{-1}$)	Maximum flux density ($\text{erg cm}^{-2} \text{s}^{-1}$)	Variability amplitude
γ -rays	5.91×10^{-13} (MJD 57177–57181)	3.02×10^{-9} (MJD 57752–57756)	5110
X-ray	7.60×10^{-12} (MJD 57386)	6.81×10^{-11} (MJD 57759)	9
W2	1.95×10^{-12} (MJD 56958)	4.92×10^{-10} (MJD 57751)	253
M2	3.41×10^{-12} (MJD 56958)	6.90×10^{-10} (MJD 57752)	202
W1	2.55×10^{-12} (MJD 56958)	5.95×10^{-10} (MJD 57751)	233
U	2.50×10^{-12} (MJD 56958)	3.37×10^{-10} (MJD 57752)	135
B	2.98×10^{-13} (MJD 56893)	7.20×10^{-10} (MJD 57750)	2416
V	1.97×10^{-13} (MJD 56874)	7.71×10^{-10} (MJD 57750)	3920
R	2.20×10^{-13} (MJD 56785)	7.76×10^{-10} (MJD 57750)	3523
I	3.62×10^{-13} (MJD 56785)	8.01×10^{-10} (MJD 57750)	2210
J	6.18×10^{-13} (MJD 56879)	6.96×10^{-10} (MJD 57752)	1126
H	8.59×10^{-13} (MJD 56879)	7.10×10^{-10} (MJD 57752)	827
K	1.09×10^{-12} (MJD 56879)	5.73×10^{-10} (MJD 57751)	526
230 GHz	2.25×10^{-12} (MJD 56832)	1.62×10^{-11} (MJD 57754)	7
103 GHz	1.63×10^{-12} (MJD 56837)	6.93×10^{-12} (MJD 57649)	4.3
91 GHz	1.51×10^{-12} (MJD 56837)	5.84×10^{-12} (MJD 57649)	3.9
37 GHz	7.92×10^{-13} (MJD 56839)	1.89×10^{-12} (MJD 57671)	2
15 GHz	4.28×10^{-13} (MJD 56651)	5.99×10^{-13} (MJD 57708)	1.5

Optical and near-IR flux densities were dereddened following the prescriptions of the NASA/IPAC Extragalactic Database⁶ (NED) and corrected for the thermal emission contribution according to the model of Raiteri et al. (2017).

Radio and mm observations were done at the Metsähovi Radio Observatory (Finland) at 37 GHz, and at the 30-m IRAM telescope (Spain) and the Sub-millimeter Array (Hawaii, USA) at 230 GHz. We also added the ALMA data collected at 91 and 103 GHz (Band 3) during 2013–2017 and included in the ALMA calibrator source catalogue.⁷

As part of an ongoing blazar monitoring program, the OVRO 40-Meter Telescope has observed CTA 102 at 15 GHz regularly since the beginning of 2009. The OVRO 40-Meter Telescope uses off-axis dual-beam optics and a cryogenic receiver with 2 GHz equivalent noise bandwidth centred at 15 GHz. Atmospheric and ground contributions as well as gain fluctuations are removed with the double switching technique (Readhead et al. 1989) where the observations are conducted in an ON–ON fashion so that one of the beams is always pointed on the source. Until 2014 May the two beams were rapidly alternated using a Dicke switch. Since 2014 May, when a new pseudo-correlation receiver replaced the old receiver, a 180 deg phase switch is used. Relative calibration is obtained with a temperature-stable noise diode to compensate for gain drifts. The primary flux density calibrator is 3C 286, with an assumed value of 3.44 Jy (Baars et al. 1977); DR21 is used as secondary calibrator source. Details of the observation and data reduction schemes are given in Richards et al. (2011). Observations acquired at 15 GHz by OVRO were used in this paper together with those obtained within the WEBT project. The radio flux at 15 GHz varied between 2.85 and 3.88 Jy during 2013–2017.

Radio-to-optical light curves collected by WEBT, REM, ALMA, and OVRO will be compared to the γ -ray light curve obtained by *Fermi*-LAT in the Section 5.

5 MULTIFREQUENCY FLUX VARIABILITY

Variability studies of radio-to- γ -ray emission from blazars can provide important insights into the physics of the jet and the mechanisms at work in these sources. Flares can be explained e.g. by a shock propagating downstream the jet and/or by variations of the Doppler factor, which depends on the bulk Lorentz factor of the relativistic plasma in the jet and on the viewing angle. During flares, blazars usually show greater variability amplitudes in the high-energy part of the spectrum than in the low-energy one (e.g. Wehrle et al. 1998; Raiteri et al. 2012). However, some sources increased their brightness by hundreds of times also in infrared and optical bands. In this context, the 2016–2017 outburst of CTA 102 presented here is one of the best cases to study.

We quantify the observed variability of the CTA 102 jet emission in the different energy bands through the variability amplitude, calculated as the ratio of maximum to minimum flux. Values in the γ -ray band are based on the light curve with five-day time bins. Near-infrared-to-UV fluxes are corrected for Galactic extinction. Moreover, the contribution of the thermal emission from the disc, BLR, and torus is removed to properly consider only the jet contribution to the flux. In Table 1 and Fig. 5, we report the variability amplitude estimated over the period 2013 January 1–2017 February 9 in the different bands. The variability amplitude may depend on the sampling of the light curves at the different frequencies. In the case of CTA 102, observations were available in all energy bands at the peak of the flare, making the values obtained representative of the increase of activity of the source. The variability amplitude shows a rising trend with increasing frequency in the radio-to-optical range and it declines in the UV. The X-ray band has a small variability amplitude, in particular if compared to the γ -ray one. This can be related to the lower energies of the electrons producing X-rays with respect to those producing γ -rays. The similar variability amplitude at 230 GHz and in the X rays may be a hint that they are produced by the same electron population in the same jet region through the synchrotron and IC emission mechanism, respectively, as found e.g. for BL Lacertae (Raiteri et al. 2013).

⁶<http://ned.ipac.caltech.edu/>

⁷<https://almascience.eso.org/alma-data/calibrator-catalogue>

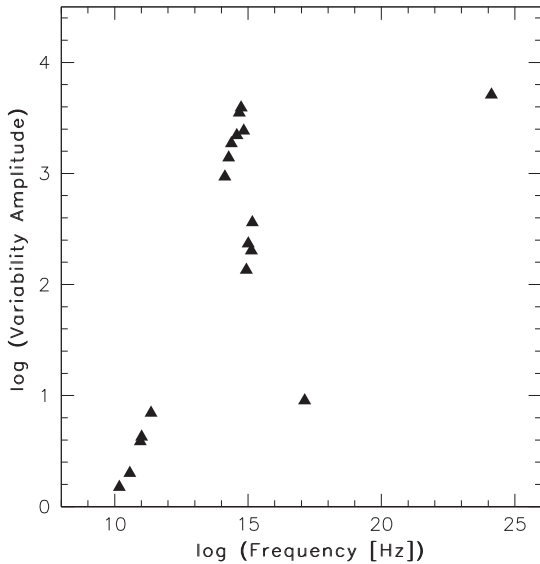


Figure 5. Variability amplitude versus frequency in the different energy bands estimated over the period 2013 January 1–2017 February 9. Values are corrected for Galactic extinction and the thermal emission contribution.

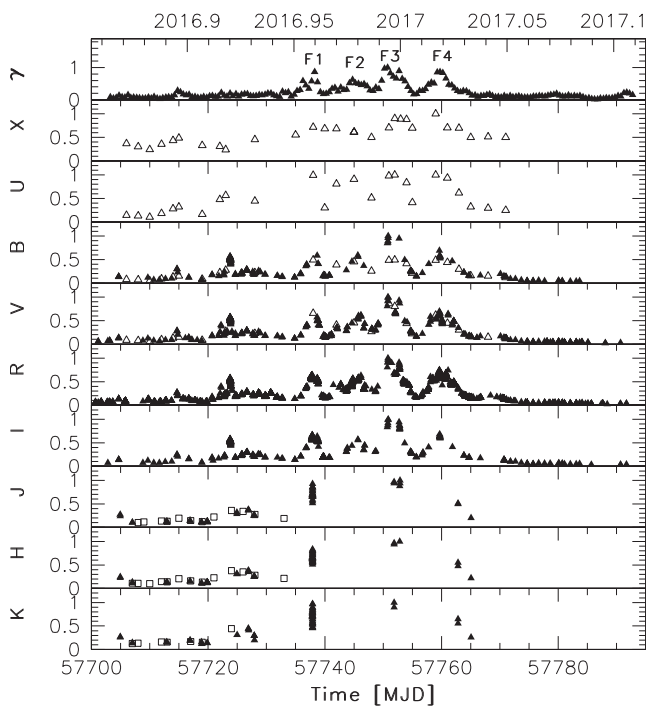


Figure 6. Multifrequency light curve normalized to the maximum value observed for the period 2016 November 11–2017 February 8 (MJD 57003–57792) in the following energy bands (from top to bottom): γ -rays (100 MeV–300 GeV), X-rays (0.3–10 keV), *B*, *V*, *R*, *I*, *J*, *H*, and *K*. Filled triangles: *Fermi-LAT* data; open triangles: *UVOT* data; open squares: *WEBT* data; filled circles: *REM* data. Main γ -ray outbursts are labelled as F1, F2, F3, and F4 in the top panel.

Simultaneous flux variations at low and high energies indicate that their emission comes from the same region of the jet and that the same electrons produce both the synchrotron and IC fluxes (e.g. Fossati et al. 2008). However, flaring events in the optical band with no counterpart at high energies were observed in some blazars (e.g. Chatterjee et al. 2013; D’Ammando et al. 2013). Strong variability characterizes the emission over the entire electromagnetic spectrum

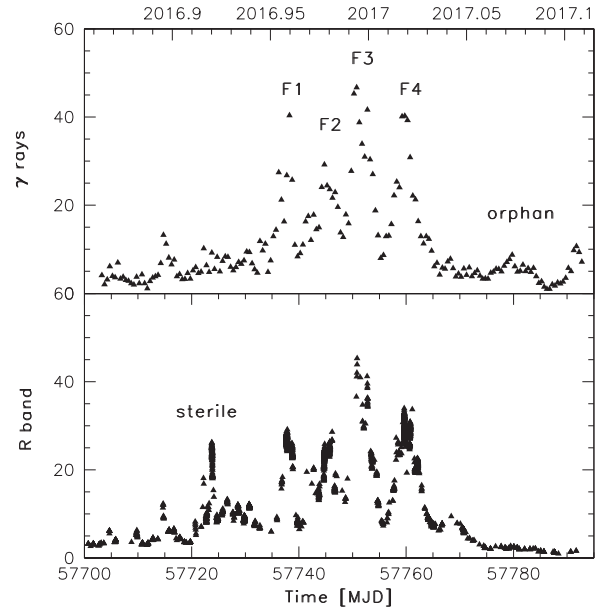


Figure 7. Comparison of the *Fermi-LAT* γ -ray light curve with 12-h time bins (top panel) and *R*-band light curve (bottom panel) normalized to the lowest value observed in the period 2016 November 11–2017 February 8. Main γ -ray outbursts and ‘orphan’ flares are labelled as F1, F2, F3, F4, and orphan in the top panel. The ‘sterile’ flare is labelled as sterile in the bottom panel.

of CTA 102 in 2016–2017, in particular during the period 2016 November 11–2017 February 8 (MJD 57003–57792), making this an ideal target to investigate the connection of the flux behaviour observed in γ -rays with the flux behaviour at lower energies.

In Fig. 6, we compare the γ -ray light curve obtained by *Fermi-LAT* with 12-h time bins during the highest activity period, 2016 November 11–2017 February 8 (MJD 57003–57792, corresponding to the outburst VI in Fig. 2), to the infrared-to-X-ray light curves. All fluxes are normalized to the maximum value observed in the considered period in order to compare when and how much the flux increased in the different energy bands. In the γ -ray light curve we can see four major outbursts peaked on 2016 December 15 (MJD 57737; F1), 2016 December 22 (MJD 57744; F2), 2016 December 27 (MJD 57749; F3), and 2017 January 4 (MJD 57757; F4). The third outburst appears more prominent and shows a larger increase with respect to the others. These four outbursts have corresponding events in optical, with the peaks observed at the same time. In *J*, *H*, and *K* bands the sampling is sparse and only two of the four peaks are observed. A high X-ray flux has been observed in the period that covers the γ -ray flares F1 and F2, and two X-ray peaks are evident at the time of the γ -ray flares F3 and F4.

If we compare the γ -ray and optical (*R* band, the best sampled band) fluxes normalized to the respective lowest values observed during 2016 November 11–2017 February 9 (Fig. 7), it is evident that the four main flares occurred at the same time. A similar amplitude has been observed in the two bands, except for the first flare. In particular, the same variability amplitude has been observed during the main peak. On the other hand, not all the events observed in the optical band have a counterpart in γ -rays and vice versa. In addition to the ‘sterile’ optical flare⁸ occurred around 2016 December 1 (MJD 57723), no significant optical

⁸With ‘sterile flare’ and ‘orphan flare’ we mean a flare observed in the optical band with no counterpart at γ -ray frequencies, and a flare that is observed at the high energies only, respectively.

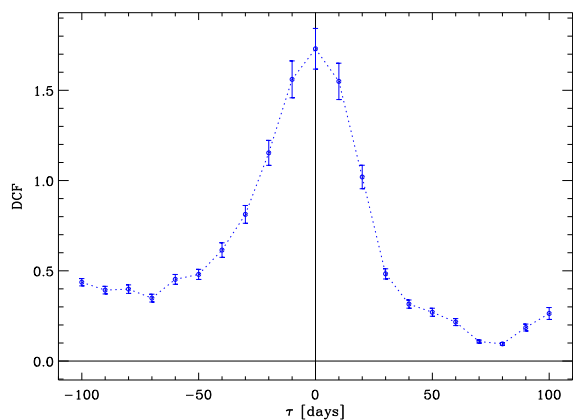


Figure 8. DCF between the γ -ray fluxes obtained with five-day time bins and the R -band flux densities with one day binning over the whole 2013–2017 period.

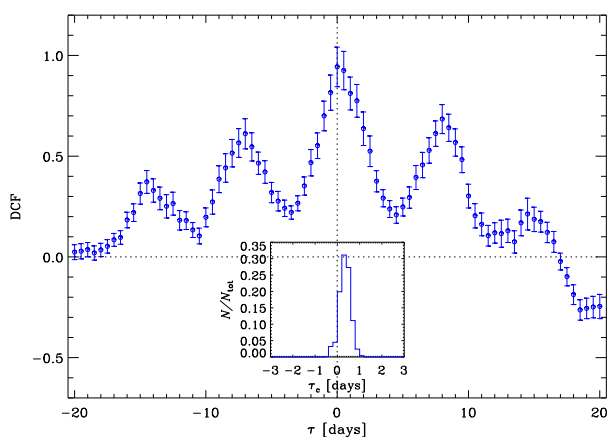


Figure 9. DCF between the γ -ray fluxes obtained with 12-h time bins and the R -band flux densities with one-hour binning during the 2016–2017 flaring period. The inset shows the result of cross-correlating 1000 Monte Carlo realizations of the two data sets according to the ‘flux redistribution/random subset selection’ technique.

activity corresponds to the increase of γ -ray activity peaked on 2017 January 24 (MJD 57777) and 2017 February 6 (MJD 57790) (‘orphan’ flares). This indicates that the interpretation of the source variability must be more complicated than the fair overall optical– γ correlation would suggest.

Cross-correlation analysis between flux variations in different bands can allow us to determine whether the emissions come from the same region of the jet or not. We used the discrete correlation function (DCF; Edelson & Krolik 1988; Hufnagel & Bregman 1992) to analyse cross-correlations. Correlation produces positive peaks in the DCF and is strong if the peak value approaches or even exceeds one. The DCF between the γ -ray and the optical (R -band) light curves over the whole 2013–2017 period is displayed in Fig. 8, showing a main peak compatible with no time lag. When comparing the γ -ray light curve with 12-h time bin with the optical light curve with one-hour binning in the high-activity period of Fig. 7, the DCF shows again a main peak compatible with no time lag, with $\text{DCF}_p = 0.94$ (Fig. 9). This indicates strong correlation between γ -ray and optical emission, with no evidence of delay between the flux variations in the two bands, in agreement with the results presented in Larionov et al. (2017). We determine the uncertainty in this

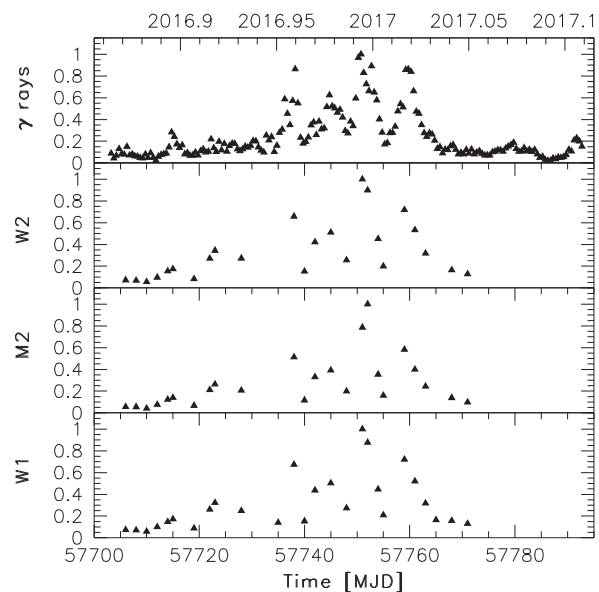


Figure 10. Multifrequency light curve normalized to the maximum value observed for the period 2016 November 11–2017 February 8 (MJD 57003–57792) in the following energy bands (from top to bottom): γ -rays (100 MeV–300 GeV), w_2 , m_2 , and w_1 bands.

result by performing 1000 Monte Carlo simulations according to the ‘flux redistribution/random subset selection’ technique (Peterson et al. 1998; Raiteri et al. 2003), which tests the importance of sampling and data errors. Among the 1000 simulations, we obtain that 78.3 percent of simulations ($>1\sigma$) give a time lag between 0 and 0.6 d, as shown in the inset of Fig. 9. This is compatible with no delay between optical and γ -ray emission. The secondary DCF peaks in Fig. 9 are due to the multi-peaked structure of the outburst.

Although the UV data collected by *Swift*-UVOT are sparser than the optical ones, we can recognize a similar behaviour in the γ -ray and UV light curves with similar increase of flux during the flaring period when normalized to the maximum value (Fig. 10), even though the variability amplitude is smaller in UV with respect to the γ -ray band.

The sparse X-ray data in 2013–2015 indicate a low flux, in keeping with the relatively low activity observed also in γ -rays (see Fig. 2). The comparison between the γ -ray and the X-ray light curves during the high-activity period shows a general agreement, with the γ -ray peaks corresponding to high X-ray fluxes (Fig. 11). Cross-correlation of the γ -ray (12-h time bins) and X-ray light curves in the high-activity period shows a good correlation with a time lag compatible to zero within the DCF bin size of six days (Fig. 12). The different sampling of the light curves does not allow a more detailed comparison. However, the X-ray variability amplitude appears much smaller than at γ -rays.

The correlation between the radio-mm fluxes on one side and the optical and γ -ray fluxes on the other side is rather puzzling. In general, they present a different behaviour, but sometimes they share common features. As one can see in Fig. 13, the mm data at 230 GHz show a steady flux increase starting from the end of 2015 and culminating with a prominent outburst peaking on 2017 January 1 (MJD 57754). A comparison with the γ -ray light curve reveals that the end of 2015 also marks the beginning of the activity in this band, with the major peak observed at the same time of the 230 GHz one.

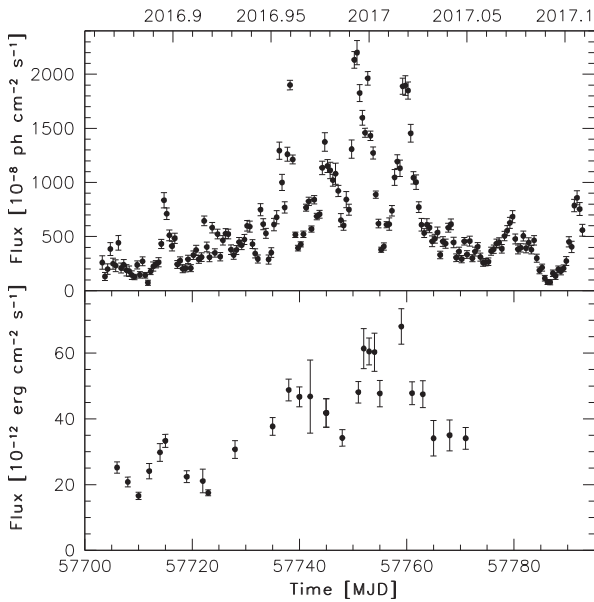


Figure 11. *Fermi*-LAT γ -ray light curve with 12-h time bins in the 0.1–300 GeV energy range (top panel) and X-ray light curve in the 0.3–10 keV energy range (bottom panel) in the period 2016 November 11–2017 February 9.

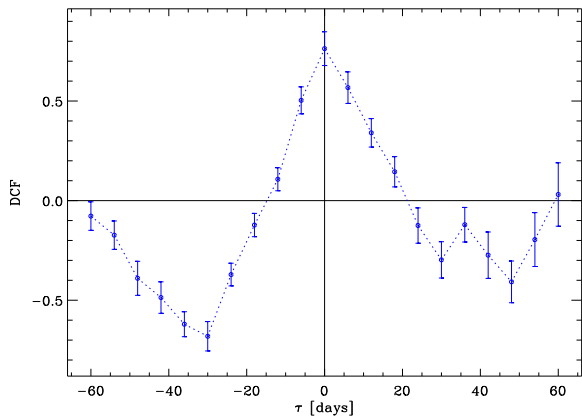


Figure 12. DCF between the γ -ray fluxes obtained with 12-h time bins and the X-ray flux.

A steady flux increase starting from the end of 2015 is observed also at 91–103 GHz, is marginally detectable at 37 GHz, and vanishes at 15 GHz. Enhanced activity is present at the beginning of 2014 at 230, 91–103, and 37 GHz, when the light curves at both lower and higher frequencies appear rather flat.

The light curves at 91–103, 37, and 15 GHz present peaks in 2016 October–November. The increase of delay of the radio peaks going to lower frequencies is in agreement with synchrotron self-absorption opacity effects. The decrease of the flux variation amplitudes towards lower frequencies is expected, if the radio emission at lower frequencies comes from more external and extended regions of the jet, in average less aligned to our line of sight. In and around the same period, the sampling at 230 GHz is poor. The closest events at γ -ray and optical frequencies date 2016 August (flare V in Fig. 2), and, before, there is a stronger γ -ray flare in 2016 March (flare IV) during a seasonal gap in the optical light curve.

The DCF between the γ -ray and 15 GHz fluxes (see Fig. 14) shows a small peak at a negative time lag of about two months,

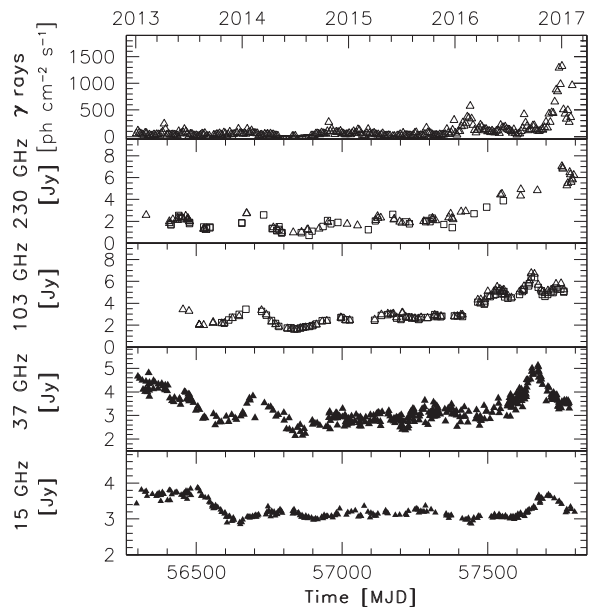


Figure 13. Multifrequency light curve for the period 2013 January 1–2017 February 9 in the following energy bands (from top to bottom): γ -rays (100 MeV–300 GeV; five-day time bins, in units of 10^{-8} ph cm $^{-2}$ s $^{-1}$; *Fermi*-LAT data), 230 GHz (in units of Jy; triangles: SMA data, squares: IRAM data), 91 and 103 GHz (in units of Jy; ALMA data), 37 GHz (in units of Jy; Metsähovi data), 15 GHz (in units of Jy; OVRO data).

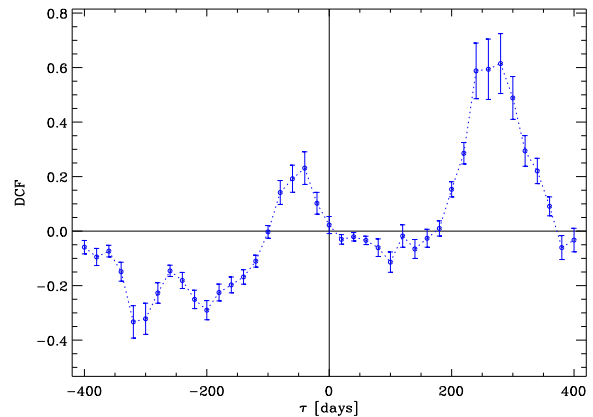


Figure 14. DCF between the γ -ray fluxes obtained with five-day time bins and the 15 GHz flux densities.

indicating radio variations preceding the γ -ray ones. This signal comes from the cross-match of the 15 GHz flare peaking at the beginning of 2016 November with the γ -ray acme two months later. A stronger DCF maximum occurs at time lag of about 250 d, indicating radio variations following the γ -ray ones by about eight to nine months. This suggests that linking the 2016 October–November radio flare observed from 103 to 15 GHz with the 2016 March γ -ray flare is more likely. Therefore, a delayed radio outburst at 15 GHz can be expected also some months after the 2017 January main flare observed in the γ -ray, optical, and 230 GHz band.

However, extending the OVRO light curve at 15 GHz up to 2018 July (see Fig. D1), a radio outburst is visible only in 2018 February, more than one year after the 2017 γ -ray, optical and mm peaks. Its peak flux is only a few per cent greater than the maximum flux reached in 2016 October–November. On the basis of the delay between γ -ray emission and radio emission at 15 GHz found here

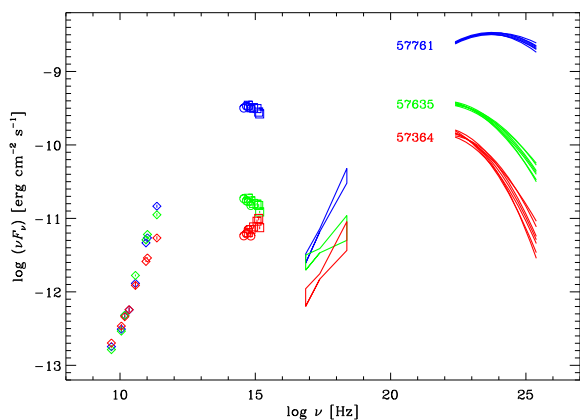


Figure 15. Broad-band SED of CTA 102 in three different brightness states labelled with their MJD. In the optical-UV bands, ground-based data are shown as open circles, while UVOT data are displayed with squares. The X-ray spectra are represented by PL fits, while the *Fermi*-LAT spectra are plotted according to LP models; in both cases we took the uncertainties on the parameters into account.

and usually observed in blazar objects (e.g. Pushkarev et al. 2010; Fuhrmann et al. 2014), it is unlikely that the 2018 radio outburst at 15 GHz is related to the main flaring activity observed at the beginning of 2017 in γ -ray, optical, and at 230 GHz. Therefore, we conclude that the γ -ray flaring activity in 2017 has no (delayed) counterpart in the 15 GHz light curve.

In the framework of the geometrical model, the difference in behaviour between radio and higher energy emission would be ascribed to different viewing angle (with consequent different Doppler boosting of the emission) of the jet regions producing their emission. The extent of misalignment between the emitting jet regions can be inferred from the corresponding light curves, as will be shown in Section 7.

6 MULTIFREQUENCY SPECTRAL VARIABILITY

Fig. 15 shows the broad-band SED of CTA 102 in three brightness states with near-contemporaneous data in the optical, UV, X-ray, and γ -ray bands. The optical-to-radio data set presented in Raiteri et al. (2017) has been complemented with data at 15 GHz by the OVRO telescope, at 91 and 103 GHz by ALMA, and in the near-IR by the REM telescope, in the optical-to-X-rays by the *Swift* satellite, and at γ -rays by the *Fermi* satellite. In addition to SMA, Metsähovi, ALMA, and OVRO data, radio observations collected by RATAN-600 radio telescope (Mingaliev et al. 2001) from 1.0 to 21.7 GHz have been considered. Because of the longer variability time-scales of the radio light curves, radio data are included also if taken within a few days from the reference epoch.

The highest state corresponds to MJD = 57761 (2017 January 8). Optical data were acquired at the Tjarafe Observatory and fairly overlap with the UVOT data. The intermediate state dates MJD = 57635 (2016 September 4), and comes from the declining phase of the small flare preceding the big outburst (flare V in Fig. 2). The optical data are from the Mt. Maidanak Observatory and are in satisfactory agreement with the UVOT data. For the low state, we chose MJD = 57364 (2015 December 8), about one year before the culmination of the big outburst. Optical data are from the St. Petersburg Observatory; the *B*-band point appears a bit fainter than the corresponding UVOT value, but they agree within errors. For

the LAT data the spectra are extracted on five-day time-scale as done in Fig. 2, except for the high state in which the daily LAT spectrum is included.

The intermediate- and the low-state SED become very close in the UV, where the emission contribution of the big blue bump peaks in coincidence of the Ly α λ 1216 broad emission lines. The X-ray spectral shape in the intermediate state is softer than expected, but it is affected by large errors. Finally, the peak of the IC component shifts at a much higher energy in the high state, confirming the result found for the synchrotron component by Raiteri et al. (2017).

7 GEOMETRICAL MODEL APPLIED TO γ -RAY, OPTICAL, AND RADIO DATA

In Raiteri et al. (2017) we interpreted the long-term variability of the CTA 102 synchrotron flux in terms of variation of the Doppler factor because of changes of the viewing angle of the jet-emitting regions. The intrinsic flux is assumed to be constant on time-scales of months or longer in the rest frame, while fast flares can be due to intrinsic, energetic processes. From the observed multiwavelength light curves we derived how the jet moves, i.e. how the regions emitting at different frequencies align with respect to the line of sight. Support to this twisting jet scenario comes from both observations and theory. Examples of helical jet structures and wobbling motion have been observed with high angular resolution images in the radio band in both extragalactic and Galactic sources (see e.g. Agudo et al. 2007, 2012; Perucho et al. 2012; Fromm et al. 2013; Britzen et al. 2017, 2018; Miller-Jones et al. 2019).

In numerical magnetohydrodynamics (MHD) simulations of relativistic jets in 3D, instabilities can develop which distort the jet itself and produce wiggled structures (Nakamura, Uchida & Hirose 2001; Mignone et al. 2010). Moreover, orbital motion in a binary black hole system or a warped accretion disc can lead to jet precession, which modifies the jet orientation with respect to the line of sight (Liska et al. 2018).

Raiteri et al. (2017) performed their analysis on radio–optical data, concentrating on the light curves at 37 and 230 GHz, and in the *R* band. In the following we investigate the outcome of the proposed geometrical model when applied to both higher and lower frequencies. We examine the γ -ray and 15 GHz flux variability; the X-ray data are too sparse for a meaningful analysis. We consider the γ -ray light curve from 2013 January 1 (MJD 56293), with a time bin of five days before 2016 November 11 (MJD 57703) and 12 h after. The γ -ray light curve is compared to the optical (*R* band) and radio (15 GHz) light curves in Fig. 16.

As in Raiteri et al. (2017), we modelled the optical long-term trend with a cubic spline interpolation through the data binned with a variable time interval, which shortens as the flux rises: $\Delta t = \Delta t_0/n$ when $F > F_{\min}n^{2+\alpha}$, where the exponent 2 applies to a continuous jet and $\alpha = 1.7$ is the spectral index in the *R* band. We used the same binning to obtain the spline in the γ -ray band, while for 15 GHz case we adopted a 30-d bin because of the smoother behaviour, as done by Raiteri et al. (2017) for the 37 and 230 GHz light curves.

From the splines we derived the Doppler factors⁹ $\delta(t)$ displayed in Fig. 16 as

$$\delta(t) = \delta_{\min} (F_{\text{spline}}/F_{\min})^{1/(2+\alpha)},$$

⁹The Doppler factor is defined as $\delta = 1/[\Gamma(1 - \beta \cos \theta)]$, where Γ is the bulk Lorentz factor, β the velocity normalized to the speed of light, and θ the viewing angle.

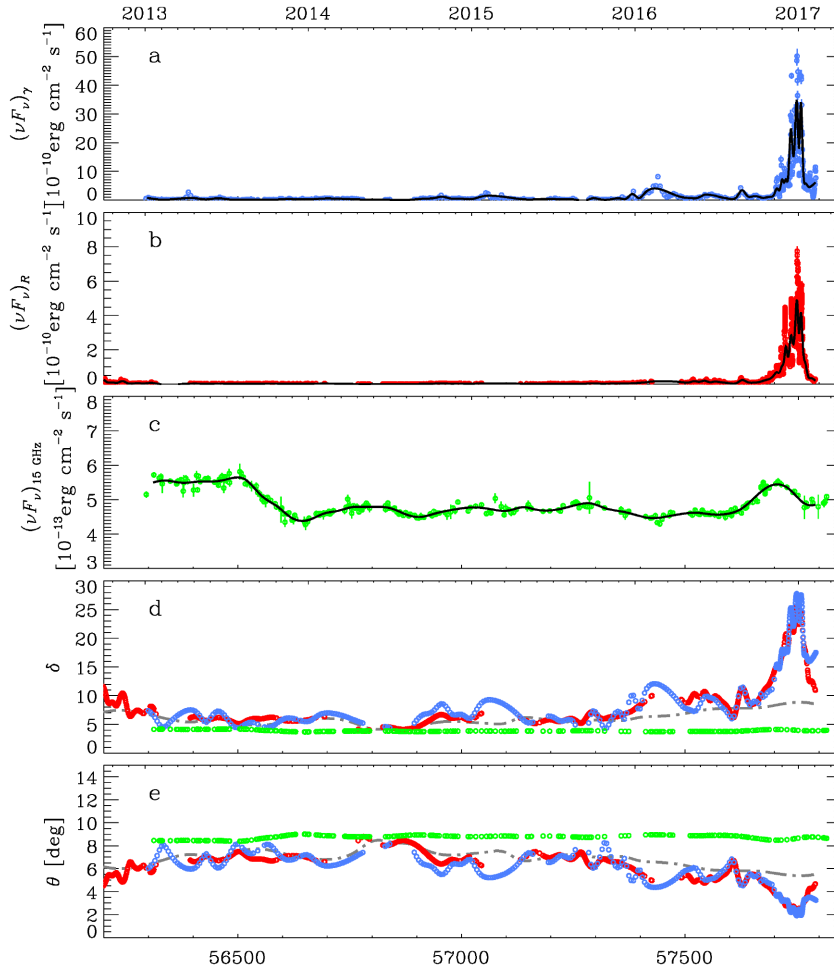


Figure 16. Light curves of CTA 102 in the γ -ray (a), optical (b), and 15 GHz radio (c) bands. The black curves indicate spline interpolations with variable time bin in the optical and γ -ray bands, and 30-d bins at 15 GHz; they represent the long-term trends. The Doppler factor δ for the γ -ray (blue), the optical (red), and the radio (green) bands are plotted in panel (d), while (e) shows the corresponding viewing angles. In panel (d) and (e) the grey dot–dashed curve shows the trend obtained for the 230 GHz data according to Raiteri et al. (2017).

where F_{spline} are the flux densities defined by the spline interpolations, F_{min} are their minimum values, and $\delta_{\text{min}} = 3.7$ is obtained by assuming a bulk Lorentz factor $\Gamma = 20$ and a maximum jet viewing angle $\theta_{\text{max}} = 9$ deg (Raiteri et al. 2017). We adopted a spectral index equal to the optical one for the γ -ray band and equal to zero for the 15 GHz case.

The behaviour of $\delta(t)$ in the optical and γ -ray bands are in fair general agreement, as expected if the optical and γ -ray photons are produced in the same jet region. Small differences between the Doppler factor estimated in the optical and γ -ray bands are justified by the fact that we derived the Doppler factors by interpolating through data affected by errors and collected in bands with different samplings. There is some discordance only in the last part of the considered period, where some γ -ray activity has no optical counterpart (see discussion in the next section).

In contrast with the optical and γ -ray cases, the Doppler factor resulting from the 15 GHz long-term trend is only marginally variable. Actually, in general the Doppler factor and its variability decrease from 230 to 15 GHz, in agreement with the decrease of their flux variability amplitude.

We interpret the time variability of the Doppler factor as due to changes in the jet viewing angle, which implies a twisting jet. The trend of the viewing angle is derived from the definition of the

Doppler factor and is shown in Fig. 16. The flux maxima correspond to maxima in the Doppler factor and minima in the viewing angle. The plots of $\theta(t)$ suggest that the part of the jet producing the optical and γ -ray radiation is characterized by intense wiggling, the viewing angle ranging from about nine to two degrees. In contrast, the viewing angle remains more stable as we proceed towards longer wavelengths, i.e. towards outer and larger jet regions. At 15 GHz $\theta(t)$ varies between 8.4 and nine degrees. Indeed, the viewing angle of the radio-emitting regions can be seen as an average over extended zones of the curved jet. This would also be the reason why the rise of the 230 GHz flux towards the 2016–2017 peak starts much earlier than in the optical and γ -ray bands. Indeed, while the optical and γ -ray fluxes reach the minimum viewing angle abruptly, the larger and curved jet section emitting the millimetre flux starts to align with the line of sight even before the optical and γ -ray-emitting zone. The maximum ‘misalignment’ between the γ -optical and 15 GHz emitting regions is reached during the culmination of the 2016–2017 outburst and is about seven degrees.

In Fig. 17 we show the relationship between γ -ray and optical fluxes starting from 2013 January 1 (MJD 56293). Each γ -ray flux is associated with the average of the optical fluxes acquired within 2.5 d from the time of the γ data point when the γ -ray bin is five days, within six hours when the bin is 12 h. The slope of

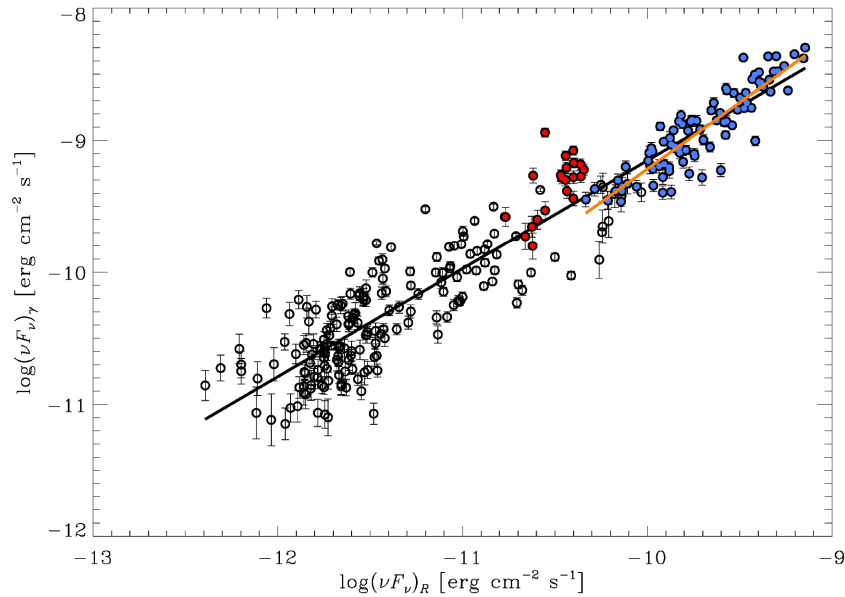


Figure 17. The relationship between γ -ray and optical fluxes. The γ -ray fluxes have been associated with the average optical fluxes obtained by considering optical data close in time to the γ -ray optical points. The blue dots refer to the outburst period, the red dots to the period of the γ -ray ‘orphan’ flare (MJD > 57775). The black and orange solid lines represent linear fits to all the data and to the data in the outburst period, respectively.

the linear fit is 0.82 and the linear Pearson correlation coefficient is 0.95.

The geometrical effect is expected to be more evident during the outburst, when we also have better sampling. If we restrict the linear fit to the outburst data in the time interval 2016 November 23–2017 January 22 (MJD 57715–57775¹⁰), we obtain a linear fit with slope equal to 1.00 and linear Pearson correlation coefficient equal to 0.90. A unity slope is what one expects if both the γ -ray and optical long-term trends are due to Doppler factor variations (Larionov et al. 2016), so this result supports the idea that the variability during the outburst is mainly caused by changes in δ , as predicted by the geometrical model.

8 DISCUSSION AND CONCLUSIONS

In Raiteri et al. (2017) the results of radio-to-optical monitoring of the FSRQ CTA 102 in 2013–2017 were presented and a geometrical model was applied to those data. In this paper, that data set has been complemented with data at 15 GHz by the OVRO telescope, at 91 and 103 GHz by ALMA, in the near-IR by the REM telescope, in the optical-to-X-rays by the *Swift* satellite, and at γ -rays by the *Fermi* satellite. These new data have been analysed in view of the above geometrical interpretation.

Since 2013 April, the source showed significant flux and spectral variability in γ -rays on a monthly time-scale, with several periods of high activity. A general correlation is found between the optical, infrared, and γ -ray flux variations, which are consistent with being simultaneous, suggesting that the observed emission is produced in the same region of the jet.

The source showed strong activity in the period mid 2016–February 2017 at all frequencies. In particular, an unprecedented γ -ray flaring activity was observed, reaching a peak flux of $(2158 \pm 63) \times 10^{-8} \text{ ph cm}^{-2} \text{ s}^{-1}$ in the 0.1–300 GeV energy

range on 2016 December 28, corresponding to an apparent isotropic luminosity of $(2.2 \pm 0.1) \times 10^{50} \text{ erg s}^{-1}$. Comparable values are obtained on 12-h time bin in the same day. The peak luminosity observed for CTA 102 is comparable to the highest values observed in blazars so far. Four main outbursts are observed in γ -rays between 2016 November 11 and 2017 February 9, and corresponding events are observed in near-IR, optical, and UV with the peaks at the same time. A common trend was observed also between the X-ray and γ -ray emission in the high-activity state. No significant harder-when-brighter behaviour was observed in X-rays, indicating that a change in the electron energy distribution is not the main driver of the variability in this band.

The same variability amplitude was observed in the optical (R band) and γ -ray bands during the high-activity period. DCF analysis suggests a strong correlation between the flux variations in optical and γ -rays, with no detectable lag between the emission in the two bands. However, not all the events observed in the optical band have a counterpart in γ -rays and vice versa. The interpretation of these ‘orphan flares’ is a challenge for all theoretical models aiming to explain blazar variability. They are likely produced in a different emitting region or by a different emission process (e.g. magnetic reconnection; Petropoulou, Giannios & Sironi 2016) with respect to the emitting region and mechanism responsible for the long-term behaviour.

On the other hand, the ‘sterile’ optical flare observed around 2016 December 1 (MJD 57723) can be due to the fact that the optical emitting region presents substructures (e.g. Narayan & Piran 2012), and not all of them produce significant γ -ray emission. Alternatively, magnitude and direction of a turbulent magnetic field should affect mostly the synchrotron emission, producing an increase of flux in optical not observed in γ -rays (e.g. Marscher et al. 2014). These ‘sterile’ and ‘orphan’ flares are superposed to the long-term variability well explained by the geometrical model adopted here.

We have investigated the source behaviour at higher (γ -ray) and lower (15 GHz) frequencies than those analysed in Raiteri et al.

¹⁰The range corresponds to a γ -ray spline flux exceeding $5 \times 10^{-10} \text{ erg cm}^{-2} \text{ s}^{-1}$.

(2017) by means of their geometrical interpretation of the source variability. This model implies that different emitting regions can change their alignment with respect to the line of sight, leading to a different Doppler boosting and thus enhancement of the observed flux from one region with respect to that from another region. We have derived the trends in time of the Doppler factor and of the viewing angle for the jet regions responsible for the γ -ray and 15 GHz emission. The trends inferred from the γ -ray data are in fair agreement with the optical ones and the relationship between the γ -ray and optical fluxes is linear, as predicted by the model, confirming it. We note that a γ -ray/optical linear correlation during the outburst may be obtained also with a change of the electron density within a leptonic, one-zone model, where the γ -rays are produced by an external Compton mechanism. However, the geometrical model also accounts for the continuous time evolution of the multiwavelength flux and not only for single snap-shots of the source behaviour.

A change in the direction of the jet, which became oriented more closely to our line of sight ($\theta \sim 1.2$ deg), has been observed with Very Long Baseline Array images at 43 GHz during the γ -ray flaring activity of CTA 102 in 2012 September–October (Casadio et al. 2015). These orientation changes can be due to MHD instabilities developing in the jet, precession, or orbital motions in a binary system of supermassive black holes.

Alternative theoretical scenarios have been proposed to explain the flaring activity observed during 2016–2017 in CTA 102. In particular, the multiwavelength flares from 2016 December to 2017 January are explained by Casadio et al. (2019) as the interaction between a new jet component and a possible recollimation shock at ~ 0.1 mas. The variability Doppler factor associated with such interaction (i.e. $\delta_{\text{var}} = 34 \pm 4$) is compatible with the values obtained applying our geometrical model (see Fig. 16). However, Casadio et al. (2019) did not try to reproduce the evolution in time of the flaring activity or the long-term behaviour of the multiwavelength light curves with their model.

The long-term trend in optical, X-ray, and γ -ray band has been discussed in a scenario in which the increase of activity is due to the ablation of a gas cloud by the relativistic jet within a hadronic emission model in Zacharias et al. (2019). However, the proposed hadronic model results in super-Eddington jet powers at all times. This is a common problem in the application of hadronic models to the SED modelling of blazars (e.g. Böttcher et al. 2013). These extreme jet powers obtained in hadronic models are in conflict with the estimates of the jet power based on radio lobes and X-ray cavities (e.g. Merloni & Heinz 2007; Godfrey & Shabala 2013), and the corresponding accretion rates should imply a very short accretion mode and/or a very small duty cycle in the SMBH evolution compared to estimated lifetimes of active phases of AGNs (e.g. Zdziarski & Boettcher 2015). Moreover, the optical and X-ray coverage, both in the flaring and long-term periods, at which the theoretical model proposed in Zacharias et al. (2019) has been applied appears not adequate to obtain robust results due to long gaps of data and relatively small number of data. The details of the model should be tested with more complete data set like that presented in this paper.

We conclude that the observed long-term flux and spectral variability of CTA 102 at both low and high energies can well be explained by an inhomogeneous curved jet where the observed emission at different frequencies is modulated by changes in the orientation of the corresponding emitting regions with respect to our line of sight.

The main strength of this geometrical model is that it can explain the long-term flux and spectral evolution of CTA 102 in a simple

way, with very few assumptions. Its main justification is its ability to explain the contraction of the variability time-scales and the increase of variability amplitude during outburst found by Raiteri et al. (2017). That is the signature of Doppler factor variations which cannot be justified by other models. The analysis performed in this paper, on a wider data set extending to high energies, confirms the model, showing in particular that the relationship between the γ -ray and optical fluxes is linear, as predicted by the model.

ACKNOWLEDGEMENTS

The data collected by the WEBT collaboration are stored in the WEBT archive at the Osservatorio Astrofisico di Torino - INAF (<http://www.oato.inaf.it/blazars/webt/>); for questions regarding their availability, contact the WEBT President Massimo Villata (massimo.villata@inaf.it). We acknowledge financial contribution from the agreement ASI-INAF n. 2017-14-H.0 and from the contract PRIN-SKA-CTA-INAF 2016.

This research was partially supported by the Bulgarian National Science Fund of the Ministry of Education and Science under grants DN 08-1/2016, DN 18-13/2017, and KP-06-H28/3 (2018). The Skinakas Observatory is a collaborative project of the University of Crete, the Foundation for Research and Technology – Hellas, and the Max-Planck-Institut für Extraterrestrische Physik. The Abastumani team acknowledges financial support by the Shota Rustaveli National Science Foundation under contract FR/217554/16. The St. Petersburg University team acknowledges support from Russian Science Foundation grant 17-12-01029. GD and OV gratefully acknowledge the observing grant support from the Institute of Astronomy and Rozhen National Astronomical Observatory, Bulgarian Academy of Sciences, via bilateral joint research project ‘Study of ICRF radio-sources and fast variable astronomical objects’ (head - G.Damljanovic). This work is a part of the Projects No. 176011 (‘Dynamics and Kinematics of Celestial Bodies and Systems’), No. 176004 (‘Stellar Physics’), and No. 176021 (‘Visible and Invisible Matter in Nearby Galaxies: Theory and Observations’) supported by the Ministry of Education, Science and Technological Development of the Republic of Serbia. JE is indebted to DGAPA (Universidad Nacional Autónoma de México) for financial support, PAPIIT project IN114917. The Submillimeter Array is a joint project between the Smithsonian Astrophysical Observatory and the Academia Sinica Institute of Astronomy and Astrophysics and is funded by the Smithsonian Institution and the Academia Sinica. Data from the Steward Observatory blazar monitoring project were used. This program is supported by NASA/Fermi Guest Investigator grants NNX12AO93G and NNX15AU81G. We acknowledge support by Bulgarian National Science Programme ‘Young Scientists and Postdoctoral Students 2019’, Bulgarian National Science Fund under grant DN18-10/2017 and National RI Roadmap Projects DO1-157/28.08.2018 and DO1-153/28.08.2018 of the Ministry of Education and Science of the Republic of Bulgaria. This publication makes use of data obtained at Metsähovi Radio Observatory, operated by Aalto University in Finland. The Astronomical Observatory of the Autonomous Region of the Aosta Valley (OAVdA) is managed by the Fondazione Clment Fillietroz-ONLUS, which is supported by the Regional Government of the Aosta Valley, the Town Municipality of Nus and the ‘Unit des Communes valdtaines Mont-milius’. The research at the OAVdA was partially funded by two ‘Research and Education’ grants from Fondazione CRT. RR acknowledges support from CONICYT project Basal AFB-170002. MM and TM acknowledge support

through the Russian Government Program of Competitive Growth of Kazan Federal University.

The *Fermi* LAT Collaboration acknowledges generous ongoing support from a number of agencies and institutes that have supported both the development and the operation of the LAT as well as scientific data analysis. These include the National Aeronautics and Space Administration and the Department of Energy in the United States, the Commissariat à l’Energie Atomique and the Centre National de la Recherche Scientifique / Institut National de Physique Nucléaire et de Physique des Particules in France, the Agenzia Spaziale Italiana and the Istituto Nazionale di Fisica Nucleare in Italy, the Ministry of Education, Culture, Sports, Science and Technology (MEXT), High Energy Accelerator Research Organization (KEK) and Japan Aerospace Exploration Agency (JAXA) in Japan, and the K. A. Wallenberg Foundation, the Swedish Research Council and the Swedish National Space Board in Sweden. Additional support for science analysis during the operations phase is gratefully acknowledged from the Istituto Nazionale di Astrofisica in Italy and the Centre National d’Études Spatiales in France. This work performed in part under DOE Contract DE-AC02-76SF00515.

The OVRO 40-m monitoring program is supported in part by NASA grants NNX08AW31G, NNX11A043G, and NNX14AQ89G, and NSF grants AST-0808050 and AST-1109911. We thank the *Swift* team for making these observations possible, the duty scientists, and science planners. This research has made use of the NASA/IPAC Extragalactic Database (NED) which is operated by the Jet Propulsion Laboratory, California Institute of Technology, under contract with the National Aeronautics and Space Administration. FD thanks S. Covino for his help with the REM data reduction. This research has made use of data obtained from the high-energy Astrophysics Science Archive Research Center (HEASARC) provided by NASA’s Goddard Space Flight Center.

We regret to mention that K. Kuratov passed away while this paper was under review.

REFERENCES

Abdo A. A. et al., 2011, *ApJ*, 733, L26
 Acero F. et al., 2016, *ApJS*, 223, 26
 Ade P. A. R. et al., 2016, *A&A*, 594, 63
 Agudo I. et al., 2007, *A&A*, 476, L17
 Agudo I., Marscher A. P., Jorstad S. G., Gómez J. L., Perucho M., Piner B. G., Rioja M., Dodson R., 2012, *ApJ*, 747, 63
 Aleksic J. et al., 2015, *A&A*, 578A, 22
 Aleksic J. et al., 2017, *A&A*, 603A, 29
 Atwood W. B. et al., 2009, *ApJ*, 697, 1071
 Atwood W. B. et al., 2013, in Brandt T. J., Omodei N., Wilson-Hodge C., eds, 2012 Fermi Symposium proceedings - eConf C121028, 4th International Fermi Symposium. Monterey, USA
 Baars J. W. M., Genzel R., Pauliny-Toth I. I. K., Witzel A., 1977, *A&A*, 61, 99
 Barthelmy S. D. et al., 2005, *Space Sci. Rev.*, 120, 143
 Blandford R. D., Rees M. J., 1978, in Wolfe A. M., ed., Pittsburgh Conference on BL Lac Objects. University Pittsburgh Press, Pennsylvania, p. 328
 Blom J. J. et al., 1995, *A&A*, 295, 330
 Böttcher M., Reimer A., Sweeney K., Prakash A., 2013, *ApJ*, 768, 54
 Breeveld A. A. et al., 2010, *MNRAS*, 406, 1687
 Britzen S., Fendt C., Eckart A., Karas V., 2017, *A&A*, 601, A52
 Britzen S. et al., 2018, *MNRAS*, 478, 3199
 Bulgarelli A. et al., 2016, *Astron. Telegram*, 9911, 1

Burrows D. N. et al., 2005, *Space Sci. Rev.*, 120, 165
 Calciolone P., Raiteri C. M., Villata M., Carnerero M. I., Acosta-Pulido J. A., GASP-WEBT Collaboration 2016, *Astron. Telegram*, 9868, 1
 Carnerero M. I. et al., 2017, *MNRAS*, 450, 2677
 Casadio C. et al., 2015, *ApJ*, 813, 51
 Casadio C. et al., 2019, *A&A*, 622, A158
 Chatterjee R. et al., 2013, *ApJ*, 763, L11
 Ciprini S., 2016, *Astron. Telegram*, 9869, 1
 Covino S. et al., 2004, in Moorwood A. F. M., Iye M., eds, *Proc. SPIE Conf. Ser.* Vol. 5492, *Ground-based Instrumentation for Astronomy*. SPIE, Bellingham, p. 1613
 D’Ammando F. et al., 2011, *A&A*, 529A, 145
 D’Ammando F. et al., 2013, *MNRAS*, 431, 2481
 Edelson R. A., Krolik J. H., 1988, *ApJ*, 333, 646
 Fossati G. et al., 2008, *ApJ*, 677, 906
 Fromm C. M., Ros E., Perucho M., Savolainen T., Mimica P., Kadler M., Lobanov A. P., Zensus J. A., 2013, *A&A*, 557, A105
 Fuhrmann L. et al., 2014, *MNRAS*, 441, 1899
 Gasparyan S., Sahakyan N., Baghmanyan V., Zargaryan D., 2018, *ApJ*, 863, 114
 Gehrels N. et al., 2004, *ApJ*, 611, 1005
 Ghisellini G., Tavecchio F., Foschini L., Ghirlanda G., 2011, *MNRAS*, 414, 2674
 Godfrey L. E. H., Shabala S. S., 2013, *ApJ*, 767, 12
 Hartman R. C. et al., 1999, *ApJS*, 123, 79
 Hayashida M. et al., 2012, *ApJ*, 754, 114
 Hayashida M. et al., 2015, *ApJ*, 807, 79
 Hufnagel B. R., Bregman J. N., 1992, *ApJ*, 386, 473
 Kalberla P. M. W., Burton W. B., Hartmann D., Arnal E. M., Bajaja E., Morras R., Pöppel W. G. L., 2005, *A&A*, 440, 775
 Katajainen S. et al., 2000, *A&AS*, 143, 357
 Krawczynski H. et al., 2004, *ApJ*, 601, 151
 Larionov V. M. et al., 2016, *MNRAS*, 461, 3047
 Larionov V. M. et al., 2017, *Galaxies*, 5, 91
 Liska M., Hesp C., Tchekhovskoy A., Ingram A., van der Klis M., Markoff S., 2018, *MNRAS*, 474, L81
 Marscher A. P., 2014, *ApJ*, 780, 87
 Mattox J. R. et al., 1996, *ApJ*, 461, 396
 Merloni A., Heinz S., 2007, *MNRAS*, 381, 589
 Meyer M., Scargle J. D., Blandford R. D., 2019, *ApJ*, 877, 39
 Mignone A., Rossi P., Bodo G., Ferrari A., Massaglia S., 2010, *MNRAS*, 402, 7
 Miller-Jones J. C. A. et al., 2019, *Nature*, 569, 374
 Mingaliyev M. G., Stolyarov V. A., Davies R. D., Melhuish S. J., Bursov N. A., Zhekanis G. V., 2001, *A&A*, 370, 78
 Moretti A. et al., 2005, in Siegmund O. H. W., ed., *Proc. SPIE Conf. Ser.* Vol. 5898, UV, X-Ray, and Gamma-Ray Space Instrumentation for Astronomy XIV. SPIE, Bellingham, p. 360
 Nakamura M., Uchida Y., Hirose S., 2001, *New Astron.*, 6, 61
 Narayan R., Piran T., 2012, *MNRAS*, 420, 604
 Oh K. et al., 2018, *ApJS*, 235, 4
 Ojha R., Carpenter B., D’Ammando F., 2016, *Astron. Telegram*, 9924, 1
 Orienti M., D’Ammando F., Giroletti M., Dallacasa D., Giovannini G., Ciprini S., 2019, *MNRAS*, in press ([arXiv:1910.08568](https://arxiv.org/abs/1910.08568))
 Osterman Meyer A., Miller H. R., Marshall K., Ryle W. T., Aller H., Aller M., Balonek T., 2009, *AJ*, 138, 1902
 Perucho M., Martí-Vidal I., Lobanov A. P., Hardee P. E., 2012, *A&A*, 545, A65
 Peterson B. M., Wanders I., Horne K., Collier S., Alexander T., Kaspi S., Maoz D., 1998, *PASP*, 110, 660
 Petropoulou M., Giannios D., Sironi L., 2016, *MNRAS*, 462, 3325
 Pica A. J., Smith A. G., Webb J. R., Leacock R. J., Clements S., Gombola P. P., 1988, *AJ*, 96, 1215
 Poole T. S. et al., 2008, *MNRAS*, 383, 627
 Pushkarev A. B., Kovalev Y. Y., Lister M. L., 2010, *ApJ*, 722, L7
 Raiteri C. M. et al., 2003, *A&A*, 402, 151
 Raiteri C. M. et al., 2010, *A&A*, 524, A43
 Raiteri C. M. et al., 2011, *A&A*, 534, A87

Raiteri C. M. et al., 2012, *A&A*, 545, A48
 Raiteri C. M. et al., 2013, *MNRAS*, 436, 1530
 Raiteri C. M. et al., 2014, *MNRAS*, 442, 629
 Raiteri C. M. et al., 2017, *Nature*, 552, 374
 Readhead A. C. S., Lawrence C. R., Myers S. T., Sargent W. L. W., Hardebeck H. E., Moffet A. T., 1989, *ApJ*, 346, 566
 Richards J. L. et al., 2011, *ApJS*, 194, 29
 Righini S., Giroletti M., D'Ammando F., Raiteri C., Villata M., Bach U., 2016, *Astron. Telegram*, 9884, 1
 Roming P. W. A. et al., 2005, *Space Sci. Rev.*, 120, 95
 Schmidt M., 1965, *ApJ*, 141, 1295
 Shukla A. et al., 2018, *ApJ*, 854, L26
 Stickel M., Padovani P., Urry C. M., Fried J. W., Kuehr H., 1991, *ApJ*, 374, 431
 Villata M. et al., 1997, *A&AS*, 121, 119
 Wehrle A. E. et al., 1998, *ApJ*, 497, 178
 Wilms J., Allen A., McCray R., 2000, *ApJ*, 542, 914
 Xu Z.-L. et al., 2016, *Astron. Telegram*, 9901, 1

Zacharias M., Böttcher M., Jankowsky F., Lenain J.-P., Wagner S. J., Wierzholska A., 2017, *ApJ*, 851, 72
 Zacharias M., Böttcher M., Jankowsky F., Lenain J.-P., Wagner S. J., Wierzholska A., 2019, *ApJ*, 871, 19
 Zdziarski A. A., Böttcher M., 2015, *MNRAS*, 450, L21
 Zerbi R. M. et al., 2001, *Astron. Nachr.*, 322, 275

SUPPORTING INFORMATION

Supplementary data are available at [MNRAS](https://www.mra-s.org) online.

ms_edits.pdf

Please note: Oxford University Press is not responsible for the content or functionality of any supporting materials supplied by the authors. Any queries (other than missing material) should be directed to the corresponding author for the article.

APPENDIX A: SWIFT-XRT RESULTS

Table A1. Log and fitting results of *Swift*-XRT observations of CTA 102 using a PL model with N_{H} fixed to Galactic absorption. Fluxes are corrected for the Galactic absorption. Full table available online.

Date (UT)	MJD	Net exposure time (s)	Flux 0.3–10 keV ($\times 10^{-13}$ erg cm $^{-2}$ s $^{-1}$)	Photon index (Γ_{X})
2013 May 24	56436	1041	8.2 ± 1.4	1.42 ± 0.20
2013 June 20	56463	3019	11.2 ± 1.2	1.39 ± 0.12
2013 June 23	56466	2974	8.3 ± 1.1	1.36 ± 0.18
2014 Oct 28	56958	4942	10.3 ± 0.7	1.38 ± 0.08
2014 Oct 30	56960	4942	9.9 ± 0.7	1.36 ± 0.09
2015 Dec 06	57362	1940	12.7 ± 1.4	1.46 ± 0.14
2015 Dec 08	57364	1793	9.0 ± 1.2	1.45 ± 0.16
2015 Dec 09	57365	1970	11.4 ± 1.3	1.39 ± 0.15
2015 Dec 12	57368	1616	12.2 ± 2.0	1.14 ± 0.20
2015 Dec 14	57370	1603	9.3 ± 1.6	1.31 ± 0.21

APPENDIX B: SWIFT-UVOT RESULTS

Table B1. Observed magnitude of CTA 102 obtained by *Swift*-UVOT. Full table available online.

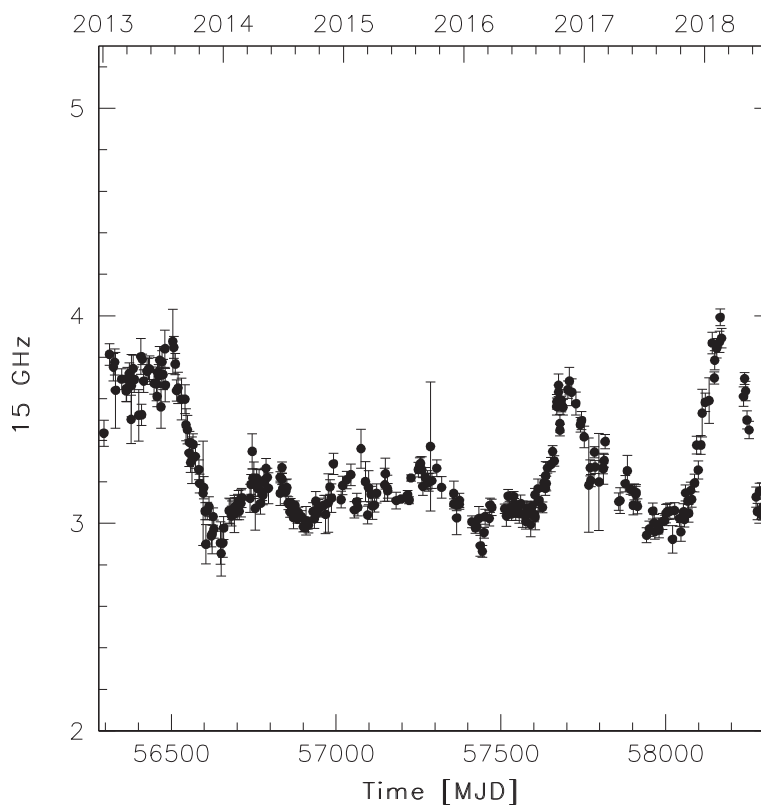
Date (UT)	MJD	<i>v</i>	<i>b</i>	<i>u</i>	<i>w1</i>	<i>m2</i>	<i>w2</i>
2013 May 24	56436	16.86 ± 0.12	17.18 ± 0.09	16.17 ± 0.07	16.04 ± 0.08	16.09 ± 0.06	16.28 ± 0.07
2013 June 20	56463	–	–	–	16.03 ± 0.06	–	16.06 ± 0.06
2013 June 23	56466	–	–	–	–	16.06 ± 0.06	–
2014 Oct 28	56958	16.77 ± 0.11	17.11 ± 0.09	16.27 ± 0.08	16.18 ± 0.09	16.17 ± 0.06	16.46 ± 0.08
2014 Oct 30	56960	16.55 ± 0.08	17.01 ± 0.07	16.03 ± 0.06	16.02 ± 0.07	15.99 ± 0.08	16.29 ± 0.07
2015 Dec 06	57362	15.82 ± 0.08	16.46 ± 0.08	15.49 ± 0.07	15.45 ± 0.08	15.61 ± 0.09	15.81 ± 0.09
2015 Dec 08	57364	16.49 ± 0.11	16.83 ± 0.09	15.90 ± 0.08	15.73 ± 0.09	15.71 ± 0.09	16.07 ± 0.08
2015 Dec 09	57365	16.61 ± 0.14	16.99 ± 0.11	15.94 ± 0.09	15.80 ± 0.10	15.98 ± 0.11	16.13 ± 0.09
2015 Dec 12	57368	16.78 ± 0.13	17.04 ± 0.10	15.95 ± 0.08	15.93 ± 0.09	15.91 ± 0.10	16.11 ± 0.08
2015 Dec 14	57370	16.57 ± 0.09	17.24 ± 0.08	16.17 ± 0.07	15.89 ± 0.07	16.05 ± 0.09	16.15 ± 0.07

APPENDIX C: REM RESULTS

Table C1. Log and fitting results of REM observations of CTA 102 in *J*, *H*, and *K* bands.

Date (UT)	MJD	<i>J</i> (mag)	<i>H</i> (mag)	<i>K</i> (mag)
2016-11-15	57707	–	11.062 ± 0.038	10.251 ± 0.206
2016-11-16	57708	11.889 ± 0.036	11.089 ± 0.042	10.209 ± 0.071
2016-11-17	57709	11.762 ± 0.040	–	–
2016-11-18	57710	–	11.181 ± 0.038	–
2016-11-20	57712	11.559 ± 0.020	10.776 ± 0.032	10.017 ± 0.090
2016-11-21	57713	11.635 ± 0.018	10.791 ± 0.035	10.032 ± 0.156
2016-11-23	57715	11.167 ± 0.036	10.394 ± 0.035	–
2016-11-25	57717	11.498 ± 0.037	10.671 ± 0.059	9.938 ± 0.151
2016-11-27	57719	11.672 ± 0.034	10.863 ± 0.028	10.051 ± 0.119
2016-11-29	57721	11.042 ± 0.045	10.293 ± 0.072	–
2016-12-02	57724	10.510 ± 0.034	9.727 ± 0.044	8.903 ± 0.265
2016-12-04	57726	10.573 ± 0.033	9.808 ± 0.054	–
2016-12-06	57728	10.811 ± 0.057	10.040 ± 0.065	–
2016-12-11	57733	11.193 ± 0.056	10.345 ± 0.048	–

APPENDIX D: EXTENDED OVRO LIGHT CURVE


Figure D1. OVRO light curve of CTA 102 at 15 GHz between 2013 January 1 (MJD 56293) and 2018 July 21 (MJD 58320).

- ¹INAF - Istituto di Radioastronomia, Via Gobetti 101, I-40129 Bologna, Italy
- ²INAF - Osservatorio Astrofisico di Torino, Via P. Torinese, I- Torino, Italy
- ³Instituto de Astrofísica de Canarias (IAC), La Laguna, E-38200 Tenerife, Spain
- ⁴Departamento de Astrofísica, Universidad de La Laguna, La Laguna, E-38205 Tenerife, Spain
- ⁵Instituto de Astrofísica de Andalucía (CSIC), E-18080 Granada, Spain
- ⁶Pulkovo Observatory, 196140 St. Petersburg, Russia
- ⁷Institute of Astronomy and NAO, Bulgarian Academy of Sciences, 1784 Sofia, Bulgaria
- ⁸Crimean Astrophysical Observatory RAS, P/O Nauchny 298409, Russia
- ⁹Instituto de Astronomía, Universidad Nacional Autónoma de México, México
- ¹⁰INAF, TNG Fundación Galileo Galilei, E-38712 La Palma, Spain
- ¹¹Faculty of Physics, Department of Astronomy, University of Sofia, BG-1164 Sofia, Bulgaria
- ¹²Osservatorio Astronomico della Regione Autonoma Valle d'Aosta, I-11020 Nus, Italy
- ¹³EPT Observatories, Tijarafe, E-38780 La Palma, Spain
- ¹⁴Max-Planck-Institut für Radioastronomie, D-53121 Bonn, Germany
- ¹⁵School of Physics and Astronomy, University of Southampton, Southampton SO17 1BJ, UK
- ¹⁶Graduate Institute of Astronomy, National Central University, Jhongli City, Taoyuan County 32001, Taiwan
- ¹⁷Astronomical Observatory, 11060 Belgrade, Serbia
- ¹⁸INAF, Osservatorio Astronomico di Roma, I-00040 Monte Porzio Catone, Italy
- ¹⁹Ulugh Beg Astronomical Institute, Maidanak Observatory, Tashkent 100052, Uzbekistan
- ²⁰Astronomical Institute, St. Petersburg State University, 198504 St. Petersburg, Russia
- ²¹Harvard-Smithsonian Center for Astrophysics, 60 Garden Street, Cambridge, MA 02138 USA
- ²²Astrophysics Research Institute, Liverpool John Moores University, Liverpool L3 5RF, UK
- ²³School of Cosmic Physics, Dublin Institute For Advanced Studies, Ireland
- ²⁴Institute for Astrophysical Research, Boston University, Boston, MA 02215, USA
- ²⁵Abastumani Observatory, Mt. Kanobili, 0301 Abastumani, Georgia
- ²⁶NNLOT, Al-Farabi Kazakh National University, 050040 Almaty, Kazakhstan
- ²⁷Fesenkov Astrophysical Institute, Almaty, Kazakhstan
- ²⁸Engelhardt Astronomical Observatory, Kazan Federal University, 422526 Tatarstan, Russia
- ²⁹Landessternwarte, Zentrum für Astronomie der Universität Heidelberg, D-69117 Heidelberg, Germany
- ³⁰Center for Astrophysics, Guangzhou University, Guangzhou 510006, China
- ³¹Aalto University Metsähovi Radio Observatory, FI-02540 Kylmälä, Finland
- ³²Aalto University Dept of Electronics and Nanoengineering, FI-00076 Aalto, Finland
- ³³Astronomical Institute, Osaka Kyoiku University, Osaka 582-8582, Japan
- ³⁴UCD School of Physics, University College Dublin, Dublin 4, Ireland
- ³⁵Department of Physics and Astronomy, Brigham Young University, Provo, UT 84602, USA
- ³⁶Michael Adrian Observatorium, Astronomie Stiftung Trebur, D-65468 Trebur, Germany
- ³⁷University of Applied Sciences, Technische Hochschule Mittelhessen, D-61169 Friedberg, Germany
- ³⁸Command Module Observatory, Tempe AZ, USA
- ³⁹Nordic Optical Telescope, E-38700 Santa Cruz de La Palma, Santa Cruz de Tenerife, Spain
- ⁴⁰Osservatorio Astronomico Sirio, I-70013 Castellana Grotte, Italy
- ⁴¹LESIA, Observatoire de Paris, Université PSL, CNRS, Sorbonne Université, Univ. Paris Diderot, Sorbonne Paris Cité, 5 place Jules Janssen, F-92195 Meudon, France
- ⁴²Department of Physics, University of Colorado, Denver, CO 80217-3364, USA
- ⁴³Lowell Observatory, Flagstaff, AZ 85751, USA
- ⁴⁴Steward Observatory, University of Arizona, Tucson, AZ 85721, USA
- ⁴⁵Instituto de Radio Astronomía Milimétrica, E-18012 Granada, Spain
- ⁴⁶Finnish Center for Astronomy with ESO (FINCA), University of Turku, FI-20014 Turku, Finland
- ⁴⁷Aalto University Metsähovi Radio Observatory, Metshovintie 114, FI-02540 Kylmälä, Finland
- ⁴⁸Owens Valley Radio Observatory, California Institute of Technology, Pasadena, CA 91125, USA
- ⁴⁹Departamento de Astronomía, Universidad de Chile, Camino El Observatorio 1515, Las Condes, Santiago, Chile
- ⁵⁰Departamento de Astronomía, Universidad de Concepción, Concepción, Chile
- ⁵¹Shanghai Astronomical Observatory, Chinese Academy of Sciences, Shanghai 200030, China
- ⁵²Kazan Federal University, 18 Kremlyovskaya St, Kazan 420044, Russia
- ⁵³Special Astrophysical Observatory of RAS, Nizhniy Arkhyz 369167, Russia

This paper has been typeset from a $\text{\TeX}/\text{\LaTeX}$ file prepared by the author.



GROWTH on S190425z: Searching Thousands of Square Degrees to Identify an Optical or Infrared Counterpart to a Binary Neutron Star Merger with the Zwicky Transient Facility and Palomar Gattini-IR

Michael W. Coughlin¹, Tomás Ahumada², Shreya Anand¹, Kishalay De¹, Matthew J. Hankins¹, Mansi M. Kasliwal¹, Leo P. Singer^{3,4}, Eric C. Bellm⁵, Igor Andreoni¹, S. Bradley Cenko^{3,4}, Jeff Cooke^{6,7}, Christopher M. Copperwheat⁸, Alison M. Dugas¹, Jacob E. Jencson¹, Daniel A. Perley⁸, Po-Chieh Yu⁹, Varun Bhalerao¹⁰, Harsh Kumar¹⁰, Joshua S. Bloom^{11,12}, G. C. Anupama¹³, Michael C. B. Ashley¹⁴, Ashot Bagdasaryan¹, Rahul Biswas¹⁵, David A. H. Buckley^{16,17}, Kevin B. Burdge¹, David O. Cook¹⁸, John Cromer¹⁹, Virginia Cunningham², Antonino D’Ai²⁰, Richard G. Dekany¹⁹, Alexandre Delacroix¹⁹, Simone Dichiara^{2,3}, Dmitry A. Duev¹, Anirban Dutta¹³, Michael Feeney¹⁹, Sara Frederick², Pradip Gatkine², Shaon Ghosh²¹, Daniel A. Goldstein¹, V. Zach Golkhou^{5,22,40}, Ariel Goobar¹⁵, Matthew J. Graham¹, Hidekazu Hanayama²³, Takashi Horiuchi²³, Tiara Hung²⁴, Saurabh W. Jha^{25,26}, Albert K. H. Kong²⁷, Matteo Giomì²⁸, David L. Kaplan²¹, V. R. Karambelkar¹⁰, Marek Kowalski^{29,30}, Shrinivas R. Kulkarni¹, Thomas Kupfer³¹, Frank J. Masci¹⁸, Paolo Mazzali⁸, Anna M. Moore³², Moses Mogotsi^{16,17}, James D. Neill¹, Chow-Choong Ngeow⁹, Jorge Martínez-Palomera³³, Valentina La Parola²⁰, M. Pavana¹³, Eran O. Ofek³⁴, Atharva Sunil Patil⁹, Reed Riddle¹⁹, Mickael Rigault³⁵, Ben Rusholme¹⁸, Eugene Serabyn³⁶, David L. Shupe¹⁸, Yashvi Sharma¹⁰, Avinash Singh¹³, Jesper Sollerman³⁷, Jamie Soon³², Kai Staats³⁸, Kirsty Taggart⁸, Hanjie Tan⁹, Tony Trvouillon³², Eleonora Troja^{2,3}, Gaurav Waratkar¹⁰, and Yoichi Yatsu³⁹

¹ Division of Physics, Mathematics, and Astronomy, California Institute of Technology, Pasadena, CA 91125, USA

² Department of Astronomy, University of Maryland, College Park, MD 20742, USA

³ Astrophysics Science Division, NASA Goddard Space Flight Center, MC 661, Greenbelt, MD 20771, USA

⁴ Joint Space-Science Institute, University of Maryland, College Park, MD 20742, USA

⁵ DIRAC Institute, Department of Astronomy, University of Washington, 3910 15th Avenue NE, Seattle, WA 98195, USA

⁶ Australian Research Council Centre of Excellence for Gravitational Wave Discovery (OzGrav), Swinburne University of Technology, Hawthorn, VIC, 3122, Australia

⁷ Centre for Astrophysics and Supercomputing, Swinburne University of Technology, Hawthorn, VIC, 3122, Australia

⁸ Astrophysics Research Institute, Liverpool John Moores University, IC2, Liverpool Science Park, 146 Brownlow Hill, Liverpool L3 5RF, UK

⁹ Graduate Institute of Astronomy, National Central University, 32001, Taiwan

¹⁰ Indian Institute of Technology Bombay, Powai, Mumbai 400076, India

¹¹ Department of Astronomy, University of California, Berkeley, CA 94720-3411, USA

¹² Physics, Lawrence Berkeley National Laboratory, 1 Cyclotron Road, MS 50B-4206, Berkeley, CA 94720, USA

¹³ Indian Institute of Astrophysics, II Block Koramangala, Bengaluru 560034, India

¹⁴ School of Physics, University of New South Wales, Sydney NSW 2052, Australia

¹⁵ The Oskar Klein Centre, Department of Physics, Stockholm University, AlbaNova, SE-106 91 Stockholm, Sweden

¹⁶ South African Astronomical Observatory, P.O. Box 9, Observatory 7935, Cape Town, South Africa

¹⁷ Southern African Large Telescope Foundation, P.O. Box 9, Observatory 7935, Cape Town, South Africa

¹⁸ IPAC, California Institute of Technology, 1200 E. California Blvd, Pasadena, CA 91125, USA

¹⁹ Caltech Optical Observatories, California Institute of Technology, Pasadena, CA 91125, USA

²⁰ INAF/IASF-Palermo, via Ugo La Malfa 153, I-90146, Palermo, Italy

²¹ Center for Gravitation, Cosmology and Astrophysics, Department of Physics, University of Wisconsin–Milwaukee, P.O. Box 413, Milwaukee, WI 53201, USA

²² The eScience Institute, University of Washington, Seattle, WA 98195, USA

²³ Ishigakijima Astronomical Observatory, National Astronomical Observatory of Japan, 1024-1 Arakawa, Ishigaki, Okinawa 907-0024, Japan

²⁴ Department of Astronomy and Astrophysics, University of California, Santa Cruz, CA 95064, USA

²⁵ Department of Physics and Astronomy, Rutgers, the State University of New Jersey, 136 Frelinghuysen Road, Piscataway, NJ 08854, USA

²⁶ Center for Computational Astrophysics, Flatiron Institute, 162 5th Avenue, New York, NY 10010, USA

²⁷ Institute of Astronomy, National Tsing Hua University, Hsinchu 30013, Taiwan

²⁸ Humboldt Universität zu Berlin, Newtonstraße 15, D-12489 Berlin, Germany

²⁹ Institute of Physics, Humboldt-Universität zu Berlin, Newtonstr. 15, D-124 89 Berlin, Germany

³⁰ Deutsches Elektronensynchrotron, Platanenallee 6, D-15738, Zeuthen, Germany

³¹ Kavli Institute for Theoretical Physics, University of California, Santa Barbara, CA 93106, USA

³² Research School of Astronomy and Astrophysics, Australian National University, Canberra, ACT 2611, Australia

³³ Department of Astronomy, University of California, Berkeley, CA 94720-3411, USA

³⁴ Department of Particle Physics & Astrophysics, Weizmann Institute of Science, Rehovot 76100, Israel

³⁵ Université Clermont Auvergne, CNRS/IN2P3, Laboratoire de Physique de Clermont, F-63000 Clermont-Ferrand, France

³⁶ Jet Propulsion Laboratory, California Institute of Technology, Pasadena, CA 91109, USA

³⁷ The Oskar Klein Centre & Department of Astronomy, Stockholm University, AlbaNova, SE-106 91 Stockholm, Sweden

³⁸ Center for Interdisciplinary Exploration and Research in Astrophysics and Department of Physics and Astronomy, Northwestern University, 2145 Sheridan Road, Evanston, IL 60208, USA

³⁹ Department of Physics, Tokyo Institute of Technology, 2-12-1, Ookayama, Meguro, Tokyo 152-8551, Japan

Received 2019 July 29; revised 2019 September 24; accepted 2019 October 4; published 2019 October 30

⁴⁰ Moore-Sloan, WRF, and DIRAC Fellow.

Abstract

The third observing run by LVC has brought the discovery of many compact binary coalescences. Following the detection of the first binary neutron star merger in this run (LIGO/Virgo S190425z), we performed a dedicated follow-up campaign with the Zwicky Transient Facility (ZTF) and Palomar Gattini-IR telescopes. The initial skymap of this single-detector gravitational wave (GW) trigger spanned most of the sky observable from Palomar Observatory. Covering 8000 deg² of the initial skymap over the next two nights, corresponding to 46% integrated probability, ZTF system achieved a depth of $\approx 21 m_{AB}$ in *g*- and *r*-bands. Palomar Gattini-IR covered 2200 square degrees in *J*-band to a depth of 15.5 mag, including 32% integrated probability based on the initial skymap. The revised skymap issued the following day reduced these numbers to 21% for the ZTF and 19% for Palomar Gattini-IR. We narrowed 338,646 ZTF transient “alerts” over the first two nights of observations to 15 candidate counterparts. Two candidates, ZTF19aarykbb and ZTF19aarzaod, were particularly compelling given that their location, distance, and age were consistent with the GW event, and their early optical light curves were photometrically consistent with that of kilonovae. These two candidates were spectroscopically classified as young core-collapse supernovae. The remaining candidates were ruled out as supernovae. Palomar Gattini-IR did not identify any viable candidates with multiple detections only after merger time. We demonstrate that even with single-detector GW events localized to thousands of square degrees, systematic kilonova discovery is feasible.

Unified Astronomy Thesaurus concepts: [Gravitational wave astronomy \(675\)](#); [Transient detection \(1957\)](#); [Optical telescopes \(1174\)](#)

1. Introduction

The third observing run (O3) by the network of gravitational-wave (GW) detectors with Advanced LIGO (Aasi et al. 2015) and Advanced Virgo (Acernese et al. 2015) began in 2019 April. This detector network has already observed over a score binary black holes thus far (LIGO Scientific Collaboration & Virgo Collaboration 2019a, 2019b, 2019c, 2019d, 2019e, 2019f). The current discovery rate builds on the success of the first few observing runs, which yielded 10 binary black hole detections (Abbott et al. 2019).

In addition, the coincident discovery of the binary neutron star (BNS) merger GW170817 (Abbott et al. 2017a), a short gamma-ray burst (SGRB) GRB170817A (Abbott et al. 2017b; Goldstein et al. 2017; Savchenko et al. 2017), with an afterglow (Alexander et al. 2017; Haggard et al. 2017; Hallinan et al. 2017; Margutti et al. 2017; Troja et al. 2017) and “kilonova” (KN) counterpart, AT2017gfo (Chornock et al. 2017; Coulter et al. 2017; Cowperthwaite et al. 2017; Drout et al. 2017; Evans et al. 2017; Kasliwal et al. 2017; Kilpatrick et al. 2017; Lipunov et al. 2017; McCully et al. 2017; Nicholl et al. 2017; Pian et al. 2017; Shappee et al. 2017; Smartt et al. 2017; Utsumi et al. 2017), initiated a new era of multi-messenger astronomy. Among many other science cases, measurements of the equation of state of neutron stars (Bauswein et al. 2013, 2017; Abbott et al. 2017a; Radice et al. 2018; Coughlin et al. 2019f), the formation of heavy elements (Just et al. 2015; Wu et al. 2016; Abbott et al. 2017c; Roberts et al. 2017; Rosswog et al. 2017; Kasliwal et al. 2019a), and the expansion rate of the universe (Abbott et al. 2017d; Hotokezaka et al. 2018; Coughlin et al. 2019e) are all important results of the first BNS detection.

Following the success of GW170817, the Zwicky Transient Facility (ZTF; Bellm et al. 2018; Masci et al. 2018; Dekany et al. 2019; Graham et al. 2019) on the Palomar 48 inch telescope, and Palomar Gattini-IR, a new wide-field near-infrared survey telescope at Palomar observatory, have been observing both SGRBs from the *Fermi* Gamma-ray Burst Monitor (Ahumada et al. 2018; Coughlin et al. 2018b, 2018c, 2018d, 2018e, 2019a; Cenko et al. 2018) and GW events from LIGO. In addition to finding the “afterglow” associated with a

highly relativistic jet powered by an SGRB (Wijers et al. 1997; Mészáros & Rees 1998; Ascenzi et al. 2019), our goal has been to identify a KN, the ultraviolet/optical/near-infrared (near-IR) emission generated by the radioactive decay of *r*-process elements (Lattimer & Schramm 1974; Li & Paczynski 1998; Metzger et al. 2010; Roberts et al. 2011; Rosswog 2015; Kasen et al. 2017). The ZTF and Palomar Gattini-IR surveys are our discovery engines, and the Global Relay of Observatories Watching Transients Happen (GROWTH) network⁴¹ is our follow-up network. GROWTH uses a variety of facilities worldwide across various wavelengths to perform rapid follow-up and classification of objects.

There are many survey systems participating in the searches for GW counterparts. Among many others, the Dark Energy Camera (DECam; Flaugher et al. 2015), the Gravitational-wave Optical Transient Observer (GOTO; O’Brien 2018), the Panoramic Survey Telescope and Rapid Response System (Pan-STARRS; Kaiser et al. 2010; Chambers et al. 2016), the All-Sky Automated Survey for Supernovae (ASASSN; Shappee et al. 2014) and Asteroid Terrestrial-impact Last Alert System (ATLAS; Tonry et al. 2018) all have performed observations of events during the third observing run. ZTF provides a competitive addition to these systems, given its depth ($m_{AB} \sim 20.6$ in 30 s), wide field of view (FOV ≈ 47 deg² per exposure), and average cadence of ~ 3 days over the entire accessible sky. In particular, the cadence is important for establishing candidate history when performing target of opportunity (ToO) observations. The SGRB program, that has covered localization regions spanning thousands of square degrees (Coughlin et al. 2019a), demonstrated that ZTF is capable of detecting GW170817-like sources out to the Advanced LIGO/Virgo detection horizon at about (~ 200 Mpc; Abbott et al. 2018). In addition, Palomar Gattini-IR (K. De et al. 2019, in preparation; Moore & Kasliwal 2019) is covering the entire visible northern sky every two nights to a *J*-band depth of ≈ 15.5 –16 AB mag. With its 25 deg² FOV and near-IR sensitivity, Palomar Gattini-IR provides a complementary system for objects that are expected to be as red as KNe

⁴¹ <http://growth.caltech.edu/>

Table 1
Telescope Specifications, Including Name, FOV, Pixel Scale, Telescope Aperture, and Available Filters

Name	FOV	Pixel Scale	Aperture	Filters
ZTF	47 deg ²	1''0	48 in	<i>g, r, i</i>
Palomar Gattini-IR	25 deg ²	8''7	30 cm	<i>J</i>
GROWTH-India	0.5 deg ²	0''67	70 cm	<i>u, g, r, i, z</i>
LOT	13'2 × 13'2	0''39	1 m	<i>g, r, i</i>
KPED	4'4 × 4'4	0''26	2.1 m	<i>g, r, U, B, V, I</i>

(Metzger 2017), albeit at lower sensitivity (a source as bright as GW170817 would be detected at ~ 20 Mpc).

The first BNS detection of O3, LIGO/Virgo S190425z, was a single-detector event discovered by the Advanced LIGO-Livingston detector, with Virgo also observing at the time (LIGO Scientific Collaboration & Virgo Collaboration 2019f). Occurring at 2019 April 25 08:18:05 UTC, the estimated false alarm rate was 1 in 70,000 yr, with a high likelihood of being a BNS. The first reported BAYESTAR skymap provided an extremely coarse localization, resulting from the low signal-to-noise ratio in Advanced Virgo; it spanned $\sim 10,000$ deg², which is nearly a “pi of the sky.” The updated LALInference skymap (LIGO Scientific Collaboration & Virgo Collaboration 2019g), released at 2019 April 26 15:32:37 UTC, reduced the localization region requiring coverage by $\approx 25\%$ to ~ 7500 deg². The all-sky averaged distance to the source is 156 ± 41 Mpc.

In this Letter, we describe an ~ 8000 square degree search for the KN counterpart to a single-detector GW event. Our campaign emphasizes the key role played by both large FOV telescopes like ZTF and Palomar Gattini-IR, as well as the associated follow-up systems. We demonstrate that our strategy for tiling the sky, vetting candidates, and pursuing follow-up is robust, and capable of promptly reducing 338,646 transient alerts from ZTF to a handful of interesting candidates for follow-up. Our Letter is structured as follows. We describe our observing plan in Section 2. The identified candidates, including their follow-up, are detailed in Section 3. We summarize our conclusions and future outlook in Section 4.

2. Observing Plan

Because S190425z came during Palomar night-time (2019 April 25 08:18:05 UTC), it occurred concurrently with ongoing survey observations by both ZTF and Palomar Gattini-IR. Within the 90% localization, approximately 44% of the original BAYESTAR map was observable from Palomar over the whole night, corresponding to ≈ 5000 deg². The GW event was automatically ingested into the GROWTH ToO Marshal, a database that we specifically designed to perform target-of-opportunity follow-up of events localized to large sky-error regions, including GW, neutrino, and gamma-ray burst events (Coughlin et al. 2019a). Among several other features, the ToO marshal allows us to directly trigger the telescope queue for certain facilities to which GROWTH has access, namely ZTF, Palomar Gattini-IR, DECam, Kitt Peak EMCCD Demonstrator (KPED) on the Kitt Peak 84-inch telescope (Coughlin et al. 2019d), the Lulin One-meter Telescope (LOT) in Taiwan, and the GROWTH-India telescope⁴² (V. Bhalerao et al. 2019, in preparation). We provide a brief description of each instrument in Table 1.

Triggering ToO observations for survey instruments like ZTF and Palomar Gattini-IR halts their ongoing survey observations and redirects them to observe only certain fields as directed by an observation plan. The observation plan generated by the ToO marshal relies on `gwemopt` (Coughlin et al. 2018a, 2019c), a code that optimizes the telescope scheduling process for GW follow-up. `gwemopt` handles both synoptic and galaxy-targeted search strategies; we employed the former to conduct observations with some of our facilities, Palomar Gattini-IR, GROWTH-India and ZTF, and the latter for scheduling observations with KPED. The coverage for both ZTF and Palomar Gattini-IR is shown in Figure 1, and the limiting magnitudes as a function of time in Figure 2.

2.1. ZTF

Serendipitously, after the BNS merger time and before the GW alert was distributed, ZTF had already observed 1920 deg² of the sky in the *r*-band, corresponding to $\sim 19\%$ of the initial BAYESTAR map and $\sim 12\%$ of the LALInference map. This overlap between ongoing survey observations and the LIGO-Livingston-only localization is unsurprising as both of the Advanced LIGO interferometers have maximum sensitivity in the sky overhead in North America (Finn & Chernoff 1993; Kasliwal & Nissanke 2014).

ZTF triggered ToO observations lasting three hours starting at 2019 April 25 09:19:07.161 UT, one hour after the trigger time. On night 1, our observing strategy involved a sequence of *g-r-g* band exposure blocks; each exposure was 30 s, with a typical depth of 20.4 mag, which is the normal duration of exposures during ZTF survey operation. The *g-r-g* sequence is the baseline observing strategy for GW follow-up with ZTF as it is specifically designed to capture the inter- and intra-night color evolution of GW170817-like KNe and to distinguish them from supernovae (Kilpatrick et al. 2017; Shappee et al. 2017). Due to the size of the localization, we obtained a *g-r* sequence, requiring references for each scheduled field. In addition, we required a 30 minutes gap between observations in *g* and *r* to avoid asteroids. Accounting for the loss in probability due to chip gaps and the processing success, ZTF covered 3250 deg², corresponding to about 36% of the initial BAYESTAR and 19% of the LALInference maps on night 1.

Motivated by the increase in available observation time (~ 5 more hours than the first night), we modified our strategy on night 2 by taking longer integrations of 90 s each, corresponding to an average depth of 21.0 mag. We obtained one epoch in each of *g*- and *r*-band, corresponding to about 46% probability in the initial BAYESTAR or 21% of the LALInference maps.

After our observations on both nights were complete, a new LALInference skymap was released at 2019 April 26 14:51:42

⁴² <https://sites.google.com/view/growthindia/>

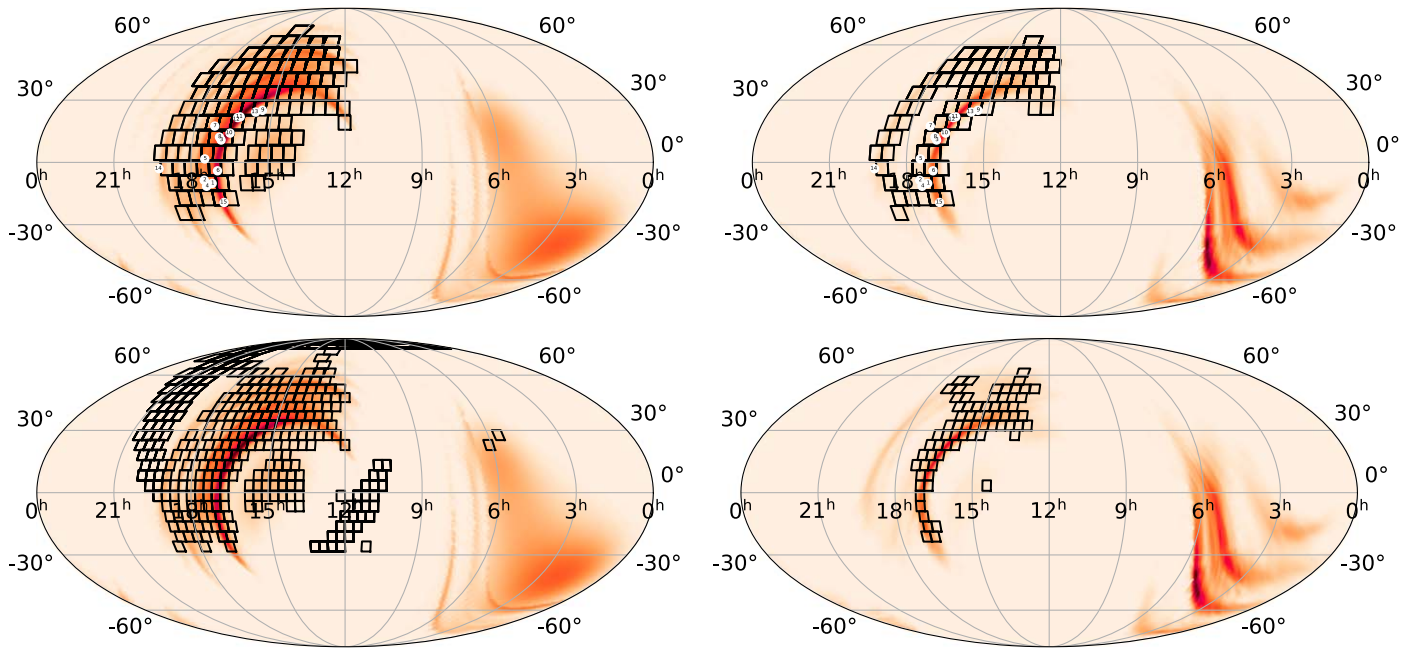


Figure 1. Coverage of S190425z. Left: the top and bottom rows show the $\approx 47 \text{ deg}^2$ ZTF tiles and the $\approx 25 \text{ deg}^2$ Palomar Gattini-IR tiles, respectively, on the 90% probability region of the initial BAYESTAR skymap, along with the identified transients highlighted in Table 3. For the ZTF observations, the numbering scheme is 1: ZTF19aarykkb, 2: ZTF19aarzaod, 3: ZTF19aasckwd, 4: ZTF19aasfogv, 5: ZTF19aasejil, 6: ZTF19aaryxfj, 7: ZTF19aascxux, 8: ZTF19aasdajo, 9: ZTF19aasbamy, 10: ZTF19aasckkq, 11: ZTF19aarycuy, 12: ZTF19aasbphu, 13: ZTF19aasbaui, 14: ZTF19aarxxwb, 15: ZTF19aashlts. Right: tilings of the two telescopes on the final LALInference map. We only include the tiles in the inner 90% probability region for each skymap.

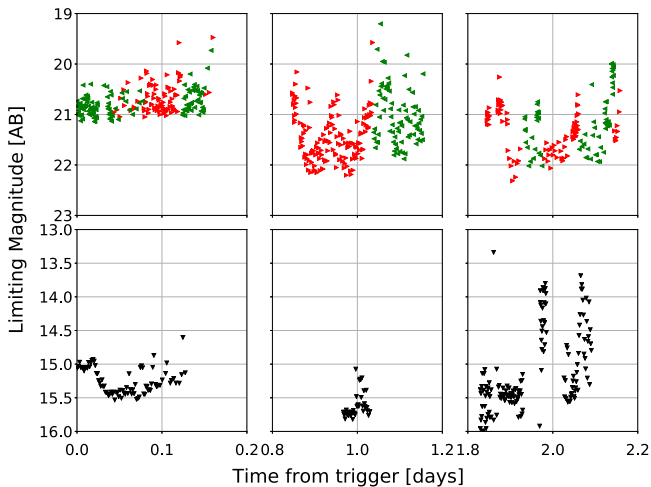


Figure 2. Limiting magnitude as a function of time for S190425z. On the top row is ZTF, while the bottom row is Palomar Gattini-IR, with the left, middle, and right panels corresponding to observations on the first, second, and third nights, respectively. The red and green triangles correspond to the r - and g -band limits from ZTF, while the black triangles correspond to the J -band limits from Palomar Gattini-IR.

UT (LIGO Scientific Collaboration & Virgo Collaboration 2019h). The LALInference runs reduced the skymap to $\sim 7500 \text{ deg}^2$ and shifted more of the probability to two lobes near the Sun and in the Southern hemisphere (see Figure 1). In summary, ZTF covered about 8000 deg^2 within the 99% integrated probability region within its two nights of observations. This corresponds to 46% of the probability in the original BAYESTAR skymap and 21% of the probability in the LALInference skymap. Our observations with ZTF over the two nights covered a 5σ median depth of $m_{AB} = 21.0$ in r -band and $m_{AB} = 20.9$ in g -band.

2.2. Palomar Gattini-IR

Palomar Gattini-IR initiated ToO observations of the localization region at 2019 April 25 09:12:09 UT, 11 minutes after the initial notice time. The synoptic tiling strategy was determined in the same way as for ZTF (Coughlin et al. 2018a). Palomar Gattini-IR imaged a total of 2401 deg^2 of the localization region spread over 227 field tiles, covering 32% of the probability region of the BAYESTAR skymap and 19% for the LALInference localization. Each field visit consisted of a sequence of eight dithered exposures of 8.1 s each, amounting to a total exposure time of 64.8 s per field. This resulted in a median stacked depth of $m_{AB} = 15.5$ in J -band. The real-time data reduction pipeline (K. De et al. 2019, in preparation) reduced the data and identified transient candidates through the application of difference imaging using reference images of the fields.

2.3. Galaxy-targeted Follow-up

In addition to the synoptic surveys for counterparts, a subset of the available systems performed galaxy-targeted follow-up. This strategy was used by a number of teams to observe GW170817 (Arcavi et al. 2017b; Coulter et al. 2017; Valenti et al. 2017). The galaxy-targeted follow-up program relies on the Census of the Local Universe catalog (Cook et al. 2019); it is complete to 85% in star formation and 70% in stellar mass at 200 Mpc. The sky area coverage of galaxies is $\approx 1\%$ within these local volumes (Cook et al. 2019). This makes targeted galaxy pointing tractable for small FOV telescopes (see Arcavi et al. 2017a or Golkhou et al. 2018 for example). Of the galaxies within the volume, our work prioritizes them for follow-up as follows.

The GROWTH ToO Marshal uses an algorithm modified from LCO's galaxy-targeted follow-up of GW events (Arcavi et al. 2017a), which uses a combination of a galaxy's location

in the GW localization region (including the distance), S_{loc} , the galaxy’s absolute B -band luminosity, S_{lum} , and the likelihood of detecting a counterpart at the galaxy’s distance S_{det} . We define S_{det} as a prioritization of a transient’s potential brightness, taking a fiducial limiting magnitude, m_{lim} , for the exposures of $m_{\text{AB}} = 22$, and convert it to a limiting apparent luminosity L_{lim} . We also compute the luminosity for a potential transient with an absolute magnitude between -12 and -17 , using wide bounds to be robust against differences in intrinsic brightness. Then, S_{det} becomes $S_{\text{det}} = \frac{L_{\text{KNmax}} - L_{\text{KNmin}}}{L_{\text{KNmax}} - L_{\text{lim}}}$, which we limit to be between 0.01 and 1. Our final metric is therefore $S = S_{\text{loc}} \times S_{\text{lum}} \times S_{\text{det}}$.

Beginning 4 hr after the event, LOT observed 85 galaxies in the initial 90% localization (Tan et al. 2019a, 2019b). LOT used 180 s exposures in R -band with seeing varying between $1''.5$ and $2''.5$. Using comparisons to Pan-STARRS images, these exposures yielded a typical 5σ limiting magnitude of $m_{\text{AB}} = 20$. Similarly, KPED started the galaxy-targeted follow-up 1.9 hr after the merger and continued until the first ZTF candidates came online. KPED imaged 10 galaxies in the r -band filter for 300 s, finding no visible transients up to $r = 20.8$ (Ahumada et al. 2019a). 300 s is the fiducial time chosen for KPED to potentially reach limiting magnitudes of $m_{\text{AB}} = 22$, useful for both the transient discovery and follow-up (Coughlin et al. 2019d).

3. Candidates

We now briefly describe the candidate filtering criteria for the ToO program for ZTF and Palomar Gattini-IR (see Coughlin et al. 2019a for further details). For GROWTH-India, LOT, and KPED, we did not identify any viable counterparts without previous history of variability in the analysis.

3.1. Candidates from ZTF

A ZTF transient alert is defined as a 5σ change in brightness in the image relative to the reference epoch. For ZTF, all transient alerts flagged for follow-up required at least two detections separated by 15 minutes in order to remove asteroids and other transient objects. We used the Pan-STARRS1 point source catalog (PS1 PSC; Tachibana & Miller 2018) to remove candidates located less than $2''$ from likely point sources (i.e., stars). Full details on the PS1 PSC can be found in Tachibana & Miller (2018); briefly, the authors build a machine learning model that determines the relative likelihood that a PS1 source is a point source or extended based on PS1 colors and shape measurements. The model is trained using sources observed with the *Hubble Space Telescope*, achieving an overall accuracy of $\sim 94\%$, and classifying $\sim 1.5 \times 10^9$ total sources.

We also used a real-bogus (RB) classifier to remove common image subtraction artifacts (Mahabal et al. 2019). This method consists of a random forest classifier trained with real objects and artifacts from ZTF images, separating objects with an accuracy of $\sim 89\%$. In order to capture the majority of real events, the threshold was set to $\text{RB} > 0.25$. In addition, the transients must have brightened relative to the reference image, leading to a positive residual after the image subtraction. Furthermore, the program excluded all objects within $20''$ of $m_{\text{AB}} < 15$ stars to avoid artifacts from blooming, thus excluding $\sim 2\%$ – 5% of the imaged region, which depends

Table 2
Filtering Results for Both ZTF Nights

Filtering Criteria	# of Alerts on April 25	# of Alerts on April 26
ToO alerts	50,802	287,844
Positive subtraction	33,139	182,095
Real	19,990	118,446
Not stellar	10,546	61,583
Far from a bright source	10,045	58,881
Not moving	990	5815
No previous history	28	234

Note. The quantities represent the number of alerts that passed a particular step in the filter. Each step is run over the remaining alerts from the previous stage. The criteria are described in Section 3.1 and the total number of relevant candidates is highlighted. In particular, “Real” indicates an RB score greater than 0.25, and “not moving” indicates that there are more than two detections separated by at least 30 minutes. The bold values refer to the final number of candidates remaining after our initial filter process.

significantly on stellar density.⁴³ The final step involved constraining the search to events that have no historical detections prior to three days before the trigger.

This filtering scheme reduced the number of ZTF alerts from 50802 to 28 for the first night and from 287844 to 234 relevant candidates for the second night. A more detailed breakdown on the number of alerts that successfully met the criteria at each filtering step can be found in Table 2.

The candidates that passed these criteria were filtered and displayed by the GROWTH Marshal (Kasliwal et al. 2019b), a database used to display historical lightcurves (including upper limits) for each object that also performs cross-matches with external catalogs. We subjected each of the remaining candidates to a thorough human vetting process to determine whether the transient could be a viable counterpart to S190425z. Through this vetting process, we removed candidates whose coordinates were outside the 90% contour in the GW localization, and candidates that had archival detections in the Pan-STARRS1 Data Release 2 (Flewelling 2018). We flagged active galactic nuclei based on the *WISE* colors (Wright et al. 2010) for each transient and its offset from the nucleus of the galaxy. Furthermore, we prioritized candidates whose photometric/spectroscopic redshift was consistent with the GW distance estimate, and whose extinction-corrected light curve exhibited rapid color evolution initially. For the most promising candidates in our vetted list, we performed forced photometry at the position of the source to ensure that there were no historical detections with ZTF.

Our first night of observations yielded only two such candidates that passed both the automatic filtering and human vetting processes. These two candidates were ZTF19aarykbb and ZTF19aarzaod. The second night of observations allowed us to identify additional candidates detected on the first night that were consistent with the new skymap, thereby increasing our candidate list from two to 13 from the first night to the second. We describe the most promising of these 15 candidates in more detail in Section 3.3.

⁴³ Estimates of the amount of excluded area rely on the assumption that the sky fraction excluded around $m_{\text{AB}} < 15$ stars, within a few circular regions of 1 deg^2 in the skymap that we checked, is representative of the overall sky fraction excluded from the entire imaged region.

Table 3

Follow-up Table for the Palomar Gattini-IR Candidate Described in Section 3.2 and the 15 Most Interesting ZTF Candidates from Kasliwal et al. (2019c) and Anand et al. (2019)

Candidate	Coordinates (R.A., Decl.)	Discov. Mag.	Classification	Spec. Facilities	Phot. Evol.	Redshift/Host
ZTF19aarykbb	17:13:21.95 −09:57:52.1	$r = 18.63$	SNII $z = 0.024$	HCT, LT, DCT	...	0.024 (s)
ZTF19aarzaod	17:31:09.96 −08:27:02.6	$r = 20.11$	SNIIn $z = 0.028$	SALT	...	0.028 (s)
ZTF19aasckwd	16:52:39.45 +10:36:08.3	$r = 20.15$	SN Ia $z = 0.145$	SOAR	...	0.15 (s)
ZTF19aasckkq	16:33:39.14 +13:54:36.7	$g = 20.86$	SN Iib $z = 0.052$	P200, SOAR	...	0.053 (s)
ZTF19aasbphu	16:22:19.95 +21:24:29.5	$r = 19.71$	Nuclear*	...	0.11	0.0971 (p)
ZTF19aaryxjf	16:58:22.87 −03:59:05.1	$g = 19.95$	SN*	...	−0.014	0.07791 (s, GLADE)
ZTF19aarxxwb	19:14:46.40 −03:00:27.0	$g = 18.89$	SN*	...	0.12	hostless
ZTF19aasdajo	16:57:25.21 +11:59:46.0	$g = 20.7$	SN*	...	0.045	0.292 (p)
ZTF19aasbamy	15:25:03.76 +24:55:39.3	$g = 20.66$	SN*	...	0.01	0.201 (p)
ZTF19aarycuy	16:16:19.97 +21:44:27.4	$r = 20.07$	SN*	...	0.02	0.127 (p)
ZTF19aasbau	15:40:59.91 +24:04:53.8	$g = 20.49$	SN*	...	0.01	0.04 (s, CLU)
ZTF19aasejil	17:27:46.99 +01:39:13.4	$g = 20.53$	SN*	...	0.01	0.199 (p)
ZTF19aascxux	17:13:10.39 +17:17:37.9	$g = 20.56$	SN*	...	0.06	0.165 (p)
ZTF19aashlts	16:52:45.01 −19:05:38.9	$r = 19.95$	SN*	...	0.03	hostless
ZTF19aasfogv	17:27:22.32 −11:20:01.9	$g = 20.53$	SN*	...	0.01	hostless

Note. The sources with a star (*) have photometric evolution (in units of mag/day) that is inconsistent with the evolution of a KN (Section 3.3). Spectra obtained with SOAR (Nicholl et al. 2019) were critical in classifying ZTF19aasckwd and ZTF19aasckkq while spectra from SALT (Buckley et al. 2019) allowed the classification of ZTF19aarzaod. GROWTH teams acquired spectra of ZTF19aarykbb with HCT, LT, and DCT (Dichiara et al. 2019; Pavana et al. 2019; Perley et al. 2019a) and also provided useful photometric data toward the classification of these transients (Ahumada et al. 2019a, 2019b; Bhalariao et al. 2019; Perley et al. 2019b; Tan et al. 2019b). We monitored the transients on average for seven days. The redshift, spectroscopic (s) or photometric, (p) of the host galaxy is also listed.

To double-check that we did not miss any candidates, we used Kowalski,⁴⁴ an open-source system used internally at Caltech (primarily) to archive and access ZTF’s alerts and light curves (Duez et al. 2019). Specifically, we used Kowalski’s web-based GUI called the ZTF Alert Lab, with which users can efficiently query, search, and preview alerts. Our results were consistent with the results above. To triple-check that we did not miss any candidates, we also carried out an additional automatic search of the AMPEL alert archive (Nordin et al. 2019) for transients that might have escaped. No additional candidates from either night were found.

3.2. Candidates from Palomar Gattini-IR

For Palomar Gattini-IR, we adopted the following selection criteria for human vetting of sources identified in the difference imaging.

1. We selected candidates that were at least $1'$ away from bright stars with $m_j < 10$, excluding $\sim 0.7\%$ – 2% of the imaged region, in order to remove contamination from subtraction artifacts.⁴⁵
2. The first detection of the candidate must have been after the GW trigger time.
3. An object must have at least two detections with a signal-to-noise ratio greater than 5 or a signal-to-noise ratio greater than 7 in one detection. Among sources with single detections, we also rejected known asteroids.

No viable counterparts were identified in this search.

⁴⁴ <https://github.com/dmitryduez/kowalski>

⁴⁵ Estimates of the amount of excluded area rely on the assumption that the sky fraction excluded around $m_{AB} < 10$ stars, within a few circular regions of 1 deg^2 in the skymap that we checked, is representative of the overall sky fraction excluded from the entire imaged region.

3.3. Follow-up of ZTF Candidates

The 15 sources that were identified from ZTF observations are shown in Table 3 and on Figure 1. Using a variety of resources including the spectral energy distribution (SED) Machine (SEDM; Blagorodnova et al. 2018; Rigault et al. 2019) on the Palomar 60 inch (P60) telescope, the Double Beam Spectrograph (DBSP; Oke & Gunn 1982) on the Palomar 200 inch (P200) telescope, the Robert Stobie Spectrograph (RSS; Smith et al. 2006) on the Southern African Large Telescope (SALT), the Liverpool telescope (LT; Steele et al. 2004), the GROWTH-India telescope, the KPED, the Himalayan Chandra Telescope (HCT), the Discovery Channel Telescope (DCT), and LOT, we followed up each of these candidates with further photometry and/or spectroscopy.

A total of five objects were classified using spectroscopy (Buckley et al. 2019; Nicholl et al. 2019; Perley et al. 2019a) and we tracked the color evolution of 15 objects using photometry for about seven days on average. A KN is expected to show a rapid evolution in magnitude (Metzger 2017); GW170817 faded $\Delta r \sim 1$ mag per day over the first three days and by $\Delta r \sim 4.2$ mag total around day 10. Thus, we can use photometric light curves to determine whether a transient is consistent with the expected evolution for a KN. Some photometrically monitored transients showed evolution that was too slow ($\Delta r \sim 0.1$ mag per day) to be consistent with GW170817 or KN model predictions. Many other candidates highlighted in Kasliwal et al. (2019c) were observed with GROWTH facilities; however, they were later excluded by the updated LALInference skymap. In addition to these sources, we reported objects in Kasliwal et al. (2019c) with ZTF detections before the event time to the community in order to limit the number of false positives identified by other surveys that may not have recently imaged those areas of the sky.

We now provide a broad summary of the most promising candidates ruled out by spectroscopy, as examples of the follow-up performed by the GROWTH facilities when vetting candidates.

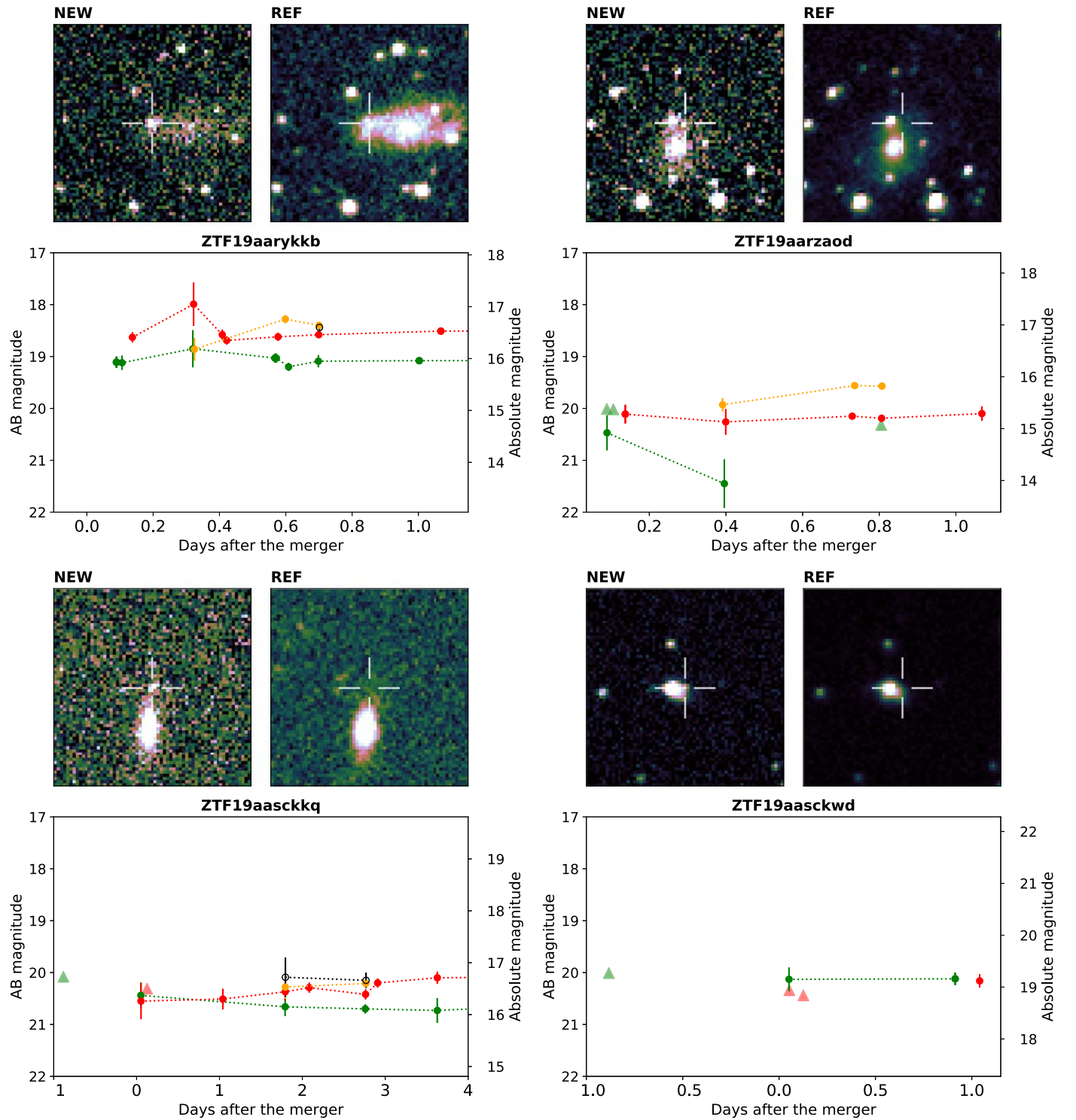


Figure 3. Light curves and *r*-band cutouts for the ZTF candidates discussed in Section 3.3. The light curves are constructed with data acquired with GROWTH facilities: for ZTF19aarykkb, the data is from ZTF, LOT, GIT, and LT; for ZTF19aarzaod, ZTF, LOT, and LT; for ZTF19aasckkq, ZTF, KPED, and LT; and for ZTF19aasckwd, ZTF and KPED. We used colors to represent each band in the light curves: green for *g*-band, red for *r*-band, yellow for *i*-band, and black for *z*-band. While triangles in the light curve represent upper limits, filled circles are the magnitudes of the object. For each transient, the cutout on the left corresponds to the ZTF discovery image and the right cutout corresponds to the ZTF reference image of the host. A cross marks the location of the transient in the reference image. The cutouts are 0.7 sq. arcmin with north being up and east to the left.

In particular, we highlight the light curves of ZTF19aarykkb, ZTF19aarzaod, ZTF19aasckkq, and ZTF19aasckwd in the top-left, top-right, lower-left and lower-right panels, respectively, in Figure 3 and discuss them briefly below. The associated spectra

are shown in the top panel of Figure 5; the spectrum of ZTF19aasckwd is not shown as we only have a spectrum of the galaxy host. We used the value of $H_0 = 67.4 \text{ km s}^{-1} \text{ Mpc}^{-1}$ (Aghanim et al. 2018) to calculate absolute magnitudes.

3.3.1. ZTF19aarykkb

We first detected the transient ZTF19aarykkb 2.13 hr after the merger and highlighted it in the first ZTF GCN (Kasliwal et al. 2019c). ZTF19aarykkb is $12''$ offset from the host galaxy, which is at a redshift of $z = 0.024$, corresponding to a luminosity distance of 106 Mpc. The absolute magnitude of the discovery is $g = -15.9$, which is broadly consistent with GW170817 and KNe predictions. We ran forced photometry in archival ZTF images of the region, finding no variability at the coordinates before the merger. The last upper limit at this location was 5.8 days before the LVC alert in g -band ($m_{AB} > 18.74$ in g -band). Due to its distance and discovery mag, several facilities followed up this source (Burke et al. 2019; Chang et al. 2019a; Dichiara et al. 2019; Morihana et al. 2019a; Nicholl et al. 2019; Perley et al. 2019a; Rhodes et al. 2019). The LOT group in Taiwan imaged the object 6 hr after the transient set in Palomar (Tan et al. 2019b); later that day, the LT continued the monitoring. This object was imaged 18 times within the first 26 hr after the merger. The first spectrum for this object came from the Himalayan Chandra Telescope (HCT) about 10.67 hr after the trigger (Pavana et al. 2019), showing a strong $H\alpha$ line at a redshift of $z = 0.024$. This was confirmed 8 hr later by the LT team with the Spectrograph for the Rapid Acquisition of Transients (SPRAT; Piascik et al. 2014), who classified it as a young SN Type II (Perley et al. 2019a), based on the characteristic P-Cygni profile in the LT spectrum. An additional spectrum was taken about 10 hr later with the DeVeny spectrograph mounted on the 4.3 m DCT (Dichiara et al. 2019), showing similar strong $H\alpha$, furthermore confirming the SN classification (see Figure 5).

3.3.2. ZTF19aarzaod

ZTF19aarzaod was first detected by ZTF 2.15 hr after the merger (Kasliwal et al. 2019c) with its last upper limit ($m_{AB} > 20.01$ in g -band) six days prior the merger. Forced photometry did not show previous history of variability at the transient location. The redshift of the host galaxy is $z = 0.028$, putting the transient at a distance of 128.7 Mpc. The transient is offset by $8''$ from the host galaxy and its absolute magnitude at discovery was $r = -15.3$, which is also consistent with a GW170817-like KN. ZTF19aarzaod was extensively followed up with various observatories (Buckley et al. 2019; Castro-Tirado et al. 2019; Hiramatsu et al. 2019; Izzo et al. 2019; Morihana et al. 2019a; Nicholl et al. 2019; Rhodes et al. 2019; Wiersema et al. 2019) and was imaged 13 times during the first day. Spectroscopic observations of ZTF19aarzaod were taken with RSS mounted on SALT on UT 2019 April 26.0 under a special GW follow-up program 2018-2-GWE-002 and reduced with a custom pipeline based on PyRAF routines and the PySALT package (Crawford et al. 2010). The spectrum covered a wavelength range of 470–760 nm with a spectral resolution of $R = 400$. The spectrum shows broad $H\alpha$ emission along with some He I features (see Figure 5) classifying it as a type II supernova at $z = 0.028$ (Buckley et al. 2019).

3.3.3. ZTF19aasckkq

The transient ZTF19aasckkq (Anand et al. 2019) was first detected by ZTF 1.23 hr after the merger. It is offset from the host galaxy by $10''$, and its last upper limit ($m_{AB} > 20.1$ in g -band) was the night before the merger. We ran forced

photometry at the location of the transient, finding no activity before the merger. The discovery absolute mag is $r = -16.3$, similar to GW170817 at peak. ZTF19aasckkq was followed up 18 hr after the last ZTF detection by LT and KPED (Ahumada et al. 2019b). This transient was imaged 16 times for a period of 3.8 days by a variety of observing groups (Ahumada et al. 2019b, 2019c; Perley et al. 2019b, 2019c). Nicholl et al. (2019) first classified ZTF19aasckkq as a Type IIb SN at $z \sim 0.05$, which is consistent with the galaxy redshift (Hosseinzadeh et al. 2019). In Figure 5, we highlight the presence of He I, $H\alpha$, and $H\beta$ absorption features in the first spectrum we acquired with P200+DBSP, confirming its classification as a SN IIb at a redshift of $z = 0.0528$. The source was still bright at $r = 19.8$, 14 days after S190425z.

3.3.4. ZTF19aasckwd

ZTF19aasckwd was detected 1.23 hr after the merger about $4''$ from its host galaxy (Anand et al. 2019). Its last upper limit ($m_{AB} > 20.1$ in g -band) was the night before the trigger. The forced photometry search did not show activity prior to the merger. This transient was imaged five times during the first 24 hr and it was classified as a SN Ia by Nicholl et al. (2019) at a redshift of $z = 0.145$ (Hosseinzadeh et al. 2019). The absolute magnitude at discovery was $r = -19.2$, a few magnitudes brighter than what is expected from a KN.

3.4. Follow-up of Non-ZTF Candidates

Here, we report on the follow-up triggered by the GROWTH team of a number of transients discovered by other facilities to be consistent with the LALInference skymap. We queried the GROWTH follow-up marshal at the positions of the most promising transients announced in order to determine whether (1) the transient had historical detections with ZTF, or (2) our concurrent photometry of the object also supported the KN hypothesis. Additionally, we used LT, GROWTH-India Telescope, and DECam to obtain photometry of the candidates that were not detected with ZTF because they were either fainter than the ZTF average upper limits or inaccessible due to their sky location. Table 4 summarizes the most relevant non-GROWTH objects followed up by the GROWTH collaboration, and we briefly discuss them below.

3.4.1. Swift's Ultraviolet/Optical Telescope (UVOT) Candidate

We followed up photometrically the *Swift*/UVOT candidate (Breeveld et al. 2019), discovered at R.A. = 17:02:19.2, decl. = $-12:29:08.2$ in u -band with $m_{Vega} = 17.7 \pm 0.2$. The transient was within a few hundred arcseconds of two galaxies within the localization volume. After its initial detection with *Swift*, several other facilities (Andreoni et al. 2019b; Arcavi et al. 2019; Breeveld et al. 2019; Chang et al. 2019b; De et al. 2019; Hu et al. 2019; Im et al. 2019; Kann et al. 2019; Kong et al. 2019; Morihana et al. 2019b; Shappee et al. 2019; Tanvir et al. 2019; Troja et al. 2019; Waratkar et al. 2019), including ZTF and Palomar Gattini-IR, reported non-detections or pre-discovery upper limits that indicated the transient might be rapidly fading in the ultraviolet. Palmese et al. (2019) reported an object offset by $<1''$ from the position of the reported UVOT candidate after visually inspecting archival DECam optical images. Using the GROWTH-DECam program, Bloom et al. (2019) detected a source that is consistent with the coordinates reported by Palmese et al.

Table 4
GROWTH Follow-up Table for Candidates Reported by Other Surveys

Candidate	Coordinates (R.A., Decl.)	Discovery Mag.	GROWTH Follow-up	Upper Limits
UVOT	17:02:19.21 –12:29:08.2	$u = 17.74$	GIT, LOT, DECam	DECam $g > 24.0$ DECam $r > 24.0$ DECam $i > 23.7$ DECam $z > 23.1$
...
...
...
AT2019ebq-PS19qp	17:01:18.33 –07:00:10.4	$i = 20.40$	Keck spectrum SN Ib/c	...
Gaia19bpt	14:09:41.88 +55:29:28.1	$o = 18.49$	ZTF19aarioci (4.12)	...
AT2019ebu-PS19pp	14:19:49.43 +33:00:21.7	$i = 20.77$	ZTF19aasbgll (2.10)	$r = 20.60$
AT2019ebw-PS19pq	15:02:17.02 +31:14:51.6	$i = 20.92$	ZTF19aasazok (11.95)	$g = 20.91$
AT2019ecc-PS19pw	15:26:29.53 +31:39:47.5	$i = 20.10$	ZTF19aapwpgg (17.96)	$r = 20.14$
AT2019eck-PS19qe	15:44:24.53 +32:41:11.0	$i = 20.81$	ZTF19aapfrw (24.97)	$g = 20.13$
AT2019ecl-PS19qg	15:48:11.85 +29:12:07.1	$i = 20.51$	ZTF19aasgwnp (25.89)	$g = 21.02$
AT2019ebr-PS19qj	16:35:26.48 +22:21:36.4	$i = 19.79$	ZTF18aaoxrvr (25.86)	$g = 20.83$
AT2019ebo-PS19qn	16:54:54.71 +04:51:31.5	$i = 20.02$	ZTF19aarpgau (9.87)	$g = 20.40$
AT2019eao-ATLAS19hyo	13:01:18.63 +52:09:02.1	$o = 19.36$	LT	$g > 22.1$
AT2019ebn-ATLAS19hwh	13:54:47.42 +44:46:27.3	$o = 19.07$	LT	$g > 22.1$
AT2019ebm-ATLAS19hwn	12:59:58.58 +29:14:30.7	$o = 19.42$	LT	$g > 22.3$
AT2019ebl-ATLAS19hyx	14:32:31.53 +55:45:00.1	$o = 19.28$	LT	$g > 22.3$
AT2019dzv-ATLAS19hxm	14:01:45.02 +46:12:56.1	$o = 19.23$	LT	$g > 22.2$

Note. GROWTH-India, LOT, and DECam-GROWTH follow-up of the *Swift*/Ultraviolet/Optical Telescope (UVOT) candidate discovered by Breeveld et al. (2019) helped confirm its classification as a likely M-dwarf flare (Andreoni et al. 2019b; Arcavi et al. 2019; Bloom et al. 2019; Breeveld et al. 2019; Chang et al. 2019b; De et al. 2019; Hu et al. 2019; Im et al. 2019; Kann et al. 2019; Kong et al. 2019; Lipunov et al. 2019b; Morihana et al. 2019b; Palmese et al. 2019; Shappee et al. 2019; Tanvir et al. 2019; Troja et al. 2019; Waratkar et al. 2019). Our initial Keck spectrum of another promising candidate, AT2019ebq/PS19qp (Smith et al. 2019) showed it was a Type II SN (Jencson et al. 2019). Several of the PS1 candidates reported by Smith et al. (2019), as well as Gaia19bpt (Kostrzewa-Rutkowska et al. 2019) were found to have previous detections with ZTF (Andreoni & Bellm 2019; Coughlin et al. 2019b). For these sources, we list the number of days before S190425z that they were detected in parentheses. LT provided constraining upper limits of some reported ATLAS candidates (McBrien et al. 2019; Perley & Copperwheat 2019).

(2019), but no transient at the coordinates reported by *Swift* (Kong et al. 2019; see Table 4). The slight trailing observed in images of the original UVOT source (which introduced uncertainty in the astrometry) strongly hinted at the physical association between the transient and the offset source. The colors of the associated source ($r - z = 1.53$ and $g - r > 0.97$) are consistent with those of a M2-dwarf (West et al. 2011). For this reason, a likely explanation for the observed ultraviolet transient is that it was a galactic M2-dwarf flare (Bloom et al. 2019; Lipunov et al. 2019b), unassociated with the GW event. The photometry of the UVOT candidate is shown with a Sloan Digital Sky Survey (SDSS) spectra of a M2-dwarf in Figure 4.

3.4.2. AT2019ebq/PS19qp

We also obtained spectroscopy of AT2019ebq/PS19qp (Smith et al. 2019) with the Near-Infrared Echelle Spectrometer (NIRES) on Keck II. This candidate was initially claimed to be exceptional in that its optical spectrum taken with the Gran Telescopio Canarias (GTC) contained broad absorption features “unlike normal supernovae;” therefore Jonker et al. (2019) highlighted it as a promising KN candidate. Our near-IR spectrum taken ~ 1.5 days after the trigger, however, exhibited broad P-Cygni SN-like features of He I that indicated that the transient was a Type Ib/c SN (Jencson et al. 2019), ruling out its association with S190425z (see the bottom panel of Figure 5). Several other facilities that also followed up this source helped verify its classification (Carini et al. 2019; Dimitriadis et al. 2019; Jencson et al. 2019; Lipunov et al. 2019a; McCully et al. 2019; Morokuma et al. 2019; Schady et al. 2019).

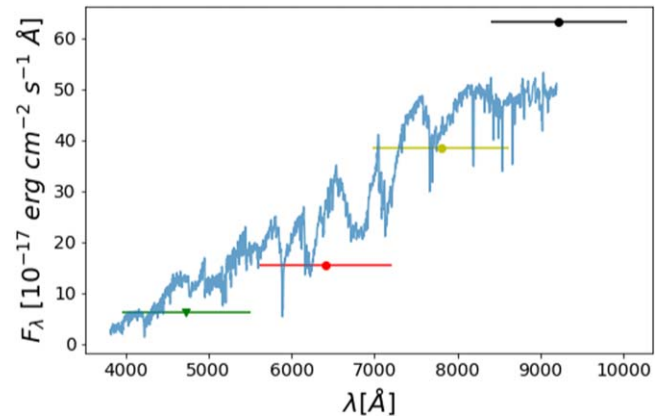


Figure 4. DECam (g , r , i and z -band) fluxes of the UVOT candidate discussed on Section 3.4.1 are over-plotted on the spectra of an SDSS M2-dwarf.

Seven additional PS1 candidates (out of the 20 transients reported by Smith et al. 2019) were ruled out based on previous ZTF detections (Andreoni et al. 2019a; see Table 4).

3.4.3. Marginal ATLAS Candidates

Additionally, we acquired a short sequence (40 s each in gri filters) of imaging at the locations of all five of the marginal ATLAS transients reported by McBrien et al. (2019) using IO: O (Steele et al. 2004) on the 2 m Liverpool Telescope (Perley & Copperwheat 2019). No significant source was detected at the location of any of them (to typical depths of 22 mag; see Table 4). Combined with the fact that none of these transients had a detectable host galaxy, this suggests these transients were

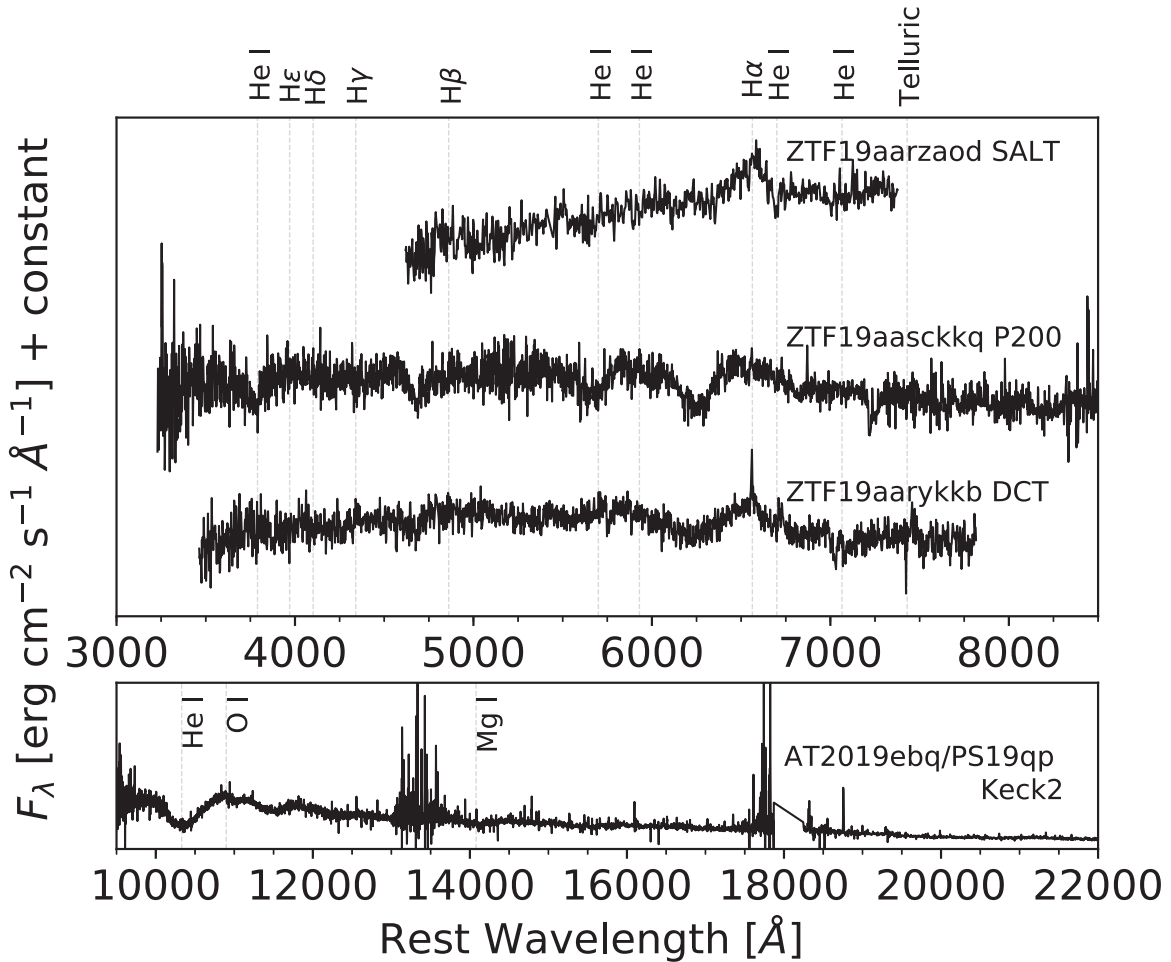


Figure 5. Spectra of all the candidates for which spectroscopic data were taken. The transient name and instrument used to obtain the spectrum are noted on the right-hand side of the plot. We show the spectrum for AT2019ebq/PS19qp in its own panel given the different wavelengths covered from the other transients. The dotted gray lines show the characteristic features in each spectrum that helped with its classification. These four transients were all classified as core-collapse SNe. The classification and phase for each transient is as follows: ZTF19aascckq—SN I Ib, seven days; ZTF19aarykkb—SN II, one day (Dichiara et al. 2019); ZTF19aarzaod—SN II, zero days (Buckley et al. 2019); AT2019ebq/PS19qp—SN Ib/c, one day (Jencson et al. 2019).

likely to be spurious or perhaps short-timescale flares from faint stars.

4. Conclusions

In this Letter, we have described the first follow-up of a binary neutron star event with ZTF and Palomar Gattini-IR. Covering more than 8000 deg² with ZTF and 2400 deg² with Palomar Gattini-IR over two nights, we show how these systems in combination with follow-up facilities are capable of rapidly identifying and characterizing transients on hour to day timescales over sky regions of this size. We show how it is possible to reduce 338,646 alerts to 15 previously unidentified candidate counterparts. We also show how with the follow-up resources available to GROWTH, we can rule out these objects as viable candidates.

Assuming an optical/near-IR counterpart with a luminosity similar to that of GW170817, which had an absolute magnitude of about -16 in g -, r -, and J -bands, the apparent magnitude in these bands for the distribution of distances to S190425z is $m_{AB} \approx 19$ – 20.5 . This varies between 1 mag brighter than to near the detection limit for ZTF for this analysis, indicating ZTF is well primed for detecting a GW170817-like source at these distances. We expect that a closer or brighter than

expected source (GW170817 would be detected at ~ 20 Mpc) should be detectable with Palomar Gattini-IR.

As a cross-check of the number of sources that we are identifying, we compare to the fiducial SN rate of $\approx 10^{-4}$ Mpc⁻³ yr⁻¹ (Li et al. 2011). The 90% localization volume of the GW skymap is $\sim 2.1 \times 10^7$ Mpc³. As stated above, ZTF covered about 46% of the skymap, meaning that we expect to detect $\sim 2.1 \times 10^7$ Mpc³ $\times 1.04 \times 10^{-4}$ Mpc⁻³ yr⁻¹ $\times 0.46 \approx 2.7$ day⁻¹. Because the distribution of Type II SNe at peak luminosity falls between absolute magnitudes of ≈ -15 to -20 mag (Richardson et al. 2014), brighter than the expected distribution at peak for KNe, our follow-up observations with ZTF should have detected all of the bright, and most of the dim Type II SNe. Having taken images for about 12 hr during the nights, we would expect to detect ~ 1 – 2 , which is consistent with the two young SNe highlighted in this Letter.

Going forward, prioritizing further automatized classification of objects can lead to more rapid follow-up and dissemination of the most interesting objects. For example, the inclusion of machine-learning-based photometric classification codes such as RAPID (Muthukrishna et al. 2019) will help facilitate candidate selection and prioritization. We are also actively improving the scheduling optimization, and have since added a

feature to schedule using the “secondary” ZTF grid, that is designed to fill in the chip gaps.

The follow-up of S190425z highlights two important points. The first is that rapid dissemination of updated GW sky maps is useful for tiling prioritization. This helps mitigate the effects of shifting localization regions, including potentially decreasing sky areas. The second is that we are capable of performing nearly all-sky searches with ZTF and Palomar Gattini-IR and conducting the necessary follow-up with partner facilities, even in the case of a single-detector GW trigger. This event serves to extend the frontier in searches for optical transients in large areas. The intermediate Palomar Transient Factory found optical counterparts to eight long GRBs localized to $\sim 100 \text{ deg}^2$ (Singer et al. 2015), with GRB 130702A (Singer et al. 2013) being the first of its kind, and this event has shown it is possible to cover more than an order of magnitude larger sky area. One caveat to this conclusion is that in general, single-detector localizations will include regions on the sky that are not accessible to one ground-based facility alone; this motivates the use of coordinated networks of telescopes with worldwide coverage (Nissanke et al. 2013; Kasliwal & Nissanke 2014). However, we have demonstrated that the network on hand is capable of overcoming the challenges of rapidly and efficiently searching for electromagnetic counterparts in this new era of GW astronomy.

We would like to thank Peter Nugent for comments on an early version of this Letter.

This work was supported by the GROWTH (Global Relay of Observatories Watching Transients Happen) project funded by the National Science Foundation under PIRE grant No. 1545949. GROWTH is a collaborative project among California Institute of Technology (USA), University of Maryland College Park (USA), University of Wisconsin Milwaukee (USA), Texas Tech University (USA), San Diego State University (USA), University of Washington (USA), Los Alamos National Laboratory (USA), Tokyo Institute of Technology (Japan), National Central University (Taiwan), Indian Institute of Astrophysics (India), Indian Institute of Technology Bombay (India), Weizmann Institute of Science (Israel), The Oskar Klein Centre at Stockholm University (Sweden), Humboldt University (Germany), Liverpool John Moores University (UK) and University of Sydney (Australia).

Based on observations made with the Liverpool Telescope operated on the island of La Palma by Liverpool John Moores University in the Spanish Observatorio del Roque de los Muchachos of the Instituto de Astrofísica de Canarias with financial support from the UK Science and Technology Facilities Council. Based on observations obtained with the Samuel Oschin Telescope 48 inch and the 60 inch Telescope at the Palomar Observatory as part of the Zwicky Transient Facility project. ZTF is supported by the National Science Foundation under grant No. AST-1440341 and a collaboration including Caltech, IPAC, the Weizmann Institute for Science, the Oskar Klein Center at Stockholm University, the University of Maryland, the University of Washington, Deutsches Elektronen-Synchrotron and Humboldt University, Los Alamos National Laboratories, the TANGO Consortium of Taiwan, the University of Wisconsin at Milwaukee, and Lawrence Berkeley National Laboratories. Operations are conducted by COO, IPAC, and UW. This research used resources of the National Energy Research Scientific

Computing Center, a DOE Office of Science User Facility supported by the Office of Science of the U.S. Department of Energy under Contract No. DE-AC02-05CH11231. The 0.7 m GROWTH-India Telescope (GIT) is set up by the Indian Institute of Astrophysics (IIA) and the Indian Institute of Technology Bombay (IITB) with support from the Indo-US Science and Technology Forum (IUSSTF) and the Science and Engineering Research Board (SERB) of the Department of Science and Technology (DST), Government of India grant No. IUSSTF/PIRE Program/GROWTH/2015-16. It is located at the Indian Astronomical Observatory, IIA at Hanle, Ladakh (India). This publication has made use of data collected at Lulin Observatory, partly supported by MoST grant 105-2112-M-008-024-MY3. The KPED team thanks the National Science Foundation and the National Optical Astronomical Observatory for making the Kitt Peak 2.1 m telescope available. We thank the observatory staff at Kitt Peak for their efforts to assist Robo-AO KP operations. The KPED team thanks the National Science Foundation, the National Optical Astronomical Observatory, the Caltech Space Innovation Council, and the Murty family for support in the building and operation of KPED. SED Machine is based upon work supported by the National Science Foundation under grant No. 1106171. The Palomar Gattini-IR project thanks the Mount Cuba Foundation, Heising-Simons Foundation, the ANU Futures Scheme, the Binational Science Foundation, and Caltech for generous support.

G.C.A. and V.B. acknowledge partial support from SERB and IUSSTF. J.S. acknowledges support from the Knut and Alice Wallenberg Foundation. E.O. is grateful for support by a grant from the Israeli Ministry of Science, ISF, Minerva, BSF, BSF transformative program, and the I-CORE Program of the Planning and Budgeting Committee and The Israel Science Foundation (grant No. 1829/12). P.G. is supported by NASA Earth and Space Science Fellowship (ASTRO18F-0085). C.-C.N., A.P., and P.-C.Y. thank the funding from Ministry of Science and Technology (Taiwan) under grants 104-2923-M-008-004-MY5, 106-2112-M-008-007, 107-2119-M-008-012, 107-2119-M-008-014-MY2. E.B. and V.Z.G. acknowledge support from the University of Washington College of Arts and Sciences, Department of Astronomy, and the DIRAC Institute. University of Washington’s DIRAC Institute is supported through generous gifts from the Charles and Lisa Simonyi Fund for Arts and Sciences, and the Washington Research Foundation. E.B. acknowledges support from the Large Synoptic Survey Telescope, which is supported in part by the National Science Foundation through Cooperative Agreement 1258333 managed by the Association of Universities for Research in Astronomy (AURA), and the Department of Energy under Contract No. DE-AC02-76SF00515 with the SLAC National Accelerator Laboratory. Additional LSST funding comes from private donations, grants to universities, and in-kind support from LSSTC Institutional Members. E.B. is supported in part by the NSF AAG grant 1812779 and grant #2018-0908 from the Heising-Simons Foundation. M.W.C. is supported by the David and Ellen Lee Postdoctoral Fellowship at the California Institute of Technology. Part of this research was carried out at the Jet Propulsion Laboratory, California Institute of Technology, under a contract with the National Aeronautics and Space Administration. D.L.K. was supported by NSF grant AST-1816492. A.K.H.K. acknowledges support from the Ministry of Science and Technology of the Republic of

China (Taiwan) under grants 106-2628-M-007-005 and 107-2628-M-007-003. J.S.B. and J.M.-P. are partially supported by a Gordon and Betty Moore Foundation Data-Driven Discovery grant. H.K. thanks the LSSTC Data Science Fellowship Program, which is funded by LSSTC, NSF Cybertraining Grant #1829740, the Brinson Foundation, and the Moore Foundation; his participation in the program has benefited this work. S.A. acknowledges support from the PMA Division Medberry Fellowship at the California Institute of Technology. R.B., A.G., and J.S. acknowledge support from the G.R.E.A.T research environment funded by the Swedish National Science Foundation. J.S. acknowledges support by an Australian Government Research Training Program (RTP) Scholarship. M.R. acknowledges support from the European Research Council (ERC) under the European Union's Horizon 2020 research and innovation programme (grant agreement No. 759194 - USNAC).

ORCID iDs

Michael W. Coughlin <https://orcid.org/0000-0002-8262-2924>
 Tomás Ahumada <https://orcid.org/0000-0002-2184-6430>
 Matthew J. Hankins <https://orcid.org/0000-0001-9315-8437>
 Mansi M. Kasliwal <https://orcid.org/0000-0002-5619-4938>
 Leo P. Singer <https://orcid.org/0000-0001-9898-5597>
 Eric C. Bellm <https://orcid.org/0000-0001-8018-5348>
 Igor Andreoni <https://orcid.org/0000-0002-8977-1498>
 S. Bradley Cenko <https://orcid.org/0000-0003-1673-970X>
 Jeff Cooke <https://orcid.org/0000-0001-5703-2108>
 Christopher M. Copperwheat <https://orcid.org/0000-0001-7983-8698>
 Jacob E. Jencson <https://orcid.org/0000-0001-5754-4007>
 Daniel A. Perley <https://orcid.org/0000-0001-8472-1996>
 Po-Chieh Yu <https://orcid.org/0000-0001-8894-0854>
 Varun Bhalerao <https://orcid.org/0000-0002-6112-7609>
 Michael C. B. Ashley <https://orcid.org/0000-0003-1412-2028>
 Rahul Biswas <https://orcid.org/0000-0002-5741-7195>
 David O. Cook <https://orcid.org/0000-0002-6877-7655>
 Virginia Cunningham <https://orcid.org/0000-0003-2292-0441>
 Antonino D'Ai <https://orcid.org/0000-0002-5042-1036>
 Dmitry A. Duv <https://orcid.org/0000-0001-5060-8733>
 Sara Frederick <https://orcid.org/0000-0001-9676-730X>
 Pradip Gatkine <https://orcid.org/0000-0002-1955-2230>
 Shaon Ghosh <https://orcid.org/0000-0001-9901-6253>
 Daniel A. Goldstein <https://orcid.org/0000-0003-3461-8661>
 V. Zach Golkhou <https://orcid.org/0000-0001-8205-2506>
 Ariel Goobar <https://orcid.org/0000-0002-4163-4996>
 Matthew J. Graham <https://orcid.org/0000-0002-3168-0139>
 Hidekazu Hanayama <https://orcid.org/0000-0001-8221-6048>
 Saurabh W. Jha <https://orcid.org/0000-0001-8738-6011>
 Albert K. H. Kong <https://orcid.org/0000-0002-5105-344X>
 David L. Kaplan <https://orcid.org/0000-0001-6295-2881>
 Shrinivas R. Kulkarni <https://orcid.org/0000-0001-5390-8563>
 Thomas Kupfer <https://orcid.org/0000-0002-6540-1484>
 Frank J. Masci <https://orcid.org/0000-0002-8532-9395>
 Paolo Mazzali <https://orcid.org/0000-0001-6876-8284>
 James D. Neill <https://orcid.org/0000-0002-0466-1119>
 Chow-Choong Ngeow <https://orcid.org/0000-0001-8771-7554>

M. Pavana <https://orcid.org/0000-0002-0000-1543>
 Eran O. Ofek <https://orcid.org/0000-0002-6786-8774>
 Reed Riddle <https://orcid.org/0000-0002-0387-370X>
 Mickael Rigault <https://orcid.org/0000-0002-8121-2560>
 David L. Shupe <https://orcid.org/0000-0003-4401-0430>
 Jesper Sollerman <https://orcid.org/0000-0003-1546-6615>
 Eleonora Troja <https://orcid.org/0000-0002-1869-7817>
 Gaurav Waratkar <https://orcid.org/0000-0003-3630-9440>
 Yoichi Yatsu <https://orcid.org/0000-0003-1890-3913>

References

- Aasi, J., Abbott, B. P., Abbott, R., et al. 2015, *CQGra*, 32, 074001
 Abbott, B. P., Abbott, R., Abbott, T. D., et al. 2017a, *PhRvL*, 119, 161101
 Abbott, B. P., Abbott, R., Abbott, T. D., et al. 2017b, *ApJL*, 848, L13
 Abbott, B. P., Abbott, R., Abbott, T. D., et al. 2017c, *ApJL*, 850, L39
 Abbott, B. P., Abbott, R., Abbott, T. D., et al. 2017d, *Natur*, 551, 85
 Abbott, B. P., Abbott, R., Abbott, T. D., et al. 2018, *LRR*, 21, 3
 Abbott, B. P., Abbott, R., Abbott, T. D., et al. 2019, *PhRvX*, 9, 031040
 Acernese, F., Agathos, M., Agatsuma, K., et al. 2015, *CQGra*, 32, 024001
 Aghanim, N., Akrami, Y., Ashdown, M., et al. 2018, arXiv:1807.06209
 Ahumada, T., Coughlin, M. W., Cenko, S. B., et al. 2018, GCN, 23515, 1
 Ahumada, T., Coughlin, M. W., Staats, K., et al. 2019b, GCN, 24320, 1
 Ahumada, T., Coughlin, M. W., Staats, K., et al. 2019c, GCN, 24343, 1
 Ahumada, T., Coughlin, M. W., Staats, K., & Dekany, R. G. 2019a, GCN, 24198, 1
 Alexander, K. D., Berger, E., Fong, W., et al. 2017, *ApJL*, 848, L21
 Anand, S., Kasliwal, M., Coughlin, M. W., et al. 2019, GCN, 24311, 1
 Andreoni, I., Anand, S., & Kasliwal, M. 2019a, GCN, 24349, 1
 Andreoni, I., & Bellm, E. 2019, GCN, 24356, 1
 Andreoni, I., Cenko, S. B., Masci, F., & Graham, M. 2019b, GCN, 24302, 1
 Arcavi, I., Hosseinzadeh, G., Howell, D. A., et al. 2017b, *Natur*, 551, 64
 Arcavi, I., Howell, D. A., McCully, C., et al. 2019, GCN, 24307, 1
 Arcavi, I., McCully, C., Hosseinzadeh, G., et al. 2017a, *ApJL*, 848, L33
 Ascenzi, S., Coughlin, M. W., Dietrich, T., et al. 2019, *MNRAS*, 486, 672
 Bauswein, A., Baumgarte, T. W., & Janka, H.-T. 2013, *PhRvL*, 111, 131101
 Bauswein, A., Just, O., Janka, H.-T., & Stergioulas, N. 2017, *ApJL*, 850, L34
 Bellm, E. C., Kulkarni, S. R., Graham, M. J., et al. 2018, *PASP*, 131, 018002
 Bhalerao, V., Kumar, H., Karambelkar, V., et al. 2019, GCN, 24201, 1
 Blagorodnova, N., Neill, J. D., Walters, R., et al. 2018, *PASP*, 130, 035003
 Bloom, J. S., Zucker, C., Schlafly, E., et al. 2019, GCN, 24337, 1
 Breeveld, A. A., Kuin, N. P. M., Marshall, F. E., et al. 2019, GCN, 24296, 1
 Buckley, D., Jha, S. W., Cooke, J., & Mogotsi, M. 2019, GCN, 24205, 1
 Burke, J., Hiramatsu, D., Arcavi, I., et al. 2019, GCN, 24206, 1
 Carini, R., Izzo, L., Palazzi, E., et al. 2019, GCN, 24252, 1
 Castro-Tirado, A. J., Hu, Y. D., Li, X. Y., et al. 2019, GCN, 24214, 1
 Cenko, B. S., Coughlin, M. W., Ghosh, S., et al. 2018, GCN, 22969, 1
 Chambers, K. C., Magnier, E. A., Metcalfe, N., et al. 2016, arXiv:1612.05560
 Chang, S. W., Wolf, C., Onken, C. A., et al. 2019a, GCN, 24260, 1
 Chang, S.-W., Wolf, C., Onken, C. A., Luvaul, L., & Scott, S. 2019b, GCN, 24325, 1
 Chornock, R., Berger, E., Kasen, D., et al. 2017, *ApJL*, 848, L19
 Cook, D. O., Kasliwal, M. M., Van Sistine, A., et al. 2019, *ApJ*, 880, 7
 Coughlin, M. W., Ahumada, T., Cenko, S. B., et al. 2019a, *PASP*, 131, 048001
 Coughlin, M. W., Ahumada, T., Cenko, S. B., et al. 2018d, GCN, 23379, 1
 Coughlin, M. W., Anand, S., & Ahumada, T. 2019b, GCN, 24223, 1
 Coughlin, M. W., Antier, S., Corre, D., et al. 2019c, *MNRAS*, 489, 5775
 Coughlin, M. W., Cenko, S. B., Ahumada, T., et al. 2018c, GCN, 23324, 1
 Coughlin, M. W., Dekany, R. G., Duv, D. A., et al. 2019d, *MNRAS*, 485, 1412
 Coughlin, M. W., Dietrich, T., Heinzel, J., et al. 2019e, arXiv:1908.00889
 Coughlin, M. W., Dietrich, T., Margalit, B., & Metzger, B. D. 2019f, *MNRAS*, 489, L91
 Coughlin, M. W., Singer, L. P., Ahumada, T., et al. 2018b, GCN, 22871, 1
 Coughlin, M. W., Singer, L. P., Cenko, S. B., et al. 2018e, GCN, 22739, 1
 Coughlin, M. W., Tao, D., Chan, M. L., et al. 2018a, *MNRAS*, 478, 692
 Coulter, D. A., Foley, R. J., Kilpatrick, C. D., et al. 2017, *Sci*, 358, 1556
 Cowperthwaite, P. S., Berger, E., Villar, V. A., et al. 2017, *ApJL*, 848, L17
 Crawford, S. M., Still, M., Schellart, P., et al. 2010, *Proc. SPIE*, 7737, 25
 De, K., Hankins, M., Adams, S. M., et al. 2019, GCN, 24306, 1
 Dekany, R., Smith, R. M., Riddle, R., et al. 2019, *PASP*, submitted
 Dichiaro, S., Gatkine, P., Durbak, J., et al. 2019, GCN, 24220, 1
 Dimitriadis, G., Jones, D. O., Siebert, M. R., et al. 2019, GCN, 24358, 1

- Drout, M. R., Piro, A. L., Shappee, B. J., et al. 2017, *Sci*, **358**, 1570
- Duev, D. A., Mahabal, A., Masci, F. J., et al. 2019, *MNRAS*, **489**, 3582
- Evans, P. A., Cenko, S. B., Kennea, J. A., et al. 2017, *Sci*, **358**, 1565
- Finn, L. S., & Chernoff, D. F. 1993, *PhRvD*, **47**, 2198
- Flaugher, B., Diehl, H. T., Honscheid, K., et al. 2015, *AJ*, **150**, 150
- Flewelling, H. 2018, AAS Meeting, **231**, 436.01
- Goldstein, A., Veres, P., Burns, E., et al. 2017, *ApJL*, **848**, L14
- Golkhou, V. Z., Butler, N. R., Strausbaugh, R., et al. 2018, *ApJ*, **857**, 81
- Graham, M. J., Kulkarni, S. R., Bellm, E. C., et al. 2019, *PASP*, **131**, 078001
- Haggard, D., Nynka, M., Ruan, J. J., et al. 2017, *ApJL*, **848**, L25
- Hallinan, G., Corsi, A., Mooley, K. P., et al. 2017, *Sci*, **358**, 1579
- Hiramatsu, D., Arcavi, I., Burke, J., et al. 2019, GCN, 24194, 1
- Hosseinzadeh, G., Cowperthwaite, P. S., Gomez, S., et al. 2019, *ApJL*, **880**, L4
- Hotokezaka, K., Nakar, E., Gottlieb, O., et al. 2018, arXiv:1806.10596
- Hu, Y. D., Castro-Tirado, A. J., Li, X. Y., et al. 2019, GCN, 24324, 1
- Im, M., Kim, J., Paek, G. S. H., et al. 2019, GCN, 24318, 1
- Issa, L., Carini, R., Benetti, S., et al. 2019, GCN, 24208, 1
- Jencson, J., De, K., Anand, S., et al. 2019, GCN, 24233, 1
- Jonker, P., Mata-Sanchez, D., Fraser, M., et al. 2019, GCN, 24221, 1
- Just, O., Bauswein, A., Pulpillo, R. A., Goriely, S., & Janka, H.-T. 2015, *MNRAS*, **448**, 541
- Kaiser, N., Burgett, W., Chambers, K., et al. 2010, *Proc. SPIE*, **7733**, 77330E
- Kann, D. A., Thoene, C., Stachie, C., et al. 2019, GCN, 24459, 1
- Kasliwal, M. M., Cannella, C., Bagdasaryan, A., et al. 2019b, *PASP*, **131**, 038003
- Kasliwal, M. M., Coughlin, M. W., Bellm, E. C., et al. 2019c, GCN, 24191, 1
- Kasliwal, M. M., Kasen, D., Lau, R. M., et al. 2019a, *MNRAS*, in press
- Kasen, D., Metzger, B., Barnes, J., Quataert, E., & Ramirez-Ruiz, E. 2017, *Natur*, **551**, 80
- Kasliwal, M. M., Nakar, E., Singer, L. P., et al. 2017, *Sci*, **358**, 1559
- Kasliwal, M. M., & Nissanke, S. 2014, *ApJL*, **789**, L5
- Kilpatrick, C. D., Foley, R. J., Kasen, D., et al. 2017, *Sci*, **358**, 1583
- Kong, A., Tan, H.-J., Yu, P.-C., Ngeow, C.-C., & Ip, W.-H. 2019, GCN, 24301, 1
- Kostrzewa-Rutkowska, Z., Hodgkin, S., Delgado, A., et al. 2019, GCN, 24354, 1
- Lattimer, J. M., & Schramm, D. N. 1974, *ApJL*, **192**, L145
- Li, L.-X., & Paczynski, B. 1998, *ApJL*, **507**, L59
- Li, W., Leaman, J., Chornock, R., et al. 2011, *MNRAS*, **412**, 1441
- LIGO Scientific Collaboration & Virgo Collaboration 2019a, GCN, 24141, 1
- LIGO Scientific Collaboration & Virgo Collaboration 2019b, GCN, 24237, 1
- LIGO Scientific Collaboration & Virgo Collaboration 2019c, GCN, 24377, 1
- LIGO Scientific Collaboration & Virgo Collaboration 2019d, GCN, 24098, 1
- LIGO Scientific Collaboration & Virgo Collaboration 2019e, GCN, 24069, 1
- LIGO Scientific Collaboration & Virgo Collaboration 2019f, GCN, 24168, 1
- LIGO Scientific Collaboration & Virgo Collaboration 2019g, GCN, 24228, 1
- LIGO Scientific Collaboration & Virgo Collaboration 2019h, GCN, 24228, 1
- Lipunov, V., Gorbvskoy, E., Tyurina, N., et al. 2019a, GCN, 24241, 1
- Lipunov, V., Tyurina, N., Gorbvskoy, E., et al. 2019b, GCN, 24326, 1
- Lipunov, V. M., Gorbvskoy, E., Kornilov, V. G., et al. 2017, *ApJL*, **850**, L1
- Mahabal, A., Rebbapragada, U., Walters, R., et al. 2019, *PASP*, **131**, 038002
- Margutti, R., Berger, E., Fong, W., et al. 2017, *ApJL*, **848**, L20
- Masci, F. J., Laher, R. R., Rusholme, B., et al. 2018, *PASP*, **131**, 018003
- McBrien, O., Smartt, S., Smith, K. W., et al. 2019, GCN, 24197, 1
- McCully, C., Hiramatsu, D., Howell, D. A., et al. 2017, *ApJL*, **848**, L32
- McCully, C., Hiramatsu, D., Howell, D. A., et al. 2019, GCN, 24295, 1
- Mészáros, P., & Rees, M. J. 1998, *ApJL*, **502**, L105
- Metzger, B. D. 2017, *LRR*, **20**, 3
- Metzger, B. D., Martínez-Pinedo, G., Darbha, S., et al. 2010, *MNRAS*, **406**, 2650
- Moore, A. M., & Kasliwal, M. M. 2019, *NatAs*, **3**, 109
- Morihana, K., Jian, M., & Nagayama, T. 2019a, GCN, 24219, 1
- Morihana, K., Jian, M., & Nagayama, T. 2019b, GCN, 24328, 1
- Morokuma, T., Ohta, K., Yoshida, M., et al. 2019, GCN, 24230, 1
- Muthukrishna, D., Narayan, G., Mandel, K. S., Biswas, R., & Hložek, R. 2019, *PASP*, **131**, 118002
- Nicholl, M., Berger, E., Kasen, D., et al. 2017, *ApJL*, **848**, L18
- Nicholl, M., Cartier, R., Pelisoli, I., et al. 2019, GCN, 24321, 1
- Nissanke, S., Kasliwal, M., & Georgieva, A. 2013, *ApJ*, **767**, 124
- Nordin, J., Brinnel, V., van Santen, J., et al. 2019, arXiv:1904.05922
- O'Brien, P. 2018, in 42nd COSPAR Scientific Assembly, Abstract E1.15-18-18
- Oke, J. B., & Gunn, J. E. 1982, *PASP*, **94**, 586
- Palmese, A., Soares-Santos, M., Santana-Silva, L., et al. 2019, GCN, 24312, 1
- Pavana, M., Kiran, B., Anupama, G., & Bhalerao, V. 2019, GCN, 24200, 1
- Perley, D. A., & Copperwheat, C. M. 2019, GCN, 24202, 1
- Perley, D. A., Copperwheat, C. M., & Taggart, K. L. 2019a, GCN, 24204, 1
- Perley, D. A., Copperwheat, C. M., & Taggart, K. L. 2019b, GCN, 24314, 1
- Perley, D. A., Copperwheat, C. M., & Taggart, K. L. 2019c, GCN, 24314, 1
- Pian, E., D'Avanzo, P., Benetti, S., et al. 2017, *Natur*, **551**, 67
- Piascik, A., Steele, I. A., Bates, S. D., et al. 2014, *Proc. SPIE*, **9147**, 91478H
- Radice, D., Perego, A., Zappa, F., & Bernuzzi, S. 2018, *ApJL*, **852**, L29
- Rhodes, L., Fender, R., Williams, D., et al. 2019, GCN, 24226, 1
- Richardson, D., III, R. L. J., Wright, J., & Maddox, L. 2014, *AJ*, **147**, 118
- Rigault, M., Neill, J. D., Blagorodnova, N., et al. 2019, *A&A*, **627**, A115
- Roberts, L. F., Kasen, D., Lee, W. H., & Ramirez-Ruiz, E. 2011, *ApJL*, **736**, L21
- Roberts, L. F., Lippuner, J., Duez, M. D., et al. 2017, *MNRAS*, **464**, 3907
- Rosswog, S. 2015, *IJMPD*, **24**, 1530012
- Rosswog, S., Feindt, U., Korobkin, O., et al. 2017, *CQGra*, **34**, 104001
- Savchenko, V., Ferrigno, C., Kuulkers, E., et al. 2017, *ApJL*, **848**, L15
- Schady, P., Chen, T. W., Schweyer, T., Malesani, D. B., & Bolmer, J. 2019, GCN, 24229, 1
- Shappee, B. J., Kochanek, C. S., Stanek, K. Z., et al. 2019, GCN, 24313, 1
- Shappee, B. J., Prieto, J. L., Grupe, D., et al. 2014, *ApJ*, **788**, 48
- Shappee, B. J., Simon, J. D., Drout, M. R., et al. 2017, *Sci*, **358**, 1574
- Singer, L. P., Cenko, S. B., Kasliwal, M. M., et al. 2013, *ApJL*, **776**, L34
- Singer, L. P., Kasliwal, M. M., Cenko, S. B., et al. 2015, *ApJ*, **806**, 52
- Smartt, S. J., Chen, T.-W., Jerkstrand, A., et al. 2017, *Natur*, **551**, 75
- Smith, K. W., Young, D. R., McBrien, O., et al. 2019, GCN, 24210, 1
- Smith, M. P., Nordisiek, K. H., Burgh, E. B., et al. 2006, *Proc. SPIE*, **6269**, 62692A
- Steele, I. A., Smith, R. J., Rees, P. C., et al. 2004, *Proc. SPIE*, **5489**, 679
- Tachibana, Y., & Miller, A. A. 2018, *PASP*, **130**, 128001
- Tan, H.-J., Yu, P.-C., Kong, A., et al. 2019a, GCN, 24274, 1
- Tan, H.-J., Yu, P.-C., Ngeow, C.-C., & Ip, W.-H. 2019b, GCN, 24193, 1
- Tanvir, N. R., Gonzalez-Fernandez, C., Levan, A. J., Malesani, D. B., & Evans, P. A. 2019, GCN, 24334, 1
- Tonry, J. L., Denneau, L., Heinze, A. N., et al. 2018, *PASP*, **130**, 064505
- Troja, E., Piro, L., van Eerten, H., et al. 2017, *Natur*, **551**, 71
- Troja, E., Watson, A. M., Becerra, R. L., et al. 2019, GCN, 24335, 1
- Utsumi, Y., Tanaka, M., Tominaga, N., et al. 2017, *PASJ*, **69**, 101
- Valenti, S., Sand, D. J., Yang, S., et al. 2017, *ApJL*, **848**, L24
- Waratkar, G., Kumar, H., Bhalerao, V., Stanzin, J., & Anupama, G. C. 2019, GCN, 24304, 1
- West, A. A., Morgan, D. P., Bochanski, J. J., et al. 2011, *AJ*, **141**, 97
- Wiersema, K., Levan, A. J., Fraser, M., et al. 2019, GCN, 24209, 1
- Wijers, R. A. M. J., Rees, M. J., & Mészáros, P. 1997, *MNRAS*, **288**, L51
- Wright, E. L., Eisenhardt, P. R. M., Mainzer, A. K., et al. 2010, *AJ*, **140**, 1868
- Wu, M.-R., Fernández, R., Martínez-Pinedo, G., & Metzger, B. D. 2016, *MNRAS*, **463**, 2323



Evidence for Late-stage Eruptive Mass Loss in the Progenitor to SN2018gep, a Broad-lined Ic Supernova: Pre-explosion Emission and a Rapidly Rising Luminous Transient

Anna Y. Q. Ho¹ , Daniel A. Goldstein^{1,27} , Steve Schulze² , David K. Khatami³ , Daniel A. Perley⁴ , Mattias Ergon⁵, Avishay Gal-Yam² , Alessandra Corsi⁶ , Igor Andreoni¹ , Cristina Barbarino⁵, Eric C. Bellm⁷ , Nadia Blagorodnova⁸ , Joe S. Bright⁹ , E. Burns¹⁰, S. Bradley Cenko^{11,12} , Virginia Cunningham¹³ , Kishalay De¹ , Richard Dekany¹⁴, Alison Dugas¹, Rob P. Fender⁹, Claes Fransson⁵ , Christoffer Fremling¹⁵ , Adam Goldstein¹⁶ , Matthew J. Graham¹⁵ , David Hale¹⁴, Assaf Horesh¹⁷, Tiara Hung¹⁸, Mansi M. Kasliwal¹ , N. Paul M. Kuin¹⁹, S. R. Kulkarni¹ , Thomas Kupfer²⁰ , Ragnhild Lunnan⁵ , Frank J. Masci²¹ , Chow-Choong Ngeow²² , Peter E. Nugent²³ , Eran O. Ofek² , Maria T. Patterson⁷ , Glen Petitpas²⁴, Ben Rusholme²¹, Hanna Sai²⁵, Itai Sfaradi¹⁷, David L. Shupe²¹, Jesper Sollerman⁵ , Maayane T. Soumagnac² , Yutaro Tachibana²⁶, Francesco Taddia⁵, Richard Walters¹, Xiaofeng Wang²⁵ , Yuhan Yao¹ , and Xinhan Zhang²⁵

¹ Cahill Center for Astrophysics, California Institute of Technology, MC 249-17, 1200 E California Boulevard, Pasadena, CA 91125, USA

² Department of Particle Physics and Astrophysics, Weizmann Institute of Science, 234 Herzl Street, 76100 Rehovot, Israel

³ Department of Astronomy, University of California, Berkeley, CA 94720, USA

⁴ Astrophysics Research Institute, Liverpool John Moores University, IC2, Liverpool Science Park, 146 Brownlow Hill, Liverpool L3 5RF, UK

⁵ The Oskar Klein Centre & Department of Astronomy, Stockholm University, AlbaNova, SE-106 91 Stockholm, Sweden

⁶ Department of Physics and Astronomy, Texas Tech University, Box 1051, Lubbock, TX 79409-1051, USA

⁷ DIRAC Institute, Department of Astronomy, University of Washington, 3910 15th Avenue NE, Seattle, WA 98195, USA

⁸ Department of Astrophysics/IMAPP, Radboud University, Nijmegen, The Netherlands

⁹ Department of Physics, University of Oxford, Denys Wilkinson Building, Keble Road, Oxford OX1 3RH, UK

¹⁰ NASA Postdoctoral Program Fellow, Goddard Space Flight Center, Greenbelt, MD 20771, USA

¹¹ Astrophysics Science Division, NASA Goddard Space Flight Center, Mail Code 661, Greenbelt, MD 20771, USA

¹² Joint Space-Science Institute, University of Maryland, College Park, MD 20742, USA

¹³ Astronomy Department, University of Maryland, College Park, MD 20742, USA

¹⁴ Caltech Optical Observatories, California Institute of Technology, MC 11-17, 1200 E. California Boulevard, Pasadena, CA 91125, USA

¹⁵ Division of Physics, Mathematics and Astronomy, California Institute of Technology, Pasadena, CA 91125, USA

¹⁶ Science and Technology Institute, Universities Space Research Association, Huntsville, AL 35805, USA

¹⁷ Racah Institute of Physics, Hebrew University, Jerusalem 91904, Israel

¹⁸ Department of Astronomy and Astrophysics, University of California, Santa Cruz, CA 95064, USA

¹⁹ Mullard Space Science Laboratory, University College London, Holmbury St. Mary, Dorking, Surrey RH5 6NT, UK

²⁰ Kavli Institute for Theoretical Physics, University of California, Santa Barbara, CA 93106, USA

²¹ IPAC, California Institute of Technology, 1200 E. California Boulevard, Pasadena, CA 91125, USA

²² Graduate Institute of Astronomy, National Central University, 32001, Taiwan

²³ Lawrence Berkeley National Laboratory, 1 Cyclotron Road, Berkeley, CA 94720, USA

²⁴ Harvard-Smithsonian Center for Astrophysics, 60 Garden Street, Cambridge, MA 02138, USA

²⁵ Physics Department/Tsinghua Center for Astrophysics, Tsinghua University, Beijing, 100084, People's Republic of China

²⁶ Department of Physics, Tokyo Institute of Technology, 2-12-1 Ookayama, Meguro-ku, Tokyo 152-8551, Japan

Received 2019 April 24; revised 2019 September 17; accepted 2019 October 1; published 2019 December 18

Abstract

We present detailed observations of ZTF18abukavn (SN2018gep), discovered in high-cadence data from the Zwicky Transient Facility as a rapidly rising (1.4 ± 0.1 mag hr⁻¹) and luminous ($M_{g,\text{peak}} = -20$ mag) transient. It is spectroscopically classified as a broad-lined stripped-envelope supernova (Ic-BL SN). The high peak luminosity ($L_{\text{bol}} \gtrsim 3 \times 10^{44}$ erg s⁻¹), the short rise time ($t_{\text{rise}} = 3$ days in g band), and the blue colors at peak ($g-r \sim -0.4$) all resemble the high-redshift Ic-BL iPTF16asu, as well as several other unclassified fast transients. The early discovery of SN2018gep (within an hour of shock breakout) enabled an intensive spectroscopic campaign, including the highest-temperature ($T_{\text{eff}} \gtrsim 40,000$ K) spectra of a stripped-envelope SN. A retrospective search revealed luminous ($M_g \sim M_r \approx -14$ mag) emission in the days to weeks before explosion, the first definitive detection of precursor emission for a Ic-BL. We find a limit on the isotropic gamma-ray energy release $E_{\gamma,\text{iso}} < 4.9 \times 10^{48}$ erg, a limit on X-ray emission $L_X < 10^{40}$ erg s⁻¹, and a limit on radio emission $\nu L_\nu \lesssim 10^{37}$ erg s⁻¹. Taken together, we find that the early (<10 days) data are best explained by shock breakout in a massive shell of dense circumstellar material ($0.02 M_\odot$) at large radii (3×10^{14} cm) that was ejected in eruptive pre-explosion mass-loss episodes. The late-time (>10 days) light curve requires an additional energy source, which could be the radioactive decay of Ni-56.

Key words: methods: observational – shock waves – stars: mass-loss – supernovae: individual – surveys

Supporting material: machine-readable tables

²⁷ Hubble Fellow.

1. Introduction

Recent discoveries by optical time-domain surveys challenge our understanding of how energy is deposited and transported in stellar explosions (Kasen 2017). For example, over 50 transients have been discovered with rise times and peak luminosities too rapid and too high, respectively, to be explained by radioactive decay (Poznanski et al. 2010; Drout et al. 2014; Arcavi et al. 2016; Shivvers et al. 2016; Tanaka et al. 2016; Pursiainen et al. 2018; Rest et al. 2018). Possible powering mechanisms include interaction with extended circumstellar material (CSM; Chevalier & Irwin 2011), and energy injection from a long-lived central engine (Kasen & Bildsten 2010; Woosley 2010; Kasen et al. 2016). These models have been difficult to test because the majority of fast-luminous transients have been discovered *post facto* and located at cosmological distances ($z \sim 0.1$).

The discovery of iPTF16asu (Wang et al. 2017; Whitesides et al. 2017) in the intermediate Palomar Transient Factory (iPTF; Law et al. 2009) showed that at least some of these fast-luminous transients are energetic (10^{52} erg) high-velocity (“broad-lined”; $v \gtrsim 20,000$ km s $^{-1}$) stripped-envelope (Ic) supernovae (Ic-BL SNe). The light curve of iPTF16asu was unusual among Ic-BL SNe in being inconsistent with ^{56}Ni -decay (Cano 2013; Taddia et al. 2019). Suggested power sources include energy injection by a magnetar, ejecta-CSM interaction, cooling-envelope emission, and an engine-driven explosion similar to low-luminosity gamma-ray bursts—or some combination thereof. Unfortunately, the high redshift ($z = 0.187$) precluded a definitive conclusion.

Today, optical surveys such as ATLAS (Tonry et al. 2018) and the Zwicky Transient Facility (ZTF; Bellm et al. 2019a; Graham et al. 2019) have the areal coverage to discover rare transients *nearby*, as well as the cadence to discover transients when they are young (<1 day). For example, the recent discovery of AT2018cow at 60 Mpc (Smartt et al. 2018; Prentice et al. 2018) represented an unprecedented opportunity to study a fast-luminous optical transient up close, in detail, and in real time. Despite an intense multiwavelength observing campaign, the nature of AT2018cow remains unknown—possibilities include an engine-powered stellar explosion (Prentice et al. 2018; Ho et al. 2019; Margutti et al. 2019; Perley et al. 2019), the tidal disruption of a white dwarf by an intermediate-mass black hole (Kuin et al. 2019; Perley et al. 2019), and an electron capture SN (Lyutikov & Toonen 2019). Regardless of the origin, it is clear that the explosion took place within dense material (Ho et al. 2019; Margutti et al. 2019; Perley et al. 2019) confined to $\lesssim 10^{16}$ cm (Ho et al. 2019).

Here we present SN2018gep, discovered as a rapidly rising (1.4 ± 0.1 mag hr $^{-1}$) and luminous ($M_{g,\text{peak}} = -20$) transient in high-cadence data from ZTF (Ho et al. 2018c). The high inferred velocities ($>20,000$ km s $^{-1}$), the spectroscopic evolution from a blue continuum to a Ic-BL SN (Costantin et al. 2018), and the rapid rise ($t_{\text{rise}} = 3$ days in g band) to high peak luminosity ($L_{\text{bol}} \gtrsim 3 \times 10^{44}$ erg s $^{-1}$) all suggest that SN2018gep is a low-redshift ($z = 0.03154$) analog to iPTF16asu. The early discovery enabled an intensive follow-up campaign within the first day of the explosion, including the highest-temperature ($T_{\text{eff}} \gtrsim 40,000$ K) spectra of a stripped-envelope SN to date. A retrospective search in ZTF data revealed the first definitive detection of pre-explosion activity in a Ic-BL.

The structure of the paper is as follows. We present our radio through X-ray data in Section 2. In Section 3 we outline basic properties of the explosion and its host galaxy. In Section 4 we attribute the power source for the light curve to shock breakout

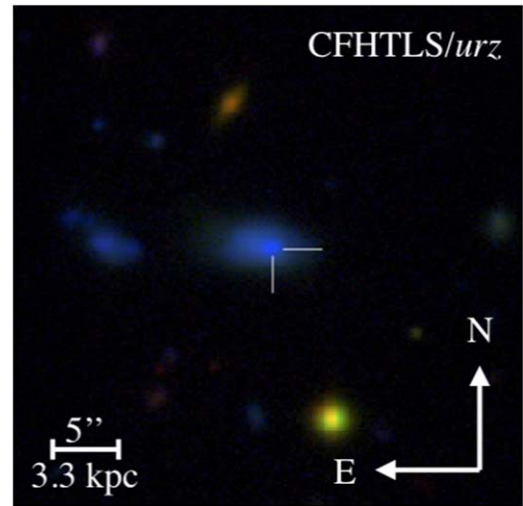


Figure 1. The position of SN2018gep (white crosshairs) in its host galaxy. Images from the Canada–France–Hawaii Telescope Legacy Survey (2004–2012), combined using the prescription in Lupton et al. (2004).

in extended CSM. In Section 5 we compare SN2018gep to unidentified fast-luminous transients at high redshift. Finally, in Section 6 we summarize our findings and look to the future. Throughout the paper, absolute times are reported in UTC and relative times are reported with respect to t_0 , which is defined in Section 2.1. We assume a standard Λ CDM cosmology (Planck Collaboration et al. 2016).

2. Observations

2.1. ZTF Discovery

ZTF observing time is divided between several different surveys, conducted using a custom mosaic camera (Dekany et al. 2016) on the 48 inch Samuel Oschin Telescope (P48) at Palomar Observatory. See Bellm et al. (2019a) for an overview of the observing system, Bellm et al. (2019b) for a description of the surveys and scheduler, and Masci et al. (2019) for details of the image processing system.

Every 5σ point-source detection is saved as an “alert.” Alerts are distributed in avro format (Patterson et al. 2019) and can be filtered based on a machine learning–based real-bogus metric (Duv et al. 2019; Mahabal et al. 2019), light-curve properties, and host characteristics (including a star-galaxy classifier; Tachibana & Miller 2018). The ZTF collaboration uses a web-based system called the GROWTH marshal (Kasliwal et al. 2019) to identify and keep track of transients of interest.

ZTF18abukavn was discovered in an image obtained at UT 2018 September 9 03:55:18 (start of exposure) as part of the ZTF extragalactic high-cadence partnership survey, which covers 1725 deg 2 in six visits (3g, 3r) per night (Bellm et al. 2019b). The discovery magnitude was $r = 20.5 \pm 0.3$ mag, and the source position was measured to be $\alpha = 16^{\text{h}}43^{\text{m}}48.22^{\text{s}}$, $\delta = +41^{\text{d}}02^{\text{m}}43.4^{\text{s}}$ (J2000), coincident with a compact galaxy (Figure 1) at $z = 0.03154$ or $d \approx 143$ Mpc. As described in Section 2.3, the redshift was unknown at the time of discovery; we measured it from narrow galaxy emission lines in our follow-up spectra. The host redshift along with key observational properties of the transient are listed in Table 1.

As shown in Figure 2, the source brightened by over two magnitudes within the first three hours. These early detections passed a filter written in the GROWTH marshal that was

Table 1
Key Observational Properties of SN2018gcp and Its Host Galaxy

Parameter	Value	Notes
z	0.03154	From narrow host emission lines
L_{peak}	$\gtrsim 3 \times 10^{43}$ erg	Peak UVOIR bolometric luminosity
t_{rise}	0.5–3 days	Time from t_0 to L_{peak}
E_{rad}	10^{50} erg	UVOIR output, $\Delta t = 0.5$ –40 days
$M_{r,\text{prog}}$	–15	Peak luminosity of pre-explosion emission
$E_{\gamma,\text{iso}}$	$< 4.9 \times 10^{48}$	Limit on prompt gamma-ray emission from <i>Fermi</i> /GBM
L_X	$< 2.5 \times 10^{41}$ erg s $^{-1}$	X-ray upper limit from <i>Swift</i> /XRT at $\Delta t = 0.4$ –14 days
	$< 10^{40}$ erg s $^{-1}$	X-ray upper limit from <i>Chandra</i> at $\Delta t = 15$ and $\Delta t = 70$ days
νL_ν	$\approx 10^{37}$ erg s $^{-1}$	9 GHz radio luminosity from VLA at $\Delta t = 5$ and $\Delta t = 16$
$M_{*,\text{host}}$	$1.3 \times 10^8 M_\odot$	Host stellar mass
SFR_{host}	$0.12 M_\odot \text{ yr}^{-1}$	Host star formation rate
Host metallicity	1/5 solar	Oxygen abundance on O3N2 scale

designed to find young SNe. We announced the discovery and fast rise via the Astronomer’s Telegram (Ho et al. 2018c), and reported the object to the IAU Transient Server (TNS²⁸), where it received the designation SN2018gcp.

We triggered ultraviolet (UV) and optical observations with the UV/Optical Telescope (UVOT; Roming et al. 2005) aboard the *Neil Gehrels Swift Observatory* (Gehrels et al. 2004), and observations began 10.2 hr after the ZTF discovery (Schulze et al. 2018a). A search of IceCube data found no temporally coincident high-energy neutrinos (Blaufuss 2018).

Over the first two days, the source brightened by two additional magnitudes. A linear fit to the early g -band photometry gives a rise of 1.4 ± 0.1 mag hr $^{-1}$. This rise rate is second only to the IIb SN 16 gkg (Bersten et al. 2018) but several orders of magnitude more luminous at discovery ($M_{g,\text{disc}} \approx -17$ mag).

To establish a reference epoch, we fit a second-order polynomial to the first three days of the g -band light curve in flux space, and define t_0 as the time at which the flux is zero. This gives t_0 as being 25 ± 2 minutes prior to the first detection, or $t_0 \approx$ UT 2018 September 9 03:30. The physical interpretation of t_0 is not straightforward, since the light curve flattens out at early times (see Figures 2 and 3). We proceed using t_0 as a reference epoch but caution against assigning it physical meaning.

2.2. Photometry

From $\Delta t \approx 1$ day to $\Delta t \approx 60$ days, we conducted a photometric follow-up campaign at UV and optical wavelengths using *Swift*/UVOT, the Spectral Energy Distribution Machine (SEDM; Blagorodnova et al. 2018) mounted on the automated 60 inch telescope at Palomar (P60; Cenko et al. 2006), the optical imager (IO:O) on the Liverpool Telescope (LT; Steele et al. 2004), and the Lulin 1 m Telescope (LOT).

Basic reductions for the LT IO:O imaging were performed by the LT pipeline.²⁹ Digital image subtraction and photometry for the SEDM, LT, and LOT imaging was performed using the

Fremling Automated Pipeline (FPipe; Fremling et al. 2016). FPipe performs calibration and host subtraction against Sloan Digital Sky Survey reference images and catalogs (SDSS; Ahn et al. 2014). SEDM spectra were reduced using *pysedm* (Rigault et al. 2019).

The UVOT data were retrieved from the NASA *Swift* Data Archive³⁰ and reduced using standard software distributed with HEASOFT version 6.19.³¹ Photometry was measured using UVOTMAGHIST with a 3'' circular aperture. To remove the host contribution, we obtained a final epoch in all broadband filters on UT 2018 October 18 and built a host template using UVOTISUM and UVOTSOURCE with the same aperture used for the transient.

Figure 3 shows the full set of light curves, with a cross denoting the peak of the r -band light curve for reference. The position of the cross is simply the time and magnitude of our brightest r -band measurement, which is a good estimate given our cadence. The photometry is listed in Table 5 in Appendix A. Note that despite the steep spectral energy distribution (SED) at early times, the K-correction is minimal. We estimate that the effect is roughly 0.03 mag, which is well within our uncertainties. In Figure 4 we compare the rise time and peak absolute magnitude to other rapidly evolving transients from the literature.

2.3. Spectroscopy

The first spectrum was taken 0.7 day after discovery by the Spectrograph for the Rapid Acquisition of Transients (SPRAT; Piascik et al. 2014) on the LT. The spectrum showed a blue continuum with narrow galaxy emission lines, establishing this as a luminous transient ($M_{g,\text{peak}} = -19.7$). Twenty-three optical spectra were obtained from $\Delta t = 0.7$ –61.1 days using SPRAT, the Andalusia Faint Object Spectrograph and Camera (ALFOC) on the Nordic Optical Telescope (NOT), the Double Spectrograph (DBSP; Oke & Gunn 1982) on the 200 inch Hale telescope at Palomar Observatory, the Low Resolution Imaging Spectrometer (LRIS; Oke et al. 1995) on the Keck I 10 m telescope, and the Xinglong 2.16 m telescope (XLT+BFOSC) of NAOC, China (Wang et al. 2018). As discussed in Section 3.2, the early $\Delta t < 5$ days spectra show broad absorption features that evolve redward with time, which we attribute to carbon and oxygen. By $\Delta t \sim 8$ days, the spectrum resembles a stripped-envelope SN, and the usual broad features of a Ic-BL emerge (Costantin et al. 2018).

We use the automated LT pipeline reduction and extraction for the LT spectra. LRIS spectra were reduced and extracted using *Lpipe* (Perley 2019). The NOT spectrum was obtained at parallactic angle using a 1'' slit, and was reduced in a standard way, including wavelength calibration against an arc lamp, and flux calibration using a spectrophotometric standard star. The XLT+BFOSC spectra were reduced using the standard IRAF routines, including corrections for bias, flat field, and removal of cosmic rays. The Fe/Ar and Fe/Ne arc lamp spectra obtained during the observation night are used to calibrate the wavelength of the spectra, and the standard stars observed on the same night at similar airmasses as the supernova were used to calibrate the flux of the spectra. The spectra were further corrected for continuum atmospheric extinction during flux calibration, using mean extinction curves obtained at Xinglong Observatory. Furthermore, telluric lines were removed from the data.

²⁸ <https://wis-tns.weizmann.ac.il>

²⁹ <https://telescope.livjm.ac.uk/TelInst/Pipelines/#ioo>

³⁰ <https://heasarc.gsfc.nasa.gov/cgi-bin/W3Browse/swift.pl>

³¹ <https://heasarc.nasa.gov/lheasoft/>

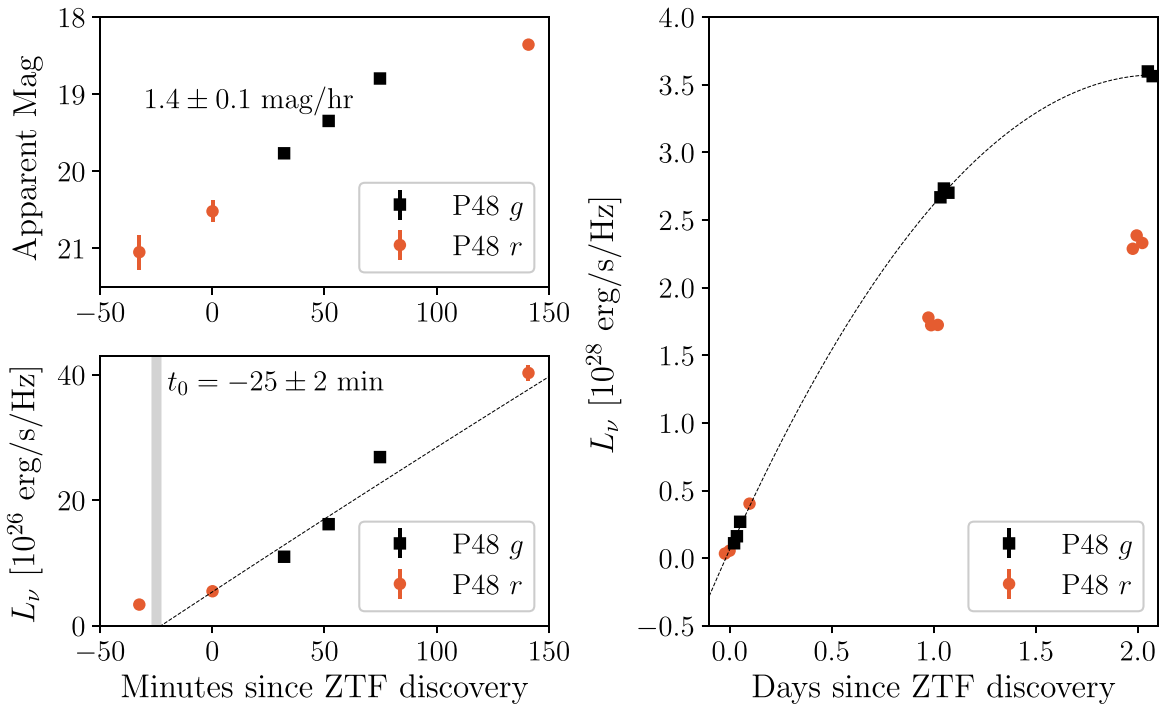


Figure 2. The rapid rise in the first few minutes and first few days after the ZTF discovery of SN2018gep. We also show an r -band point from prior to discovery that was found in retrospect by lowering the detection threshold from 5σ to 3σ . Top left: the rise in magnitudes gives an almost unprecedented rate of $1.4 \pm 0.1 \text{ mag hr}^{-1}$. Bottom left: the rise in flux space together with the quadratic fit and definition of t_0 . Right: the rise in flux space showing the quadratic fit.

Swift obtained three UV-grism spectra between UT 2018 September 15 3:29 and 6:58 ($\Delta t \approx 6.4$ days) for a total exposure time of 3918 s. The data were processed using the calibration and software described by Kuin et al. (2015). During the observation, the source spectrum was centered on the detector, which is the default location for *Swift*/UVOT observations. Because of this, there is second-order contamination from a nearby star, which was reduced by using a narrow extraction width ($1''.3$ instead of $2''.5$). The contamination renders the spectrum unreliable at wavelengths longer than 4100 \AA , but is negligible in the range $2850\text{--}4100 \text{ \AA}$ due to absorption from the interstellar medium. Below 2200 \AA , the spectrum overlaps with the spectrum from another star in the field of view.

The resulting spectrum (Figure 5) shows a single broad feature between 2200 \AA and 3000 \AA (rest frame). One possibility is that this is a blend of the UV features seen in superluminous supernovae (SLSNe). Line identifications for these features vary in the SLSN literature, but are typically blends of Ti III, Si III, C II, C III, and Mg II (Quimby et al. 2011; Howell et al. 2013; Mazzali et al. 2016; Yan et al. 2017).

The spectral log and a figure showing all the spectra are presented in Appendix B. In Section 3.2 we compare the early spectra to spectra at similar epochs in the literature. We model one of the early spectra, which shows a “W” feature that has been seen in SLSNe, to measure the density, density profile, and element composition of the ejecta. From the Ic-BL spectra, we measure the velocity evolution of the photosphere.

2.4. Search for Pre-discovery Emission

The nominal ZTF pipeline only generates detections above a 5σ threshold. To extend the light curve further back in time, we performed forced photometry at the position of SN2018gep on single-epoch difference images from the IPAC ZTF difference imaging pipeline. The ZTF forced photometry point spread functions (PSF)-fitting code will be described in

Y. Yao et al. (2019, in preparation). As shown in Figure 2, forced photometry uncovered an earlier 3σ r -band detection.

Next, we searched for even fainter detections by constructing deeper reference images than those used by the nominal pipeline, and subtracting them from 1 to 3 day stacks of ZTF science images. The reference images were generated by performing an inverse-variance weighted coaddition of 298 R -band and 69 g -band images from PTF/iPTF taken between 2009 and 2016 using the CLIPPED combine strategy in SWarp (Bertin 2010; Gruen et al. 2014). PTF/iPTF images were used instead of ZTF images to build references as they were obtained years prior to the transient, and thus less likely to contain any transient flux. No cross-instrument corrections were applied to the references prior to subtraction. Pronounced regions of negative flux on the PTF/iPTF references caused by crosstalk from bright stars were masked out manually.

We stacked ZTF science images obtained between UT 2018 February 22 and 2018 August 31 in a rolling window (segregated by filter) with a width of 3 days and a period of 1 day, also using the CLIPPED technique in SWarp. Images taken between 2018 Sep 01 and t_0 were stacked in a window with a width of 1 day and a period of 1 day. Subtractions were obtained using the HOTPANTS (Becker 2015) implementation of the Alard & Lupton (1998) PSF matching algorithm. Many of the ZTF science images during this period were obtained under exceptional conditions, and the seeing on the ZTF science coadds was often significantly better than the seeing on the PTF/iPTF references. To correct for this effect, ZTF science coadds were convolved with their own PSFs, extracted using PSFEX, prior to subtraction. During subtraction, PSF matching and convolution were performed on the template and the resulting subtractions were normalized to the photometric system of the science images. We show two example subtractions in Figure 6.

Using these newly constructed deep subtractions, PSF photometry was performed at the location of SN2018gep using the PSF

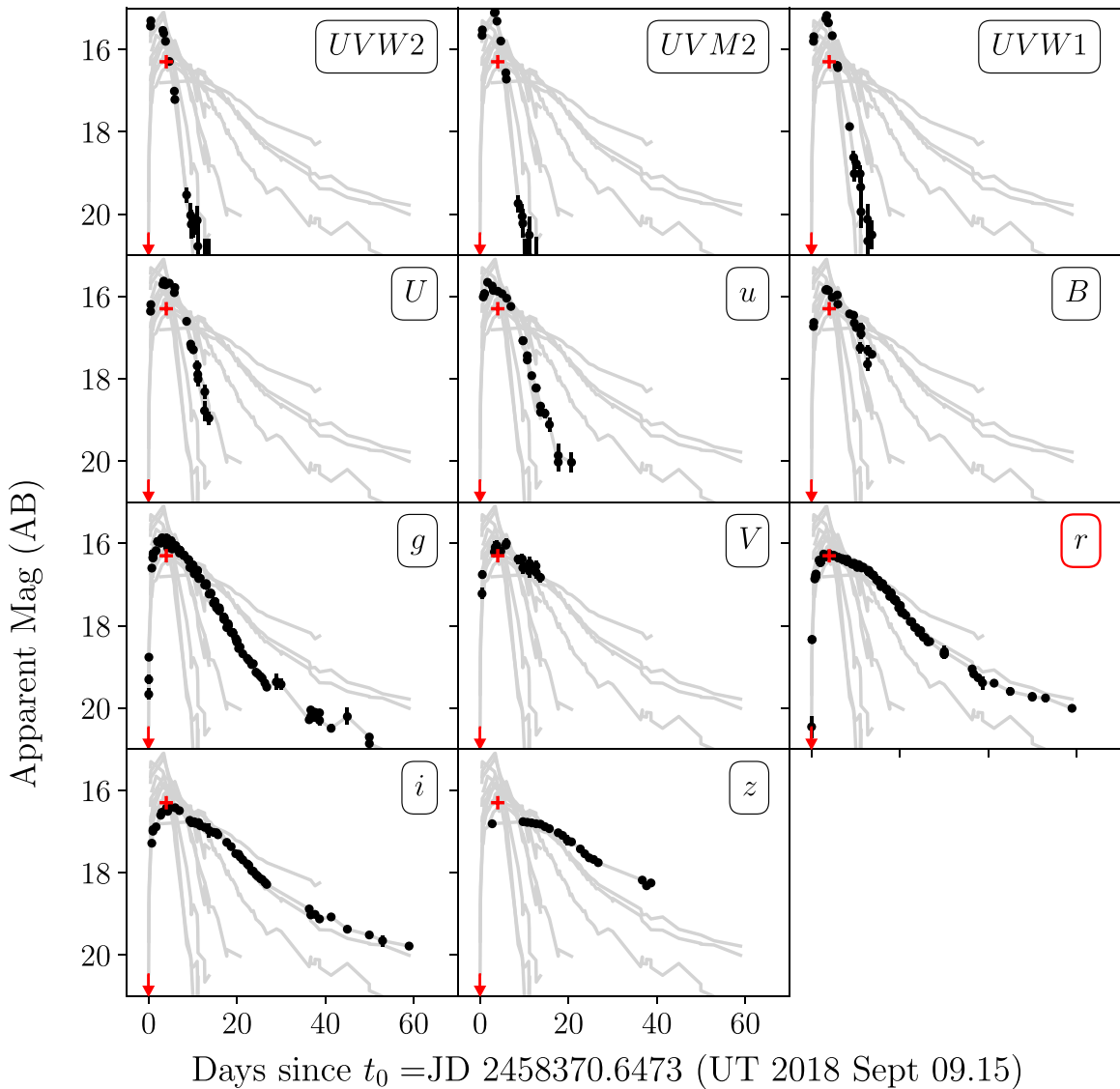


Figure 3. UV and optical light curves from *Swift* and ground-based facilities. The arrow marks the last nondetection, which was in *r* band. The red cross marks the peak of the *r*-band light curve, which is 16.3 mag at $\Delta t = 4$ days. The full set of light curves is shown as gray lines in the background, and each panel highlights an individual filter in black. We correct for Galactic extinction using the attenuation curve from Fitzpatrick (1999) and $E_{B-V} = R_V/A_V = 0.01$ for $R_V = 3.1$ and $A_V = 0.029$ (Schlafly & Finkbeiner 2011).

of the science images. To estimate the uncertainty on the flux measurements made on these subtractions, we employed a Monte Carlo technique, in which thousands of PSF fluxes were measured at random locations on the image, and the PSF-flux uncertainty was taken to be the 1σ dispersion in these measurements. We loaded this photometry into a local instance of SkyPortal (Van der Walt et al. 2019), an open-source web application that interactively displays astronomical data sets for annotation, analysis, and discovery.

We detected significant flux excesses at the location of SN2018gep in both *g* and *r* bands in the weeks preceding t_0 (i.e., its first detection in single-epoch ZTF subtractions). The effective dates of these extended prediscovery detections are determined by taking an inverse-flux variance weighted average of the input image dates. The detections in the week leading up to explosion are $m_g \sim m_r \approx 22$, which is approximately the magnitude limit of the coadd subtractions. However, in an *r*-band stack of images from August 24–26 (inclusive), we detect emission at $m_r \sim 21.5$ at 5σ above the background.

Assuming that the rapid rise we detected was close to the time of explosion, this is the first definitive detection of pre-explosion emission in a Ic-BL SN. There was a tentative detection in another source, PTF 11qej (Corsi et al. 2014), 1.5 and 2.5 yr prior to the SN. In Section 4 we discuss possible mechanisms for this emission, and conclude that it is likely related to a period of eruptive mass loss immediately prior to the explosion. We note that it is unlikely that this variability arises from active galactic nucleus (AGN) activity, due to the properties of the host galaxy (Section 3.3).

With forced photometry and faint detections from stacked images and deep references, we can construct a light curve that extends weeks prior to the rapid rise in the light curve, shown in Figure 7.

2.5. Radio Follow-up

We observed the field of SN2018gep with the Karl G. Jansky Very Large Array (VLA) on three epochs: on 2018 September 14 UT under the Program ID VLA/18A-242 (PI: D. Perley;

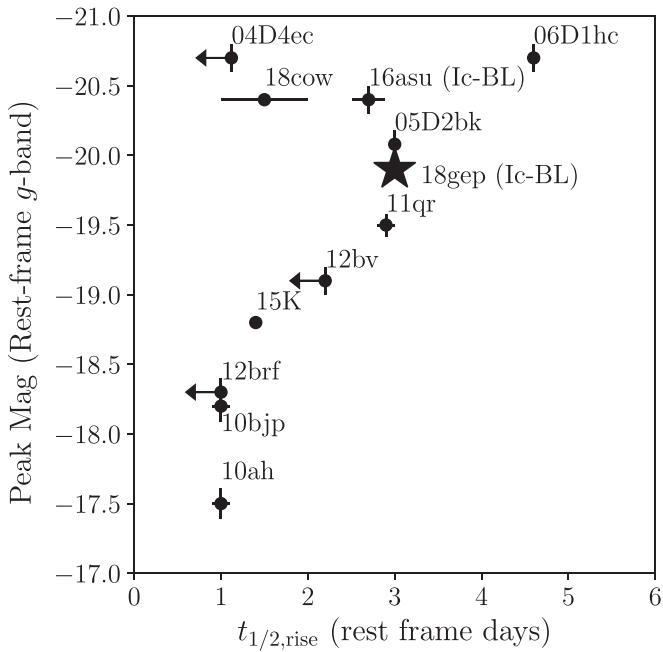


Figure 4. The rise time and peak absolute magnitude of SN2018gep, iPTF16asu (a high-redshift analog), and unclassified fast-luminous transients from Drout et al. (2014), Arcavi et al. (2016), Rest et al. (2018), and Perley et al. (2019). When possible, we report measurements in rest-frame g band, and define “rise time” as time from half-max to max. For iPTF16asu, we use the quadratic fit to the early g -band light curve from Whitesides et al. (2017) as well as their reported peak magnitude, but caution that this is rest-frame r band. For KSN2015K, there are only observations in the *Kepler* white filter (Rest et al. 2018).

Ho et al. 2018b), and on 2018 September 25 and 2018 November 23 UT under the Program ID VLA/18A-176 (PI: A. Corsi). We used 3C286 for flux calibration, and J1640+3946 for gain calibration. The observations were carried out in X- and Ku-band (nominal central frequencies of 9 GHz and 14 GHz, respectively) with a nominal bandwidth of 2 GHz. The data were calibrated using the automated VLA calibration pipeline available in the CASA package (McMullin et al. 2007) then inspected for further flagging. The CLEAN procedure (Högbom 1974) was used to form images in interactive mode. The image rms and the radio flux at the location of SN2018gep were measured using `imstat` in CASA. Specifically, we report the maximum flux within pixels contained in a circular region centered on the optical position of SN2018gep with radius comparable to the FWHM of the VLA synthesized beam at the appropriate frequency. The source was detected in the first two epochs, but not in the third (see Table 2). As we discuss in Section 4, the first two epochs were conducted in a different array configuration than the third epoch, and may have had a contribution from host galaxy light.

We also obtained three epochs of observations with the AMI large array (AMI-LA; Zwart et al. 2008; Hickish et al. 2018), on UT 2018 September 12, 2018 September 23, and 2018 October 20. AMI-LA is a radio interferometer comprised of eight 12.8 m diameter antennas that extend from 18 m up to 110 m in length and operates with a 5 GHz bandwidth around a central frequency of 15.5 GHz.

We used a custom AMI data reduction software package `reduce_dc` (e.g., Perrott et al. 2013) to perform initial data reduction, flagging, and calibration of phase and flux. Phase calibration was conducted using short interleaved observations of J1646+4059, and for absolute flux calibration we used 3C286. Additional flagging and imaging were performed using CASA. All three observations resulted in null detections with

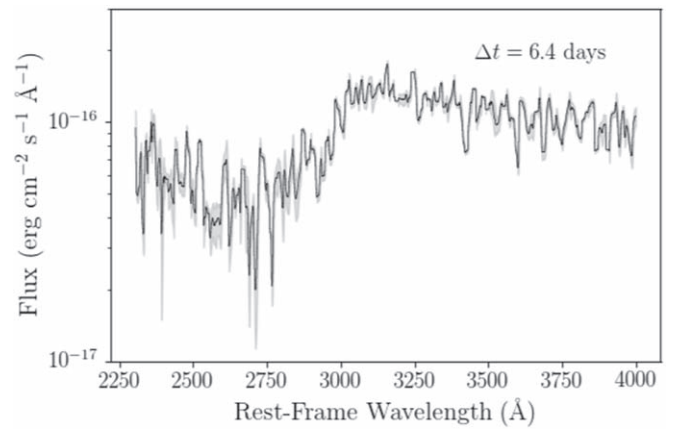


Figure 5. *Swift*/UVOT grism spectrum shifted to the rest frame. The black line shows the data binned such that each bin size is 10 Å. Light gray represents 1σ uncertainties after binning. The spectrum has been scaled to match the UVOT u -band flux at this epoch (integrated from 3000 Å to 3900 Å), which was determined by interpolating the *Swift* u -band light curve.

3σ upper limits of $\approx 120 \mu\text{Jy}$ in the first two observations, and a 3σ upper limit of $\approx 120 \mu\text{Jy}$ in the last observation.

Finally, we observed at higher frequencies using the Submillimeter Array (SMA; Ho et al. 2004) on UT 2018 September 15 under its target-of-opportunity program. The project ID was 2018A-S068. Observations were performed in the sub-compact configuration using seven antennas. The observations were performed using RxA and RxB receivers tuned to LO frequencies of 225.55 GHz and 233.55 GHz, respectively, providing 32 GHz of continuous bandwidth ranging from 213.55 to 245.55 GHz with a spectral resolution of 140.0 kHz per channel. The atmospheric opacity was around 0.16–0.19 with system temperatures around 100–200 K. The nearby quasars 1635+381 and 3C345 were used as the primary phase and amplitude gain calibrators with absolute flux calibration performed by comparison to Neptune. Passband calibration was derived using 3C454.3. Data calibration was performed using the MIR IDL package for the SMA, with subsequent analysis performed in MIRIAD (Sault et al. 1995). For the flux measurements, all spectral channels were averaged together into a single continuum channel and an rms of 0.6 mJy was achieved after 75 minutes on-source.

The full set of radio and submillimeter measurements are listed in Table 2.

2.6. X-Ray Follow-up

We observed the position of SN2018gep with *Swift*/XRT from $\Delta t \approx 0.4$ –14 days. The source was not detected in any epoch. To measure upper limits, we used web-based tools developed by the *Swift*-XRT team (Evans et al. 2009). For the first epoch, the 3σ upper limit was 0.003 ct s^{-1} . To convert the upper limit from count rate to flux, we assumed³² a Galactic neutral hydrogen column density of $1.3 \times 10^{20} \text{ cm}^{-2}$, and a power-law spectrum with photon index $\Gamma = 2$. This gives³³ an unabsorbed 0.3–10 keV flux of $< 9.9 \times 10^{-14} \text{ erg cm}^{-2} \text{ s}^{-1}$, and $L_X < 2.5 \times 10^{41} \text{ erg s}^{-1}$.

We obtained two epochs of observations with the Advanced CCD Imaging Spectrometer (Garmire et al. 2003) on the *Chandra X-ray Observatory* via our approved program (Proposal No.

³² <https://heasarc.gsfc.nasa.gov/cgi-bin/Tools/w3nh/w3nh.pl>

³³ <https://heasarc.gsfc.nasa.gov/cgi-bin/Tools/w3pimms/w3pimms.pl>

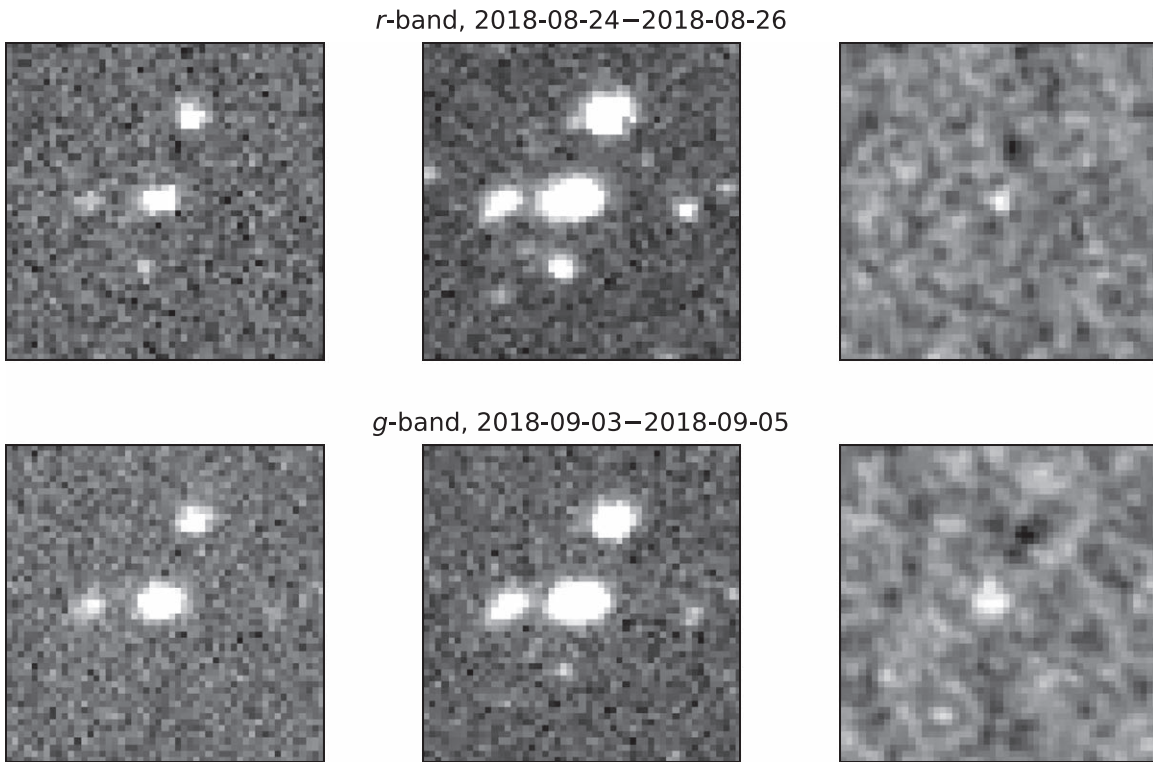


Figure 6. Sample pre-explosion subtractions of deep PTF/iPTF references from ZTF science images stacked in 3 days bins (see Section 2.4). Each cutout is centered on the location of SN2018gep. The subtractions show clear emission at the location of the SN in both *g* and *r* bands days to weeks before the discovery of the SN in ZTF.

19500451; PI: Corsi). The first epoch began at 9:25 UTC on 2018 10 October ($\Delta t \approx 15$ days) under ObsId 20319 (integration time 12.2 ks), and the second began at 21:31 UTC on 2018 December 4 ($\Delta t \approx 70$ days) under ObsId 20320 (integration time 12.1 ks). No X-ray emission is detected at the location of SN2018gep in either epoch, with 90% upper limits on the 0.5–7.0 keV count rate of $\approx 2.7 \times 10^{-4}$ ct s^{-1} . Using the same values of hydrogen column density and power-law photon index as in our XRT measurements, we find upper limits on the unabsorbed 0.5–7 keV X-ray flux of $< 3.2 \times 10^{-15}$ erg cm^{-2} s^{-1} , or (for a direct comparison to the XRT band) a 0.3–10 keV X-ray flux of $< 4.2 \times 10^{-15}$ erg cm^{-2} s^{-1} . This corresponds to a 0.3–10 keV luminosity upper limit of $L_X < 1.0 \times 10^{40}$ erg s^{-1} .

2.7. Search for Prompt Gamma-Ray Emission

We created a tool to search for prompt gamma-ray emission (GRBs) from *Fermi*-Gamma-ray Burst Monitor (GBM) (Gruber et al. 2014; von Kienlin et al. 2014; Narayana Bhat et al. 2016), the *Swift* Burst Alert Telescope (BAT; Barthelmy et al. 2005), and the IPN, which we have made available online.³⁴ We did not find any GRB consistent with the position and t_0 of SN2018gep.

Our tool also determines whether a given position was visible to BAT and GBM at a given time, using the spacecraft pointing history. We use existing code³⁵ to determine the BAT history. We find that the position of SN2018gep was in the BAT field of view from UTC 03:13:40 to 03:30:38, before *Swift* slewed to another location.

We also find that at t_0 SN2018gep was visible to the *Fermi* GBM (Meegan et al. 2009). We ran a targeted GRB search in 10–1000 keV *Fermi*/GBM data from three hours prior to t_0 to

half an hour after t_0 . We use the soft template, which is a smoothly broken power law with low-energy index -1.9 and high-energy index -2.7 , and an SED peak at 70 keV. The search methodology (and parameters of the other templates) are described in Blackburn et al. (2015) and Goldstein et al. (2016). No signals with a consistent location were found. For the 100 s integration time, the fluence upper limit is 2×10^{-6} erg cm^{-2} . This limit corresponds to a 10–1000 keV isotropic energy release of $E_{\gamma, \text{iso}} < 4.9 \times 10^{48}$ erg. Limits for different spectral templates and integration times are shown in Figure 8.

2.8. Host Galaxy Data

We measure line fluxes using the Keck optical spectrum obtained at $\Delta t \approx 61$ days (Figure 25). We model the local continuum with a low-order polynomial and each emission line by a Gaussian profile of FWHM ~ 5.3 Å. This is appropriate if Balmer absorption is negligible, which is generally the case for starburst galaxies. For the host of SN2018gep, the Balmer decrement between $H\beta$, $H\gamma$, and $H\delta$ does not show any excess with respect to the expected values in Osterbrock & Ferland (2006). The resulting line fluxes are listed in Table 7.

We retrieved archival images of the host galaxy from *Galaxy Evolution Explorer* (GALEX) Data Release (DR) 8/9 (Martin et al. 2005), SDSS DR9 (Ahn et al. 2012), Panoramic Survey Telescope And Rapid Response System (PanSTARRS, PS1) DR1 (Chambers et al. 2016), Two-Micron All Sky Survey (2MASS; Skrutskie et al. 2006), and *Wide-Field Infrared Survey Explorer* (WISE; Wright et al. 2010). We also used UVOT photometry from *Swift*, and NIR photometry from the Canada–France–Hawaii Telescope Legacy Survey (CFHTLS; Hudelot et al. 2012).

The images are characterized by different pixel scales (e.g., SDSS $0''.40/\text{px}$, GALEX $1''/\text{px}$) and different point spread

³⁴ https://github.com/annayqho/HE_Burst_Search

³⁵ https://github.com/lanl/swiftbat_python

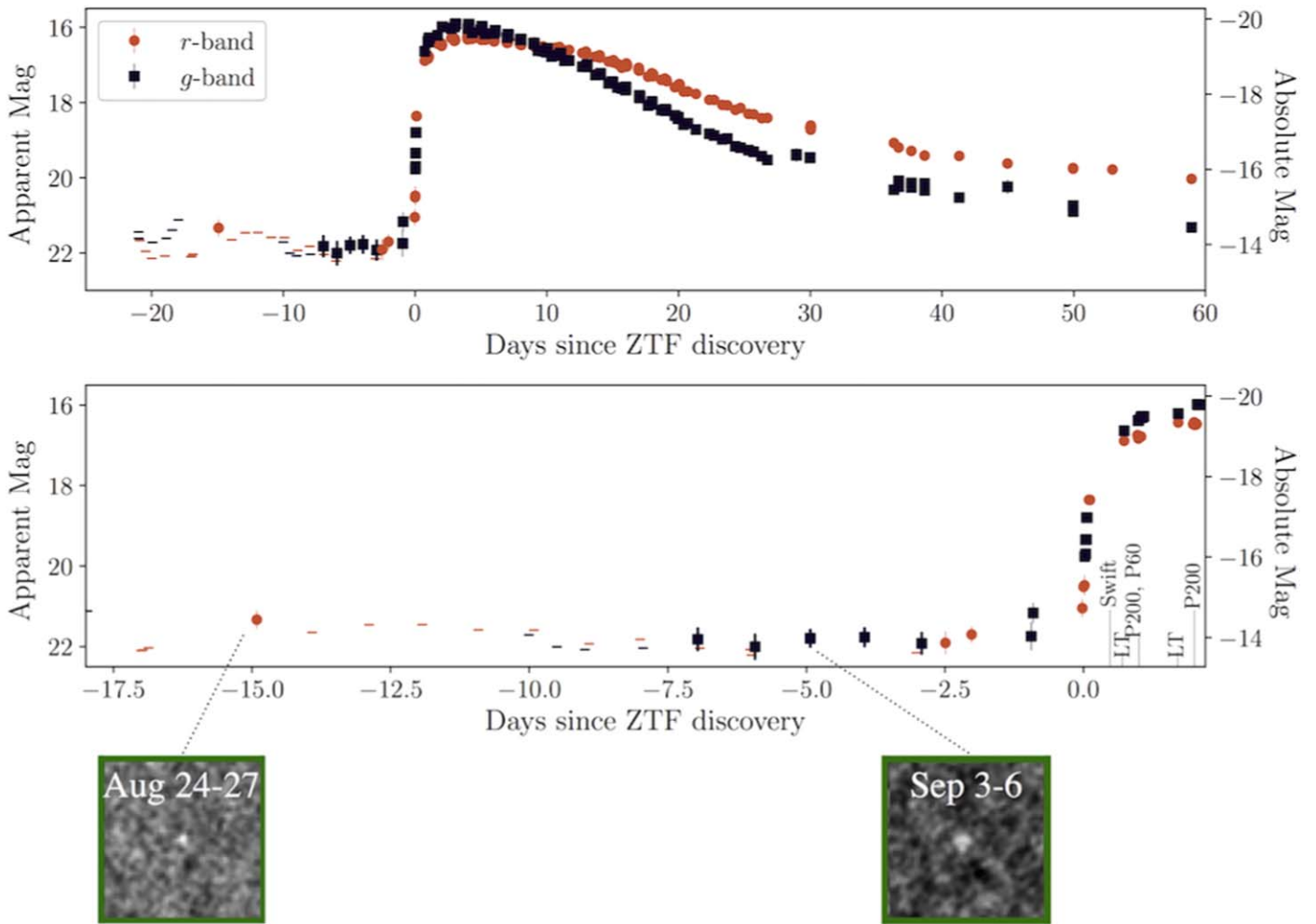


Figure 7. Full r and g -band light curves of SN2018gep. Horizontal lines show 3σ upper limits. Points at $t < 0$ are from 3 days stacks of ZTF/P48 data as described in Section 2.4. Sample subtractions from two of these stacks are shown in the bottom row.

functions (e.g., SDSS/PS1 $1''$ – $2''$, WISE/W2 $6''$.5). To obtain accurate photometry, we use the matched-aperture photometry software package LAMBDA ADAPTIVE MULTI-BAND DEBLENDING ALGORITHM IN R (LAMBDAAR; Wright et al. 2016) that is based on a photometry software package developed by Bourne et al. (2012). To measure the total flux of the host galaxy, we defined an elliptical aperture that encircles the entire galaxy in the SDSS/ r' -band image. This aperture was then convolved in LAMBDAAR with the PSF of a given image that we specified directly (*GALEX* and *WISE* data) or that we approximated by a two-dimensional Gaussian (2MASS, SDSS and PS1 images). After instrumental magnitudes were measured, we calibrated the photometry against instrument-specific zero-points (*GALEX*, SDSS, and PS1 data), or, as in the case of 2MASS and *WISE* images, against a local sequence of stars from the 2MASS Point Source Catalogue and the AllWISE catalog. The photometry from the UVOT images was extracted with the command UVOTSOURCE in HEASOFT and a circular aperture with a radius of $8''$. The photometry of the CFHT/WIRCAM data was performed with the software tool presented in Schulze et al. (2018b).³⁶ To convert the 2MASS, UVOT, WIRCAM, and *WISE* photometry to the AB system, we applied the offsets reported in Blanton & Roweis (2007),

Breeveld et al. (2011), and Cutri et al. (2013). The resulting photometry is summarized in Table 8.

3. Basic Properties of the Explosion and Its Host Galaxy

The observations we presented in Section 2 constitute some of the most detailed early time observations of a stripped-envelope SN to date. In this section we use this data to derive basic properties of the explosion: the evolution of bolometric luminosity, radius, and effective temperature over time (Section 3.1), the velocity evolution of the photosphere and the density and composition of the ejecta as measured from the spectra (Section 3.2), and the mass, metallicity, and star formation rate (SFR) of the host galaxy (Section 3.3). These properties are summarized in Table 1.

3.1. Physical Evolution from Blackbody Fits

By interpolating the UVOT and ground-based photometry, we construct multiband SEDs and fit a Planck function on each epoch to measure the evolution of luminosity, radius, and effective temperature. To estimate the uncertainties, we perform a Monte Carlo simulation with 600 trials, each time adding noise corresponding to a 15% systematic uncertainty on each data point, motivated by the need to obtain a combined $\chi^2/\text{dof} \sim 1$ across all epochs. The uncertainties for each parameter are taken

³⁶ https://github.com/steveschulze/aperture_photometry

Table 2
Radio Flux Density Measurements for SN2018gep

Start Time (UTC)	Δt (days)	Instrument	ν (GHz)	f_ν (μJy)	L_ν ($\text{erg s}^{-1} \text{Hz}^{-1}$)	θ_{FWHM}	Int. Time (hr)
2018-09-12 17:54	3.6	AMI	15	<120	$<2.9 \times 10^{27}$	43.53×30.85	4
2018-09-23 15:35	14.5	AMI	15	<120	$<2.9 \times 10^{27}$	39.3×29.29	4
2018-10-20 14:01	41.4	AMI	15	<120	$<2.9 \times 10^{27}$	43.53×30.85	4
2018-09-15 02:33	6.0	SMA	230	<590	$<1.4 \times 10^{28}$	4.828×3.920	1.25
2018-09-14 01:14	4.9	VLA	9.7	34 ± 4	8.3×10^{26}	7.06×5.92	0.5
2018-09-25 00:40	15.9	VLA	9	24.4 ± 6.8	6.0×10^{26}	7.91×6.89	0.7
2018-09-25 00:40	15.9	VLA	14	26.8 ± 6.8	6.6×10^{26}	4.73×4.26	0.5
2018-11-23 13:30	75.4	VLA	9	<16	$<3.9 \times 10^{26}$	3.52×2.08	0.65
2018-11-23 13:30	75.4	VLA	14	<17	$<4.2 \times 10^{26}$	2.77×1.32	0.65

Note. For VLA measurements: the quoted errors are calculated as the quadrature sums of the image rms, plus a 5% nominal absolute flux calibration uncertainty. When the peak flux density within the circular region is less than three times the rms, we report an upper limit equal to three times the rms of the image. For AMI measurements: nondetections are reported as 3σ upper limits. For SMA measurements: nondetections are reported as a 1σ upper limit.

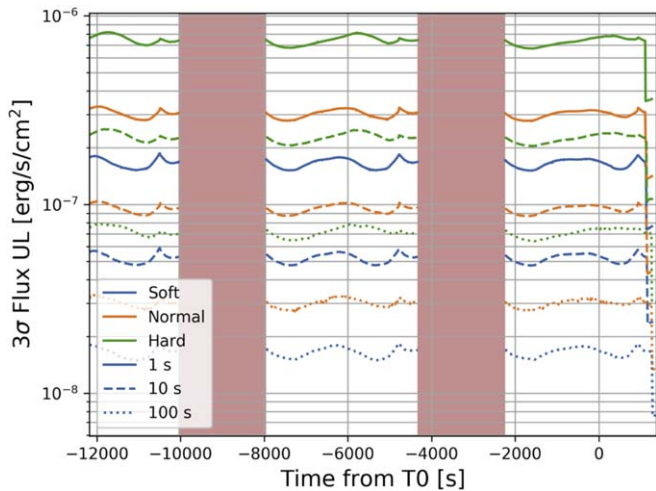


Figure 8. 3σ upper limits from GBM GRB search, which we performed for three hours prior to t_0 . The red vertical bars indicate epochs when GBM was not taking data due to passing through the South Atlantic Anomaly. The time of t_0 was estimated from a fit to the early data (Figure 7), and is 26 ± 5 minutes prior to the first detection.

as the 16-to-84 percentile range from this simulation. The SED fits are shown in Appendix A, and the resulting evolution in bolometric luminosity, photospheric radius, and effective temperature is listed in Table 3. We plot the physical evolution in Figure 9, with a comparison to iPTF16asu and AT2018cow.

The bolometric luminosity peaks between $\Delta t = 0.5$ day and $\Delta t = 3$ days, at $>3 \times 10^{44} \text{ erg s}^{-1}$. In Figure 10 we compare this peak luminosity and time to peak luminosity with several classes of stellar explosions. As in iPTF16asu, the bolometric luminosity falls as an exponential at late times ($t > 10$ days). The total integrated UV and optical ($\approx 2000\text{--}9000 \text{ \AA}$) blackbody energy output from $\Delta t = 0.5\text{--}40$ days is $\sim 10^{50} \text{ erg}$, similar to that of iPTF16asu. The earliest photospheric radius we measure is $\sim 20 \text{ au}$, at $\Delta t = 0.05$ day. Until $\Delta t \approx 17$ days the radius expands over time with a very large inferred velocity of $v \approx 0.1c$. After that, it remains flat, and even appears to recede. This possible recession corresponds to a flattening in the temperature at $\sim 5000 \text{ K}$, which is the recombination temperature of carbon and oxygen. This effect was not seen in iPTF16asu, which remained hotter (and more luminous) for longer. Finally, the effective temperature rises before falling as $\sim t^{-1}$. We interpret these properties in the context of shock-cooling emission in Section 4.

Table 3
Physical Evolution of AT2018gep from Blackbody Fits

Δt	$L(10^{10}L_\odot)$	R (au)	T (kK)
0.05	$0.04^{+0.04}_{-0.02}$	21^{+14}_{-6}	13^{+5}_{-4}
0.48	$7.4^{+8.6}_{-4.1}$	22^{+7}_{-5}	46^{+16}_{-13}
0.73	$4.5^{+5.5}_{-2.8}$	31^{+11}_{-6}	35^{+12}_{-11}
1.0	$2.2^{+2.1}_{-1.2}$	46^{+18}_{-9}	24^{+6}_{-6}
1.7	$3.5^{+4.7}_{-2.1}$	46^{+22}_{-10}	27^{+9}_{-8}
2.7	$1.3^{+1.2}_{-0.4}$	78^{+22}_{-20}	16^{+5}_{-3}
3.2	$3.5^{+2.2}_{-1.3}$	50^{+14}_{-8}	26^{+6}_{-5}
3.8	$2.9^{+1.7}_{-0.8}$	56^{+11}_{-11}	23^{+5}_{-3}
4.7	$1.7^{+0.7}_{-0.3}$	69^{+16}_{-14}	18^{+3}_{-2}
5.9	$0.88^{+0.17}_{-0.08}$	100^{+14}_{-21}	13^{+1}_{-0}
8.6	$0.46^{+0.08}_{-0.06}$	220^{+46}_{-39}	$7.4^{+0.6}_{-0.5}$
9.6	$0.33^{+0.04}_{-0.03}$	200^{+33}_{-24}	$7.1^{+0.4}_{-0.4}$
10.0	$0.31^{+0.04}_{-0.03}$	210^{+34}_{-28}	$6.9^{+0.4}_{-0.4}$
11.0	$0.28^{+0.04}_{-0.03}$	220^{+35}_{-33}	$6.5^{+0.4}_{-0.3}$
13.0	$0.25^{+0.04}_{-0.03}$	260^{+50}_{-42}	$5.8^{+0.3}_{-0.3}$
14.0	$0.22^{+0.04}_{-0.03}$	270^{+60}_{-47}	$5.5^{+0.4}_{-0.3}$
16.0	$0.17^{+0.04}_{-0.03}$	260^{+76}_{-58}	$5.3^{+0.5}_{-0.5}$
18.0	$0.15^{+0.04}_{-0.02}$	300^{+77}_{-64}	$4.7^{+0.4}_{-0.4}$
21.0	$0.11^{+0.03}_{-0.02}$	250^{+83}_{-58}	$4.7^{+0.4}_{-0.4}$
25.0	$0.073^{+0.02}_{-0.013}$	240^{+95}_{-85}	$4.5^{+0.9}_{-0.5}$
38.0	$0.034^{+0.012}_{-0.007}$	180^{+86}_{-55}	$4.2^{+0.6}_{-0.5}$

(This table is available in machine-readable form.)

3.2. Spectral Evolution and Velocity Measurements

3.2.1. Comparisons to Early Spectra in the Literature

We obtained nine spectra of SN2018gep in the first five days after discovery. These early spectra are shown in Figure 11, when the effective temperature declined from 50,000 K to 20,000 K. To our knowledge, our early spectra have no analogs in the literature, in that there has never been a spectrum of a stripped-envelope SN at such a high temperature (excluding spectra during the afterglow phase of GRBs).³⁷ Two of the earliest spectra in the literature, one at $\Delta t = 2$ days for Type Ic SN PTF10vgv (Corsi et al. 2012) and one at $\Delta t = 3$ days for Type Ic SN PTF12gzk (Ben-Ami et al. 2012) are redder and exhibit more features than

³⁷ There is however a spectrum of a Type II SN at a comparable temperature: iPTF13dqy was $\sim 50,000 \text{ K}$ at the time of the first spectrum (Yaron et al. 2017).

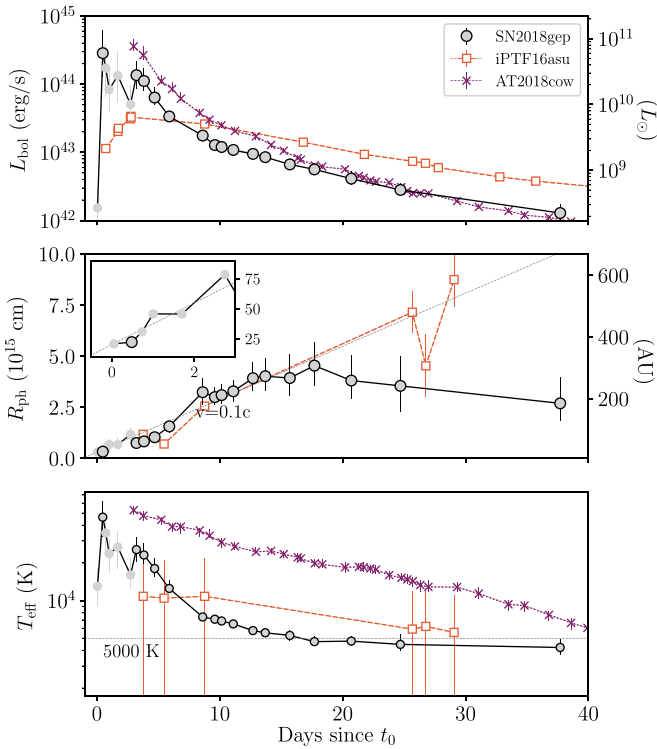


Figure 9. Evolution of blackbody properties (luminosity, radius, temperature) over time compared to the Ic-BL SN iPTF16astu and the fast–luminous optical transient AT2018cow. The light gray circles are derived from optical data only. The outlined circles are derived from UV and optical data. Middle panel: dotted line shows $v = 0.1c$. Note that $R \neq 0$ at t_0 , and instead $R(t = 0) = 3 \times 10^{14}$ cm. Due to the scaling of our plot we do not show the radius evolution of AT2018cow, which drops from 8×10^{14} cm to 10^{14} cm on this timescale. Bottom panel: dotted horizontal line shows 5000 K, the recombination temperature for carbon and oxygen. Once this temperature is reached, the photosphere flattens out (and potentially begins to recede).

the spectrum of SN2018gep. We show the comparison in Figure 11.

At $\Delta t \approx 4$ days, a “W” feature emerges in the rest-frame wavelength range 3800–4350 Å. In the second-from-bottom panel of Figure 11 we make a comparison to “W” features seen in SN 2008D (e.g., Modjaz et al. 2009), which was a Type Ib SN associated with an X-ray flash (Mazzali et al. 2008), and in a typical pre-max stripped-envelope SLSN (Type I SLSN; Moriya et al. 2018; Gal-Yam 2019b). The absorption lines are broadened much more than in PTF12dam (Nicholl et al. 2013) and probably more than in SN2008D as well. Finally, SN2018gep cooled more slowly than SN2008D: only after 4.25 days did it reach the temperature that SN 2008D reached after >2 days.

3.2.2. Origin of the “W” feature

The lack of comparison data at such early epochs (high temperatures) motivated us to model one of the early spectra in order to determine the composition and density profile of the ejecta. We used the spectral synthesis code JEKYLL (Ergon et al. 2018), configured to run in steady state using a full NLTE solution. An inner blackbody boundary was placed at a high continuum optical depth (~ 50), and the temperature at this boundary was iteratively determined to reproduce the observed luminosity. The atomic data used is based on what was specified in Ergon et al. (2018), but has been extended as described in Appendix C. We explored models with C/O (mass fractions: 0.23/0.65) and O/Ne/Mg (mass fractions: 0.68/0.22/0.07)

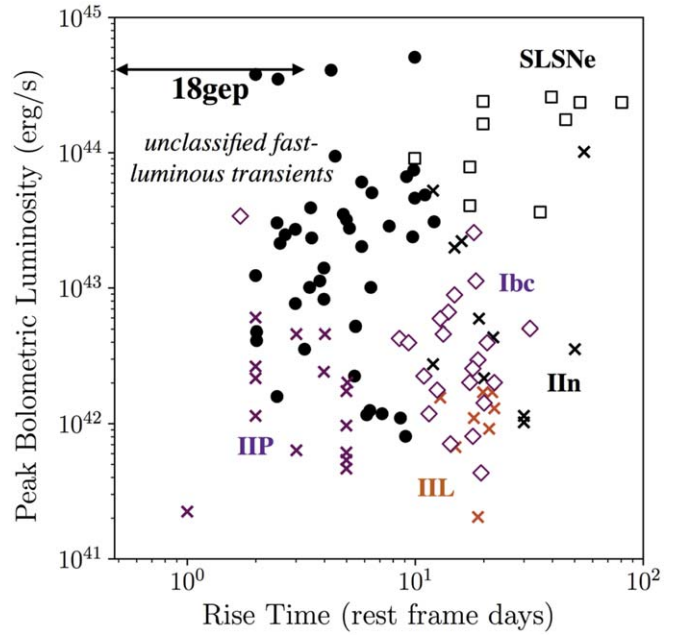


Figure 10. Rise to peak bolometric luminosity compared to other classes of transients. Modified from Figure 1 in Margutti et al. (2019).

compositions taken from a model by Woosley & Heger (2007)³⁸ and a power-law density profile, where the density at the inner border was adjusted to fit the observed line velocities. Except for the density at the inner border, various power-law indices were also explored, but in the end an index of -9 worked out best.

Figures 12 and 13 show the model with the best overall agreement with the spectra and the SED (as listed in Table 6 the spectrum was obtained at high airmass, making it difficult to correct for telluric features). The model has a C/O composition, an inner border at $22,000 \text{ km s}^{-1}$ (corresponding to an optical depth of ~ 50), a density of $4 \times 10^{-12} \text{ g cm}^{-3}$ at this border, and a density profile with a power-law index of -9 . In Figure 12 we show that the model does a good job of reproducing both the spectrum and the SED of SN2018gep. In particular, it is interesting to note that the “W” feature seems to arise naturally in C/O material at the observed conditions. A similar conclusion was reached by Dessart (2019), whose magnetar-powered SLSN-I models, calculated using the NLTE code CMFGEN, show the “W” feature even when nonthermal processes were not included in the calculation (as in our case).

In the model, the “W” feature mainly arises from the O II $2p^2(3P)3s\ 4P \leftrightarrow 2p^2(3P)3p\ 4D^\circ$ (4639–4676 Å), O II $2p^2(3P)3s\ 4P \leftrightarrow 2p^2(3P)3p\ 2D$ (4649 Å), and O II $2p^2(3P)3s\ 4P \leftrightarrow 2p^2(3P)3p\ 4P^\circ$ (4317–4357 Å) transitions. The departure from LTE is modest in the line-forming region, and the departure coefficients for the O II states are small. The spectrum redward of the “W” feature is shaped by carbon lines, and the features near 5700 and 6500 Å arise from the C II $3s\ 2S \leftrightarrow 3p\ 2P^\circ$ (6578, 6583 Å) and C III $2s3p\ 1P^\circ \leftrightarrow 2s3d\ 1D$ (5696 Å) transitions, respectively. In the model, the C II feature is too weak, suggesting that the ionization level is too high in the model. There is also a contribution from the C III $2s3s\ 3S \leftrightarrow 2s3p\ 3P^\circ$ (4647–4651 Å) transition to the red part of the “W” feature, which could potentially be what is seen in the spectra from earlier epochs. In

³⁸ The model was divided into compositional zones by Jerkstrand et al. (2015) and a detailed specification of the C/O and O/Ne/Mg zones is given in Table D.2 therein.

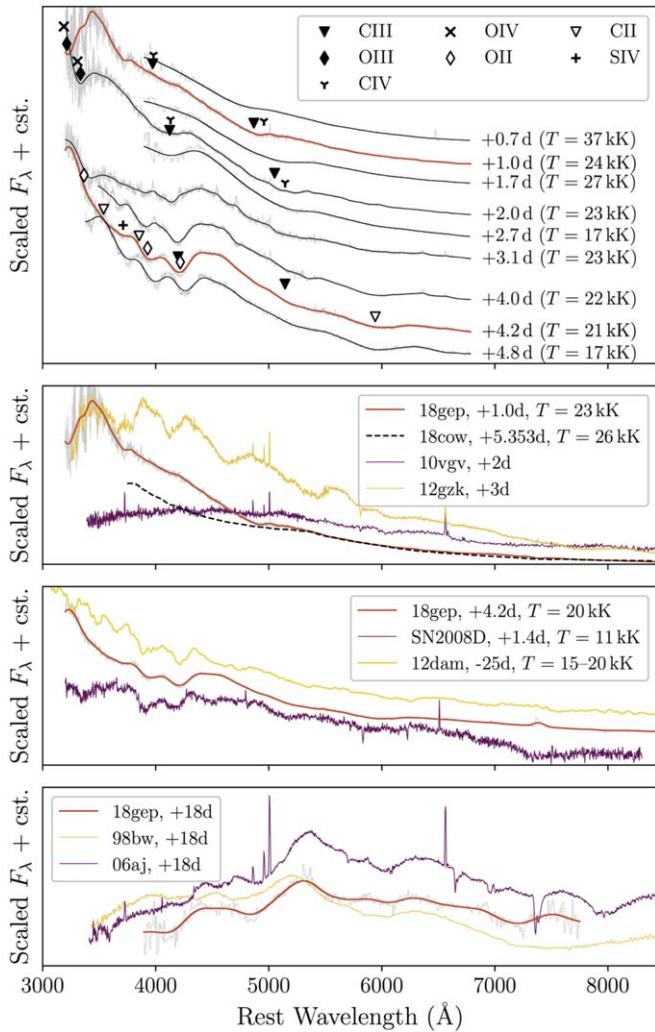


Figure 11. Top panel: spectra of SN2018gep taken in the first five days. Broad absorption features are consistent with ionized carbon and oxygen, which evolve redward with time. Second-from-top panel: an early spectrum of 18gep compared to spectra from other stellar explosions at a comparable phase. Second-from-bottom panel: the spectrum at $\Delta t = 4.2$ days shows a “W” feature, which we compare to similar “W” features seen in an early spectrum of SN2008D from Modjaz et al. (2009), and a typical pre-max spectrum of a SLSN-I (PTF12dam, from Nicholl et al. 2013). We boost the SLSN spectrum by an additional expansion velocity of $\sim 15,000$ km s $^{-1}$, and apply reddening of $E(B - V) = 0.63$ to SN 2008D. Weak features in the red are also similar to what are seen in PTF12dam, and are consistent with arising from CII and CIII lines, following the analysis of Gal-Yam (2019a). The lack of narrow carbon features as well as the smooth spectrum below 3700 Å suggest a large velocity dispersion leading to significant line broadening, compared to the intrinsically narrow features observed in SLSNe-I (Gal-Yam 2019a; Quimby et al. 2018).

addition, there is a contribution from Si IV $4s\ 2S \leftrightarrow 4p\ 2P^\circ$ (4090, 4117 Å) near the blue side of the “W” feature, which produces a distinct feature in models with lower velocities and which could explain the observed feature on the blue side of the “W” feature.

In spite of the overall good agreement, there are also some differences between the model and the observations. In particular the model spectrum is bluer and the velocities are higher. These two quantities are in tension and a better fit to one of them would result in a worse fit to the other. As mentioned above, the ionization level might be too high in the model, which suggests that the temperature might be too high as well. It should be noted that adding host extinction (which is assumed to be zero) or reducing the distance (within the error bars) would help in making

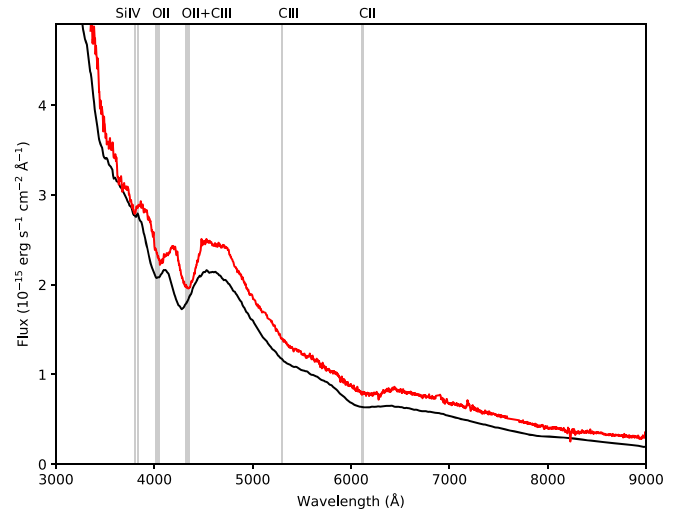


Figure 12. Observed spectrum (red) at 4.2 days, compared to our model spectrum (black) from the spectral synthesis code JEKYLL configured to run in steady state using a full NLTE solution. The model has a C/O composition, an inner border at 22,000 km s $^{-1}$, a density of 4×10^{-12} g cm $^{-3}$, and a density profile with a power-law index of -9 . The absolute (but not relative) flux of the spectrum was calibrated using the interpolated P48 g and r magnitudes. We also show the O II, C II, C III, and Si IV lines discussed in the text shifted to the velocity of the model photosphere.

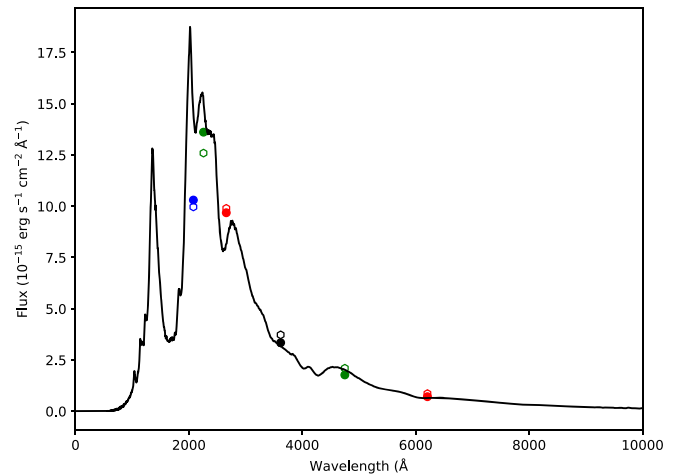


Figure 13. Comparison of model (filled circles) and observed (unfilled circles) mean fluxes through the *Swift* UVW1 (blue), UVM2 (green), UVW2 (red), and the SDSS u (black), g (green), and r (red) filters. We also show the model spectrum in black.

the model redder (in the observer frame), and the latter would also help in reducing the temperature. The (modest) differences between the model and the observations could also be related to physics not included in the model, like a nonhomologous velocity field, departures from spherical asymmetry, and clumping.

The total luminosity of the model is 6.2×10^{43} erg s $^{-1}$, the photosphere is located at $\sim 33,000$ km s $^{-1}$, and the temperature at the photosphere is $\sim 17,500$ K, which is consistent with the values estimated from the blackbody fits (although the blackbody radius and temperature fits refer to the thermalization layer). As mentioned, we have also tried models with an O/Ne/Mg composition. However, these models failed to reproduce the carbon lines redwards of the “W” feature. We therefore conclude that the (outer) ejecta probably have a C/O-like composition, and that this composition in combination with a standard power-law density profile reproduces the spectrum of SN2018gep at the

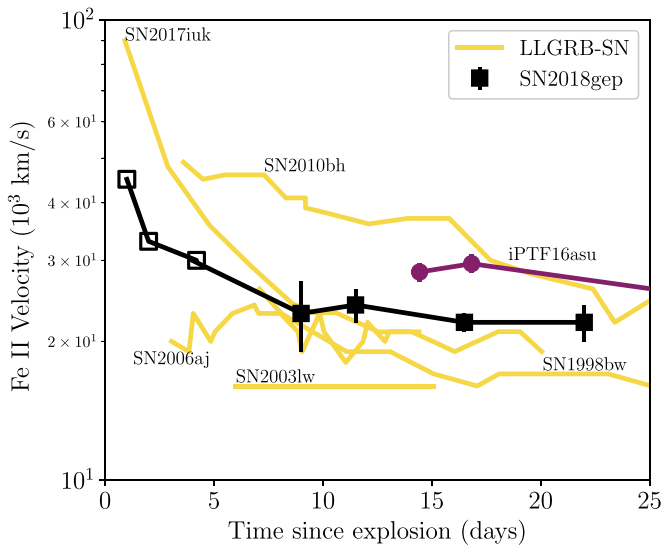


Figure 14. Velocity evolution over time as measured from spectral absorption features. Open symbols for SN2018gep come from C/O velocities measured from line minima. Closed symbols come from the Fe II feature in the Ic-BL spectra. The velocities are comparable to those measured for Ic-BL SNe associated with low-luminosity GRBs (LLGRBs). The velocity evolution for SN2017iuk is taken from Izzo et al. (2019). Velocities for iPTF16asu are taken from Whitesides et al. (2017). Velocities for the other Ic-BL SNe are taken from Modjaz et al. (2016) and shifted from V-band max using data from Galama et al. (1998), Campana et al. (2006), Malesani et al. (2004), and Bufano et al. (2012).

observed conditions (luminosity and velocity) 4.2 days after explosion.

In our model, the broad feature seen in our *Swift* UVOT grism spectrum is dominated by the strong Mg II (2796, 2803 Å) resonance line. However, a direct comparison is not reliable because the ionization is probably lower at this epoch than what we consider for our model.

3.2.3. Photospheric Velocity from Ic-BL Spectra

At $\Delta t \gtrsim 7.8$ days, the spectra of SN2018gep qualitatively resemble those of a stripped-envelope SN. We measure velocities using the method in Modjaz et al. (2016), which accommodates blending of the Fe II $\lambda 5169$ line (which has been shown to be a good tracer of photospheric velocity; Branch et al. 2002) with the nearby Fe II $\lambda \lambda 4924, 5018$ lines.

At earlier times, when the spectra do not resemble typical Ic-BL SNe, we use our line identifications of ionized C and O to measure velocities. As shown in Figure 14, the velocity evolution we measure is comparable to that seen in Ic-BL SNe associated with GRBs (more precisely, low-luminosity GRBs; LLGRBs) which are systematically higher than those of Ic-BL SNe lacking GRBs (Modjaz et al. 2016). However, as discussed in Section 2.7, no GRB was detected.

3.3. Properties of the Host Galaxy

We infer a star formation rate of $0.09 \pm 0.01 M_{\odot} \text{ yr}^{-1}$ from the H α emission line using the Kennicutt (1998) relation converted to use a Chabrier initial mass function (IMF); (Chabrier 2003; Madau & Dickinson 2014). We note that this is a lower limit as the slit of the Keck observation did not enclose the entire galaxy. We estimate a correction factor of 2–3: the slit diameter in the Keck spectra was $1''.0$, and the extraction radius was $\sim 1''.75$ in the February observation and $\sim 1.21''$ in the March observation. The host diameter is roughly $4''$.

We derive an electron temperature of $13,100^{+900}_{-1000}$ K from the flux ratio between [O III] $\lambda 4641$ and [O III] $\lambda 5007$, using the software package PYNEB version 1.1.7 (Luridiana et al. 2015). In combination with the flux measurements of [O II] $\lambda \lambda 3226, 3729$, [O III] $\lambda 4364$, [O III] $\lambda 4960$, [O III] $\lambda 5008$, and H β , we infer a total oxygen abundance of $8.01^{+0.10}_{-0.09}$ (statistical error; using Equations (3) and (5) in Izotov et al. 2006). Assuming a solar abundance of 8.69 (Asplund et al. 2009), the metallicity of the host is $\sim 20\%$ solar.

We also compute the oxygen abundance using the strong-line metallicity indicator O3N2 (Pettini & Pagel 2004) with the updated calibration reported in Marino et al. (2013). The oxygen abundance in the O3N2 scale is $8.05 \pm 0.01(\text{stat}) \pm 0.10(\text{sys})$.³⁹

We also estimate mass and star formation rate by modeling the host SED; see Appendix D for a table of measurements, and details on where we obtained them. We use the software package LEPHARE version 2.2 (Arnouts et al. 1999; Ilbert et al. 2006). We generated 3.9×10^6 templates based on the Bruzual & Charlot (2003) stellar population synthesis models with the Chabrier IMF (Chabrier 2003). The star formation history (SFH) was approximated by a declining exponential function of the form $\exp(t/\tau)$, where t is the age of the stellar population and τ the e-folding timescale of the SFH (varied in nine steps between 0.1 and 30 Gyr). These templates were attenuated with the Calzetti attenuation curve (Calzetti et al. 2000) varied in 22 steps from $E(B - V) = 0$ to 1 mag.

As shown in Figure 15, the SED is well characterized by a galaxy mass of $\log M/M_{\odot} = 8.11^{+0.07}_{-0.08}$ and an attenuation-corrected star formation rate of $0.12^{+0.08}_{-0.05} M_{\odot} \text{ yr}^{-1}$. The derived star formation rate is comparable to the measurement inferred from H α . The attenuation of the SED is marginal, with $E(B - V)_{\text{star}} = 0.05$, and consistent with the negligible Balmer decrement (Section 2.8).

Figure 16 shows that the host galaxy of SN2018gep is even more low-mass and metal-poor than the typical host galaxies of Ic-BL SNe, which are low-mass and metal-poor compared to the overall core-collapse SN population. The figure uses data for 28 Ic-BL SNe from PTF and iPTF (Modjaz et al. 2019; Taddia et al. 2019) and a sample of 11 long-duration GRBs (including LLGRBs, all at $z < 0.3$). We measured the emission lines from the spectra presented in Taddia et al. (2019) and used line measurements reported in Modjaz et al. (2019) for objects with missing line fluxes. The photometry was taken from S. Schulze et al. (2019, in preparation). Photometry and spectroscopy were taken from a variety of sources.⁴⁰ The oxygen abundances were measured in the O3N2 scale like for SN2018gep and their SEDs were modeled with the same set of galaxy templates. For reference, the mass and SFR of the host of AT2018cow was $1.4 \times 10^9 M_{\odot}$ and $0.22 M_{\odot} \text{ yr}^{-1}$, respectively (Perley et al. 2019). The mass and SFR of the host of iPTF16asu was $4.6^{+6.5}_{-2.3} \times 10^8 M_{\odot}$ and $0.7 M_{\odot} \text{ yr}^{-1}$, respectively (Whitesides et al. 2017).

³⁹ Note, the oxygen abundance of SN2018gep's host lies outside of the domain calibrated by Marino et al. (2013). However, we will use the measurement from the O3N2 indicator only to put the host in context of other galaxy samples that are on average more metal enriched.

⁴⁰ Gorosabel et al. (2005), Bersier et al. (2006), Margutti et al. (2007), Ovaldsen et al. (2007), Kocevski et al. (2007), Thöne et al. (2008), Michałowski et al. (2009), Han et al. (2010), Levesque et al. (2010), Starling et al. (2011), Hjorth et al. (2012), Thöne et al. (2014), Schulze et al. (2014), Krühler et al. (2015), Stanway et al. (2015), Toy et al. (2016), Izzo et al. (2017), and Cano et al. (2017).

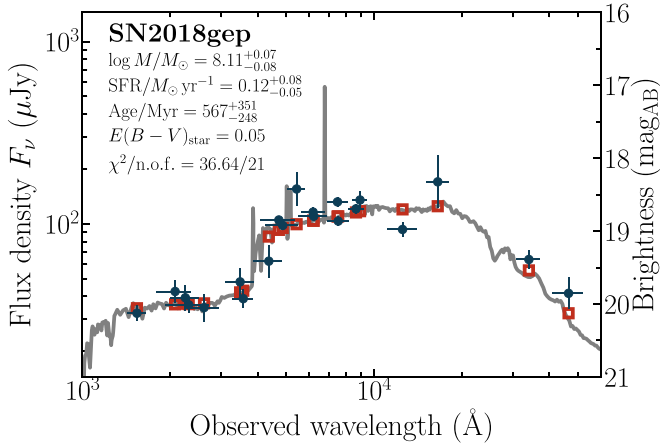


Figure 15. The spectral energy distribution of the host galaxy of SN2018gep from 1000 to 60000 Å and the best fit (solid line) in the observer frame. Filled data points represent photometric measurements. The error bars in the “x” direction indicate the FWHM of each filter response function. The open data points signify the model-predicted magnitudes. The quoted values of the host properties represent the median values and the corresponding 1σ errors.

4. Interpretation

In Sections 2 and 3, we presented our observations and basic inferred properties of SN2018gep and its host galaxy. Now we consider what we can learn about the progenitor, beginning with the power source for the light curve.

4.1. Radioactive Decay

The majority of stripped-envelope SNe have light curves powered by the radioactive decay of ^{56}Ni . As discussed in Kasen (2017), this mechanism can be ruled out for light curves that rise rapidly to a high peak luminosity, because this would require the unphysical condition of a nickel mass that exceeds the total ejecta mass. With a peak luminosity exceeding 10^{44} erg s^{-1} and a rise to peak of a few days, SN2018gep clearly falls into the disallowed region (see Figure 1 in Kasen 2017). Thus, we rule out radioactive decay as the mechanism powering the peak of the light curve.

We now consider whether radioactive decay could dominate the light curve at late times ($t \gg t_{\text{peak}}$). The left panel of Figure 17 shows the bolometric light curve of SN2018gep compared to several other Ic-BL SNe from the literature (Cano 2013), whose light curves are thought to be dominated by the radioactive decay of ^{56}Ni (although see Moriya et al. 2017 for another possible interpretation). The luminosity of SN2018gep at $t \sim 20$ days is about half that of SN1998bw, and double that of SN2010bh and SN2006aj. By modeling the light curves of the three Ic-BL SNe shown, Cano (2013) infers nickel masses of $0.42 M_{\odot}$, $0.12 M_{\odot}$, and $0.21 M_{\odot}$, respectively. On this scale, SN2018gep has $M_{\text{Ni}} \sim 0.1\text{--}0.2 M_{\odot}$.

The right panel of Figure 17 shows the light curve of SN2018gep compared to that of AT2018cow (Perley et al. 2019). To estimate the nickel mass of AT2018cow, Perley et al. (2019) compared the bolometric luminosity at $t \sim 20$ days to that of SN2002ap (whose nickel mass was derived via late-time nebular spectroscopy; Foley et al. 2003) and found $M_{\text{Ni}} < 0.05 M_{\odot}$. On this scale, we would expect $M_{\text{Ni}} \lesssim 0.05 M_{\odot}$ for SN2018gep as well.

Finally, Katz et al. (2013) and Wygoda et al. (2019) present an analytical technique for testing whether a light curve is powered by radioactive decay. At late times, the bolometric luminosity is equal to the rate of energy deposition by

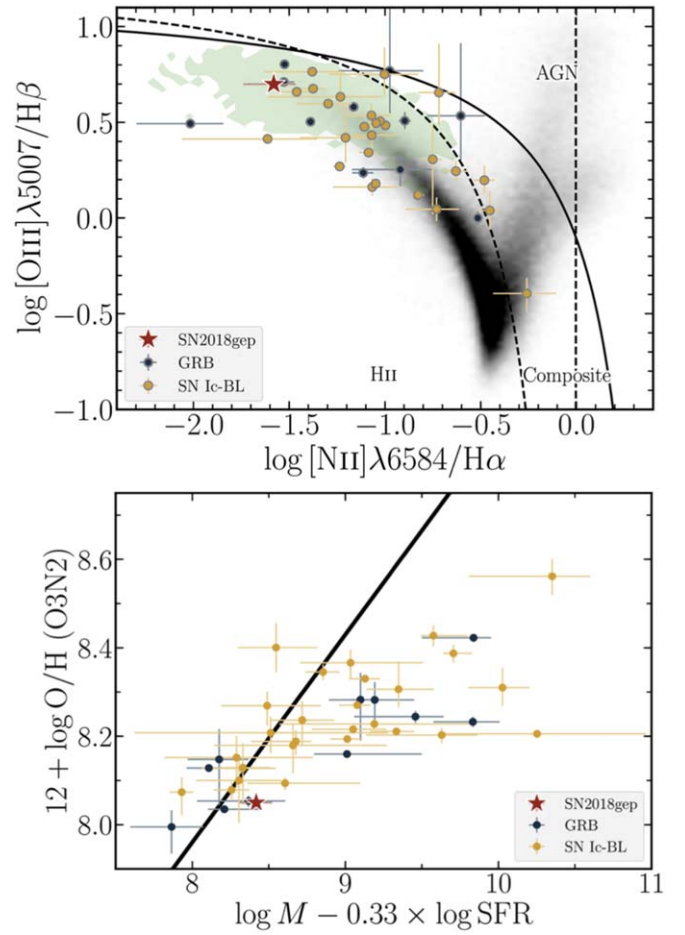


Figure 16. Top: BPT diagram. The host of SN2018gep is a low-metallicity galaxy with an intense ionizing radiation field (green shaded region indicates extreme emission line galaxies). The majority of Ic-BL SNe and long-duration GRBs are found in more metal enriched galaxies (parameterized by $[\text{N II}]/\text{H}\alpha$), and galaxies with less intense radiation fields (parameterized by $[\text{O III}]/\text{H}\alpha$). Field galaxies from SDSS DR15 are shown as a background density distribution. The thick solid line separates star formation- and AGN-dominated galaxies (Kewley et al. 2001). Bottom: the mass–metallicity–star formation-rate plane. The bulk of the SN-Ic-BL and GRB host populations are found in hosts that are more metal enriched. For reference, the host of AT2018cow had $\log M - 0.33 \times \log \text{SFR} \approx 9.4$. The black line is the fundamental metallicity relation in Mannucci et al. (2010).

radioactive decay $Q(t)$, because the diffusion time is much shorter than the dynamical time: $L_{\text{bol}}(t) = Q(t)$. At any given time, the energy deposition rate $Q(t)$ is

$$Q(t) = Q_{\gamma}(t)(1 - e^{-(t_0/t)^2}) + Q_{\text{pos}}(t) \quad (1)$$

where $Q_{\gamma}(t)$ is the energy release rate of gamma-rays and t_0 is the time at which the ejecta becomes optically thin to gamma-rays. The expression for $Q_{\gamma}(t)$ is

$$\frac{Q_{\gamma}(t)}{10^{43} \text{ erg s}^{-1}} = \frac{M_{\text{Ni}}}{M_{\odot}} (6.45e^{-t/8.76 \text{ days}} + 1.38e^{-t/111.4 \text{ days}}). \quad (2)$$

$Q_{\text{pos}}(t)$ is the energy deposition rate of positron kinetic energy, and the expression is

$$\frac{Q_{\text{pos}}(t)}{10^{41} \text{ erg s}^{-1}} = 4.64 \frac{M_{\text{Ni}}}{M_{\odot}} (-e^{-t/8.76 \text{ days}} + e^{-t/111.4 \text{ days}}). \quad (3)$$

The dotted line in Figure 17 shows a model track with $M_{\text{Ni}} = 0.28 M_{\odot}$ and $t_0 = 30$ days. Lower nickel masses produce tracks that are too low to reproduce the data, and

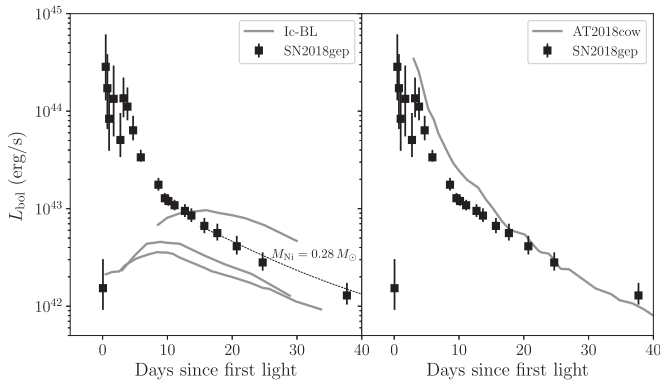


Figure 17. The bolometric light curve of SN2018gep compared to (left) other Ic-BL SNe from the literature (Cano 2013) and (right) to AT2018cow (Perley et al. 2019). The dotted line shows the expected contribution from the radioactive decay of ^{56}Ni , for a gamma-ray escape time of 30 days and $M_{\text{Ni}} = 0.28 M_{\odot}$. In order of decreasing L_{bol} , the three Ic-BL SNe are SN1998bw, SN2010bh, and SN2006aj.

larger values of t_0 produce tracks that drop off too rapidly. Thus on this scale it seems that $M_{\text{Ni}} \sim 0.3 M_{\odot}$, similar to other Ic-BL SNe (Lyman et al. 2016). Because the data have not yet converged to model tracks, we cannot solve directly for t_0 and M_{Ni} using the technique for Ia SNe in Wygoda et al. (2019).

We can also try to solve directly for t_0 and M_{Ni} using the technique for Ia SNe in Wygoda et al. (2019). The first step is to solve for t_0 using Equation (1) and a second equation resulting from the fact that the expansion is adiabatic,

$$\int_0^t Q(t') t' dt' = \int_0^t L_{\text{bol}}(t') t' dt'. \quad (4)$$

The ratio of Equation (1) to Equation (4) removes the dependence on M_{Ni} , and enables t_0 to be measured. However, as shown in Figure 18, the data have not yet converged to model tracks.

4.2. Interaction with Extended Material

One way to power a rapid and luminous light curve is to deposit energy into CSM at large radii (Nakar & Sari 2010; Nakar & Piro 2014; Piro 2015). Since this is a Ic-BL SN, we expect the progenitor to be stripped of its envelope and therefore compact ($R \sim 0.5 R_{\odot} \sim 10^{10}$ cm; Groh et al. 2013), although there have never been any direct progenitor detections for a Ic-BL SN.

With this expectation, extended material at larger radii would have to arise from mass loss. This would not be surprising, as massive stars are known to shed a significant fraction of their mass in winds and eruptive episodes; see Smith (2014) for a review.

First we perform an order-of-magnitude calculation to see whether the rise time and peak luminosity could be explained by a model in which shock interaction powers the light curve (“wind shock breakout”). Assuming that the progenitor ejected material with a velocity v_w at a time t prior to explosion, the radius of this material at any given time is

$$\begin{aligned} R_{\text{sh}} &= R_* + v_w t \\ &\approx (8.64 \times 10^{12} \text{ cm}) \left(\frac{v_w}{1000 \text{ km s}^{-1}} \right) \left(\frac{t}{\text{day}} \right). \end{aligned} \quad (5)$$

For material ejected 15 days prior to explosion, traveling at 1000 km s^{-1} , the radius would be $R_{\text{CSM}} \sim 10^{14}$ cm at the time

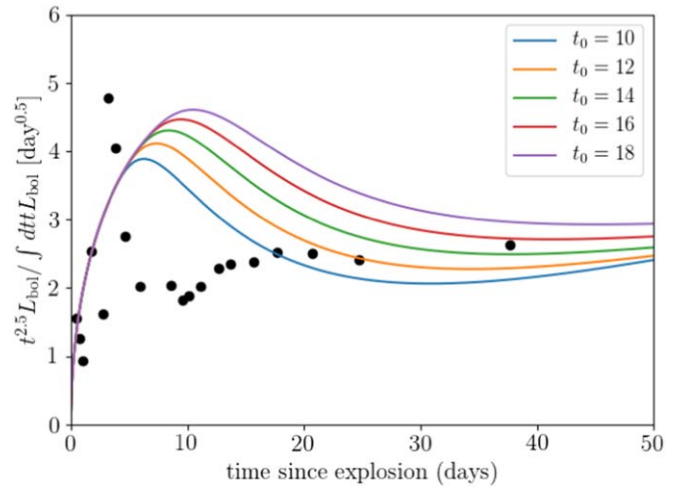


Figure 18. To test whether a light curve is powered by radioactive decay, the ratio of the bolometric luminosity to the time-weighted integrated bolometric luminosity should converge to model tracks, as described in Katz et al. (2013) and Wygoda et al. (2019). This enables a direct measurement of the gamma-ray escape time t_0 and the nickel mass M_{Ni} . However, our data have not converged to these tracks, suggesting that either radioactive decay is not dominant, or that we are not yet in a phase where we can perform this measurement.

of explosion. The shock crossing timescale is t_{cross} :

$$t_{\text{cross}} \sim R_{\text{CSM}}/v_s \approx (0.4 \text{ day}) \left(\frac{R}{10^{14} \text{ cm}} \right) \left(\frac{v_s}{0.1c} \right)^{-1} \quad (6)$$

where v_s is the velocity of the shock. The shock heats the CSM with an energy density that is roughly half of the kinetic energy of the shock, so $e_s \sim (1/2)(\rho v_s^2/2)$. The luminosity is the total energy deposited divided by t_{cross} ,

$$\begin{aligned} L_{\text{BO}} &\sim \frac{E_{\text{BO}}}{t_{\text{cross}}} \sim \frac{v_s^3 dM}{4 dR} \\ &= (8 \times 10^{44} \text{ erg s}^{-1}) \left(\frac{v_s}{0.1c} \right)^3 \left(\frac{dM}{M_{\odot}} \right) \left(\frac{dR}{10^{14} \text{ cm}} \right)^{-1} \end{aligned} \quad (7)$$

assuming a constant density. Thus, for shock velocities on the order of the observed photospheric radius expansion ($0.1c$), and a CSM radius on the order of the first photospheric radius that we measure (3×10^{14} cm), it is easy to explain the rise time and peak luminosity that we observe.

To test whether shock breakout (and subsequent post-shock cooling) can explain the evolution of the physical properties we measured in Section 3, we ran one-dimensional numerical radiation hydrodynamics simulations of an SN running into a circumstellar shell with CASTRO (Almgren et al. 2010; Zhang et al. 2011). We assume spherical symmetry and solve the coupled equations of radiation hydrodynamics using a gray flux-limited nonequilibrium diffusion approximation. The setup is similar to the models presented in Rest et al. (2018) but with parameters modified to fit SN2018gep.

The ejecta is assumed to be homologously expanding, characterized by a broken power-law density profile, an ejecta mass M_{ej} , and energy E_{ej} . The ejecta density profile has an inner power-law index of $n = 0$ (that is, $\rho(r) \propto r^{-n}$) then steepens to an index $n = 10$, as is appropriate for core collapse SN explosions (Matzner & McKee 1999). The circumstellar shell is assumed to be uniform in density with radius R_{CSM} and mass M_{CSM} . We adopt a uniform opacity of $\kappa = 0.2 \text{ cm}^2 \text{ g}^{-1}$, which is characteristic of hydrogen-poor electron scattering.

The best-fit model, shown in Figure 19, used the following parameters: $M_{\text{ej}} = 8 M_{\odot}$, $E_{\text{ej}} = 2 \times 10^{52}$ erg, $M_{\text{CSM}} = 0.02 M_{\odot}$, and $R_{\text{CSM}} = 3 \times 10^{14}$ cm. The inferred kinetic energy is consistent with typical values measured for Ic-BL SNe (e.g., Cano et al. 2017; Taddia et al. 2019), and R_{CSM} is similar in value to the first photospheric radius we measure (at $\Delta t = 0.05$ day; see Figure 9).

The inferred values presented here are likely uncertain to within a factor of a few, given the degeneracies of the rise time and peak luminosity with the CSM mass and radius. Qualitatively, a larger CSM radius will result in a higher peak luminosity and longer rise time. The peak luminosity is relatively independent of the CSM mass, which instead affects the photospheric velocity and temperature (i.e., a larger CSM mass slows down the post-interaction velocity to a greater extent and increases the shock-heated temperature). A full discussion of the dependencies of the light curve and photospheric properties on the CSM parameters will be presented in an upcoming work (D. Khatami et al. 2019, in preparation.).

In this framework, the shockwave sweeps through the CSM prior to peak luminosity, so that at maximum luminosity the outer parts of the CSM have been swept into a dense shell moving at SN-like velocities ($v_{\text{post-shock}} \approx 3v_s/4$). This scenario was laid out in Chevalier & Irwin (2011) and discussed in Kasen (2017). This explains the high velocities we measure at early times and the absence of narrow emission features in our spectra. For another discussion of the absence of narrow emission lines due to an abrupt cutoff in CSM density, see Moriya & Tominaga (2012). Following Chevalier & Irwin (2011), the rapid rise corresponds to shock breakout from the CSM, and begins at a time $R_{\text{CSM}}/v_{\text{sh}}$ after the explosion, where v_{sh} is the velocity of the shock. The time to peak luminosity (1.2 days) is longer than this delay time by a factor (R_w/R_d). Given the best-fit $R_w = 3 \times 10^{14}$ cm, and assuming $R_d \sim R_w$, we find $v_{\text{sh}} = 0.1c$, and an explosion time ~ 1 day prior to t_0 . This model also predicts an increasing temperature while the shock breaks out (i.e., during the rise to peak bolometric luminosity).

Other Ic SNe have shown early evidence for interaction in their light curves, but in other cases the emission has been attributed to post-shock cooling in expanding material rather than shock breakout itself. For example, the first peak observed in iPTF14gqr (De et al. 2018) was short-lived ($\lesssim 2$ days) and attributed to shock-cooling emission from material stripped by a compact companion. iPTF14gqr is different in a number of ways from SN2018gep: the spectra showed high-ionization emission lines, including He II, and the explosion had a much smaller kinetic energy ($E_k \approx 10^{50}$ erg) and smaller velocities ($10,000 \text{ km s}^{-1}$). The main peak in iPTF16asu was also modeled as shock-cooling emission rather than shock breakout (Whitesides et al. 2017).

Under the assumption that the light curve represented post-shock cooling emission, De et al. (2018) and Whitesides et al. (2017) both used one-zone analytic models from Piro (2015) to estimate the properties of the explosion and the CSM. This approximation assumes that the emitting region is a uniformly heated expanding sphere. In iPTF14gqr the inferred properties of the extended material were $M_e \sim 8 \times 10^{-3} M_{\odot}$ at $R_e \sim 3 \times 10^{13}$ cm. In iPTF16asu the inferred properties of the extended material were $M_e \sim 0.45 M_{\odot}$ at $R_e \sim 1.7 \times 10^{12}$ cm. The fit also required a more energetic explosion than iPTF14gqr (4×10^{51} erg). By applying the same framework to the decline of the bolometric light curve of SN2018gep, we arrive at similar values to those inferred for iPTF16asu, as shown in Figure 20.

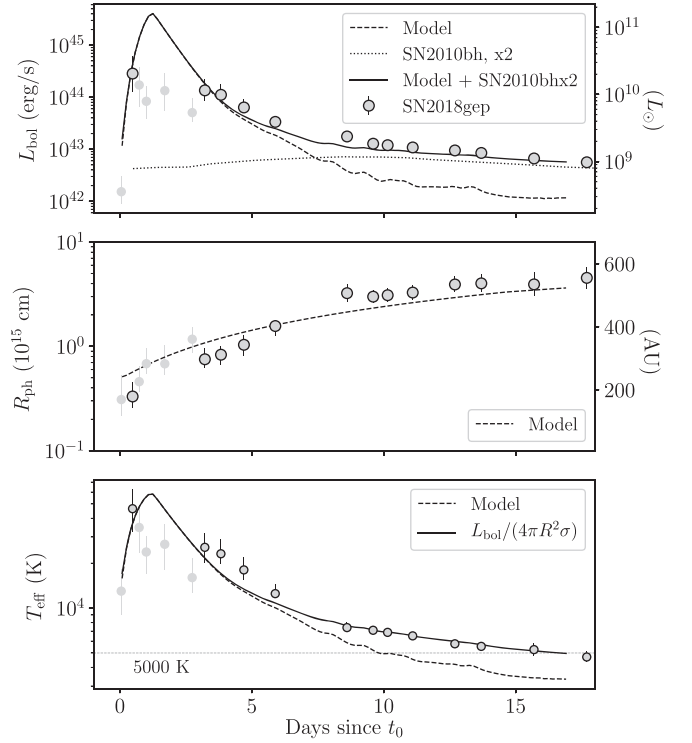


Figure 19. Best-fit CSM interaction model with the light curve of the Ic-BL SN 2010bh (Cano 2013) scaled up by a factor of two. The model parameters are $M_{\text{ej}} = 8 M_{\odot}$, $E_{\text{ej}} = 2 \times 10^{52}$ erg, $M_{\text{CSM}} = 0.02 M_{\odot}$, and $R_{\text{CSM}} = 3 \times 10^{14}$ cm. As in Figure 9, the outlined circles are derived from UV and optical data, while the light gray circles are derived from optical data only.

We model the main peak of SN2018gep as shock breakout rather than post-shock cooling emission. Our motivation for this choice is that the timescale over which we detect the precursor emission is more consistent with a large radius and lower shell mass. From the shell mass and radius, we can also estimate the mass-loss rate immediately prior to explosion,

$$\frac{\dot{M}}{M_{\odot} \text{ yr}^{-1}} \approx 32 \left(\frac{M_{\text{sh}}}{M_{\odot}} \right) \left(\frac{v_w}{1000 \text{ km s}^{-1}} \right) \left(\frac{R_{\text{sh}}}{10^{14} \text{ cm}} \right)^{-1}. \quad (8)$$

For our best-fit parameters $M_{\text{sh}} = 0.02 M_{\odot}$ and $R_{\text{sh}} = 3 \times 10^{14}$ cm, and taking $v_w = 1000 \text{ km s}^{-1}$, we find $\dot{M} \approx 0.6 M_{\odot} \text{ yr}^{-1}$, 4–6 orders of magnitude higher than what is typically expected for Ic-BL SNe (Smith 2014).

In the shock breakout model, the shock sweeps through confined CSM and passes into lower density material. Thus, it is not surprising that we do not observe the X-ray or radio emission that would indicate interaction with high-density material. From our VLA observations of SN2018gep, the radio flux marginally decreased from $\Delta t = 5$ days to $\Delta t = 75$ days. This could be astrophysical, but could also be instrumental (change in beam size due to change in VLA configuration). Using the relation of Murphy et al. (2011), the estimated contribution from the host galaxy (for an SFR of $0.12^{+0.08}_{-0.05} M_{\odot} \text{ yr}^{-1}$; see Section 3.3) is

$$\left(\frac{L_{1.4 \text{ GHz}}}{\text{erg s}^{-1} \text{ Hz}^{-1}} \right) \approx 1.57 \times 10^{28} \left(\frac{\text{SFR}_{\text{radio}}}{M_{\odot} \text{ yr}^{-1}} \right) \approx 1.9 \times 10^{27} \text{ erg s}^{-1} \text{ Hz}^{-1}. \quad (9)$$

Taking a spectral index of -0.7 (a synchrotron spectrum), the expected 9 GHz luminosity would be between $3.0 \times 10^{26} \text{ erg s}^{-1} \text{ Hz}^{-1}$ and $8.6 \times 10^{26} \text{ erg s}^{-1} \text{ Hz}^{-1}$. From Table 2,

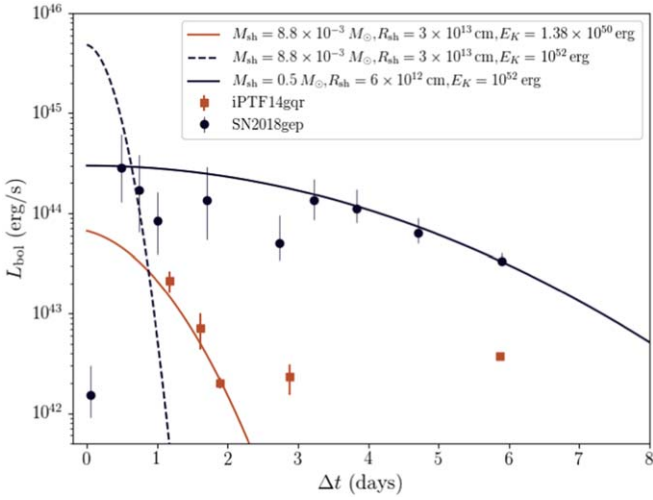


Figure 20. Estimated CSM and explosion properties using models from Piro (2015). The shell mass is much larger than the one in iPTF14gqr, which is the reason for the more extended shock-cooling peak.

the measured spectral luminosity is $8.3 \times 10^{26} \text{ erg s}^{-1} \text{ Hz}^{-1}$ (at 10 GHz) in the first epoch, and $6 \times 10^{26} \text{ erg s}^{-1} \text{ Hz}^{-1}$ (at 9 GHz) in the second epoch. The slit covering fraction of our LRIS observations is again relevant here; as discussed in Section 3.3, the true SFR is likely a factor of a few higher than what we inferred from modeling the galaxy SED. So, it is plausible that the first two radio detections are entirely due to the host galaxy.

In the third epoch, the luminosity (at 9 GHz) is $< 3.9 \times 10^{26} \text{ erg s}^{-1} \text{ Hz}^{-1}$, although the difference from the first two epochs may be due to the different array configuration. Taking the peak of the 9–10 GHz light curve to be $8.3 \times 10^{26} \text{ erg s}^{-1} \text{ Hz}^{-1}$ at $\Delta t \approx 5$ days, Figure 21 shows that SN2018gep would be an order of magnitude less luminous in radio emission than any other Ic-BL SN. If the luminosity truly decreased, then the implied mass-loss rate is $\dot{M} \sim 3 \times 10^{-6}$, consistent with the idea that the shock has passed from confined CSM into much lower density material.

If the emission is constant and due entirely to the host galaxy, the point shown in Figure 21 is an upper limit in luminosity. Assuming that the peak of the SED of any radio emission from the SN is not substantially different from the frequencies we measure (i.e., that the spectrum is not self-absorbed at these frequencies), we have a limit on the 9 GHz radio luminosity of $L_p \lesssim 10^{27} \text{ erg s}^{-1} \text{ Hz}^{-1}$ at $\Delta t \approx 5\text{--}15$ days.

The shell mass and radius also give an estimate of the optical depth: $\tau \approx \kappa M / r^2 \approx 100 \gg 1$, which means that the shell would be optically thick. The lack of detected X-ray emission is consistent with the expectation that any X-ray photons produced in the collision would be thermalized by the shell and reradiated as blackbody emission.

Finally, assuming that the rapid rise to peak is indeed caused by shock breakout, we examine whether our model is consistent with our detections in the weeks prior to explosion. Material ejected 10 days prior to the explosion at the escape velocity of a Wolf-Rayet star ($v_{\text{esc}} \sim 1000 \text{ km s}^{-1}$) would lie at $R \sim 10^{14} \text{ cm}$, which is consistent with our model. Assuming that the emission mechanism is internal shocks between shells of ejected material traveling at different velocities, we can estimate the amount of mass required:

$$\frac{1}{2} \epsilon M v^2 = L \tau \quad (10)$$

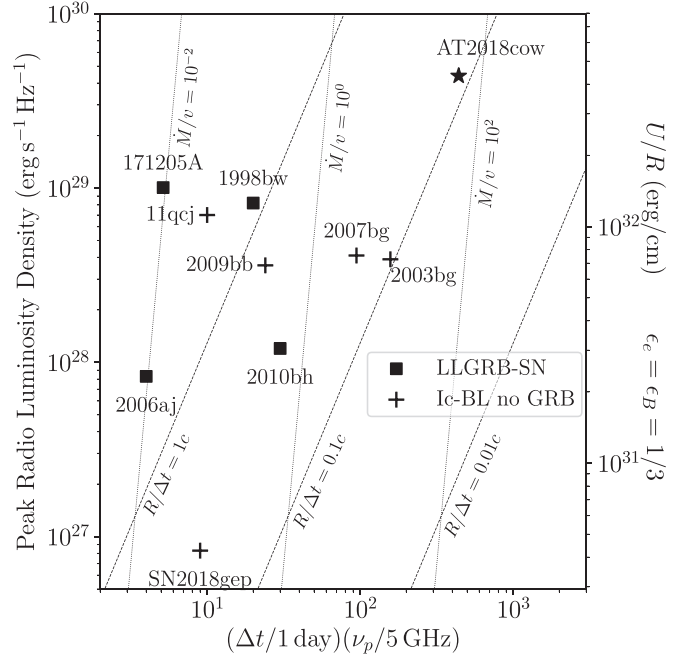


Figure 21. The radio luminosity of SN2018gep compared to AT2018cow and radio-loud Ic-BL SNe (assuming $\epsilon_e = \epsilon_B = 1/3$, see Chevalier 1998; Soderberg et al. 2010; Ho et al. 2019). Lines of constant mass-loss rate (scaled to wind velocity) are shown in units of $10^{-4} M_{\odot} \text{ yr}^{-1} / 1000 \text{ km s}^{-1}$. The radio luminosity for GRB 171205A was taken from VLA observations reported by Laskar et al. (2017), but we note that this is a lower limit in luminosity and in peak frequency because the source was heavily self-absorbed at this epoch.

where $v \approx 1000 \text{ km s}^{-1}$, $\epsilon \approx 0.5$ is the efficiency of thermalizing the kinetic energy of the shells, M is the shell mass, $L \approx 10^{39} \text{ erg s}^{-1}$ is the luminosity we observe, and $\tau \approx 10$ days is the timescale over which we observe the emission. We find $M \approx 0.02 M_{\odot}$, again consistent with our model.

We conclude that the data are consistent with a scenario in which a compact Ic-BL progenitor underwent a period of eruptive mass loss shortly prior to explosion. In the terminal explosion, the light curve was initially dominated by shock breakout through (and post-shock cooling of) this recently ejected material.

Finally, we return to the question of the emission detected in the first few minutes, which showed an inflection point prior to the rapid rise to peak (Figure 2). Given the pre-explosion activity and inference of CSM interaction, it is not surprising that the rise is not well-modeled by a simple quadratic function. One possibility is that we are seeing ejecta already heated from earlier precursor activity. Another possibility is that we are seeing the effects of a finite light travel time. For a sphere of $R \sim 3 \times 10^{14} \text{ cm}$, the light-crossing time is ~ 20 minutes. The slower rising phase could represent the time for photons to reach us across the extent of the emitting sphere.

In Table 4, we summarize the key properties inferred from Section 4.

5. Comparison to Unclassified Rapidly Evolving Transients at High Redshift

In terms of the timescale of its light curve evolution, SN2018gep is similar to AT2018cow in fulfilling the criteria that optical surveys use to identify rapidly evolving transients (e.g., Drout et al. 2014; Tanaka et al. 2016; Pursiainen et al. 2018). However, there are a number of ways in which SN2018gep is more of a “typical” member of these populations

Table 4
Key Model Properties of SN2018gep

Parameter	Value	Notes
t_{rise}	1.2 days	
E_{SN}	2×10^{52} erg	
M_{ej}	$8 M_{\odot}$	
M_{CSM}	$0.02 M_{\odot}$	
R_{CSM}	3×10^{14} cm	
\dot{M}	$0.6 M_{\odot} \text{ yr}^{-1}$	Assuming $v_w = 1000 \text{ km s}^{-1}$
M_{Ni}	$< 0.2\text{--}0.3 M_{\odot}$	

than AT2018cow. In particular, SN2018gep has an expanding photospheric radius and declining effective temperature. By contrast, one of the challenges in explaining AT2018cow as a stellar explosion was its nearly constant temperature (persistent blue color) and *declining* photospheric radius. In Figure 22 we show these two different kinds of evolution as very different tracks in color–magnitude space. We also show a late-time point for KSN2015K (Rest et al. 2018), which shows blue colors even after the transient had faded to half-max. The mass-loss rate inferred for Rest et al. (2018) was $2 \times 10^{-3} M_{\odot} \text{ yr}^{-1}$.

Of the PS-1 events, most appear to expand, cool, and redden with time (Drout et al. 2014). That said, there are few coeval data points in multiple filters, even in the gold sample transients. The transients are also faint; all but one lie at $z > 0.1$. Of the DES sample, most also show evidence for declining temperatures and increasing radii, although three show evidence of a constant temperature and decreasing radius: 15X3mxf, 16X1eho, and 15C3opk. The peak bolometric luminosities for these three transients are reported as $3 \times 10^{43} \text{ erg s}^{-1}$, $9 \times 10^{43} \text{ erg s}^{-1}$, and $5 \times 10^{43} \text{ erg s}^{-1}$, respectively (Pursiainen et al. 2018).

To estimate a rate of Ic-BL SNe that have a light curve powered by shock breakout, we used the sample of 25 nearby ($z < 0.1$) Ic-BL SNe from PTF (Taddia et al. 2019), because these were found in an untargeted survey. Of these, we could not draw a conclusion about eight (either because the peak was not resolved or there was no multicolor photometry available around peak, or both). The remaining clearly lacked the rise time or blue colors of SN2018gep. Furthermore, SN2018gep is unique among the sample of 12 nearby ($z < 0.1$) Ic-BL SNe from ZTF discovered so far, which will be presented in a separate publication. From this, we estimate that the rate of Ic-BL SNe with a main peak dominated by shock breakout is no more than 10% of the rate of Ic-BL SNe.

6. Summary and Future Work

In this paper, we presented an unprecedented data set that connects late-stage eruptive mass loss in a stripped massive star to its subsequent explosion as a rapidly rising luminous transient. Here we summarize our key findings:

1. High-cadence dual-band observations with ZTF (six observations in 3 hr) captured a rapid rise ($1.4 \pm 0.1 \text{ mag hr}^{-1}$) to peak luminosity, and a corresponding increase in temperature. This rise rate is second only to that of SN 2016gkg (Bersten et al. 2018), which was attributed to shock breakout in extended material surrounding a Type IIb progenitor. However, the signal in SN2018gep is two magnitudes more luminous.
2. A retrospective search in ZTF data revealed clear detections of precursor emission in the days and months leading up to the terminal explosion. The luminosity of

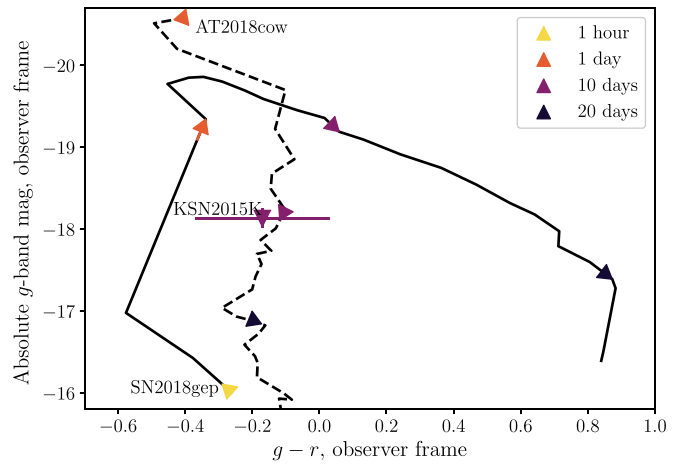


Figure 22. A “color–magnitude” diagram of AT2018cow and SN2018gep, showing the evolution of color with time from first light (t_0). Like AT2018cow, the fast transient KSN2015K stayed persistently blue even after it had faded to half-maximum. SN2018gep has more typical SN evolution, reddening with time (cooling in temperature).

these detections ($M = -14$) and evidence for variability suggests that they arise from eruptive mass loss, rather than the luminosity of a quiescent progenitor. This is the first definitive pre-explosion detection of a Ic-BL SN.

3. The bolometric light curve peaks after a few days at $> 3 \times 10^{44} \text{ erg s}^{-1}$. At late times, a power-law and an exponential decay are both acceptable fits to the data.
4. The temperature rises to 50,000 K in the first day, then declines as t^{-1} then flattens at 5000 K, which we attribute to recombination of carbon and oxygen.
5. The photosphere expands at $v = 0.1c$, and flattens once recombination sets in.
6. We obtained nine spectra in the first five days of the explosion, as the effective temperature declined from 50,000 K to 20,000 K. To our knowledge, these represent the earliest-ever spectra of a stripped-envelope SN, in terms of temperature evolution.
7. The early spectra exhibit a “W” feature similar to what has been seen in stripped-envelope superluminous SNe. From an NLTE spectral synthesis model, we find that this can be reproduced with a carbon and oxygen composition.
8. The velocities inferred from the spectra are among the highest observed for stripped-envelope SNe, and are most similar to the velocities of Ic-BL SNe accompanied by GRBs.
9. The host galaxy has a star formation rate of $0.12 M_{\odot} \text{ yr}^{-1}$, and a lower mass and lower metallicity than galaxies hosting GRB-SNe, which are low-mass and low-metallicity compared to the overall CC SN population.
10. The early light curve is best described by shock breakout in extended but confined CSM, with $M = 0.02 M_{\odot}$ at $R = 3 \times 10^{14} \text{ cm}$. The implied mass-loss rate is $0.6 M_{\odot} \text{ yr}^{-1}$ in the days leading up to the explosion, consistent with our detections of precursor emission. After the initial breakout, the shock runs through CSM of much lower density, hence the lack of narrow emission features and lack of strong radio and X-ray emission.
11. Although SN2018gep is similar to AT2018cow in terms of its bolometric light curve, it has a very different color evolution. In this sense, the “rapidly evolving transients”

in the PS-1 and DES samples are more similar to SN2018gep than to AT2018cow.

12. The late-time light curve seems to require an energy deposition mechanism distinct from shock interaction. Radioactive decay is one possibility, but further monitoring is needed to test this.

The code used to produce the results described in this paper was written in Python and is available online in an open-source GitHub repository⁴¹ and it is archived on Zenodo (doi:10.5281/zenodo.3534067). When the paper has been accepted for publication, the data will be made publicly available via WISEREP, an interactive repository of supernova data (Yaron & Gal-Yam 2012).

The authors would like to thank the anonymous referee whose comments improved the flow, precision, and clarity of the paper. It is a pleasure to thank Tony Piro, Dan Kasen, E. Sterl Phinney, Eliot Quataert, Maryam Modjaz, Jim Fuller, Lars Bildsten, Udi Nakar, Paul Duffell, and Luc Dessart for helpful discussions. A.Y.Q.H. is particularly grateful to Tony Piro and the community at Carnegie Observatories for their hospitality on Tuesdays during the period in which this work was performed. Thank you to the staff at the SMA, AMI, the VLA, *Swift*, and *Chandra* for rapidly scheduling and executing the observations. Thank you to David Palmer (LANL) for his assistance in searching the pointing data for *Swift*/BAT. Thank you to Michael J. Koss (Eureka Scientific Int), Andrew Drake (Caltech), Scott Adams (Caltech), Matt Hankins (Caltech), Kevin Burdge (Caltech), and Kirsty Taggart (LJMU) for assisting with optical spectroscopic observations. Thank you to Erik Petigura and David Hogg for their advice on figure aesthetics. Thank you to David Alexander Kann (IAA-CSIC) for pointing out an error in an early version of the paper posted to the arXiv. D.A.G. thanks Stéfan van der Walt and Ari Crellin-Quick for assistance with skyportal, which enabled the search for pre-explosion emission.

A.Y.Q.H. is supported by a National Science Foundation Graduate Research Fellowship under grant No. DGE1144469. This work was supported by the GROWTH project funded by the National Science Foundation under PIRE grant No. 1545949. A. G.-Y. is supported by the EU via ERC grant No. 725161, the ISF, the BSF Transformative program, and by a Kimmel award. Y.T. studied as a GROWTH intern at Caltech during the summer and fall of 2017. C.C.N. thanks the funding from *MOST* grant 104-2923-M-008-004-MY5. R.L. is supported by a Marie Skłodowska-Curie Individual Fellowship within the Horizon 2020 European Union (EU) Framework Programme for Research and Innovation (H2020-MSCA-IF-2017-794467). A.H. acknowledges support by the I-Core Program of the Planning and Budgeting Committee and the Israel Science Foundation, and support by the ISF grant 647/18. This research was supported by a grant from the GIF, the German-Israeli Foundation for Scientific Research and Development. This research was funded in part by the Gordon and Betty Moore Foundation through Grant GBMF5076, and a grant from the Heising-Simons Foundation. A.C. acknowledges support from the NSF CAREER award N. 1455090 and from the NASA/*Chandra* GI award N. GO8-19055A. Research support to I.A. is provided by the GROWTH project, funded by the National Science Foundation under grant No 1545949.

This work is based on observations obtained with the Samuel Oschin Telescope 48 inch and the 60 inch Telescope at the Palomar

Observatory as part of the Zwicky Transient Facility project. Major funding has been provided by the U.S. National Science Foundation under grant No. AST-1440341 and by the ZTF partner institutions: the California Institute of Technology, the Oskar Klein Centre, the Weizmann Institute of Science, the University of Maryland, the University of Washington, Deutsches Elektronen-Synchrotron, the University of Wisconsin–Milwaukee, and the TANGO Program of the University System of Taiwan. Partially based on observations made with the Nordic Optical Telescope, operated by the Nordic Optical Telescope Scientific Association at the Observatorio del Roque de los Muchachos, La Palma, Spain, of the Instituto de Astrofísica de Canarias. The Liverpool Telescope is operated by Liverpool John Moores University with financial support from the UK Science and Technology Facilities Council. LT is located on the island of La Palma, in the Spanish Observatorio del Roque de los Muchachos of the Instituto de Astrofísica de Canarias. The scientific results reported in this article are based in part on observations made by the *Chandra X-ray Observatory*. The data presented here were obtained in part with ALFOSC, which is provided by the Instituto de Astrofísica de Andalucía (IAA) under a joint agreement with the University of Copenhagen and NOTSA. The Submillimeter Array is a joint project between the Smithsonian Astrophysical Observatory and the Academia Sinica Institute of Astronomy and Astrophysics and is funded by the Smithsonian Institution and the Academia Sinica. We acknowledge the support of the staff of the Xinglong 2.16 m telescope. This work is supported by the National Natural Science Foundation of China (NSFC grants 11325313 and 11633002), and the National Program on Key Research and Development Project (grant No. 2016YFA0400803). SED Machine is based upon work supported by the National Science Foundation under grant No. 1106171. This publication has made use of data collected at Lulin Observatory, partly supported by MoST grant 105-2112-M-008-024-MY3. The JEKYLL simulations were performed on resources provided by the Swedish National Infrastructure for Computing (SNIC) at Paralleldatorcentrum (PDC).

Facilities: CFHT, Keck:I (LRIS), Hale (DBSP), AMI, Liverpool:2 m (IO:O, SPRAT), DCT, *Swift* (UVOT, XRT), Beijing:2.16 m, EVLA, SMA, LO:1 m, NOT (ALFOSC).

Software: Astropy (Astropy Collaboration et al. 2013, 2018), IPython (Pérez & Granger 2007), matplotlib (Hunter 2007), numpy (Oliphant 2006), scipy (Jones et al. 2001), extinction (Barbary 2016) SkyPortal (Van der Walt et al. 2019).

Appendix

In Appendix A we provide the full set of optical and UV photometry and the blackbody fits to this photometry. In Appendix B we provide the log of optical and UV spectroscopic observations, as well as a figure showing all of our optical spectra. In Appendix C we include more details about the atomic data used for our spectral modeling. In Appendix D we show the spectrum, line-flux measurements, and photometry that was used to derive the properties of the host galaxy.

Appendix A UV and Optical Photometry

Here we provide our optical and UV photometry (Table 5) and the blackbody fits to this photometry used to derive the photospheric evolution (Figure 23).

⁴¹ <https://github.com/annayqho/SN2018gep>

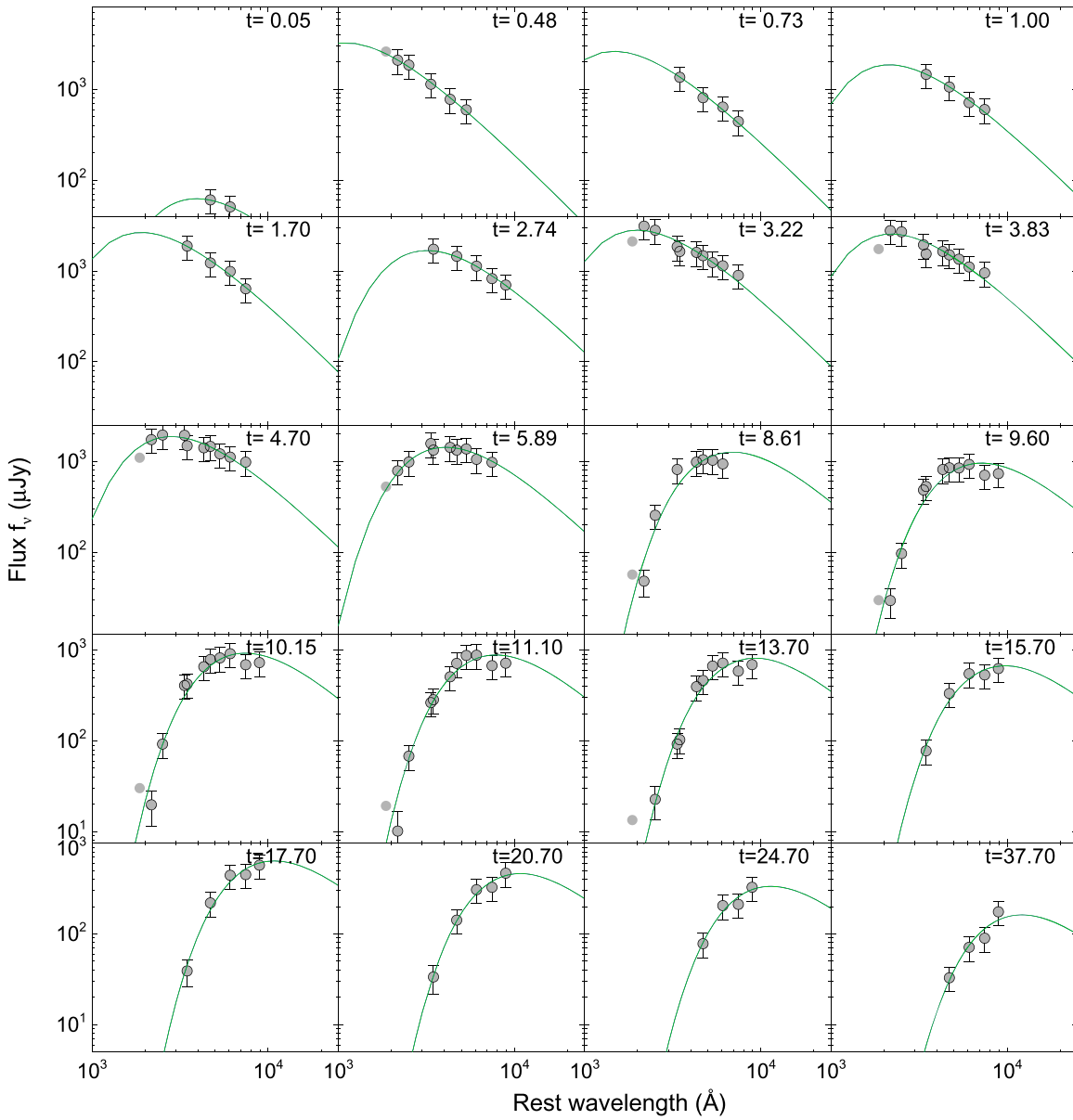


Figure 23. Blackbody fits to *Swift*/UVOT and optical photometry for SN2018gep. Since the UVOT and ground-based observations were taken at slightly different epochs, we interpolated the data in time using UVOT epochs at early times and LT epochs at later times.

Table 5
Optical and Ultraviolet Photometry for SN2018gep

Date (JD)	Δt	Instrument	Filter	AB Mag	Error in AB Mag
2458370.6634	0.02	P48+ZTF	<i>r</i>	20.48	0.26
2458370.6856	0.04	P48+ZTF	<i>g</i>	19.70	0.14
2458370.6994	0.05	P48+ZTF	<i>g</i>	19.34	0.11
2458370.7153	0.07	P48+ZTF	<i>g</i>	18.80	0.08
2458370.7612	0.11	P48+ZTF	<i>r</i>	18.36	0.08
2458370.7612	0.11	P48+ZTF	<i>r</i>	18.36	0.08
2458371.6295	0.98	P60+SEDM	<i>r</i>	16.78	0.01
2458371.6323	0.99	P60+SEDM	<i>g</i>	16.39	0.02
2458371.6351	0.99	P60+SEDM	<i>i</i>	17.01	0.01
2458371.6369	0.99	P48+ZTF	<i>r</i>	16.83	0.03
2458371.6378	0.99	P48+ZTF	<i>r</i>	16.81	0.04

Note. Table 5 is published in its entirety in the machine-readable format. A portion is shown here for guidance regarding its form and content.

(This table is available in its entirety in machine-readable form.)

Appendix B UV and Optical Spectroscopy

The observation log of our UV and optical spectra is provided in Table 6. A plot showing the full sequence of optical spectra is shown in Figure 24.

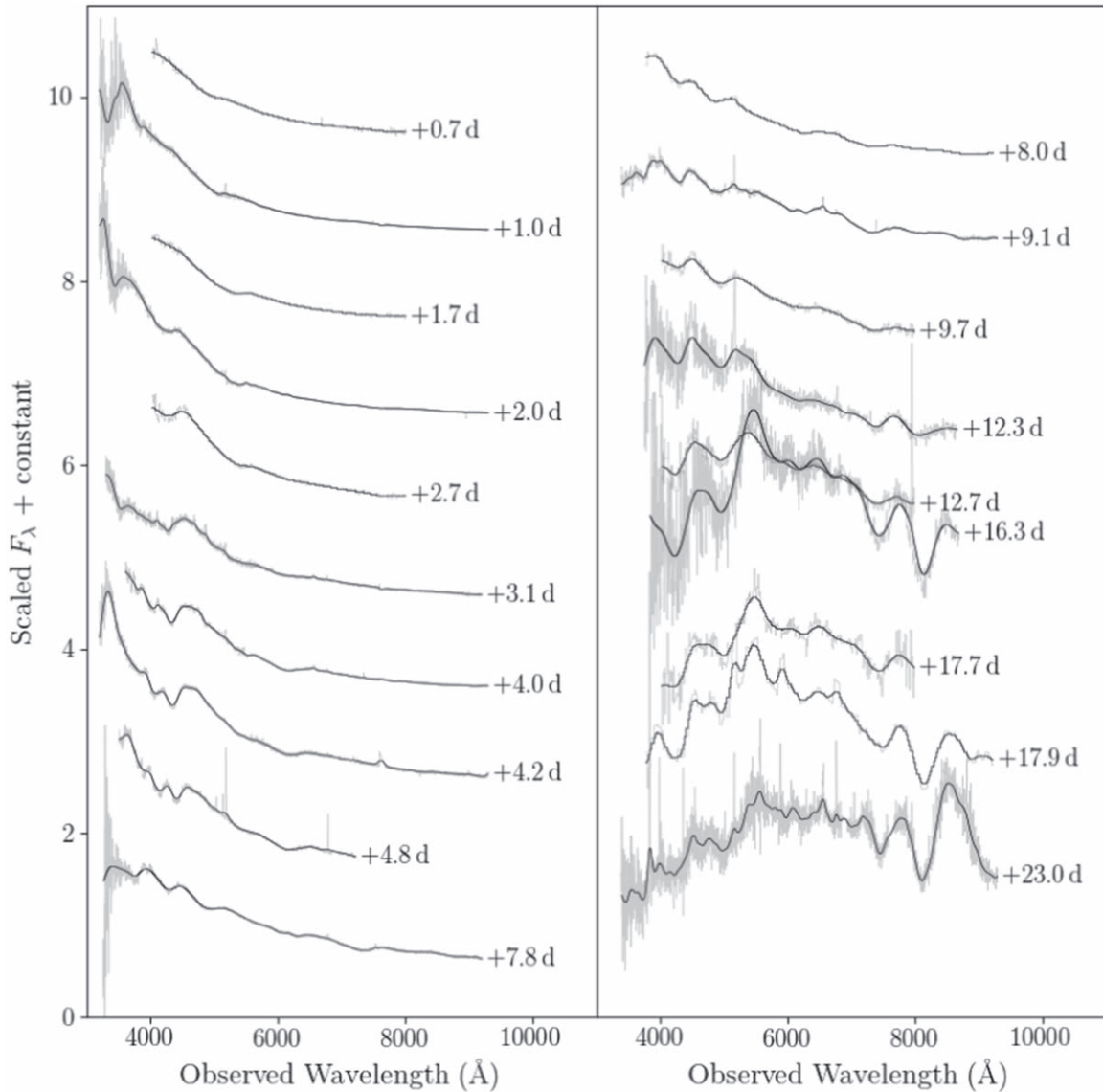


Figure 24. Ground-based optical spectra of SN2018gep. The light gray represents the observed spectrum, interpolating over host emission lines and telluric features. The black line is a Gaussian-smoothed version of the spectrum, using a Gaussian width that is several times the width of a galaxy emission line at that resolution. For more details on the smoothing procedure, see Section 2.1 of Ho et al. (2017).

Table 6
Log of SN2018gep Optical Spectra

Start Time (UTC)	Δt	Instrument	Exp. Time (s)	Airmass
2018 Sep 09 20:30:01	0.7	LT+SPRAT	1200	1.107
2018 Sep 10 04:28:51	1.0	P200+DBSP	600	1.283
2018 Sep 10 21:03:42	1.7	LT+SPRAT	900	1.182
2018 Sep 11 04:59:19	2.0	P200+DBSP	600	1.419
2018 Sep 11 20:22:35	2.7	LT+SPRAT	900	1.107
2018 Sep 12 06:09:59	3.1	P200+DBSP		
2018 Sep 13 03:52:58	4.0	P200+DBSP	300	1.209
2018 Sep 13 09:17:25	4.2	Keck I+LRIS	300	3.483
2018 Sep 14 02:44:24.24	4.8	DCT+Deveny+LMI	300	1.11
2018 Sep 17 04:38:40	8.0	P60+SEDM	1440	1.435
2018 Sep 17 20:40:25.750	8.7	NOT+ALFOSC	1800	1.19
2018 Sep 18 05:21:58	9.1	P200+DBSP	600	1.720
2018 Sep 18 20:14:35	9.7	LT+SPRAT	1000	1.143
2018 Sep 21 11:15:10	12.3	XLT+BFOSC	3000	1.181
2018 Sep 21 20:58:21	12.7	LT+SPRAT	1000	1.293
2018 Sep 25 11:16:43	16.3	XLT+BFOSC	3000	1.225
2018 Sep 26 20:22:54	17.7	LT+SPRAT	1000	1.242
2018 Sep 27 02:42:29	17.9	P60+SEDM	1440	1.172
2018 Oct 02 04:34:35	23.0	P200+DBSP	600	1.780
2018 Nov 09 05:26:17	61.1	Keck I+LRIS	900	3.242

Note. Gratings used: Wasatch600 (LT+SPRAT), Gr4 (NOT+ALFOSC), 600/4000 (P200+DBSP; blue side), 316/7500 (P200+DBSP; red side), 400/8500 (Keck I+LRIS; red side). Filters used: 400 nm (LT+SPRAT), open (NOT+ALFOSC), clear (Keck I+LRIS). Wavelength range: 4020–7995 Å (LT+SPRAT), 3200–9600 Å (NOT+ALFOSC), 1759–10311 Å (Keck I+LRIS), 3777–9223 Å (P60+SEDM). Resolution: 20 (LT+SPRAT), 710 (NOT+ALFOSC).

Appendix C Atomic Data for Spectral Modeling

The atomic data used for the spectral modeling in Section 3.2 is the same as described in Appendix A.4 of Ergon et al. (2018), but with the following modifications. The stage II–IV ions were (whenever possible) updated to include at least 50 levels for N, Na, Al, Ar, and Ca, at least 100 levels for C, O, Ne, Mg, Si, and S, and at least 300 levels for Sc, Ti, V, Cr, Mn, Fe, Co, and Ni. In addition we updated the C II–C IV and O II–O III ions with specific recombination rates from the online table by S. Nahar.⁴²

Appendix D Data for Measuring Host Properties

In this section we provide the data that we used to derive properties of the host galaxy of SN2018gep: the host-galaxy spectrum (Figure 25), line fluxes extracted from this spectrum (Table 7), and host-galaxy photometry (Table 8).

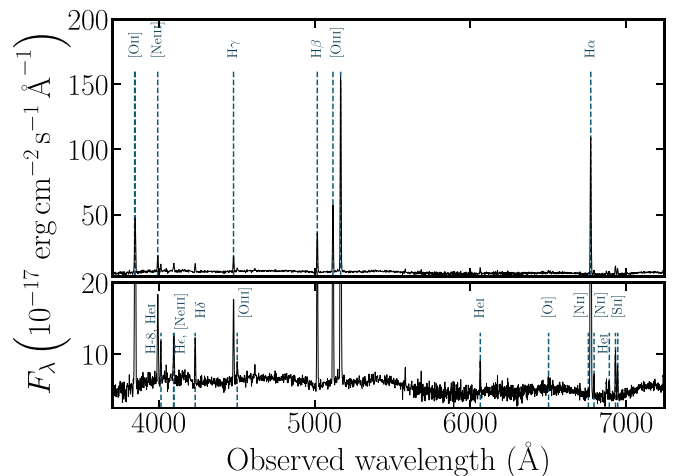


Figure 25. Host spectrum of SN2018gep obtained with Keck/LRIS on 2018 November 9, about two months after explosion. Strong emission lines from the host galaxy are labeled. The low host metallicity of 0.1 solar is reflected by very small N II/H α flux ratio. The large rest-frame [O III] λ 5007 equivalent width of >160 Å puts the host also in regime of extreme emission-line galaxies. This galaxy class constitutes $<2\%$ of all star-forming galaxies at $z < 0.3$ in the SDSS DR15 catalog. The undulations are due to the supernova. The spectrum is truncated at 7250 Å for presentation purposes, and it is corrected for Galactic reddening.

⁴² http://www.astronomy.ohio-state.edu/~nahar/_naharradiativeatomicdata/

Table 7
Line Fluxes from the Host Galaxy of SN2018gep Extracted from the Keck/LRIS Spectrum Obtained on 2018 November 9

Transition	λ_{obs} (Å)	F (10^{-17} erg cm $^{-2}$ s $^{-1}$)
[O II] $\lambda\lambda$ 3726, 3729	3848.17 \pm 0.05	334.5 \pm 6.23
[Ne III] λ 3869	3993.50 \pm 0.16	82.34 \pm 6.18
He I λ 3889, H-8	4014.49 \pm 0.16	29.01 \pm 4.73
[Ne III] λ 3968, He	4096.66 \pm 0.26	36.61 \pm 3.98
H δ	4233.87 \pm 0.13	44.88 \pm 2.59
H γ	4480.20 \pm 0.10	81.95 \pm 3.74
[O III] λ 4364	4503.68 \pm 0.10	15.01 \pm 2.69
H β	5017.87 \pm 0.08	213.41 \pm 10.53
[O III] λ 4960	5118.61 \pm 0.04	352.42 \pm 6.50
[O III] λ 5008	5168.04 \pm 0.04	1066.70 \pm 19.50
He I λ 5877	6064.21 \pm 0.20	27.04 \pm 2.30
O I λ 6302	6502.18 \pm 1.08	6.72 \pm 2.94
[N II] λ 6549	6758.16 \pm 0.02	11.15 \pm 6.73
H α	6773.40 \pm 0.02	723.85 \pm 7.65
[N II] λ 6585	6794.67 \pm 0.02	19.01 \pm 5.76
[He I] λ 6678	6890.29 \pm 0.14	7.88 \pm 2.19
[S II] λ 6718	6931.83 \pm 0.10	41.76 \pm 2.38
[S II] λ 6732	6946.68 \pm 0.10	28.15 \pm 2.19

Note. All measurements are corrected for Galactic reddening.

Table 8
Brightness of the Host Galaxy from UV to IR Wavelengths

Instrument/ Filter	λ_{eff} (Å)	Brightness (mag)	Instrument/ Filter	λ_{eff} (Å)	Brightness (mag)
GALEX/FUV	1542.3	20.20 \pm 0.03	SDSS/ i'	7439.5	18.62 \pm 0.04
GALEX/NUV	2274.4	20.09 \pm 0.03	SDSS/ z'	8897.1	18.59 \pm 0.12
UVOT/ $w2$	2030.5	19.91 \pm 0.12	PS1/ g_{PS1}	4775.6	18.96 \pm 0.04
UVOT/ $m2$	2228.1	20.00 \pm 0.14	PS1/ r_{PS1}	6129.5	18.82 \pm 0.04
UVOT/ $w1$	2589.1	20.11 \pm 0.16	PS1/ i_{PS1}	7484.6	18.88 \pm 0.04
UVOT/ u	3501.2	19.74 \pm 0.16	PS1/ z_{PS1}	8657.8	18.71 \pm 0.05
UVOT/ b	4328.6	19.45 \pm 0.20	WIRCam/ J	12481.5	18.99 \pm 0.09
UVOT/ v	5402.1	18.45 \pm 0.21	2MASS/ H	16620.0	18.33 \pm 0.36
SDSS/ u'	3594.9	19.97 \pm 0.12	WISE/ $W1$	33526.0	19.39 \pm 0.08
SDSS/ g'	4640.4	18.88 \pm 0.02	WISE/ $W2$	46028.0	19.85 \pm 0.19
SDSS/ r'	6122.3	18.76 \pm 0.05			

Note. All measurements are reported in the AB system and are not corrected for reddening. For guidance, we report the effective wavelengths of each filter.

ORCID iDs

Anna Y. Q. Ho  <https://orcid.org/0000-0002-9017-3567>
 Daniel A. Goldstein  <https://orcid.org/0000-0003-3461-8661>
 Steve Schulze  <https://orcid.org/0000-0001-6797-1889>
 David K. Khatami  <https://orcid.org/0000-0003-4307-0589>
 Daniel A. Perley  <https://orcid.org/0000-0001-8472-1996>
 Avishay Gal-Yam  <https://orcid.org/0000-0002-3653-5598>
 Alessandra Corsi  <https://orcid.org/0000-0001-8104-3536>
 Igor Andreoni  <https://orcid.org/0000-0002-8977-1498>
 Eric C. Bellm  <https://orcid.org/0000-0001-8018-5348>
 Nadia Blagorodnova  <https://orcid.org/0000-0003-0901-1606>
 Joe S. Bright  <https://orcid.org/0000-0002-7735-5796>
 S. Bradley Cenko  <https://orcid.org/0000-0003-1673-970X>
 Virginia Cunningham  <https://orcid.org/0000-0003-2292-0441>
 Kishalay De  <https://orcid.org/0000-0002-8989-0542>
 Claes Fransson  <https://orcid.org/0000-0001-8532-3594>
 Christoffer Fremling  <https://orcid.org/0000-0002-4223-103X>
 Adam Goldstein  <https://orcid.org/0000-0002-0587-7042>
 Matthew J. Graham  <https://orcid.org/0000-0002-3168-0139>
 Mansi M. Kasliwal  <https://orcid.org/0000-0002-5619-4938>
 S. R. Kulkarni  <https://orcid.org/0000-0001-5390-8563>
 Thomas Kupfer  <https://orcid.org/0000-0002-6540-1484>
 Ragnhild Lunnan  <https://orcid.org/0000-0001-9454-4639>
 Frank J. Masci  <https://orcid.org/0000-0002-8532-9395>
 Chow-Choong Ngeow  <https://orcid.org/0000-0001-8771-7554>
 Peter E. Nugent  <https://orcid.org/0000-0002-3389-0586>
 Eran O. Ofek  <https://orcid.org/0000-0002-6786-8774>
 Maria T. Patterson  <https://orcid.org/0000-0002-4753-3387>
 Jesper Sollerman  <https://orcid.org/0000-0003-1546-6615>
 Maayane T. Soumagnac  <https://orcid.org/0000-0001-6753-1488>
 Xiaofeng Wang  <https://orcid.org/0000-0002-7334-2357>
 Yuhan Yao  <https://orcid.org/0000-0001-6747-8509>

References

- Ahn, C. P., Alexandroff, R., Allende Prieto, C., et al. 2012, *ApJS*, 203, 21
 Ahn, C. P., Alexandroff, R., Allende Prieto, C., et al. 2014, *ApJS*, 211, 17
 Alard, C., & Lupton, R. H. 1998, *ApJ*, 503, 325
 Almgren, A. S., Beckner, V. E., Bell, J. B., et al. 2010, *ApJ*, 715, 1221
 Arcavi, I., Wolf, W. M., Howell, D. A., et al. 2016, *ApJ*, 819, 35
 Arnouts, S., Cristiani, S., Moscardini, L., et al. 1999, *MNRAS*, 310, 540
 Asplund, M., Grevesse, N., Sauval, A. J., & Scott, P. 2009, *ARA&A*, 47, 481
 Astropy Collaboration, Price-Whelan, A. M., Sipőcz, B. M., et al. 2018, *AJ*, 156, 123
 Astropy Collaboration, Robitaille, T. P., Tollerud, J. E., et al. 2013, *A&A*, 558, A33
 Barbary, K. 2016, Extinction, v0.3.0, Zenodo, doi:10.5281/zenodo.804967
 Barthelmy, S. D., Barbier, L. M., Cummings, J. R., et al. 2005, *SSRv*, 120, 143
 Becker, A. 2015, HOTPANTS: High Order Transform of PSF and Template Subtraction, Astrophysics Source Code Library, ascl:1504.004
 Bellm, E. C., Kulkarni, S. R., Barlow, T. R., et al. 2019b, *PASP*, 131, 1000
 Bellm, E. C., Kulkarni, S. R., Graham, M. J., et al. 2019a, *PASP*, 131, 018002
 Ben-Ami, S., Gal-Yam, A., Filippenko, A. V., et al. 2012, *ApJL*, 760, L33
 Bersier, D., Fruchter, A. S., Strolger, L.-G., et al. 2006, *ApJ*, 643, 284
 Bersten, M. C., Folatelli, G., García, F., et al. 2018, *Natur*, 554, 497
 Bertin, E. 2010, SWarp: Resampling and Co-adding FITS Images Together, Astrophysics Source Code Library, ascl:1010.068
 Blackburn, L., Briggs, M. S., Camp, J., et al. 2015, *ApJS*, 217, 8
 Blagorodnova, N., Neill, J. D., Walters, R., et al. 2018, *PASP*, 130, 035003
 Blanton, M. R., & Roweis, S. 2007, *AJ*, 133, 734
 Blaufuss, E. 2018, *ATel*, 12062, 1
 Bourne, N., Maddox, S. J., Dunne, L., et al. 2012, *MNRAS*, 421, 3027
 Branch, D., Benetti, S., Kasen, D., et al. 2002, *ApJ*, 566, 1005
 Breeveld, A. A., Landsman, W., Holland, S. T., et al. 2011, AIP Conf. Ser., Gamma Ray Bursts 2010 (Melville, NY: AIP), 373
 Bruzual, G., & Charlot, S. 2003, *MNRAS*, 344, 1000
 Bufano, F., Pian, E., Sollerman, J., et al. 2012, *ApJ*, 753, 67
 Calzetti, D., Armus, L., Bohlin, R. C., et al. 2000, *ApJ*, 533, 682
 Campana, S., Mangano, V., Blustin, A. J., et al. 2006, *Natur*, 442, 1008
 Cano, Z. 2013, *MNRAS*, 434, 1098
 Cano, Z., Izzo, L., de Ugarte Postigo, A., et al. 2017, *A&A*, 605, A107
 Cano, Z., Wang, S.-Q., Dai, Z.-G., & Wu, X.-F. 2017, *AdAst*, 2017, 8929054
 Cenko, S. B., Fox, D. B., Moon, D.-S., et al. 2006, *PASP*, 118, 1396
 Chabrier, G. 2003, *PASP*, 115, 763
 Chambers, K. C., Magnier, E. A., Metcalfe, N., et al. 2016, arXiv:1612.05560
 Chevalier, R. A. 1998, *ApJ*, 499, 810
 Chevalier, R. A., & Irwin, C. M. 2011, *ApJL*, 729, L6
 Corsi, A., Ofek, E. O., Gal-Yam, A., et al. 2012, *ApJL*, 747, L5
 Corsi, A., Ofek, E. O., Gal-Yam, A., et al. 2014, *ApJ*, 782, 42
 Costantin, L., Avramova-Bonche, A., Pinter, V., et al. 2018, *ATel*, 12047, 1
 Cutri, R. M., Wright, E. L., & Conrow, T. 2013, Explanatory Supplement to the ALLWISE Data Release Products
 De, K., Kasliwal, M. M., Ofek, E. O., et al. 2018, *Sci*, 362, 201
 Dekany, R., Smith, R. M., Belicki, J., et al. 2016, Proc. SPIE, 9908, 99085M
 Dessart, L. 2019, *A&A*, 621, A141
 Drout, M. R., Chornock, R., Soderberg, A. M., et al. 2014, *ApJ*, 794, 23
 Duev, D. A., Mahabal, A., Masci, F. J., et al. 2019, *MNRAS*, 489, 3582
 Ergon, M., Fransson, C., Jerkstrand, A., et al. 2018, *A&A*, 620, A156
 Evans, P. A., Beardmore, A. P., Page, K. L., et al. 2009, *MNRAS*, 397, 1177
 Fitzpatrick, E. L. 1999, *PASP*, 111, 63
 Foley, R. J., Papenkova, M. S., Swift, B. J., et al. 2003, *PASP*, 115, 1220
 Fremling, C., Sollerman, J., Taddia, F., et al. 2016, *A&A*, 593, A68
 Galama, T. J., Vreeswijk, P. M., van Paradijs, J., et al. 1998, *Natur*, 395, 670
 Gal-Yam, A. 2019a, *ApJ*, 882, 102
 Gal-Yam, A. 2019b, *ARA&A*, 57, 305
 Garmire, G. P., Bautz, M. W., Ford, P. G., Nousek, J. A., & Ricker, G. R., Jr. 2003, Proc. SPIE, 4851, 28
 Gehrels, N., Chincarini, G., Giommi, P., et al. 2004, *ApJ*, 611, 1005
 Goldstein, A., Burns, E., Hamburg, R., et al. 2016, arXiv:1612.02395
 Gorosabel, J., Pérez-Ramírez, D., Sollerman, J., et al. 2005, *A&A*, 444, 711
 Graham, M. J., Kulkarni, S. R., Bellm, E. C., et al. 2019, *PASP*, 131, 1001
 Groh, J. H., Meynet, G., Georgy, C., & Ekström, S. 2013, *A&A*, 558, A131
 Gruber, D., Goldstein, A., Weller von Ahlefeld, V., et al. 2014, *ApJS*, 211, 12
 Gruen, D., Seitz, S., & Bernstein, G. M. 2014, *PASP*, 126, 158
 Han, X. H., Hammer, F., Liang, Y. C., et al. 2010, *A&A*, 514, A24
 Hickish, J., Razavi-Ghods, N., Perrott, Y. C., et al. 2018, *MNRAS*, 475, 5677
 Hjorth, J., Malesani, D., Jakobsson, P., et al. 2012, *ApJ*, 756, 187
 Ho, A. Y. Q., Ness, M. K., Hogg, D. W., et al. 2017, *ApJ*, 836, 5
 Ho, A. Y. Q., Perley, D. A., Hallinan, G., et al. 2018b, *ATel*, 12056, 1
 Ho, A. Y. Q., Phinney, E. S., Ravi, V., et al. 2019, *ApJ*, 871, 73
 Ho, A. Y. Q., Schulze, S., Perley, D. A., et al. 2018c, *ATel*, 12030, 1
 Ho, P. T. P., Moran, J. M., & Lo, K. Y. 2004, *ApJL*, 616, L1
 Högbom, J. A. 1974, *A&AS*, 15, 417
 Howell, D. A., Kasen, D., Lidman, C., et al. 2013, *ApJ*, 779, 98
 Hudelot, P., Cuillandre, J.-C., Withington, K., et al. 2012, *yCat*, 2317, 0
 Hunter, J. D. 2007, *CSE*, 9, 90
 Ilbert, O., Arnouts, S., McCracken, H. J., et al. 2006, *A&A*, 457, 841
 Izotov, Y. I., Stasińska, G., Meynet, G., Guseva, N. G., & Thuan, T. X. 2006, *A&A*, 448, 955
 Izzo, L., de Ugarte Postigo, A., Maeda, K., et al. 2019, *Natur*, 565, 324
 Izzo, L., Thöne, C. C., Schulze, S., et al. 2017, *MNRAS*, 472, 4480
 Jerkstrand, A., Ergon, M., Smartt, S. J., et al. 2015, *A&A*, 573, A12
 Jones, E., Oliphant, E., Peterson, P., et al. 2001, SciPy, <http://www.scipy.org/>
 Kasen, D. 2017, in Handbook of Supernovae, ed. A. W. Alsabti & P. Murdin (Cham: Springer Int. Publishing AG), 939
 Kasen, D., & Bildsten, L. 2010, *ApJ*, 717, 245
 Kasen, D., Metzger, B. D., & Bildsten, L. 2016, *ApJ*, 821, 36
 Kasliwal, M. M., Cannella, C., Bagdasaryan, A., et al. 2019, *PASP*, 131, 038003
 Katz, B., Kushnir, D., & Dong, S. 2013, arXiv:1301.6766
 Kauffmann, G., Heckman, T. M., Tremonti, C., et al. 2003, *MNRAS*, 346, 1055
 Kennicutt, R. C., Jr. 1998, *ARA&A*, 36, 189
 Kewley, L. J., Dopita, M. A., Sutherland, R. S., et al. 2001, *ApJ*, 556, 121
 Kocevski, D., Modjaz, M., Bloom, J. S., et al. 2007, *ApJ*, 663, 1180
 Krühler, T., Malesani, D., Fynbo, J. P. U., et al. 2015, *A&A*, 581, A125
 Kuin, N. P. M., Wu, K., Oates, S., et al. 2019, *MNRAS*, 487, 2505

- Kuin, N. P. M., Landsman, W., Breeveld, A. A., et al. 2015, *MNRAS*, **449**, 2514
- Laskar, T., Coppejans, D. L., Margutti, R., & Alexander, K. D. 2017, *GCN*, **22216**, 1
- Law, N. M., Kulkarni, S. R., Dekany, R. G., et al. 2009, *PASP*, **121**, 1395
- Levesque, E. M., Kewley, L. J., Graham, J. F., & Fruchter, A. S. 2010, *ApJL*, **712**, L26
- Lupton, R., Blanton, M. R., Fekete, G., et al. 2004, *PASP*, **116**, 133
- Luridiana, V., Morisset, C., & Shaw, R. A. 2015, *A&A*, **573**, A42
- Lyman, J. D., Bersier, D., James, P. A., et al. 2016, *MNRAS*, **457**, 328
- Lyutikov, M., & Toonen, S. 2019, *MNRAS*, **487**, 5618
- Madau, P., & Dickinson, M. 2014, *ARA&A*, **52**, 415
- Mahabal, A., Rebbapragada, U., Walters, R., et al. 2019, *PASP*, **131**, 038002
- Malesani, D., Tagliaferri, G., Chincarini, G., et al. 2004, *ApJL*, **609**, L5
- Mannucci, F., Cresci, G., Maiolino, R., Marconi, A., & Gnerucci, A. 2010, *MNRAS*, **408**, 2115
- Margutti, R., Chincarini, G., Covino, S., et al. 2007, *A&A*, **474**, 815
- Margutti, R., Metzger, B. D., Chornock, R., et al. 2019, *ApJ*, **872**, 18
- Marino, R. A., Rosales-Ortega, F. F., Sánchez, S. F., et al. 2013, *A&A*, **559**, A114
- Martin, D. C., Fanson, J., Schiminovich, D., et al. 2005, *ApJL*, **619**, L1
- Masci, F. J., Laher, R. R., Rusholme, B., et al. 2019, *PASP*, **131**, 018003
- Matzner, C. D., & McKee, C. F. 1999, *ApJ*, **510**, 379
- Mazzali, P. A., Sullivan, M., Pian, E., et al. 2016, *MNRAS*, **458**, 3455
- Mazzali, P. A., Valentí, S., Della Valle, M., et al. 2008, *Sci*, **321**, 1185
- McMullin, J. P., Waters, B., Schiebel, D., Young, W., & Golap, K. 2007, *adass XVI*, **376**, 127
- Meegan, C., Lichti, G., Bhat, P. N., et al. 2009, *ApJ*, **702**, 791
- Michałowski, M. J., Hjorth, J., Malesani, D., et al. 2009, *ApJ*, **693**, 347
- Modjaz, M., Bianco, F. B., Siwek, M., et al. 2019, arXiv:1901.00872
- Modjaz, M., Li, W., Butler, N., et al. 2009, *ApJ*, **702**, 226
- Modjaz, M., Liu, Y. Q., Bianco, F. B., & Graur, O. 2016, *ApJ*, **832**, 108
- Moriya, T. J., Chen, T.-W., & Langer, N. 2017, *ApJ*, **835**, 177
- Moriya, T. J., Sorokina, E. I., & Chevalier, R. A. 2018, *SSRv*, **214**, 59
- Moriya, T. J., & Tominaga, N. 2012, *ApJ*, **747**, 118
- Murphy, E. J., Condon, J. J., Schinnerer, E., et al. 2011, *ApJ*, **737**, 67
- Nakar, E., & Piro, A. L. 2014, *ApJ*, **788**, 193
- Nakar, E., & Sari, R. 2010, *ApJ*, **725**, 904
- Narayana Bhat, P., Meegan, C. A., von Kienlin, A., et al. 2016, *ApJS*, **223**, 28
- Nicholl, M., Smartt, S. J., Jerkstrand, A., et al. 2013, *Natur*, **502**, 346
- Oke, J. B., Cohen, J. G., Carr, M., et al. 1995, *PASP*, **107**, 375
- Oke, J. B., & Gunn, J. E. 1982, *PASP*, **94**, 586
- Oliphant, T. E. 2006, *A Guide to NumPy* (Trelgol Publishing)
- Osterbrock, D. E., & Ferland, G. J. 2006, in *Astrophysics of Gaseous Nebulae and Active Galactic Nuclei*, II., ed. D. E. Osterbrock & G. J. Ferland (Sausalito, CA: Univ. Science Books)
- Ovaldsen, J.-E., Jaunsen, A. O., Fynbo, J. P. U., et al. 2007, *ApJ*, **662**, 294
- Patterson, M. T., Bellm, E. C., Rusholme, B., et al. 2019, *PASP*, **131**, 018001
- Pérez, F., & Granger, B. E. 2007, *CSE*, **9**, 21
- Perley, D. A. 2019, *PASP*, **131**, 1002
- Perley, D. A., Mazzali, P. A., Yan, L., et al. 2019, *MNRAS*, **484**, 1031
- Perrott, Y. C., Scaife, A. M. M., Green, D. A., et al. 2013, *MNRAS*, **429**, 3330
- Pettini, M., & Pagel, B. E. J. 2004, *MNRAS*, **348**, L59
- Piascik, A. S., Steele, I. A., Bates, S. D., et al. 2014, *Proc. SPIE*, **9147**, 91478H
- Piro, A. L. 2015, *ApJL*, **808**, L51
- Planck Collaboration, Ade, P. A. R., Aghanim, N., et al. 2016, *A&A*, **594**, A13
- Poznanski, D., Chornock, R., Nugent, P. E., et al. 2010, *Sci*, **327**, 58
- Prentice, S. J., Maguire, K., Smartt, S. J., et al. 2018, *ApJL*, **865**, L3
- Pursiainen, M., Childress, M., Smith, M., et al. 2018, *MNRAS*, **481**, 894
- Quimby, R. M., De Cia, A., Gal-Yam, A., et al. 2018, *ApJ*, **855**, 2
- Quimby, R. M., Kulkarni, S. R., Kasliwal, M. M., et al. 2011, *Natur*, **474**, 487
- Rest, A., Garnavich, P. M., Khatami, D., et al. 2018, *NatAs*, **2**, 307
- Rigault, M., Neill, J. D., Blagorodnova, N., et al. 2019, *A&A*, **627**, A115
- Roming, P. W. A., Kennedy, T. E., Mason, K. O., et al. 2005, *SSRv*, **120**, 95
- Sault, R. J., Teuben, P. J., & Wright, M. C. H. 1995, *adass IV*, **77**, 433
- Schlafly, E. F., & Finkbeiner, D. P. 2011, *ApJ*, **737**, 103
- Schulze, S., Ho, A. Y. Q., & Mill, A. A. 2018a, *ATel*, **12032**, 1
- Schulze, S., Krühler, T., Leloudas, G., et al. 2018b, *MNRAS*, **473**, 1258
- Schulze, S., Malesani, D., Cucchiara, A., et al. 2014, *A&A*, **566**, A102
- Shivvers, I., Zheng, W. K., Mauerhan, J., et al. 2016, *MNRAS*, **461**, 3057
- Skrutskie, M. F., Cutri, R. M., Stiening, R., et al. 2006, *AJ*, **131**, 1163
- Smartt, S. J., Clark, P., Smith, K. W., et al. 2018, *ATel*, **11727**, 1
- Smith, N. 2014, *ARA&A*, **52**, 487
- Soderberg, A. M., Chakraborti, S., Pignata, G., et al. 2010, *Natur*, **463**, 513
- Stanway, S. R., Levan, A. J., Tanvir, N., et al. 2015, *MNRAS*, **446**, 3911
- Starling, R. L. C., Wiersema, K., Levan, A. J., et al. 2011, *MNRAS*, **411**, 2792
- Steele, I. A., Smith, R. J., Rees, P.-C., et al. 2004, *Proc. SPIE*, **5489**, 679S
- Tachibana, Y., & Miller, A. A. 2018, *PASP*, **130**, 128001
- Taddia, F., Sollerman, J., Fremling, C., et al. 2019, *A&A*, **621**, A71
- Tanaka, M., Tominaga, N., Morokuma, T., et al. 2016, *ApJ*, **819**, 5
- Thöne, C. C., Christensen, L., Prochaska, J. X., et al. 2014, *MNRAS*, **441**, 2034
- Thöne, C. C., Fynbo, J. P. U., Östlin, G., et al. 2008, *ApJ*, **676**, 1151
- Tonry, J. L., Denneau, L., Heinze, A. N., et al. 2018, *PASP*, **130**, 064505
- Toy, V. L., Cenko, S. B., Silverman, J. M., et al. 2016, *ApJ*, **818**, 79
- Van der Walt, S. J., Crellin-Quick, A., & Bloom, J. S. 2019, *JOSS*, **4**, 1247
- von Kienlin, A., Meegan, C. A., Paciesas, W. S., et al. 2014, *ApJS*, **211**, 13
- Wang, J., Xin, L., Ren, J., et al. 2018, *ATel*, **12055**, 1
- Wang, L. J., Wang, X. F., Cano, Z., et al. 2017, *MNRAS*, **489**, 1110
- Whitesides, L., Lunnan, R., Kasliwal, M. M., et al. 2017, *ApJ*, **851**, 107
- Woosley, S. E. 2010, *ApJL*, **719**, L204
- Woosley, S. E., & Heger, A. 2007, *PhR*, **442**, 269
- Wright, A. H., Robotham, A. S. G., Bourne, N., et al. 2016, *MNRAS*, **460**, 765
- Wright, E. L., Eisenhardt, P. R. M., Mainzer, A. K., et al. 2010, *AJ*, **140**, 1868
- Wygoda, N., Elbaz, Y., & Katz, B. 2019, *MNRAS*, **484**, 3941
- Yan, L., Quimby, R., Gal-Yam, A., et al. 2017, *ApJ*, **840**, 57
- Yaron, O., & Gal-Yam, A. 2012, *PASP*, **124**, 668
- Yaron, O., Perley, D. A., Gal-Yam, A., et al. 2017, *NatPh*, **13**, 510
- Zhang, W., Howell, L., Almgren, A., Burrows, A., & Bell, J. 2011, *ApJS*, **196**, 20
- Zwart, J. T. L., Barker, R. W., Biddulph, P., et al. 2008, *MNRAS*, **391**, 1545

工作報告

鹿林天文台觀測時數統計(2003-2019)

林宏欽、蕭翔耀、林啟生、侯偉傑

鹿林天文台自 2002 年 9 月開始人員常駐，2003 年鹿林一米望遠鏡(LOT)上線，開始有正式觀測時數紀錄，可供瞭解鹿林長期的天氣狀況。依 2003-2019 共 17 年的統計結果，鹿林天文台年平均觀測時數為 1146 小時。一年可分為四個觀測季，

- 最佳觀測季：10-12 月。
- 次佳觀測季：1-3 月。
- 最差觀測季：4-6 月。4 月開始進入雨季，5-6 月受梅雨影響，天氣最差。
- 次差觀測季：7-9 月。主要受颱風及西南氣流影響，天氣變化大。此外夏季晝長夜短，每晚可觀測時間比冬季為短。

詳細統計資料及統計如下：

表 1 每月觀測時數統計 (2003-2019)

Month	2003	2004	2005	2006	2007	2008	2009	2010	2011	2012	2013	2014	2015	2016	2017	2018	2019	Average
1	78.75	125	163.25	129	127.32	179	234.52	206.9	90.8	113.42	153.58	269.62	188.55	75.4	160.85	110.4	196.3	150.51
2	142.5	145.98	94.75	149	128.55	118.25	165.7	100.6	123.8	64.88	183.63	109.8	131.65	60.25	105.3	66.7	136.35	118.92
3	147.5	163	143	126.05	116.4	138.5	146.75	181.3	75.9	168.23	134.26	78.7	111.1	72.8	96.4	173.7	124	129.57
4	126.5	110.5	144.75	86.8	53.75	85.25	71.8	75.8	151.45	32.75	55.83	135.95	124	82.9	86.9	125.7	124.35	99.39
5	129.75	106.25	136.25	59.5	106.6	98.25	167.4	86.05	56.6	74.3	41.02	32.4	64.2	86.05	84.55	190.7	39.1	89.06
6	24	133	45	39.3	54	37	81.75	26.5	61.5	35.15	80.14	33.7	146.9	114.05	76.1	70.35	56.55	62.94
7	222.5	48	167.75	91.57	128.88	88.4	76.6	99.85	81.75	106.4	88.05	114.65	87.45	123.95	105.25	80.65	77.35	101.24
8	137.75	142	76	111.65	56.6	118.95	6.8	98.3	97.9	35.7	72.2	110.9	45.1	61	139.9	50.35	58.2	84.70
9	142	116	129.25	60.05	69.55	59.8	0	109.95	90.1	117.35	107.84	134.39	93.25	42.85	128.2	93.45	137.45	99.30
10	149.25	219.75	210.25	150.6	172.63	191.38	175.6	139.8	136.95	214.51	200.57	232.33	145.4	142.2	187.8	142.05	193.75	175.70
11	166.5	214.5	216.25	71.75	160.55	152.55	175.8	163.65	87.2	93.81	136.1	166.15	197.05	171.85	134.55	148.15	200.29	157.91
12	271.5	232.45	129	132	261.09	211.17	169.8	169.65	115.25	132.21	86	137.3	161.2	193.27	156.7	170.05	180.2	170.09
Total	1738.5	1756.43	1655.5	1207.27	1435.92	1478.5	1472.52	1458.35	1169.2	1188.71	1339.22	1555.89	1495.85	1226.57	1462.5	1422.25	1523.89	

* 2009 年因受莫拉克颱風八八風災影響，自八月八日起至十月初約 2 個月期間道路中斷並停電，無法觀測。所以 2009 年之八、九月觀測時數很少，甚至為 0。

**Average 值為扣除最高及最低值後取平均。

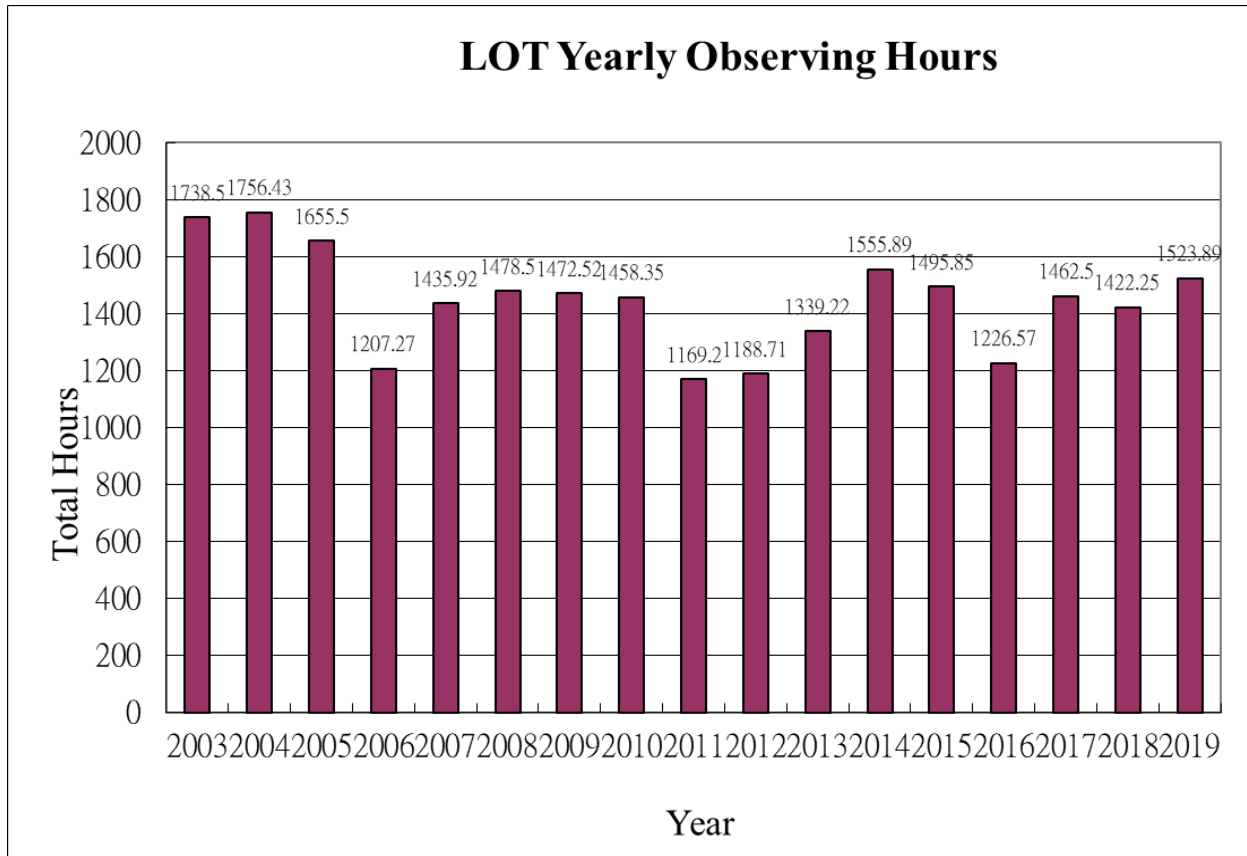


圖 1 鹿林天文台年平均觀測時數統計圖(2003-2019)

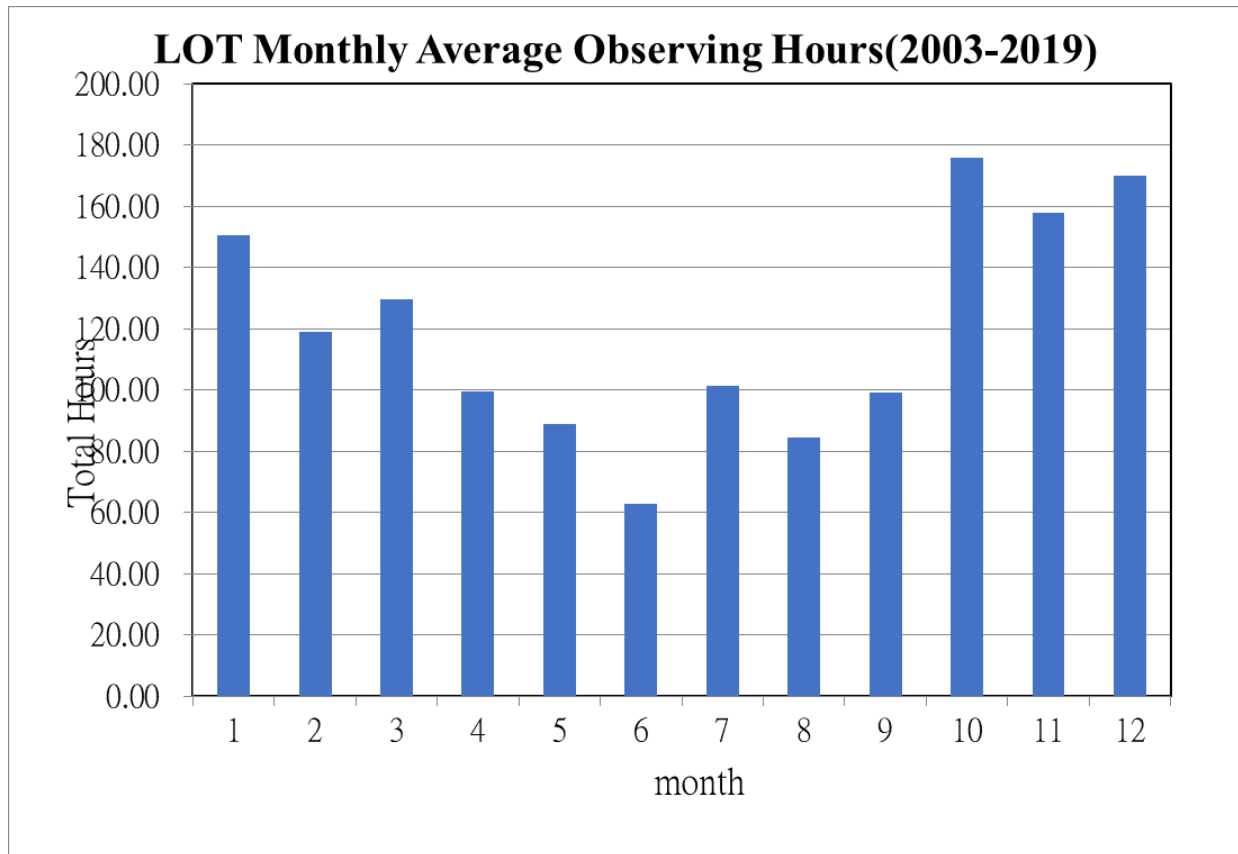
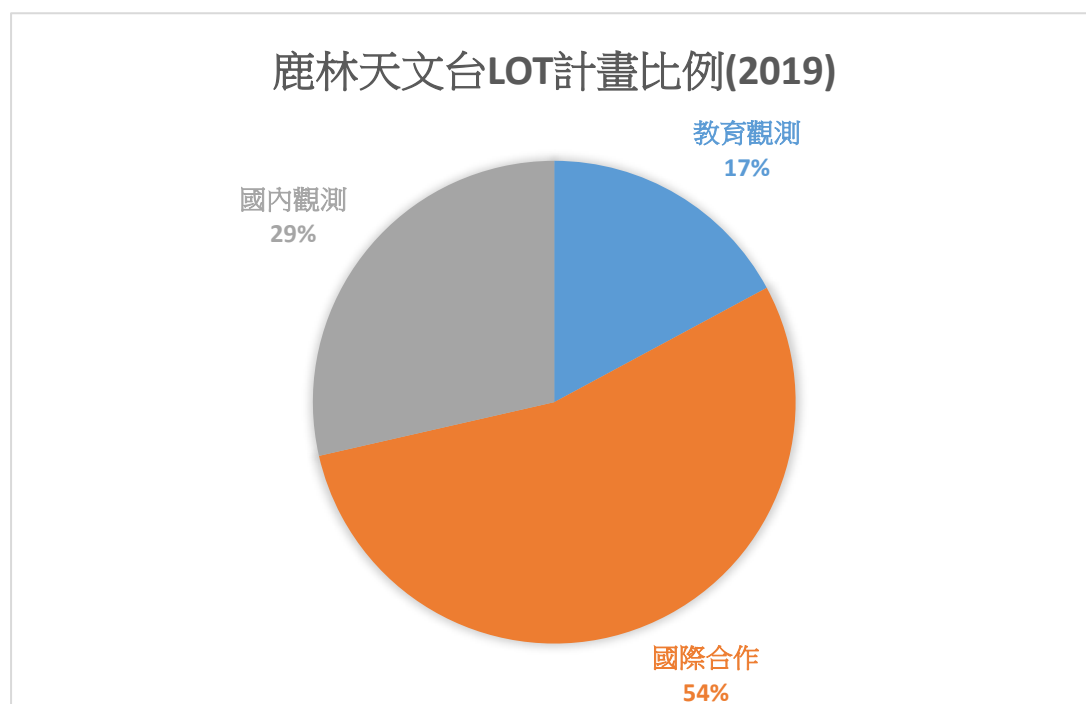


圖 2 鹿林天文台月平均觀測時數統計圖 (2003-2019)

鹿林天文台 LOT 觀測研究計畫統計 (2019)

鹿林天文台一米望遠鏡(LOT)觀測研究計畫時間安排以 4 個月為一個觀測期，一年分為三期 (A = 1-4 月、B = 5-8 月、C = 9-12 月)，其中字母 E、R 和 *R 分別為天文觀測教學、國內研究計畫與國際合作計畫。

2018 年的觀測計畫如下，統計結果：E 天文觀測教學有 6 個，佔 17%。R 國內研究計畫有 10 個，佔 29%。*R 國際合作計畫有 19 個，佔 54%。



LOT2019A Semester (01 January – 30 April, 2019)

Education Program:

E01 – Training School with Chenggong Senior High School for Observational Astronomy

PI: Chih-Hao Hsia (chhsia@must.edu.mo)

E02 – Observing Training for “Advanced Observational Astronomy” Course

PI: Chow-Choong Ngeow (cngeow@astro.ncu.edu.tw)

E03 – Practical Class of "Fundamentals of Observational Astronomy"

PI: Albert Kong (akong@phys.nthu.edu.tw)

Research Program:

*EDEN – Exo-earth Discovery and Exploration Network

PI: W-P Chen (wchen@astro.ncu.edu.tw)

*R01 – ToO and Follow-Up Observations of GROWTH and ZTF Targets

PI: Chow-Choong Ngeow (cngeow@astro.ncu.edu.tw)

R02 – An Observation of Comet 46P/Wirtanen During its Outbound Orbit in 2019

PI: Zhong-Yi Lin (zylin@astro.ncu.edu.tw)

*R03 – Transients within Hours of Explosion

PI: Yen-Chen Pan (yenchen.pan@nao.ac.jp)

*R04 – Lulin One-meter Telescope Follow-up of Microlensing Events detected by Gaia

PI: Paweł Zieliński (pzielinski@astrouw.edu.pl)

*R05 – In-Depth Study of Millisecond Pulsar J1048+2339

PI: Yee-Xuan Yap (yapyeexuan@gapp.nthu.edu.tw)

R06 – Photopolarimetric Observations of Known UXor and Potential Candidates. II

PI: Po-Chieh Huang (pochiehuang1@gmail.com)

R07 – ToO Observations of Galactic Transient Events

PI: Albert Kong (akong@phys.nthu.edu.tw)

LOT2019B Semester (01 May – 31 August, 2019)

Education Program:

E01 – Students Training for Astro Summer Camp 2019

PI: Chow-Choong Ngeow (cngeow@astro.ncu.edu.tw)

E02 – Observation Training for Lin-kou Senior High School Students

PI: Hao-Yuan Duan (hyduan@gapp.nthu.edu.tw)

Research Program:

*EDEN – Exo-earth Discovery and Exploration Network

PI: W-P Chen (wchen@astro.ncu.edu.tw)

R01 – ToO Observations of Cosmic Transient Events

P.I.: Albert Kong (akong@phys.nthu.edu.tw)

*R02 – Transients within Hours of Explosion

P.I.: Yen-Chen Pan (yenchchen.pan@nao.ac.jp)

*R03 – ToO and Follow-Up Observations of GROWTH and ZTF Transients

P.I.: Chow-Choong Ngeow (cngew@astro.ncu.edu.tw)

R04 – The rotation period confirmations for large super-fast rotating asteroids

P.I.: Ting-Shuo Yeh (tsyeh@astro.ncu.edu.tw)

*R05 – Monitoring of comet 29P/SW1 for activity trends and outburst

P.I.: Zhong-Yi Lin (zylin@astro.ncu.edu.tw)

R06 – Multi-phase angle polarimetric observations of multi-taxonomic main belt asteroids

P.I.: Kang-Shian Pan (m989005@astro.ncu.edu.tw)

R07 – The search for the C-type superfast rotators

P.I.: Kang-Shian Pan (m989005@astro.ncu.edu.tw)

*R08 – Taxonomical Study for Unclassified Near-Earth Asteroids (III)

P.I.: Chih-Hao Hsia (chhsia@must.edu.mo)

*R09 – Lulin One-meter Telescope Follow-up of Microlensing Events detected by Gaia

P.I.: Po-Chieh Huang (pochiehhuang1@gmail.com)

LOT2019C Semester (01 September – 31 December, 2019)

Education Program:

E01 – Practical Class of "Fundamentals of Observational Astronomy"

PI: Albert Kong (akong@phys.nthu.edu.tw)

Research Program:

- *EDEN – Exo-earth Discovery and Exploration Network
PI: W-P Chen (wchen@astro.ncu.edu.tw)

- *R01 – Dedicated Follow-Up Observations of GW Optical Counterparts with LOT
P.I.: Chow-Choong Ngeow (cngeow@astro.ncu.edu.tw)

- *R02 – Activity and Physical Properties of Comet 160P/LINEAR and 260P/McNaught
P.I.: Jian-Chun Shi (jcschi@pmo.ac.cn)

- *R03 – Search for Rotation-powered Compact Millisecond Pulsar Binaries
P.I.: Yee-Xuan Yap (yapyeexuan@gapp.nthu.tw.edu)

- *R04 – Monitoring of Comet 29P/SW1 for Activity Trends and Outburst
P.I.: Zhong-Yi Lin (zylin@astro.ncu.edu.tw)

- R05 – ToO Observations of Cosmic Transient Events
PI: Albert Kong (akong@phys.nthu.edu.tw)

- *R06 – Lulin One-meter Telescope Follow-up of Microlensing Events detected by Gaia
P.I.: Kotryna Siskauskaite (k.siskauskaite@gmail.com)

- *R07 – Transients within Hours of Explosion
P.I.: Yen-Chen Pan (yencheng.pan@nao.ac.jp)

- *R08 – Taxonomical Study for Unclassified Near-Earth Asteroids (IV)
P.I.: Chih-Hao Hsia (chhsia@must.edu.mo)

- R09 – The Rotation Period Confirmations for Large Super-Fast Rotating Asteroids
P.I.: Ting-Shuo Yeh (tsyeh@astro.ncu.edu.tw)

- R10 – The Search for the C-type Super-Fast Rotators
P.I.: Kang-Shian Pan (m989005@astro.ncu.edu.tw)

鹿林天文台工作報告 2019

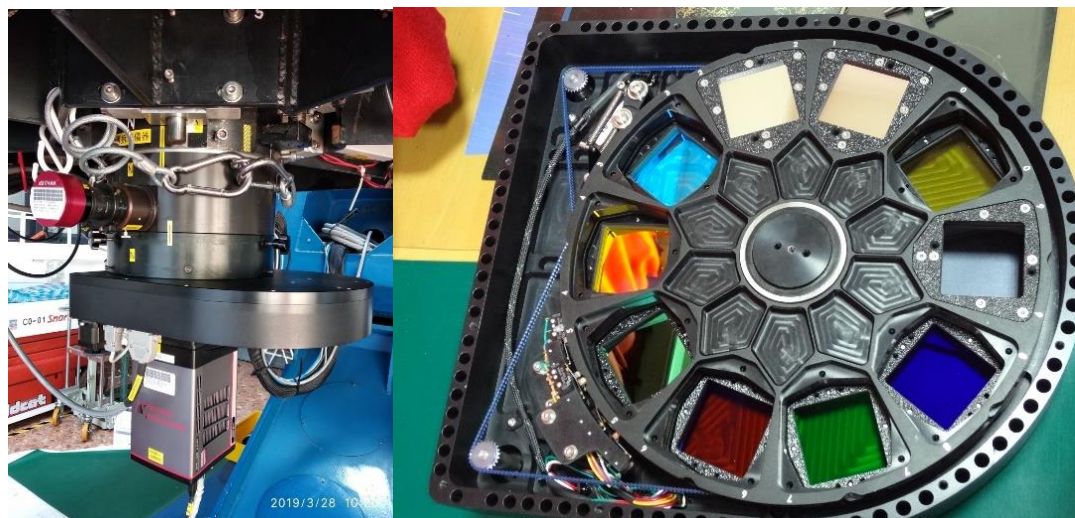
林宏欽、侯偉傑

鹿林天文台一米望遠鏡（LOT）自 2002 年 9 月開始運作以來已歷 17 年，2019 年將 LOT 濾鏡盤與全天相機更新，使觀測過程更順利進行。並將周圍影響觀測的樹木移除提高了低角度天體觀測的可能。控制中心屋頂與圓頂漏水問題也於年初進行修繕。

1. 具體工作

1.1 LOT 濾鏡盤更新

一米望遠鏡(LOT)舊濾鏡盤已使用超過 15 年，故障率漸增，一但故障許多需要使用科學濾鏡的計畫將都無法執法，影響十分嚴重，因此更換新濾鏡盤勢在必行！LOT 新濾鏡盤可安裝 18 片濾鏡，可減少濾鏡更換的頻次，盡量避免系統參數修改及設定出錯之機率。



LOT 新濾鏡盤外觀與內部結構

1.2 LOT 天文觀測障礙木移除

鹿林天文台 20 多年發展，基地內小樹也逐漸變成大樹，天文台周圍許多樹木已經長高超過圓頂下緣，遮擋了低角度的天體，嚴重影響天文望遠鏡之觀測！經過多年協商及會勘，終於得到台大實驗林的大力幫忙移除 LOT 天文台周圍的障礙木。接下來待爭取另一半區域樹木管理單位林務局的同意與協助。



LOT 天文台全景(障礙木移除前)



LOT 天文台全景(障礙木移除後)

1.3 鹿林全天相機更新

全天相機配備魚眼鏡頭，用於監測 180 度夜間天空狀態，以供瞭解實時觀測條件，並可作為天文台長期觀測條件之重要佐證。鹿林舊款全天相機為十多年前所購，只能提供夜間黑白低解析影像，經多年使用因相機進水損壞，更新後的全天相機可提供高解析的彩色日夜間影像，能夠更完整紀錄天文台觀測狀態，並於流星雨等重要天象提供直播畫面供大眾科普科教使用。



新全天相機外觀與夜空實際影像

1.4 LOT 控制中心屋頂漏水修繕

鹿林天文台 LOT 控制中心自 2002 年啟用迄今已 17 年，圓頂、屋頂均有不同程度的漏水問題，已於 2019 年初進行全面修繕，保障了天文台運作的基礎。



修繕工程作業進行

2. 科學成果(2019)

標題、作者、年份、期刊名稱、卷期、起(迄)頁數

(Title, authors, year, journal, volume, first page)

1. The resolution to the paradox of the sprite polarity, Chen, A. B. C.; Chen, H.; Chuang, C. W.; Cummer, S.; Lu, G.; Su, H. T.; Hsu, R. R., American Geophysical Union, Fall Meeting 2018, December 2018
2. Face changing companion of the redback millisecond pulsar PSR J1048+2339, Yap, Y. X.; Li, K. L.; Kong, A. K. H.; Takata, J.; Lee, J.; Hui, C. Y., *Astronomy & Astrophysics*, Volume 621, id.L9, 6 pp., January 2019
3. Diagnosing the Clumpy Protoplanetary Disk of the UXor Type Young Star GM Cephei, P. C. Huang, W. P. Chen, M. Mugrauer, R. Bischoff, J. Budaj, O. Burkhonov, S. Ehgamberdiev, R. Errmann, Z. Garai, H. Y. Hsiao, 2019 February, *The Astrophysical Journal*, 871:183 (12pp)
4. 2012 TC4 - An unusual fast-rotating PHA with C-type taxonomy, Lin, Zhong-Yi; Ip, Wing-Huen; Ngeow, Chow-Choong, February 2019, *Planetary and Space Science*, Volume 166, p. 54-58.,
5. The fast, luminous ultraviolet transient AT2018cow: extreme supernova, or disruption of a star by an intermediate-mass black hole? Daniel A Perley, Paolo A Mazzali, Lin Yan, et al., *Monthly Notices of the Royal Astronomical Society*, Volume 484, Issue 1, March 2019, Pages 1031–1049
6. Research of activity of Main Belt Comets 176P/LINEAR, 238P/Read and 288P/(300163) 2006 VW139, Shi, Jianchun; Ma, Yuehua; Liang, He; Xu, Ruiqi, *Scientific Reports*, Volume 9, id. 5492, April 2019
7. LIGO/Virgo S190425z: Lulin Follow-Up Observations., Mansi M., Tan, H. -J.; Yu, P. -C.; Ngeow, C. -C.; Ip, W. -H., GRB Coordinates Network, Circular Service, No. 24193, #1 (2019/April)
8. LIGO/Virgo S190425z: Lulin Observations of Counterpart Search., Tan, H. -J.; Yu, P. -C.; Patil, A. S.; Ngeow, C. -C.; Kong, A.; Ip, W. -H., GRB Coordinates Network, Circular Service, No. 24274, #1 (2019/April-0)
9. LIGO/Virgo S190425z: Lulin observations of the Swift/UVOT transient., Kong, A.; Tan, H. -J.; Yu, P. -C.; Ngeow, C. -C.; Ip, W. -H., GRB Coordinates Network, Circular Service, No. 24301, #1 (2019/April-0)

10. Correction to GCN Circular 24301: LIGO/Virgo S190425z: Lulin observations of the Swift/UVOT transient., Kong, A., GRB Coordinates Network, Circular Service, No. 24303, #1 (2019/April-0)
11. LIGO/Virgo S190510g: Lulin Optical Follow-up Observations., Yu, P. -C.; Tan, H. -J.; Kong, A.; Patil, A. S.; Ngeow, C. -C.; Ip, W. -H., GRB Coordinates Network, Circular Service, No. 24461, #1 (2019/May-0)
12. 鹿林廣角望遠鏡 (LWT)：追蹤近地天體的自動化望遠鏡, 黃健峯, 饒兆聰, 2019/06 國立中央大學天文所碩士論文, 105229005
13. 利用星團中已知造父變星在顏色-星等圖上的位置尋找新的造父變星, 駱世昌, 饒兆聰, 2019/06, 國立中央大學天文所碩士論文, 104229008
14. The beamed jet and quasar core of the distant blazar 4C 71.07, Raiteri, C M, Villata, M and Carnerero, et al. August 2019, Monthly Notices of the Royal Astronomical Society, Volume 489, Issue 2
15. Triple Range Imager and POLarimeter (TRIPOL)—a compact and economical optical imaging polarimeter for small telescopes, Sato, Shuji; Chieh Huang, Po; Chen, Wen Ping; Zenno, Takahiro; Eswarajah, Chakali; Su, Bo He; Abe, Shinsuke; Kinoshita, Daisuke; Wang, Jia Wei, September 2019, Research in Astronomy and Astrophysics, Volume 19, Issue 9, article id. 136 (2019).
16. Investigating the multiwavelength behaviour of the flat spectrum radio quasar CTA 102 during 2013–2017, D’Ammando, F, Raiteri, C M, Villata, M, et al., October 2019, Monthly Notices of the Royal Astronomical Society, Volume 489, Issue 2
17. Swift J1845.7-0037: Lulin optical observation, Yap, Y. X., Kong, A., Li, K. L., The Astronomer's Telegram, No. 13223 (2019/Oct)
18. GROWTH on S190425z: Searching Thousands of Square Degrees to Identify an Optical or Infrared Counterpart to a Binary Neutron Star Merger with the Zwicky Transient Facility and Palomar Gattini-IR, Michael W. Coughlin¹, Tomás Ahumada², Shreya Anand, et al., 2019 November, The Astrophysical Journal Letters, 885:L19 (13pp)
19. LIGO/Virgo S191213g: Lulin Follow-up Observations of AT2019wxt, Kong, A.; Tan, H. -J.; Ngeow, C. -C.; Ip, W. -H., GRB Coordinates Network, Circular Service, No. 26503, #1 (2019/Dec)
20. Evidence for Late-stage Eruptive Mass Loss in the Progenitor to SN2018gep, a Broad-lined Ic Supernova: Pre-explosion Emission and a Rapidly Rising Luminous Transient, Anna Y. Q. Ho, Daniel A. Goldstein, Steve Schulze et al., 2019 December, The Astrophysical Journal, 887:169 (24pp)

3. 其他成果

3.1 目前參與之國際合作計畫

台灣位處太平洋西側，由於廣大的太平洋上（橫跨 6 個時區）只有夏威夷有天文台，對於觀測隨時間變化的天文現象或是全球不同經度的天文台（甚至太空望遠鏡）針對特定天體的聯合觀測，鹿林天文台扮演舉足輕重的角色。多年來鹿林天文台積極參與國際合作計畫，與各國天文台建立良好合作模式，並取得優良成果。這一年我們參與的幾個主要國際合作計畫如下，

1. 全球蠍虎 BL 類星體聯合觀測計畫(The Whole Earth Blazar Telescope, WEBT)：監測活躍星系核，藉此研究黑洞與噴流的性質。
2. 史維基瞬變探測器計畫(Zwicky Transient Facility, ZTF)：將天文研究推進到時間加上空間的 4D 階段，可望對可見光時域天文學作出重大的科學貢獻。
3. 伊甸園觀測網(Exoearth Discovery and Exploration Network, EDEN)：搜尋鄰近太陽之 M 型恆星可能位於適居區內的系外行星。

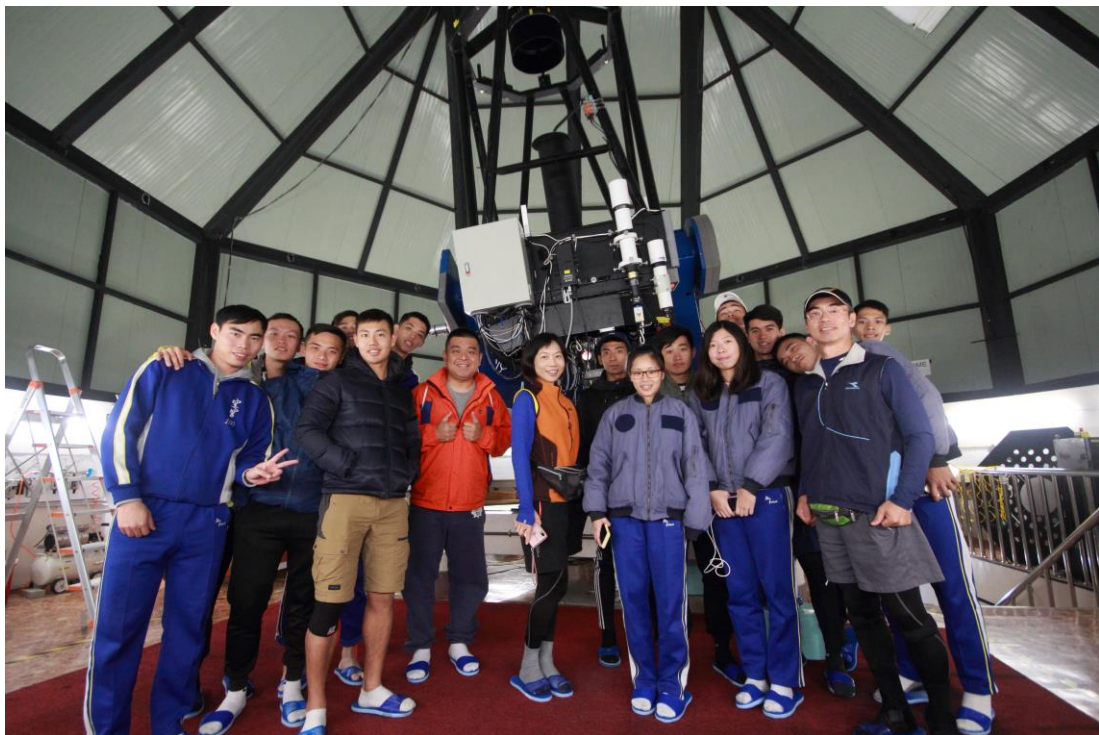
鹿林天文台參訪團體統計(2019)

日期	單位	人數
1月5日	中和+海山高中	39
1月12日	逢甲大學天文社	10
1月15日	海洋大學天文社	16
1月20日	中大 EMBAx5	5
1月26日	彰興國中	27
1月30日	交大天文社	22
1月31日	台大天文社	34
1月31日 2月1日	成功高中	15
2月2日	北一女北集星	48
2月15日	群創光電	11
3月1日 3月2日	中原天文社	31
3月23日	空軍官校航太系	33
4月13日	新竹女中天文社	16
4月26日 4月27日	清大天文所	26 18
4月29日	華德福中學	13
5月23日	台中四育國中	22
6月7日	新竹光復高中	17
6月7日 6月8日	親子觀星會	13
6月25日 6月26日	華德福中學	27 26
6月28日	環保署背景站	10
6月29日	中大天文營	18
7月14日	武陵高中	18
7月24日 7月25日	環保署背景站(大物所德國教授參訪)	19 18
7月25日	台南女中天文社南十字	21
7月27日 7月28日	林口高中	23
7月29日	麗山高中	23
8月01日	香港港青基信書院	7

8月02日	北區多所大學天文社	28
8月15日	上海上南中學	17
8月26日 8月27日	交大天文社	8
8月27日	清境觀光協會	7
8月31日	國家太空中心通訊實驗	17
9月21日	週六菁英隊	9
9月21日	台中市五權社區大學	25
9月28日	文山社區大學	22
10月02日	水利署	21
10月03日	台南重溪國小	14
10月10日 10月11日	中原大學天文社	16
10月19日	台北市天文協會	21
10月21日	亞熱帶生態學會	2
10月26日	苗栗社大天文班	23
10月30日	營建署	11
11月02日	台南市天文協會	45
11月03日	屏東縣祥暉關懷協會	15
11月08日 11月09日	清大天文所	14 15
11月10日	蝸噪家族	19
11月16日	新竹中學天文社	25
11月20日	營建署	15
11月30日	海山高中	35
11月30日	台中一中	18
12月07日	嘉義高中教師群	26
12月12日	紐西蘭 Waihi Academy 學院	13
12月13日	中大理學院謝發坤副院長，化學系 侯敦仁教授，Prof. Norbert Reich	3
12月14日	嘉中嘉女天文社	29
12月14日	中大國際處大陸交換學生	30
12月14日	荒野保護協會	12



北區多所大學天文社參觀



空軍官校航太系參觀

doi: 10.3969/j.issn.1000-8349.2016.z1.16

鹿林天文台三色偏振相机 (TRIPOL) 介绍

李建德¹, 陈文屏¹, 佐藤修二², ESWARAI AH Chakali¹

(1. 台湾“中央大学”天文研究所, 桃园 32001; 2. 名古屋大学 理学部, 名古屋 464-8602)

摘要: 偏振技术被认为是近代天文研究最强大的工具之一, 藉由测量多波段光源的偏振比率及偏振角度可以追踪散射源的大小、形状, 以及是磁场的分布, 从环星尘埃到星系介质乃至宇宙背景辐射, 偏振光的研究在各种天文学尺度都扮演非常重要的角色。鹿林天文台 1m 望远镜近年新安置的偏振相机, 全名为三色成像偏振仪 (TRI-color imaging POLarimeter, 简称 TRIPOL), 系由名古屋大学佐藤教授团队设计制作并且开发控制软件。此相机使用波板以及线栅偏振片来撷取偏振的分量, 再用两片分色镜将光束分为 g' - r' - i' 三色光, 在三台 SBIG ST-9XE 相机同时成像, 相机的视野 4.2 平方角分。每组资料含有 0° , 22.5° , 45° 和 67.5° 的测量, 由此可以导出偏振率以及偏振角。TRIPOL 最重要的特色是 25 kg 的机身极其轻薄短小, 并且拥有三色偏光一次成像的高效率。如此轻便及多色同步的设计, 非常适合约 1 m 级的望远镜, 观测分子云气磁场的强度和分布, 监测瞬变天体的光度以及偏光变化, 或是探测随波长变化的散色源, 例如游离气体的密度或是尘埃大小的分布。介绍了 TRIPOL 的设计以及实际量测偏振的表现。

关键词: 可见光; 偏振; 恒星形成

中图分类号: P112 **文献标识码:** A

1 引 言

天文学获取的观测资料主要分为成像、光谱以及偏振。即使成像细节无法解析, 偏振光可以判断邻近散射源的形状, 甚至可以协助光谱分析, 了解环绕星体的气体与尘埃的特性。偏振光主要源自于光被相当于波长大小的粒子散射, 如气体或是尘埃。光被偏振的程度与散射的方向相关, 与入射方向相同的散射光无偏极化, 与入射方向垂直的散射光则是完全的偏极化, 而介于两者之间的则是部分偏极化。偏振程度是光的偏极化的流量与总流量的比率。

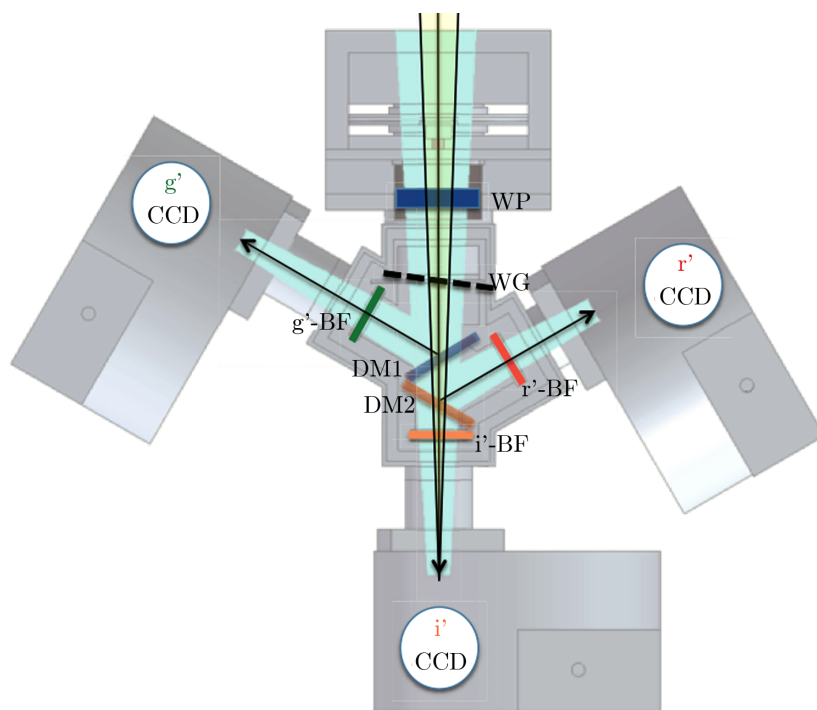
三色成像偏振仪 (TRI-color imaging POLarimeter, 简称 TRIPOL), 其设计的理念为结构简单、功能多样以及成本低廉。视宁度在 $1''$ 以下, 焦比在 $f/6 \sim f/15$ 之间, 像素比例约

通讯作者: 李建德, cdlee@astro.ncu.edu.tw

为 $0.5''$, 所以适合用于小望远镜。TRIPOL 的设计者是日本名古屋大学的佐藤修二教授。除了结构极轻极小之外, 它拥有非常高效率的光学组合。在没有利用反射镜与透镜的设计下, 此仪器能够同时取得天体三色成像以及偏振的信息。TRIPOL 的原形在 2011 年完成并且于鹿林天文台 1 m 望远镜测试。第二套于 2012 年完成, 目前已发表的结果包括了伽玛暴余辉的测光^[1], 以及金牛 T 型星 GM Cep 环星物质的偏振测量^[2]。

2 偏振仪的设计及表现

TRIPOL 由三个部分组成: (1) 偏光元件包括了一个可以旋转的波板, 以及线栅偏振片; (2) 颜色元件则有两片分光镜和三片滤镜; (3) 资料元件包括三台感光耦合元件 (CCD) 相机, 以及一台桌上型电脑。图 1 展示了仪器内部元件的安排, 以及光学路径。来自于望远镜的光, 通过波板和线栅偏极片, 然后被两片分光镜分解到三个路径, 再经由三色滤镜 (g' , r' , i') 最后进入 CCD 相机。TRIPOL 的重量只有 25 kg, 体积大约是 $40 \times 40 \times 40 \text{ cm}^3$ 。



图中主要部分: WP——波板; WG——线栅偏振片; DM1——分光镜一; DM2——分光镜二; g' -BF—— g' 波段滤镜; r' -BF—— r' 波段滤镜; i' -BF—— i' 波段滤镜; CCD——感光元件。

图 1 TRIPOL 的设计概要图

TRIPOL 使用三台商用 SBIG ST 9-XEi 相机, CCD 的尺寸为 $512 \times 512 \times 20 \mu\text{m}$ (见表 1), 安装在鹿林 1 m 望远镜 ($f/8$) 上的视野大小为 4.2 平方角分。相机的操作以及偏光元件的转

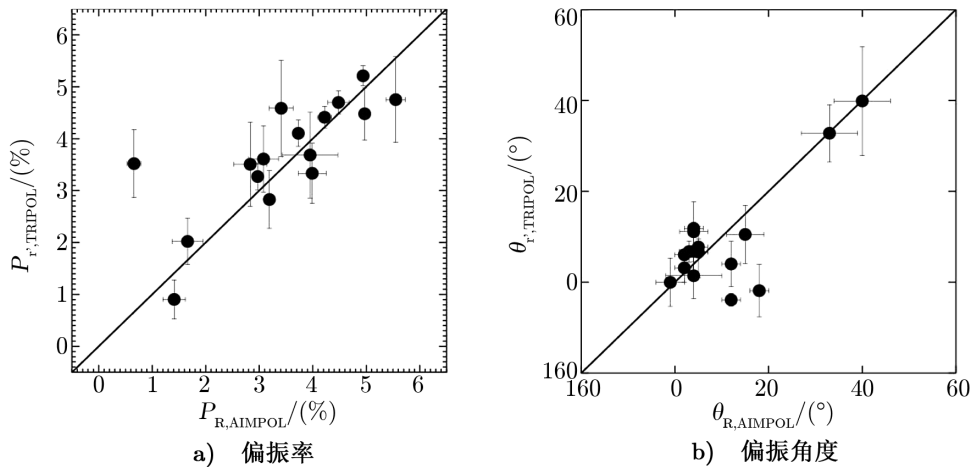
动, 是由一台 Intel DN 2800MT 桌上型电脑所控制。波板可以旋转的角度分别是 0° , 22.5° , 45° 以及 67.5° 。观测时依序取得每个角度的影像, 处理资料时才能取得天体偏振结果。

表 1 CCD 相机参数

参数	值
CCD 大小	$512 \times 512 \times 20 \mu\text{m}$
最大阱容	约 65 000 e
暗电流	10 e/pixel/s 在 0°C
增益值	1.6 e/ADU
读取杂信	16 e RMS
全幅数据采集时间	1 s

由观测偏振及无偏振的标准星^[4], 我们可以推导 TRIPOL 在鹿林 1 m 望远镜上的仪器所造成的偏振, 以及测光和偏振的探测极限。从 2015 年 2 月的结果来看, 仪器自身造成的偏振程度约为 0.3%, 而角度的平移量约为 $30^\circ \sim 40^\circ$ 。在 3 倍标准差下, 偏振探测极限约为 15 mag, 极限偏振率及角度大约是 0.3% 和 3° 。若只测光而不测量偏振, 可将偏振片取出, 灵敏度可达到 18~19 mag。

为了强化 TRIPOL 的可靠性, 除了观测标准星比较之外, 也与印度的 ARIES (Aryabhata Research Institute of Observational Sciences) 的偏振仪 AIMPOL (ARIES imaging polarimeter)^[3] 相比较 (见图 2)。对恒星形成区的星团 NGC 6823 的观测, 无论是偏振率还是偏振角度, 两个仪器的表现都相当一致。

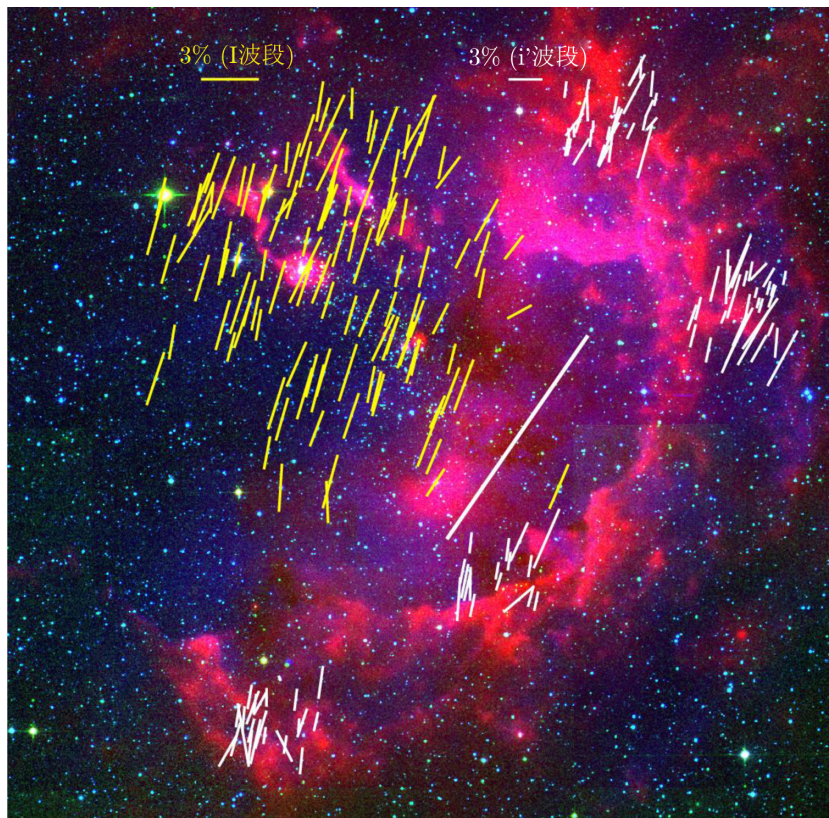


注: 对角线表示完全一致的比较基准。

图 2 AIMPOL 的 R 波段 (横轴) 与 TRIPOL 的 r' 波段 (纵轴) 观测 NGC 6823 的偏振结果比较

3 应用与总结

目前 TRIPOL 在实际应用上, 分别观测被原行星团块环绕的年轻恒星 GM Cep, 以及恒星形成区。例如位于氢二区的 NGC 1893, 在此区域不同的位置上我们分别利用 AIMPOL 以及 TRIPOL 做偏振观测, 见图 3。结果显示, 这个区域的磁场一致性, 并且与银河较大尺度的偏振方向有些许的偏振角平移。除了可见光之外, 期待将来可以使用红外及亚毫米的偏振, 多波段观测恒星形成区更深处的磁场, 再整合由浅到深的观测结果, 绘制磁场的三维分布, 进一步研究磁场在恒星形成过程所扮演的角色。



注: TRIPOL 的 i' 波段以及 AIMPOL 的 I 波段分别观测不同区域, 偏振角度分别由黄线以及白线表示。图内标示出 3% 的偏振率, 以及银河大尺度的偏振方向 (HII 区的空洞处)。

图 3 恒星形成区 NGC 1893 的偏振观测

TRIPOL 是鹿林天文台目前最新的仪器, 提供观测者可见光 $g'-r'-i'$ 三色偏振同步的成像, 简单多功能的设计非常适合小型望远镜。在探索星际磁场、星球环星物质以及其偏振变化方面, TRIPOL 是非常合适且优异的观测工具。

参考文献:

- [1] Cenko S B, Urban A L, Perley D A, et al. ApJ, 2015, 803: L24
- [2] Chen W P, Hu S C L. Formation, Detection, and Characterization of Extrasolar Habitable Planets, 2014, 293: 74
- [3] Rautela B S, Joshi G C, Pandey J C. Bulletin of the Astronomical Society of India, 2004, 32: 159
- [4] Schmidt G D, Elston R, Lupie O L. AJ, 1992, 104: 1563

Introduction to the TRI-color Imaging POLarimeter for the Lulin Observatory

LEE Chien-De¹, CHEN Wen-Ping¹, SATO Shuji², ESWARAI AH Chakali¹

(1. Graduate Institute of Astronomy, "Central University", Taoyuan 32001; 2. Department of Astrophysics, Nagoya University, Chikusa-ku 464-8602)

Abstract: Polarization technique is one of the most powerful tool in modern astronomy. Multicolor polarimetry traces the properties of scattering sources including size, geometry, magnetic field and even the distribution of the gravitational wave. Investigation of the polarized light crucially probes the universe in different scale from circumstellar dust, interstellar medium to cosmic microwave background. Recently, we have set up a polarimeter called TRI-color imaging POLarimeter (TRIPOL) at Lulin one meter telescope. The device and control software were designed and constructed by a group of Nagoya university leading by prof. Sato. TRIPOL measures the polarized component of light with its wave plate and wire grid. Using the two dichroic mirrors and g'-r'-i' filters, three colors images can be collected simultaneously in three SBIG ST-9XE cameras in a field of view with $4.2' \times 4.2'$. To derive the degree of polarization and position angle, each data set includes four measurements from 0° , 22.5° , 45° and 67.5° . TRIPOL is not only a simultaneous imager of polarized light but also a compact and light instrument only 25 kg in weight, so it is extremely fit for the small telescopes with diameter around one meter. It is suitable for studying the magnetic field distribution of molecular cloud, polarimetric and photometric variation of transiting objects, the wavelength dependence of the scattering sources of the astrophysical objects, e.g., the density of ionized gas or the size distribution of the dust grain. In this work, we introduce the instrumental design and observing performance of TRIPOL.

Key words: optical; polarimetry; star formation

Follow-Up Observations of Gravitational Wave Events from Lulin Observatory

The Lulin One-meter Telescope (LOT), via the GROWTH network, is participating the follow-up observations of gravitational wave (GW) events detected by LIGO. During its O3 run (April 2019 to April 2020), LIGO detected ~39 and ~14 GW events in 2019 and 2020, respectively. LOT did not, and cannot, follow-up all these events but preferentially selected the events that were suitable to be observed (e.g. the events are visible from Lulin Observatory at night, the events are located within 1000Mpc, and etc). Nevertheless, LOT has performed follow-up observations for 4 GW events (S190425z, S190510g, S190930t & S191213g) in 2019, resulting in 8 GCN published (see the screenshots below; Note: we omitted the galaxies list in the screenshots). The work on S190425z was also included in a refereed paper: "GROWTH on S190425z: Searching Thousands of Square Degrees to Identify an Optical or Infrared Counterpart to a Binary Neutron Star Merger with the Zwicky Transient Facility and Palomar Gattini-IR" by Coughlin et al (2019, ApJL 885:L19).

TITLE: GCN CIRCULAR
NUMBER: 24193
SUBJECT: LIGO/Virgo S190425z: Lulin Follow-Up Observations
DATE: 19/04/25 19:55:03 GMT
FROM: Mansi M. Kasliwal at Caltech/Carnegie <manskasliwal@gmail.com>

Han-Jie Tan (NCU), Po-Chieh Yu (NCU), Chow-Choong Ngeow (NCU), Wing-Huen Ip (NCU)

On behalf of Global Relay of Observatories Watching Transients Happen (GROWTH) collaborations

We report the photometric measurements of two promising candidates ZTF19aarykbb and ZTF19aarzaod (GCN 24191) associated with the gravitational wave trigger S190425z (GCN 24168) using Lulin One-meter Telescope (LOT) in Taiwan. The observations were conducted using g, r, i filters at 2019-04-25 15:57:19 UT, ~7.65 hours after the trigger, and 2019-04-25 17:25:43, ~9.12 hours after the trigger, respectively. Preliminary photometry were obtained by calibrating with Pan-STARRS catalog.

We would like to thank the staff in Lulin Observatory for helping the observations.

Summary of ZTF19aarykbb:	Filter	Exp(s)	
2019-04-25 15:58:49	g	180	18.84+/-0.04
2019-04-25 16:02:11	r	180	18.23+/-0.02
2019-04-25 16:05:33	i	180	17.92+/-0.02
Summary of ZTF19aarzaod:			
2019-04-25 17:48:24	g	300	21.45+/-0.47
2019-04-25 17:53:45	r	300	
			20.26+/-0.25
2019-04-25 17:41:56	i	300	
			19.93+/-0.13

Also, we searched for optical counterpart in 90% localization area of LIGO/Virgo S190425z (GCN 24168). The observation started at 2019-04-25 12:27:23 UT, 249 minutes after the trigger, and 27 galaxies were observed in R-band with 180 second exposure time. No obvious transient can be identified brighter than R=20 mag (AB). The galaxy coordinates are listed below.

TITLE: GCN CIRCULAR
NUMBER: 24461
SUBJECT: LIGO/Virgo S190510g: Lulin Optical Follow-up Observations
DATE: 19/05/10 20:13:15 GMT
FROM: Albert Kong at NTHU <akhkong@gmail.com>

Po-Chieh Yu (NCU), Han-Jie Tan (NCU), Albert Kong (NTHU), Atharva Sunil Patil (NCU), Chow-Choong Ngeow (NCU), Wing-Huen Ip (NCU), on behalf of the Global Relay of Observatories Watching Transients Happen (GROWTH) collaboration

We report observations of 81 galaxies in the 90% localization of the BNS merger candidate, S190510g, detected by LIGO/Virgo (GCN #24442; GCN #24448) using the Lulin One-meter Telescope (LOT) in Taiwan. The observation started at 2019-05-10 12:54:43 UT, ~10 hours after the trigger. The observations were conducted using the r-band filter with 180 second exposure time. By comparing with Pan-STARRS images, we do not detect transient candidates brighter than r=21 mag (AB). We thank the staff in Lulin Observatory for helping the observations. The galaxy coordinates are listed below.

TITLE: GCN CIRCULAR
NUMBER: 24274
SUBJECT: LIGO/Virgo S190425z: Lulin Observations of Counterpart Search
DATE: 19/04/27 09:17:29 GMT
FROM: Albert Kong at NTHU <akhkong@gmail.com>

Han-Jie Tan (NCU), Po-Chieh Yu (NCU), Atharva Sunil Patil (NCU), Chow-Choong Ngeow (NCU), Albert Kong (NTHU), Wing-Huen Ip (NCU)

On behalf of Global Relay of Observatories Watching Transients Happen (GROWTH) collaborations

We report observations of 58 galaxies in 90% localization of the BNS merger candidate, S190425z, detected by LIGO/Virgo (GCN #24168) using the Lulin One-meter Telescope (LOT) in Taiwan. The observation started at 2019-04-25 14:11:07 UT, ~5.9 hours after the trigger. All images were taken in R-band with 180 second exposure time. No significant transient can be identified brighter than R=20 mag (AB). The galaxy coordinates are listed below.

We thank the staff in Lulin Observatory for helping the observations.

TITLE: GCN CIRCULAR
NUMBER: 24301
SUBJECT: LIGO/Virgo S190425z: Lulin observations of the Swift/UVOT transient
DATE: 19/04/27 20:39:41 GMT
FROM: Albert Kong at NTHU <akhkong@gmail.com>

Albert Kong (NTHU), Han-Jie Tan (NCU), Po-Chieh Yu (NCU), Chow-Choong Ngeow (NCU), Wing-Huen Ip (NCU)

On behalf of Global Relay of Observatories Watching Transients Happen (GROWTH) collaborations

We used the 1m telescope at the Lulin Observatory in Taiwan to obtain g- and r-band images of the transient found by Swift/UVOT (GCN 24296). The observations started at 2019-04-28 19:30 UT and the exposure time is 300s for both filters. With a limiting magnitude of about 21.5 (AB) by comparing to PS1 images, we do not detect the UVOT transient.

TITLE: GCN CIRCULAR
NUMBER: 24487
SUBJECT: LIGO/Virgo S190510g: Non-detection of the OT in PGC 094244
DATE: 19/05/11 17:20:02 GMT
FROM: Albert Kong at NTHU <akhkong@gmail.com>

Po-Chieh Yu (NCU), Han-Jie Tan (NCU), Albert Kong (NTHU), Atharva Sunil Patil (NCU), Chow-Choong Ngeow (NCU), Wing-Huen Ip (NCU), on behalf of the Global Relay of Observatories Watching Transients Happen (GROWTH) collaboration

We observed the possible OT in PGC 094244 (GCN #24470, Lipunov et al.) at 2019-05-11 12:50:12 UT using the Lulin One-meter Telescope (LOT) in Taiwan. We obtained g-, r-, i-band images with 300s exposure time, and the transient is not detected in all images. The r-band limiting magnitude is about 21 by comparing with Pan-STARRS images. This is consistent with the results of Tucker et al. (GCN #24477).

We thank the staff in Lulin Observatory for helping the observations.

TITLE: GCN CIRCULAR
NUMBER: 26431
SUBJECT: LIGO/Virgo S191213g: Lulin Follow-up Observations of ZTF19acykzsk/AT2019wqj
DATE: 19/12/15 02:17:28 GMT
FROM: Albert Kong at NTHU <akhkong@gmail.com>

Han-Jie Tan (NCU), Albert Kong (NTHU), Chow-Choong Ngeow (NCU),
Wing-Huen Ip (NCU)

On behalf of the Global Relay of Observatories Watching Transients
Happen (GROWTH) collaborations

We report the photometric measurements of the Type II supernova
ZTF19acykzsk/AT2019wqj previously associated with the gravitational
wave event S191213g (GCN #26402, #26424) using the Lulin One-meter
Telescope (LOT) in Taiwan. The observations were conducted using g, r,
i filters starting at 2019-12-14 10:13:37 UT and were repeated 7 hours
later. Preliminary photometry was obtained by calibrating with the
APASS catalog.

Its r magnitude is slightly fainter than the observation by Andreoni
et al. (GCN #26424) ~14hr earlier and suggests a slow decay. We
confirm the report from Andreoni of a red color $g-r=0.26$.

Summary of ZTF19acykzsk/AT2019wqj :

UT	JD	Filter	Exp(s)	Mag (AB)
2019-12-14 10:16:07	2458831.928	g	300	19.37+/-0.10
2019-12-14 10:21:13	2458831.931	r	300	19.11+/-0.16
2019-12-14 10:26:20	2458831.935	i	300	19.10+/-0.11
2019-12-14 17:21:07	2458832.223	g	300*2	19.51+/-0.11
2019-12-14 17:32:47	2458832.231	r	300*2	19.10+/-0.14
2019-12-14 17:35:24	2458832.233	i	300	19.06+/-0.24

We would like to thank the staff in Lulin Observatory for helping the
observations.

TITLE: GCN CIRCULAR
NUMBER: 26503
SUBJECT: LIGO/Virgo S191213g: Lulin Follow-up Observations of AT2019wxt
DATE: 19/12/19 14:44:06 GMT
FROM: Albert Kong at NTHU <akhkong@gmail.com>

Albert Kong (NTHU), Han-Jie Tan (NCU), Chow-Choong Ngeow (NCU),
Wing-Huen Ip (NCU)

On behalf of the Global Relay of Observatories Watching Transients
Happen (GROWTH) collaborations

We report the photometric measurements of AT2019wxt (GCN #26485)
associated with the gravitational wave event S191213g (GCN #26402)
using the Lulin One-meter Telescope (LOT) in Taiwan. The observations
were conducted using g, r, i filters for 300 sec each starting at
2019-12-19 10:42:45 UT. Preliminary photometry (AB) was obtained by
calibrating with the PS1 catalogue. We obtained $g=19.50+/-0.04$,
 $r=19.40+/-0.03$, and $i=19.47+/-0.06$.

Compared to the Palomar observations taken 6 hours earlier (GCN
#26500), AT2019wxt remains at the same brightness level.

We would like to thank the staff in Lulin Observatory for helping the
observations.

TITLE: GCN CIRCULAR
NUMBER: 25916
SUBJECT: LIGO/Virgo S190930t: Lulin Follow-up Observations of AT2019rpn and AT2019rpj
DATE: 19/10/01 23:55:00 GMT
FROM: Albert Kong at NTHU <akhkong@gmail.com>

Han-Jie Tan (NCU), Albert Kong (NTHU), Chow-Choong Ngeow (NCU),
Wing-Huen Ip (NCU)

On behalf of the Global Relay of Observatories Watching Transients
Happen (GROWTH) collaborations

We report the photometric measurements of two optical counterpart
candidates ZTF19acbpqlh (AT2019rpn) and ATLAS19wyn/ZTF19acbpsuf
(AT2019rpj) associated with the gravitational wave event S190930t (GCN
#25876, #25899) using the Lulin One-meter Telescope (LOT) in Taiwan.
The observations were conducted using g, r, i filters starting at
2019-10-01 14:12:14 UT. Preliminary photometry was obtained by
calibrating with the Pan-STARRS catalog.

Summary of ZTF19acbpqlh:

UT	Filter	Exp(s)	Mag (AB)
2019-10-01 14:14:56	g	300	20.80+/-0.25
2019-10-01 14:20:16	r	300	20.67+/-0.33
2019-10-01 14:25:36	i	300	20.80+/-0.39

Summary of ATLAS19wyn/ZTF19acbpsuf:

2019-10-01 14:31:53	g	300	19.65+/-0.08
2019-10-01 14:37:14	r	300	19.58+/-0.09
2019-10-01 14:42:35	i	300	19.55+/-0.12

We would like to thank the staff in Lulin Observatory for helping the
observations.

利用鹿林廣視場望遠鏡對近地天體做自動化的追蹤觀測

黃健峯

鹿林廣視場望遠鏡(Lulin Widefield Telescope, 簡稱 LWT)是新購置的望遠鏡並在 2017/10/17 安裝於鹿林天文台,是一個口徑 40 公分的小型望遠鏡,配備一台 FLI PL16803 相機,使得望遠鏡視野達到約 2 平方度,極限星等可達約 19 等。我們的追蹤目標為待確認的近地天體,列於 Minor Planet Center (MPC)的 NEO Confirmation Page (NEOCP)網站裡面。

由 GROWTH 計畫啟發兩個想法,分別為「鹿林天文台改造計畫」與「時序天文學的前沿研究」,前者目標使位於鹿林天文台的研究用望遠鏡改造成全自動觀測與分析,後者為對瞬變天體與近地小行星做追蹤觀測。為了朝這兩個目標前進,我們先從比較簡單的計畫開始實行,也就是利用 LWT 對近地天體做追蹤觀測。

為了瞭解新望遠鏡的性能,我們做了一系列測試,其中相機特性包括讀出雜訊在讀出速度慢(1MHz)為 8.4 個電子與讀出速度快(8MHz)為 13.2 個電子、增益值為 1.4 e/ADU、暗電流約為 0.01 e/s 和曝光要長於 3 秒以避免測光受快門圖案影響;而望遠鏡極限星等對於訊噪比 10 的星體曝光 5 分鐘可達約 18 等(滿月)與 19 等(新月)。

硬體結構包含有一台觀測用電腦(LWTobs)與一台分析用電腦(LWTanaly),利用 LWTobs 控制望遠鏡做自動觀測,資料儲存於 LWTobs 並即時地備份至 LWTanaly, LWTanaly 即時地處理分析後,將近地天體的天球座標及其亮度上報給 MPC。

自動觀測與自動分析個別由三個 Python 程式負責,以下分別介紹各步驟,觀測步驟:

1. 首先從 NEOCP 篩選可觀測的目標,然後產生出一個 ACP Observatory Control Software 可以執行的腳本,最後通知使用者當日的觀測資訊,隔日更新觀測資料至 LWT 網站。
2. 拍攝校正照片需要的資料,包括偏壓與暗電流。
3. 觀測開始,首先開啟所有觀測程式,黃昏時拍攝平場,晚上追蹤近地天體,清晨拍攝平場,太陽升起前關閉天文台。

分析步驟：

1. 尋找可使用的偏壓場、暗場與平場並處理，隨後即時處理近地天體相照片。
2. 對校正後的近地天體照片進行疊加，尋找其天球座標。
3. 利用膠囊形狀的測光區域對近地天體做測光。
4. 產生 ADES 格式的報告給 MPC。

未來工作包括：

1. 改善與強化自動化系統。
2. 因為比我們的極限星等(18 等)還亮的近地天體很少，所以有些天沒有觀測目標可以追蹤，近期會將已知的近地小行星包含在觀測目標裡面。
3. 利用更好的方法來尋找近地天體在照片裡面的位置，例如利用較差影像分析 (Difference-Imaging Analysis)或機器學習辨識的方法，提高辨識成功率。



Lulin Widefield Telescope (LWT): a Robotic Telescope for the Near-Earth Object Follow-up Observation

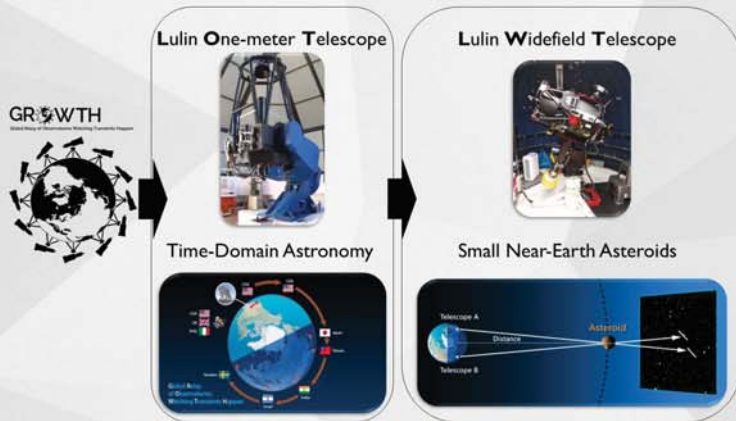


Jian-Fong Huang^{1*}, Chow-Choong Ngeow¹, Ting-Chang Yang¹, Hung-Chin Lin¹
¹Graduate Institute of Astronomy, National Central University, Taoyuan, Taiwan

ABSTRACT

The Lulin Widefield Telescope (LWT, observatory code: D37^[1]), a 0.4-m Officina Stellare 400 RiFast telescope, was installed at the Lulin Observatory on October 17th, 2017. The telescope is equipped with the FLI ProLine PLI 6803 monochrome CCD camera such that the field of view is about 2 degree squared and can reach to a limiting magnitude of 19-mag in V-band. Our goal is to automatically follow up Near-Earth Objects (NEOs), including automated observation, image reduction, calibration and analysis. We also present an example of automated observation of a known Near-Earth Asteroid (NEA) with the LWT.

MOTIVATION

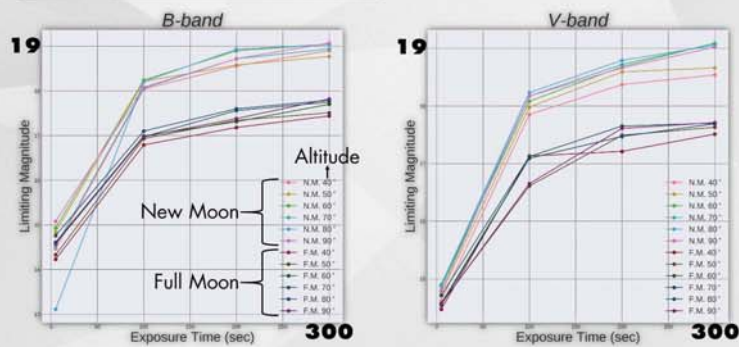


CCD CHARACTERISTICS

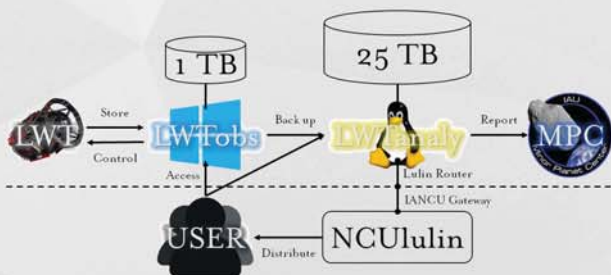
[-30°C]	Readout Noise	Gain	Dark Current
1 MHz	8.4 e ⁻	1.4 $\frac{e^-}{ADU}$	0.0077 $\frac{e^-}{sec}$
8 MHz	13.2 e ⁻		0.011 $\frac{e^-}{sec}$

• Shutter pattern will appear if exposure time is shorter than 3 seconds.
 *The above values are the results based on several CCD testings.

TELESCOPE PERFORMANCE



SYSTEM ARCHITECTURE



AUTOMATION DESIGN

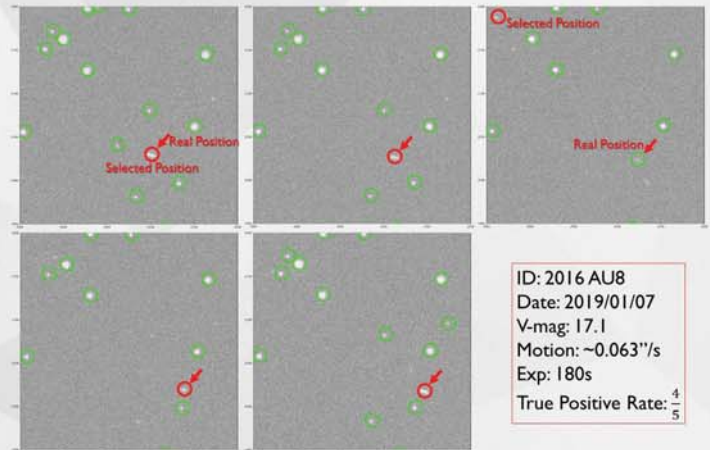
Automatic Observation

- I. Select the NEOs from the NEOCP^[2] → create the ACP^[3] script → inform users → update the LWT's website
- II. take bias and dark frames
- III. Open astronomical softwares → take dusk flats → run the ACP script → take dawn flats → close observatory

Automatic Analysis

- I. Copy and process calibration data → calibrate science images in real time
- II. Reduce science images & stack the images → photometric calibration → find the NEO
- III. Perform the pill aperture photometry of the TRIPPy^[4] Python package
- IV. Submit the astrometric observation report to the MPC

AN EXAMPLE OF KNOWN NEAs



FUTURE WORKS

- A. Improve and enhance the automation system.
- B. Include known NEAs into our candidates.
- C. Seek better ways to find the NEOs, such as difference-imaging analysis or the M.L.

REFERENCES

- [1] Minor Planet Center – List of Observatory Codes (<https://minorplanetcenter.net/iau/lists/ObsCodesF.html>)
- [2] Minor Planet Center – The NEO Confirmation Page (https://www.minorplanetcenter.net/iau/NEO/toconfirm_tabular.html)
- [3] DC-3 Dreams – ACP Observatory Control Software (<http://acp.dc3.com/index2.html>)
- [4] TRIPPy: Trailed Image Photometry in Python (DOI: 10.3847/0004-6256/151/6/158)



新聞報導

好山好水好宇宙，臺灣展望宇宙之眼：鹿林天文臺

2019/12/23 泛科學

鹿林天文臺位於臺灣南投縣與嘉義縣交界之鹿林前山，緊鄰玉山國家公園，是臺灣最重要的光學天文基地，兼具研究與教育功能。

為什麼選在高山上建立鹿林天文臺？

鹿林天文臺的基本檔案

地理位置：東經 120°52'25"，北緯 23°28'07"

海拔：2,862 公尺

夜天光背景 1：每平方角秒的視星等為 21.28 星等

大氣寧靜度 2：星點平均視角為 1.39 角秒

年平均觀測時間：1,450 小時（約 180 個夜晚，以每晚 8 小時計）

此地受冬季東北季風、夏季西南氣流和颱風的影響較小；受惠於國家公園的優越環境，加上位處高山，空氣汙染和塵埃少，大氣透明度高，光害也較小；由於海拔高、大氣稀薄，所以消光較小，大氣寧靜度較好，秋冬兩季尤其適合觀測。

鹿林天文臺的開發緣起於 1990 年，由當時任職於中央大學天文所的蔡文祥教授與張光祥先生，考量臺灣各地的晴天率、海拔、後勤支援等因素，並歷經 3 年的大氣寧靜度、氣候、夜天光背景等條件調查後才選定臺址。

天文臺所使用的電力由臺電提供，玉山國家公園和中華電信的基地臺則分別提供用水和網路通訊服務。此外，天文臺內也設有自動氣象站、全天域相機以及雲量監測儀等儀器設備，可作為觀測參考。

鹿林天文臺有哪些設備？

基地內設置了數座小型可見光望遠鏡。除了有：

鹿林一米望遠鏡（Lulin Onemeter Telescope，簡稱 LOT）

中美掩星計畫（Taiwanese American Occultation Survey，簡稱 TAOS）的 4 座

0.5 米自動望遠鏡

0.4 米超輕型望遠鏡（Super Light Telescope，簡稱 SLT40）

鹿林廣角望遠鏡（Lulin Widefield Telescope，簡稱 LWT）

進行天文觀測外，另有成功大學的紅色精靈 3 地面觀測與極低頻無線電波偵測

系統（ELF）、中央大學的氣暉全天相機、土石流偵測預警系統，以及環保署的鹿林山大氣背景測站（LABS）等設備，記錄大氣、環境、太空、地震等觀測數據，為我國珍貴的高山科學基地。

鹿林一米望遠鏡（LOT）：

鹿林天文臺最大的望遠鏡—LOT，同時也是目前臺灣口徑最大的通用型光學望遠鏡。

LOT 具備良好的光學成像品質、指向和追蹤精度，並配備高靈敏儀器，包括專業天文相機，以取得天體影像，並測量在不同可見光波段的亮度。另外也配置低色散光譜儀及偏振儀等，藉以取得天體光譜或偏振訊息。

LOT 由德國 APM 公司製作，屬於卡塞格林反射式望遠鏡，由於採用鏡後端對焦座，因此卡焦儀器限重 50 公斤。LOT 觀測目標包括太陽系天體、銀河系中的恆星、變星、星團及鄰近星系等，除了提供中央大學師生研究與教學之用，也開放國內、外學者申請使用。

某些宇宙現象有時效性，例如星球爆發、掩星等，隨著地球自轉，只有面對該天體的觀測者才能夠看到。由於臺灣位處西太平洋，向東 6 個時區內缺乏其他天文臺，因此對於會隨時間變化，需連續監測的天象，或是國際間需要位在不同經度的天文臺（或太空望遠鏡）針對特定天體聯合觀測時，鹿林天文臺便扮演著舉足輕重的角色。

多年來，鹿林天文臺的望遠鏡積極參與此類計畫，例如：全球望遠鏡聯合觀測（Whole Earth Telescope，簡稱 WET）聯合不同時區的望遠鏡，接力監測恆星的亮度變化，以星震 5 手段探討恆星內部結構；全球蝎虎 BL 類星體聯合觀測（Whole Earth Blazar Telescope，簡稱 WEBT）監測活躍星系核，藉此研究黑洞與噴流的性質；年輕系外行星掩星觀測計畫（Young Exoplanet Transit Initiative，簡稱 YETI）則監測星團成員、搜尋系外行星造成的凌星事件等，均與國際天文臺建立良好合作模式，並取得優良成果。

啟用至今，鹿林天文臺的望遠鏡共發現 15 顆超新星、800 餘顆小行星，以及一顆彗星。每年通常約有十幾個研究計畫利用 LOT 執行，使用 LOT 數據發表的研究論文已超過百篇。除了研究之外，LOT 也支援大學、高中及社教機構進行觀測教學實習，另有多座小型望遠鏡提供特定課題使用。

中美掩星計畫（TAOS）：

天文臺原來設有 4 座 TAOS 望遠鏡，由中央研究院天文所、中央大學天文所、美國哈佛史密松天文物理中心，以及韓國延世大學共同合作。每座望遠鏡的口

徑 50 公分，具備 3 平方度 6 的超廣角視野，全年監測可能由柯伊伯帶天體造成的掩星事件，藉以估計分布在太陽系外圍的小型天體數量。

TAOS 計畫自 2005 年開始運行，累積 6 年的觀測結果一共收集超過 10 億筆恆星光度的測量數據，因為沒有偵測到任何掩星事件，提供了柯伊伯帶天體的數量上限。

第一代 TAOS 的設備已於 2016 年拆除、撤離，第二代的海王星外自動掩星普查計畫（Transneptunian Automated Occultation Survey，簡稱 TAOSII）選在墨西哥的聖彼德羅瑪蒂爾天文臺（San Pedro Mártir Observatorio）落腳，一共有 3 座口徑 1.3 米的望遠鏡。

超輕型望遠鏡（SLT）：

中央大學天文研究所於 1997 年獲得太空計畫室（現在的國家太空中心）補助，興建鹿林第一座天文臺“SLT”。1999 年 SLT 完工後，內部安裝自行設計、製造的 76 公分超輕型望遠鏡（SLT76），並從 2000 年開始進行觀測，是鹿林天文臺初期最重要的觀測設備。

SLT76 於 2005 年換裝口徑 40 公分的超輕型望遠鏡（SLT40），並自 2006 年開始進行鹿林巡天計畫（Lulin Sky Survey，簡稱 LUSS），搜尋太陽系小天體。計畫進行 3 年期間共發現 800 多顆小行星，其中有 400 多顆已獲得永久編號，小行星發現數量排名世界第 47。

目前鹿林天文臺發現的小行星已有 100 多顆得到永久命名，名稱涵蓋臺灣的代表性人物、團體、地理、山水及原住民族等。2007 年 LUSS 首度發現彗星（C/2007 N3）與近地小行星（2007 NL1），該彗星後來被命名為鹿林彗星（Comet Lulin）。LUSS 計畫結束後，自 2010 年起 SLT40 投入變星、彗星的長期監測工作。

除了硬體設備，還能善用地理優勢進行觀測

鹿林天文臺的主要策略是利用小型望遠鏡的機動性，以及臺灣本身的觀測條件優勢，與其他的天文臺合作、競爭。

臺灣的地理位置緯度較低，因此可以觀測範圍較大的南半球天空；而經度方面則可以跟國際間的其他天文臺互補。對於需要長期監測或瞬變的天文現象（如超新星及伽瑪射線爆等），鹿林天文臺參與跨國合作，在全球天文觀測網和太空與地面的聯合觀測中占據不可或缺的位置。

比如 2006 年中央大學天文所參加夏威夷大學主導的泛星計畫（PanSTARRS），另外近年加入由加州理工學院主導的茲威基瞬變探測利器（Zwicky Transient Facility，簡稱 ZTF），並加入伊甸園觀測網（Exoearth Discovery and Exploration Network，簡稱 EDEN），以搜尋鄰近太陽之 M 型恆星周圍可能位於適居區內的系外行星等，都因為地理位置的優勢，能藉由鹿林天文臺的設備追蹤並確認新的科學發現。

在臺灣近百年的天文發展史上，鹿林天文臺締造了多項紀錄，包括首度發現小行星、首度發現超新星、首度發現彗星、首度發現近地小行星及首度進行小行星命名。天文臺的望遠鏡口徑雖然小，但做為天文教育與基本研究工具，多年來配合規劃的課題立基，亦取得良好的成果。

註解：

夜天光背景：夜空背景的亮度。星等數字越大，表示亮度愈低，意即光害愈小，能夠觀測愈暗的天體。

大氣寧靜度：大氣擾動對星光成像的影響程度。以星點的視角表示，視角愈小表示大氣寧靜度愈好，觀測到的星像愈清晰。

紅色精靈：積雨雲層上方發生的放電現象，由於主要發出紅光，而且發生的時間非常短暫不易捉摸，因此被稱為紅色精靈。

焦比：口徑與焦距的比值。

星震：利用亮度變化或光譜都卜勒效應研究天體的震動，藉此瞭解無法直接觀測的恆星內部結構，其原理類似利用地震波研究地球的內部結構。

平方度：一度乘以一度的天空範圍。例如滿月的張角約半度，3 平方度相當於 10 個滿月的天空面積。

「南瀛天文館」小行星光照 全臺首創的《星動時課》上路

2019/12/03 HiNet 新聞

擁有全台灣平地最大 76 公分望遠鏡的台南市立南瀛天文館，長期致力台灣基礎天文教育的扎根，串連鄰近的人文景觀、豐富的自然生態資源，創造多元教育價值的「南瀛星故鄉」。為肯定南瀛天文館在天文教育上之貢獻，中央大學特將鹿林天文台所發現的編號 281569 號小行星，命名為「南瀛天文館」小行星，並經國際天文學聯合會（IAU）通過。

12 月 1 日上午在台南市忠義國小，台南市政府教育局特舉辦「玩轉天文」星動時課天文課程博覽會，除有一系列精彩活動之外，另有「南瀛天文館」小行星

頒贈儀式，由中央大學副校長陳志臣致贈小行星銘板給台南市長黃偉哲。

秉持著「天文好好玩」的信念，臺南市政府教育局轄下南瀛天文館以國小一至六年級學生為目標，把讓老師苦惱的天文課程教學，透過團康、桌遊、故事或教具操作，轉化為好玩易懂的《星動時課》。歷經兩年的教案編寫、課程試教修正及教具研發製作，終於在今年 7 月完成全部 36 套課程。這是全臺第一個系統性開發完成的國小天文課程，同時自 108 學年度起，臺南市共有 15 間國民小學正式實施《星動時課》。

中央大學副校長陳志臣肯定台南市政府這項創舉，有助於天文教育向下扎根。他表示，小行星目前為唯一可由發現者命名的天體，中大目前已取得近 50 顆命名，表彰許多對台灣有重要貢獻的人，如陳樹菊女士、鄧雨賢先生...等等。同時全台灣各縣市名稱，也即將命名完成。

中央大學天文所所長黃崇源說，「南瀛天文館」小行星 2008 年 10 月 23 日由蕭翔耀與葉泉志於鹿林天文台所發現，發現時在金牛座位置，目前已運行到獵戶座。大小約在 1-2 公里之間，繞行太陽一圈 3.59 年（軌道週期），離太陽最近時（近日點）為 2.6 億公里，最遠時（遠日點）為 4.4 億公里。

黃崇源說，要在宇宙蒼穹間發現新星體，一如大海撈針般困難，同時要經長時間的軌道確認，才能確認是新天體。尤其在海拔 2,862 公尺的高山觀測相當克難，工作型態更是日夜顛倒，十分辛苦。

小行星是目前各類天體中唯一可以由發現者進行命名並得到世界公認的天體。觀測者發現小行星後，需先通報國際小行星中心，經初步確認後，會按發現時的年份與順序配予暫時編號。當該小行星至少 4 次在回歸中被觀測到，軌道又可以精確測定時，它就會得到一個永久編號，發現者便擁有該小行星的命名權。提出的名稱必須經過國際天文學聯合會（IAU）的小天體命名委員會（CSBN）審查通過並公告生效。

小行星命名南瀛天文館 中央大學贈台南銘板

2019/12/02 中央通訊社

中央大學鹿林天文台將 2008 年發現的小行星命名為「南瀛天文館」，副校長陳志臣今天致贈小行星銘板給台南市長黃偉哲，以推許台南市天文教育的突出及南瀛天文館的貢獻。

陳志臣今天出席在台南市中西區忠義國中舉辦的「星動時課」天文課程博覽會，當場致贈小行星銘板給黃偉哲，且盛讚台南天文教育的突出。

陳志臣表示，自己是南部人，卻沒去過南瀛天文館，昨天一到台南就去參觀，果真是小而美，辦得很有特色；南瀛天文館雖僅有 12 年歷史，卻有平地最大直徑的天文望遠鏡、天文博物館及 3D 劇院，且結合在地人文，更有豐富的自然生態資源。

陳志臣同時介紹中央大學鹿林天文台說，鹿林天文台是台灣最高的天文台，位於玉山山脈的鹿林山，海拔 2800 多公尺，工作人員與世隔絕，日夜顛倒。

他表示，鹿林天文台迄今發現近 50 顆小行星，已命名 38 顆，「南瀛天文館」就是第 38 顆；鹿林天文台發現小行星的命名，都是對台灣有貢獻或重要地名，讓世界看到台灣，也讓台灣天文教育發光發亮。

「南瀛天文館」小行星於 2008 年 10 月 23 日由蕭翔耀、葉泉志在鹿林天文台發現，當時在金牛座位置，目前已運行到獵戶座。小行星大小約在 1 公里至 2 公里之間，繞行太陽 1 圈 3.59 年（軌道週期），離太陽最近時（近日點）為 2.61 億公里，最遠時（遠日點）為 4.41 億公里，命名也經國際天文學聯合會（IAU）通過。

南瀛天文館位於台南市大內區，前身是台南縣政府創設的「南瀛天文教育園區」，2010 年台南縣市合併時改名為「南瀛天文館」，天文館設施包括天文觀測館、天文展示館、星象館等。

小行星命名南瀛天文館 中央大學贈台南銘板

2019/12/02 芋傳媒

中央大學鹿林天文台將 2008 年發現的小行星命名為「南瀛天文館」，副校長陳志臣今天致贈小行星銘板給台南市長黃偉哲，以推許台南市天文教育的突出及南瀛天文館的貢獻。

陳志臣今天出席在台南市中西區忠義國中舉辦的「星動時課」天文課程博覽

會，當場致贈小行星銘板給黃偉哲，且盛讚台南天文教育的突出。

陳志臣表示，自己是南部人，卻沒去過南瀛天文館，昨天一到台南就去參觀，果真是小而美，辦得很有特色；南瀛天文館雖僅有 12 年歷史，卻有平地最大直徑的天文望遠鏡、天文博物館及 3D 劇院，且結合在地人文，更有豐富的自然生態資源。

陳志臣同時介紹中央大學鹿林天文台說，鹿林天文台是台灣最高的天文台，位於玉山山脈的鹿林山，海拔 2800 多公尺，工作人員與世隔絕，日夜顛倒。

他表示，鹿林天文台迄今發現近 50 顆小行星，已命名 38 顆，「南瀛天文館」就是第 38 顆；鹿林天文台發現小行星的命名，都是對台灣有貢獻或重要地名，讓世界看到台灣，也讓台灣天文教育發光發亮。

「南瀛天文館」小行星於 2008 年 10 月 23 日由蕭翔耀、葉泉志在鹿林天文台發現，當時在金牛座位置，目前已運行到獵戶座。小行星大小約在 1 公里至 2 公里之間，繞行太陽 1 圈 3.59 年（軌道週期），離太陽最近時（近日點）為 2.61 億公里，最遠時（遠日點）為 4.41 億公里，命名也經國際天文學聯合會（IAU）通過。

南瀛天文館位於台南市大內區，前身是台南縣政府創設的「南瀛天文教育園區」，2010 年台南縣市合併時改名為「南瀛天文館」，天文館設施包括天文觀測館、天文展示館、星象館等。

台南市領先全國首創國小天文課程 黃偉哲邀請親子大眾一同玩轉

星動時課

2019/12/02 蕃薯藤 yamNews

台南市政府教育局與南瀛天文館合作推廣天文教育，南瀛天文館歷時 2 年成功開發全國第一套完整的國小天文課程－「星動時課」，1 日上午 9 時在忠義國小舉辦「玩轉天文·星動時課」天文課程博覽會，黃偉哲市長出席代表台南市接受國立中央大學頒贈「南瀛天文館」小行星，此小行星為中央大學鹿林天文台於 2008 年發現，以「南瀛天文館」進行命名，象徵市府教育局及南瀛天文館致力推廣天文教育的成果備受肯定。現場還有教育局鄭新輝局長、國立中央大學陳志臣副校長、國立成功大學科教中心許瑞榮主任、沈震東議員、李啟維議員及各界貴賓共襄盛舉一同參與開幕。

市長黃偉哲表示，台南市對於科學教育積極落實扎根，非常感謝中央大學、成功大學以及各位校長、老師的付出，讓台南的大朋友、小朋友都能夠在浩瀚的天文領域裡找到自己喜歡的方向，勇於付出、投入，未來市府也願意在有限的經費預算下盡可能再增加教育的支出。

秉持著「天文好好玩」的信念，南瀛天文館以國小一至六年級學生為目標，把讓老師苦惱的天文課程教學，透過團康、桌遊、故事或教具操作，轉化為好玩易懂的《星動時課》，歷經 2 年的教案編寫、課程試教修正及教具研發製作，終於在今年 7 月完成全部 36 套課程。教育局長鄭新輝表示，這是全台第一個系統性開發完成的國小天文課程，自 108 學年度起，台南市共有 15 所國民小學正式實施《星動時課》課程。

「玩轉天文·星動時課」天文課程博覽會內容涵蓋 8 大項別開生面的活動，藉由展示解說、擂台競賽、闖關體驗及課程示範教學等豐富有趣的方式，展現台南市天文課程研發成果。活動現場的「南瀛藏星閣」，透過別具巧思的設計，完整展示課程內容與教材教具；「鬥天機-天文達人擂台賽」由國小學生組隊報名參加，藉由擂台方式比鬥天文知識；「大天文小教室」則是國小教師實際帶領學生，依教案進行班級實作教學；其他如「戲說天文」、「星光遊樂園」、「奧林帕斯競技場」、「阿緹米絲的異想世界」及「黑洞之密室脫逃」等，全部都是由「星動時課」教材教具所設計的精彩趣味活動。

活動當天，民眾只要喊出「玩轉天文，天文好好玩」口號，音量超過 80 分貝，就可獲得闖關卡及滿天星 1 份。憑闖關卡體驗活動完成集章，還可進行轉轉樂兌換天文館精緻好禮。此外，現場還有許多免費報名的競賽及手做活動，提供親子大眾豐富的選擇，如「奧林帕斯競技場」天文競賽、「熊尾巴的七顆星」DIY 和「大天文小教室」示範教學等，讓親子大眾開心享受學習天文的樂趣。

星動時課 全台首創國小天文課程

2019/12/02 Yahoo 奇摩新聞

你知道有一顆行星以南瀛天文館命名嗎？中央大學鹿林天文台 2008 年發現編號 281569 號小行星，命名「南瀛天文館」並經國際天文學聯合會（IAU）通過，12 月 1 日將由中央大學致贈小行星銘板給台南市長黃偉哲，肯定南瀛天文館對

天文教育貢獻；同時，南瀛天文館花 2 年打造《星動時課》（見圖，曹婷婷攝），今年 7 月共完成 36 套，是全台首創系統性的國小天文課程。

中央大學天文所所長黃崇源說，「南瀛天文館」小行星 2008 年 10 月 23 日由蕭翔耀與葉泉志於鹿林天文台發現，發現時在金牛座位置，目前已運行到獵戶座，大小約在 1-2 公里間，繞行太陽 1 圈 3.59 年，離太陽最近時（近日點）為 2.6 億公里，最遠時（遠日點）為 4.4 億公里。

黃崇源說，發現新星體如大海撈針，同時要經長時間才能確認，小行星是目前各類天體中，唯一可由發現者命名並得到世界公認的天體，提出名稱需經國際天文學聯合會小天體命名委員會（CSBN）審查通過並公告生效。

中央大學副校長陳志臣表示，中大目前取得近 50 顆命名，表彰對台灣有重要貢獻的人，如陳樹菊女士、鄧雨賢先生等，同時全台灣各縣市名稱也即將命名完成。

南瀛天文館以國小一至六年級學生為目標，把艱深天文課程教學透過團康、桌遊、故事或教具操作，轉化為好玩易懂的《星動時課》，歷經 2 年教案編寫、課程試教及教具研發，終在今年 7 月完成 36 套課程，108 學年度起，台南市共有 15 所國小正式實施《星動時課》。

星動時課博覽會 12 月 1 日登場

2019/12/02 Yahoo 奇摩新聞

「希望孩子能更輕鬆有趣地認識星空，有系統地學習天文！」南瀛天文館開發全臺第一套完整的國小天文課程，將於 12 月 1 日在忠義國小舉辦「玩轉天文·星動時課」天文課程博覽會，以「黑洞密室逃脫」、「阿提米斯的異想世界」等好玩的遊樂園主題概念呈現給學童與民眾，歡迎闔家前往，體驗玩轉天文的樂趣。

秉持著「天文好好玩」的信念，南瀛天文館以國小一至六年級學生為目標，把讓老師苦惱的天文課程教學，透過團康、桌遊、故事或教具操作，轉化為好玩易懂的《星動時課》。

歷經兩年的教案編寫、課程試教修正及教具研發製作，終於在今年 7 月完成全部 36 套課程。教育局長鄭新輝表示，這是全臺第一個系統性開發完成的國小天文課程，自 108 學年度起，南市共有 15 所國民小學正式實施《星動時課》課程。

週末想要 FUN 輕鬆，開心體驗天文主題遊樂園，觀賞鬥天機天文達人競賽，大玩黑洞密室逃脫，進行月球角色裝扮及聆聽專業解說員講述超獵奇天文故事嗎？12 月 1 日當天從上午 9 時到下午 4 時，在忠義國小舉辦「玩轉天文·星動時課」天文課程博覽會，36 套課程結合遊樂園主題活動，提供民眾免費體驗，只要喊出「玩轉天文，天文好好玩」口號，音量超過 80 分貝，就可獲得闖關卡以及滿天星 1 份。憑闖關卡體驗活動完成集章，還可進行轉轉樂兌換天文館精緻好禮。

此外，現場還有許多免費報名的競賽及手做活動，提供親子大眾豐富的選擇。如「奧林帕斯競技場」天文競賽、「熊尾巴的七顆星」DIY 和「大天文小教室」示範教學等，歡迎民眾提早到場登記領取號碼牌，以免向隅。

活動當日上午 10 時，黃偉哲市長將代表臺南市接受國立中央大學頒贈「南瀛天文館」小行星，此小行星為中央大學鹿林天文台於 2008 年發現，並以南瀛天文館進行命名，象徵南瀛天文館致力於推廣天文教育，成果備受肯定，歡迎民眾前往觀禮，一同為臺南市喝采。更多活動詳情請上南瀛天文館官網 <https://taea.tn.edu.tw/>，或撥 06-5761076 致電洽詢。

中央大學發現新小行星 IAU 通過命名「南瀛天文館」

2019/11/29 自由時報

v 中央大學鹿林天文台將 2008 年發現的編號 281569 號小行星，命名為「南瀛天文館」，並經國際天文學聯合會（IAU）通過。12 月 1 日上午將在台南市忠義國小舉辦頒贈儀式，由中央大學副校長陳志臣致贈小行星銘板給台南市長黃偉哲。

中央大學天文所所長黃崇源說，「南瀛天文館」小行星於 2008 年 10 月 23 日由蕭翔耀與葉泉志在鹿林天文台所發現，當時在金牛座位置，目前已運行到獵戶

座。大小約在 1-2 公里之間，繞行太陽一圈 3.59 年（軌道週期），離太陽最近時（近日點）為 2.6 億公里，最遠時（遠日點）為 4.4 億公里。

黃崇源說，小行星是目前各類天體中唯一可以由發現者進行命名並得到世界公認的天體。以南瀛天文館命名，肯定南瀛天文館在天文教育的貢獻。

陳志臣表示，中央大學目前已取得近 50 顆命名，表彰許多對台灣有重要貢獻的人，如陳樹菊、鄧雨賢等。

12 月 1 日當天，台南市教育局也規劃「玩轉天文」星動時課天文課程博覽會，一系列活動供民眾體驗。

南瀛天文館花費 2 年，以國小一至六年級學生為目標，把天文課程教學透過團康、桌遊、故事或教具操作，轉化為好玩易懂的《星動時課》，今年 7 月完成全部 36 套課程，為全台第一個系統性開發完成的國小天文課程，同時自 108 學年度起，全市共有 15 間國民小學正式實施《星動時課》。

小行星命名南瀛天文館 中央大學 12/1 頒贈銘板

2019/11/29 中央通訊社

台南市南瀛天文館推廣天文教育，中央大學鹿林天文台更將 2008 發現的小行星命名為「南瀛天文館」，中央大學副校長陳志臣 12 月 1 日將致贈小行星銘板給台南市。

台南市南瀛天文館人員今天告訴中央社記者，小行星銘板頒贈儀式 12 月 1 日上午 10 時將在台南市中西區忠義國小舉行。這個小行星是中央大學鹿林天文台 2008 年發現的，命名為「南瀛天文館」，並經國際天文學聯合會（IAU）通過。

「南瀛天文館」小行星於 2008 年 10 月 23 日由蕭翔耀、葉泉志在鹿林天文台發現，當時在金牛座位置，目前已運行到獵戶座。小行星大小約在 1 公里至 2 公

里之間，繞行太陽 1 圈 3.59 年（軌道週期），離太陽最近時（近日點）為 2.61 億公里，最遠時（遠日點）為 4.41 億公里。

中央大學表示，南瀛天文館是台南市的公立天文博物館，從創立以來，除致力台灣基礎天文教育的扎根，更串連鄰近的人文景觀、豐富的自然生態資源，創造一個結合天文、科學、人文與生態之多面向教育價值的「南瀛星故鄉」。

中央大學表示，中大長年來致力於天文研究，也曾將發現的行星以名人為命名，這次為了表達南瀛天文館對天文教育的奉獻與付出，將在台南市舉辦頒贈儀式。

台南市教育局人員表示，南瀛天文館 2017 年著手開發適合國小 1 年級至 6 年級學生的天文課程，今年 7 月完成 36 套「星動時課」課程，這是全台第一個系統性開發完成的國小天文課程，台南市有 15 所國小已於 108 學年度開始授課。

南瀛天文館位於台南市大內區，前身是台南縣政府創設的「南瀛天文教育園區」，2010 年台南縣市合併時改名為「南瀛天文館」，天文館設施包括天文觀測館、天文展示館、星象館等。

12 月 1 日當天除小行星銘板頒贈外，台南市政府教育局也將舉辦「玩轉天文」的天文課程博覽會，將南瀛天文館開發的 36 套「星動時課」課程結合遊樂園主題，讓民眾免費體驗。

小行星命名南瀛天文館 中央大學 12 月 1 日頒贈銘板

2019/11/29 udn 聯合新聞網

台南市南瀛天文館推廣天文教育，中央大學鹿林天文台更將 2008 發現的小行星命名為「南瀛天文館」，中央大學副校長陳志臣 12 月 1 日將致贈小行星銘板給台南市。

台南市南瀛天文館人員今天告訴中央社記者，小行星銘板頒贈儀式 12 月 1 日上午 10 時將在台南市中西區忠義國小舉行。這個小行星是中央大學鹿林天文台 2008 年發現的，命名為「南瀛天文館」，並經國際天文學聯合會（IAU）通過。

「南瀛天文館」小行星於 2008 年 10 月 23 日由蕭翔耀、葉泉志在鹿林天文台發現，當時在金牛座位置，目前已運行到獵戶座。小行星大小約在 1 公里至 2 公里之間，繞行太陽 1 圈 3.59 年（軌道週期），離太陽最近時（近日點）為 2.61 億公里，最遠時（遠日點）為 4.41 億公里。

中央大學表示，南瀛天文館是台南市的公立天文博物館，從創立以來，除致力台灣基礎天文教育的扎根，更串連鄰近的人文景觀、豐富的自然生態資源，創造一個結合天文、科學、人文與生態之多面向教育價值的「南瀛星故鄉」。

中央大學表示，中大長年來致力於天文研究，也曾將發現的行星以名人為命名，這次為了表達南瀛天文館對天文教育的奉獻與付出，將在台南市舉辦頒贈儀式。

台南市教育局人員表示，南瀛天文館 2017 年著手開發適合國小 1 年級至 6 年級學生的天文課程，今年 7 月完成 36 套「星動時課」課程，這是全台第一個系統性開發完成的國小天文課程，台南市有 15 所國小已於 108 學年度開始授課。

南瀛天文館位於台南市大內區，前身是台南縣政府創設的「南瀛天文教育園區」，2010 年台南縣市合併時改名為「南瀛天文館」，天文館設施包括天文觀測館、天文展示館、星象館等。

12 月 1 日當天除小行星銘板頒贈外，台南市政府教育局也將舉辦「玩轉天文」的天文課程博覽會，將南瀛天文館開發的 36 套「星動時課」課程結合遊樂園主題，讓民眾免費體驗。

天文主題遊樂園免費體驗《星動時課》博覽會周日登場

2019/11/27 中時電子報

周末想要 FUN 輕鬆，開心體驗天文主題遊樂園，玩黑洞密室逃脫，觀賞鬥天機天文達人競賽，進行月球角色裝扮及聆聽專業解說員講述超獵奇天文故事嗎？「玩轉天文」《星動時課》天文課程博覽會將於 12 月 1 日在台南忠義國小登場，規畫了許多豐富有趣的活動供民眾免費體驗，還有精緻好禮可兌換。

秉持著「天文好好玩」的信念，台南市政府教育局轄下南瀛天文館以國小一至六年級學生為目標，把讓老師苦惱的天文課程教學，透過團康、桌遊、故事或

教具操作，轉化為好玩易懂的《星動時課》。

歷經兩年的教案編寫、課程試教修正及教具研發製作，終於在今年 7 月完成全部 36 套課程，這是全台第一個系統性開發完成的國小天文課程，同時自本學年度起，台南市共有 15 間國民小學正式實施《星動時課》。

教育局為了讓孩童更輕鬆有趣地認識星空，學習天文，12 月 1 日上午 9 點到下午 4 點在忠義國小舉辦星動時課天文課程博覽會，36 套課程結合遊樂園主題，以「黑洞密室逃脫」、「阿提米斯的異想世界」等好玩的「遊樂園」主題概念呈現給學童與民眾。

現場還有許多免費報名的競賽及手作活動，提供親子大眾豐富的選擇。如「奧林帕斯競技場」天文競賽、「熊尾巴的七顆星」手作 DIY 和「大天文小教室」示範教學等，歡迎當日提早到場登記領取號碼牌，以免向隅。

活動當天只要喊出「玩轉天文，天文好好玩」口號，音量超過 80 分貝，就可獲得闖關卡以及滿天星 1 份。憑闖關卡體驗活動完成集章，還可進行轉轉樂兌換天文館精緻好禮。

活動當日上午 10 點市長黃偉哲將代表台南市接受國立中央大學頒贈「南瀛天文館」小行星，此小行星為中央大學鹿林天文台於 2008 年發現，並以南瀛天文館進行命名，象徵南瀛天文館致力於推廣天文教育，成果備受肯定。

原文轉載自【2019-11-27/中時電子報】

打造假日天文遊樂園！星動時課博覽會 12 月 1 日歡樂登場

2019/11/25 Hinet

「希望孩子能更輕鬆有趣地認識星空，學習天文！」臺南市政府教育局將於 12 月 1 日在忠義國小舉辦「玩轉天文」星動時課天文課程博覽會，以「黑洞密室逃脫」、「阿提米斯的異想世界」等好玩的「遊樂園」主題概念呈現給學童與民眾，歡迎闔家前往，體驗「玩轉天文」的樂趣。

秉持著「天文好好玩」的信念，臺南市政府教育局轄下南瀛天文館以國小一至六年級學生為目標，把讓老師苦惱的天文課程教學，透過團康、桌遊、故事或教具操作，轉化為好玩易懂的《星動時課》。歷經兩年的教案編寫、課程試教修正及教具研發製作，終於在今年 7 月完成全部 36 套課程。這是全臺第一個系統性開發完成的國小天文課程，同時自 108 學年度起，臺南市共有 15 間國民小學

正式實施《星動時課》。

週末想要 FUN 輕鬆，開心體驗天文主題遊樂園，觀賞鬥天機天文達人競賽，大玩黑洞密室逃脫，進行月球角色裝扮及聆聽專業解說員講述超獵奇天文故事嗎？12 月 1 日當天從上午 9 點到下午 4 點，在忠義國小將舉辦「玩轉天文」星動時課天文課程博覽會，36 套課程結合遊樂園主題，規劃了許多豐富有趣的活動，提供到場民眾免費體驗，只要喊出「玩轉天文，天文好好玩」口號，音量超過 80 分貝，就可獲得闖關卡以及滿天星 1 份。憑闖關卡體驗活動完成集章，還可進行轉轉樂兌換天文館精緻好禮。

此外，現場還有許多免費報名的競賽及手作活動，提供親子大眾豐富的選擇。如「奧林帕斯競技場」天文競賽、「熊尾巴的七顆星」手作 DIY 和「大天文小教室」示範教學等，歡迎當日提早到場登記領取號碼牌，以免向隅。

活動當日上午 10 點黃偉哲市長將代表臺南市接受國立中央大學頒贈「南瀛天文館」小行星，此小行星為中央大學鹿林天文台於 2008 年發現，並以南瀛天文館進行命名，象徵南瀛天文館致力於推廣天文教育，成果備受肯定，歡迎民眾前往觀禮，一同為臺南市喝采。

更多活動詳情請上南瀛天文館官網 <https://taea.tn.edu.tw/>，或撥 06-5761076 致電洽詢。

全球首例！台高中生發現「海王星外」新天體 IAU 正式命名「燭龍」

2019/11/08 大紀元

國立中興大學附屬高中 5 名學生，2014 年參與國立中央大學主持的國際「泛星計畫」搜尋未知天體，新發現一顆遠在海王星軌道外的小行星，國際天文學聯盟（IAU）近日正式認可學生的提議，將該天體命名為「燭龍」。不僅創下台灣高中生紀錄，也是全球首次由高中生發現的海王星之外太陽系天體。

國際「泛星計畫」是利用泛星望遠鏡取得的第一手影像，透過分析影像尋找未知天體。5 年前，興大附中指導老師林士超帶領 5 名學生薛竹珺、紀政杰、林筠皓、謝昕蕙、何艾玲，分析泛星計畫的影像，發現了一顆比海王星更遙遠的小行星，為全球首例由高中生發現的「海王星之外太陽系天體」。

當年參與「泛星計畫」的興大附中團隊學生，現在都快大學畢業，目前就讀於台灣大學地質系 4 年級的何艾玲就是其中之一。她表示，永遠也忘不了當年在螢幕上尋找星點的辛苦，以及與同學討論的樂趣，很高興能為這個「世界第一的發現」做出貢獻。

中央大學說，這顆小行星大小約兩百公里，距離太陽平均距離為 56 個天文單位，意即地球與太陽距離的 56 倍，比海王星甚至冥王星更遠。這種新型態的小行星，不同於一般位於火星與木星之間的小行星，IAU 經過冗長討論才決定命名規則。

據悉，興大附中 2017 年曾在校內舉辦過一次命名票選，全校師生當時原本希望將小行星命名為「媽祖」，但未被 IAU 認可。經過多年驗證軌道與命名討論，位於巴黎 IAU 於 2018 年給予小行星永久編號，並於近日正式接受興大附中學生投票命名該天體為「燭龍」(2014 GE45 = 472235 Zhulong “Torch Dragon”)。

「燭龍」為《山海經·大荒北經》記載的紅色妖神，書中描述其人面蛇身，張閉眼控制了日夜，吸吐氣則控制了冬夏，發出火焰照亮了九幽重暗。

中央大學天文所教授陳文屏表示，「燭龍」的發現相當幸運，但好運掉下來時，準備好的人才能伸手接住。今年 10 月到 11 月，台灣也有三十多所學校、超過百名學生參與小行星搜尋活動，期待有更多發現。

天文迷跨國際小行星搜尋賽 國立中興高中發現 4 顆大放光芒

2019/11/07 Yahoo 奇摩新聞

由國際天文搜尋組織(International Astronomical Search Collaboration (IASC))舉辦的國際性聯合搜尋賽事，自 10 月 21 日起展開五週的競賽，南投縣國立中興高中數理資優班二年級同學組隊參加，目前為止全台 29 所國高中學校共發現 10 顆從未被觀測過的小行星，其中中興高中即發現 4 顆，於競賽中大放光芒。

這項國際尋星的競賽，讓參與的同學發揮高度天文知識，每年均有來自 10 多個不同國家的高中生組隊參加，台灣地區的賽事承辦人為國立中央大學天文研究所陳文屏教授。今年度的賽事(IASC2019)於 10 月 21 日起至 11 月 18 日止，為期將近五週，截至 11 月 2 日止目前公布結果全台找到 10 顆主要小行星帶上從未被觀測過的小行星，其中國立中興高中發現 4 顆、北一女中發現 3 顆，另臺中一中、彰化高中與羅東高中各貢獻 1 顆。

中興高中今年度尋星隊員為高二數理資優班 6 位同學，分別是張簡苑昌、陳宥翔、林佑安、張晏蓁、李佩儒與林懷昇。

指導老師李欣珮組長指出，此競賽於台灣已進行 10 年，修正去年經驗，今年讓高二同班同學參加以強化效率。同學被付予不同任務，經過此次歷練，並以英文與國外教授對談，獲得跨出台灣的機會，實際有成果與貢獻並獲國際認證，讓同學更有動力向前。

與賽同學在每筆天文圖資公布後都於 12 小時內各分組分析完資料後比對並統整出最佳化數據，回傳夏威夷大學天文台之承辦教授 Dr. Cassidy Davis，學生不但能學習如何分析處理天文資料，也藉此與夏威夷大學教授用英文溝通發現成果，極具挑戰和成就。

同學接獲四張不同圖片後，透過疊圖藉資料的差異找出不曾被觀測過的小行星，同學說點選小行星對比資料庫，如果是資料庫中沒有的檔，即回報到主辦單位，再行對比是否為不曾被找到的小行星，由主辦單位確認，並經過也許數年的觀測確定為新發現者始予命名。

這些同學已經能擔任指導小老師，陳宥翔表示從國中沒有任何經驗，到後來能從容表達，也指導國中同學製作濾鏡觀測太陽等。張簡苑昌也表示，去年參加時偶遇瓶頸，今年略為修正縮短時間，更見效率，未來希望朝此方向持續研究努力，加深對地科的熱愛。

校長陳江海表示，目前成果顯示學校資優教育成果，可以讓知識應用在實際操作上，也應證學校獲資優評鑑一等的佳績。參與競賽讓同學了解團隊合作的重要與創意的啟發，未來學校仍會持續拓展資源，讓同學有更多參與國際活動的機會。

此次競賽時程頗長，考驗著學生的耐心與毅力，全台灣共 29 所國高中參與競賽，中興高中、北一女、中大壠中、羅東高中、臺中一中、興大附中、彰化高中、嘉義高中、台南二中等校。

原文轉載自【2019-11-07/Yahoo 奇摩新聞】

破世界紀錄！興大附中學生發現「海王星外」新天體 正式命名

「燭龍」

國立中興大學附屬高中 5 名學生，5 年前參與國立中央大學主持的國際「泛星計畫」搜尋未知天體，果然新發現一顆遠在海王星軌道外的小行星，不僅創下台灣高中生紀錄，也是全球首例。國際天文學聯盟（IAU）近日正式認可學生的提議，將該天體命名為「燭龍」。

國際「泛星計畫」是利用泛星望遠鏡取得的第一手影像，透過分析影像尋找未知天體。2014 年，興大附中指導老師林士超帶領 5 名學生薛竹珺、紀政杰、林筠皓、謝昕蕓、何艾玲，分析泛星計畫的影像，發現了一顆比海王星更遙遠的小行星，為全球首次由高中生發現的海王星之外太陽系天體。

中央大學說，這顆小行星大小約 200 公里，距離太陽平均距離為 56 個天文單位，意即地球與太陽距離的 56 倍，比海王星甚至冥王星更遠。這種新型態的小行星，不同於一般位於火星與木星之間的小行星，IAU 經過冗長討論才決定命名規則，當年參與的高中生，如今也快從大學畢業。

據悉，興大附中 2017 年曾在校內舉辦過一次命名票選，全校師生當時原本希望將小行星命名為「媽祖」，但未被 IAU 認可。經過多年驗證軌道與命名討論，位於巴黎 IAU 於 2018 年給予小行星永久編號，並於近日正式接受興大附中學生投票命名該天體為「燭龍」（2014 GE45 = 472235 Zhulong “Torch Dragon”）。

「燭龍」為《山海經•大荒北經》記載的紅色妖神，書中描述其人面蛇身，張閉眼控制了日夜，吸吐氣則控制了冬夏，發出火焰照亮了九幽重暗。

當年參與發現小行星的學生何艾玲，目前就讀台灣大學地質系四年級。她表示，永遠也忘不了當年在螢幕上尋找星點的辛苦，以及與同學討論的樂趣，很高興能為這個世界第一的發現作出貢獻。

興大附中指導老師林士超說明，海王星軌道之外的這些小天體，也被稱為「古柏帶天體」，有助於研究太陽系的形成與演化。林士超回憶，當初剛發現這顆小行星時，因為位置變化慢，團隊一度以為該天體往直直往地球而來，誤認是近地小行星，經過後續觀測，才證實是位在海王星軌道之外的遙遠天體。

世界第一台灣高中生發現小行星命名「燭龍」

中央大學參加國際「泛星計畫」，利用泛星望遠鏡尋找未知天體，2014年中興大學附屬高中學生分析泛星計畫的影像，發現了一顆比海王星還遙遠的小行星，國際天文學聯盟 (IAU) 於近日正式接受興大附中學生投票命名該天體為「燭龍」。

中興大學附屬高中學生發現的這顆小行星，大小約 200 公里，距離太陽平均是地球與太陽距離的 56 倍（56 個天文單位），比海王星甚至冥王星更遠。這是全球首次由高中生發現海王星之外的太陽系天體。

這種新型態的小行星，不同於一般位於火星與木星之間的小行星，國際天文學聯合會經過冗長討論才決定命名規則，當年參與的高中生，現在已經快要大學畢業。

小行星發現之後，經過多年驗證軌道與命名討論，位於巴黎的國際天文學聯盟終於在 2018 年給予永久編號，並於近日正式接受興大附中學生投票命名該天體為「燭龍」。燭龍是山海經當中的紅色妖神，人面蛇身，張閉眼控制了日夜，吸吐氣則控制了冬夏，發出火焰照亮了九幽重暗。

當年參與的學生何艾玲，現就讀台大地質系四年級，仍忘不了當年在螢幕上尋找移動星點的辛苦，以及與同學討論的樂趣，很高興貢獻了這個世界第一的發現指，也希望之後能夠繼續類似的學術研究，再續小行星緣。

指導老師中興大學附屬高中林士超老師說明，研究位於海王星軌道之外的這些小天體，也稱為古柏帶天體，有助於研究太陽系的形成與演化。林士超老師清楚記得這顆小行星剛被發現時因為位置變化很慢，有可能是因為往地球直直而來，而被誤認為近地小行星，但經過後續觀測，才證實是位在海王星軌道之外的遙遠太陽天體。

中央大學天文所教授陳文屏是泛星計畫台灣的共同主持人，他表示，這次的發現很幸運，小行星分類印證了小心求證的科學過程，而一旦好運掉下來，準備好的人才能伸手接住。這次的命名過程蜿蜒曲折，很高興神話燭龍躍向太空變身為燭龍小行星。

全球首例！台灣高中生發現小行星命名「燭龍」

2019/11/06 自由時報

國立興大附中高中生，5年前參加中央大學主導的「泛星計畫」，在分析泛星計畫的影像後，發現了一顆寬度約 200 公里，比海王星還遙遠的小行星，這是全球首次由高中生發現海王星之外的太陽系天體，經多年驗證軌道與命名討論，位於巴黎的國際天文學聯盟（IAU）終於在 2018 年給予永久編號，取得命名權的興大附中學生，近日並正式命名該天體為「燭龍」。

國立興大附中天文社學生在指導老師林士超帶領下，2014 年參加中央大學天文所陳文屏教授擔任共同主持人的「泛星計畫」，利用泛星望遠鏡取得的第一手影像尋找未知天體，5 名學生經不斷觀察、比對，發現一顆距離是地球與太陽距離的 56 倍，比海王星甚至冥王星更遠的小行星，此發現是全球高中生首例。

這顆小行星發現後，經過多年驗證軌道與命名討論，位於巴黎的國際天文學聯盟終於在去年給予永久編號。因這種新型態的小行星，不同於一般位於火星與木星間的小行星，國際天文學聯合會經過冗長討論才決定命名規則，當年發現的學生都已經快大學畢業。

因 5 名興大附中發現學生取得命名權，5 人原本想命名為「媽祖」，但國際天文學聯盟告知此是小行星，不可用大神命名，討論後覺得中國古籍《山海經》中描述的紅色妖神「燭龍」，外型人面蛇身，張閉眼控制了日夜，吸吐氣則控制了冬夏，發出火焰還能照亮九幽重暗，與此小行星相當類似，決定命名為「燭龍」，近日並正式獲得認可。

當年發現學生之一的何艾玲，現已就讀台大地質系 4 年級，對當年在螢幕尋找移動星點的辛苦仍印象深刻，很高興能成為全球首次發現的一份子，希望以後能有機會繼續從事類似的學術研究。

林士超老師說，這顆小行星剛被發現時因位置變化很慢，有可能因往地球直直而來，而被誤認為近地小行星，但經持續觀測，才證實是位在海王星軌道之外的遙遠太陽天體，此研究有助於探索太陽系的形成與演化。

興大附中團隊發現小行星 取山海經典故命名燭龍

2019/11/06 Yahoo 奇摩新聞

中興大學附屬高中師生組成的團隊，於民國 103 年分析「泛星計畫」影像，發現一顆海王星外太陽系天體，這顆小行星近日透過學生投票，取「山海經」典故命名為「燭龍」。

在中央大學主導下，廣招台灣學生參與「泛星計畫」，利用泛星望遠鏡取得的第一手影像尋找未知天體。興大附中團隊於 103 年發現了一顆比海王星還遙遠的小行星，大小約 200 公里，距離太陽平均距離是 56 個天文單位（地球與太陽距離的 56 倍），甚至比冥王星更遠。

中央大學今天發布新聞稿指出，這是全球首次由高中生發現海王星之外的太陽系天體。不同於一般位於火星與木星之間的小行星，國際天文學聯合會（IAU）經過冗長討論才決定命名規則，於 107 年給予永久編號，並於近日透過興大附中團隊投票，正式命名為「燭龍」（2014 GE45 = 472235 Zhulong “Torch Dragon”）。

中央大學指出，「燭龍」是「山海經」中的紅色妖神，人面蛇身。傳說中祂張眼、閉眼間就控制了日夜，吸氣、吐氣之際便控制了冬夏，並會發出火焰照亮黑暗。

當年參與「泛星計畫」的興大附中團隊學生，現在都快大學畢業，目前就讀於台灣大學地質系 4 年級的何艾玲就是其中之一。她忘不了當年在螢幕上尋找移動星點的辛苦，以及與同學討論的樂趣，很高興貢獻了「發現指」，希望之後還能繼續類似的學術研究，再續小行星緣。

興大附中指導教師林士超回憶，「燭龍」剛被發現時，位置變化很慢，有可能是往地球直直而來，而被誤認為近地小行星。但經過後續觀測，才證實是位在海王星軌道之外的遙遠太陽天體。

中央大學天文所教授陳文屏表示，「燭龍」的發現相當幸運，但好運掉下來時，準備好的人才能伸手接住。今年 10 月到 11 月，台灣也有 30 多所學校、超過百名學生參與小行星搜尋活動，期待有更多發現。

夏天就要賞銀河看星星！全台 8 大觀星勝地推薦

2019/08/12 新頭殼 newtalk

台灣夏天是適合觀星的季節，6~9 月也是觀察、拍攝銀河的好時機，基本上，只要沒有光害的地方，抬頭隨便都可以見到星空，而在高山上只要天氣不糟就可以望見滿天星斗。《新頭殼》挑選全台較容易抵達、有特色的觀星景點，一一為大家介紹。

北部

台北市擎天崗

對住在大台北地區的人來說，擎天崗可說是距離最近的觀星地點，從市區開車、騎車上山大約一小時就可抵達，下山後要去北投泡溫泉，或是去士林夜市逛逛都很順路，可以輕鬆安排豐富的行程。

擎天崗可以眺望台北盆地夜景，但因為距離地面有一些高度，雖然難免還是會受到光害影響，但以需花費的時間和心力來說，依舊是 **cp** 值很高的觀星點。因為視野遼闊、空地廣大，加上有規劃完善的公共設施，交通容易，每逢流星雨總有許多人湧入，將夜晚的山頭點綴得熱鬧。

基隆大武崙砲台

大武崙砲台離基隆市區約半小時車程，因為位於高地、夜間光害少，加上離市區很近，大武崙砲台停車場就成為很受歡迎、老少咸宜的觀星景點，不必上高山就能輕鬆抵達。北觀處在 2017 幸福北海岸系列活動中，首度於基隆大武崙舉辦觀星活動，今年依然持續舉辦，相當受歡迎，很適合想觀星的入門者參加。

大武崙砲台附近有情人湖、八斗子、外木山、大武崙漁港，不妨在白天安排行程，遊覽基隆白天景色，晚上再以觀星結束充實的一天。

中部

玉山國家公園塔塔加

塔塔加位於玉山國家公園，遠離都市喧囂，加上空氣純淨不受光害侵擾，容易辨識星體、星座，每到夜晚就是群星上演華麗表演的時刻。塔塔加的停車場、遊客服務中心都是熱門的觀星點，更有許多人喜愛以「夫妻樹」為前景，長時間曝光拍出星軌拖曳的奇幻效果。因為塔塔加的優良觀測環境，中央大學天文所還在鹿林前山設置了鹿林天文台，更吸引許多天文團體來此舉辦觀星活動。

大雪山森林遊樂區

大雪山不僅是景色秀麗、生態豐富的森林遊樂區，到夜幕低垂，更是變身為星空劇場，可在無光害的環境下盡情欣賞遼闊星空之美。大雪山林道 43K 遊客服務中心區及 48-50K 小雪山區域，沿線有不少的觀星地點，可謂一條名符其實的

星光大道！東勢林區管理處不定期會舉辦星空講座，邀請專家為遊客解說星空特色和背後的故事，規劃兩天一夜的旅行，住宿山上，白天欣賞風景、追尋帝雉、藍腹鵲的蹤跡，晚上觀賞璀璨星空，抽空遠離繁忙都市生活。

東部

台東大坡池

大坡池是全台唯一斷層形成的淡水濕地，提供多種動植物良好生長環境，也是留鳥與候鳥的天堂，是相當重要的國家級重要濕地。而遠離市區的位置和特殊濕地景觀，讓大坡池變成有別於高山的特色觀星景點。樹木、山景環繞濕地，夜裡星星、月亮倒映在池中的反射令人屏息，同時也是自行車道的來往樞紐，是池上自行車小旅行的必經之地。

台東三仙台

憑著曾入選「台東 14 個最美星空」和知名旅遊平台選出的「台灣 5 大觀星聖地」，就可以瞭解三仙台是多麼強大的觀星景點。三仙台位於台東成功鎮東北方，原先是一處岬角，因為海水侵蝕將岬角與岸邊連結處切斷，形成現今離岸的小島，後來興建的拱型跨海步行橋將它與本島連接，遂成為成功鎮最具代表性的景觀。三仙台是欣賞日出、觀星的好地方，躺在岸邊聽著浪濤聲，看著星星移動，更有許多攝影人喜愛用拱橋作為地景，拍出一張張精彩的夜空照片。

南部

恆春貓鼻頭

貓鼻頭位於台灣南端的西側岬角，由於沿岸有一塊自海崖崩落的礁石，因形似一隻面海伏伏的貓，因此命名為貓鼻頭。貓鼻頭觀景台可以眺望恆春許多知名景點，如難灣、墾丁國家森林遊樂區、船帆石、香蕉灣海岸林、鵝鑾鼻等地方，因為遠離光害，到了晚上也成為恆春半島熱門的觀星景區。邊聽著海浪聲，帶一塊墊布鋪在身下，看著遠方閃爍的星光，是夏天夜晚的獨家體驗。

阿里山森林遊樂區小笠原觀景台

去阿里山不僅可以看日出，觀星也是近年來非常熱門的活動。因為海拔高、位於光害稀少的山區，加上漫步於森林間的愜意，搭乘世界級的森林鐵道小火車上山，比起單純的森林遊樂區，更兼具豐富的人文氣息，讓行程有更多變化。

小笠原觀景台坐擁 360 度無遮蔽景觀，對觀星來說是非常適合的地點。阿里山森林遊樂區每年會推出觀星活動，可搭乘電動遊園車，在專業導覽員的講說下對星空和阿里山森林鐵道歷史有更詳盡的認識。

中央大學鹿林天文台發現小行星 浩瀚宇宙現雪霸

2019/07/01 中時電子報

今年為雪霸國家公園管理處第 27 週年處慶，中央大學特將鹿林天文台所發現的第 278956 號小行星命名為「雪霸 (Shei-Pa)」，希望傳達國家公園對自然資源保育的精神，將臺灣的青山、綠水、藍天和美麗星空，世世代代的流傳下去。

雪霸國家公園位於台灣本島之中北部，以雪山和大霸尖山的「雪」、「霸」兩字命名，總面積 7 萬 6850 公頃，境內高山林立，景觀壯麗，為台灣第五座國家公園。區內 3000 公尺以上高山就有 51 座，其中還有 19 座更名列台灣百岳，並有臺灣獨一無二國寶魚「櫻花鉤吻鮭」及「觀霧山椒魚」等保育物種，是一座自然資源極為豐富的國家公園。

中央大學表示，「雪霸」小行星為 2008 年 10 月 22 日由國立中央大學鹿林天文台蕭翔耀觀測員及加州理工學院葉泉志博士所發現，大小約 3.7 公里。雪霸小行星繞行太陽一圈 5.71 年（軌道週期），離太陽最近時（近日點）為 4.26 億公里，最遠時（遠日點）為 5.33 億公里。「雪霸」小行星 2008 年 10 月 22 日發現時在鯨魚座，11 年後的今天繞太陽兩圈後又回到同一星座。

適逢管理處 27 週年處慶，於 6 月 29 日舉辦了一系列慶祝活動，除了針對數 10 年來雪霸國家公園對於「櫻花鉤吻鮭」保育歷程和生態研究的座談外，中央大學也將於同日頒贈小行星銘版，並邀請發現者蒞臨分享小行星的發現及鹿林天文台的介紹，活動內容十分精彩，一同慶賀雪霸國家公園 27 歲生日快樂。

中央大學指出，小行星的命名提出後需經過國際天文學聯合會（IAU）的小天體命名委員會（CSBN）審查通過並公告生效，因此從發現到命名確認往往需時數年，其過程並不容易，而持續自然保育及環境教育推動多年的雪霸國家公園的精神同樣值得敬佩。

中央大學提到，雪霸國家公園如同一座大型的自然博物館，境內無光害、少污染的特點讓其成為最天然的觀星教室，將 278956 號小行星以此命名，從今以後雪霸小行星將在浩瀚的星空中閃爍，照耀著雪霸國家公園。

雪霸處 27 週年 發表雪霸小行星命名

2019/07/01 自由時報

雪霸國家公園管理處今天辦 27 週年系列活動，會中雪霸處也發表當時鹿林天文台所發現的第 278956 號小行星命名為「雪霸 (Shei-Pa)」，雪霸處指出，期盼藉此傳達國家公園對自然資源保育的精神。

中央大學表示，「雪霸」小行星為 2008 年 10 月 22 日由國立中央大學鹿林天文台蕭翔耀及加州理工學院葉泉志博士所發現，於去年正式通過命名。「雪霸」小行星 2008 年 10 月 22 日發現時在鯨魚座，而 11 年後的今天繞太陽兩圈後又回到同一星座。

其中雪霸小行星繞行太陽一圈 5.71 年（軌道週期），離太陽最近時（近日點）為 4.26 億公里，最遠時（遠日點）為 5.33 億公里。

由於小行星的命名提出後需經過國際天文學聯合會的小天體命名委員會審查通過並公告生效，從發現到命名確認往往需時數年，過程不易。

今天舉辦的「雪霸小行星命名發表會」也邀請鹿林天文台所長林宏欽、發現者蕭翔耀分享介紹。

雪霸處期望雪霸國家公園如境內少光害、少污染，而雪霸小行星今後將於浩瀚的星空中照耀雪霸國家公園。

影／無盡蒼穹 從今多了顆「雪霸小行星」

2019/07/01 udn 聯合新聞網

雪霸國家公園管理處今天歡慶成立 27 周年，同時收到中央大學送來一份最珍貴的生日禮物「雪霸小行星」，央大鹿林天文台 2008 年 10 月發現、編號 278956 號的小行星，去年通過國際審查及命名，今天在雪霸管理處發表「雪霸」的名稱，從此浩瀚無盡的蒼穹裡，多了顆特別以國家公園為名的小行星。

國立中央大學指出，「雪霸」小行星 2008 年 10 月 22 日由央大鹿林天文台觀測員蕭翔耀及加州理工學院葉泉志博士發現，這顆小行星約 3.7 公里大，繞行太陽一圈需 5.71 年（軌道周期），離太陽最近（近日點）為 4.26 億公里，最遠時（遠日點）5.33 億公里。

央大表示，「雪霸」小行星 2008 年發現時位在鯨魚座，繞太陽 2 圈後今天又回到同一星座；小行星命名提出後需經國際天文學聯合會（IAU）的小天體命名委員會（CSBN）審查通過並公告生效，因此從發現到命名確認往往需時數年，過程並不容易。

中央大學校長周景揚率主秘周立德、天文研究所長黃崇源及雪霸小行星發現者蕭翔耀等人，今天下午在雪霸管理處頒贈小行星銘板給雪霸處長楊模麟，作為雪霸國家公園管理處慶生禮物，會場請來新民高中音樂班 5 名學生演奏，雪霸管理處企畫課長楊國華並以竹笛吹奏韓劇「來自星星的你」主題曲。

央大表示，中央大學迄今已發現約 800 顆小行星，因命名限額，目前已為 50 顆命名，包括台灣一些縣市，未來央大盼為全省各縣市都命名；小行星是各類天體中，唯一可由發現者提出命名審查的天體，目前命名的小行星名稱有地名、知名人物、古人、團體、學校、原住民族等。

2012 年央大也曾將編號 246643 的編號的小行星命名為「苗栗」，因央大在台復校時最早就在苗栗市，當初舊校地現已成為國立聯合大學；過去有小行星以「玉山」為名，但因玉山兼具山脈、國家公園之名，這次雪霸獲小行星命名，也可視為國內第一顆特別以國家公園命名的小行星。

雪霸處表示，雪霸國家公園如同一座大型的自然博物館，境內無光害、少污染的特點，也成為最天然的觀星教室，278956 號小行星以雪霸命名，此後雪霸小行星在浩瀚的星空中閃爍，也照耀著雪霸國家公園。

2019 年春季「年輕天文學者獎」 郭兆林博士榮獲

2019/06/11 新浪新聞

由國立中央大學與台達電子文教基金會共同頒發的「年輕天文學者講座」，2019 年春季獲獎者為美國史丹佛大學的郭兆林博士，對宇宙論有深入的研究的

他，將來台展開三場演講，6月10日並接受中央大學校長周景揚頒獎。

此講座表彰國際上在天文學領域有卓越表現之年輕學者，邀請具潛力的學術菁英來台與國內學界互動，並啟發年輕心靈。講座獎金由台達電子文教基金會提供，由國際甄選委員會推薦候選人，並由中央大學天文所執行邀訪活動。獲獎者將在中央大學天文所發表學術演講，與國內學者進行交流，另在台達電子文教基金會，以及台中一中進行科普演講，讓民眾與學生接觸最前沿的天文課題，並與講者互動、瞻仰其學術風範。

郭兆林博士 (Dr. Chao-Lin) 於 2003 年取得加州大學柏克萊分校天文物理學博士學位，目前在美國史丹佛大學擔任副教授。目前最為接受的理論是宇宙來自大霹靂，之後時間與空間剎那暴脹，持續膨脹，而成了現在的情形，這是什麼意思呢？有哪些證據已經觀測到，又有哪些仍待證實？郭兆林的演講，將帶領大家進一步探索。

他來台的三場演講，分別是 6 月 14 日(五)下午 2 點在中央大學天文所健雄館 1013 室，講題是 “Gravitational Wave from Big Bang”。另外兩場為科普演講，內容為大霹靂及南極研究之旅，分別是 6 月 11 日(二)下午 2 點，在台達電子台北總公司，以及 6 月 15 日(六)上午 9 點，在台中一中。第二場與第三場以中文進行，歡迎民眾參加。

小行星以台灣博物館命名 取名科博館

2019/05/20 udn 聯合新聞網

昨天是「國際博物館日」，中央大學、國立自然科學博物館在這天共同發表將新發現小行星命名為「科博館 (Kerboguan)」。科博館長孫維新說，這是真正的台灣科普之光，「科博館星」成為首顆以台灣博物館命名的小行星，昨天運行到雙子座。

「小行星」是目前各類天體中，唯一可由發現者命名的天體。觀測者發現小行星後，須先通報國際小行星中心，確認後，按發現年份與順序，配給「暫時編號」。

「科博館星」編號第二〇七六五五號，由中央大學鹿林天文台林啟生、加州理

工學院博士葉泉志共同發現，繞行太陽一圈的軌道周期三點四五年，離太陽最近是二點七億公里、最遠四點一億公里。

中央大學指出，目前台灣命名的小行星約五十顆，例如雲門、慈濟、李國鼎、陳樹菊、孫維新等；也有以地名命名，如台北、台中。

鹿林天文台台長林宏欽表示，國際天文學聯合會（I A U）訂下的國際公約規定，若要以政治人物命名小行星，須等他死後一百年再考慮，主因是政治人物褒貶不一，百年之後的歷史評價較為確定，才不會有爭議。另如以軍事、商業命名，前者擔心有挑釁意味，後者有商業利益糾葛之虞，所以都會避免；目前以科學、教育、慈善、地理、娛樂等命名為原則。

2 顆小行星 分別命名科博館及孫維新

2019/05/20 中時電子報

「科博館」星成首顆以台灣博物館命名的小行星！中央大學將鹿林天文台所發現的第 207655 號小行星及第 185364 號小行星，各命名為「科博館」

（Kerboguan）及科博館館長的名字「孫維新」（Sunweihsin），已經由國際天文學聯合會（IAU）通過，18 日「國際博物館日」在科博館發表。

科博館館長孫維新在發表會致詞時說，現在有顆小行星代表科博館在天際間，顯示科博館責任更重大，期勉同仁要更加努力。

中央大學表示，「科博館」小行星為 2007 年 7 月 25 日鹿林天文台林啟生及加州理工學院葉泉志博士發現，大小約在 1 至 3 公里之間，繞行太陽一圈 3.45 年（軌道週期），離太陽最近時（近日點）為 2.7 億公里，最遠時（遠日點）為 4.1 億公里。「孫維新」小行星為 2006 年 11 月 12 日鹿林天文台林宏欽及葉泉志博士所發現，大小約在 1 至 3 公里之間，繞行太陽一圈 3.76 年，離太陽最近時為 3.1 億公里，最遠時為 4.2 億公里。

科博館表示，小行星是目前各類天體中唯一可以由發現者進行命名，台灣過去曾有以「陳樹菊」、「雲門」及地名等命名，這是首次以台灣的博物館命名。

〈中部〉《台中》12 年前發現小行星 獲以「科博館」命名

2019/05/20 自由時報

國際天文學聯合會（IAU）通過「科博館」與「孫維新」為小行星之名。中央大學日前將鹿林天文台發現的第 207655 號小行星命名為「科博館」

（Kerboguan），將第 185364 號小行星命名為「孫維新」（Sunweihsin），昨天是天文年會、也是國際博物館日，科博館與中央大學共同舉辦小行星命名儀式，見證台灣科學教育與科普推廣歷史性的一刻。

中央大學表示，「科博館」小行星在二〇〇七年七月廿五日由鹿林天文台林啟生及加州理工學院葉泉志博士所發現，大小約在一至三公里之間，繞行太陽一圈三·四五年，離太陽最近時為二·七億公里，最遠時為四·一億公里。「孫維新」小行星為二〇〇六年十一月十二日鹿林天文台台長林宏欽及葉泉志博士發現，繞行太陽一圈三·七六年，離太陽最近時為三·一億公里，最遠時為四·二億公里。

台灣命名的行星約有 50 顆

過去行星多以人名、地名命名，除了陳樹菊、雲門，也有林書豪，台北、台中、屏東。目前台灣命名的約有五十顆，還有名為慈濟、李國鼎，數年前也以現任科博館館長孫維新命名，孫維新除主持小行星的命名揭幕儀式，也演講小行星的前世今生。

科博館指出，「科博館」目前已運行到雙子座，「孫維新」則來到巨蟹座，兩者一同在夜空中閃耀天際。

獲得永久編號 需耗時數年

小行星是目前各類天體中唯一可由發現者命名並得到世界公認的天體，但從發現到命名確認，往往耗時數年。從觀測者發現小行星，通報國際小行星中心，初步確認後按發現年份與順序配予暫時編號，經過至少四次在回歸中被觀測到、且軌道可精確測定時，才有永久編號，命名再經過國際天文學聯合會的小天體命名委員會審查通過並公告生效。

正港臺灣之光!科博館與孫維新躍上天際閃耀 科博館星成首顆以臺灣博物館命名的小行星

2019/05/20 新浪新聞

國立中央大學特將鹿林天文台所發現的第 207655 號小行星命名為「科博館」"Kerboguan"，將第 185364 號小行星命名為「孫維新」"Sunweihsin"，已經由國際天文學聯合會（IAU）通過；而 5 月 18 日天文年會的這天，也恰是 2019 年的「國際博物館日」，科博館與中央大學共同舉辦小行星命名儀式，見證臺灣科學教育與科普推廣歷史性的一刻！

科博館 18 日以國際博物館協會（ICOM）所提出的主題：「博物館做為文化樞紐：傳統的未來」當作推廣主題，辦理「自然探索」、「文化體驗」，及「天文蒐秘」、「天文觀測」等活動；下午 2 時館長孫維新在科博館多用途劇場親自上陣，接續「小行星」的話題進行一場專題演講，主題是「小行星的前世今生 - 心理上的威脅，實質上的財富？」

由於「科博館」小行星在 5 月 18 日這天剛好運行到雙子座，「孫維新」小行星則來到了巨蟹座，兩者一同在夜空中閃耀天際，別具意義！中央大學表示，「科博館」小行星為 2007 年 7 月 25 日鹿林天文台林啟生及加州理工學院葉泉志博士所發現，大小約在 1-3 公里之間；「科博館」小行星繞行太陽一圈 3.45 年（軌道週期），離太陽最近時（近日點）為 2.7 億公里、最遠時（遠日點）為 4.1 億公里。

「孫維新」小行星則為 2006 年 11 月 12 日鹿林天文台林宏欽及葉泉志所發現，大小約在 1-3 公里之間。繞行太陽一圈 3.76 年，離太陽最近時為 3.1 億公里、最遠時為 4.2 億公里。

小行星是目前各類天體中唯一可以由發現者進行命名、並得到世界公認的天體。觀測者發現小行星後，需先通報國際小行星中心（Minor Planet Center，MPC），經初步確認後，MPC 會按發現時的年份與順序配予暫時編號。當該小行星至少 4 次在回歸中被觀測到，軌道又可以精確測定時，它就會得到一個永久編號；一旦取得永久編號，發現者便擁有該小行星的命名權。

但因提出的名稱必須經過國際天文學聯合會（IAU）的小天體命名委員會（CSBN）審查通過、並公告生效，所以從發現到命名確認往往需時數年。臺灣過去曾有以「陳樹菊」、「雲門」等命名；這回首次以臺灣的博物館命名，尤其剛好在「國際博物館日」發表，別具意義！

科博館指出，該館是臺灣首座及最大的自然科學博物館。自 1986 年開館以來，每年參觀人數超過 300 萬人次，迄今已近 1 億人次。該館也是行政院於民國 66 年公布國家 12 項建設的文化建設計畫中，3 座科學博物館其中最先落成的 1 座，是臺灣主要的自然科學教育基地之一。

而孫維新則是一位以科學教育聞名的天文學者，除了教學研究工作之外，他擅長以多元創意、趣味活潑的方式推動科普教育；由於孫館長累積了許多科學教育和科普活動的經驗，在科博館的良好基礎上，引入先進的展教科技，創造精彩特展，還以舞台劇和國際學遊的方式推動科普教育，更親自策劃《漫步太陽系》等大型特展，引導社會大眾和各級學生接觸科技新知，培養科學精神。這次科博館和孫維新同時獲獎，可謂實至名歸。

小行星命名 科博館與孫維新閃耀天際

2019/05/20 Yahoo 奇摩新聞

中央大學 18 日宣布，將鹿林天文台發現的第 207655 號小行星和第 185364 號小行星分別命名為「科博館 Kerboguan」和「孫維新 Sunweihsin」。

五四運動百年 中央大學「羅家倫小行星」永恆誌念

2019/04/26 中時電子報

今年適逢五四運動一百週年，中央大學有感於羅家倫校長揭櫫的五四精神，以及對中大的重大貢獻，特將該校鹿林天文台所發現的 204711 號小行星，經國際天文學聯合會(IAU/CSBN)通過，命名為「羅家倫 (Luojiulun)」。25 日由中央大學校長周景揚頒贈給其次女羅久華女士，肯定羅家倫校長在近代歷史上的重要事蹟，也彰顯了他對中央大學的無私奉獻。

「羅家倫小行星」為中央大學鹿林天文台林宏欽及加州理工學院葉泉志博士於 2006 年 4 月 1 日所發現，大小約在 2-4 公里之間。小行星軌道位在火星與木星之間，繞行太陽一圈 4.68 年（軌道週期），離太陽最近時（近日點）為 3.3 億公里，最遠時（遠日點）為 5.1 億公里。發現時是在室女座，目前已運行到雙子座。

羅家倫先生是五四健將，在北京大學求學期間，曾與傅斯年等人合辦《新潮》雜誌，繼承並發揚新文學、新文化運動「使中國現代化」之精神；後留學美、歐，曾任清華、中央大學校長、駐印度大使、國史館館長等要職。任職中大校長近十年，建樹良多，對日抗戰期間，費盡千辛萬苦，將整個學校西遷重慶沙坪壩。因為他的高瞻遠矚、臨危不亂，以及有完整的思考，使得中央大學因此成為當時最完整也是最好的綜合大學。

中央大學在文學院大講堂舉辦「羅家倫與五四運動研討會」，發表張堂錡、羅秀美、林秋芳三篇論文，探討羅家倫的文學與思想、婦女解放觀點以及羅家倫眼中的五四師友；並安排一場座談會，邀請吳玉山、周玉山和李瑞騰主講羅家倫在整個五四運動和新文化運動過程中的關鍵角色與地位。

根據文獻來看，五四運動有三個層面的影響：首先是激起年輕學子對國家大事的關心，第二是從學生運動擴展到民眾運動，第三是他們提出的白話文學運動，把文學的力量擴及到一般社會與民眾。

此外，中央大學同時出版《羅家倫與五四運動》（史料篇）一書，由文學院李瑞騰院長和中文系莊宜文老師主編，特邀請羅家倫長女羅久芳女士為序。這是一本珍貴的書，用最具體的文獻帶讀者回到五四歷史現場，體會羅校長在時代變遷中不變的思維，以及心境的轉折。在小行星頒贈儀式中作新書發表，相得益彰。

中央大學命名羅家倫小行星 感念對五四運動貢獻

2019/04/26 中央社

今年適逢五四運動 100 週年，中央大學有感於已故前校長羅家倫對五四運動的貢獻，將鹿林天文台發現的小行星命名為「羅家倫」，今天將此殊榮頒贈給羅家倫的女兒。

204711 號小行星為中央大學鹿林天文台台長林宏欽及美國加州理工學院博士葉泉志於 2006 年 4 月 1 日發現，大小約在 2 至 4 公里之間。經國際天文學聯合會通過，中央大學將這個小行星命名「羅家倫（Luojialun）」，今天將此殊榮頒贈給羅家倫的次女羅久華，肯定羅家倫對五四運動和學校的奉獻。

中央大學表示，羅家倫是五四運動的健將，在北京大學求學期間，曾與傅斯年等人合辦「新潮」雜誌，繼承並發揚新文學、新文化運動，曾任清華大學、中央大學校長、駐印度大使、國史館館長等要職；任職中大校長近 10 年，建樹良多，使中大成為當時最完整也是最好的綜合大學。

適逢五四運動 100 週年，中央大學規劃一系列活動，包括舉辦「羅家倫與五四運動研討會」，探討羅家倫的文學與思想、婦女解放觀點等，並安排座談會，邀請專家學者分享羅家倫在五四運動和新文化運動過程中的關鍵角色與地位。

此外，中央大學出版「羅家倫與五四運動（史料篇）」一書，由中央大學文學院院長李瑞騰和中文系教師莊宜文主編，並邀請羅家倫的長女羅久芳寫序，用具體文獻帶讀者回到五四歷史現場，體會羅家倫在時代變遷中不變的思維及心境轉折。

它真的存在 人類不用再想像

2019/04/11 Yahoo 奇摩新聞

美國電影「星際效應」，劇中很多黑洞的場景是依照諾貝爾獎得主基普的指導而模擬出來，黑洞的樣子有憑有據，中研院全球首張黑洞照片，讓人類不再想像、電腦不用模擬，改變了科幻小說與電影的呈現手法。

不了解黑洞又想知道黑洞，主要是它可望為人們找到另一個自己的希望所在！黑洞是通向平行宇宙的入口、一個連接眾多宇宙的通道，讓宇宙的誕生推翻「大爆炸論」，而從平行宇宙中通過黑洞而轉移的一部分，人類有可能找到另一個世界。

中央大學天文所教授周翊表示，黑洞是愛因斯坦相對論預說出來，任何東西想辦法壓縮，壓到某個大小就變成黑洞，現在問題是如何將一個東西壓縮到那麼小的空間，比較有可能在天上的天體，因為重力場強，有足夠支撐體，例如太陽。

中研院發表的黑洞照片在天文界可能又是一個謎，因為質量非常大，一般黑洞是太陽的幾倍，中研院拍到的黑洞是天文界另一種黑洞，質量超過太陽的 65 億倍。

周翊說，黑洞與人類生活沒有相關，但算是天文的重大發現，就像幾年前發現重力波一樣，重力波不會改變生活，它在人們周遭隨時都有但偵測不到，現在用非常的技術測到了，而中研院也以很高的技術讓人看到了黑洞，拍了照片，證明它的存在與樣貌。

星際效應電影模擬盤狀大漩渦包覆黑洞的上方、下方，電影在模擬畫面時，有著「事實與虛構更離奇」的感覺，電影要給天文學界一個電腦特效呈現的參考，現在中研院給了電影界全新的視覺震撼。

黑洞引力強光線無法穿透 觀測難度高更添神秘

2019/04/11 中央社

科幻電影裡從黑洞穿越時空的情節屢見不鮮，這是因為科學界推測黑洞有彎曲時間和空間的特性，而黑洞密度大、引力強，光線無法穿透，更增添觀測的難度。

中央研究院今天晚間舉辦「事件視界望遠鏡（EHT）」計畫全球同步記者會，發表最新取得的重大成果，會中公布人類史上首張黑洞影像。

究竟何謂黑洞？中央大學天文研究所教授陳文屏解釋，當某個空間內塞進很多物質，使得密度很高且萬有引力很強，連光線都跑不出來，這就是「黑洞」。

陳文屏指出，由於光線跑不出黑洞，因此黑洞很難直接觀測到，科學界只能從繞著黑洞外圍轉的天體或物質著手，由於黑洞很小且距離遙遠，很難光靠單一的望遠鏡進行觀測，而中研院參與的跨國合作研究就集結各國力量，利用在地球不同角度的頂尖望遠鏡共同觀測黑洞外的情形。

「事件視界望遠鏡（EHT）」計畫成功拍到人類史上首次的超大質量黑洞影像，10日晚間正式公布，中研院表示，這個黑洞位於 M87 星系，距離地球 5500 萬光年，質量為太陽的 65 億倍。（中研院提供）中央社記者余曉涵傳真 108 年 4 月 10 日

在「星際效應」等科幻電影中，因為黑洞的特性，讓黑洞經常成為穿越時空的捷徑。陳文屏舉例，假如 4 個人抬起一張懸空的床單，在床單中間丟下鉛球，床單就會凹下去，原本的平面床單形狀被改變了，從不同角度去看這張床單，看到的樣子也會有所差異。

陳文屏進一步說明，原本一張白紙上從 A 點走到 B 點的距離是固定的，但在紙張扭曲後，兩點間的距離就可能變短，根據科學家推測，太空是個四度空間，黑洞可以將時間和空間彎曲，因此有可能藉由黑洞找到穿越時空的捷徑，雖然在理論上講得通，但至今仍無法證實。

關於黑洞的研究，陳文屏表示，科學家在幾十年前就猜測有黑洞存在，現在越來越多證據顯示真的有黑洞，而中研院參與的跨國研究拍攝到首張黑洞照片，更讓黑洞研究往前一大步，透過逐步認識黑洞，才有機會解答黑洞的許多特殊性。

快訊／黑洞照片首度曝光！人類歷史重大發現

2019/04/11 東森新聞

科幻電影裡從黑洞穿越時空的情節屢見不鮮，這是因為科學界推測黑洞有彎曲時間和空間的特性，而黑洞密度大、引力強，光線無法穿透，更增添觀測的難度。

中央研究院今天晚間舉辦「事件視界望遠鏡（EHT）」計畫全球同步記者會，發表最新取得的重大成果，會中公布人類史上首張黑洞影像。

究竟何謂黑洞？中央大學天文研究所教授陳文屏解釋，當某個空間內塞進很多物質，使得密度很高且萬有引力很強，連光線都跑不出來，這就是「黑洞」。

陳文屏指出，由於光線跑不出黑洞，因此黑洞很難直接觀測到，科學界只能從繞著黑洞外圍轉的天體或物質著手，由於黑洞很小且距離遙遠，很難光靠單一的望遠鏡進行觀測，而中研院參與的跨國合作研究就集結各國力量，利用在地球不同角度的頂尖望遠鏡共同觀測黑洞外的情形。

在「星際效應」等科幻電影中，因為黑洞的特性，讓黑洞經常成為穿越時空的捷徑。陳文屏舉例，假如 4 個人抬起一張懸空的床單，在床單中間丟下鉛球，床單就會凹下去，原本的平面床單形狀被改變了，從不同角度去看這張床單，看到的樣子也會有所差異。

陳文屏進一步說明，原本一張白紙上從 A 點走到 B 點的距離是固定的，但在紙張扭曲後，兩點間的距離就可能變短，根據科學家推測，太空是個四度空間，黑洞可以將時間和空間彎曲，因此有可能藉由黑洞找到穿越時空的捷徑，雖然在理論上講得通，但至今仍無法證實。

關於黑洞的研究，陳文屏表示，科學家在幾十年前就猜測有黑洞存在，現在越來越多證據顯示真的有黑洞，而中研院參與的跨國研究拍攝到首張黑洞照片，更讓黑洞研究往前一大步，透過逐步認識黑洞，才有機會解答黑洞的許多特殊性。

中研院有貢獻！人類史上首張黑洞照公布 黑洞研究跨一大步

2019/04/11 風傳媒

科幻電影裡從黑洞穿越時空的情節屢見不鮮，這是因為科學界推測黑洞有彎曲時間和空間的特性，而黑洞密度大、引力強，光線無法穿透，更增添觀測的難度。

中央研究院今天晚間舉辦「事件視界望遠鏡（EHT）」計畫全球同步記者會，發表最新取得的重大成果，會中公布人類史上首張黑洞影像。

光線無法穿透黑洞 觀測難度高

究竟何謂黑洞？中央大學天文研究所教授陳文屏解釋，當某個空間內塞進很多物質，使得密度很高且萬有引力很強，連光線都跑不出來，這就是「黑洞」。

陳文屏指出，由於光線跑不出黑洞，因此黑洞很難直接觀測到，科學界只能從繞著黑洞外圍轉的天體或物質著手，由於黑洞很小且距離遙遠，很難光靠單一的望遠鏡進行觀測，而中研院參與的跨國合作研究就集結各國力量，利用在地球不同角度的頂尖望遠鏡共同觀測黑洞外的情形。

從黑洞穿越時空 「理論上行得通」

在「星際效應」等科幻電影中，因為黑洞的特性，讓黑洞經常成為穿越時空的捷徑。陳文屏舉例，假如 4 個人抬起一張懸空的床單，在床單中間丟下鉛球，床單就會凹下去，原本的平面床單形狀被改變了，從不同角度去看這張床單，看到的樣子也會有所差異。

陳文屏進一步說明，原本一張白紙上從 A 點走到 B 點的距離是固定的，但在紙張扭曲後，兩點間的距離就可能變短，根據科學家推測，太空是個四度空間，黑洞可以將時間和空間彎曲，因此有可能藉由黑洞找到穿越時空的捷徑，雖然在理論上講得通，但至今仍無法證實。

關於黑洞的研究，陳文屏表示，科學家在幾十年前就猜測有黑洞存在，現在越來越多證據顯示真的有黑洞，而中研院參與的跨國研究拍攝到首張黑洞照片，更讓黑洞研究往前一大步，透過逐步認識黑洞，才有機會解答黑洞的許多特殊性。

小行星以合歡山命名

2019/04/09 中時電子報

南投縣政府積極爭取合歡山成為亞洲第 2 座國際認證的暗空公園，台北市天文協會常務理事劉志安在臉書「台灣星空守護聯盟」推文，表示得到香港方面的發布消息，台灣又有 3 顆小行星通過命名，其中一顆命名為「合歡山小行星」，這顆行星由鹿林天文台林啟生與葉泉志於 2007 年 8 月 6 日發現。

根據香港天文新聞，2019 年 4 月 6 日出版的《小行星通告》，新增了 9 顆中文小行星名稱，其中 3 顆與台灣的機構、地點有關，分別是編號 207655 科博館星、編號 281569 南瀛天文館小行星及編號 207661 合歡山小行星，專文說明合歡山星是由鹿林天文台林啟生、葉泉至在 2007 年 8 月 6 日所發現，並註明合歡山是台灣中部一座 3416 米的高山，最高峰位於南投縣和花蓮縣的邊界，位於太魯閣峽谷國家公園內。台灣每年的「星空饗宴」大型觀星活動都在合歡山進行。

得知此消息的劉志安表示，合歡山有小行星命名了，相信中央大學很快也會發布這項好消息，真是太棒了！接下來希望暗空公園的認證一切順利。

台灣參與「ZTF」觀測 捕捉公轉週期迄今最短的近地小行星

2019/02/11 Hinet

中央大學天文所與清華大學天文所共組的「探高 (TANGO)」團隊參與美國加州理工學院主導之「史維基瞬變設備」(Zwicky Transient Facility, 簡稱為 ZTF)，透過前所未有的廣視野觀測，可捕捉到充滿動態的夜空。近一年來，ZTF 已發現 1100 多個超新星，50 個近地小行星，其中近地小行星 2019 AQ3 的公轉週期只有 165 天，是迄今最短者。

加州理工學院之史維基瞬變設備 (ZTF) 在 2018 年 3 月開始科學觀察工作，該計畫的核心儀器是一部有 47 平方度超廣角視野的相機，讓天文觀測如虎添翼，成果相當豐碩。目前初步成果的論文，已被國際天文期刊 (Publications of the Astronomical Society of the Pacific, 簡稱 PASP) 接受刊登，其中 2 篇便由台灣天文學工作者參與。

台灣「探高」計畫的主持人中央大學天文所葉永烜院士表示，他相當贊同 ZTF 總計畫主持人 Sri Kulkarni 教授的說法，認為 ZTF 每三晚便將整個可視北天巡察

一次，能發現很多有趣、甚至前所未見的天文瞬變現象，並使時域天文學獲得極大的發展。

「探高」團隊的主要科學目標在於太陽系小物體、變星、超新星和重力波的光學對應體的追蹤觀察。中央大學天文所饒兆聰教授主持的 GROWTH 國際合作計畫便是將鹿林天文台與全球十多個天文台連結，成為一個很重要的重力波天文學觀察網。

中大天文所俞伯傑博士後研究員曾參與重力波源 GW20170817 的搜尋認證工作，他與其 ZTF 合作者非常期望鹿林天文台的相關觀測資料能在該領域有所貢獻，能夠幫助未來更多重力波源的辨識與認證工作。

中大天文所章展誥博士也說，ZTF 是前所未有的廣視野觀測，能非常有效率的收集時序天文資料，這是天文學中亟待開發的領域，對於小行星的時序學習提供了一個絕佳的機會。

中大研究團隊感謝國科會/科技部在 ZTF 構想階段便已經支持這個重要天文計畫，成為台灣與加州理工學院長期合作的一個成功例子。

台灣參與國際天文觀測 發現近地小行星公轉周期僅 165 天

2019/02/11 中時電子報

中央大學與清華大學兩校天文所共組的「探高」團隊參與美國加州理工學院主導之「史維基瞬變設備」(ZTF)，透過廣視野觀測捕捉動態夜空，近一年來，發現 1100 多個超新星，50 個近地小行星，其中近地小行星 2019AQ3 的公轉周期只有 165 天，是迄今最短者。

ZTF 在 2018 年 3 月開始進行科學觀察，核心儀器是一部有 47 平方度超廣角視野的相機，讓天文觀測如虎添翼。目前初步成果的論文，已被國際天文期刊《PASP》接受刊登，其中 2 篇便由台灣天文學工作者參與。

台灣「探高」計畫的主持人中央大學天文所教授葉永烜表示，他相當贊同 ZTF 總計畫主持人 SriKulkarni 教授的說法，認為 ZTF 每三晚便將整個可視北天巡察一次，能發現很多有趣、甚至前所未見的天文瞬變現象，並使時域天文學獲得極大的發展。

「探高」團隊的主要科學目標在於太陽系小物體、變星、超新星和重力波的光學對應體的追蹤觀察。中央大學天文所教授饒兆聰主持的 GROWTH 國際合作計

畫便是將鹿林天文台與全球十多個天文台連結，成為一個很重要的重力波天文學觀察網。

中大天文所博士後研究員俞伯傑曾參與重力波源 GW20170817 的搜尋認證工作，他與其 ZTF 合作者非常期望鹿林天文台的相關觀測資料能在該領域有所貢獻，能夠幫助未來更多重力波源的辨識與認證工作。

中大天文所博士章展誥也說，ZTF 是前所未有的廣視野觀測，能非常有效率的收集時序天文資料，這是天文學中亟待開發的領域，對於小行星的時序學習提供了一個絕佳的機會。

中大研究團隊感謝國科會／科技部在 ZTF 構想階段便已經支持這個重要天文計畫，成為台灣與加州理工學院長期合作的一個成功例子。

延禧攻略、陳樹菊小行星也入題 學測國文古今雅俗兼備

2019/01/28 自由時報

08 年大學學測國文科選擇考題中，大考中心提升整體閱讀量，並重視跨領域、多元文本，不僅表格、文章、漫畫等，包含羅大佑及李宗盛歌詞，以及陳樹菊小行星、電視劇《延禧攻略》等都入題，要考生擴展閱讀素材多元、調整閱讀習慣。

大考中心統計，國文選擇題有 13 萬 8248 人報名，到考人數 13 萬 6142 人，缺考率 1.52%。

大考中心主任劉孟奇說，今年國文出題在閱讀上比重增加，去年 5603 字，今年來到 6560 字，但經闖場內的老師與試考生測試，閱讀量增加，難度並未上升，反而呈現素養導向的反思應用，考驗考生理解力。

其中，入闈的教師分析，今年是國文選擇題單獨成卷的第 2 年，題目聚合古今、兼容雅俗，文學、藝術文本作為基礎，另有天文及社會科學探究，難度中間偏易，不少人文藝術精神底蘊在試題展露無遺。

例如時事題考中央大學天文觀測並將新發現的小行星命名為「陳樹菊」，藉此讓樹菊阿嬤的善行照亮全世界；也談論羅大佑、李宗盛的民歌故事及歌詞創作意涵；甚至更將去年火熱的中國電視劇《延禧攻略》也列入題材，呈現考生需透過閱讀，進而理解運用。

闈場試考生則分析，今年國文文言文的篇幅短小，淺顯易懂，較無死板單純記憶題，平常若廣泛閱讀，可快速理解文章，再加上充實的國學背景知識，就可輕鬆答題，整體而言很靈活。

中山女高老師李明慈認為，看出試卷把國文科當作語文工具，命題符合即將上路的 108 課綱素養導向，素養題跟傳統題型各半，雖閱讀無超長文章，平易近人，並且多元題材如科普、經濟、藝術、史地等領域兼備，但選項誘答具鑑別度，有樂評人馬世芳談羅大佑與李宗盛來呈現當代；取材多元下對學生是挑戰，高中老師也須教導學生閱讀策略，才能應對靈活多變的試題。

中央大學與國際合作高精度太空望遠鏡 將隨微衛星發射

2019/01/17 Yahoo 奇摩新聞

國立中央大學和日本北海道大學、東北大學共同合作的高精度望遠鏡（簡稱 HPT），安裝在總重量僅 60kg 的微衛星 RISESAT 上，預計臺灣時間 18 號上午 8 點 50 分隨日本宇航局 (JAXA) 的 Epsilon 火箭四號機發射，進入太陽同步軌道，執行地面及天文觀測。中央大學天文所指出，總重只 3kg、口徑 10 公分的高精度望遠鏡，繞射極限約 1.5 角秒，可不受天氣限制或大氣不穩定所造成的干擾，依需求進行觀測，在某些波段因無大氣強烈吸收，可望獲得更好的成果。

中大高密度望遠鏡 18 日隨微衛星發射

2019/01/17 中時電子報

中央大學和日本北海道大學、東北大學共同合作的高精度望遠鏡（簡稱 HPT），安裝在總重量僅 60 公斤的微衛星 RISESAT 上，預計在臺灣時間 1 月 18 日上午 8 點 50 分隨日本宇航局(JAXA)的 Epsilon 火箭四號機發射，進入太陽同步軌道，執行地面及天文觀測。

中央大學表示，微衛星是一個日益受重視的領域，因電子、電機元件技術不斷進步，使微衛星的功能不斷增加，相對於傳統的大型衛星任務，微衛星的研發製程時間短、成本低，可作為技術試驗的良好平台，或針對特定任務設計酬載，不管在科學研究、教育與商業層面都可以運用，加上近年來商業發射日漸普及，發射費用也隨著競爭而降低，相關科技、研究已是新興太空發展的重要趨勢。

中央大學指出，總重僅 3kg、口徑為 10 公分的高精度望遠鏡，繞射極限約在 1.5 角秒，可不受天氣的限制或大氣不穩定所造成的干擾，依需求進行觀測，在某些波段因無大氣強烈之吸收，可望獲得更好的成果。

台灣計畫主持人中央大學天文所葉永烜院士表示，該計畫主要受教育部五年五百億之補助，中央大學天文研究所、太空及遙測研究中心與國家太空中心等單位共同合作。科學目標初期將以氣膠觀測為主，水氣、森林、地表環境等觀測為輔。天文方面，將以觀測亮星、行星為目標，特別針對於南半球星空，對中大鹿林天文台所難以觀測的天體加以研究，希望能培養優秀人才，並有好的研究成果。

中央大學攜日合作望遠鏡 18 日隨微衛星發射太空

2019/01/17 udn 聯合新聞網

中央大學和日本北海道大學、東北大學合作的高精度望遠鏡，將安裝在微衛星上，台灣時間 18 日上午隨日本宇航局的 Epsilon 火箭 4 號機發射，進入太陽同步軌道，執行地面及天文觀測。

中央大學天文研究所新聞資料指出，因電子、電機元件技術不斷進步，使微衛星的功能不斷增加，相對於傳統大型衛星，微衛星研發製程時間短、成本低，可作為技術試驗的良好平台，也使得微衛星相關科技和研究日益受到重視。

中央大學和日本北海道大學、東北大學共同合作的高精度望遠鏡，總重僅 3 公斤、口徑 10 公分，繞射極限約在 1.5 角秒，可不受天氣限制或大氣不穩定所造成的干擾，依需求進行觀測，在某些波段因無大氣強烈的吸收，可望獲得更好的觀測成果。

台灣計畫主持人、中央大學天文研究所教授葉永烜表示，此計畫由中大天文所、太空及遙測研究中心與國家太空中心等單位共同合作，初期目標將以氣膠觀測為主，水氣、森林、地表環境等觀測為輔，天文方面以觀測亮星、行星為目標，特別針對中大鹿林天文台所難以觀測的天體加以研究，希望能培養優秀人才，並有好的研究成果。

感念前校長貢獻 中央大學把小行星命名「劉兆漢」

2019/01/04 udn 聯合新聞網

中央大學感念前校長劉兆漢對學校和永續發展的貢獻，將鹿林天文台發現的小行星命名為「劉兆漢 (Liuchaohan)」，已經國際天文學聯合會審查通過。

中央大學將鹿林天文台發現的編號第 207603 小行星命名為「劉兆漢 (Liuchaohan)」，並選在劉兆漢 80 大壽的今天舉行小行星頒贈儀式，同時邀請前行政院院長劉兆玄（劉兆漢的胞弟）、前中央大學校長蔣偉寧、李羅權等人與會。

中央大學校長周景揚表示，劉兆漢在中央大學掌舵 12 年，帶領中大從教學型大學轉型為研究型大學，學生人數足足成長 1 倍多，他也是國內推動「永續發展」的先驅，20 多年前就帶領中大，集合 6 個學院、上百位教師，向教育部提出永續發展的跨領域整合計畫，成為台灣創舉，退休後仍以中大學術基金會董事長身分協助學校發展。

劉兆漢指出，自 1981 年與中大結緣以來，「中大給了我太多東西」，讓他學習用宏觀思維去做研究工作，尤其領悟到「跨領域研究」的重要性，許多人類待解決的問題，其實都需要跨領域合作，未來他希望繼續幫助中大將特色領域推到世界前端。

感念前校長貢獻 中央大學把小行星命名劉兆漢

2019/01/04 Yahoo 奇摩新聞

中央大學感念前校長劉兆漢對學校和永續發展的貢獻，將鹿林天文台發現的小行星命名為「劉兆漢 (Liuchaohan)」，已經國際天文學聯合會審查通過。

中央大學將鹿林天文台發現的編號第 207603 小行星命名為「劉兆漢 (Liuchaohan)」，並選在劉兆漢 80 大壽的今天舉行小行星頒贈儀式，同時邀請前行政院院長劉兆玄（劉兆漢的胞弟）、前中央大學校長蔣偉寧、李羅權等人與會。

中央大學校長周景揚表示，劉兆漢在中央大學掌舵 12 年，帶領中大從教學型大學轉型為研究型大學，學生人數足足成長 1 倍多，他也是國內推動「永續發展」的先驅，20 多年前就帶領中大，集合 6 個學院、上百位教師，向教育部提出永續發展的跨領域整合計畫，成為台灣創舉，退休後仍以中大學術基金會董事長身分協助學校發展。

劉兆漢指出，自 1981 年與中大結緣以來，「中大給了我太多東西」，讓他學習用宏觀思維去做研究工作，尤其領悟到「跨領域研究」的重要性，許多人類待解決的問題，其實都需要跨領域合作，未來他希望繼續幫助中大將特色領域推到世界前端。

「劉兆漢小行星」光照 永續在宇宙運行

2019/01/04 蕃薯藤

中央大學為感念劉兆漢校長對該校以及永續發展的卓越貢獻，特將天文所鹿林天文台所發現的編號第 207603 小行星命名為「劉兆漢 (Liuchaohan)」，並經國際天文學聯合會 (IAU/CSBN) 通過。特選在其八十大壽的今 (三) 日，舉辦溫馨的頒贈儀式。

中央大學校長周景揚說，劉兆漢校長在中央大學掌舵十二年，帶領中大從教學型大學轉型為研究型大學，在他的任內，學生人數足足成長了一倍多。他同時是國內推動「永續發展」的先驅，早在廿多年前，中大便開風氣之先，集合六個學院一百多位老師，向教育部提出永續發展之跨領域整合計畫，成為台灣創舉！

為提振士氣，找出中大特色，他治校期間喊出「中大第一」的信念，樹立中大許多拔尖的地位。即使退休後，仍以中大學術基金會董事長身份協助母校發展，每一次的重要活動，重要會議無役不與，以實際行動來支持母校發展，成為中大發展最堅實的後盾！

劉兆漢院士感性地說，從 1981 年與中大結緣以來，「中大給了我太多東西」，學習到用宏觀思維去做研究工作，尤其領悟到「跨領域研究」的重要性，人類待解決的問題，其實都需要跨領域合作。也很開心在結交許多好友，大家一心一意都希望中大更好，將中大的特色領域推到世界前沿，看到更多的中大第一。

劉兆漢小行星，2006 年 8 月 27 日由鹿林天文台站長林宏欽和葉泉志共同發現，位在火星與木星之間，大小約 2-5 公里，距離我們大約 4.2 億公里，繞太陽一圈大約 5.38 年 (軌道週期)，發現時在鯨魚座，目前已運行到雙子座方向。

小行星的頒贈儀式，邀請了劉兆漢的胞弟—前行政院院長劉兆玄和東元電機副會長劉兆凱，以及前中大校長蔣偉寧和李羅權院士，還有葉永烜院士等人出席，加上一些以往的舊識，眾人共同創作一幅「生命樹」，齊祝他生日快樂，場面熱鬧而溫馨。